

**Faradaic electrode materials  
for next-generation  
electrochemical water desalination**

Dissertation  
zur Erlangung des Grades  
des Doktors der Naturwissenschaften  
der Naturwissenschaftlich-Technischen Fakultät  
der Universität des Saarlandes

**von**

**Pattarachai Srimuk**

Saarbrücken

2019

**Tag des Kolloquims:** 21.08.2019

**Dekan:** Prof. Dr Guido Kickelbick

**Berichterstatter:** Prof. Dr. Volker Presser  
Priv-Doz. Dr.-Ing. Guido Falk  
Assist. Prof. Xiao Su

**Akad. Mitglied:** Dr.-Ing. Frank Aubertin

**Vorsitz:** Prof. Dr. Guido Kickelbick

## **Abstract**

An ever-growing global population leads to higher water consumption and demand for advanced remediation technologies. Thus, water stress intensifies in many countries around the world. Most global water remediation is accomplished by established techniques, such as reverse osmosis and thermal desalination. To lower the energy consumption per processed water volume, engineers and scientists investigate novel techniques like capacitive deionization technology (CDI). CDI based on carbon electrodes promises energy-efficient desalination by ion electrosorption but is limited to the remediation of brackish water, that is, very low salt concentration media. My doctoral thesis explores next-generation electrodes for electrochemical water desalination based on Faradaic materials. Unlike carbon, these materials accomplish ion removal by reversible electrochemical processes, such as ion insertion of crystalline structures or redox-reactions of dissolved ions. Faradaic materials not only provide a large potential for enhanced desalination capacity but also enable the remediation of seawater, that is, aqueous media with high molar strength. These features can be accomplished while maintaining a low level of energy consumption to enable energy-efficient water desalination for a more sustainable future.

## **Zusammenfassung**

Das weltweite Bevölkerungswachstum führt zu einem höheren Wasserverbrauch und erhöhtem Bedarf an effektiven Aufbereitungstechnologien. Entsprechend verschärfen sich die Probleme in Bezug auf Zugang und Verfügbarkeit von Trinkwasser in vielen Ländern der Welt. Wissenschaftler\*Innen erforschen daher Wasserentsalzungstechnologien, die bessere Energieeffizienz bieten können als die derzeit gängigen Methoden wie Umkehrosmose oder thermische Verfahren. Eine besonders vielversprechende, energie-effiziente Technologie zur Entsalzung ist die kapazitive Deionisierung (CDI). CDI basiert auf Ionenelektrosorption, kann aber nur für Brackwasser eine hohe Energieeffizienz und Entsalzungsleistung darstellen. Die vorliegende Dissertationsschrift erforscht daher neue Faraday'sche Elektrodenmaterialien um Wasser effizient und effektiv zu entsalzen. Hierzu eignen sich insbesondere Kristallstrukturen, die Ionen durch Insertation aufnehmen können, oder redox-aktive Ionen, welche im wässrigen Medium in Lösung sich befinden. Solche Materialien bieten nicht nur eine hohe Entsalzungskapazität sondern sind auch nicht mehr auf Brackwasser limitiert: sie erlauben sogar die energie-effiziente Entsalzung von Meerwasser und haben damit das Potential, eine vielversprechende Technologie für eine nachhaltigere Zukunft zu sein.

## **Acknowledgments**

I kindly thank my supervisor Prof. Volker Presser who gave me the opportunity for working on a very interesting topics in the Energy Materials Group at the INM - Leibniz Institute for New Materials. Thanks to his guidance and patience, I was fortunate to accomplish many achievements, including publications and great presentation at international conferences or summer school.

I thank Dr. Guido Falk (Saarland University) to be the second reviewer of my Ph.D. thesis. I am very grateful for Prof. Eduard Arzt, CEO of the INM, for his continuing support. Further, I thank Prof. Frank Mücklich and Dr. Flavio Andrés Soldera (both at Saarland University) for their support in the DocMase program. Also, I kindly acknowledge financial support via the German Academic Exchange Organization (DAAD) via award number 91579066. This fellowship was part of the Graduate School Scholarship Program (GSSP), awarded to Prof. Frank Mücklich.

During my time of almost four years working at the INM, it has been my pleasure and honor to learn and work with wonderful and incredible people. My special thanks to Dr. Mesut Aslan, my great mentor in the laboratory. I am also grateful to my kind INM colleges and good friends: Dr. Juhan Lee, Dr. Soumyadip Choudhury, Dr. Choonsoo Kim, Dr. Marco Zeiger, Dr. Simon Fleischmann, Dr. Aura Tolosa, Dr. Nicolas Jäckel, Dr. Benjamin Krüner, Dr. Rafael Linzmeyer Zornitta, Öznil Budak, Yuan Zhang, Anna Schreiber, Hwirim Shim, Sylvain Badie, and Robert Drumm. The work would have been difficult without great contributions from master students and intern students (in alphabetical order): Sidonie Carpier, Jaehoon Choi, Lucie Ries, Maike Ulbricht, and Rose Zwingelstein.

I am also grateful for the opportunity to network and collaborate with great scientists across the world. Particularly, I thank Prof. Matthew E. Suss, one of the pioneers in CDI field, for the great discussion. Many thanks also to Dr. Joseph Halim and Prof. Johanna Rosen at Linköping University for providing Mo-MXene to explore novel desalination electrodes materials. I also kindly thank Dr. Christian Prehal for useful discussions and helpful comments for my work!

Finally, my life would be impossible if it were not for the unconditional support from my big "Srimuk" family. Huge thanks to my great aunt, uncle, and granddad! Finally, I dedicate my thesis to my grandma, who passed away at the beginning of my Ph.D. She has always been my motivation and positive energy.

## List of content

1.	Motivation: water resources and lack thereof .....	6
2.	State-of-the-art .....	7
2.1.	Water desalination .....	7
2.2.	Electrochemical desalination via ion electrosorption .....	10
2.2.1.	<i>Concept and history</i> .....	10
2.2.2.	<i>Ion removal mechanism</i> .....	13
2.2.3.	<i>Electrochemical (parasitic) side-reactions</i> .....	21
2.2.4.	<i>Correlation between electrode pore structure and desalination performance</i> .....	24
2.2.5.	<i>Carbon electrode materials</i> .....	25
2.2.5.1.	Activated carbon .....	26
2.2.5.2.	Templated carbons .....	27
2.2.5.3.	Carbide-derived carbons .....	29
2.2.5.4.	Carbon aerogels .....	30
2.2.5.5.	Graphene .....	30
2.2.5.6.	Carbon nanotubes .....	31
2.2.5.7.	Summary .....	32
2.3.	Electrochemical desalination via ion insertion .....	33
2.3.1.	<i>A brief history of insertion materials for electrochemical desalination</i> .....	33
2.3.2.	<i>Ion insertion mechanism and basic concepts</i> .....	36
2.3.2.1.	Thermodynamics of Faradaic materials .....	38
2.3.2.2.	Correlation between charge capacity and ion removal .....	41
2.3.2.3.	Cell charge balancing .....	43
2.3.3.	<i>Ion-insertion electrode materials</i> .....	44
2.3.3.1.	1-D insertion materials .....	45
2.3.3.1.1.	<i>Sodium manganese oxide</i> .....	45
2.3.3.1.2.	<i>Tunnel-structure manganese oxide</i> .....	46
2.3.3.2.	2-D insertion materials .....	47
2.3.3.2.1.	<i>Layered metal carbides/nitrides (MXene)</i> .....	47
2.3.3.2.2.	<i>Transition metal dichalcogenides (TMDs)</i> .....	49
2.3.3.2.3.	<i>Layered transition metal oxides</i> .....	50
2.3.3.3.	3-D insertion materials .....	51
2.3.3.3.1.	<i>Prussian Blue and Prussian Blue analogs</i> .....	51
2.3.3.3.2.	<i>Polyanionic phosphates</i> .....	52
2.3.3.3.3.	<i>Summary</i> .....	53
2.4.	Electrochemical desalination via reconstitution/conversion reactions .....	53
2.4.1.	<i>Concept and mechanism</i> .....	53
2.4.3.	<i>A brief history of conversion materials for water desalination</i> .....	55
2.5.	Electrochemical desalination via redox electrolytes .....	56
3.	Outline and scope of this thesis .....	58
4.	Peer-reviewed research papers .....	62
4.1.	Enhanced performance stability of carbon/titania hybrid electrodes during capacitive deionization of oxygen saturated saline water .....	62
4.2.	High performance stability of titania decorated carbon for desalination with capacitive deionization in oxygenated water .....	62

4.3.	MXene as a novel intercalation-type pseudocapacitive cathode and anode for capacitive deionization	62
4.4.	Two-dimensional molybdenum carbide (MXene) with divacancy ordering for brackish and seawater desalination via cation and anion intercalation .....	62
4.5.	Faradaic deionization of brackish and sea water via pseudocapacitive cation and anion intercalation into few-layered molybdenum disulfide.....	62
4.6.	Titanium disulfide: a promising low-dimensional electrode material for sodium Ion Intercalation for seawater desalination .....	62
4.7.	Potential-dependent, switchable ion selectivity in aqueous media using titanium disulfide	62
4.8.	Sodium ion removal by hydrated vanadyl phosphate for electrochemical water desalination	62
4.9.	Low voltage operation of a silver/silver chloride battery with high desalination capacity in seawater	62
4.10.	Confined redox reactions of Iodide in carbon nanopores for fast and energy-efficient desalination of brackish water and seawater .....	62
4.1	Enhanced performance stability of carbon/titania hybrid electrodes during capacitive deionization of oxygen saturated saline water .....	63
4.2	High performance stability of titania decorated carbon for desalination with capacitive deionization in oxygenated water.....	88
4.3	MXene as a novel intercalation-type pseudocapacitive cathode and anode for capacitive deionization	100
4.4	Two-dimensional molybdenum carbide (MXene) with divacancy ordering for brackish and seawater desalination via cation and anion intercalation .....	108
4.5	Faradaic deionization of brackish and sea water via pseudocapacitive cation and anion intercalation into few-layered molybdenum disulfide.....	120
4.6	Titanium disulfide: a promising low-dimensional electrode material for sodium ion intercalation for seawater desalination .....	138
4.7	Potential-dependent, switchable ion selectivity in aqueous media using titanium disulfide	155
4.8	Sodium ion removal by hydrated vanadyl phosphate for electrochemical water desalination	171
4.9	Low voltage operation of a silver/silver chloride battery with high desalination capacity in seawater	187
4.10	Confined redox reactions of iodide in carbon nanopores for fast and energy-efficient desalination of brackish water and seawater .....	204
5.	Summary, conclusions, and outlook.....	231
6.	References .....	235

## 1. Motivation: water resources and lack thereof

Water is one of the most fundamental resources for humankind besides food, medicine, and energy. It does not only sustain the livelihood but also supports the future growth of the economy and the development of public health. However, the global demand for water has constantly increased as the global population has increased. According to the United Nations World Water Development Report 2018, an estimated 3.6 billion people across the world live in a potentially water-shortage area at least one month per year.[1] This issue will intensify in the future due to climate change and ever-growing water consumption.[2] In 2007, the European Environment Agency reported that the annual precipitation of water in northern Europe has increased since 1960, resulting in a 10-40% wetter climate, while southern Europe has become 20% drier. Many countries across the globe must adapt to lower availability of surface water. For example, the United States of America, Mexico, Iran, China, and India, show a groundwater depletion rate in excess of 30 km<sup>3</sup>/year.[1] In addition to the negative effects of climate change on water access, the higher water consumption of our world population causes even greater water stress. Globally, most water is being used for agriculture (50-60% of total water withdraw), 5-10% for industry, and 10-20% for urban purposes (e.g., drinking water, sanitation).[3] Also, many of those activities lead to polluted water that may contaminate underground or surface water.

With less water available and more water being polluted, there is an ever-increasing demand for energy efficient water remediation. To this end, various kinds of water technology have been intensively developed, for example, reverse osmosis, multi-stage flash distillation, multiple effect evaporation, and electrochemical desalination (i.e., electrodialysis, capacitive deionization, and Faradaic deionization).

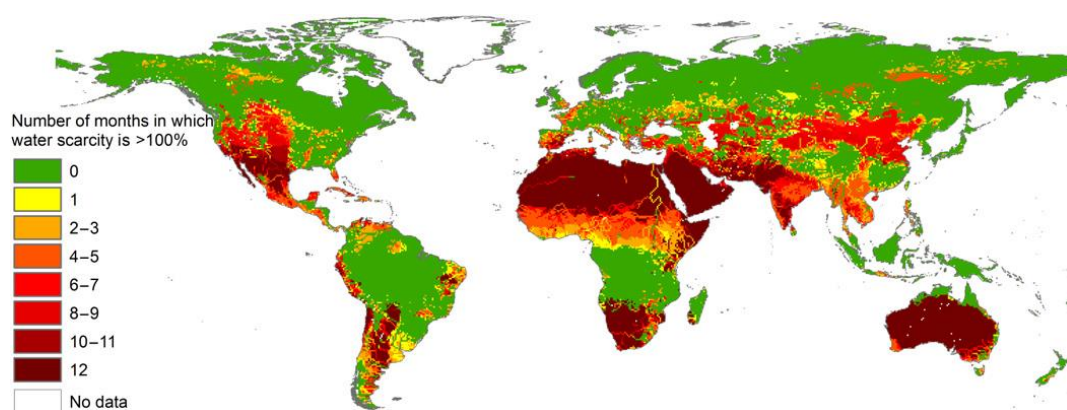


**Figure 1.** The blue water scarcity in months per year from 1996 to 2005 .From Ref. [4]. Reprinted with permission from AAAS.

## 2. State-of-the-art

### 2.1. Water desalination

Water desalination removes dissolved ions from saline media to obtain potable water or otherwise useable water. Depending on the source of water, the salt concentration differs; for example, sea water has total dissolved solids (TDS) of 30-45 g/L and brackish water of 1-10 g/L. According to the World Health Organization, the drinkable water should contain less than 250 mg/L of salt.[5] Hence, about 99% of all salt ions must be removed from seawater to render it potable. This value decreases to 66-97% for the desalination of brackish water, that is found in river basins or some other bodies of water (e.g., Baltic Sea). The feed water for desalination highly depends on the desalination method, pretreatment steps (i.e., micro-filtration, and pH alteration), and product recovery (the ratio between produced-freshwater and feed water). The following briefly compares three basic desalination approaches: thermal-based desalination, membrane-based desalination, and electrochemical desalination.

**Thermal desalination**, also known as distillation, is likely the oldest desalination process in human history. The process of using a heat source to separate water from salt toward enthalpy of vaporization or latent heat. In the 18<sup>th</sup> century, engineers began to develop advanced distillation, and in the 1950s, seawater distillation plants were established.[5] The main principle of this technology is that the input energy must be large enough to overcome the latent heat of saline water, which is around 2.400 MJ/kg (677 kWh/m<sup>3</sup>).[6] The best-known thermal based desalination technique is multistage flash desalination (MSF) and multiple effect evaporation desalination (MED). As seen from **Figure 2Ai**, MSF consists of a series of stages where each flash evaporation of seawater takes place at about 110 °C. The vapor from the first stage is then demisted to remove brine droplets and condensed to fresh water. The connection between the first stage and the second stage is the heat exchanger that transfers heat from the first stage to the second stage. The temperature and the pressure of the second stage should be lower than the first stage; otherwise, flash evaporation will not occur. MSF usually employs 7-9 stages depending on the system design and target application.[7] The power consumption is about 18 kWh/m<sup>3</sup> at a fresh water capacity of 50,000-75,000 m<sup>3</sup>/day.[8]

The principle of MED is that the saline water (feed) is directly evaporated in the first stage at the temperature of around 60-100 °C (**Figure 2Aii**)[9]. After that, the as-produced vapor from the first chamber flows to a condenser. At this step, the latent heat of condensation is transferred to the feed saline water through the heat exchanger. MED and MSF differ by the evaporation method and heat transfer process. Instead of flash evaporation (convective heating), MED relies on the heat transfer at the heat exchanger of each effect, and thus the heat transfer is highly important for MED technique. The calculated water production using six effects in series is 20,000 m<sup>3</sup>/day whereas the power consumption of MED is of 2-4.5 kWh/m<sup>3</sup>. [7, 8] Yet, MSF consumes much less energy than MED, but MSF has much larger freshwater capacity than MED.

**Reverse osmosis** (RO) as a membrane-based desalination technology was developed in the 1950s. In 1957, Reid et al. used a cellulose acetate membrane having the NaCl (100 mM) rejection of 96% for an applied pressure of about 7 MPa to the membrane.[10] Although the salt rejection was high, the water permeability was low so that the membrane requires very high pressure to let water pass through. Also, the cellulose acetate membrane can only be used within a pH value range of 4-6 due to the hydrolysis reaction in both alkaline and acidic media. Later, the research brought forth a membrane that consists of a thin surface layer with a porous structure and a higher chlorine resistance.[11-13] In the early 1980s, John Cadotte developed the interfacial polyamide chemistry (**Figure 2B**) on the thin film polysulfone (tens of nanometer) for RO membrane application.[14] This approach involves the interfacial polymerization between difunctional amide in the water phase and trifunctional acid chloride in the organic phase. The membrane is then assembled on top of the porous polysulfone and porous polyethylene terephthalate as the reinforcement layer. In contrast to other filtration membranes operating by size discrimination, RO membranes achieve the water/salt separation not only by the sieving but also by capitalizing on the different mass transport rates of salt and water. Prior to the implementation of the RO process, filtration like microfiltration (MF) or ultrafiltration (UF) were required[15] because untreated seawater typically contains colloidal particles, biological species, mud, and sand which cause the degradation and fouling of RO membrane.

The basic principle of RO is the filtration of seawater through the pores of the membrane by force imposed with an external pump (**Figure 2B**). The water flux depends on the porosity, the hydrophilicity, and the thickness of the membrane and correlates the osmotic pressure, hydraulic pressure, and membrane performance via **Equation 1**. [5, 16]

$$N_{H_2O} = A(\Delta p - \Delta\pi) \quad \text{Equation 1}$$

where  $N_{H_2O}$  is the water flux through the membrane,  $A$  is the permeability of the membrane,  $\Delta p$  is the net hydraulic pressure, and  $\Delta\pi$  is the net osmotic pressure. The term  $A$  in **Equation 1** represents the water production performance of the membrane. When the  $A$  value is high, the water productivity is also high. The osmotic pressure for the remediation of seawater is in the range between 6 MPa and 80 MPa; thus, the net hydraulic pressure should be at least greater than 6 MPa. In order to calculate the water permeability of the membrane, **Equation 2** is employed. [17]

$$N_{H_2O} = \frac{\Delta V}{S\Delta t} \quad \text{Equation 2}$$

where  $\Delta V$  is the total volume of permeate solution,  $S$  is the effective area of the membrane, and  $\Delta t$  is the duration of the permeation process.

Another important parameter for evaluating the performance of the RO membrane is the mass flux of salt that passes across the membrane (**Equation 3**). [5, 16]

$$N_{salt} = B(c_{feed} - c_{permeate}) \quad \text{Equation 3}$$

where  $N_{salt}$  is the salt flux across the membrane,  $B$  is a salt permeability which is a function of the salt diffusivity through the membrane, salt separation coefficient, and membrane thickness.  $c_{feed}$  is the salt concentration of the feed water, and  $c_{permeate}$  is the salt concentration of treated water. The  $B$  value represents the ability of salt rejection ( $R_s$ ) that can be simply calculated using **Equation 4**.

$$R_s = 1 - \left( \frac{c_{permeate}}{c_{feed}} \right) \cdot 100\% \quad \text{Equation 4}$$

RO desalination can reach a salt rejection of 98-99.8% with the water production rate up to 129,000 m<sup>3</sup>/day. [5] The energy consumption of RO stands in between 2 kWh/m<sup>3</sup> and 5 kWh/m<sup>3</sup> [15] which is about three times lower than for MED. Despite the large-volume water production, relatively low energy consumption, and large salt rejection, polyamide-based RO membranes suffer from low chlorine resistance: the water permeability and salt rejection strongly decay when the membrane is exposed to chlorine. [18]

Seeking alternative materials for RO membranes, scientists have explored nanoporous graphene[18], carbon nanotubes[19], or layered two-dimension materials[20]. For example, molecular dynamics simulations have shown for nanoporous graphene a 100- to 1,000-times greater water permeability than recent RO membranes. Thereby, nanoporous graphene as the RO membrane may significantly reduce the overall energy consumption. The challenge remains to scale-up such a process as the membrane requires a large defect-free area before the etching.

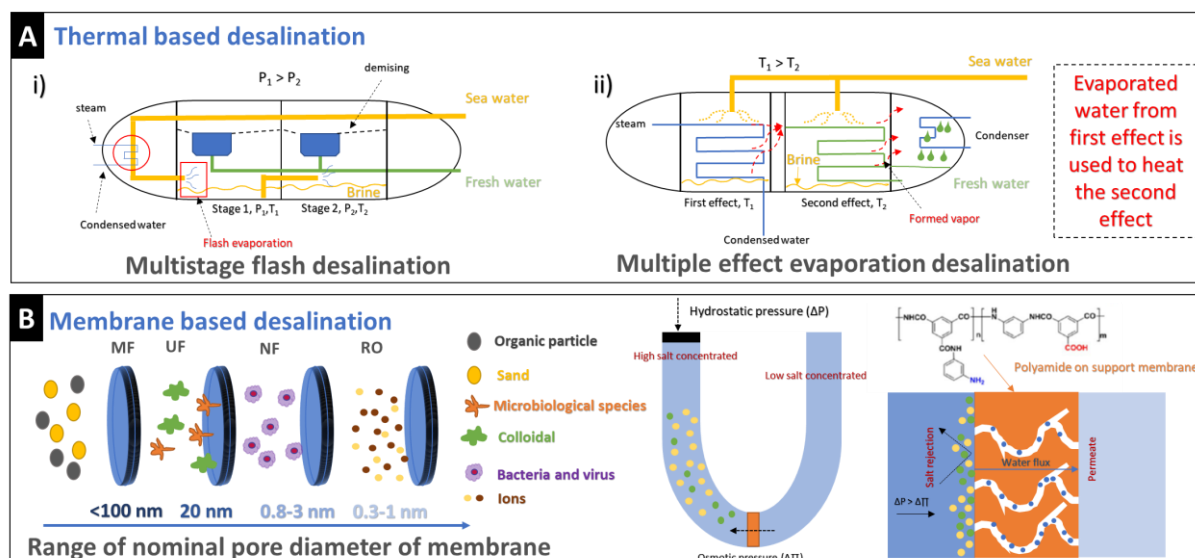


**Figure 2.** A) Schematic illustration of multistage flash desalination (MFS), and multiple effect evaporation desalination (MED),[7, 8] B) schematic of all range of membranes and reverse osmosis[15, 16].

## 2.2. Electrochemical desalination via ion electrosorption

### 2.2.1. Concept and history

Following their conference contribution of 1959, Blair and Murphy established for the first time the electrochemical deionization of saline water in 1960. They used tannin acid functionalized-graphite as the working electrode and a silver/silver chloride as the counter electrode to remove sodium and chloride, respectively (**Figure 3A**).[22] Not knowing about the importance of ion electrosorption for the charge storage and desalination mechanism, Blair and Murphy assumed ion-response as the indication for an electrode that shows the electrode/ion interaction. It was believed that most of the carbon behaves only cation-responsive (sodium ion removal) due to the negatively charged functional group like quinone-type, and tannic acid (**Figure 3B**).

For chloride removal, Blair and Murphy used graphite modified by tetramethyl phenylenediamine to capitalize the desalination on positively charged functional groups or immobilized dissolved chloride at an Ag/AgCl electrode via a conversion reaction.[22, 23] By this way, the first works on what later became capacitive deionization employed (at least in parts) Faradaic reactions.[22-25]

In 1971, Johnson and Newman introduced the concept of ion electrosorption as the working principle governing electrochemical desalination with carbon electrodes. Their cell design was the same as the work by Blair and Murphy: a stack of the activated carbon electrode was connected to a power source while the brackish water was flown axially along the electrode (**Figure 3C**).[26] The proposed ion removal mechanism was that ions are tightly attracted to the surface of the charged electrode following the formation of an electrical double-layer in agreement with the Gouy-Chapman-Stern model (**Figure 3D**).[27] The amount of ion depletion in the solution was correlated with the interfacial area of carbon and the applied potential. However, later works have shown the limited applicability of the Gouy-Chapman-Stern model for ion electrosorption in narrow micropores (e.g., pores below 2 nm; **Figure 3D**).[28]

In 2011, the modified Donnan model was proposed to more accurately describe electrical double-layer formation in micropores.[28, 29] This model differs from the original Donnan model in two aspects.[29, 30] First, the modified Donnan model includes a charge-free Stern layer between micropore and macropore. Second, the Coulombic interaction between an ion and the conductive electrode, which is the driving force for ion transport from macropore to micropore. It is responsible for the increased ion concentration in the micropore even at an applied voltage of 0 V. Such model explained the structure of the electrical double-layer very well for ions confined within micropores. During electro-adsorption, a strong overlapping double-layer potential profile in the pores results in approximately constant electrostatic potential in the middle of the pore (**Figure 3D**). In the modified Donnan model, micropores are not defined as the recommendation from the International Union of Pure and Applied Chemistry (IUPAC); the IUPAC definition classifies pores per their size with micropores being smaller than 2 nm, mesopores are between 2 nm and 50 nm, and macropores are any pores exceeding 50 nm. In the modified Donnan model, micropores are treated as intraparticle pores while macropores are treated as interparticle pores; while it is reasonable to assume larger pores between particles than within them, the modified Donnan model definition fails to clarify actual pore sizes. Within this thesis, we adhere to the IUPAC definition of pore types.

At equilibrium, the ion concentration in the micropores is related to the bulk concentration via **Equation 5**:

$$c_{mi,j} = c_{j,bulk} \exp(-z_j \cdot \Delta\varphi_D + \mu_{att}) \quad \text{Equation 5}$$

where  $c_{mi,j}$  is the concentration of an individual ion in the micropore,  $c_{j,bulk}$  is the bulk ion concentration,  $z_j$  is the valence of ion (e.g.,  $\text{Na}^+$  gives  $z_{\text{Na}^+} = +1$ ),  $\Delta\varphi_D$  is the dimensionless Donnan potential difference between intraparticle and interparticle pore and,  $\mu_{att}$  is the dimensionless parameter indicating the ratio between energy density and total micropore ion concentration. As the ions populate the micropores, the ionic charge density is derived by **Equation 6**.

$$\delta_{mi} = \sum_j z_j \cdot c_{j,mi} \quad \text{Equation 6}$$

where  $\delta_{mi}$  is the ionic charge in micropores. The ionic charge should be neutralized by the electronic charge at the pore surface (**Equation 7**):

$$\delta_{mi} = -\delta_{electronic} \quad \text{Equation 7}$$

The ionic charge is the relation between stern potential, Stern capacitance, and thermal voltage (**Equation 8**):

$$\delta_{mi} = -C_s \cdot \varphi_s \cdot \frac{V_T}{F} \quad \text{Equation 8}$$

where  $C_s$  is the stern capacitance,  $\varphi_s$  is the Stern potential,  $V_T$  is the thermal potential, and  $F$  is the Faraday constant. Now, the charge balance between electronic and ionic charge at equilibrium is achieved by solving **Equation 5** and **Equation 6** to give **Equation 9**.

$$\delta_{mi} = c_{cation,mi} - c_{anion,mi} = -2c_{bulk} \cdot \exp(\mu_{att}) \cdot \sinh(\Delta\varphi_D) \quad \text{Equation 9}$$

The total ion density in the micropore is given by **Equation 10**:

$$c_{ion,mi} = c_{cation,mi} + c_{anion,mi} = 2c_{salt,bulk} \cdot \exp(\mu_{att}) \cdot \cosh(\varphi_D) \quad \text{Equation 10}$$

For the Stern potential and Donnan potential, the cell voltage is given by **Equation 11**:

$$\frac{V}{V_T} = 2|\Delta\varphi_D + \Delta\varphi_S| \quad \text{Equation 11}$$

The in-pore ion concentration (ion removal) and charges depend on the applied voltage for a certain bulk salt concentration. The influence of the applied voltage and the bulk salt concentration on the desalination performance will be subject of the next section.

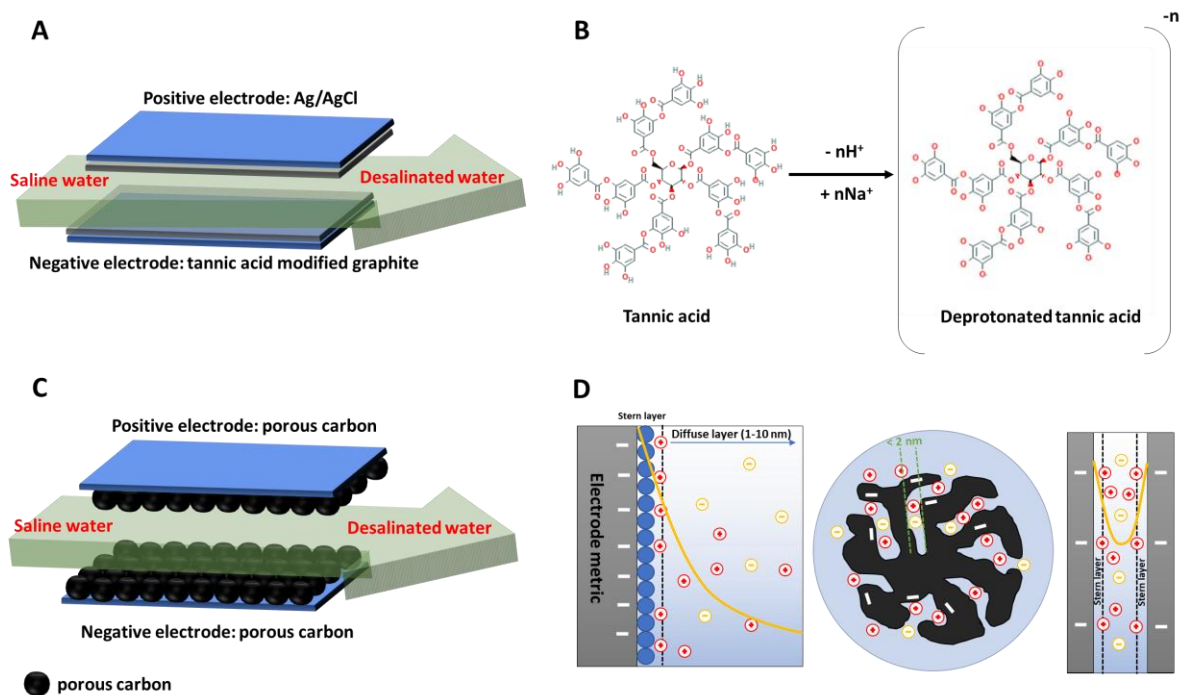


**Figure 3.** A) Scheme of the electrochemical desalination cell using modified graphite and Ag/AgCl as electrodes, B) molecular structure of graphite modifier and redox mechanism, C) capacitive deionization cell demonstration using activated porous carbon electrode, and D) concept of activated porous particle during cation adsorption and structure of electrical double-layer according to the Gouy-Chapman-Stern theory at the flat surface and modified Donnan model describing ion storage in micropores.

### 2.2.2. Ion removal mechanism

While ion electrosorption always involves charge storage (or recovery), it does not always have to be a permselective process. We cannot assume, for example, that each positive charge will be used fully just for the adsorption of anions. A suitable tool to quantify the degree of permselectivity is the charge efficiency ( $\eta$ ) which represents the accumulated charge that contributes to the ion adsorption (**Equation 12**).

$$\eta = \frac{F \cdot z \cdot N_{cation}}{C^-} \cdot 100\% \quad \text{Equation 12}$$

where  $F$  is the Faraday constant (96,485 C/mol),  $N_{cation}$  is the removed cations according to the mole of negative charge (mol),  $z$  is the charge state of cation ion (e.g.,  $Na^+$  give  $z = 1$ ), and  $C^-$  is accumulated negatively charge at the electrode (C).

The parameter of charge efficiency is the product of different ways (permselective and non-permselective) by which ion electrosorption can be accomplished. Ideally, the perfect capacitive deionization process yields a charge efficiency of 100% which indicates that all invested charge is used to adsorb counter ions, those with an ionic charge opposite to the electric charge of the electrode. In the initial (uncharged) state, there is usually an equal number of anions and cations in micropores of the electrode. This means, we can also accomplish charge storage by ejecting co-ions, that is, ions with the same charge as the electrode. As a third way, instead of just adsorbing counter-ions or just ejecting co-ions, we may also have a concurrence of both processes. This scenario is known as ion-swapping, where one desorbing co-ion is accompanied by an adsorbing counter-ion to compensate the electric charges.

The 1:1 exchange of cations and anions (co-ions vs. counter-ions; ion swapping) is for many electrolytes the predominant mechanism at high molar strength (usually 1 M) in a supercapacitor.[31-33] Since the same amount of co-ions is desorbing as the amount of adsorbed counter-ions, the net ion concentration between the electrodes remains unchanged, and no desalination can be accomplished (**Figure 4**). A negative value of charge efficiency will be effectively consumed if the charge storage process is accomplished only by co-ion expulsion (**Figure 4**). The best scenario for capacitive deionization would be the ideal counter-ion adsorption (**Figure 4**). Thereby, we would see a decreasing salt concentration in the feed stream. When operating with a rather low molar strength (<50 mM in typical CDI), we can see a transition in the predominant charge storage mechanism (**Figure 5**): as the charge increases from the uncharged state, co-ions are ejected from the pores and counter-ion are electro-adsorbed following the ion-swapping scenario. Yet, as the in-pore co-ion population is depleted, the process of counter-ion electroadsorption becomes dominant, and the system transitions towards permselective ion removal.

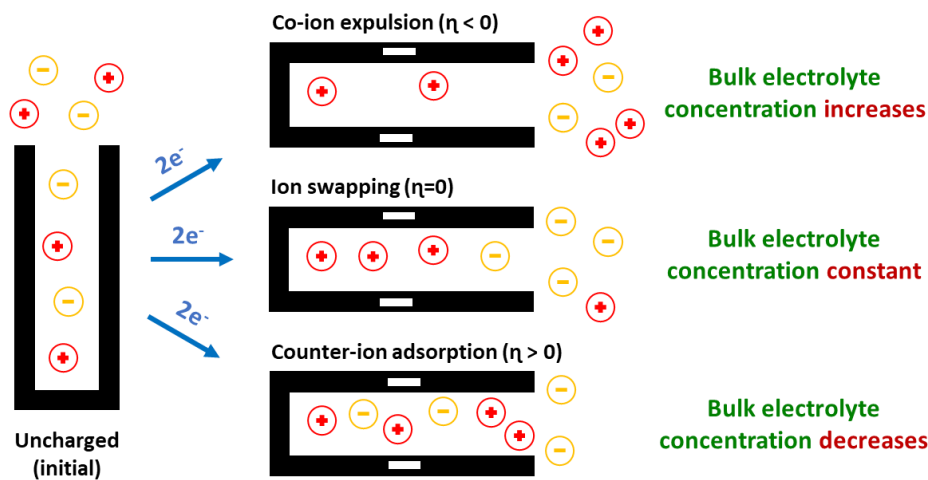


**Figure 4.** The principle of electrical charge/ions interaction in the micropore: ion swapping, counter-ion adsorption, and co-ion expulsion.

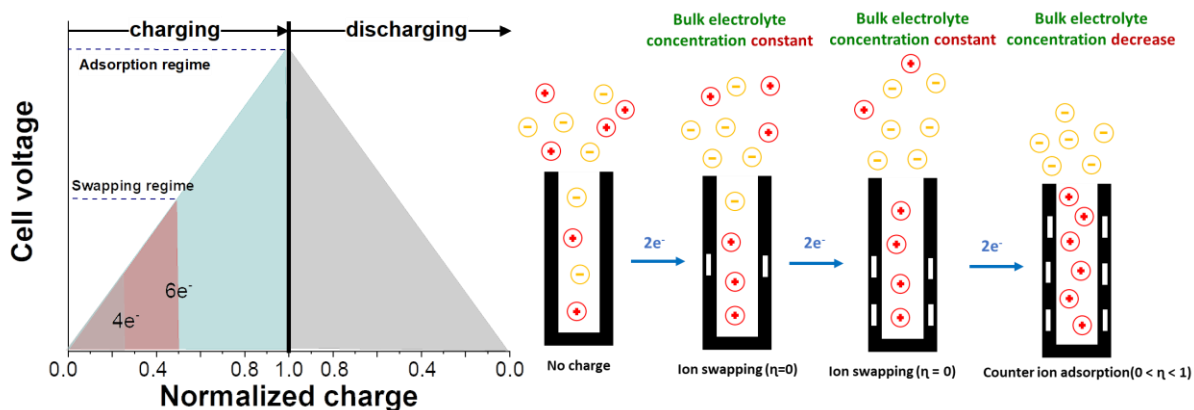


**Figure 5.** Voltage profile of capacitive response with different charge/voltage regime and the combination mechanism of ion swapping and counter-ion adsorption.

The permselective or non-permselective ion electroadsorption regimes can be identified by measuring the concentration of anions and cations within carbon micropores.[32, 34, 35] At high molar strength (e.g., aqueous 1 M NaCl), as found in supercapacitors or highly saline media, we see that the entire charge regime allowed by the electrochemical stability window of water is dominated by ion swapping (**Figure 6A**).[35, 36] This is why capacitive deionization cannot be applied for seawater remediation where we would operate at a molar concentration of about 600 mM. At low molar concentration (e.g., aqueous 20 mM NaCl), as found in brackish water, we first see a regime of non-permselectivity (ion swapping), which transitions to preferred counter-ion adsorption once the population of co-ions has been depleted in the micropores at higher charged states (**Figure 6B**).

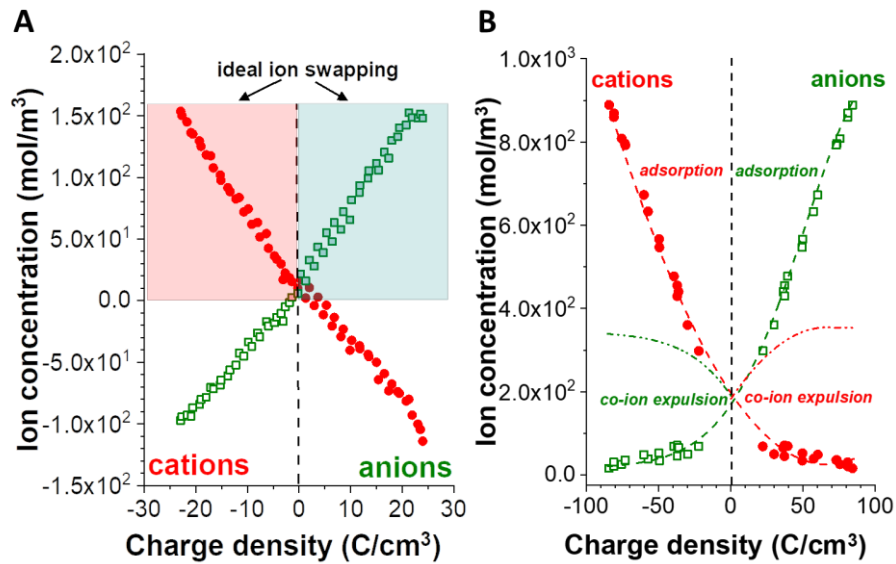


**Figure 6.** Cation and anion concentration changes inside micropores as a function of the applied charge A) at a concentration of aqueous 1 M NaCl (data adapted from Ref. [32]), and B) at aqueous 20 mM NaCl (data adapted from Ref. [34]).

There is a strong influence of the molar strength on the desalination performance. If we consider the cation-to-anion ratio of the negative electrode at 1 M NaCl, the intrinsic ion swapping result in the cation-to-anion ratio of around 1 (**Figure 7A**). At lower NaCl concentration, the non-permselective regime is easier to overcome compared to high salt concentration so that more charge can be contributed to the ion removal. Another important parameter on the desalination performance is the applied voltage per which a certain charge is applied to the electrodes. As seen from **Figure 7B**, at 20 mM NaCl, a larger cell voltage results in a larger charge and a higher cation-to-anion ratio at the negative electrode; thereby, a higher desalination capacity is accomplished.

As illustrated for microporous carbon,[37] we see in **Figure 7C** the strong decrease of the salt removal capacity with increasing salinity for a cell voltage of 0.8 V. The ability to remove significant amounts of salt is lost when exceeding a molar strength of 100 mM, while a high charge efficiency is only achieved below 10 mM. As depicted in **Figure 7D**, activated porous carbon perform desalination capacity of 2 mg/g at a cell voltage of 0.6 V with a charge efficiency of around 35%. These data indicate that ion swapping is mitigated as the cell voltage is well above 0.6 V. Obviously, higher cell voltage leads to higher accumulated charge, and more salt is removed. At 1.2 V, the desalination performance is optimized at 14 mg/g with a charge efficiency of 90%.

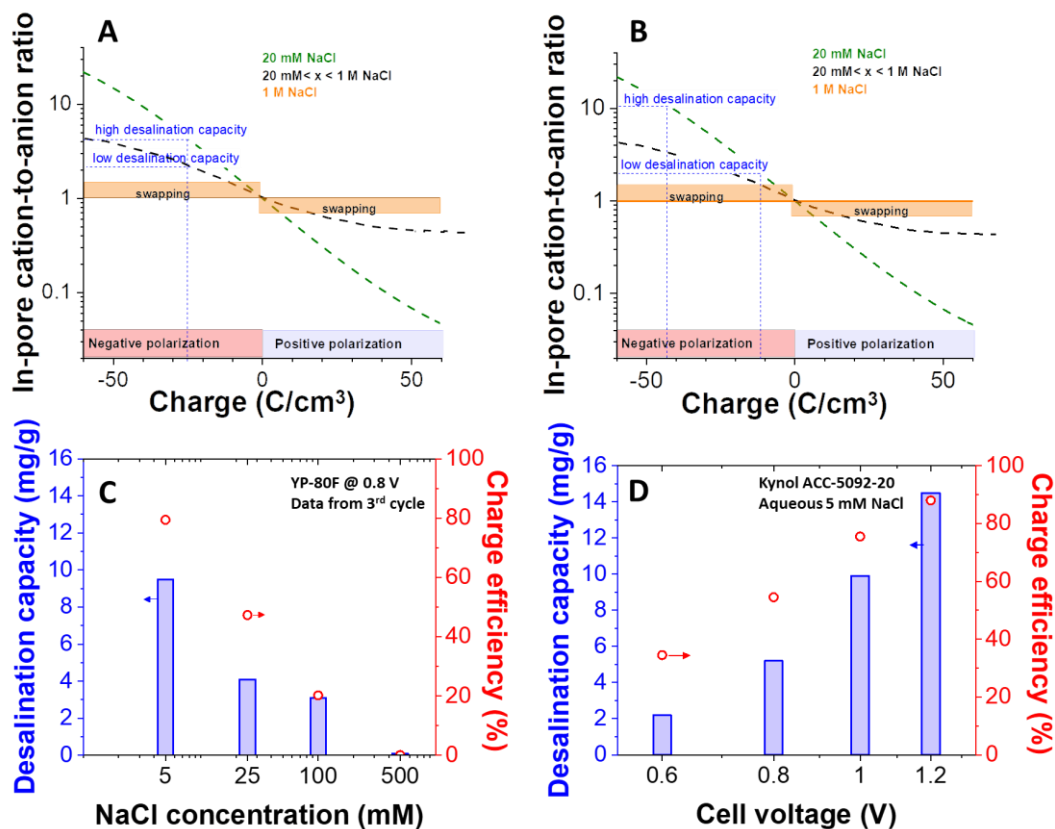


**Figure 7.** A-B) Cation-to-anion ratio inside a micropore as a function of applied charge demonstrating the influence of salt concentration and applied charge, C) desalination capacity and charge efficiency of porous carbon in different NaCl concentration, the data adapted from Ref. [37, 38], D) desalination capacity and charge efficiency of porous carbon in 5 mM NaCl at different cell voltages (data adapted from Ref. [38]).

So far, we have only considered an ideally polarizable electrode surface, that is, assuming the absence of positively or negatively charged surface groups. The potential distribution between the positive electrode and the negative electrode should be equal so that the accumulated charge in both electrodes are quantitatively the same. In such a case, the potential of zero charge ( $E_{PZC}$ ) is close to  $E_0$  (**Figure 8A**). However,  $E_{PZC}$  can be adjusted by surface functional groups at the fluid/solid interface (**Figure 8A**).[39] Once the surface of carbon is modified, an extra charge is added onto the carbon surface, causing already ion adsorption at uncharged state. Thereby, the  $E_{PZC}$  is shifted towards a positive or negative direction depending on the type of functional group. For example, in **Figure 8A**, the  $E_{PZC}$  at the positive electrode ( $E^+_{PZC}$ ) is shifted, resulting in an asymmetric charge distribution during charging and discharging.

Upon discharge via short-circuiting, the potentials of both electrodes decrease and intersect, where the potential of the positive electrode is smaller than  $E^+_{PZC}$  ( $E^+ < E^+_{PZC}$ ). As a result, we observe an inverted adsorption behavior: instead of removing ions from the saline medium, we expel extra-ions.

Bouhadana et al. [40] investigated the influence of electrochemical oxidation at a positive electrode to the dynamic changing of  $E^+_{PZC}$ . The electro-oxidation of the positive electrode creates carboxylic groups on the surface of the carbon. Such functional groups yield (slightly) negatively charged surface and thus, a positively shifted potential of zero charge ( $E_{PZC}$ ; **Figure 8A**). During desalination operation, cycle by cycle, the absolute salt adsorption decreases due to the shifting of  $E_{PZC}$  as well as  $E_0$ . As a result, the potential distribution between  $E^+$  and  $E^-$  becomes asymmetric, causing a lower desalination capacity and  $\eta$ . To restore the desalination performance, one can inverse the polarity of the applied cell voltage. By that way, the positive electrode becomes effectively the negative electrode and vice versa. The values of  $E_{PZC}$  and  $E_0$  are changed in a way that the potential distribution between both electrodes becomes symmetric again. Clearly, the presence of surface functional groups on the positive electrode triggers the inverted adsorption phenomenon in combination with regular adsorption.

It is also possible to fully invert the CDI system in such a way that both  $E^-_{PZC}$  and  $E^+_{PZC}$  shift away from each other (**Figure 8B**). At open circuit cell voltage, positively charged surface groups at the negative electrode adsorb anions while the negatively charged surface group at the positive electrode adsorb cations. During charging, the potential of the positive electrode increases toward  $E^+_{PZC}$ , causing ejection of adsorbed cations, and the mirrored effects are seen at the opposite electrode. During discharging, the potential for positive and negative electrode decreases to  $E_0$ . The cations and anions are again adsorbed at the positive and negative electrode, respectively. The limit of electrode potential should not exceed  $E^+_{PZC}$  and  $E^-_{PZC}$ ; otherwise, the “normal” adsorption process will occur and diminish the net desalination capacity.[41]

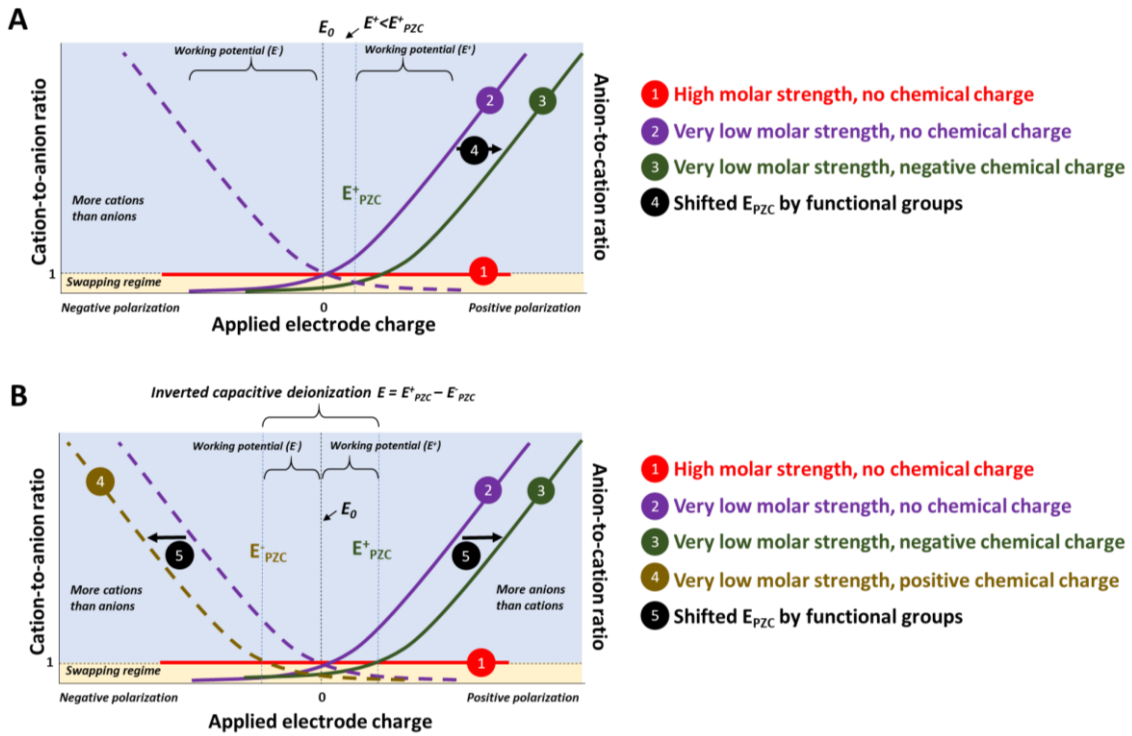


**Figure 8** A) An idealized charge/ion concentration vs. charge correlation representing the influence of concentration and the shifting of potential at zero charge ( $E_{PZC}$ ) due to the surface functional group. B) Visualization of inverted adsorption regime due to the surface functional group at both positive and negative electrode.

Several studies have explored inverted CDI so far. For example, Gao et al.[41] modified the  $E_{PZC}$  using different functional groups by use of acid-treated porous carbon as the negative electrode and carbon modified with tetraethyl orthosilicate as the positive electrode. The operational cell voltage of such electrode configuration is determined by the difference between  $E_{PZC}$  of the positive and the negative electrode (**Figure 9A**). In such case, the  $E^+_{PZC}$  value is +0.62 V vs. SHE, while  $E^-_{PZC}$  is at -0.17 V vs. SHE; hence, the operational cell voltage of inverted desalination is 0.79 V ( $\Delta = E^+_{PZC} - E^-_{PZC}$ ). The desalination capacity of this system has been reported to be 1.7 mg/g for a charging voltage of 0.8 V and when discharging to 0 V.

The performance can be further optimized by capitalizing on the dependency of the desalination capacity on the cell voltage.[42] For example, oxidation of carbon in nitric acid creates carboxylic surface groups which can be treated with ethylenediamine to generate positively charged amine groups. In a desalination cell, one can use carboxylated carbon as the positive electrode and carbon with amine groups as the negative electrode (**Figure 9B**). The operational voltage is enhanced to 1.1 V resulting from the large difference between  $E_{PZC}^+$  and  $E_{PZC}^-$ , and this cell yielded a desalination capacity of 5.3 mg/g. Once the operating cell voltage is larger than 1.1 V, the inverted desalination behavior (**Figure 9C**) will be mixed with regular desalination. The potential of the positive electrode is now larger than  $E_{PZC}^+$ , whereas the potential of the negative electrode is lower than  $E_{PZC}^-$ . Thereby, both electrodes enter the regular desalination regime. At the beginning of the discharge step, an inversion peak appears before the ion adsorption is established (**Figure 9D**).

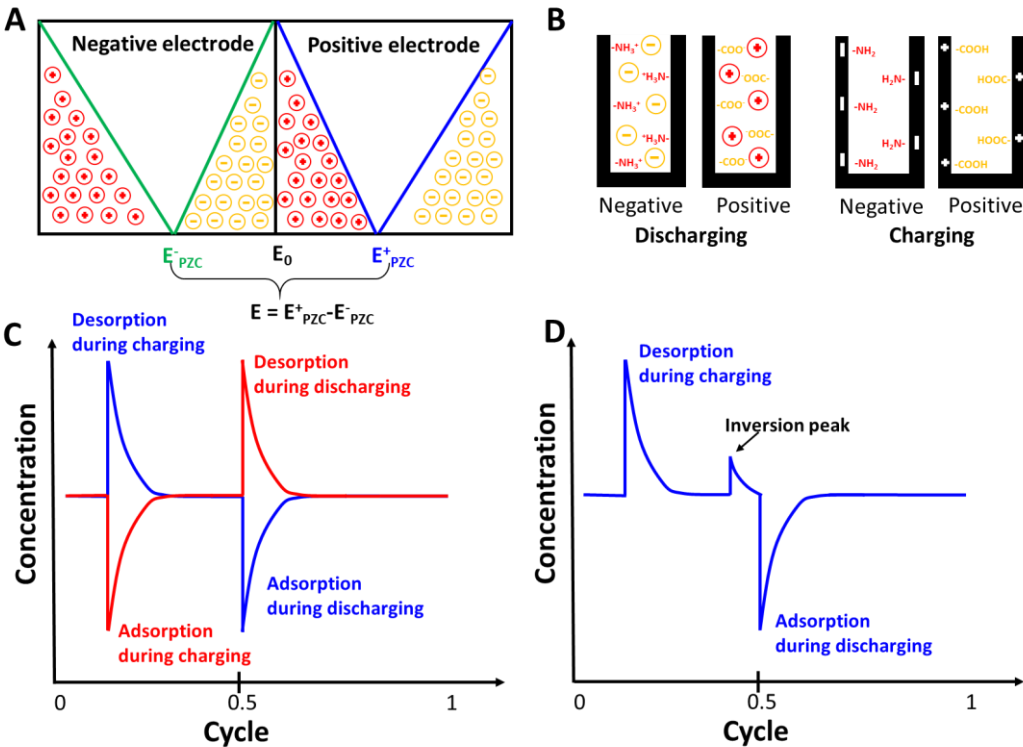


**Figure 9** A) Schematic showing the potential distribution and ionic distribution of inverted desalination, B) demonstration of surface functional groups that use as positive and negative electrode in inverted desalination, C) the effluence concentration profile of conventional capacitive deionization and inverted desalination, and D) effluence concentration of inverted desalination, in the case of cell voltage is large than  $E_{PZC}^+ - E_{PZC}^-$ .

### 2.2.3. Electrochemical (parasitic) side-reactions

Desalination by capacitive deionization is based on physical ion electrosorption and may be off-set or modified by the electric charge of surface groups. Electrically charged electrode surfaces in contact with an electrolyte may also experience redox reactions per Faradaic processes. Such a process may relate to water splitting, and we can use Pourbaix diagrams to show the relation between pH and thermodynamic window potential of water (**Figure 10A**). Not considering an over-potential, water splitting occurs at an electrode potential difference (cell voltage) of 1.23 V. Depending on the electrode potential, we will see hydrogen gas evolution reaction (HER) or oxygen gas evolution reaction (OER). Such reactions will consume an electric charge without contributing towards actual ion removal, thereby lowering the charge efficiency. In most cases, feed water for capacitive deionization has a neutral pH (pH 7); thus, the limitation of positive potential is at +0.69 V vs. standard hydrogen electrode (SHE) while the limitation of negative potential is at -0.4 V vs. SHE. The reaction mechanism of OER and HER is given per **Equation 13** and **Equation 14**.



Once the positive and/or negative potential exceeds the limit, hydrogen gas and/or oxygen gas evolve and diffuse away from the electrode surface.

Feed water for CDI does often not only contain dissolved ions but also a significant amount of dissolved oxygen. The latter greatly affects charge efficiency, pH, and cyclic stability of capacitive deionization towards oxygen reduction reaction (ORR). ORR is the electrochemical reaction between the electron and the adsorbed oxygen. As the electrode is biased to the negative potential, oxygen gas reacts electrochemically at the solid/liquid interface to form hydrogen peroxide at  $E_0$  of +0.29 V vs. SHE at pH 7 (**Figure 10B** and **Equation 15**).



The as-formed peroxide ion can be further reduced to form hydroxyl ion at  $E_0$  of 1.14 V vs. SHE (**Equation 16**).



The potential of peroxide reduction is even higher than that of the oxygen evolution potential. Thus, the oxygen reduction in most cases is limited to a two-electron transfer with negative consequences to the electrode stability and performance.[43, 44] Yet, the effect can be specifically triggered as well to enable use for electrolyte disinfection or degradation of an organic compound in water.[45] Hydrogen peroxide formation further oxidizes the carbon surface and causes the creation of surface functionalities like hydroxyl and carboxylic groups.[44] In that way, the  $E_{PZC}$  of the positive electrode shifts, and this effect decreases the desalination performance.[43, 44, 46, 47]

The carbon functional groups may not only shift the  $E_{PZC}^+$  but are also subject to oxidation reactions (**Equation 17-19**), resulting in pronounced charge consumption and degradation of the overall desalination performance.[48]



where  $R^1$  and  $R^2$  indicate the phenol, anhydride, lactone, quinone, and carbonyl groups.[49]

One can see that the reaction mechanism yields  $CO_2$  and  $CO$  gases (**Equation 17-18**) following irreversible reactions. At a neutral pH value, the functional group decomposition begins at the potential of +0.25 V vs. SHE which is below the oxygen evolution reaction (+0.69 V vs. SHE, **Equation 14**). Hence, it is very difficult to avoid such oxidation processes because the potential is low compared to the positive potential at the cell voltage of 1.2 V (**Figure 10A**).

We must separately consider the processes that occur at each electrode. For a symmetric setup (i.e., using two electrodes identical in size, material, and mass), a cell voltage of 1.2 V is accomplished by the positive electrode being at a relative potential of +0.6 V vs. SHE and the other at -0.6 V vs. SHE. This cell voltage of 1.2 V is commonly used in the CDI literature but may already exceed the actual electrochemical stability window of carbon in water. As seen from **Figure 10A**, a cell voltage of 1.2 V would at an initial pH value of 7 cause a parasitic Faradaic process, namely, hydrogen gas evolution at the negatively charged electrode. At the same time, the positively charged electrode is not exhausting the maximum window width by ca. 200 mV.

However, low molar saline media will provide a significant over-potential for Faradaic processes, and we may also benefit from reversible electrochemical hydrogen storage in the electrode micropores. Therefore, exceeding the hydrogen evolution reaction potential may not necessarily cause the irreversible formation of hydrogen gas. Still, using an asymmetric mass balance between the positively and negatively charged electrode may be needed to optimize the CDI process.[50]

In addition, functional groups of carbon at the positive electrode will experience performance degradation due to carbon oxidation and oxygen reduction reaction. The latter may cause a shift of  $E_{PZC}$ , inverted desalination, and/or low charge efficiency (**Figure 10B-D**).

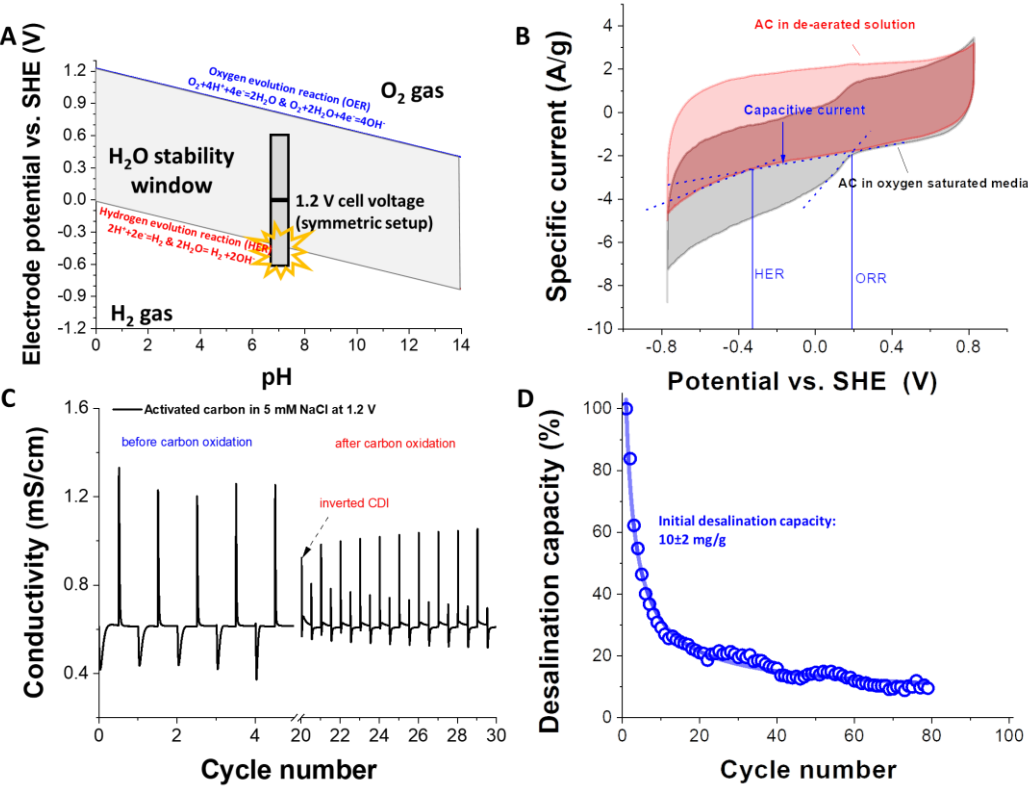


**Figure 10.** A) Pourbaix diagram of water, B) cyclic voltammogram of activated carbon in 1 M NaCl with and without saturated oxygen, data modified from Ref. [44], C) concentration profile during CDI operation in oxygen-saturated aqueous solution 5 mM NaCl, data modified from Ref. [44], and D) the desalination performance of high surface area carbon black operating in saturated  $O_2$  5 mM NaCl, data modified from Ref. [43].

#### 2.2.4. Correlation between electrode pore structure and desalination performance

There is no direct correlation between desalination performance and total pore volume or total surface area. In addition to the presence of a chemical (surface) charge and (possibly: irreversible) surface reactions, however, there is a significant influence of the pore size on the ion electrosorption process. Adopting the knowledge of a pore size dependent specific capacitance in the supercapacitor field, it is reasonable to translate the influence of nanoconfinement also to the ion immobilization (and desalination) performance via ion electrosorption.[51, 52] Accordingly, there is a strong increase in desalination capacity for micropores (**Figure 11A**). As established by Porada et al.[53], there is a good match between predicted and measured desalination capacity, based on the micro-mesoporosity quantified by nitrogen gas sorption (**Figure 11B**). This predictive tool remains very useful even for different cell voltages (up to 1.2 V),[38] but fails to work when there is a significant contribution of surface redox processes which reduce the charge efficiency.[54]

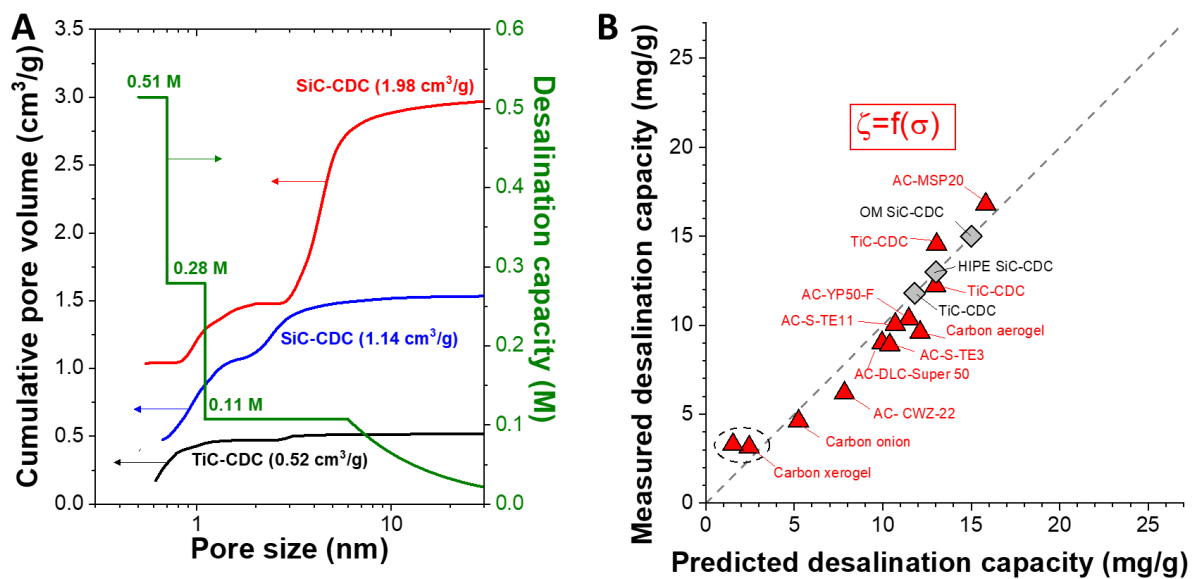


**Figure 11.** A) Cumulative pore size distribution calculated from quenched solid density functional theory (QSDFT) models of the tested nanoporous carbon materials with different pore dispersity and total pore volume values and correlation function for ion adsorption capacity adapted from Ref. [53], B) parity plot between measured desalination capacity and predicted desalination capacity using the function in **Figure 11A**, data adapted from Ref. [53].

### 2.2.5. Carbon electrode materials

Research on carbon electrodes for capacitive deionization has developed alongside the supercapacitor research field [55, 56] as it shares the same fundamental charge storage concept (i.e., the electrical double-layer). Thereby, carbon material development has focused on achieving a high specific surface area, optimized pore structure, high pore volume, good electrical conductivity, and facile scalability. The current literature encompasses carbon materials with large inner porosity, such as activated carbon, carbon aerogels, carbide-derived carbon (CDC), and templated carbons. In addition, there are carbons with (only/mostly) an outer surface area, such as carbon nanotubes, carbon onions, or graphene (**Figure 12**). The next sections will provide a general overview of carbon materials for CDI, and **Table 1** provides data on the desalination performances.

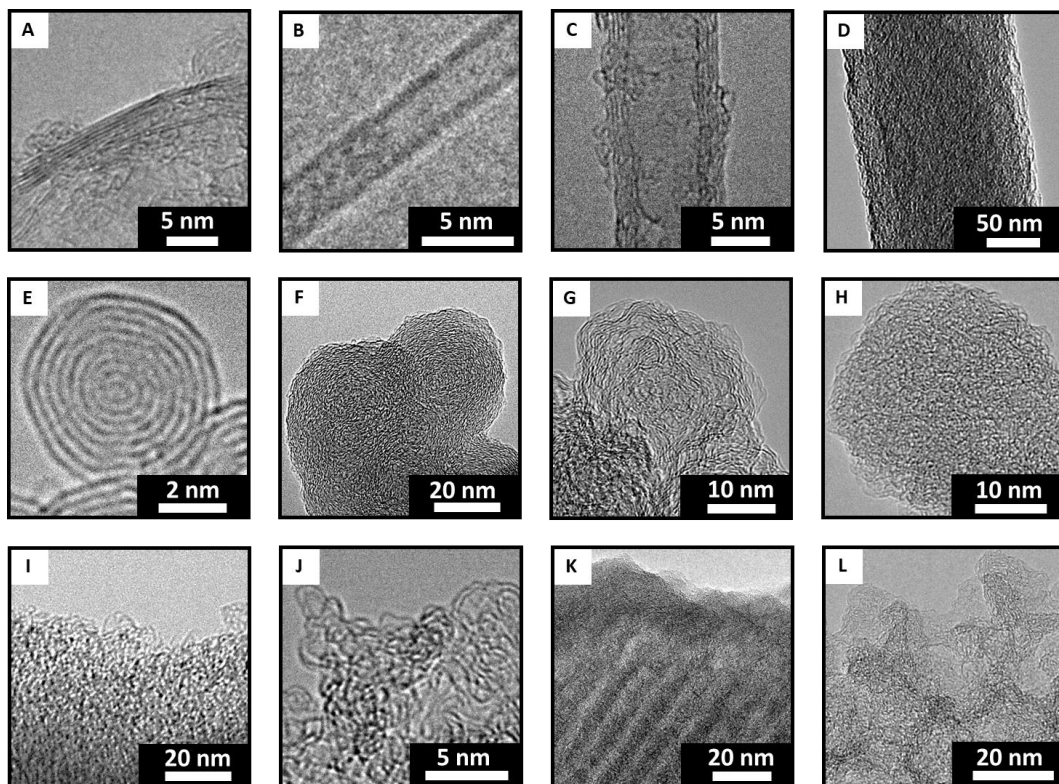


**Figure 12.** Transmission electron micrographs of A) multi-layer graphene (nano graphite flakes), B) single-wall carbon nanotube (SWCNT), C) multi-wall carbon nanotube (MWCNT), D) electro-spun carbon fiber from polyacrylonitrile (PAN), E) carbon onion, F) carbon black (CB), G) activated carbon black, H) carbide-derived carbon nanobeads, I) microporous activated carbon (AC) from coconut shells, J) microporous titanium carbide-derived carbon (TiC-CDC), K) ordered mesoporous carbon (OMC), and L) non-ordered mixed micro- and mesoporous carbon. Images courtesy of the Presser Group.

#### 2.2.5.1. Activated carbon

Activated carbon is the most common and large-scale available carbon material used for supercapacitor applications.[57] The synthesis of activated carbon generally involves two steps: first, the pyrolysis of a carbon precursor and second, the creation of a large specific surface area via physical or chemical activation. Many activated carbons are derived from a natural source (organic precursor) such as coconut shell[58] and wood[59] by pyrolysis below 1,000 °C. As an alternative to natural precursors, activated carbon can also be converted from petroleum coke,[60] polyacrylonitrile,[61] or phenolic resin.[62] The as-carbonized product is subsequently activated by an oxidizing gas (physical activations; e.g., CO<sub>2</sub> or water steam)[61] or by other reactive media (chemical activation; e.g., KOH).[50] Polymer-derived activated carbons can often be synthesized with different morphology, including the shapes of beads, fibers, or monoliths; in contrast, common biomass-derived activated carbon is conveniently obtained after the activation as a granular powder. Activated carbon beads, for example, are synthesized towards self-emulsion technique using a polymer resin solution as the carbon precursor. The cross-linked polymer is then pyrolyzed at 1,000 °C under Ar atmosphere. The as-carbonized product is then activated in the CO<sub>2</sub> atmosphere at 1,000 °C.[62] The same precursor can be used to prepare activated carbon cloth, as, for example, phenolic polymer resin can be shaped into fiber or textile. The cross-linked polymer textiles are carbonized and subsequently activated to obtain activated carbon cloth.[38, 63]

As seen in **Table 1**, the total pore volume of activated carbons is in the range of 0.3 cm<sup>3</sup>/g to above 1 cm<sup>3</sup>/g while the surface area ranges from about 400 m<sup>2</sup>/g to more than 2,000 m<sup>2</sup>/g. The higher surface area and pore volume lead to higher desalination capacity (i.e., amount of salt removed from the saline medium per electrode mass) at the evaluated cell voltage (up to 1.2 V). For example, activated carbon cloth derived from a polymer resin shows a desalination capacity from 10 mg/g to 17 mg/g in 5 mM NaCl when the total pore volume is increased from 0.5 cm<sup>3</sup>/g to 1.2 cm<sup>3</sup>/g.[38]

#### 2.2.5.2. Templated carbons

Templated carbons use a sacrificial template to exert control over the resulting pore structure which may be ordered. It follows many steps, including template impregnation, carbonization, and template removal. Hard templates must be removed after the carbon synthesis by chemical etching (e.g., removal of a silica template by HF etching). When using soft templates, self-assembly of carbon precursor occurs through the co-condensation of soft matter. During carbonization, the soft template is thermally decomposed. The resulting carbon (from a hard and soft template) may show ordered, or non-ordered mesopores and additional micropores can be obtained by applying further (chemical or physical) activation.[64, 65]

To obtain ordered micro/mesoporous carbons, one can use zeolites, aluminosilicates, and silicates as a hard template. Zeolites and well-ordered mesoporous silicates offer periodically ordered pore with different cage morphology resulting in various pore structures. For example, by filling zeolite cages with carbon sources like furfuryl alcohol and carbonization, carbon materials are obtained that are embedded within the zeolite network. Finally, the zeolite is removed by chemical etching, and we obtain carbon with well-ordered (micro)pores. The porosity reflects the initially used template (e.g., zeolite Y, zeolite X13, and zeolite L).[66-68] The specific surface area of zeolite-templated carbons may reach 3,600 m<sup>2</sup>/g.[66] Besides silica-based zeolite, zeolite imidazolate framework (ZIF) has also been used as self-sacrificed carbon template. ZIF share the same topology as zeolite. It is built from the coordination of a transition metal (e.g., Zn and Co)[69] and an organic molecule (imidazole) having ordered micropores.[70] Due to the high carbon content that already exists in the ZIF structure, the carbon precursor loading before pyrolysis is not necessary. Thereby, highly porous carbon can be directly obtained by carbonization of ZIF and subsequent removal of transition metal using HCl acid.[69, 71, 72]

Similar to zeolite template, porous silica like MCM-41 and porous aluminosilicate (MCM-48) exhibit ordered cylindrical mesopores,[73, 74] so that infiltration or impregnation of the carbon precursor followed by carbonization results in the well-ordered mesoporous carbon. For example, the ordered mesoporous carbon CMK-1 was synthesized by impregnation of MCM-48 into sucrose and sulfuric acid solution and subsequently carbonization. The resulting carbon shows a specific surface area of 1,380 m<sup>2</sup>/g.[75] Silica gel or silica colloidal templating is an alternative hard template to the as mentioned above.[76, 77] Silica colloidal templating results in spherical pores with a pore size distribution between 5 nm and 50 nm. A good dispersion of silica particles and the carbon precursor leads to high pore volume up to 6 cm<sup>3</sup>/g after silica etching.[78] The silica particle is also employed as the template for microporous carbon with a hollow structure.[79-81]

Soft templating may involve amphiphilic molecules like surfactants and block copolymers. The absence of (harsh) chemical etching for removal of the template makes soft templating a much more attractive synthesis strategy. The polymer itself becomes nanostructured during the self-assembling process. For example, poly(ethylene oxide)-b-poly(propylene oxide)-b-poly(ethylene oxide) triblock copolymer induces organic/organic self-assembly with carbon sources (e.g., phenolic resin) in ethanol. The hydroxyl group of phenolic resin promotes hydrogen bonding with polyethylene oxide in the triblock copolymer resulting in microphase formation.[65] Thereby, highly ordered mesoporous carbon is obtained after pyrolysis.

Ordered mesoporous carbon derived from silica/copolymer/metal composites with a specific surface area of 1,491 m<sup>2</sup>/g has been explored for capacitive deionization showing a desalination capacity of 1 mg/g (**Table 1**).[82] While providing only a small desalination capacity, ordered mesoporous carbons provide much faster ion transport due to the well-ordered pore network.[83] By further activation of ordered mesoporous carbon, microporosity is introduced without collapsing of mesopore, yielding a high surface area of 1,700 m<sup>2</sup>/g (**Table 1**). The desalination capacity of activated ordered mesoporous carbon, therefore, reach 15 mg/g in 76 mM NaCl at 1.2 V. ZIF derived porous carbon exhibit moderate specific surface area between 790 m<sup>2</sup>/g and 930 m<sup>2</sup>/g (**Table 1**). The desalination capacity of such carbon is 9-22 mg/g at the applied cell voltage of 1.2 V (input salt concentration: 1-17 mM NaCl)

### 2.2.5.3. Carbide-derived carbons

Carbide-derived carbon is produced by selectively etching of metal or metalloid atoms out of the crystal structure of metal carbides (e.g., TiC, SiC, Ti<sub>2</sub>AlC), carbonitride (e.g., SiCN), and carboxides (e.g., SiOC). CDC materials can be obtained by use of a different synthesis path, such as leaching by halogen gas, decomposition in a vacuum, or etching with supercritical water.[84] The most common and industrially scaled technique is the leaching by chlorine gas as the resulting porosity, reaction kinetics, and carbon properties are very controllable. CDC has gained interest per the ability to obtain materials with a narrow distribution of micropores when using, for example, chlorine gas treatment at temperatures below 1,000 °C on SiC or TiC.[85] Other carbide precursors, like Mo<sub>2</sub>C and NbC, rather yield a broad pore size distribution with micro- and mesopores, when using a chlorine gas treatment temperature between 400 and 900 °C.[86, 87] Tailored combinations of micropores and mesopores can be obtained by employing a templated carbide precursor (e.g., mesoporous carbide) and then subjecting the ceramic to the chlorine gas treatment.[88-90] Via electrospinning or melt spinning techniques, carbide-derived carbon fiber mats can be made which present faster ion mobility as compared to CDC powders. For example, SiOC fiber mat is prepared towards electrospinning of silicone resin solution and subsequently pyrolyzed. After chlorine gas treatment, SiOC-CDC carbon fiber is obtained with the promising surface area of 3,089 m<sup>2</sup>/g.[91] By adapting the carbon template method[92], the hierarchical micro-mesoporous pore network shows a much higher surface area than that of regular CDC.[93] A silica template (SBA-15), for example, is infiltrated with polycarbosilane followed by pyrolysis, obtaining SiC embedded in the silica template. The resulting product is then subjected to the HF solution to remove the template. After chlorine treatment, a high surface of the CDC (2,729 m<sup>2</sup>/g) is obtained.[94]

Despite the facile access to low-cost activated carbons, carbide-derived carbons have rather served as a model material for the research field of capacitive deionization.[53, 95] As shown in **Table 1**, TiC-CDC with sub-nanometer pores, having a total pore volume of 0.5-0.6 cm<sup>3</sup>/g, show a desalination capacity of 9-12 mg/g (5 mM NaCl at 1.2 V). SiC-CDC with an ordered mesoporosity in addition to micropores with a total pore volume of 1.98 cm<sup>3</sup>/g exhibits a desalination capacity of 13 mg/g in 5 mM NaCl at the cell voltage of 1.2 V.

#### 2.2.5.4. Carbon aerogels

Carbon aerogels consist of interconnected carbon nanoparticle, and the pore volume is composed of interparticle pores. The synthesis of carbon aerogel begins with the sol-gel polymerization between resorcinol and formaldehyde using carbonate salt catalyst. After crosslinking, a wet gel of resorcinol-formaldehyde is obtained. Then, the air-dried gel is pyrolyzed to obtain the carbon aerogel. Alternative carbon precursors for the preparation of carbon aerogel are polyurea and polyvinyl chloride.[96, 97] A key synthesis parameter is the type and concentration of the catalyst in the sol-gel process, which determines the microstructure, pore size, surface area, and pore volume. For example, the pore size is decreased as the concentration of catalyst is decreased and result in higher surface area (400-1,000 m<sup>2</sup>/g).[98, 99]

Carbon aerogels are among the earliest carbon materials that have been investigated for CDI application. The first report in 1995 by Farmer et al. used carbon aerogel with a surface area of 600-800 m<sup>2</sup>/g for investigation of different anions removal (Na<sub>2</sub>SO<sub>4</sub>, Na<sub>2</sub>PO<sub>4</sub>, Na<sub>2</sub>CO<sub>3</sub>, NaNO<sub>3</sub>, NaCl, and NH<sub>4</sub>ClO<sub>4</sub>).[100-102] As seen in **Table 1**, the desalination capacity of aerogel is in the range between 2-7 mg/g in salt concentrations of 8.5-11 mM NaCl (applied cell voltage of 1.4 V) which is quite low compared to other materials like activated carbon and CDC. At that time, the CDI research focused on mesoporous carbon for which carbon aerogels are well-suited research subjects.

#### 2.2.5.5. Graphene

Graphene is defined as a monoatomic layer of carbon with sp<sup>2</sup>-hybridization.[103] There are three main routes to prepare graphene: chemical vapor deposition (CVD),[104] chemical reduction of graphene oxide,[105] and liquid phase exfoliation of bulk graphite[105]. Among these methods, chemical vapor deposition is one of the most common methods for creating large area continuous graphene film. Hydrocarbon gases like methane are chemically deposited on the nickel or copper catalyst at the temperature of 1,000 °C. This process is rather difficult to control due to the growing preference between grain and grain boundary of a metal catalyst.

Another well-established synthesis route is the reduction of exfoliated graphene oxide obtained through Hummer's method.[106, 107] Due to the plane surface and edge function groups of graphene oxide (carboxylic, epoxide, and hydroxyl), it can be simply exfoliated in water. The oxygenated functional groups can be further removed, resulting in the reduced graphene oxide, which contains many defects and wrinkles. The first use of reduced graphene oxide for capacitive deionization was reported in 2009.[108] As seen in **Table 1**, the salt adsorption is low (2 mg/g) even though the work used an applied cell voltage of 2 V (i.e., far outside the electrochemical stability window of water). Such low performance may relate to the low surface area (14 m<sup>2</sup>/g) and the high number of oxygenated functional groups. The salt adsorption of reduced graphene oxide significantly increases as the surface area is increased. As seen in **Table 1**, sponge-templated graphene exhibits a much larger surface area (305 m<sup>2</sup>/g) than flat reduced graphene oxide flakes. Consequently, the former shows a desalination capacity of 5 mg/g at a large cell voltage of 1.5 V. After nitrogen-doping, the salt adsorption can be increased to 21 mg/g at the cell voltage of 1.5 V (**Table 1**). Another approach for enhancing graphene performance is chemical activation (H<sub>2</sub>O<sub>2</sub>).[109] During hydrothermal reduction, H<sub>2</sub>O<sub>2</sub> preferentially etched the defect sites and left the in-plane pore. As a result, the surface area reached 1,261 m<sup>2</sup>/g (measured by methylene blue adsorption) with a corresponding desalination capacity of 27 mg/g at a cell voltage of 1.2 V in 85 mM NaCl.

#### 2.2.5.6. Carbon nanotubes

Carbon nanotubes (CNTs) are rolled-up graphene sheets which may contain single-, double-, or multiple-layers (single-walled, double-walled, or multi-walled CNTs). The number of walls and the structural arrangement cause different physicochemical properties. Arc discharge, laser ablation, and CVD have been the most successful methods for nanotube synthesis. The first two routes employ solid carbon as the precursor. The growth in such methods requires much higher temperature compared to CVD, which, similarly to graphene synthesis, uses temperatures around 500 °C to 1,000 °C. However, CNTs produced by CVD usually present catalyst residue that can bring a negative impact for capacitive deionization (leakage current and low charge efficiency), requiring post-synthesis treatments to remove it.

Owed to the moderate surface area (50-130 m<sup>2</sup>/g), carbon nanotubes only show a small desalination capacity below 2 mg/g for capacitive deionization (**Table 1**).[110] However, a number of works in the literature use CNTs in carbon composites[111] with activated carbon[96, 112], mesoporous carbon [113, 114], or reduced graphene oxide composite[115], for example.

### 2.2.5.7. Summary

Carbon materials are attractive electrode materials for capacitive deionization because many of them are easy to produce, the materials required for their synthesis are usually abundantly available, and they (often) combine a high specific pore volume/surface area with (sufficient) electrical conductivity. In good agreement with the modified Donnan model, microporous carbon leads to overlapping potential profiles of the in-pore electrical double-layer, and the salt adsorption depends on the pore volume with important implications of the pore size. Although the fundamental understanding of capacitive deionization has improved the desalination performance, the mechanism of ion electrosorption itself remains a limiting factor the desalination performance. This particularly pertains to the failure of desalination at high molar strength (**Figure 13A**), and the rapid performance decay in the presence of dissolved oxygen in the saline medium (**Figure 13B**). Therefore, alternative electrode materials and ion removal mechanisms are in high demand.

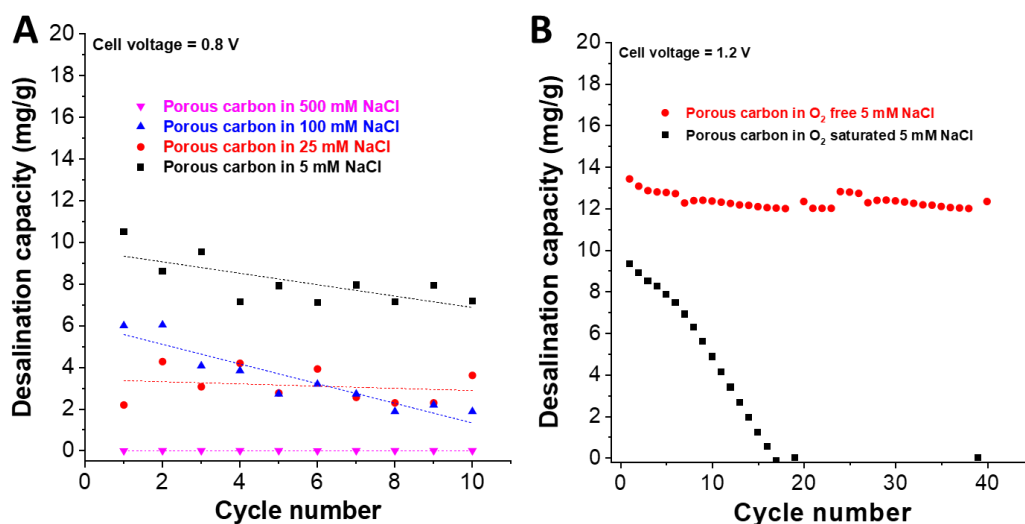


**Figure 13.** A) desalination performance of activated porous carbon as a function of salt concentration at a cell voltage of 0.8 V, data adapted from Ref.[37], B) longevity performance of activated carbon in oxygen-free and oxygen-saturated solution, data adapted from Ref. [44].

## 2.3. Electrochemical desalination via ion insertion

### 2.3.1. A brief history of insertion materials for electrochemical desalination

It is often overlooked that Blair and Murphy [22] used in 1960 in the context of the capacitive deionization already the desalination performance of an Ag/AgCl redox process and a chemically modified carbon electrode (**Figure 14A-B**). Since then, there was no dedicated work related to Faradaic material until 2012 when Pasta et al. explored insertion materials for electrochemical desalination.[116] In the latter work, Pasta et al. introduced the so-called desalination battery based on sodium manganese oxide ( $\text{Na}_{2-x}\text{Mn}_5\text{O}_{10}$ ) as the sodium removal electrode and silver as a chloride removal electrode in a cell like the ones used for conventional CDI (**Figure 14C**). Their work demonstrated the ability of Faradaic materials to desalinate aqueous media with a high molar concentration, thereby, allowing seawater desalination, which is impossible for conventional CDI based on nanoporous carbon. In 2014, the similar concept as Blair and Murphy was introduced and named hybrid capacitive deionization. Lee et al. [117] used sodium-permselective  $\text{Na}_4\text{Mn}_9\text{O}_{18}$  as the positive electrode (0-0.8 V vs. Ag/AgCl) and activated carbon with an anion-exchange membrane as the negative electrode (**Figure 14D**). This cell configuration allows an operation voltage between +1.2 V and -1.2 V, resulting in high desalination performance (31 mg/g).

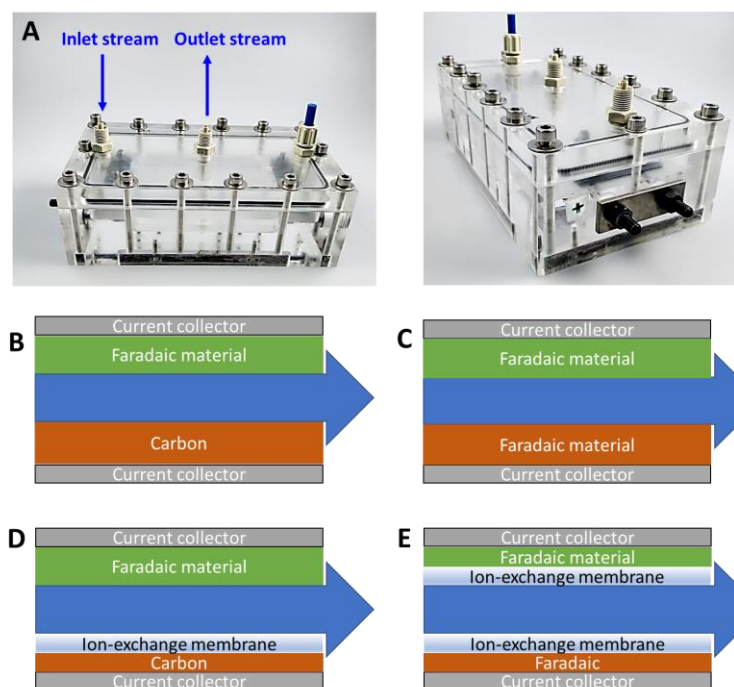


**Figure 14.** A) picture of lab-scale conventional flow-by CDI cell, B-E) the various cell configuration according to the pairing between the positive and negative electrode in the conventional CDI cell.

Another hybrid capacitive deionization cell was introduced by Kim et al. in 2016.[118] In their work, sodium insertion  $\text{Na}_2\text{FeP}_2\text{O}_7$  was paired with an activated carbon electrode and yielded a desalination performance of 30 mg/g. In this cell, it was necessary to use an anion-exchange membrane to enable the desalination process (**Figure 14D**). Yet, using an ion exchange membrane is not always needed for hybrid cells. For example, as shown by our team in 2017,[119] sodium-permselective  $\text{TiS}_2$  can be paired with activated carbon cloth without applying any membrane for desalination even at 600 mM NaCl. Considering cation insertion in  $\text{TiS}_2$  between 0 V and -0.5 V vs. Ag/AgCl, it is clear that carbon maintains the ability to remove chloride ion at the positive potential.

One can further convert from hybrid capacitive deionization to fully Faradaic deionization by applying insertion materials as both positive and negative electrode like desalination battery (**Figure 14C**). In 2016, the first such full Faradaic deionization was reported by us.[120] We used  $\text{Ti}_3\text{C}_2$  MXene, allowing the insertion of sodium and chloride in-between the layers of the electrode materials. Shortly after MXene,  $\text{MoS}_2$  was introduced by Xing et al.[121] using exfoliated  $\text{MoS}_2$ . Our work [37] revealed that the desalination capacity of exfoliated  $\text{MoS}_2$  at 500 mM NaCl was enabled by ion insertion, in alignment with work by Acerce et al. [122].

Lately, more and more works have explored Faradaic deionization. For example, Chen et al. coupled a sodium insertion material ( $\text{Na}_{0.44}\text{MnO}_2$ ) with the conversion reaction material (BiOCl).[123] To increase the selectivity of each electrode, they applied the anion-exchange membrane and cation-exchange membrane on top of BiOCl and  $\text{Na}_{0.44}\text{MnO}$ , respectively. Thereby, the desalination capacity was 70 mg/g at the cycling cell voltage of  $\pm 1.5$  V.

A novel desalination cell concept called Na-ion desalination (NID) was introduced by Smith et al. in 2016.[124] Other works have coined the same cell concept Rocking chair desalination.[125] As seen in **Figure 15A-B**, NID employs two sodium insertion electrodes at different sodiation states. Those two electrodes were separated by anion-exchange membrane resulting in two flow channels: one is desalinated while another is salinated during operation. During charge and discharge, sodium ions are released from the host material and balanced with the chloride ion that migrated from another channel and vice versa. This allows Na and Cl removal just based on reversible Na insertion processes.

Lee et al.[125] reported in 2017 a NID cell that consisted of sodium hexacyanoferrate and sodium nickel hexacyanoferrate, yielding a desalination capacity of 60 mg/g in 600 mM NaCl at a cell voltage of 0.8 V. The desalination performance is even higher when changing the materials to sodium copper hexacyanoferrate as a positive and negative electrode.[126] Within the cycling cell voltage of  $\pm 0.6$  V, this material delivers a desalination performance of 100 mg/g in 50 mM NaCl.

Instead of using sodium-insertion and a cation-exchange membrane, one can also invert the NID cell concept (**Figure 15C**). The first chloride ion desalination (CID) cell, without being called so, was reported in 2012. In the latter, Grylowicz-Pawlaw et al.[127] used a cation-exchange membrane (sulfonated tetrafluoroethylene-based fluoropolymer, Nafion) coated around the silver electrode to obtain the desalination of seawater containing 600 mM NaCl. In 2017, Figuera et al.[128] applied inkjet printing to print Ag and AgCl on conductive glass, added Nafion, and used the resulting microdevice for on-chip desalination. With these early works unacknowledged by the CDI community, Arulrajan et al. introduced the concept of CID by using chemically modified carbon electrodes instead of Faradaic materials.[129] In their work, (3-aminopropyl)triethoxysilane modified activated carbon cloth was employed as both a positive electrode and a negative electrode. The desalination capacity of this work was 50 mg/g operating in 20 mM NaCl with the cell voltage of  $\pm 0.9$  V. Our work further explored the Ag/AgCl system, showing an initial desalination capacity of almost 200 mg/g in aqueous 600 mM NaCl; however, per particle coarsening and the generation of electrochemically inert dead mass core regions, the performance drops quickly and stabilizes at 115 mg/g.[130]

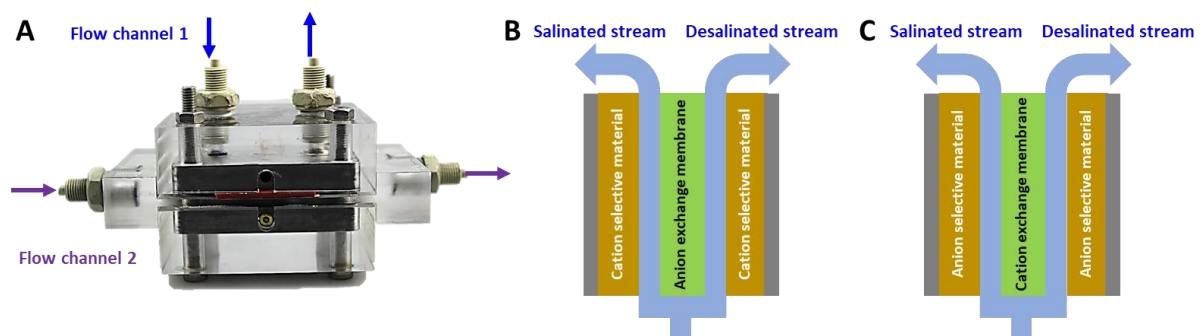


**Figure 15.** A) Lab-scale desalination cell with two flow channels. B-C) Schematic setup of B) NID and C) CID.

### 2.3.2. Ion insertion mechanism and basic concepts

Ion electrosorption is based on the attraction force between ions and excess/deficiency electron charges at the solid/liquid interface (**Figure 16A**). In conventional capacitive deionization, there is a linear correlation between the stored charge and the applied potential; consequently, ions are held (immobilized) within the electrical double-layer near the surface of the carbon electrode. Yet, charge storage and ion immobilization can also be accomplished by processes that involve the charge transfer across the fluid/solid interface of an electrode and the electrolyte. Such Faradaic processes are accompanied by chemical and/or structural changes of the electrode material, for example, by changing the oxidation state of the electroactive material.[131] Common battery electrode materials undergo extensive Faradaic processes triggered by reversible ion intercalation or ion insertion during the charging and discharging process (**Figure 16B-C**).

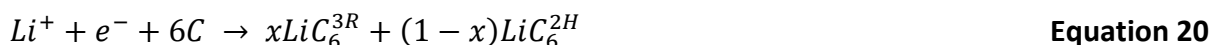
The International Union of Pure and Applied Chemistry (IUPAC) defines the following:

***“Insertion reaction.** A general term is given to a reaction involving the transfer of a guest atom, ion or molecule into a host crystal lattice.”*[132]

***“Intercalation reaction.** A reaction, generally reversible that involves the introduction of a guest species into a host structure without a major structural modification of the host. In the strictest sense, intercalation refers to the insertion of a guest into a two-dimension host”*. [132]

Therefore, the term intercalation should only be assigned to insertion processes with a minor change of the structure. More generally, the ion-uptake process is best just labeled as ion-insertion. In many materials, the insertion/extraction of ions causes volume change (expansion/contraction) and mechanical stress. One example is the insertion reaction of lithium-ions into orthorhombic  $V_2O_5$  ( $\alpha$ -phase). A phase transformation (from the  $\alpha$ -phase to the  $\delta$ -phase) is a function of the amount of inserted lithium ( $Li_xV_2O_5$ ,  $0 < x < 1$ ). [133]

A well-known example is the lithium-ion intercalation into hexagonal graphite with ABAB stacking (2H phase). Upon the intercalation process, lithium ions accumulate between the layers and centered at the benzene hexagon, causing the phase change from the hexagonal 2H phase to rhombohedral 3R phase (**Equation 20**). [134]



The electrical current-potential response of an electrode material during charge/discharge cycling can further be classified as capacitive/pseudocapacitive in the absence of redox peaks or as battery-like in the presence of clear redox peaks. A system only experiencing charge storage via ion electrosorption will, within the stable electrochemical window of the electrolyte, show cyclic voltammograms with a constant current (rectangular shape) for cathodic and anodic scan direction (**Figure 16D**). If a charge transfer process displays this capacitor-like signature, it can be called pseudocapacitive.[131] Pseudocapacitive materials include surface-redox materials like  $\text{RuO}_2$ [135] or ion insertion materials like  $\text{MoS}_2$ . [37, 121, 122]. In the occurrence of redox peaks during charge/discharge cycling, one should never assign the label pseudocapacitive, and must replace the often-used unit of F/g (capacitance) by mAh/g (capacity).[136]

For ion electrosorption and pseudocapacitive systems, any increase of the applied cell voltage will cause a linear increase of the stored charge. Accordingly, there is no limiting energy barrier impeding a capacitor-like response, either for ion electrosorption or ion insertion. In contrast, battery materials that show sharp or broad redox peaks during charge/discharge cycling employ Faradaic reactions that require to overcome a certain energy barrier (activation energy; **Figure 16E**).

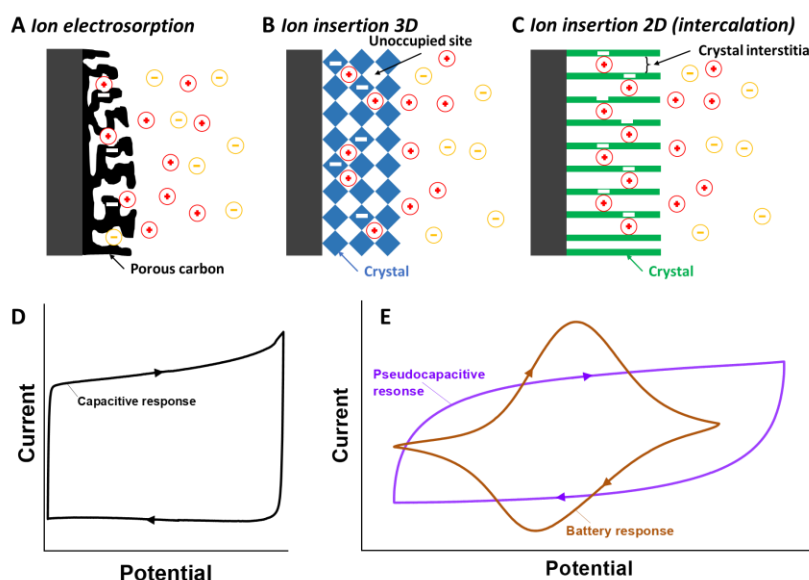


**Figure 16.** A) Ion electrosorption on the surface of nanoporous carbon, B) ion insertion into the host structure, C) ion intercalation between the layers of a two-dimensional material.[132] Cyclic voltammogram of D) a typical electrical double-layer, and E) comparison between a battery-like and a pseudocapacitive current-vs.-potential signature.

### 2.3.2.1. Thermodynamics of Faradaic materials

The characteristics of ion insertion materials with redox peaks in the electrical response require to consider the free energy of the insertion reaction. The latter depends on the electrode material, the ion concentration, and the ionic species.[137] As visualized in **Figure 17A**, the electrochemical process for insertion reaction occurs not only at the solid-liquid interfaces but also in the host material. The activation energy and free energy change depend on the lithium concentration in the interstitial site of the host material.[138] The free energy ( $G_x$ ) is given in **Equation 21**.

$$G_x = G_0 + \epsilon x + kT(x_a \ln x_a + (1 - x_a) \ln(1 - x_a)) \quad \text{Equation 21}$$

where  $G_0$  is the free energy of the host material before insertion reaction,  $\epsilon$  is the free energy difference per added ion,  $k$  is the Boltzmann constant,  $T$  is the temperature, and  $x_a$  is the concentration of ion a in the host material during insertion. The third term in the **Equation 21** includes the entropy of guest ion distribution in the interstitial sites of the host material.

**Figure 17B** shows the free energy pattern if the host material results in a solid solution with the guest ion species during insertion. Any change of the ion concentration in the structure causes no actual phase transformation or insignificant phase change. In such a case, we observe a gradual change in free energy and no potential plateau. An insertion process leading to a first-order phase transformation causes the free energy to show two local minima and one potential plateau (**Figure 17C**). In the case of a second order phase transformation during insertion, an intermediate phase may occur at a specific ion concentration. Correspondingly, we see two potential plateaus (**Figure 17D**).

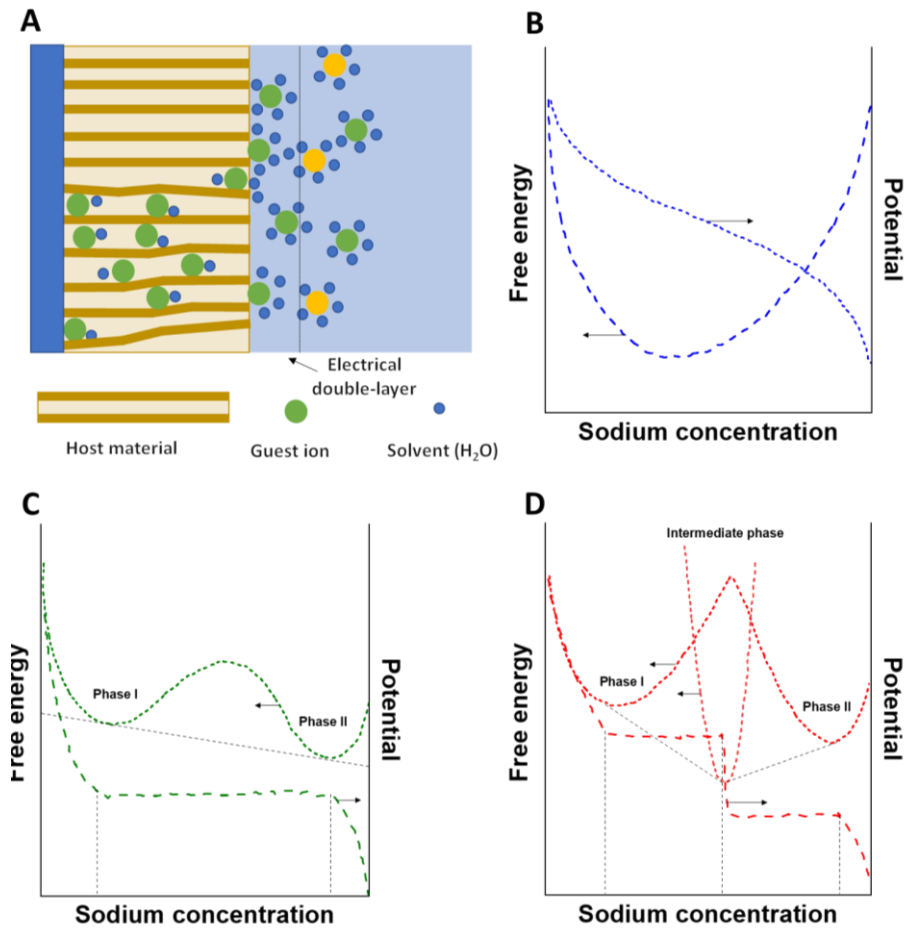
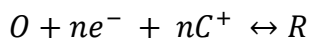


**Figure 17.** A) Schematic illustration of the ion insertion into the host material. B-D) Free energy of the material and electrochemical potential as a function of the sodium concentration in the structure considering B) a solid solution, C) first-order phase transformation, and D) second-order phase transformation[138]

The excess free energy of an insertion material (**Equation 21**) contains the activity in term of the ionic molar fraction in the structure. The interstitial site that can be free or occupied by a guest species is a part of the whole process. The free energy of solvent and ion also play a crucial role in a complete picture. Considering the electrochemical potential presented in

**Equation 22:**



**Equation 22**

where  $O$  is the oxidized state of the host material,  $n$  is the transferred charge during the insertion process,  $C^{+}$  is inserted ion, and  $R$  is the reduced state of the host material.

By assuming the electrolyte as an ideal solution, the potential ( $E$ ) is shown in **Equation 23**.

$$E = E_a^0 + \frac{RT}{nF} \ln \frac{C_a}{C_0} - \frac{RT}{nF} \ln \frac{x_a}{(1-x_a)} - \frac{1}{nF} \frac{d}{dx_a} G_x(x_a) \quad \text{Equation 23}$$

where  $E$  is the potential,  $E_a^0$  is the standard potential of ion  $a$ ,  $R$  is the gas constant,  $T$  is the temperature,  $n$  is number of transferred charges,  $F$  is the Faraday constant,  $C_a$  is the concentration of ion  $a$ ,  $C_0$  is the standard concentration of ion  $a$  (usually 1 M),  $x_a$  is the molar fraction of  $a$  in the interstitial site of the host material, and  $G_x$  is the excess free energy.

Assuming the electrolyte to be not an ideal solution, the term  $E_a^0 + \frac{RT}{nF} \ln \frac{C_a}{C_0}$  is no longer valid in **Equation 23** because the activity of the solution is not the same as the concentration ( $a_a = \gamma_a \frac{C_a}{C_0}$ ). Thereby, **Equation 23** should be transformed into **Equation 24**.

$$E = E_a^0 + \frac{RT}{nF} \ln a_a - \frac{RT}{nF} \ln \frac{x_a}{(1-x_a)} - \frac{1}{nF} \frac{d}{dx_a} G_x(x_a) \quad \text{Equation 24}$$

where  $E_a^0 + \frac{RT}{nF} \ln a_a$  is the formal potential ( $E_f$ ), and  $a_a$  is the activity of ion  $a$  in the solution.

**Figure 18** exemplifies the influence of host free energy and the activity of the ion on the insertion potential. As seen in **Figure 18A**,  $\text{TiS}_2$  exhibits the lowest insertion potential as compare with triclinic/orthorhombic  $\text{Na}_x\text{VOPO}_4 \cdot y\text{H}_2\text{O}$ , and cubic  $\text{K}_2\text{NiFe}(\text{CN})_6$ . When the same structure of a material and the type of inserted ion is fixed by using the same material, the insertion potential shifts as a function of the concentration indicating the influence of ionic activity in the solution (**Figure 18B-C**).[137]

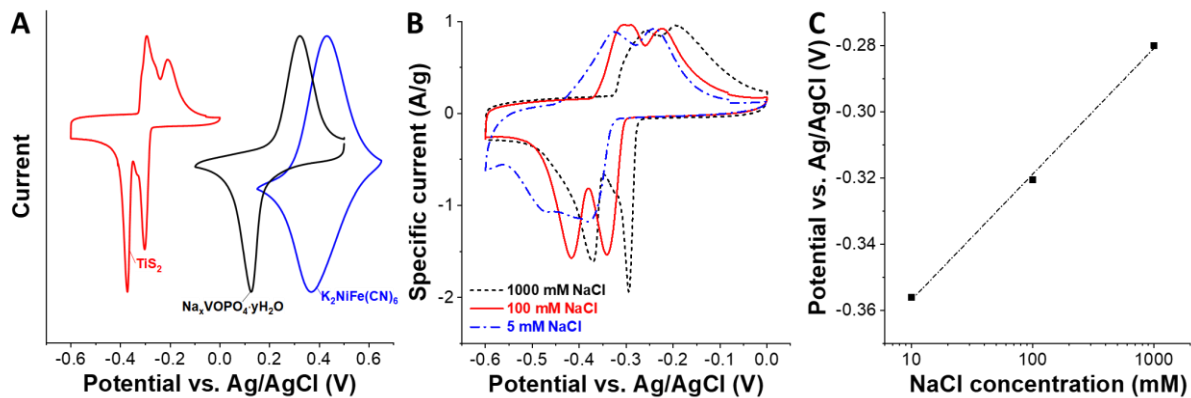


**Figure 18.** A) Cyclic voltammogram of three different insertion materials (i.e.,  $\text{TiS}_2$ ,  $\text{Na}_x\text{VOPO}_4 \cdot y\text{H}_2\text{O}$ , and  $\text{K}_2\text{NiFe}(\text{CN})_6$ ) recorded at 1 mV/s in 1 M NaCl. B) Cyclic voltammogram of  $\text{TiS}_2$  tested in different NaCl concentration at 1 mV/s, and C) formal potential of  $\text{TiS}_2$  as a linear function of the aqueous NaCl concentration.

### 2.3.2.2. Correlation between charge capacity and ion removal

Ion insertion-type materials include cation insertion materials, anion insertion materials, and materials that allow the insertion of both ion types. We first focus on the cation insertion materials. Depending on the nature of the materials (electrochemical potential and Fermi energy level), the charge storage is determined towards their composition and structure. Using aqueous electrolytes, many electrode materials show a charge capacity enabled by sodium-ion insertion between 22 mAh/g and 100 mAh/g.[139] Since ion insertion is not plagued by co-ion desorption, this charge can (ideally) be fully used for the desalination process even at high molar strength.[37, 116, 119, 125, 140, 141] In the case of sodium ion removal, the sodium uptake capacity (NUC) can be correlated by applying **Equation 26**.

$$NUC = \frac{C_{sp}Mw_{Na}}{F} \quad \text{Equation 26}$$

where  $NUC$  is the sodium uptake capacity ( $\text{mg}_{\text{Na}}/\text{g}_{\text{electrode}}$ ),  $C_{sp}$  is the specific capacity of the electrode ( $\text{mAh}/\text{g}_{\text{electrode}}$ ),  $Mw_{Na}$  is molecular weight of sodium ion (22.9 g/mol), and  $F$  is Faraday constant (22.8 Ah/mol).

The NUC can be predicted by using the charge capacity from electrochemical testings. For example,  $\text{TiS}_2$ ,  $\text{Na}_x\text{VOPO}_4 \cdot y\text{H}_2\text{O}$ , and  $\text{K}_2\text{NiFe}(\text{CN})_6$  exhibit the specific capacity in 1 M NaCl of 70 mAh/g, 34 mAh/g, and 23 mAh/g, respectively (**Figure 19A**). Assuming the charge efficiency of 100%,  $\text{TiS}_2$  gives the  $NUC$  of 60  $\text{mg}_{\text{Na}}/\text{g}$ , while  $\text{Na}_x\text{VOPO}_4 \cdot y\text{H}_2\text{O}$ , and  $\text{K}_2\text{NiFe}(\text{CN})_6$  give 34  $\text{mg}_{\text{Na}}/\text{g}$  and 21  $\text{mg}_{\text{Na}}/\text{g}$ , respectively (**Figure 19B**).

Some electrode materials, like  $\text{MoS}_2$ ,  $\text{Ti}_3\text{C}_2$ , and  $\text{Mo}_{1.33}\text{C}$ , have the ability of both cation and anion insertion.[37, 120, 121, 141, 142] Some of them present a capacitor-like (pseudocapacitive) electrical response during charge/discharge operation (**Figure 19C**).[143] Others show one or several redox peaks in the electrical response. Like the  $NUC$ , the chloride uptake capacity ( $CUC$ ) is also related to the electronic charge and can be calculated by use of **Equation 27**.

$$CUC = \frac{C_{sp}Mw_{Cl}}{F} \quad \text{Equation 27}$$

As depicted in **Figure 19D**, the ideal chloride ion removal of insertion materials stands between 18  $\text{mg}_{\text{Cl}}/\text{g}$  and 29  $\text{mg}_{\text{Cl}}/\text{g}$ . For example, few-layer  $\text{MoS}_2$  exhibits a charge storage capacity of 22 mAh/g (200 F/g) during positive polarization. Such capacity would give the  $CUC$  of 29  $\text{mg}_{\text{Cl}}/\text{g}$  when we assume a charge efficiency of 100%.[37, 119, 141]

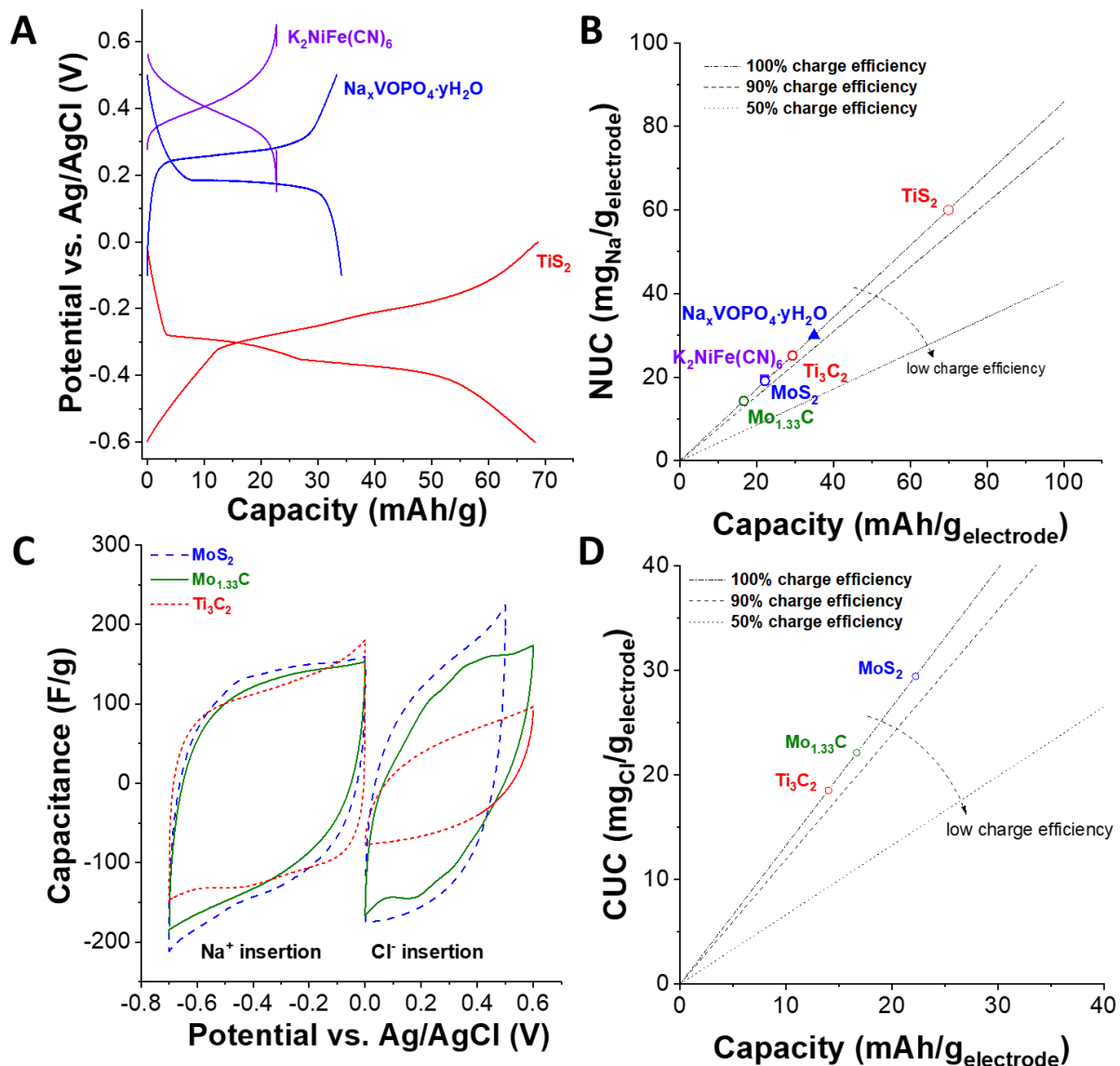


**Figure 19.** A) Galvanostatic charge/discharge profiles of three different insertion materials ( $TiS_2$ ,  $Na_xVOPO_4 \cdot yH_2O$ , and  $K_2NiFe(CN)_6$ ) in 1 M NaCl, B) calculated sodium removal according to the charge storage capacity of the materials, C) cyclic voltammogram of pseudo-capacitive insertion type materials ( $MoS_2$ ,  $Mo_{1.33}C$ , and  $Ti_3C_2$ ), and D) calculated chloride removal according to the charge storage capacity.

### 2.3.2.3. Cell charge balancing

Maximizing the desalination performance always requires careful charge balancing between the positive and the negative electrode. First, we shall consider materials with different charge storage capacity. For example, the theoretical capacity of graphite is 339 mAh/g while LiCoO<sub>2</sub> is 139 mAh/g. The maximized capacity of a graphite/LiCoO<sub>2</sub> cell assumes 1 g of graphite as an anode; thereby, the amount of LiCoO<sub>2</sub> would be 2.4 g. Accordingly, the total capacity of graphite/LiCoO<sub>2</sub> is 197 mAh/g (total mass is 3.4 g) at the fully charged state.[144] In the case of water desalination, the cell capacity must be maximized in the same way. For example, our work paired TiS<sub>2</sub> with activated carbon cloth. TiS<sub>2</sub> shows a maximum sodium ion insertion capacity of 70 mAh/g while activated carbon cloth delivers a maximum capacity of 20 mAh/g (**Figure 20A**). The ideal cell performance could be 30 mAh/g if the carbon to TiS<sub>2</sub> mass ratio was 3.5 at the cell voltage of 1.2 V (from -0.6 V to +0.6 V vs. Ag/AgCl). With the mass ratio of 5.5, TiS<sub>2</sub>/activated carbon cloth yield the cell capacity of 12 mAh/g at a cell voltage of 0.8 V (**Figure 20B**).[119] With such cell capacity, the resulting desalination capacity was measured to be 15 mg/g in 600 mM NaCl. As seen in **Figure 20C**, the desalination performance of TiS<sub>2</sub>/activated carbon cloth could bring the maximum performance of 33 mg/g when the charge between the positive electrode and the negative electrode is perfectly balanced (30 mAh/g).

Second, there are materials with identical charge storage capacity, such as symmetric cells based on MoS<sub>2</sub> or Mo<sub>1.33</sub>C MXene.[37, 141] For a voltage range up to 0.8 V, MoS<sub>2</sub> delivers an anodic and a cathodic capacity of 22 mAh/g (200 F/g) which allows a one-to-one mass ratio between positive electrode. This means that the cell capacity is of 22 mAh/g resulting in ideal desalination of 24 mg/g (**Figure 20C**). Mo<sub>1.33</sub>C MXene has a symmetric capacity of 17 mAh/g (150 F/g) corresponding to the desalination capacity of 15 mg/g at a cell voltage of 0.8 V.

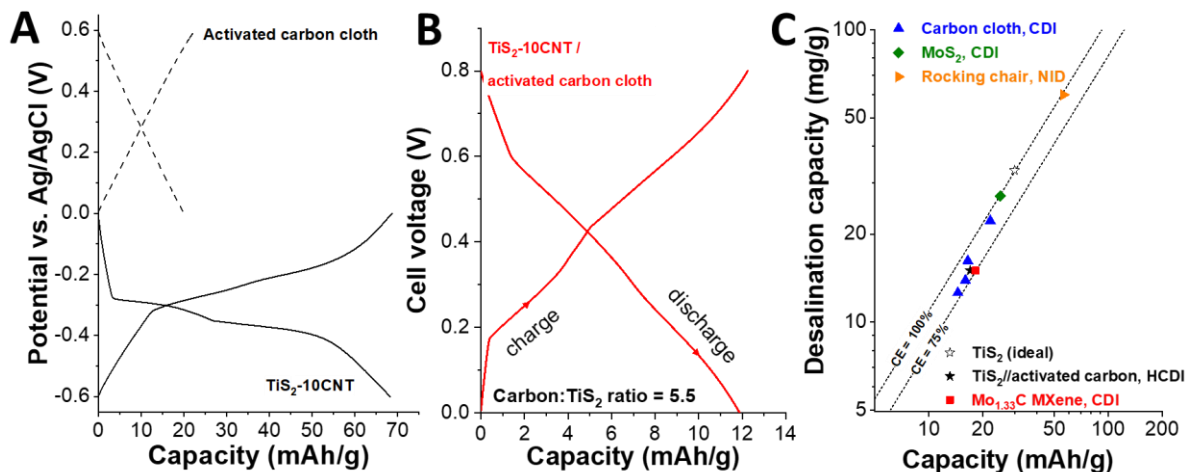


**Figure 20.** A) Galvanostatic charge/discharge of  $\text{TiS}_2$  and activated carbon cloth in 1 M NaCl at 0.1 A/g, B) Full-cell galvanostatic charge/discharge of  $\text{TiS}_2$ /activated carbon cloth in 1 M NaCl at 0.1 A/g, and C) relation between charge capacity and desalination capacity (CE = charge efficiency).

### 2.3.3. Ion-insertion electrode materials

Ion insertion materials for water desalination involve the insertion process of cation or anion into the interstitial site of the electrode materials. Most insertion materials are capable of cation insertion (e.g.,  $\text{Li}^+$ , and  $\text{Na}^+$ ) while some materials are capable of anion and cation insertion (e.g., MXenes). Robust crystal materials with large interstitial size may result in good cyclic stability, large ion storage capacity (high charge storage capacity), and fast kinetics (ion diffusion in the host material). Yet, the current state-of-the-art literature does not yet provide a rigorous confirmation or disavowing of these basic assumptions.[138]

We can classify ion insertion materials when considering the dimensionality of the insertion sites (**Figure 21**). One-dimensional (1-D) insertion materials show a tunnel structure (**Figure 21A**) with channels for the ion transport resulting from the connection between the polyhedral transition metal and oxygen, like  $\text{Na}_{0.44}\text{MnO}_2$ , or connections between tetrahedral of oxygen phosphate and polyhedron of metal and oxygen, like  $\text{NaTi}_2(\text{PO}_4)_3$ . Two-dimensional (2-D) insertion materials are layered materials like polyanion phosphates (hydrous and anhydrous), layered transition metal carbides, transition metal oxide, or layered transition metal chalcogenides (**Figure 21B**). These materials accommodate inserted ions between in-plane layers.[145]

Three-dimensional (3-D) insertion structures, for example, inorganic framework materials like Prussian blue, or NASICON-type materials (**Figure 21C**) have an open framework or cage-like structure, ions can be inserted from all direction and possess large spacing for ion accommodation. Based on those above, the next sections will outline different insertion materials.

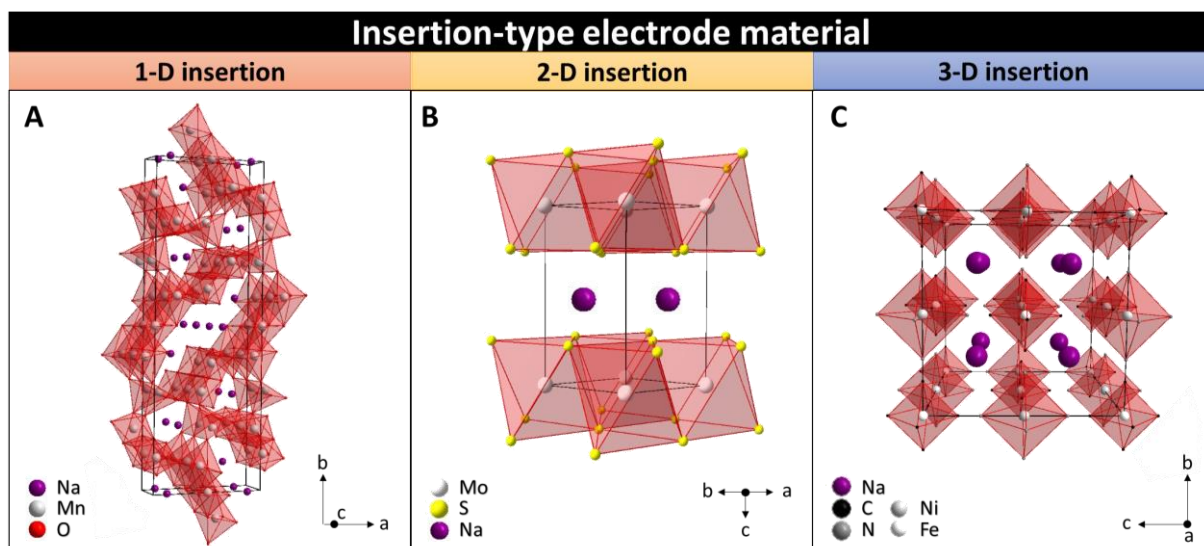


**Figure 21.** Examples for different ion insertion material classes showing the crystal structure for sodium insertion A) one-dimensional (1-D) sodium insertion into channels of  $\text{Na}_{0.44}\text{MnO}_2$ , B) two-dimensional (2-D) sodium insertion between layers of  $\text{MoS}_2$ , and C) three-dimensional sodium insertion into specific sites of cage-like  $\text{NaNi}(\text{Fe}(\text{CN})_6)$ .

### 2.3.3.1. 1-D insertion materials

#### 2.3.3.1.1. *Sodium manganese oxide*

There exist several types of Na-Mn-O compounds which have been explored for sodium-ion battery applications.[139] For example,  $\text{Na}_{0.44}\text{MnO}_2$  shows a three-dimensional structure having a space group of *Pbam*. Its crystal structure of  $\text{Na}_{0.44}\text{MnO}_2$  is built by  $\text{MnO}_6$  octahedral subunits and  $\text{MnO}_5$  square-pyramidal sites. Each unit cell contains a large ion tunnel with four sodium sites (S-type tunnel) and two pentagonal tunnels.[146] The pentagonal site is rather small and filled with sodium while the larger site is mostly half-filled, resulting in a charge storage capacity in an aqueous solution of 30-50 mAh/g.[147, 148]  $\text{Na}^+$  ions in both sites are highly mobile along the c-direction, but full insertion and de-insertion operation in aqueous solution leads to instability of the structure and subsequently capacity fading.

Within the stable potential range between -0.2 V and +0.6 V vs. Ag/AgCl, the reversible sodium uptake is 0.4 mol as accomplished the crystallographically distinct sites of the S-type tunnels.[33] The first report of  $\text{Na}_{0.44}\text{MnO}_2$  for water desalination by Pasta et al. demonstrated 50% salt removal in simulated seawater containing  $\text{Na}^+$ ,  $\text{K}^+$ ,  $\text{Mg}^{2+}$ ,  $\text{Ca}^{2+}$ ,  $\text{Cl}^-$ , and  $\text{SO}_4^{2-}$ . [116] This indicates that such material is not only  $\text{Na}^+$  selective but also allows the uptake of  $\text{K}^+$ ,  $\text{Mg}^{2+}$ , and  $\text{Ca}^{2+}$ . Later, Lee et al. coupled  $\text{Na}_{0.44}\text{MnO}_2$  with activated carbon, which has an anion-exchange membrane on top of it. [117] With the electrode potential between 0 V and 0.8 V vs. Ag/AgCl,  $\text{Na}_{0.44}\text{MnO}_2$  shows a charge storage capacity of 40-50 mAh/g corresponding to a desalination performance of 31 mg/g at the cell voltage of  $\pm 1.2$  V in 10 mM NaCl. In 2017, a similar concept was introduced by using  $\text{Na}_{0.44}\text{MnO}_2$  and AgCl electrode. [149] The authors applied the cation and anion-exchange membrane on top of  $\text{Na}_{0.44}\text{MnO}_2$  and AgCl, respectively. As a result, the desalination performance in 15 mM NaCl is of 57 mg/g using cell voltage of -1 V and +1.5 V. Not only  $\text{Na}_{0.44}\text{MnO}_2$  can be paired with AgCl but also BiOCl; as reported by Chen et al. [123], within the cell voltage of  $\pm 1.5$  V, such cell configuration showed a desalination performance of 69 mg/g in 13 mM NaCl.

#### 2.3.3.1.2. Tunnel-structure manganese oxide

Within the manganese oxide family, there are many tailorable tunnel structures. Tunnel-structured manganese oxides are built from octahedral  $\text{MnO}_6$  subunits sharing vertices and edges. It possesses different tunnel size and shapes, providing a large crystallographic volume for ion insertion. For example, hollandite  $\text{MnO}_2$  or  $\alpha\text{-MnO}_2$  consists of 4 octahedra  $2 \times 2$   $\text{MnO}_6$  per one tunnel creating a tetragonal structure with the space group of  $I4/m$ . Todorokite  $\text{MnO}_2$  exhibits a similar structure as hollandite  $\text{MnO}_2$ . It has a larger tunnel size than hollandite which constructs from  $3 \times 3$  octahedra  $\text{MnO}_6$  subunits having a monoclinic structure with a space group of  $P2/m$ . [150] By altered synthesis methods, the number of subunit octahedral can be controlled, resulting in larger tunnel size. For example,  $2 \times 3$  tunnel (romanechite), and  $2 \times 4$  tunnel  $\text{MnO}_2$ . Also, the large tunnel is usually filled with positively charged ions, like lithium, potassium, and sodium, and/or water molecules to maintain the structure. [151] Thereby, it has excellent potential for electrochemical ion exchange, energy storage, and separation technique.

The electrochemical signature of such  $\text{MnO}_2$  tunnel-structures is different to  $\text{Na}_{0.44}\text{MnO}_2$ : instead of multiple broad redox peaks seen during cyclic voltammetry,[33] tunnel-structured  $\text{MnO}_2$  typically shows a rectangular cyclic voltammogram with the specific capacitance of around 200-300 F/g.[150, 151] Such high specific capacitance would translate to the desalination capacity of 45 mg/g at 100% charge efficiency.

So far, there have been only a few works regarding tunnel structure  $\text{MnO}_2$  for water desalination. For example, Byles et al. studied the difference tunnel structure  $\text{MnO}_2$  in HCDI. In 15 mM NaCl with an applied cell voltage of  $\pm 1.2$  V, hollandite  $\text{MnO}_2$  shows a desalination capacity of 22 mg/g while the todorokite  $\text{MnO}_2$  provided 23 mg/g. By increasing the size of the tunnel  $2 \times n$   $\text{MnO}_2$  (hybrid phase where  $n=2,3,4$ ) is capable of  $\text{Mg}^{2+}$  ion insertion with the latter being about 2-times higher than that of hollandite or todorokite  $\text{MnO}_2$ . [152] Recently, Leong et al. reported hollandite  $\text{MnO}_2$  to have a desalination capacity of 10 mg/g in 5 mM NaCl when using a cell voltage between -0.6 V and +1 V. [150]

### 2.3.3.2. 2-D insertion materials

#### 2.3.3.2.1. *Layered metal carbides/nitrides (MXene)*

MXenes are of the most recent 2D materials, being introduced in 2012.[153] Their general formula is  $M_{n+1}X_nT$  ( $n=1,2,3$ ) where  $M$  refer to an early transition metal such as Ti, Mo, or Nb,  $X$  represent carbon and/or nitrogen, and  $T$  is the surface termination (usually fluoride, or oxygen). The chemical structure of MXene depends on the original ternary metal carbides/nitrides (MAX-phases; A stands for elements in group 13 or 14). Based on the composition of the corresponding MAX-phase, there are mainly three different types, namely  $M_2AX$  (211 phase),  $M_3AX_2$  (312 phase), and  $M_4AX_3$  (413 phase).[154] Because the M-A bond is weaker than that of M-X, the use of strong etchants like HF acid leads to selective removal of A atoms from the MAX structure, leaving behind the 2-D  $M_{n+1}X_nT$ . [155] The chemical structure of MXene depends on the MAX-precursor: 211 MAX results in  $M_2XT$  which is the thinnest layer among other MXenes with 3 atoms (M-X-M) in one layer. Etching 312 MAX leads to  $M_3X_2T$  with 5 atoms per MX-layer. 413 MAX is transformed into  $M_4X_3T$  which is the thickest MXene.

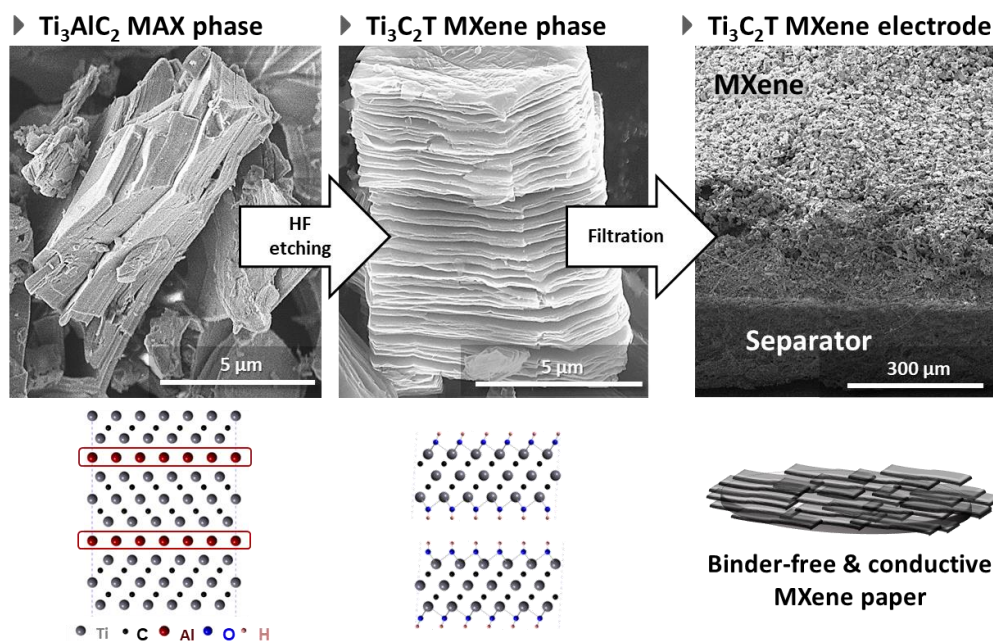


**Figure 22.** Conversion of  $\text{Ti}_3\text{AlC}_2$  MAX into  $\text{Ti}_3\text{C}_2\text{T}$  MXene via HF etching. The resulting layered material is conveniently converted to an MXene paper electrode without the use of polymer binder via filtration. Adopted from Ref. [120, 153].

Most MXenes show a hexagonal close-packed structure. The ordered of each MXene sheet  $\text{M}_2\text{XT}$  follows ABAB fashion while MXene derived from 312 and 413 MAX phases exhibit ABCABC ordering. Similar to graphene and other 2-D materials, the stacking number, and surface terminations of MXenes determine the resulting properties (including the electrical conductivity).[156-158]

MXenes store charge via ion insertion, usually by showing a pronouncedly pseudocapacitive response.[159] It shows not only high volumetric and gravimetric capacitance but also high power handling due to its high electrical conductivity[33, 160, 161] and nanoconfinement of interlayer water.[162] The latter is believed to improve the ion insertion kinetics.[107] The first MXene used for desalination was  $\text{Ti}_3\text{C}_2$  produced by HF etching of  $\text{Ti}_3\text{AlC}_2$  yielding a desalination capacity of 13 mg/g at a cell voltage of 1.2 V in 5 mM NaCl.[120] It was found that  $\text{Ti}_3\text{C}_2$  MXene is not only capable of cation insertion but also anion insertion in aqueous media. However, due to its negative surface termination via fluoride and oxygen, the specific capacitance at the positive polarization (84 F/g) is 2-fold lower than the negative polarization (176 F/g). Thereby, the anion insertion capacity of this MXene is lower than the cation insertion capacity.

By further improving the microstructure of  $\text{Ti}_3\text{C}_2$  by cryo-drying, the desalination performance was increased to 45 mg/g at a cell voltage of 1.2 V for 170 mM NaCl.[142]  $\text{Mo}_{1.33}\text{C}$  was the first report for using MXene in highly concentrated saline solution.[141] It was synthesized by HF etching of  $(\text{Mo}_{2/3}\text{Sc}_{1/3})_2\text{AlC}$  to result in so-called divacancy-ordered MXene.  $\text{Mo}_{1.33}\text{C}$  exhibits a symmetrical specific capacitance of 150 F/g for both positive and negative polarization which translates to a desalination capacity of 15 mg/g at a cell voltage of 0.8 V for aqueous 600 mM NaCl.

#### 2.3.3.2.2. *Transition metal dichalcogenides (TMDs)*

Transition metal dichalcogenides (TMDs) are layered materials built from the in-plane covalent bonding between a transition metal and chalcogen (e.g., S, Se, Te). Its typical chemical formula is  $\text{MX}_2$ , where M represents a transition metal, and X stands for chalcogen. In equivalent to the graphite layer, the bulk TMDs layers are held together by Van der Waals force allowing the exfoliation process. As a result of the exfoliation process, its electronic property can be altered to range between semiconductor and conductor.[163] Each of the TMD layers consists of a stack of 3 atoms, that is, X-M-X.

The exfoliation process can result in different phases as compared to the bulk (multilayer) TMDs.[164] Taking  $\text{MoS}_2$  as an example, the crystal structure of  $\text{MoS}_2$  are four types depending on the coordination between Mo and S and the stacking order. The 2H- $\text{MoS}_2$  phase occurs for bulk materials and is a close-packing hexagonal structure (trigonal prismatic coordination) with the ABA layer ordering. When achieving a single layer of  $\text{MoS}_2$ , the resulting 1H phase shows the same Mo-S coordination, but with octahedral coordination and tetragonal symmetry. The 1T- $\text{MoS}_2$  layer ordering differs from 2H- $\text{MoS}_2$ : Instead of ABA, 1T- $\text{MoS}_2$  has an ABC stacking order. The transition from bulk to a few layers or single layer  $\text{MoS}_2$  shows an unusual electronic structure due to the free electron in the d orbital of molybdenum. Several studies confirm that the indirect bandgap of bulk 2H- $\text{MoS}_2$  transforms into a direct bandgap in single-layer 1T- $\text{MoS}_2$ . [165-167]

1T- or single-layer 2H-MoS<sub>2</sub> have been explored as electrode materials for energy storage, especially for lithium-ion or sodium-ion batteries, and supercapacitors.[168-173] For example, MoS<sub>2</sub> is giving a pseudocapacitive electrochemical response in an aqueous system with 100-400 F/g depending on the synthesis and degree of exfoliation.[172, 174-178]. As for desalination applications, chemically-exfoliated MoS<sub>2</sub> using N-butyllithium show desalination capacity of 8 mg/g in 400 mM NaCl at a cell voltage of  $\pm 1.2$  V.[121] Electrochemical exfoliated of MoS<sub>2</sub> entangled by carbon nanotubes shows an even better performance with a desalination capacity of 25 mg/g in aqueous 500 mM NaCl at a cell voltage of 0.8 V.[37] 1T-TiS<sub>2</sub> accomplishes a desalination capacity of 15 mg/g in 600 mM NaCl at a cell voltage between 0.2 V and 0.8 V without the need for electrochemical activation.[119] The structure 1T-TiS<sub>2</sub> is also cation-selective without the ability to insert anions [137], allowing the pairing of the TMD for cation-removal with nanoporous carbon for anion-removal without the use of an ion exchange membrane.

#### 2.3.3.2.3. Layered transition metal oxides

There exist various layered transition metal oxides, typically falling into the category of dioxides, trioxides, or pentoxides. Many metal trioxides have a layered structure with the governing formula MO<sub>3</sub>, where M is the transition metal (e.g., Mo, Ta, and W).[179-181] For example, MoO<sub>3</sub> is predominantly composed of octahedra MoO<sub>6</sub> in the orthorhombic space group *Pcmn*. [182, 183] Each layer is held by Van der Waals forces having either interlayer water or interlayer cations. Perovskite metal oxides are another large family of layered metal oxide. They have general formula ABO<sub>3</sub>, where A is the occupied ion in the lattice site (e.g., Ca, and Ba), B is the transition metal bonded to oxygen. Cubic perovskite can be prepared by layer-by-layer deposition, followed by exfoliation and stabilization.[180, 184]

Orthorhombic hydrated vanadium pentoxide (h-V<sub>2</sub>O<sub>5</sub>) is composed of trigonal bipyramidal polyhedra [133] and can be prepared by electrodeposition of vanadyl sulfate solution onto the multiwall carbon nanotubes paper. The materials show an insertion-type pseudocapacitive feature with the specific capacitance of 250 F/g in 1 M NaCl. In the membrane CDI cell configuration, the desalination capacity was measured 25 mg/g in 600 mM NaCl solution at a cell voltage of -0.4 V to +0.8 V.[140]

MnO<sub>2</sub> materials with a layered structure based on edge-sharing MnO<sub>6</sub> octahedra also been explored for electrochemical desalination.[185] Birnessite MnO<sub>2</sub> synthesized onto the reduced graphene oxide was investigated for the first time in 2014.[186] The material showed a specific capacitance of 300 F/g in 1 M NaCl. By employing MnO<sub>2</sub> as the positive electrode and activated carbon as the negative electrode, the desalination capacity was 5 mg/g in 100 mM NaCl at a cell voltage of 1.2 V. In other work, layered MnO<sub>2</sub>-CNTs composites were shown to yield a capacitance of 140 F/g in 0.5 M NaCl, which translated to a desalination capacity of 6.7 mg/g at a cell voltage of 1.8 V in aqueous 0.5 mM NaCl.[187] A well-ordered buserite MnO<sub>2</sub> can be obtained by ion exchange of Na-birnessite MnO<sub>2</sub>. It exhibits large d-spacing of 0.97 nm, which results in higher desalination capacity (37 mg/g) as compared with Na-birnessite MnO<sub>2</sub> (31 mg/g).[188]

### 2.3.3.3. 3-D insertion materials

#### 2.3.3.3.1. *Prussian Blue and Prussian Blue analogs*

A<sub>x</sub>Fe[Fe(CN)<sub>6</sub>]<sub>z</sub>·nH<sub>2</sub>O (Prussian Blue, PB) has a 3-D open organometallic-like framework resulting from low spin Fe<sup>2+</sup> and high spin Fe<sup>3+</sup> coordinated to carbon and nitrogen of cyanide anions (CN<sup>-</sup>), respectively. It has a face-centered cubic structure with a space group Fm $\bar{3}$ m.[189]. The interstitial site is usually occupied by the alkaline ion (A; e.g., Na or K) or crystal water depending on the condition of preparation.[190, 191]

So far, various Prussian blue analogs have been explored.[192, 193] For example, by replacing Fe<sup>2+</sup> in the structure with Ni<sup>2+</sup>, the nickel-analog (A<sub>x</sub>NiFe(CN)<sub>6</sub>) can be prepared.[194, 195] More complex Prussian blue analog structures can be prepared by replacing Fe<sup>2+</sup>/Fe<sup>3+</sup> with another transition metal. For example, Mn<sub>3</sub>[Co(CN)<sub>6</sub>]<sub>2</sub>·nH<sub>2</sub>O is produced by the precipitation of K<sub>3</sub>[Co(CN)<sub>6</sub>]<sub>2</sub> and Mn(CH<sub>3</sub>COO)<sub>2</sub>·4H<sub>2</sub>O.[196]

PB and its analogs show interesting electrochemistry due to the redox activity of the metals within the framework. Thus, the chosen transition metal determines the redox potential. For example,  $\text{Na}_2\text{Ni}[\text{Fe}(\text{CN})_6]_2$  shows a redox activity in aqueous  $\text{Na}_2\text{SO}_4$  at +0.4 V vs. Ag/AgCl while the redox potential of  $\text{Na}_2\text{VO}_x[\text{Fe}(\text{CN})_6]_2$  is at +0.9 V vs. Ag/AgCl.[193]

For water treatment,  $\text{Na}_x\text{Ni}[\text{Fe}(\text{CN})_6]$  was coupled with the  $\text{Na}_x\text{Fe}[\text{Fe}(\text{CN})_6]$  in the NID cell and showed a desalination capacity of 60 mg/g at a cell voltage of 0.8 V using simulated seawater.[125]  $\text{Na}_2\text{NiFe}(\text{CN})_6$  was paired with  $\text{NaNiFe}(\text{CN})_6$  in a CID cell; using aqueous 20 mM NaCl, such a cell delivered a desalination performance of 35 mg/g at a cell voltage of  $\pm 1.2$  V.  $\text{K}_{0.03}\text{Cu}[\text{Fe}(\text{CN})_6]_{0.65} \cdot 0.43\text{H}_2\text{O}$  was reported to exhibit a specific capacity of 40 mAh/g. When applied such material in the conventional CDI cell with an activated carbon counter-electrode, it showed desalination performance of 23 mg/g in brackish water.[197] Nanoparticles of  $\text{Fe}_4[\text{Fe}(\text{CN})_6]_3 \cdot x\text{H}_2\text{O}$  decorated on reduced graphene were synthesized by using hydrothermal method; using a membrane CDI cell, the material exhibited a large desalination capacity of 130 mg/g in aqueous 42 mM NaCl at a cell voltage of  $\pm 1.4$  V.[198]

#### 2.3.3.3.2. Polyanionic phosphates

The 3-D framework built on the transition metal and polyanion phosphate ( $\text{PO}_4^{3-}$ ) is known as the NASICON (sodium superionic conductors) phosphates. It has a chemical formula of  $\text{A}_x\text{MM}'(\text{PO}_4)_3$  where A is the sodium ion, and M/M' are transition metals. The number of sodium in the structure is altered by the oxidation state the transition metal.[199] NASICON can accommodate up to three sodium atoms per unit cell, giving rise, for example, to  $\text{Na}_3\text{V}_2(\text{PO}_4)_2$ [200], and  $\text{Na}_3\text{Ti}_2(\text{PO}_4)_3$ .[201, 202]

For desalination, nanocomposite  $\text{NaTi}_2(\text{PO}_4)_3$ /reduced graphene oxide was synthesized via one-pot hydrothermal, and the resulting material was operated in a conventional membrane CDI cell using activated carbon as the anion removal electrode.[203] By applying a cell voltage of  $\pm 1.4$  V, the cell exhibited desalination performance in 17 mM NaCl of 120 mg/g.[203] Further,  $\text{NaTi}_2(\text{PO}_4)_3$  can be paired with BiOCl instead of carbon material to allow the desalination without the aid of membranes.[204] Another system was reported by using  $\text{NaTi}_2(\text{PO}_4)_3$ /reduced graphene oxide paired with nanoparticulate Ag/reduced graphene oxide; this configuration delivered a desalination capacity of 105 mg/g at a cell voltage between -1.2 V and +1.4 V in aqueous 42 mM NaCl.[205] Further,  $\text{Na}_3\text{V}_2(\text{PO}_4)_3$ /carbon core-shell material was studied in a membrane CDI cell having active carbon as the chloride ion removal electrode. It showed a large desalination capacity of 137 mg/g in 100 mM NaCl at a cell voltage of 1 V.[206]  $\text{Na}_3\text{V}_2(\text{PO}_4)_3$  was also coupled with an AgCl electrode in the membrane CDI cell allowing 108 mg/g desalination in 17 mM NaCl (cell voltage  $\pm 1.4$  V).[207]

#### 2.3.3.3.3. *Summary*

Desalination electrode towards insertion Faradaic material is highly promising to achieve a large desalination capacity. More importantly, Faradaic materials work very well in high ionic concentration where carbon materials fail to desalinate. Yet, actual desalination applications require much more rigorous testing of the performance stability and robustness in impurity-rich aqueous environments. Further concerns of the potential impact of the materials relate to costs, material availability, and chemical stability via the possible release of non-harmless compounds.

## 2.4. Electrochemical desalination via reconstitution/conversion reactions

### 2.4.1. *Concept and mechanism*

Instead of immobilizing an ion via electrosorption or insertion, ion removal can also be accomplished by a reconstitution reaction (conversion reaction). Thereby, the ion uptake triggers a significant change in the crystal structure of the host material, giving rise to a new compound.

There are two different types of conversion reactions, namely the formation type and the displacement type. According to Huggins,[208] the formation reaction leads to the formation of a new phase within the atomic constituents (**Figure 23A-B**). The best-known formation reaction is the silver/silver chloride redox couple (**Figure 23B**). Upon oxidation, the chloride ion reacts with bulk Ag, leading to breaking of the original Ag-Ag bond and the formation of AgCl. For Ag/AgCl, this process is accompanied by a large volume change, and repeated charge/discharge operation typically leads to the loss of initial grain boundaries and particle coarsening. Displacement reactions also cause significant phase changes. However, instead of just one new phase as a product, displacement reactions result in more than one phase. As exemplified in **Figure 23D**, FeF<sub>2</sub> in a lithium-ion battery is undergoing a displacement reaction by exchanging Fe by Li in the structure. Subsequently, LiF<sub>2</sub> and metallic Fe are being formed.[209] So far, only a few conversion or reconstitution materials have been explored for electrochemical desalination, including Ag/AgCl and Bi/BiOCl.[127, 204]

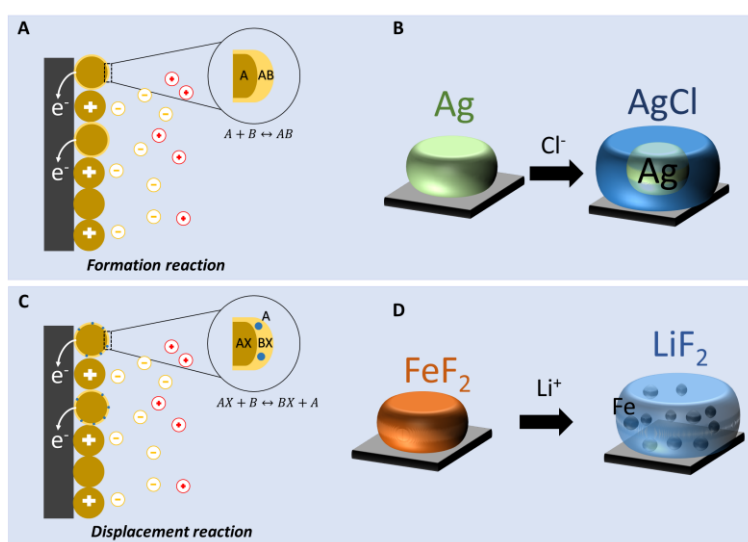


**Figure 23.** Mechanism of ion removal via reconstitution reaction (conversion reaction) A-B) represent the mechanism of formation reaction and its example (Ag/AgCl), C-D) illustration of displacement reaction and its example (FeF<sub>2</sub>/LiF<sub>2</sub>+Fe).

### *2.4.3. A brief history of conversion materials for water desalination*

The first use of a conversion material for water desalination has been documented for AgCl. Blair and Murphy investigated carbon and functionalized carbon paired with electrochlorinated (oxidized) silver mesh by use of a hybrid capacitive deionization cell in 1960.[22] This pairing allowed the authors to focus on the sodium removal by the carbon electrode while chlorine removal was accomplished by the reversible Ag/AgCl reaction.

With a few decades not further exploring this concept, the first work using Ag/AgCl again was published by Pasta et al. in 2012.[116] In the latter work, the authors introduced the desalination battery consisting of  $\text{Na}_{2-x}\text{Mn}_5\text{O}_{10}$  as sodium removal electrode via ion insertion and the Ag/AgCl reaction for the chloride removal electrode without the use of any membrane. The desalination battery showed an ability to desalinate at a high salt concentration (seawater) with low energy consumption. The work of Pasta et al. did not provide actual values for the desalination capacity; yet, the follow-up work of Chen et al. using the same pairing of sodium manganese oxide and Ag/AgCl in 2017 yielded 57 mg/g when cycling the cell voltage from -1.0 V to +1.5 V.[149]

Another hybrid CDI system was reported by Yoon et al. in 2017.[210] In their work, they enhanced the chlorine-removal ability of nanoporous activated carbon by deposition of sub-micrometer silver particles via  $\text{AgNO}_3$  decomposition. Paired with non-modified activated carbon shielded by a cation-exchange membrane, the hybrid CDI system yielded a desalination capacity of 17 mg/g for the highest loading of Ag when cycling between -0.7 V and +0.7 V in aqueous 10 mM NaCl.

In 2012, Gryglowicz-Pawlaw et al. proposed a desalination cell with the symmetric pairing of the Ag/AgCl and AgCl/Ag reactions.[127] This concept basically is the exact inversion of the Na-ion desalination (NID) introduced in 2016. Gryglowicz-Pawlaw et al. employed a silver electrode coated by a cation-exchange membrane (sulfonated tetrafluoroethylene fluoropolymer copolymer, Nafion) to desalinate aqueous 600 mM NaCl. The underlying mechanism is the depletion of chlorine at the Ag-side of the cell, upon which Na-ion cross the Nafion membrane to charge-balance the aqueous environment into which Cl-ions are released via the AgCl reaction. Thereby, a concurrent effluent stream pair of desalinated and salinated water is created, just like by use of the NID technology. The Ag/AgCl system with a Nafion membrane was also adopted for an on-chip desalination system designed by Figuera et al. in 2017.[128]

In 2016, Yuan-Cheng Tsai and Ruey-An Doong revisited the concept of Blair and Murphy by using Ag nanoparticle (ca. 30 nm) confined in the hierarchically ordered mesoporous carbon paired with activated carbon.[211] In the absence of an ion-exchange membrane, the cell accomplished a desalination capacity of 20 mg/g which is 2.8-fold better than that of just carbon in 1 mM NaCl at a cell voltage of 1.2 V. Ag can also be paired with Faradaic materials. For example,  $\text{NaTi}_2(\text{PO}_4)_3$  coupled with Ag nanoparticle in the membrane capacitive deionization cell showed a desalination capacity of 105 mg/g in 42 mM NaCl for a cell voltage cycled between -1.2 V and +1.4 V.[205] Further, the pairing of  $\text{Na}_3\text{V}_2(\text{PO}_4)_3$ /reduced graphene oxide aerogel with AgCl/reduced graphene oxide aerogel and by use of an ion-exchange membrane pair provided a desalination capacity of 108 mg/g in 17 mM NaCl when cycling the cell voltage at  $\pm 1.4$  V.[207]

The first conversion-type material outside the scope of Ag/AgCl to be explored for desalination was Bi/BiOCl, as introduced by Do-Hwan Nam and Kyoung-Shin Choi.[204] Bi was used for chloride removal and coupled with  $\text{Na}_3\text{Ti}_3(\text{PO}_4)_3$  in 600 mM NaCl, but no desalination capacity values were provided. Later work by Chen et al. paired the Bi/BiOCl redox couple with  $\text{Na}_{0.44}\text{MnO}_2$  for sodium removal using a pair of anion- and cation-exchange membranes.[123] With the aid of cation and anion-exchange membrane, the cell delivered a desalination capacity of 68 mg/g in 13 mM NaCl at a cell voltage of  $\pm 1.4$  V.

## 2.5. Electrochemical desalination via redox electrolytes

All desalination concepts presented so far immobilize salt ions either by electrosorption or by Faradaic reactions. However, it is also possible to capitalize on the large charge transfer capacity of redox-active ions dissolved in an electrolyte. As shown in **Figure 24**, the redox-active dissolved ion (e.g., iodide ion, ferricyanide, etc.) can change the oxidation state by accepting or ejecting of an electron at the solid/liquid interface. This feature is widely applied with redox flow batteries and finds more and more of use in redox-enabled supercapacitors.[56, 212, 213] Once the electrode is electrified, the highly mobile redox-active ion diffuses close to the electrode interface and rapidly transfers an electron to the electrode. Per the short diffusion pathlength and the nanoconfinement of the redox-active ion within electrically conductive carbon, this process can be very fast and even outperform conventional ion electrosorption.[212] Subsequently, the oxidation state of the redox-active ion changes and the latter may diffuse away from the solid/liquid interface.[213]



### 3. Outline and scope of this thesis

Capacitive deionization based on ion electrosorption peruse of carbon electrodes has constantly been improved since the 1960s. These developments include research on novel carbon nanomaterials, pore structure optimization, manufacturing of electrodes, cell design, and the corresponding basic understanding of the ion electrosorption process both by use of in situ experiments and modeling. However, even the best state-of-the-art materials and cells cannot remedy capacitive deionization from its intrinsic bias towards low molar strength and the limited charge storage capacity of capacitive carbons. Further, carbon ages rapidly when the feedwater stream contains dissolved oxygen at levels typical for real-world surface water. Clearly, it is important to find ways to overcome these limitations and to find better ways to capitalize on electrochemical processes. The latter hold the promise of energy efficient desalination because most of the invested charge can be used for ion removal and is conveniently recovered during the discharging step. Therefore, my work was motivated by the challenge to go beyond carbon-based capacitive deionization and to gain a glimpse in the future of electrochemical desalination technologies.

A graphical depiction of the four main segments of my work can be seen in **Figure 25**, referring to enhancing carbon (**first segment**), using two-dimensional layered electrode materials (**second segment**), using a conversion reaction material (**third segment**), and using redox-active electrolytes in combination with nanoporous carbon (**fourth segment**).

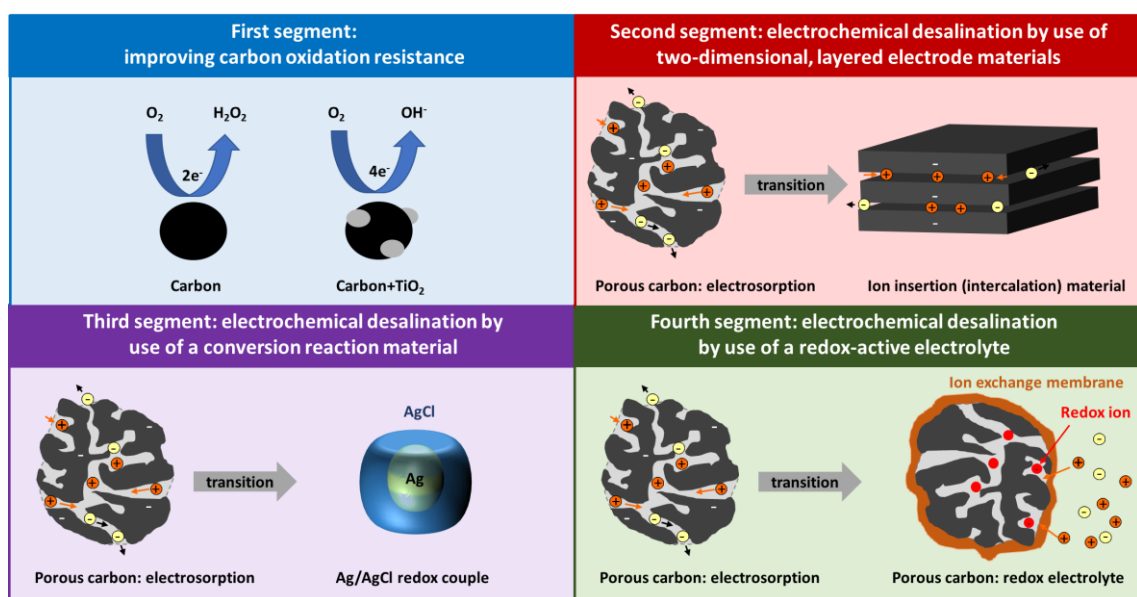


**Figure 25.** Overview of the three main segments of this dissertation.

The **first segment** of my doctoral research explored how to turn-off the rapid aging of carbon in an aqueous environment (**Chapter 4.1** and **Chapter 4.2**). From the literature, it is known that the oxygen reduction reaction (ORR) causes oxidation of the positively polarized electrode when the aqueous medium is not de-aerated. We chose high surface area activated carbons for decoration with titania nanocrystals peruse of sol-gel synthesis to selectively modify the ORR mechanism (**Chapter 4.1**). Our findings were based on kinetic analysis of the ORR process and the quantitative analysis of the cycling desalination performance. Titania-decorated activated carbons showed a significantly improved desalination capacity and significantly improved performance stability. However, we failed to completely avoid carbon oxidation and overall performance decay. The key limiting factor was the inability to reach all the carbon surface area, which is, in case of activated carbon, mostly contained as intraparticle pores. Therefore, we decorated carbon black with titania (**Chapter 4.2**). This choice was based on the much smaller size of the particles, the outer surface area, and the easier access of the surface. Although the overall desalination capacity was moderate (7 mg/g), we were able to obtain stable performance over 100 operation cycles in oxygen-saturated brackish water.

The **second segment** of my work explores two-dimensional materials capable of ion intercalation for electrochemical desalination (**Chapter 4.3-4.8**). Our electrode materials can be classified as MXene (**Chapter 4.3-4.4**), transition metal dichalcogenide (**Chapter 4.5-4.7**), and layered metal phosphate (**Chapter 4.8**).

- Among MXene materials, we first explored  $\text{Ti}_3\text{C}_2$  as the first proof-of-concept for a symmetric cell (**Chapter 4.3**). In this chapter,  $\text{Ti}_3\text{C}_2$ -MXene accomplishes on the positively polarized side chlorine insertion, while the negatively polarized side is subjected to sodium insertion. The presence of negative interlayer charges causes a strong bias towards cation insertion and an accordingly enhanced capacitance for the negative electrode. The desalination performance at low molar strength was at the same level as nanoporous carbon.  $\text{Mo}_{1\frac{1}{2}}\text{C}$ -MXene does not have negative interlayer charges, and the resulting capacitance values are virtually identical for positive and negative polarization (**Chapter 4.4**). The desalination capacity increases when the salt concentration is increased from brackish water to seawater concentration, while for activated carbon, the exact opposite is found. We also tracked the removal of sodium and the removal of chlorine by use of online monitoring via inductively coupled plasma optical emission spectroscopy (ICP-OES) to confirm the ability of MXene to insert cations and anions.

- In **Chapter 4.5-4.7**, transition metal dichalcogenides (TMDs), will be explored. MoS<sub>2</sub> is originally in the bulky form (multilayers) showing poor electrical conductivity. Therefore, in **Chapter 4.5**, a binder-free composite electrode composed of exfoliated MoS<sub>2</sub> and carbon nanotubes is used for electrochemical desalination. We compared the performance of the electrodes with the desalination via activated carbon at low and high molar strength (5-500 mM NaCl). Our data show the increased desalination performance, accompanied by an increased charge efficiency) for remediation of water by use of MoS<sub>2</sub>-CNT electrodes. In contrast, activated carbon effectively loses its desalination capability at molar concentrations exceeding 100 mM NaCl. Our work includes in situ Raman spectroscopy to track the structural changes during chlorine and sodium insertion processes. While MoS<sub>2</sub> shows a pseudocapacitive charge/discharge profile owing to its ability to insert cations and/or anions, TiS<sub>2</sub> is only capable of hosting cations and shows two redox peaks during sodiation (and two corresponding peaks during desodiation). **Chapter 4.6** explores TiS<sub>2</sub>-CNT composites for sodium-removal. The asymmetrical cell design paired with an activated carbon counter electrode, the resulting asymmetric cell design accomplished 14 mg/g NaCl removal, which was carried by a sodium-removal capacity of 36 mg/g of TiS<sub>2</sub>. The sharp redox peaks were then explored in a different context as well. In **Chapter 4.7**, we capitalized on the different sodium insertion potentials for different cations to accomplish ion selectivity by simply operating the desalination cell at different cell voltages. We exemplified this novel approach to ion selectivity by tuning the desalination cell between Cs- and Mg-uptake.
- To highlight the variety of ion insertion materials with a layered structure, we investigated hydrated vanadyl phosphate (Na<sub>x</sub>VOPO<sub>4</sub>·yH<sub>2</sub>O) for electrochemical water desalination in **Chapter 4.8**. The material synthesis was accomplished by applying a hydrothermal process, and the cell employed an ion exchange membrane and an activated carbon counter electrode. We used this study to investigate the possible contamination of the effluent stream by vanadium and/or phosphorus; however, the use of an ion exchange membrane effectively prevented both.

The **third segment** demonstrates the very high desalination capacity that can be achieved for salt removal via conversion reactions. In **Chapter 4.9**, we present the facile and well-known Ag/AgCl redox couple and used a two-channel CID setup. With a charge capacity exceeding 200 mAh/g in theory, the material system should theoretically provide a desalination capacity of about 200 mg/g. However, per grain coarsening, the system sees a rapid performance decrease from 190 mg/g to 115 m/g; the latter remains a very high value and is accomplished by a cell voltage difference of only 0.2 V.

The **fourth segment** explores a process that accomplishes ion removal (in this case: sodium-ion removal) by balancing the charge transferred by a redox process of redox-active ions within the electrolyte. In **Chapter 4.10**, the redox electrolyte NaI was studied by using activated carbon cloth as the electrode material. Our work provides the critical parameters for operating a redox electrolyte for desalination application, that is, limiting oxidation/reduction potential, maximum charge storage, and redox kinetics. We show also the potential of the system which affords a desalination capacity of 69 mg/g in aqueous 100 mM NaCl.

#### **4. Peer-reviewed research papers**

- 4.1. Enhanced performance stability of carbon/titania hybrid electrodes during capacitive deionization of oxygen saturated saline water**
- 4.2. High performance stability of titania decorated carbon for desalination with capacitive deionization in oxygenated water**
- 4.3. MXene as a novel intercalation-type pseudocapacitive cathode and anode for capacitive deionization**
- 4.4. Two-dimensional molybdenum carbide (MXene) with divacancy ordering for brackish and seawater desalination via cation and anion intercalation**
- 4.5. Faradaic deionization of brackish and sea water via pseudocapacitive cation and anion intercalation into few-layered molybdenum disulfide**
- 4.6. Titanium disulfide: a promising low-dimensional electrode material for sodium Ion Intercalation for seawater desalination**
- 4.7. Potential-dependent, switchable ion selectivity in aqueous media using titanium disulfide**
- 4.8. Sodium ion removal by hydrated vanadyl phosphate for electrochemical water desalination**
- 4.9. Low voltage operation of a silver/silver chloride battery with high desalination capacity in seawater**
- 4.10. Confined redox reactions of Iodide in carbon nanopores for fast and energy-efficient desalination of brackish water and seawater**

## 4.1 Enhanced performance stability of carbon/titania hybrid electrodes during capacitive deionization of oxygen saturated saline water

Pattarachai Srimuk,<sup>1,2</sup> Marco Zeiger,<sup>1,2</sup> Nicolas Jäckel,<sup>1,2</sup> Aura Tolosa, Benjamin Krüner,<sup>1,2</sup>  
Simon Fleischmann,<sup>1,2</sup> Ingrid Grobelsek,<sup>1</sup> Mesut Aslan,<sup>1</sup> Boris Shvartsev,<sup>3</sup>  
Matthew E. Suss,<sup>3</sup> Volker Presser<sup>1,2</sup>

<sup>1</sup> INM - Leibniz Institute for New Materials, Campus D2 2, 66123 Saarbrücken, Germany

<sup>2</sup> Saarland University, Campus D2 2, 66123 Saarbrücken, Germany

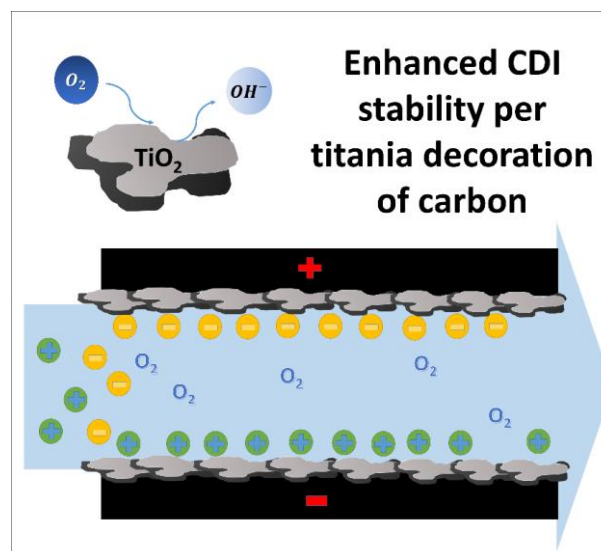
<sup>3</sup> Faculty of Mechanical Engineering, Technion-Israel Institute of Technology, Haifa, 32000, Israel

### Citation:

P. Srimuk, M. Zeiger, N. Jäckel, A. Tolosa, B. Krüner, S. Fleischmann, I. Grobelsek, M. Aslan, B. Shvartsev, M.E. Suss, V. Presser, ENHANCED PERFORMANCE STABILITY OF CARBON/TITANIA HYBRID ELECTRODES DURING CAPACITIVE DEIONIZATION OF OXYGEN SATURATED SALINE WATER, *Electrochimica Acta* 224 (1) (2017) 314-328.

### Own contribution:

Electrochemistry measurements, materials characterization, writing





## Enhanced performance stability of carbon/titania hybrid electrodes during capacitive deionization of oxygen saturated saline water



Pattarachai Srimuk<sup>a,b</sup>, Marco Zeiger<sup>a,b</sup>, Nicolas Jäckel<sup>a,b,1</sup>, Aura Tolosa<sup>a,b</sup>, Benjamin Krüner<sup>a,b</sup>, Simon Fleischmann<sup>b</sup>, Ingrid Grobelsek<sup>a</sup>, Mesut Aslan<sup>a</sup>, Boris Shvartsev<sup>c</sup>, Matthew E. Suss<sup>c,\*\*</sup>, Volker Presser<sup>a,b,\*</sup>

<sup>a</sup> INM—Leibniz Institute for New Materials, 66123 Saarbrücken, Germany

<sup>b</sup> Department of Materials Science and Engineering, Saarland University, 66123 Saarbrücken, Germany

<sup>c</sup> Faculty of Mechanical Engineering, Technion—Israel Institute of Technology, Haifa, 32000, Israel

### ARTICLE INFO

#### Article history:

Received 4 October 2016

Received in revised form 5 December 2016

Accepted 9 December 2016

Available online 10 December 2016

#### Keywords:

Capacitive deionization  
electrochemical water treatment  
titania  
nanoporous carbon

### ABSTRACT

Capacitive deionization (CDI) is a promising technology for the desalination of brackish water due to its potentially high energy efficiency and its relatively low costs. One of the most challenging issues limiting current CDI cell performance is poor cycling stability. CDI can show highly reproducible salt adsorption capacities (SACs) for hundreds of cycles in oxygen-free electrolyte, but by contrast poor stability when oxygen is present due to a gradual oxidation of the carbon anode. This oxidation leads to increased concentration of oxygen-containing surface functional groups within the micropores of the carbon anode, increasing parasitic co-ion current and decreasing SAC. In this work, activated carbon (AC) was chemically modified with titania to achieve additional catalytic activity for oxygen-reduction reactions on the electrodes, preventing oxygen from participating in carbon oxidation. Using this approach, we show that the SAC can be increased and the cycling stability prolonged in electrochemically highly demanding oxygen-saturated saline media (5 mM NaCl). The electrochemical oxygen reduction reaction (ORR) occurring in our CDI cell was evaluated by the number of electron transfers during charging and discharging. It was found that, depending on the amount of titania, different ORR pathways take place. A loading of 15 mass% titania presents the best CDI performance and also demonstrates a favorable three-electron transfer ORR.

© 2016 Elsevier Ltd. All rights reserved.

### 1. Introduction

Developing energy efficient and cost effective techniques for the desalination of brackish and wastewater is a focal point of current research activities in environmental engineering [1–7]. Several techniques have been developed in the last decades, such as reverse osmosis, multistep distillation, electrodeionization and electrodialysis, and a particularly promising, fast-emerging method is capacitive deionization (CDI) [8–10]. Among electrochemical desalination methods, CDI has the particular advantages of operating at lower cell voltage and being based on a simple cell

configuration. CDI is based on the reversible electrosorption of ions into an electrical double-layer within micropores of a saline water saturated porous carbon, typically activated carbon (AC). The fundamental principle of ion electrosorption can also be applied for energy storage in electrical double-layer capacitors (EDLCs) using electrolytes of high ionic strength. The adsorption capacity of the electrode material for CDI or the capacitance of EDLCs is dependent on the specific surface area of the carbon accessible to the ions [11,12]. Micro-mesoporous activated carbon is a widely used material due to specific surface areas (SSA) above 1000 m<sup>2</sup> g<sup>-1</sup>.

During desalination by CDI, one electrode is negatively polarized and the second positively polarized. In a micropore, electric charge accumulates and is compensated in the electrolyte by co-ion expulsion or counter-ion adsorption (or a mixture of both processes) [13]. Co-ions denote ions with the same charge sign as the electrode charge, while counter-ions have a charge sign opposite to the electrode. Once the maximum possible number of

\* Corresponding author at: INM—Leibniz Institute for New Materials, 66123 Saarbrücken, Germany.

\*\* Corresponding author.

E-mail addresses: [mesuss@tx.technion.ac.il](mailto:mesuss@tx.technion.ac.il) (M.E. Suss), [volker.presser@leibniz-inm.de](mailto:volker.presser@leibniz-inm.de) (V. Presser).

<sup>1</sup> ISE member.

ions is electrosorbed by the porous electrode, the potential of the cell can be set to zero or reversed to release the ions and to regenerate the CDI electrodes. By this alternating operation, an effective purification of influent water is achieved and particularly high energy efficiencies have been obtained for saline media with low ionic strength [14]. It should be pointed out that only the adsorption of counter-ions contributes to the overall desalination. Co-ion expulsion consumes current without any contribution to the total desalination, resulting in reduced charge and energy efficiency, that is, the ratio between adsorbed salt over the accumulated charge [15]. To suppress the co-ion depletion and increase the overall charge efficiency, charge selective membranes can be used (membrane capacitive deionization, MCDI), or charged surface function groups can be added to the carbon micropores judiciously to enable enhanced or extended-voltage CDI [16–20]. Charge efficiency is a particularly informative CDI performance parameter, which gives the ratio of charge used for effective salt removal and total charge invested. The difference to 100% is mostly because of ion swapping and possible (parasitic) Faradaic side reactions which consume charge without contributing towards actual desalination; as a secondary effect, also contributions from resistive heating may have to be considered [21].

The concentration of surface groups, such as carboxyl groups, may increase especially in micropores *in-situ* during cycling of a CDI cell [22]. Such oxygen-containing surface groups are formed at the positively charged electrode due to carbon electro-oxidation in aqueous electrolytes, which is accelerated when dissolved oxygen is present. The result is a continuous performance decrease and low cell cycle life [23,24]. The effect of positively polarized electrode oxidation on the desalination performance of electrodes during CDI process is the focus of intensive research activities, and is currently the main limitation on CDI cell cycle life [22,25–27]. Current strategies to mitigate anode corrosion include nitrogen or argon purging of the feedwater [22], a reduction of cell potential as carbon oxidation takes place between 0.7 and 0.9 V vs. NHE [25], the use of chemical treatments to increase the concentration of negatively charged surface groups at the anode [28] (inverted-CDI), and the use of thin polymeric ion exchange membrane sheaths for the anode [29]. Yet, it is not always possible during practical applications to reduce the oxygen content by argon or nitrogen bubbling, and reducing cell voltage to avoid carbon oxidation comes at the cost of severely lowered desalination capacity. In inverted CDI (i-CDI), a high initial negative chemical charge concentration in the anode micropores led to the CDI process becoming fully inverted, whereby desalination occurred upon cell discharge [30–33]. While i-CDI allowed for mitigation of anode corrosion and long CDI cycle life of approximately 600 cycles, a key disadvantage of i-CDI at present is a rather low salt adsorption capacity (SAC). As shown by Gao et al., employing thin ion exchange membrane coatings directly on nanoporous carbon felt electrodes can significantly improve stability upon cycling [29] for desalination of de-aerated saline media. Membrane-free CDI, however, would be even more attractive due to the significant costs of ion exchange membranes [32]. Thus, there is an outstanding need for techniques to mitigate anode corrosion in a CDI cell without sacrificing SAC or other performance benchmarks.

Not only anode oxidation related to oxygen-containing functionalities needs to be addressed, but also the parasitic influence of dissolved oxygen on the CDI process [26,33,34]. Under realistic conditions, atmospheric oxygen (21 vol.%) diffuses into the water and electrochemically reacts with the carbon electrode during CDI operation. The widespread use of de-aerated saline solution in scientific literature does not correspond to the oxygen content in practical water applications.

The oxygen reduction reaction (ORR) either proceeds as a four or two-electron transfer, leading to hydrogen peroxide evolution as

the intermediate product, which can modify (and degenerate) the carbon surface [35]. The addition of metal oxides to the carbon electrode may contribute to overcoming the oxidation of the positively charged electrode and ORR, thus preventing performance fading and convey good aging stability of CDI. It has already been shown that a thin layer of metal oxide on the carbon material leads to better CDI performance [36–41]. Among several different metal oxides having ORR catalyst capability, such as  $\text{MnO}_2$ ,  $\text{Co}_3\text{O}_4$ ,  $\text{Fe}_2\text{O}_3$ ,  $\text{Fe}_3\text{O}_4$ , and  $\text{NiCo}_2\text{O}_4$  [42–47], titania appears to lead to significant improvement of ORR performance [48–50]. Particularly attractive is the high natural abundance and the facile nature of titania preparation methods, for example, by sol-gel processes [51–54]. The fundamental understanding of the mechanisms governing an improved salt adsorption capacity remains fragmented at present. Several factors play a role, including improved wettability, electrocatalysis, and enhanced charge separation due to possible negatively charged surface groups [55–59].

To the best of our knowledge, the influence of titania on the electro-oxidation, ORR, and aging stability of carbon-based CDI electrodes has not been investigated so far. For that task, we prepared hybrid electrodes consisting of activated carbon with different titania loadings, following a well-established sol-gel approach. The electrochemical properties, including oxygen reduction reaction (ORR), were systematically studied. CDI performance is tested in oxygen saturated aqueous NaCl, in particular with respect to aging stability, and the influence of titania loading on the performance is investigated. The key goal of our work is to establish the promising nature of carbon/metal oxide hybrid materials for enhanced CDI performance *stability* and to explore the underpinning electrochemical mechanisms enabling such performance.

## 2. Experimental

### 2.1. Synthesis of AC-titania hybrids

YP80-F activated carbon (AC) from Kuraray was used as electrode material. Ti(IV) isopropoxide was purchased from Sigma Aldrich. AC-titania hybrid materials were prepared by sol-gel method using one and two step hydrolysis reaction [40,41,60]. Different mass ratios of Ti(IV) isopropoxide to AC, dispersed in ethanol, were used to achieve different mass loadings of titania on AC.

Ti(IV) isopropoxide was first dissolved in 400 mL absolute ethanol. In all steps, the container was backfilled with argon. The amount of Ti(IV) isopropoxide (39.6, 46.6, 55.9, and 83.9 g) was calculated based on titania formation with regard to AC, which translates to 20, 25, 30, and 45 % of titania. In a second step, AC powder (30 g for each batch) was vacuum dried at 120 °C and 20 mbar for 10 h and put in an argon backfilled glass bottle, which was stirred for 5 h after adding of 400 mL ethanol. The resulting carbon slurry was subjected to ultrasound assisted bath (Sonorex Super RK514BH, Bandelin) for 30 min and afterwards poured into the Ti(IV) isopropoxide solution (55.9 and 83.9 g of Ti(VI) propoxide in 400 mL absolute ethanol) during stirring and kept stirred for 48 h. For the one step hydrolysis process, 39.6 and 46 g of Ti(IV) isopropoxide in 400 mL ethanol was centrifuged for solid/liquid separation and the removal of the unreacted excess isopropoxide. This was repeated for two times after re-dispersion of the sediment in 800 ml absolute ethanol. For the two step hydrolysis reaction, water was added to the AC-isopropoxide mixture in the first step and stirred for another 48 h to hydrolyze the amount of isopropoxide, which did not react with the AC surface. The molar ratio of water to isopropoxide was 5:1 for all batches. The settled material obtained after centrifugation was vacuum dried at 120 °C and 20 mbar for 10 h.

## 2.2. Structural and chemical characterization

Scanning electron microscope (SEM) images were recorded with a JEOL JSM 7500F field emission scanning electron microscope (FESEM, Japan) operating at 3 kV. Energy dispersive X-ray spectroscopy (EDX) was carried out in the system with an X-Max Silicon Detector from Oxford Instruments using AZtec software. Transmission electron micrographs were taken with a JEOL 2100F transmission electron microscope at 200 kV. Powder samples were prepared by dispersing them in ethanol and drop casting them on a copper grid with lacey carbon film (Gatan).

Raman spectra were measured with a Renishaw inVia Raman microscope using a Nd-YAG laser with an excitation wavelength of 532 nm. The system employed a grating with 2400 lines  $\text{mm}^{-1}$  yielding a spectral resolution of  $\sim 1.2 \text{ cm}^{-1}$  and the spot size on the sample was in the focal plane  $\sim 2 \mu\text{m}$  with an output power of 0.2 mW. Spectra were recorded for 20 s and accumulated 10-times to obtain a high signal-to-noise and signal-to-background ratio. Peak fitting was performed by employing four Lorentzian peaks for the spectrum between  $900 \text{ cm}^{-1}$  and  $1900 \text{ cm}^{-1}$ .

X-ray diffraction (XRD) was conducted employing a D8 Advance diffractometer (Bruker AXS) with a copper X-ray source ( $\text{Cu}_{K\alpha}$ , 40 kV, 40 mA) in point focus (0.5 mm) and a Goebel mirror. A VANTEC-500 (Bruker AXS) 2D detector ( $\sim 25^\circ$  per step; measurement time 1000 s per step) was employed. The samples were dispersed in ethanol and drop casted on a sapphire wafer to obtain a homogeneous layer. The sample holder was oscillating in plane (amplitude 5 mm with the speed of  $0.5 \text{ mm s}^{-1}$  along  $x$  and  $0.2 \text{ mm s}^{-1}$  along  $y$ ) to enhance statistics.

Nitrogen gas sorption measurements at  $-196^\circ\text{C}$  were carried out with an Autosorb 6 B from Quantachrome. The powder samples were outgassed at  $250^\circ\text{C}$  for 10 h under vacuum conditions at  $10^2$  Pa to remove adsorbed water; the outgassing temperature for film electrodes was  $120^\circ\text{C}$ . Nitrogen gas sorption was performed in liquid nitrogen in the relative pressure range from 0.008 to 1.0. The BET-specific surface area (BET-SSA) was calculated with the ASiQwin-software using the Brunauer-Emmett-Teller [61] equation in the linear relative pressure range of 0.01–0.05. The DFT-specific surface area (DFT-SSA) and pore size distribution (PSD) were calculated via quenched-solid density functional theory (QSDFT) [62] with a model for slit pores.

Thermogravimetric analysis was carried out on dried hybrid samples at  $10^\circ\text{C min}^{-1}$  to  $900^\circ\text{C}$  in flowing synthetic air ( $10 \text{ cm}^3 \text{ min}^{-1}$ ) to determine the ash content, which was used to calculate the total titania content in the samples (TG 209F1, Netzsch).

## 2.3. Electrochemical measurements

For electrochemical characterization, two types of electrodes were prepared: free-standing PTFE-bound electrodes for electrochemical characterization and drop casted film electrodes on graphite current collectors using PVP and PVB as binder for CDI [63,64]. Film electrodes were prepared by mixing AC powder or AC-titania hybrid powders with 5 to 10 mass % of dissolved polytetrafluoroethylene (PTFE, 60 mass% solution in water from Sigma Aldrich) and ethanol to obtain a homogeneous carbon paste. The carbon paste was rolled with a rolling machine (MTI HR01, MIT Corp.) to 180–200  $\mu\text{m}$  thick, free standing film electrodes and dried in vacuum at  $120^\circ\text{C}$  for 24 h at 20 mbar. The electrodes for CDI experiments were  $6 \times 6 \text{ cm}^2$  in size with a hole in the middle of each electrode of  $1.5 \times 1.5 \text{ cm}^2$ , which was cut from the rolled film electrodes.

To evaluate the effect and electrochemical performance of titania in as prepared AC-titania hybrid materials, electrochemical analysis was carried out in three-electrode cells using Pt wire as a counter electrode, Ag/AgCl (3 M KCl, MF-2052 RE-5B, BASi Corp.) as

a reference electrode, and glassy carbon (3 mm diameter, MF-2012, BASi Corp) as substrate for a working electrode. Before use, the glassy carbon electrode was polished using aqueous alumina suspension on felt pad. The carbon hybrid slurry was prepared by dispersing 100 mg of as-prepared material and 2.5 mg of polyvinylpyrrolidone (PVP) in 10 mL of ethanol. After tip sonication for 10 min, 5.85 mg of polyvinyl butyral (PVB; 25 mass% in ethanol) was added into the solution and stirred for 30 min. 5  $\mu\text{L}$  of the resulting suspension was drop casted over glassy carbon electrode and dried at  $60^\circ\text{C}$  for 30 min. The stability of the PVP/PVB binder for aqueous media was established in a previous publication [63] and confirmed by recent work by the group of Likun Pan [65].

Prior to the oxygen reduction reaction measurement,  $\text{N}_2$  or  $\text{O}_2$  gas was bubbled into aqueous 1 M NaCl for 20 min to achieve the de-aerated or  $\text{O}_2$  saturated electrolytes, respectively. Cyclic voltammetry was used with a potential between  $-1.0 \text{ V}$  to  $+0.6 \text{ V}$  vs. Ag/AgCl with scan rates from  $5 \text{ mV s}^{-1}$  to  $50 \text{ mV s}^{-1}$ . The symmetric full-cell charge storage behavior of all samples was measured via cyclic voltammetry with a cell voltage from 0 to 1.2 V at scan rate of  $5 \text{ mV s}^{-1}$  and galvanostatic charge-discharge measurements with specific currents from 0.1 to  $10 \text{ A g}^{-1}$ . The as prepared free-standing electrodes were cut into  $3 \times 3 \text{ cm}^2$  pieces and placed between the graphite current collector (CC) of same size (SGL Technologies; thickness: 250  $\mu\text{m}$ ) and the porous separator (glass fiber pre-filter, Millipore, compressed thickness of a single layer is 380  $\mu\text{m}$ ) in the following order: CC/electrode/spacer/electrode/CC. The stack was compressed and soaked in de-aerated 1 M NaCl. The specific capacitance of one electrode was calculated from galvanostatic cycling by applying different specific currents (0.1–10  $\text{A g}^{-1}$ , normalized to both electrodes) and using Eq. (1):

$$C_{\text{specific}} = 4 \cdot \int_{t_1}^{t_2} I dt / U \cdot m \quad (1)$$

with  $I$  the measured current,  $t_2 - t_1$  the discharge time,  $U$  the applied cell voltage (with respect to iR drop), and  $m$  the mass of both electrodes.

## 2.4. CDI testing

A CDI setup described in Ref. [12] with flow-by electrodes was used to characterize the desalination performance. The CDI stack was built from graphite current collectors (SGL Technologies; thickness: 250  $\mu\text{m}$ ) with attached porous carbon film electrodes and a porous spacer (glass fiber pre-filter, Millipore, compressed thickness of a single layer is 380  $\mu\text{m}$ ). The measurements were carried out with three pairs of electrodes. So, each stack consisted of six electrodes, four CC and two parallel flow paths which were firmly pressed and sealed. The total masses of the CDI electrodes are 400, 844, 844, and 809 mg for AC, AC-15, AC-25, and AC-35, respectively. The total electrolyte flow rate was  $22 \text{ mL min}^{-1}$ . Ion adsorption and desorption steps were carried out using constant potential mode at 1.2 V. The electrode regeneration was accomplished at 0 V. For all electrochemical operations, we used a VSP300 potentiostat/galvanostat (Bio-Logic) and the duration of each half-cycle was 30 min. All experiments were carried out with 5 mM NaCl solution and a 10 L electrolyte tank which was flushed continuously with  $\text{O}_2$  gas to obtain oxygen saturation in the electrolyte. The salt adsorption capacity and the measured charge were defined per mass of active material in both electrodes and were calculated as an average value from adsorption and desorption step. For quantification of the electrical charge, the leakage current measured at the end of each half-cycle was subtracted.

### 3. Results and discussion

#### 3.1. Structural and chemical properties

The morphology of the electrode materials was studied with electron microscopy, see Fig. 1. The AC-15 sample reveals a smooth morphology compared to initial AC sample, indicating titania is coating the carbon surface homogenously (Fig. 1C). As depicted in Fig. 1E, G, higher titania loadings lead to smoother surfaces, as also confirmed by TEM micrographs shown in Fig. 1D, F, H. Titania formation occurs when Ti(IV) isopropoxide is hydrolyzed at oxygen containing surface groups of AC even without the need for additional water (Fig. 1D) [40]. By a two-step hydrolysis, additional

titania formation takes place on the initially formed titania layer, leading to continuous thickening of the coating (Fig. 1G, H).

The microstructure of the AC sample is clearly visible in the TEM image, with graphitic nanodomains connected by amorphous regions (Fig. 1B) [66]. After coating with titania, the AC structure is less visible due to the coverage with incompletely crystalline titania (AC-15, Fig. 1D). Once the titania mass loading is increased, nanocrystalline domains of titania occur across the surface for AC-25 and AC-35 (Fig. 1F, H). To examine the uniformity of titania coatings for all synthesis conditions, EDX mapping was conducted (Supplementary Information, Fig. S1), confirming a high uniformity of titanium and oxygen distribution.

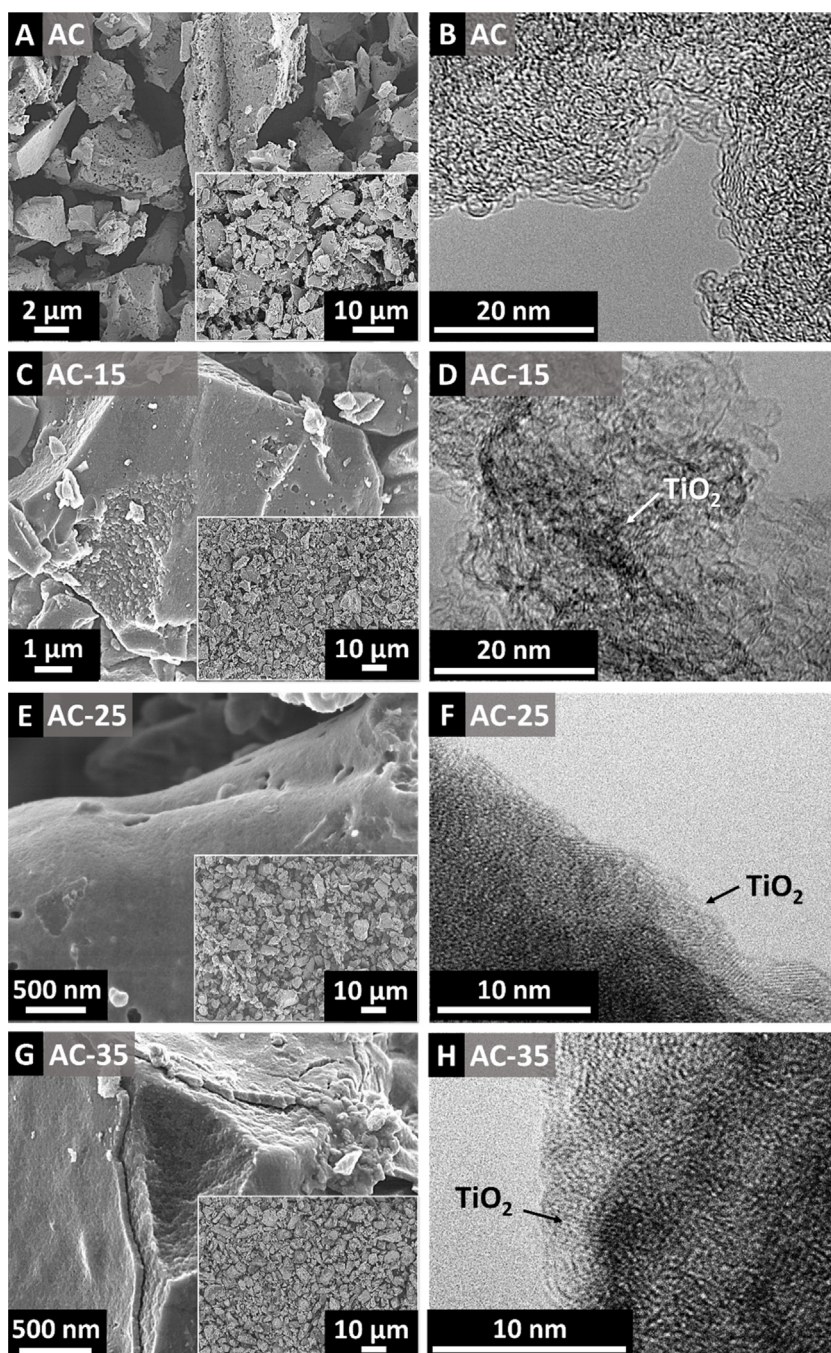
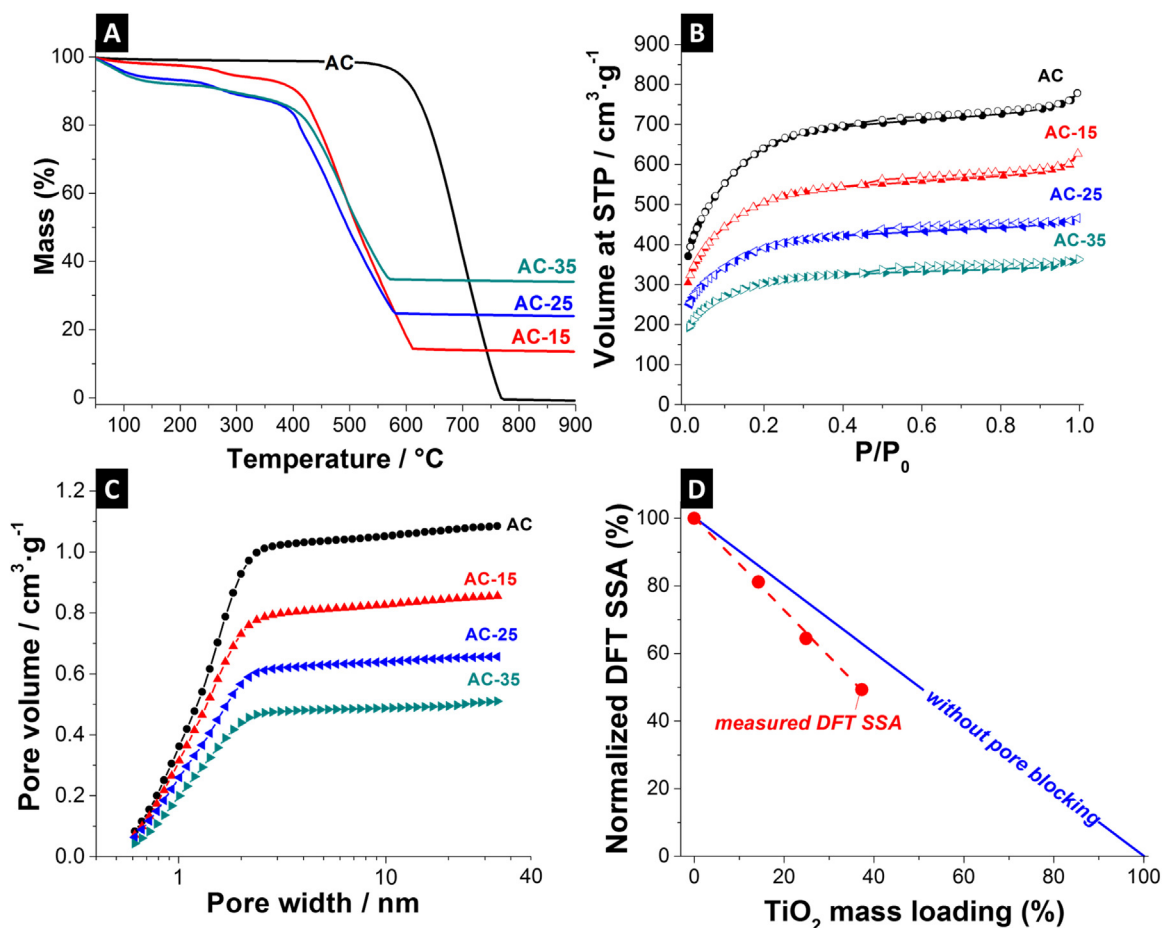


Fig. 1. Scanning electron micrographs (A,C,E,G) and transmission electron micrographs (B,D,F,H) of (A,B) AC, (C,D) AC-15, (E,F) AC-25, and (G,H) AC-35.



**Fig. 2.** (A) TGA curves, (B) nitrogen sorption isotherms at standard temperature and pressure (STP), (C) specific cumulative pore volumes, and (D) relative surface areas of AC, AC-15, AC-25, and AC-35.

The amount of titania in the AC/titania hybrids was quantified with TGA (Fig. 2A). AC is completely burned off between 600 °C and 800 °C, whereas AC-titania hybrids show a three-step mass loss. Between 50 °C and 150 °C, adsorbed water as well as unstable functional groups desorb from the surface alongside with a mass loss of 2.5–8.0 mass% [51]. Starting at 250 °C, loss of surface water and other volatile surface species accounts to ca. 5 mass% [67]. The carbon in the hybrid materials starts to burn off at 400 °C. This is a much lower temperature than the AC powder and can be explained by catalytic effects of the metal oxide [41,68]. At 600 °C, the carbon is completely removed and the titania coating remains (Table 1). It was found that the nominal (expected) titania contents of 20, 30, and 45 mass% lead to a mass loading in the hybrid material of titania mass of 14, 25, and 37 mass%, respectively (Table 1).

An increasing metal oxide loading is expected to partially block the AC nanopores and consequently decreases the specific surface area. The porosity and the surface area were analyzed using

nitrogen sorption with the respective isotherms shown in Fig. 2B. All isotherms exhibit a characteristic type I(b) shape suggesting micropores with pore sizes smaller than 1.2 nm and 2.9 nm [69]. The specific surface area (DFT and BET) and the pore volumes are summarized in Table 2. As expected, the specific surface area (SSA) is decreased with increasing titania loading. Neat AC shows a BET-SSA of 2170 m<sup>2</sup> g<sup>-1</sup> (QSDFT-SSA = 1838 m<sup>2</sup> g<sup>-1</sup>). When increasing the titania loading, the BET-SSA decreases to 1749 m<sup>2</sup> g<sup>-1</sup> (QSDFT-SSA = 1492 m<sup>2</sup> g<sup>-1</sup>) for AC-15 and 1057 m<sup>2</sup> g<sup>-1</sup> (QSDFT-SSA = 907 m<sup>2</sup> g<sup>-1</sup>) for AC-35. Due to the uniform titania covering of AC particles (Fig. 1G, H), pores are blocked when the titania content is increased (Fig. 2B, C). This is clearly seen in Fig. 2D, which shows the relative decrease of the surface area dependent on the metal oxide loading. An ideal dependency would correspond to titania addition without pore blocking; however, all hybrids fall below the ideal behavior, which indicates that pore blocking occurs for all samples to a certain degree. This pore blocking behavior is in line

**Table 1**

Results of TG analyses of AC-titania hybrids with different nominal titania contents, prepared by hydrolysis of AC Ti(IV) isopropoxide mixtures (heating rate 10 K min<sup>-1</sup>, 900 °C, flowing air 10 cm<sup>3</sup> min<sup>-1</sup>).

Sample name	Nominal titania content (mass%)	Burn off residue (mass%)	Titania residue (mass%)
AC	0	0.5	–
AC-15	20	14.8	14.3
AC-25	30	26.4	24.9
AC-35	45	37.8	37.3

**Table 2**

Summary of the results of nitrogen GSA analyses at –196 °C of all AC-titania hybrids.

Sample name	SSA (m <sup>2</sup> g <sup>-1</sup> )		Pore size (nm)	Pore volume (cm <sup>3</sup> g <sup>-1</sup> )
	BET	DFT		
AC	2170	1838	1.30	1.09
AC-15	1749	1492	1.25	0.86
AC-25	1328	1185	1.20	0.66
AC-35	1057	907	1.20	0.51

with the findings of a recent study by our group investigating the hybridization of activated carbon with vanadia [70].

Structural and phase-dependent changes caused by the titania hybridization of AC were further assessed by Raman spectroscopy (Fig. 3). The Raman spectrum of the AC sample is typical for disordered and partially amorphous carbon materials [71]. It presents a D-mode at  $1339\text{ cm}^{-1}$  and a G-mode at  $1601\text{ cm}^{-1}$ , together with a significant fraction of amorphous carbon at  $\sim 1520\text{ cm}^{-1}$ . The detailed carbon structure of this commercial AC has been described in more detail in one of our previous works [69]. For AC and AC-titania hybrids, the same position of D- and G-band are measured with  $1339\text{ cm}^{-1}$  for the D-mode and  $1601\text{ cm}^{-1}$  for the G-mode. Peak deconvolution revealed small changes of the areal intensity ratio  $I_D/I_G$ , with 2.0 for AC, 2.4 for AC-25, and 2.2 for AC-35. In addition, the FWHM of the D-mode for AC-25 and AC-35 are increased comparing to AC and AC-15 ( $101\text{ cm}^{-1}$  for AC,  $103\text{ cm}^{-1}$  for AC-15,  $121\text{ cm}^{-1}$  for AC-25, and  $108\text{ cm}^{-1}$  for AC-35). Increasing  $I_D/I_G$  ratios as well as increasing FWHM indicate that the number of defects in hexagonal rings increases when coated with titania. Due to the oxidative reaction on the surface of the AC, carbon is partially removed, and the dangling bonds may serve as nucleation centers of the titania formation.

As seen in Fig. 3B, the Raman spectra of AC-25 and AC-35 show anatase-type nanocrystalline titania at  $150\text{ cm}^{-1}$  [72,73]. Further

characteristic anatase peaks above  $400\text{ cm}^{-1}$  (see Ref. [74]) were not observed in our study because of the high disorder/small domain size and the high signal strength of the carbon material [75]. The well resolved  $E_g$  mode at  $150\text{ cm}^{-1}$  (FWHM =  $31\text{ cm}^{-1}$ ) of AC-25 and AC-35 can be used to estimate the anatase domain size to be below  $4\text{ nm}$  [74], which is in good agreement with the TEM observations (Fig. 1F, H). No anatase related Raman signals were found for AC-15 due to its low crystallinity/very small domain size resulting in very broad and overlapping peaks, making the spectrum indistinguishable from the carbon signal [75]. The incompletely crystalline nature of titania in AC-15 is also in alignment with the TEM images seen in Fig. 1D and the results in previous work [74]. It is obvious that the structure of the anatase phase is dependent on the amount coated on the carbon substrate. For very low amounts (AC-15) the titania coating starts to grow in an incompletely crystalline manner and further crystallizes to nanoscopic grains for higher loadings (AC-25). X-ray diffraction also confirms the presence of anatase, yet only for the sample with the highest titania mass loading (AC-35; Fig. 3C–G). This aligns with the high degree of disorder (esp. for AC-35) and the very small domain size (esp. for AC-15 and AC-25) when using XRD, which, as a diffraction technique, has a preferred sensitivity towards large, highly ordered scattering domains. For AC-35, we see the clear emergence of the (101) peak of anatase at  $25.2^\circ 2\theta$ .

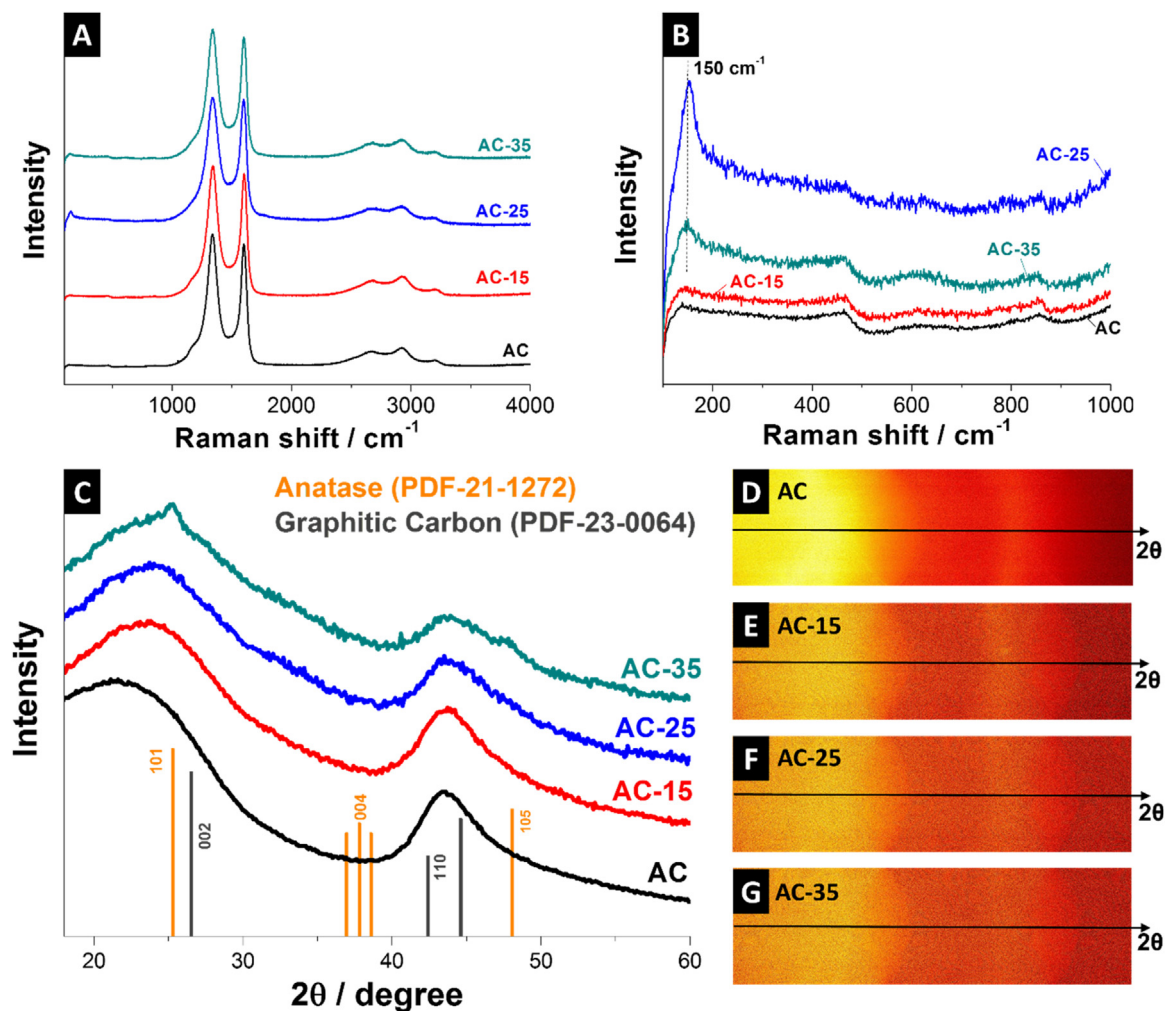


**Fig. 3.** Raman spectra of AC, AC-15, AC-25 and AC-35 showing the (A) full range and (B) just the range between  $100\text{--}1000\text{ cm}^{-1}$  (i.e., range with Raman active modes of titania). (C) X-ray diffractograms of AC and AC-titania composite. The ideal peaks position from the powder diffraction files for graphitic carbon (PDF-23-0064) and anatase-type titania (PDF-21-1272) are given. (D–G) Corresponding 2D frames from the 2D detector (covering the same range in  $2\theta$ ).

### 3.2. Electrochemical characterization in high salinity aqueous electrolyte

In aqueous CDI processes, dissolved oxygen typically shows a strong impact on cell performance, especially on the aging stability [35]. It has been proposed previously that dissolved oxygen can electrochemically react with the carbon electrode to form oxygen containing surface functional groups [76,77]. These surface functionalities affect the salt adsorption capacity by introducing local (chemical) surface charges [78,79]. To explore the potential of a metal oxide coating to mitigate the performance fading due to electrode oxidation, we tested the AC/titania hybrids as electrodes in a CDI cell. Electrodesorption experiments were performed in de-aerated 1 M NaCl solution to evaluate the specific capacitance of the fabricated electrodes. As seen in Fig. 4A, the CV curve at  $5 \text{ mV s}^{-1}$  shows typical behavior of an electric double-layer capacitor material with a rectangular shape [80]. Since no redox peaks are observed, titania in the hybrid material did not introduce any non-capacitive or non-pseudocapacitive behavior. This is underlined by galvanostatic charge-discharge measurements at  $0.1 \text{ A g}^{-1}$  (Fig. 4B) with a triangular shape.

The specific capacitances from galvanostatic measurements are plotted in Fig. 4C. At a low current density of  $0.1 \text{ A g}^{-1}$ , AC exhibits the highest specific capacitance of  $113 \text{ F g}^{-1}$ , whereas AC-15, AC-25 and AC-35 show lower specific capacitances of  $94 \text{ F g}^{-1}$ ,  $84 \text{ F g}^{-1}$ , and  $3 \text{ F g}^{-1}$ , respectively. As shown by nitrogen gas sorption (Fig. 2B–D), the pores of the AC are clogged by the additional titania coating. Thus, the lower accessible pore volume leads to lower specific capacitance values. The decrease in capacitance is further

amplified by the mass increase cause by the addition of electrochemically inactive titania (Fig. 4D).

### 3.3. Capacitive deionization performance

To evaluate the salt adsorption performance under realistic conditions, we tested the as-assembled CDI cell under saturated  $\text{O}_2$  in 5 mM NaCl (Fig. 5). As shown in Fig. 5A, AC and all hybrid electrodes exhibit a distinct salt adsorption and desorption behavior in the first three cycles. This behavior is changing significantly after 20 cycles, as the AC electrodes show a strong desorption peak before the onset of the adsorption (Fig. 5B). The latter feature, also referred to as an inversion peak, has been observed previously [20,32], and is attributed to the oxidation of the positive electrode and the consequential increase in the concentration of negatively charged surface functional groups in the micropores [23,25,26]. Post mortem EDX analysis (Fig. 5D) was carried out to give further evidence of additional oxygen-containing surface modifications. The electrodes were cycled in oxygen saturated 5 mM NaCl for 40 cycles and the positive and negative electrodes were chemically analyzed separately. We observed that after cycling, the oxygen content of the positive electrode ( $14.8 \pm 3.3 \text{ mass\%}$ ) was more than three-times higher than the negative electrode ( $4.4 \pm 0.6 \text{ mass\%}$ ), strongly indicating the formation of oxygen containing surface functional groups.

Hybrid electrodes with titania show a similar behavior [41,81], but with a much smaller inversion peak for AC-15, which vanishes entirely for electrodes with higher titania loadings (Fig. 5B). The

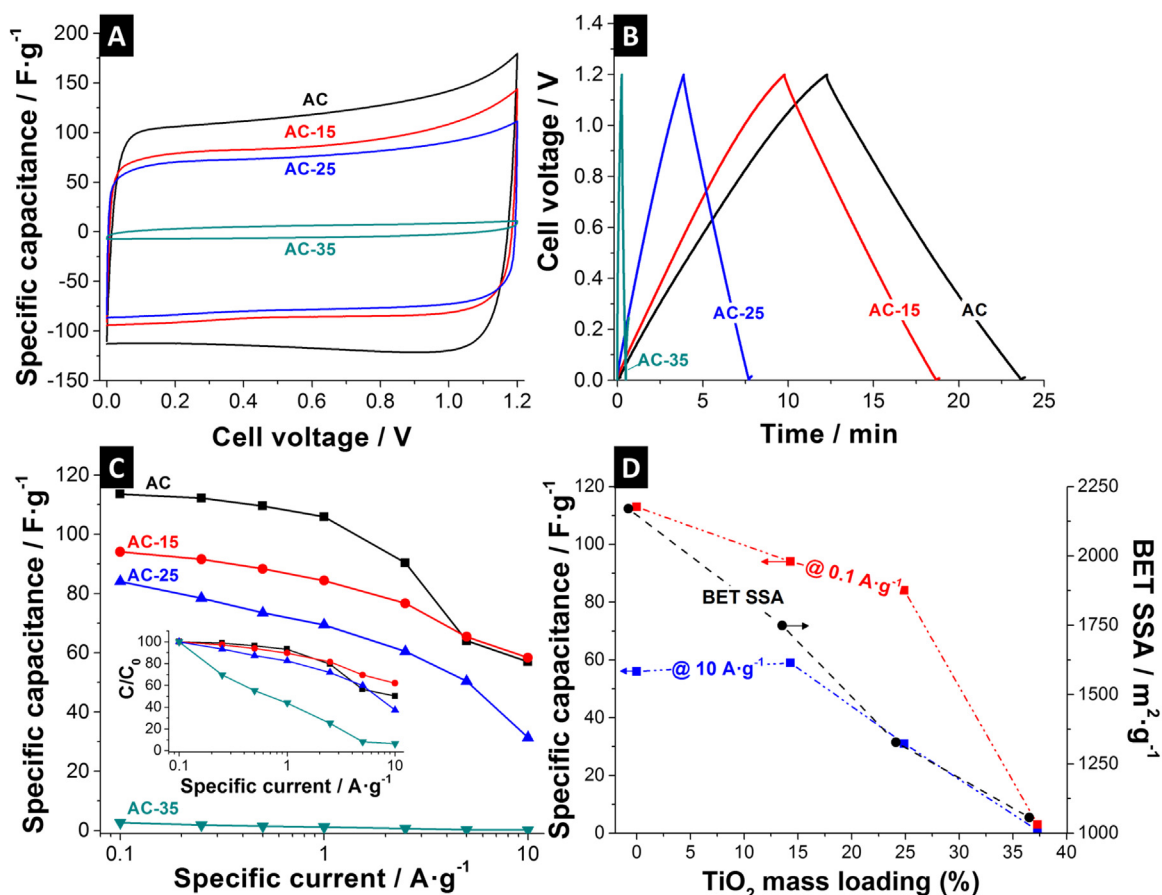


**Fig. 4.** (A) Cyclic voltammograms at  $5 \text{ mV s}^{-1}$ , (B) galvanostatic charge-discharge curves at  $0.1 \text{ A g}^{-1}$ , (C) specific capacitance versus specific current, and (D) specific capacitance and BET SSA plotted against the titania mass loading for high and low rates. All electrodes are free-standing PTFE-bond electrodes.

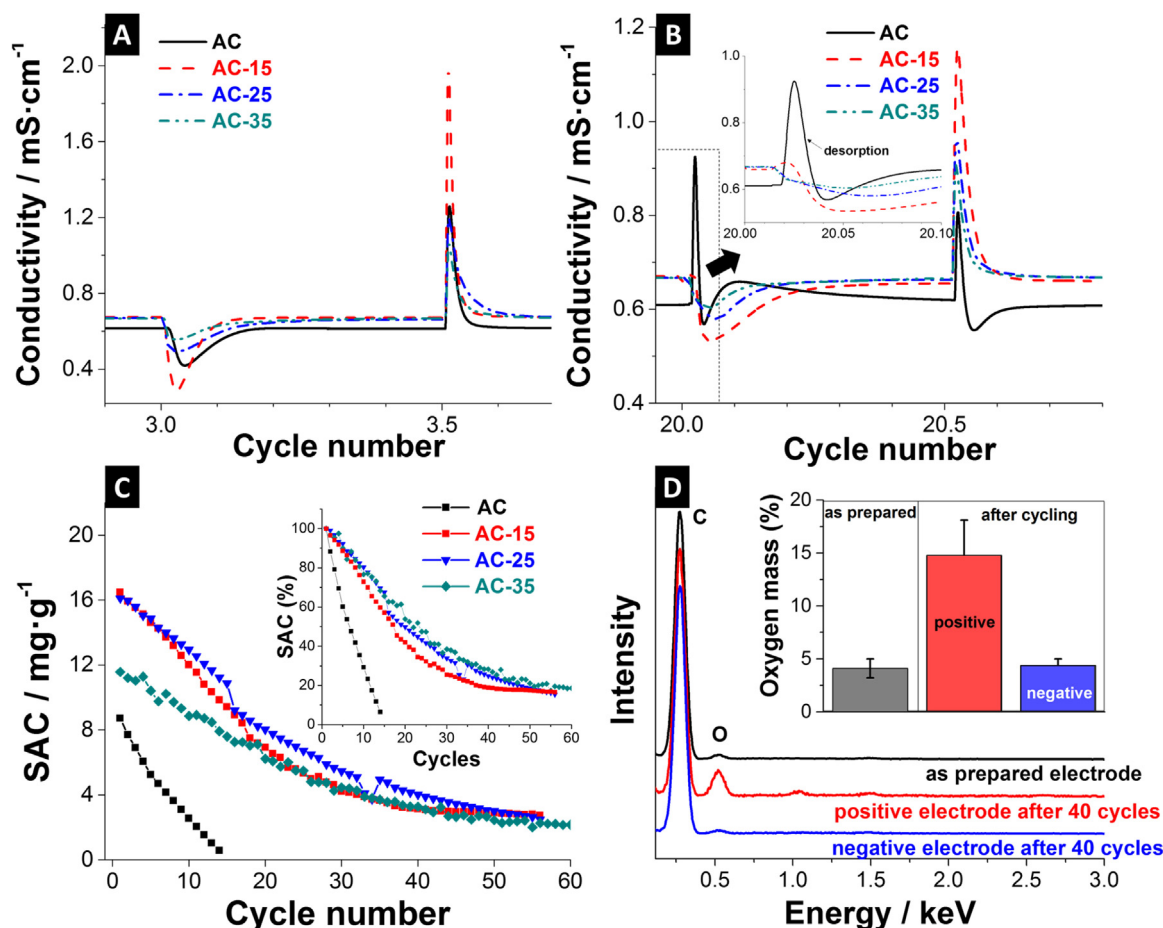


**Fig. 5.** CDI performance in oxygen saturated 5 mM NaCl at 1.2 V using free-standing PTFE-bond electrodes. Conductivity data of the outlet flow stream for (A) 3rd and (B) 20th cycle. (C) Salt adsorption capacity for 60 cycles and (D) EDX analysis of PVP/PVB-bound positive and negative electrodes after 40 desalination cycles with 5 mM oxygen saturated NaCl electrolyte at 1.2 V.

measured salt adsorption capacities exhibit values of  $17.4 \text{ mg g}^{-1}$  and  $16.2 \text{ mg g}^{-1}$  for AC-15 and AC-25, respectively, whereas AC-35 shows a smaller SAC of  $11.4 \text{ mg g}^{-1}$ . In comparison, the AC electrodes have the lowest SAC of around  $9 \text{ mg g}^{-1}$ . Earlier works (Table 4) had already reported an enhanced SAC for metal oxide/carbon hybrids (in particular titania/carbon hybrids) [55–59]. Enhanced wettability has been proposed as a cause of the improvements in the SAC of the hybrid material [39,82], and micropore surface groups may also play a role [83]. Interestingly, the measured SAC of titania containing electrodes does not follow the same general trend of the measured capacitance of the electrodes determined by galvanostatic charge/discharge experiments in oxygen-free 1 M NaCl (Fig. 4D).

As shown in Fig. 5C, the CDI performance of AC is significantly improved in oxygen saturated aqueous media by addition of titania in the first cycles. The titania containing electrodes show a much slower decrease of SAC with  $\sim 50\%$  of the initial SAC after 20 cycles and  $\sim 20\%$  after 60 cycles. While titania decoration did not fully prevent the performance degradation, there is still a remarkable performance and stability enhancement clearly visible for carbon/metal oxide hybrids. The SAC of all titania containing samples converges at ca.  $2 \text{ mg g}^{-1}$  after 60 cycles and this value seems to remain rather constant irrespective of the used amount of titania. This is in stark contrast to AC samples without titania, where the entire CDI salt removal capacity is readily lost completely after 15 cycles.

For pure AC, the performance in de-aerated 5 mM NaCl is shown in Fig. S4 (Supplementary Information). For this electrolyte, a high SAC of ca.  $13 \text{ mg g}^{-1}$  is maintained over 40 full CDI cycles (Fig. S4C, Supplementary Information), which is in stark contrast to the performance loss in oxygen saturated electrolyte with a virtually complete loss of the desalination capacity after just 15 cycles. The difference in performance stability is also seen from assessing the charge efficiency, as depicted in Fig. S4D (Supplementary Information). In de-aerated saline solution, the charge efficiency of AC remains constant at ca. 71% which is indicative of a highly reversible process of co-ion expulsion and counter-ion adsorption. For comparison, the charge efficiency of AC in oxygen saturated solution is much lower at 34% in the first cycle and fades to 0% after 15 cycles. This is in line with previous reports on the increased electrochemical degradation of carbon electrodes by dissolved oxygen [34].

To get more information on the impact of prolonged CDI cycling on AC containing titania electrodes, the potential development of the CDI cycled electrodes was benchmarked by galvanostatic charge/discharge testing at  $0.1 \text{ A g}^{-1}$  for fresh electrodes and after CDI cycling. The potential evolution of the cathode and the anode for AC-15 and AC-25 is very similar before and after CDI cycling (Fig. S6A, Supplementary Information). In both cases, we see a shift of the cell potential to +0.23 V vs. Ag/AgCl compared to fresh electrodes. As seen in Fig. S6A-B, after 60 cycles of CDI experiment, the symmetric AC-15 and AC-25 cells already exceed the theoretical oxygen evolution

potential at a cell voltage of 0.6 V. Hence, the anode is the limiting electrode. At a cell voltage of 1.2 V, AC-15 and AC-25 exhibit a potential that is 0.2 V higher than the theoretical oxygen evolution potential. AC-35 exhibits a similar cathodic and anodic potential as fresh electrodes, but the zero charge potential at a cell voltage of 1.2 V is shifted to 0.15 V vs. Ag/AgCl after 60 CDI cycles (Fig. S6C-D, *Supplementary Information*). This leads to an asymmetric potential distribution between cathode ( $\Delta E$  ca. 0.8 V at cell voltage 1.2 V) and anode ( $\Delta E$  ca. 0.4 V at cell voltage 1.2 V). This positive shifting might affect the SAC through lower accumulation of charges on the positive electrode, causing the anode to limit the total salt adsorption of the cell.

Charge efficiency, the ratio between invested charge and removed ions, is a useful tool to further characterize CDI performance and stability [21]. As shown in Fig. 5D (*Supplementary Information*), the charge efficiency of all titania containing samples is nearly three-fold higher than for pure AC at the first cycle. All three composite electrodes maintain a high charge efficiency between 90 % and 100 % for ca. 10 cycles and then gradually decrease to ca. 20 % after 60 cycles. Such high initial values for the charge efficiency cannot be explained by a pure EDL formation and ion swapping, as we see much lower values for pure AC in oxygen saturated electrolyte (Fig. S4D, *Supplementary Information*). Thereby, an electron uptake of dissolved oxygen from the cathode and the resulting effect on the SAC and charge efficiency through a Faradaic ORR is confirmed. Thus, it is indicated that the

introduction of Faradaic oxygen reduction seems to have a significant impact.

#### 3.4. ORR activity measurements

To investigate the oxygen reduction reactions (ORR) of the hybrid electrodes with different quantities of titania, cyclic voltammetry was carried out at  $5 \text{ mV s}^{-1}$  in de-aerated and in oxygen saturated 1 M NaCl. The results of these measurements are shown in Fig. 6. It was found that the CV of AC in de-aerated solution is rectangular, as it is typical for systems with purely capacitive behavior and without any Faradaic contributions (Fig. 6A). In the case of oxygen saturated electrolyte, a well-defined ORR onset potential is observed at 16 mV vs. Ag/AgCl. The results of AC-titania hybrid samples in de-aerated media are like those of AC, but with lower specific current and less potential window stability (Fig. 6). Higher mass loadings of titania lead to a lower electrochemical potential for hydrogen evolution reactions (HER) and, in turn, to a lowered applicable potential. Especially, AC-35 shows comparably low potential window stability, because the nanocrystallinity of titania favors HER [50]. In the  $\text{O}_2$  saturated solution, ORR peaks for titania hybrid electrodes (AC-15, AC-25 and AC-35) are appearing at the onset potential of +46 mV,  $-38 \text{ mV}$ , and  $-21 \text{ mV}$  vs. Ag/AgCl, respectively. Typically, for reduction potentials closer to the standard potential of oxygen reduction (between +170 mV and  $-360 \text{ mV}$  vs. Ag/AgCl depending on the mechanism) [84], the oxygen reduction reaction is favorable.

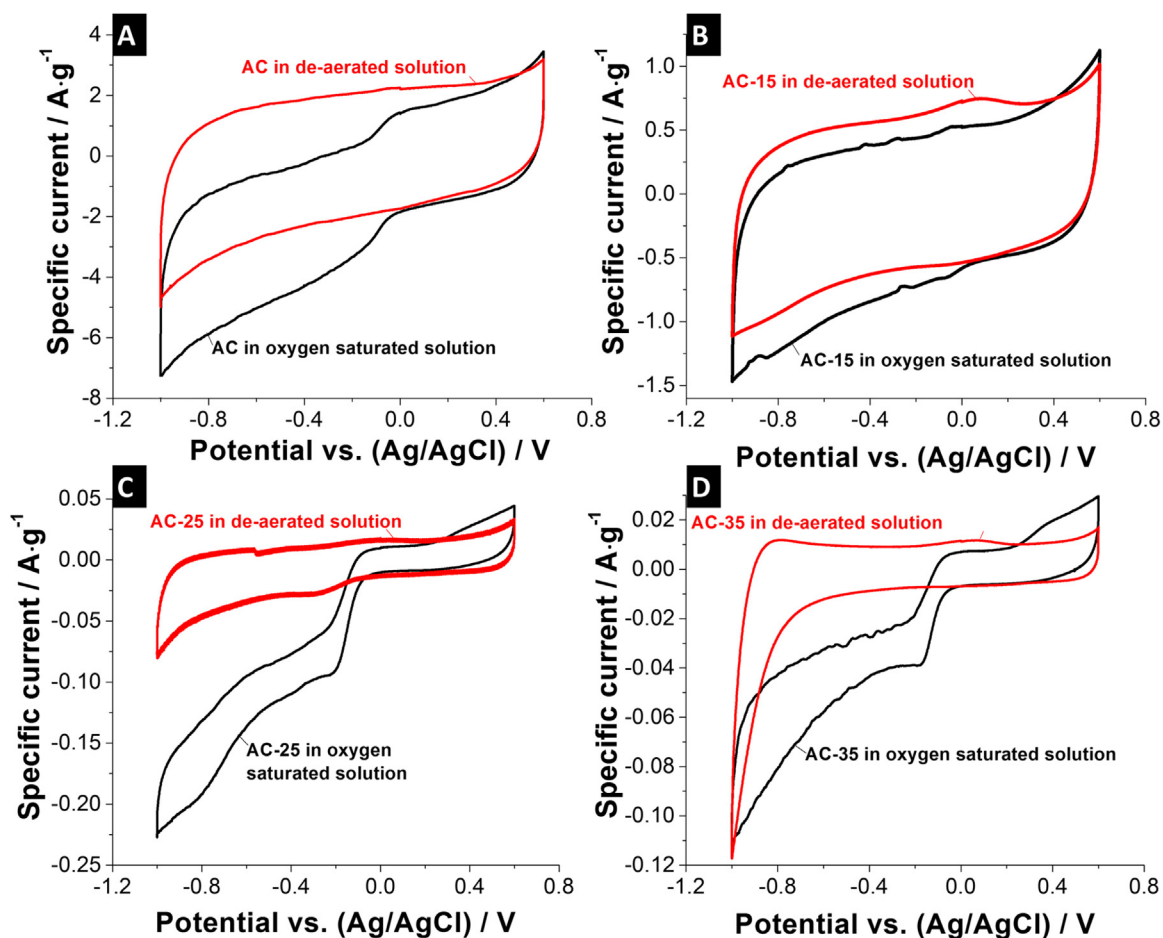


Fig. 6. Cyclic voltammograms in de-aerated and oxygen saturated aqueous 1 M NaCl at  $5 \text{ mV s}^{-1}$  for (A) AC, (B) AC-15, (C) AC-25, and (D) AC-35.

**Table 3**

Density and specific resistivity of film electrodes. Film electrodes were prepared by rolling of activated carbon and AC-titania mixtures with different amounts of PTFE binder (film thickness: 180–200  $\mu\text{m}$ ).

Sample name	PTFE binder (mass%)	Electrode density ( $\text{g cm}^{-3}$ )	Specific resistivity (ohm cm)
AC	5.0	0.42 $\pm$ 0.03	9 $\pm$ 1
AC-15	5.0	0.52 $\pm$ 0.02	18 $\pm$ 2
AC-25	7.5	0.60 $\pm$ 0.03	86 $\pm$ 7
AC-35	10.0	0.72 $\pm$ 0.05	>2000

Among all samples, AC-15 shows the highest ORR potential of +46 mV vs. Ag/AgCl, indicating a stronger oxygen reduction tendency. The onset reduction potentials of the hybrid electrodes AC-25 and AC-35 are more negative than the AC electrodes; this can be understood as an impeded ORR due to a lower accessibility of the carbon, as well as a reduced electrical conductivity (Table 3) due to the rather thick titania coating.

In Fig. 7A, B, the intrinsic ORR currents of AC and hybrid electrodes are calculated by subtracting the current in oxygen saturated electrolyte by the capacitive current in de-aerated electrolyte. When using just AC, we see a simultaneous increase of the specific ORR current as the potential becomes more negative from 16 mV to –400 mV vs. Ag/AgCl. This is commonly observed for metal-free ORR catalysts [85]. For comparison, AC-15 exhibits the same phenomenon as AC, but with a lower (more positive) ORR specific current, suggesting synergistic ORR activity between AC and titania. AC-25 and AC-35 show different ORR activities compared to AC and AC-15, with a sharp step in the specific current from the onset potential (–48 mV and –21 mV vs Ag/AgCl) to a certain potential (–220 mV and –200 mV vs. Ag/AgCl), before the constant plateau occurs (Fig. 7A, B). The plateau current demonstrates that the reaction at this scan rate (5  $\text{mVs}^{-1}$ ) is diffusion limited [86]. This suggests an impeded diffusion of oxygen species due to a faster transfer of the first electron, which is more pronounced for higher loadings.

A technique to measure the reaction rate of oxygen species on the active surface involves the Tafel equation and the Tafel slope [87]. The Tafel equation (Eq. (2)) is derived from the Butler-Volmer equation [88,89] and is typically a logarithmic plot of the current  $i$  versus the overpotential  $\eta$ , which should be linear at each rate of reaction. The ORR kinetics are obtained from the slope of the Tafel

plot via Eq. (2):

$$\log i = \log i_0 - \frac{\alpha n F}{RT} \eta \quad (2)$$

where,  $i_0$  is the exchange current,  $\alpha$  is the charge transfer coefficient,  $F$  is Faraday's constant

(96485  $\text{C mol}^{-1}$ ),  $R$  is the ideal gas constant (8.314  $\text{J mol}^{-1} \text{K}^{-1}$ ),  $T$  is the temperature (296 K), and  $n$  is number of electron transfers.

As shown in Fig. 7C, the cathodic Tafel plot of all samples exhibits two different slopes: one at low overpotential and one at high overpotential. At low overpotential, the rate-determining step is the first electron transfer leading to oxygen reduction, while at the higher over potential, the kinetics are limited by oxygen diffusion [90]. The calculated Tafel slopes for both potentials are displayed in Fig. 7D. AC-15 shows a low overpotential Tafel slope higher than AC due to multiple steps of reduction processes of the titania. For high titania loadings (i.e., AC-25 and AC-35), the catalytic activity is dominated by titania. Hence, titania might reduce oxygen in different pathways. The Tafel slopes at high overpotential increase with higher amounts of titania, potentially because of the poor conductivity (sluggish electron flow rate), as well as the diffusion limitations of oxygen (pore blocking by titania coating) within the AC-titania hybrid

In summary, AC and AC-15 show higher rates of ORR than AC-25 and AC-35 at high overpotentials, while the two latter achieve higher rates of ORR at low overpotential due to the strong influence of titania. Figs. 6 and 7 clearly show the catalytic ability for AC and AC-titania hybrids. However, the mechanism of such a reaction needs to be studied in more detail, since there are different possible ORRs between carbon and metal oxide, which can affect the CDI performance (Supporting Information equations S1–S9).

The formation of surface functional groups is a particularly critical issue affecting the aging of CDI electrodes. It is expected that, during CDI operation,  $\text{H}_2\text{O}_2$  is formed through the reduction of oxygen in the solution, and the  $\text{H}_2\text{O}_2$  then oxidizes the positive electrode (Fig. 5D) [35,91]. Thus, to understand the ORR, several reaction steps have to be considered, which are either a direct 4 electron pathway (Eq. (3)) or a two-step two-electron pathway (Eqs. (4)–(5)) [25,92]. Following a perfect ORR four-electron pathway,  $\text{O}_2$  directly reacts on the surface of the carbon and forms hydroxyl ions. In the two-step, two-electron pathway, peroxide ions are formed in an intermediate step (Eq. (4)) and then peroxide

**Table 4**

Comparison of salt adsorption capacity (SAC) of metal oxide-carbon composite.

Samples	Salt concentration	SAC	Charge efficiency	Operation voltage	Ref.
ZrO <sub>2</sub> /graphene oxide	50 $\text{mg L}^{-1}$	4.5 $\text{mg g}^{-1}$	93%	1.2 V	[97]
TiO <sub>2</sub> /CNTs	25–800 $\text{mg L}^{-1}$	4 $\text{mg g}^{-1}$	na.	1.4 V	[39]
TiO <sub>2</sub> /AC	5–560 $\text{mg L}^{-1}$	21 $\text{mg g}^{-1}$	na.	0.3–1.2 V	[40]
TiO <sub>2</sub> /AC	5.8 $\text{mg L}^{-1}$ 0.1 mM	0.5 $\text{mg g}^{-1}$	na.	1 V	[41]
MnO <sub>2</sub> /MWCNTs	87 $\text{mg L}^{-1}$	6.6 $\text{mg g}^{-1}$	na.	1.8 V	[98]
TiO <sub>2</sub> nanorod/rGO	300 $\text{mg L}^{-1}$	9.1 $\text{mg g}^{-1}$	50 %	1.2 V	[82]
TiO <sub>2</sub> nanofiber/AC	292 $\text{mg L}^{-1}$	17.7 $\text{mg g}^{-1}$	90 %	1.2 V	[99]
ZnO/AC	500 $\text{mg L}^{-1}$	9.4 $\text{mg g}^{-1}$	80.5 %	0.4–1.5 V	[36]
SnO <sub>2</sub> /rGO	na.	1.5 $\text{mg g}^{-1}$	80 %	1.4 V	[38]
MnO <sub>2</sub> /rGO	56000 $\text{mg L}^{-1}$	5 $\text{mg g}^{-1}$	93 %	1.2 V	[100]
MnO <sub>2</sub> /AC	35 $\text{mg L}^{-1}$	9.4 $\text{mg g}^{-1}$	81 %	1.2 V	[37]
TiO <sub>2</sub> /rGO	1400 $\text{mg L}^{-1}$	17.8 $\text{mg g}^{-1}$	na.	1.8 V	[101]
TiO <sub>2</sub> /AC	100 $\text{mg L}^{-1}$	11.5 $\text{mg g}^{-1}$	na.	1.2 V	[102]
AC-15	280 $\text{mg L}^{-1}$	17.4 $\text{mg g}^{-1}$	22% after 60 cycles	1.2 V	This work
		ca. 2 $\text{mg g}^{-1}$ after 60 cycles			
AC-25	280 $\text{mg L}^{-1}$	16.2 $\text{mg g}^{-1}$	22% after 60 cycles	1.2 V	This work
		ca. 2 $\text{mg g}^{-1}$ after 60 cycles			
AC-35	280 $\text{mg L}^{-1}$	11.4 $\text{mg g}^{-1}$	22% after 60 cycles	1.2 V	This work
		ca. 2 $\text{mg g}^{-1}$ after 60 cycles			

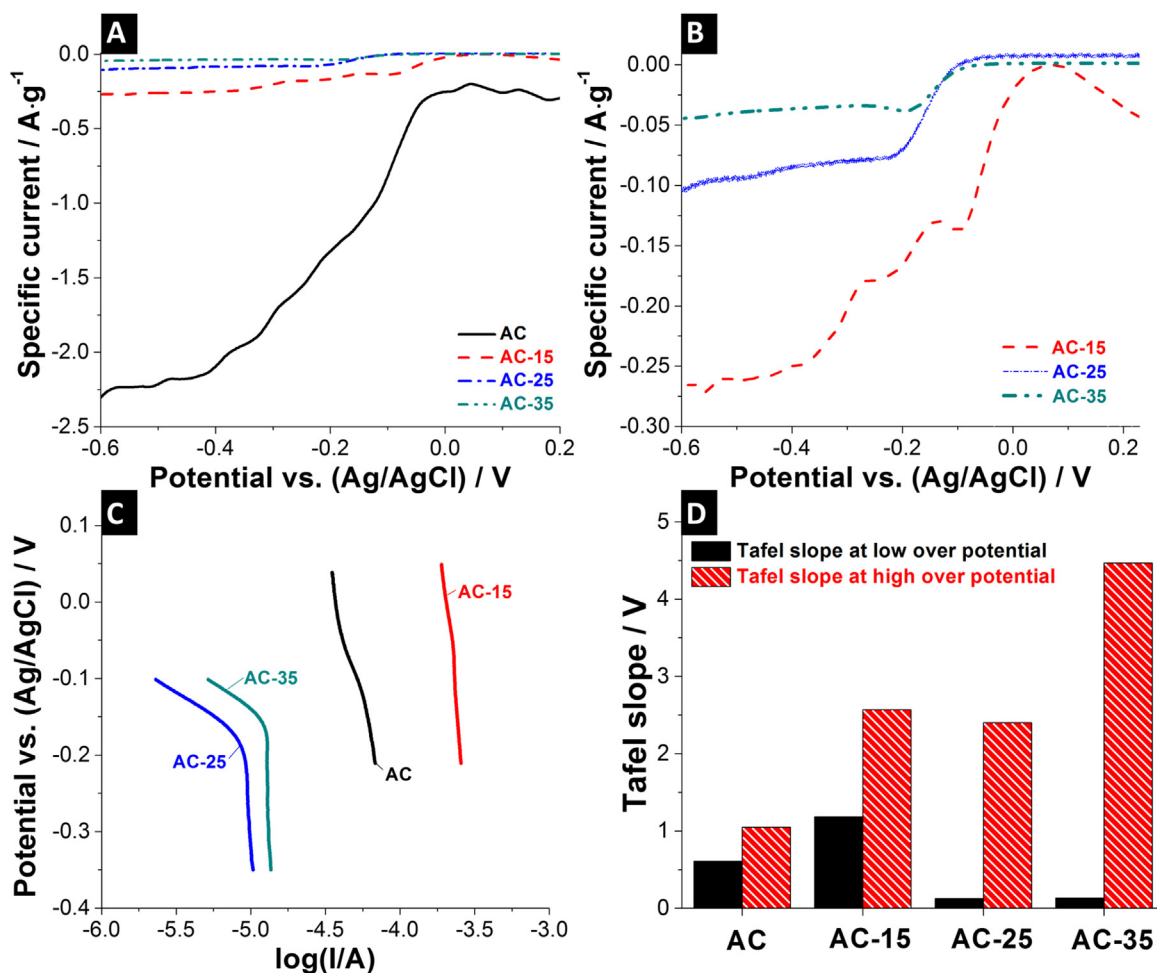
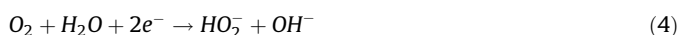


Fig. 7. (A, B) Intrinsic ORR currents at  $5 \text{ mV s}^{-1}$ , (C) Tafel plot, and (D) Tafel slopes of AC, AC-15, AC-25, and AC-35.

ions form the hydroxyl ions (Eq. (5)). However, peroxide ions in the intermediate steps cannot further be reduced due to their high reduction potential, so that the direct four electron pathway without peroxide formation would be preferable with respect to suppress the oxidation of carbon electrodes.



Hence, to see which ORR reactions takes place, the electrodes were further evaluated at various scan rates, to get further insight into the relation between the rate of electron transfer and oxygen diffusion. As can be concluded from the Tafel slope (Fig. 7D), the rate limiting step is the bulk diffusion of dissolved oxygen. To reduce such influence, the increase of the sweep rate enhances the ORR kinetics in terms of acceleration of the charge transfer. For each scan rate, the specific ORR current was calculated as described in the last section. It can clearly be observed that the diffusion-limiting specific current of AC increases with the scan rate in the range from  $-0.15 \text{ V}$  to  $-0.2 \text{ V}$  vs. Ag/AgCl, suggesting that the charge transfer rate of AC is increased at high rates and more oxygen is reduced (Fig. 8A). In addition, the peaks appeared more clearly after the scan rate is increased up to  $20 \text{ mV s}^{-1}$  (Fig. 8A). For AC-15, we could observe complementary behavior with the

specific peak current disappearing when the sweep rate is increased (Fig. 8B). For low scan rates, the rate of charge transfer at the solid/liquid interface is lower than for high scan rate. With higher scan rates, the ORR kinetics are increased to reach the equilibrium between rate of electron transfer and rate of oxygen diffusion as indicated by the absence of a peak at a high scan rate ( $50 \text{ mV s}^{-1}$ ). In case of AC-25 and AC-35 (Fig. 8C, D), the specific currents exhibit plateaus for low scan rates ( $5 \text{ mV s}^{-1}$ ) indicating the reaction reaches equilibrium. For higher rates, peaks appear since the surface reaction of titania is much faster than bulk diffusion of oxygen. This is especially seen for AC-35, where most the pores are blocked by titania. The number of transferred electrons, which indicates the specific ORR pathway, can be calculated with the Randles-Sevcik equation (Eq. (6)) [93,94]:

$$i_p = (2.99 \cdot 10^5) n(n\alpha)^{0.5} A C D^{0.5} \nu^{0.5} \quad (6)$$

$A$  is the active surface area (in this case: DFT-SSA),  $C$  is the concentration of dissolved oxygen

( $2.59 \cdot 10^{-7} \text{ mol cm}^{-2}$ ) [95],  $D$  is the diffusion coefficient of oxygen ( $2 \cdot 10^{-5} \text{ cm}^2 \text{ s}^{-1}$ ),  $\alpha$  is the charge transfer coefficient,  $n$  is number of electron transfers and  $\nu$  is the scan rate. The term  $n\alpha$  is calculated from the Tafel slope at high potential using Eq. (7) [87]:

$$\text{Tafel slope} = \frac{2.303 \cdot RT}{\alpha n F} \quad (7)$$

The reduction currents at the peak maximum are plotted versus the square root of scan rate as shown in Fig. 8E. It was found that AC, AC-15, AC-25 and AC-35 present slopes of  $-0.056$ ,  $-0.664$ ,  $-0.062$ ,

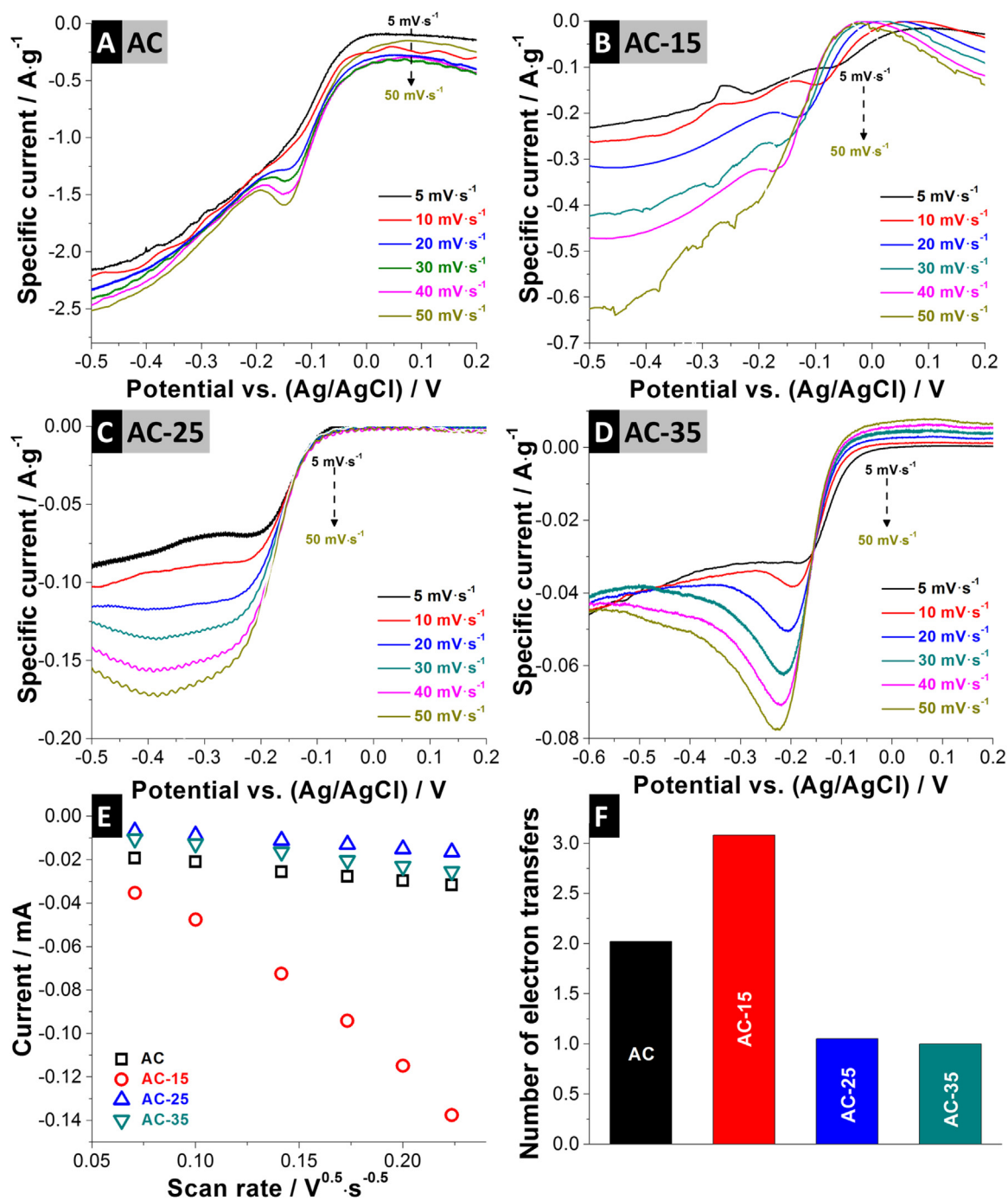


**Fig. 8.** Intrinsic ORR specific currents at different scan rates for (A) AC, (B) AC-15, (C) AC-25, and (D) AC-35. (E) ORR peak currents versus square root of scan rate, and (F) number of electron transfers.

and  $-0.101 \text{ mA}(\text{Vs}^{-1})^{0.5}$ , respectively. The number of electron transfers is calculated and plotted in Fig. 8F. AC without additional catalyst exhibits an electron transfer of 2.02, indicating a two-electron oxygen reduction reactions takes place, in which hydrogen peroxide ions are produced (Eq. (4)) [76,77]. Hydrogen peroxide strongly oxidizes the carbon surface leading to the formation of oxygen containing surface groups [78]. These functional groups create local negative charges at the positive electrode, which cause the inverse peak during the adsorption process (Fig. 5B). This verifies that during CDI operation and in the presence of oxygen in the electrolyte, hydrogen peroxide plays a crucial role at the positive electrode resulting in poor aging performance [35,96].

The catalytic role of titania during the CDI process shows different ORR mechanisms (number of electron transfers) dependent on the mass loading. As we can see in Fig. 8F, AC-15 shows the highest electron transfer of 3.08, whereas AC-25 and AC-35 show 1.05 and 1.01 electron transfers, respectively. The different mechanisms regarding the number of electron transfers of the hybrid materials can protect the oxidation of carbon at the positive electrode in different ways [49]:

- For AC-25 and AC-35, a single electron transfer is indicated due to the higher activation energy barrier leading to catalyst poisoning and incomplete reactions. Per the mechanism shown in Fig. S3

(*Supplementary Information*), the dissolved oxygen adsorbs on the titania surface and the first electron reacts with it to form superoxide. The latter strongly adsorbs on active sites which are used to transform oxygen to superoxide. Over the time, the active sites of titania are blocked and cannot be further used for ORR. Therefore, using AC-25 and AC-35 in CDI results in a continuous decrease of the SAC (Fig. 5C) because of active site blockage and the formation of hydrogen peroxide, which strongly oxidizes the carbon surface.

- In case of AC-15, 3.08 electron transfers are indicated. This could be explained by the following ORR mechanism, schematically shown in Fig. S3 (*Supplementary Information*). First, oxygen diffuses and selectively adsorbs on the surface of titania. Once an electrical potential is applied on AC-15, the first electron will react with oxygen to form superoxide. Afterwards, the second electron reacts with superoxide and water to generate hydroxyl ions and peroxide. The third electron, then, reacts with the peroxide and the water producing hydroxide and hydroxyl radicals. However, hydroxyl radicals should further be reduced to form hydroxyl ions in a perfect 4-electron process, but AC-15 presents only three-electron transfers. Therefore, hydroxyl radicals adsorb on the active site of titania and when the entire surface is blocked, the ORR cannot proceed. Hence, the SAC of AC-15 will be decreased and becomes constant at 20 % of the initial SAC after 60 cycles (Fig. 5C).

#### 4. Conclusions

We have provided a comprehensive study on the advantages of AC-titania hybrids for the CDI performance in oxygen saturated saline water (5 mM NaCl). AC-titania hybrids were successfully prepared by a sol-gel method resulting in different mass loadings of titania. It was found that higher amounts of titania lead to reduced surface areas due to pore blocking by the titania coating and thus, to lower specific capacitances measured in de-aerated electrolyte. Interestingly, CDI measurements present a contradicting behavior in O<sub>2</sub>-saturated NaCl with higher SACs for the titania coated samples and better long-time stability. For example, a 15 mass% loading of titania results in ~17.4 mg g<sup>-1</sup> SAC in the first cycles compared to AC with an initial value of ~9 mg g<sup>-1</sup>. After 15 cycles, the AC-15 hybrid demonstrates a comparably high SAC of more than ~8 mg g<sup>-1</sup> (about 50 % of the initial value), while the SAC of AC decreases to zero. Pure AC exhibits poor catalytic activity for oxygen reduction in a two-electron transfer, so that the carbon electrode is oxidized by hydrogen peroxide and surface functional groups are formed. In contrast, AC-15 leads to a three-electron transfer reaction which impedes the formation of hydrogen peroxide and partially prevents the carbon electrode from oxidizing. With this approach, higher SACs, as well as better cycling stability can be reached. Yet, the strong decay of SAC over cycles remains a challenge to be overcome and the full potential of the carbon/metal oxide is yet to be shown.

#### Acknowledgements

The authors thank Prof. Eduard Arzt (INM) for his continuing support. P.S. acknowledges financial support by the German Academic Exchange Service (DAAD award number 91579066).

#### Appendix A. Supplementary data

Supplementary data associated with this article can be found, in the online version, at <http://dx.doi.org/10.1016/j.electacta.2016.12.060>.

#### References

- [1] T.Y. Cath, A.E. Childress, M. Elimelech, Forward osmosis: Principles, applications, and recent developments, *Journal of Membrane Science* 281 (2006) 70–87.
- [2] M. Elimelech, W.A. Phillip, The Future of Seawater Desalination: Energy, Technology, and the Environment, *Science* 333 (2011) 712–717.
- [3] M.A. Shannon, P.W. Bohn, M. Elimelech, J.G. Georgiadis, B.J. Marinas, A.M. Mayes, Science and technology for water purification in the coming decades, *Nature* 452 (2008) 301–310.
- [4] N. Savage, M.S. Diallo, Nanomaterials and Water Purification: Opportunities and Challenges, *Journal of Nanoparticle Research* 7 (2005) 331–342.
- [5] K.P. Lee, T.C. Arnot, D. Mattia, A review of reverse osmosis membrane materials for desalination—Development to date and future potential, *Journal of Membrane Science* 370 (2011) 1–22.
- [6] L. Alvarado, A. Chen, Electrodeionization: Principles, Strategies and Applications, *Electrochimica Acta* 132 (2014) 583–597.
- [7] Y.S. Dzyazko, L.N. Ponomaryova, L.M. Rozhdestvenskaya, S.L. Vasilyuk, V.N. Belyakov, Electrodeionization of low-concentrated multicomponent Ni<sup>2+</sup>-containing solutions using organic–inorganic ion-exchanger, *Desalination* 342 (2014) 43–51.
- [8] B. Jia, W. Zhang, Preparation and Application of Electrodes in Capacitive Deionization (CDI): a State-of-Art Review, *Nanoscale Research Letters* 11 (2016) 1–25.
- [9] S. Porada, R. Zhao, A. van der Wal, V. Presser, P.M. Biesheuvel, Review on the science and technology of water desalination by capacitive deionization, *Progress in Materials Science* 58 (2013) 1388–1442.
- [10] Y. Oren, Capacitive deionization (CDI) for desalination and water treatment – past, present and future (a review), *Desalination* 228 (2008) 10–29.
- [11] J.K. Ewert, D. Weingarth, C. Denner, M. Friedrich, M. Zeiger, A. Schreiber, N. Jackel, V. Presser, R. Kempe, Enhanced capacitance of nitrogen-doped hierarchically porous carbide-derived carbon in matched ionic liquids, *Journal of Materials Chemistry A* 3 (2015) 18906–18912.
- [12] S. Porada, F. Schipper, M. Aslan, M. Antonietti, V. Presser, T.-P. Fellingner, Capacitive Deionization using Biomass-based Microporous Salt-Templated Heteroatom-Doped Carbons, *ChemSusChem* 8 (2015) 1867–1874.
- [13] C. Prehal, D. Weingarth, E. Perre, R.T. Lechner, H. Amenitsch, O. Paris, V. Presser, Tracking the structural arrangement of ions in carbon supercapacitor nanopores using in situ small-angle X-ray scattering, *Energy & Environmental Science* 8 (2015) 1725–1735.
- [14] P.M. Biesheuvel, S. Porada, M. Levi, M.Z. Bazant, Attractive forces in microporous carbon electrodes for capacitive deionization, *Journal of Solid State Electrochemistry* 18 (2014) 1365–1376.
- [15] M.E. Suss, S. Porada, X. Sun, P.M. Biesheuvel, J. Yoon, V. Presser, Water desalination via capacitive deionization: what is it and what can we expect from it? *Energy & Environmental Science* 8 (2015) 2296–2319.
- [16] Y.-J. Kim, J.-H. Choi, Enhanced desalination efficiency in capacitive deionization with an ion-selective membrane, *Separation and Purification Technology* 71 (2010) 70–75.
- [17] P.M. Biesheuvel, A. van der Wal, Membrane capacitive deionization, *Journal of Membrane Science* 346 (2010) 256–262.
- [18] J. Yang, L. Zou, N.R. Choudhury, Ion-selective carbon nanotube electrodes in capacitive deionization, *Electrochimica Acta* 91 (2013) 11–19.
- [19] P.M. Biesheuvel, H.V.M. Hamelers, M.E. Suss, Theory of Water Desalination by Porous Electrodes with Immobile Chemical Charge, *Colloids and Interface Science Communications* 9 (2015) 1–5.
- [20] X. Gao, S. Porada, A. Omosibi, K.L. Liu, P.M. Biesheuvel, J. Landon, Complementary surface charge for enhanced capacitive deionization, *Water Research* 92 (2016) 275–282.
- [21] R. Zhao, P.M. Biesheuvel, H. Miedema, H. Bruning, A. van der Wal, Charge Efficiency: A Functional Tool to Probe the Double-Layer Structure Inside of Porous Electrodes and Application in the Modeling of Capacitive Deionization, *The Journal of Physical Chemistry Letters* 1 (2010) 205–210.
- [22] I. Cohen, E. Avraham, Y. Bouhadana, A. Soffer, D. Aurbach, Long term stability of capacitive de-ionization processes for water desalination: The challenge of positive electrodes corrosion, *Electrochimica Acta* 106 (2013) 91–100.
- [23] K.G. Gallagher, T.F. Fuller, Kinetic model of the electrochemical oxidation of graphitic carbon in acidic environments, *Physical Chemistry Chemical Physics* 11 (2009) 11557–11567.
- [24] K.G. Gallagher, G. Yushin, T.F. Fuller, The Role of Nanostructure in the Electrochemical Oxidation of Model-Carbon Materials in Acidic Environments, *Journal of The Electrochemical Society* 157 (2010) B820–B830.
- [25] J.-H. Lee, W.-S. Bae, J.-H. Choi, Electrode reactions and adsorption/desorption performance related to the applied potential in a capacitive deionization process, *Desalination* 258 (2010) 159–163.
- [26] I. Cohen, E. Avraham, Y. Bouhadana, A. Soffer, D. Aurbach, The effect of the flow-regime, reversal of polarization, and oxygen on the long term stability in capacitive de-ionization processes, *Electrochimica Acta* 153 (2015) 106–114.
- [27] F. Duan, X. Du, Y. Li, H. Cao, Y. Zhang, Desalination stability of capacitive deionization using ordered mesoporous carbon: Effect of oxygen-containing surface groups and pore properties, *Desalination* 376 (2015) 17–24.
- [28] X. Gao, A. Omosibi, J. Landon, K. Liu, Surface charge enhanced carbon electrodes for stable and efficient capacitive deionization using inverted adsorption-desorption behavior, *Energy & Environmental Science* 8 (2015) 897–909.

- [29] X. Gao, A. Omosebi, N. Holubowitch, A. Liu, K. Ruh, J. Landon, K. Liu, Polymer-coated composite anodes for efficient and stable capacitive deionization, *Desalination* 399 (2016) 16–20.
- [30] R.R.A. Rios, D.E. Alves, I. Dalmázio, S.F.V. Bento, C.L. Donnici, R.M. Lago, Tailoring activated carbon by surface chemical modification with O, S, and N containing molecules, *Materials Research* 6 (2003) 129–135.
- [31] S. Kundu, W. Xia, W. Busser, M. Becker, D.A. Schmidt, M. Havenith, M. Muhler, The formation of nitrogen-containing functional groups on carbon nanotube surfaces: a quantitative XPS and TPD study, *Physical Chemistry Chemical Physics* 12 (2010) 4351–4359.
- [32] X. Gao, A. Omosebi, J. Landon, K. Liu, Enhanced Salt Removal in an Inverted Capacitive Deionization Cell Using Amine Modified Microporous Carbon Cathodes, *Environmental Science & Technology* 49 (2015) 10920–10926.
- [33] B. Shapira, E. Avraham, D. Aurbach, Side Reactions in Capacitive Deionization (CDI) Processes: The Role of Oxygen Reduction, *Electrochimica Acta* 220 (2016) 285–295.
- [34] Y. Bouhadana, E. Avraham, M. Noked, M. Ben-Tzion, A. Soffer, D. Aurbach, Capacitive Deionization of NaCl Solutions at Non-Steady-State Conditions: Inversion Functionality of the Carbon Electrodes, *The Journal of Physical Chemistry C* 115 (2011) 16567–16573.
- [35] T. Kim, J. Yu, C. Kim, J. Yoon, Hydrogen peroxide generation in flow-mode capacitive deionization, *Journal of Electroanalytical Chemistry* 776 (2016) 101–104.
- [36] J. Liu, M. Lu, J. Yang, J. Cheng, W. Cai, Capacitive desalination of ZnO/activated carbon asymmetric capacitor and mechanism analysis, *Electrochimica Acta* 151 (2015) 312–318.
- [37] J. Yang, L. Zou, H. Song, Z. Hao, Development of novel MnO<sub>2</sub>/nanoporous carbon composite electrodes in capacitive deionization technology, *Desalination* 276 (2011) 199–206.
- [38] A.G. El-Deen, N.A.M. Barakat, K.A. Khalil, M. Motlak, H. Yong Kim, Graphene/SnO<sub>2</sub> nanocomposite as an effective electrode material for saline water desalination using capacitive deionization, *Ceramics International* 40 (2014) 14627–14634.
- [39] H. Li, Y. Ma, R. Niu, Improved capacitive deionization performance by coupling TiO<sub>2</sub> nanoparticles with carbon nanotubes, *Separation and Purification Technology* 171 (2016) 93–100.
- [40] M.-W. Ryou, G. Seo, Improvement in capacitive deionization function of activated carbon cloth by titania modification, *Water Research* 37 (2003) 1527–1534.
- [41] C. Kim, J. Lee, S. Kim, J. Yoon, TiO<sub>2</sub> sol–gel spray method for carbon electrode fabrication to enhance desalination efficiency of capacitive deionization, *Desalination* 342 (2014) 70–74.
- [42] Y. Liang, Y. Li, H. Wang, J. Zhou, J. Wang, T. Regier, H. Dai, Co304 nanocrystals on graphene as a synergistic catalyst for oxygen reduction reaction, *Nat. Mater.* 10 (2011) 780–786.
- [43] J. Suntivich, H.A. Gasteiger, N. Yabuuchi, H. Nakanishi, J.B. Goodenough, Y. Shao-Horn, Design principles for oxygen-reduction activity on perovskite oxide catalysts for fuel cells and metal–air batteries, *Nat. Chem.* 3 (2011) 546–550.
- [44] F. Cheng, T. Zhang, Y. Zhang, J. Du, X. Han, J. Chen, Enhancing Electrocatalytic Oxygen Reduction on MnO<sub>2</sub> with Vacancies, *Angewandte Chemie International Edition* 52 (2013) 2474–2477.
- [45] Y. Liang, H. Wang, P. Diao, W. Chang, G. Hong, Y. Li, M. Gong, L. Xie, J. Zhou, J. Wang, T.Z. Regier, F. Wei, H. Dai, Oxygen Reduction Electrocatalyst Based on Strongly Coupled Cobalt Oxide Nanocrystals and Carbon Nanotubes, *Journal of the American Chemical Society* 134 (2012) 15849–15857.
- [46] Z.-S. Wu, S. Yang, Y. Sun, K. Parvez, X. Feng, K. Müllen, 3D Nitrogen-Doped Graphene Aerogel-Supported Fe<sub>3</sub>O<sub>4</sub> Nanoparticles as Efficient Electrocatalysts for the Oxygen Reduction Reaction, *Journal of the American Chemical Society* 134 (2012) 9082–9085.
- [47] S. Guo, S. Zhang, L. Wu, S. Sun, Co/CoO Nanoparticles Assembled on Graphene for Electrochemical Reduction of Oxygen, *Angewandte Chemie* 124 (2012) 11940–11943.
- [48] J. Yu, Z. Liu, L. Zhai, T. Huang, J. Han, Reduced graphene oxide supported TiO<sub>2</sub> as high performance catalysts for oxygen reduction reaction, *International Journal of Hydrogen Energy* 41 (2016) 3436–3445.
- [49] D.-N. Pei, L. Gong, A.-Y. Zhang, X. Zhang, J.-J. Chen, Y. Mu, H.-Q. Yu, Defective titanium dioxide single crystals exposed by high-energy {001} facets for efficient oxygen reduction, *Nat Commun* 6 (2015).
- [50] J. Swaminathan, R. Subbiah, V. Singaram, Defect-Rich Metallic Titania (TiO<sub>1.23</sub>)—An Efficient Hydrogen Evolution Catalyst for Electrochemical Water Splitting, *ACS Catalysis* 6 (2016) 2222–2229.
- [51] A. Satyanarayana Reddy, S. Kim, H. Young Jeong, S. Jin, K. Qadir, K. Jung, C. Ho Jung, J. Yeul Yun, J. Yeong Cheon, J.-M. Yang, S. Hoon Joo, O. Terasaki, J. Young Park, Ultrathin titania coating for high-temperature stable SiO<sub>2</sub>/Pt nanocatalysts, *Chemical Communications* 47 (2011) 8412–8414.
- [52] D. Vorkapic, T. Matsoukas, Effect of Temperature and Alcohols in the Preparation of Titania Nanoparticles from Alkoxides, *Journal of the American Ceramic Society* 81 (1998) 2815–2820.
- [53] C.-C. Wang, J.Y. Ying, Sol-Gel Synthesis and Hydrothermal Processing of Anatase and Rutile Titania Nanocrystals, *Chemistry of Materials* 11 (1999) 3113–3120.
- [54] A. Matsumoto, K. Tsutsumi, K. Kaneko, Titania coating of a microporous carbon surface by molecular adsorption-deposition, *Langmuir* 8 (1992) 2515–2520.
- [55] L. Yan, G. Chen, S. Tan, M. Zhou, G. Zou, S. Deng, S. Smirnov, H. Luo, Titanium Oxynitride Nanoparticles Anchored on Carbon Nanotubes as Energy Storage Materials, *ACS Applied Materials & Interfaces* 7 (2015) 24212–24217.
- [56] R.B. Rakhi, W. Chen, D. Cha, H.N. Alshareef, High performance supercapacitors using metal oxide anchored graphene nanosheet electrodes, *Journal of Materials Chemistry* 21 (2011) 16197–16204.
- [57] K. Laxman, L.A. Gharibi, J. Dutta, Capacitive deionization with asymmetric electrodes: Electrode capacitance vs electrode surface area, *Electrochimica Acta* 176 (2015) 420–425.
- [58] M.B. Sassin, C.N. Chervin, D.R. Rolison, J.W. Long, Redox Deposition of Nanoscale Metal Oxides on Carbon for Next-Generation Electrochemical Capacitors, *Accounts of Chemical Research* 46 (2013) 1062–1074.
- [59] M. Ramani, B.S. Haran, R.E. White, B.N. Popov, Synthesis and Characterization of Hydrrous Ruthenium Oxide–Carbon Supercapacitors, *Journal of The Electrochemical Society* 148 (2001) A374–A380.
- [60] M.-W. Ryou, J.-H. Kim, G. Seo, Role of titania incorporated on activated carbon cloth for capacitive deionization of NaCl solution, *Journal of Colloid and Interface Science* 264 (2003) 414–419.
- [61] S. Brunauer, P.H. Emmett, E. Teller, Adsorption of Gases in Multimolecular Layers, *Journal of the American Chemical Society* 60 (1938) 309–319.
- [62] G.Y. Gor, M. Thommes, K.A. Cychoz, A.V. Neimark, Quenched solid density functional theory method for characterization of mesoporous carbons by nitrogen adsorption, *Carbon* 50 (2012) 1583–1590.
- [63] M. Aslan, D. Weingarth, P. Herbeck-Engel, I. Grobelsek, V. Presser, Polyvinylpyrrolidone/polyvinyl butyral composite as a stable binder for castable supercapacitor electrodes in aqueous electrolytes, *Journal of Power Sources* 279 (2015) 323–333.
- [64] P. Srimuk, L. Ries, M. Zeiger, S. Fleischmann, N. Jäckel, A. Tolosa, B. Krüner, M. Aslan, V. Presser, High performance stability of titania decorated carbon for desalination with capacitive deionization in oxygenated water, *RSC Advances* 6 (2016) 106081–106089.
- [65] X. Xu, M. Wang, Y. Liu, T. Lu, L. Pan, Metal-organic framework-engaged formation of a hierarchical hybrid with carbon nanotube inserted porous carbon polyhedra for highly efficient capacitive deionization, *Journal of Materials Chemistry A* 4 (2016) 5467–5473.
- [66] N. Jäckel, D. Weingarth, A. Schreiber, B. Krüner, M. Zeiger, A. Tolosa, M. Aslan, V. Presser, Performance evaluation of conductive additives for activated carbon supercapacitors in organic electrolyte, *Electrochimica Acta* 191 (2016) 284–298.
- [67] Y. Wang, Y. Zou, J. Chen, G.-D. Li, Y. Xu, A flexible and monolithic nanocomposite aerogel of carbon nanofibers and crystalline titania: fabrication and applications, *RSC Advances* 3 (2013) 24163–24168.
- [68] B. Gao, G.Z. Chen, G. Li Puma, Carbon nanotubes/titanium dioxide (CNTs/TiO<sub>2</sub>) nanocomposites prepared by conventional and novel surfactant wrapping sol–gel methods exhibiting enhanced photocatalytic activity, *Applied Catalysis B: Environmental* 89 (2009) 503–509.
- [69] M. Aslan, M. Zeiger, N. Jäckel, I. Grobelsek, D. Weingarth, V. Presser, Improved capacitive deionization performance of mixed hydrophobic/hydrophilic activated carbon electrodes, *Journal of Physics: Condensed Matter* 28 (2016) 114003.
- [70] S. Fleischmann, N. Jäckel, M. Zeiger, B. Krüner, I. Grobelsek, P. Formanek, S. Choudhury, D. Weingarth, V. Presser, Enhanced Electrochemical Energy Storage by Nanoscopic Decoration of Endohedral and Exohedral Carbon with Vanadium Oxide via Atomic Layer Deposition, *Chemistry of Materials* 28 (2016) 2802–2813.
- [71] A.C. Ferrari, J. Robertson, Interpretation of Raman spectra of disordered and amorphous carbon, *Physical Review B* 61 (2000) 14095–14107.
- [72] Y. Xu, H. Lin, L. Li, X. Huang, G. Li, Precursor-directed synthesis of well-faceted brookite TiO<sub>2</sub> single crystals for efficient photocatalytic performances, *Journal of Materials Chemistry A* 3 (2015) 22361–22368.
- [73] T.A. Kandiel, A. Feldhoff, L. Robben, R. Dillert, D.W. Bahnemann, Tailored Titanium Dioxide Nanomaterials: Anatase Nanoparticles and Brookite Nanorods as Highly Active Photocatalysts, *Chemistry of Materials* 22 (2010) 2050–2060.
- [74] W.F. Zhang, Y.L. He, M.S. Zhang, Z. Yin, Q. Chen, Raman scattering study on anatase TiO<sub>2</sub> nanocrystals, *Journal of Physics D: Applied Physics* 33 (2000) 912.
- [75] Y.-H. Zhang, C.K. Chan, J.F. Porter, W. Guo, Micro-Raman Spectroscopic Characterization of Nanosized TiO<sub>2</sub> Powders Prepared by Vapor Hydrolysis, *Journal of Materials Research* 13 (2005) 2602–2609.
- [76] B. Štjukić, C.E. Banks, R.G. Compton, An overview of the electrochemical reduction of oxygen at carbon-based modified electrodes, *Journal of the Iranian Chemical Society* 2 (2005) 1–25.
- [77] R. Liu, D. Wu, X. Feng, K. Müllen, Nitrogen-Doped Ordered Mesoporous Graphitic Arrays with High Electrocatalytic Activity for Oxygen Reduction, *Angewandte Chemie* 122 (2010) 2619–2623.
- [78] Y. Zheng, Y. Jiao, J. Chen, J. Liu, J. Liang, A. Du, W. Zhang, Z. Zhu, S.C. Smith, M. Jaroniec, G.Q. Lu, S.Z. Qiao, Nanoporous Graphitic-C<sub>3</sub>N<sub>4</sub>@Carbon Metal-Free Electrocatalysts for Highly Efficient Oxygen Reduction, *Journal of the American Chemical Society* 133 (2011) 20116–20119.
- [79] R.A. Sidik, A.B. Anderson, N.P. Subramanian, S.P. Kumaraguru, B.N. Popov, O<sub>2</sub> Reduction on Graphite and Nitrogen-Doped Graphite: Experiment and Theory, *The Journal of Physical Chemistry B* 110 (2006) 1787–1793.
- [80] D. Weingarth, M. Zeiger, N. Jäckel, M. Aslan, G. Feng, V. Presser, Graphitization as a Universal Tool to Tailor the Potential-Dependent Capacitance of Carbon Supercapacitors, *Advanced Energy Materials* 4 (2014) n/a–n/a.

- [81] M.W. Ryou, G. Seo, Improvement in capacitive deionization function of activated carbon cloth by titania modification, *Water Res.* 37 (2003).
- [82] A.G. El-Deen, J.-H. Choi, C.S. Kim, K.A. Khalil, A.A. Almajid, N.A.M. Barakat, TiO<sub>2</sub> nanorod-intercalated reduced graphene oxide as high performance electrode material for membrane capacitive deionization, *Desalination* 361 (2015) 53–64.
- [83] P.B. Peters, M.Z. van Roij, P.M. Biesheuvel, Analysis of electrolyte transport through charged nanopores, *Physical Review E* 93 (2016) 053108.
- [84] E. Yeager, Electrocatalysts for O<sub>2</sub> reduction, *Electrochimica Acta* 29 (1984) 1527–1537.
- [85] J. Liang, Y. Jiao, M. Jaroniec, S.Z. Qiao, Sulfur and Nitrogen Dual-Doped Mesoporous Graphene Electrocatalyst for Oxygen Reduction with Synergistically Enhanced Performance, *Angewandte Chemie International Edition* 51 (2012) 11496–11500.
- [86] E. Benn, J. Erlebacher, Oxygen Reduction in Nanoporous Metals Under Proton Diffusion Limited Conditions, *Meeting Abstracts, MA2016-01* (2016) 1696.
- [87] S.J. Clouser, J.C. Huang, E. Yeager, Temperature dependence of the Tafel slope for oxygen reduction on platinum in concentrated phosphoric acid, *Journal of Applied Electrochemistry* 23 (1993) 597–605.
- [88] H. Geisler, A. Kromp, A. Weber, E. Ivers-Tiffée, Performance of MIEC Cathodes in SOFC Stacks Evaluated by Means of FEM Modeling, *ECS Transactions* 61 (2014) 191–201.
- [89] J. Durst, A. Siebel, C. Simon, F. Hasche, J. Herranz, H.A. Gasteiger, New insights into the electrochemical hydrogen oxidation and evolution reaction mechanism, *Energy & Environmental Science* 7 (2014) 2255–2260.
- [90] M. Jahan, Z. Liu, K.P. Loh, A Graphene Oxide and Copper-Centered Metal Organic Framework Composite as a Tri-Functional Catalyst for HER, OER, and ORR, *Advanced Functional Materials* 23 (2013) 5363–5372.
- [91] Y. Peng, H. Liu, Effects of Oxidation by Hydrogen Peroxide on the Structures of Multiwalled Carbon Nanotubes, *Industrial & Engineering Chemistry Research* 45 (2006) 6483–6488.
- [92] K. Gong, F. Du, Z. Xia, M. Durstock, L. Dai, Nitrogen-Doped Carbon Nanotube Arrays with High Electrocatalytic Activity for Oxygen Reduction, *Science* 323 (2009) 760–764.
- [93] C.O. Laoire, S. Mukerjee, K.M. Abraham, E.J. Plichta, M.A. Hendrickson, Elucidating the Mechanism of Oxygen Reduction for Lithium-Air Battery Applications, *The Journal of Physical Chemistry C* 113 (2009) 20127–20134.
- [94] C.O. Laoire, S. Mukerjee, K.M. Abraham, E.J. Plichta, M.A. Hendrickson, Influence of Nonaqueous Solvents on the Electrochemistry of Oxygen in the Rechargeable Lithium-Air Battery, *The Journal of Physical Chemistry C* 114 (2010) 9178–9186.
- [95] G.W. Hung, R.H. Dinius, Diffusivity of oxygen in electrolyte solutions, *Journal of Chemical & Engineering Data* 17 (1972) 449–451.
- [96] D. He, C.E. Wong, W. Tang, P. Kovalsky, T.D. Waite, Faradaic Reactions in Water Desalination by Batch-Mode Capacitive Deionization, *Environmental Science & Technology Letters* 3 (2016) 222–226.
- [97] A.S. Yasin, H.O. Mohamed, I.M.A. Mohamed, H.M. Mousa, N.A.M. Barakat, Enhanced desalination performance of capacitive deionization using zirconium oxide nanoparticles-doped graphene oxide as a novel and effective electrode, *Separation and Purification Technology* 171 (2016) 34–43.
- [98] B. Chen, Y. Wang, Z. Chang, X. Wang, M. Li, X. Liu, L. Zhang, Y. Wu, Enhanced capacitive desalination of MnO<sub>2</sub> by forming composite with multi-walled carbon nanotubes, *RSC Advances* 6 (2016) 6730–6736.
- [99] A.G. El-Deen, J.-H. Choi, K.A. Khalil, A.A. Almajid, N.A.M. Barakat, A TiO<sub>2</sub> nanofiber/activated carbon composite as a novel effective electrode material for capacitive deionization of brackish water, *RSC Advances* 4 (2014) 64634–64642.
- [100] A.G. El-Deen, N.A.M. Barakat, H.Y. Kim, Graphene wrapped MnO<sub>2</sub>-nanostructures as effective and stable electrode materials for capacitive deionization desalination technology, *Desalination* 344 (2014) 289–298.
- [101] W. Zhang, B. Jia, Toward anti-fouling capacitive deionization by using visible-light reduced TiO<sub>2</sub>/graphene nanocomposites, *MRS Communications* 5 (2015) 613–617.
- [102] P.-I. Liu, L.-C. Chung, C.-H. Ho, H. Shao, T.-M. Liang, R.-Y. Horng, M.-C. Chang, C.-C.M. Ma, Effects of activated carbon characteristics on the electrosorption capacity of titanium dioxide/activated carbon composite electrode materials prepared by a microwave-assisted ionothermal synthesis method, *Journal of Colloid and Interface Science* 446 (2015) 352–358.

# Enhanced performance stability of carbon/titania hybrid electrodes during capacitive deionization of oxygen saturated saline water

Pattarachai Srimuk,<sup>1,2</sup> Marco Zeiger,<sup>1,2</sup> Nicolas Jäckel,<sup>1,2,+</sup> Aura Tolosa,<sup>1,2</sup>

Benjamin Krüner,<sup>1,2</sup> Simon Fleischmann,<sup>2</sup> Ingrid Grobelsek,<sup>1</sup> Mesut Aslan,<sup>1</sup>

Boris Shvartsev,<sup>3</sup> Matthew E. Suss,<sup>3</sup> Volker Presser<sup>1,2</sup>

<sup>1</sup> *INM - Leibniz Institute for New Materials, 66123 Saarbrücken, Germany*

<sup>2</sup> *Department of Materials Science and Engineering, Saarland University, 66123 Saarbrücken, Germany*

<sup>3</sup> *Faculty of Mechanical Engineering, Technion – Israel Institute of Technology, Haifa, 32000, Israel*

<sup>+</sup> *ISE member*

## *Supporting Information*

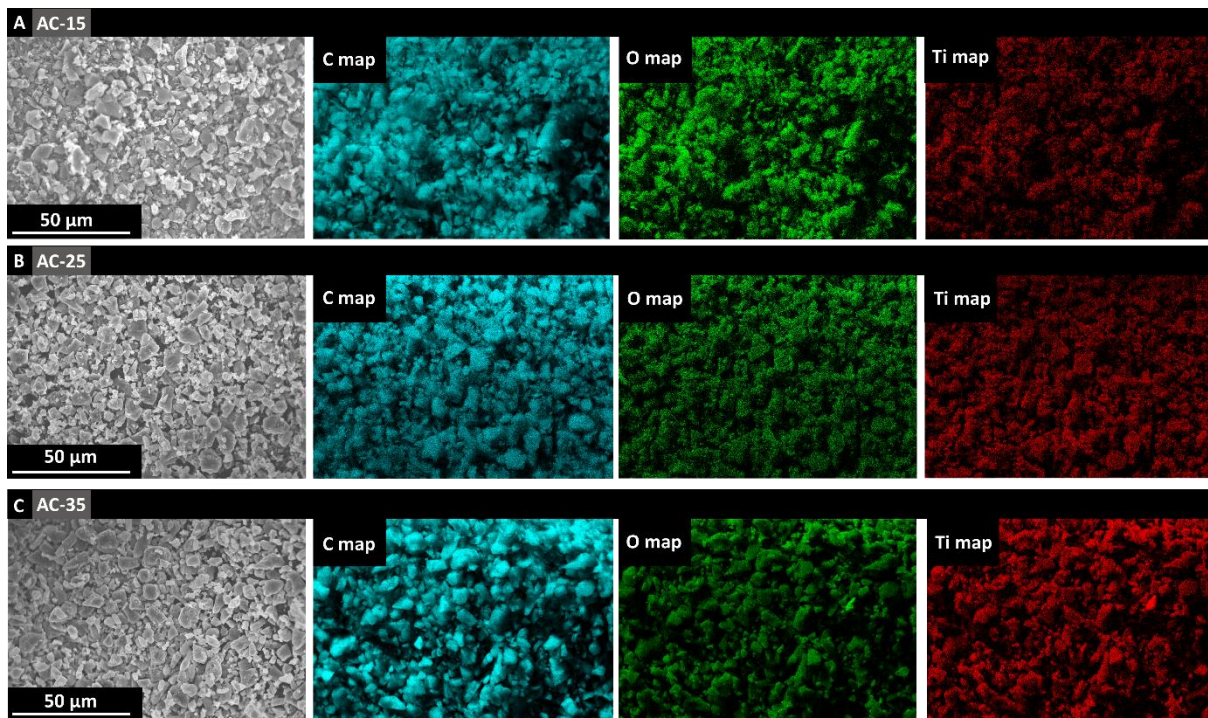


**Figure S1.** EDX mapping of (A) AC-15, (B) AC-25, and (C) AC-35. The element distribution of carbon, oxygen and titanium are illustrated including original SEM images.

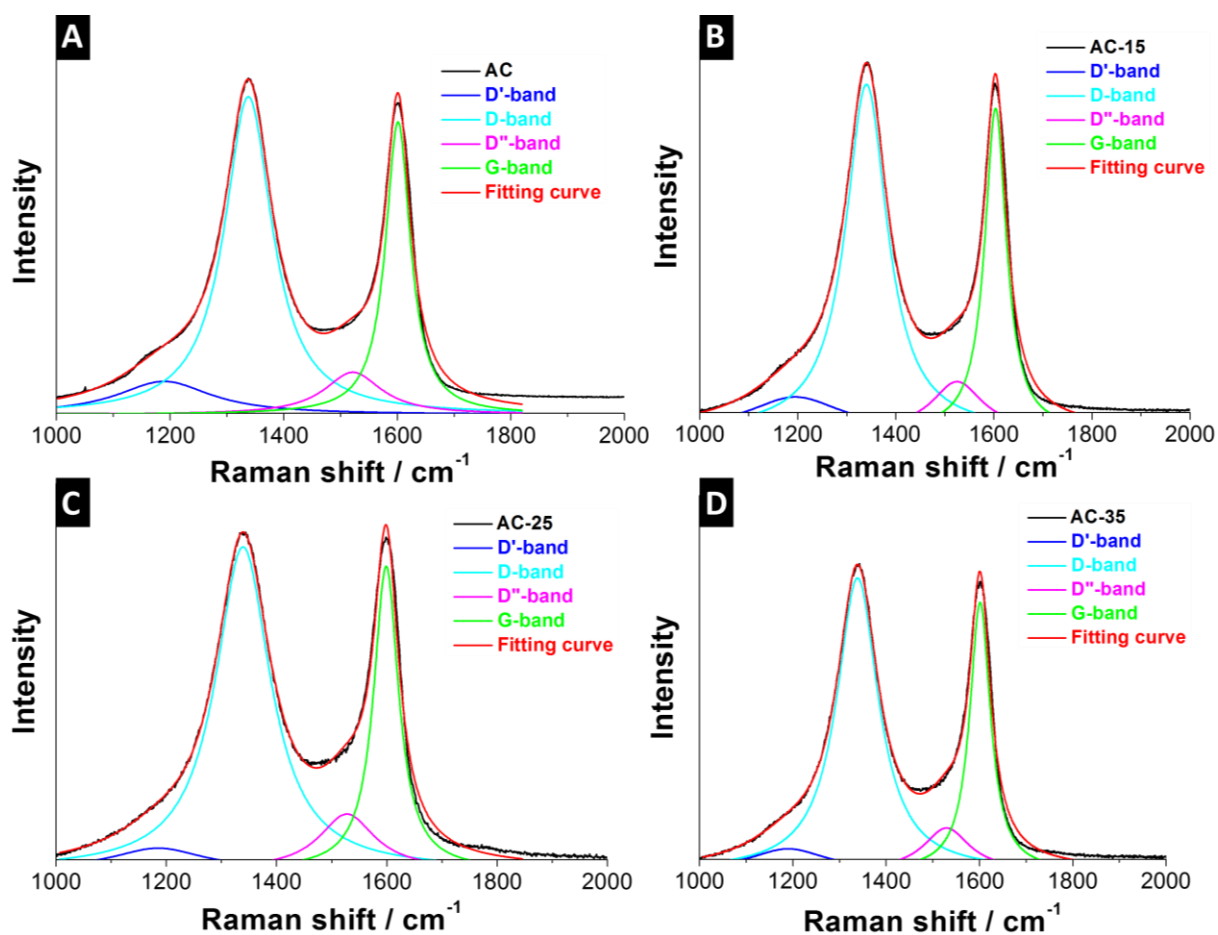
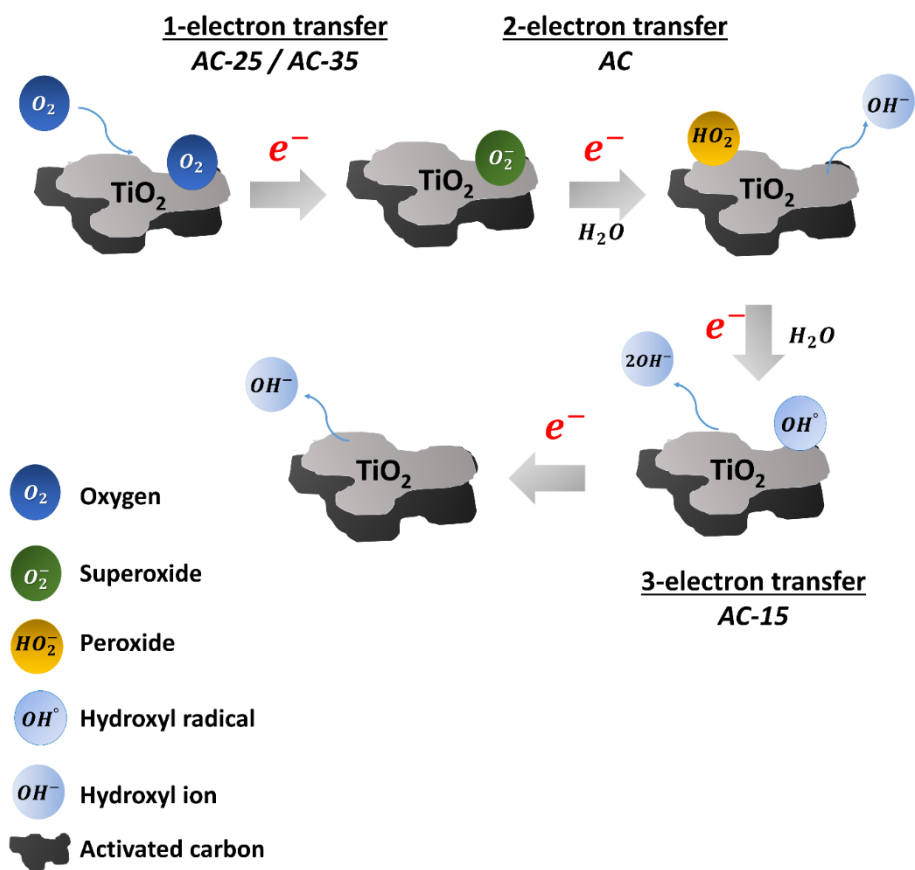
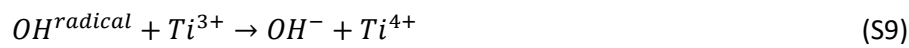
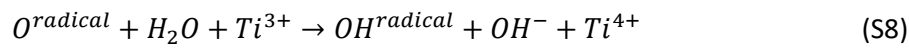
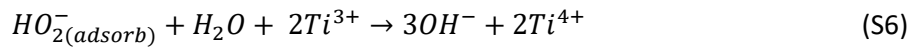
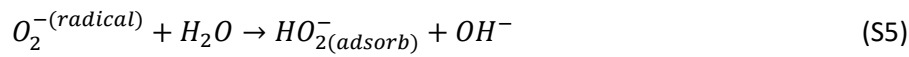
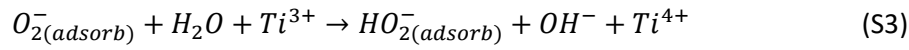
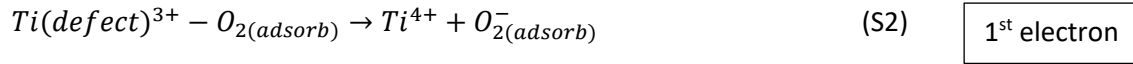


Figure S2. Cumulative fitting of carbon Raman spectra. (A) AC, (B) AC-15, (C) AC-25, and (D) AC-35.



**Figure S3.** Oxygen reduction reaction mechanism on AC-titania surfaces.

## ORR reactions



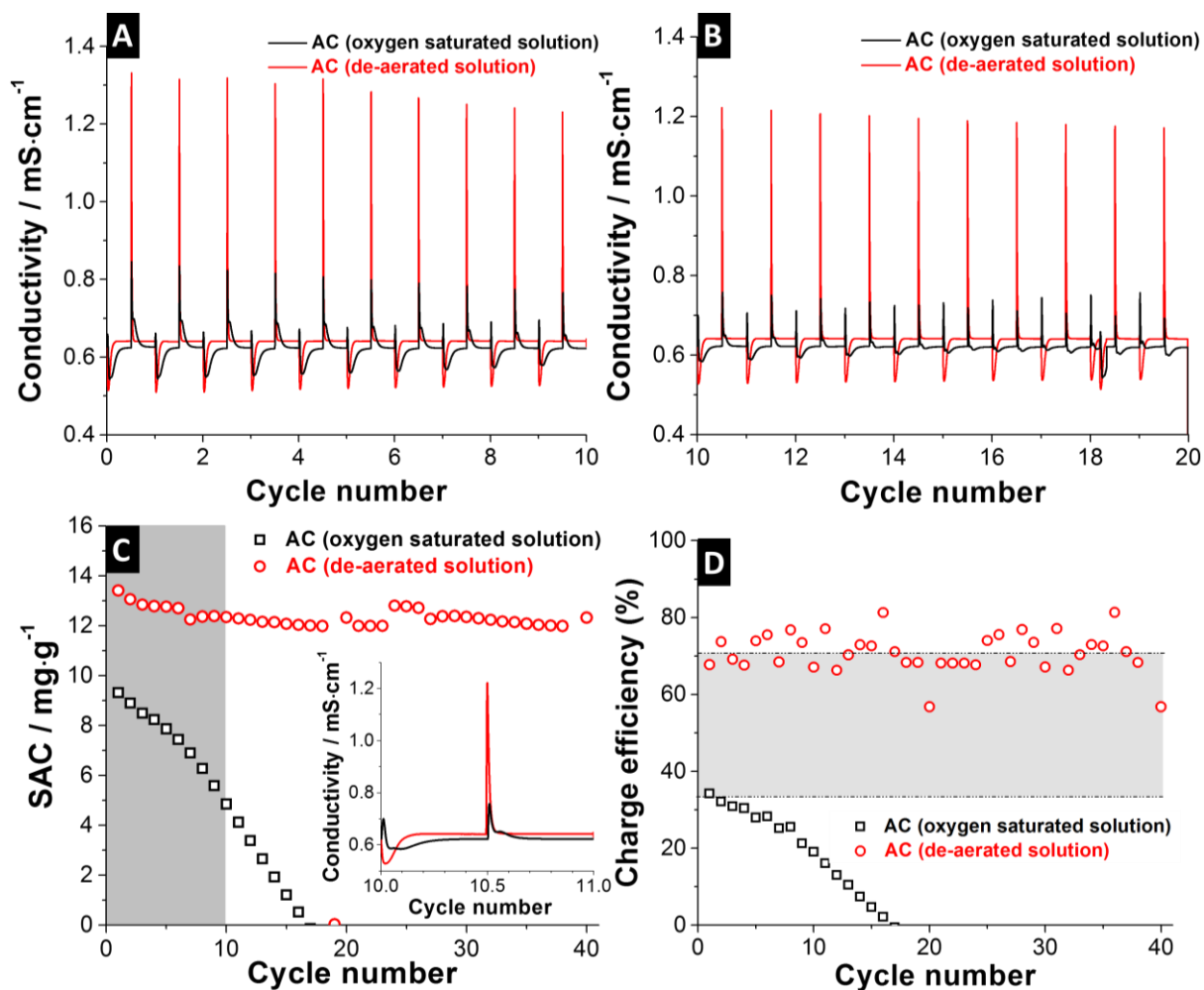


**Figure S4.** CDI performance of neat AC in de-aerated and oxygen saturated 5 mM NaCl at 1.2 V. Conductivity data of the outlet flow stream for (A) 1<sup>st</sup> to 10<sup>th</sup> and (B) 10<sup>th</sup> to 20<sup>th</sup> cycle. Data for neat AC in de-aerated and oxygen saturated 5 mM NaCl for 40 cycles regarding the (C) salt adsorption capacity and (D) charge efficiency.

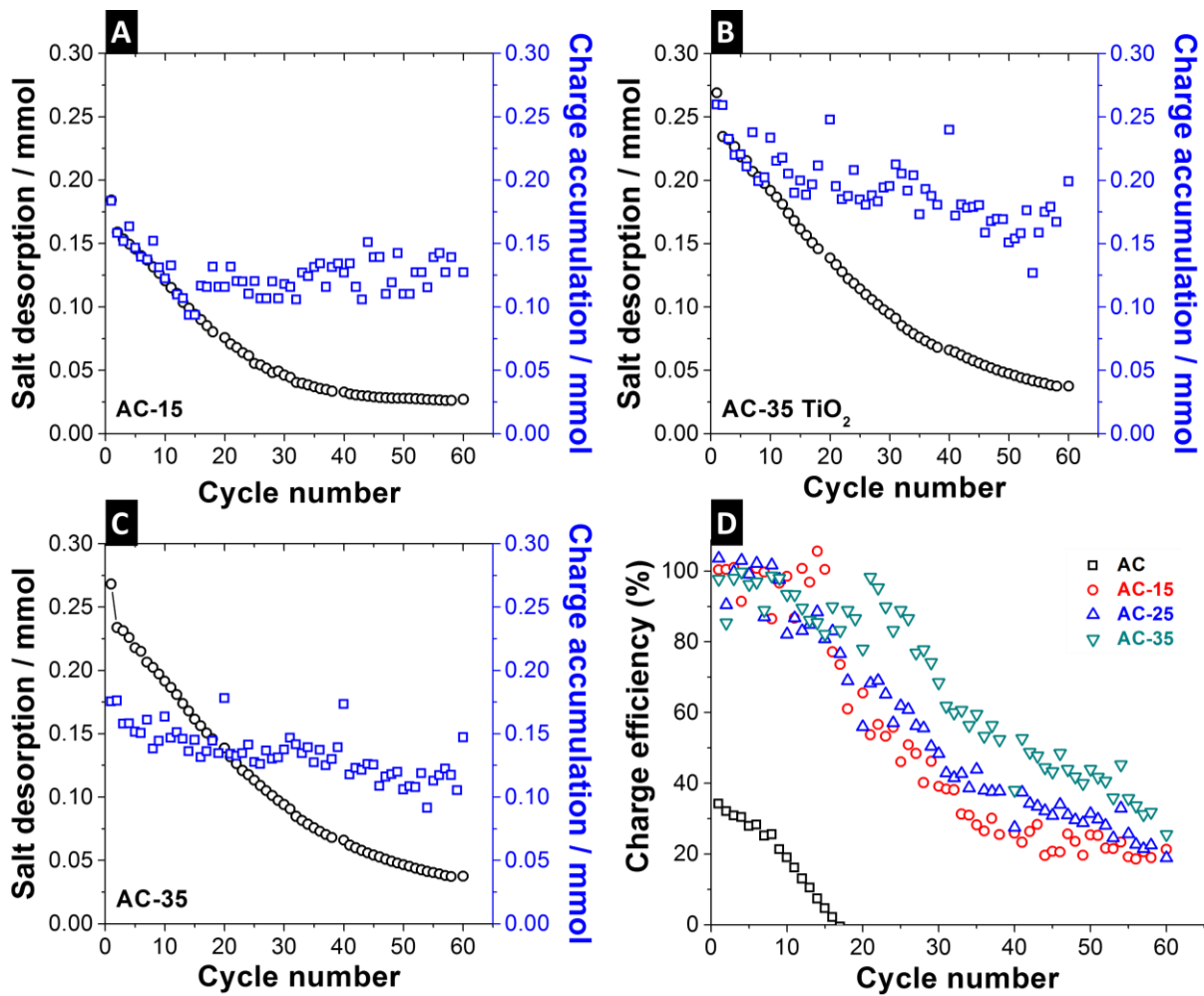


**Figure S5.** Charge and salt adsorption of (A) AC-15, (B) AC-25, (C) AC-35, and (D) corresponding charge efficiencies in O<sub>2</sub>-saturated 5 mM NaCl.

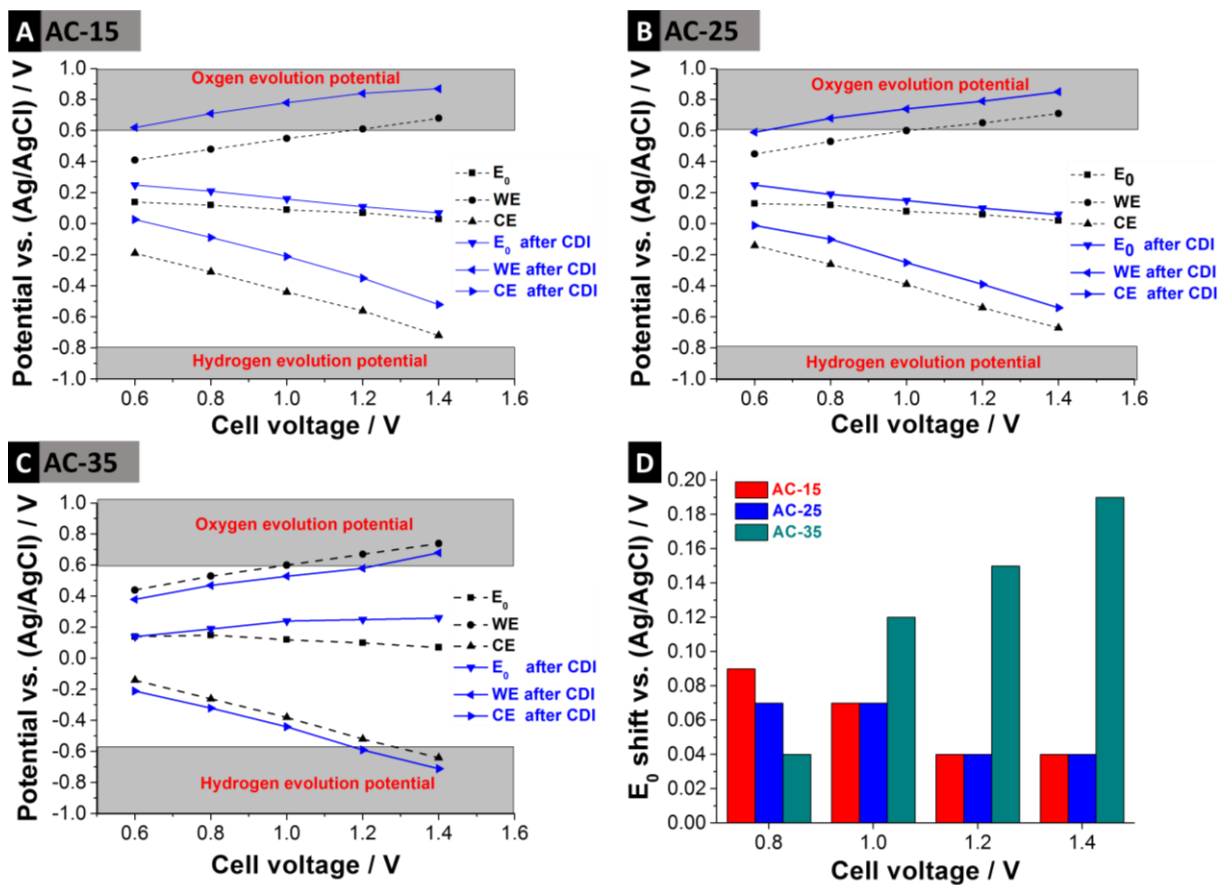
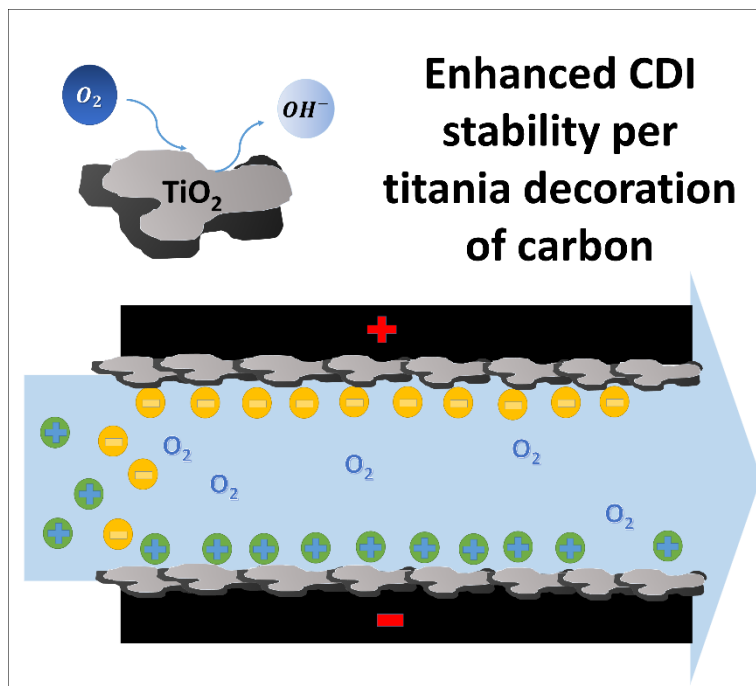


**Figure S6.** Potential monitoring of cathode and anode before and after CDI cycle at different cell voltages in 1 M NaCl for (A) AC-15, (B) AC-25, and (C) AC-35. (D) Zero charge potential shift of AC-titania before and after CDI cycle.

Graphical Abstract



## 4.2 High performance stability of titania decorated carbon for desalination with capacitive deionization in oxygenated water

Pattarachai Srimuk<sup>1,2</sup> Lucie Ries,<sup>1,2</sup> Marco Zeiger,<sup>1,2</sup> Simon Fleischmann,<sup>1,2</sup>  
Nicolas Jäckel,<sup>1,2</sup> Aura Tolosa,<sup>1,2</sup> Benjamin Krüner,<sup>1,2</sup> Mesut Aslan,<sup>1</sup> Volker Presser<sup>1,2</sup>

<sup>1</sup> INM - Leibniz Institute for New Materials, Campus D2 2, 66123 Saarbrücken, Germany

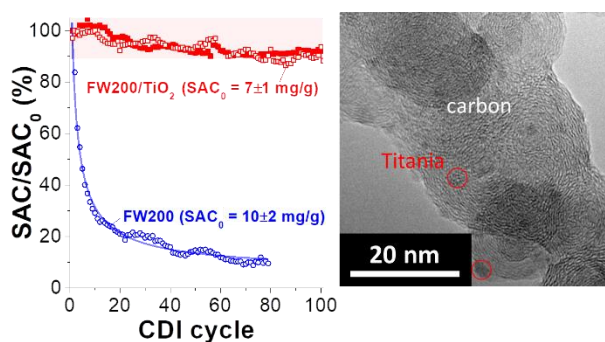
<sup>2</sup> Saarland University, Campus D2 2, 66123 Saarbrücken, Germany

### Citation:

P. Srimuk, L. Ries, M. Zeiger, S. Fleischmann, N. Jäckel, A. Tolosa, B. Krüner, M. Aslan, V. Presser, HIGH PERFORMANCE STABILITY OF TITANIA DECORATED CARBON FOR DESALINATION WITH CAPACITIVE DEIONIZATION IN OXYGENATED WATER, RSC Advances 6(108) (2016) 106081-106089.

### Own contribution:

Electrochemical measurement, CDI measurement, analysis, writing





CrossMark  
 click for updates

Cite this: *RSC Adv.*, 2016, 6, 106081

Received 12th September 2016  
 Accepted 28th October 2016

DOI: 10.1039/c6ra22800c

[www.rsc.org/advances](http://www.rsc.org/advances)

# High performance stability of titania decorated carbon for desalination with capacitive deionization in oxygenated water†

Pattarachai Srimuk,<sup>ab</sup> Lucie Ries,<sup>ab</sup> Marco Zeiger,<sup>ab</sup> Simon Fleischmann,<sup>b</sup> Nicolas Jäckel,<sup>ab</sup> Aura Tolosa,<sup>ab</sup> Benjamin Krüner,<sup>ab</sup> Mesut Aslan<sup>a</sup> and Volker Presser<sup>\*ab</sup>

Performance stability in capacitive deionization (CDI) is particularly challenging in systems with a high amount of dissolved oxygen due to rapid oxidation of the carbon anode and peroxide formation. For example, carbon electrodes show a fast performance decay, leading to just 15% of the initial performance after 50 CDI cycles in oxygenated saline solution (5 mM NaCl). We present a novel strategy to overcome this severe limitation by employing nanocarbon particles hybridized with sol-gel-derived titania. In our proof-of-concept study, we demonstrate very stable performance in low molar saline electrolyte (5 mM NaCl) with saturated oxygen for the carbon/metal oxide hybrid (90% of the initial salt adsorption capacity after 100 cycles). The electrochemical analysis using a rotating disk electrode (RDE) confirms the oxygen reduction reaction (ORR) catalytic effect of FW200/TiO<sub>2</sub>, preventing local peroxide formation by locally modifying the oxygen reduction reaction.

capacity), normalized to the electrode mass, and values of 15–21 mg g<sup>-1</sup> have been reported.<sup>6,7</sup>

CDI performance is commonly plagued by progressing degradation stemming from the electrochemical deterioration of the carbon electrodes.<sup>8–10</sup> A challenge is the aggravating difference between the positively and negatively charged electrode: the former is continuously oxidized, leading to a shift in the electrode potential towards the oxygen reduction reaction (ORR) limit and enhanced degradation.<sup>9,11</sup> One approach to mitigate the issue is the use of dissimilar electrodes.<sup>12,13</sup> For example, modifying the carbon surfaces with functional groups allows to introduce an additional chemical charge and, effectively, shifts the point of zero charge of the respective electrodes.<sup>14,15</sup> By this way, CDI can even be completely inverted to yield ion release upon charging and desalination during discharging. Yet, the main focus of research on tuning carbon surface charge and functionality has remained on enhancing the salt removal capacity or the efficiency, but the longevity and performance stability remain widely unexplored. This is even more aggravated for practical, non-ideal systems, that is, aqueous saline media with dissolved oxygen, where H<sub>2</sub>O<sub>2</sub> evolution occurs on the negatively polarized electrode.<sup>16,17</sup>

Besides other metal oxides (like manganese oxide<sup>18</sup> or zinc oxide<sup>19</sup>), titania/carbon hybrid materials have been investigated to enhance the desalination capacity<sup>20,21</sup> and/or efficiency.<sup>22,23</sup> These studies commonly cover the range of few desalination/regeneration (charge/discharge) cycles, but even for CDI with just carbon electrodes, only few works show dozens or more cycles.<sup>8</sup> So far, research has fallen short of investigating the potential for enhancing the CDI performance stability by use of metal oxide coatings.

In this study, we explore the hybridization of few-nanometer-sized carbon black particles (FW200) with titania *via* sol-gel synthesis and report on the remarkable performance stability in low molar saline media with a high amount of dissolved oxygen. We chose carbon black instead of microporous activated carbon because we wanted to avoid ion transport limitations within the network of nanopores in micrometer sized particles and to have

## Introduction

Capacitive deionization (CDI) is an emerging water treatment technology which is highly attractive for energy efficient removal of ions from aqueous media with low molar concentrations (especially below 100 mM).<sup>1–3</sup> Common CDI operation accomplishes ion removal from a feed stream *via* capacitive ion electrosorption at the electrically charged fluid/solid interface between the electrolyte and the electrode. Most commonly, CDI employs nanoporous carbon, such as activated carbon, but also other carbons have been explored, for instance, graphene, carbon nanotubes, or carbide-derived carbon.<sup>4</sup> During electrical charging of the carbon electrodes, ions are removed from the feed stream *via* electrosorption.<sup>5</sup> A key value for CDI benchmarking is the desalination capacity (SAC = salt adsorption

<sup>a</sup>INM – Leibniz Institute for New Materials, Saarbrücken, Germany. E-mail: volker.presser@leibniz-inm.de

<sup>b</sup>Department of Materials Science and Engineering, Saarland University, Saarbrücken, Germany

† Electronic supplementary information (ESI) available. See DOI: 10.1039/c6ra22800c



access for titania decoration to an exclusive outer surface area. We also study the ORR catalyst ability of FW200 and FW200/TiO<sub>2</sub> to understand the origin of longevity performance in harsh (*i.e.*, oxygenated) solution.

## Experimental

### Material synthesis

For our study, we used carbon black type FW200, which was purchased from Orion (formerly: Degussa) and used without further chemical treatment.

For FW200/TiO<sub>2</sub> synthesis, 18 g of vacuum dried carbon powder FW200 was dispersed in 200 mL ethanol and set on magnetic stirrer for 5 h. Then, 16.1 g Ti(IV) isopropoxide (Aldrich) was dissolved in 500 mL ethanol and set on magnetic stirrer which should give a carbon hybrid with 20 mass% titania. During filling, the bottles/containers were purged with argon to avoid any moisture pick up from the environment. The Ti-isopropoxide solution and carbon slurry were poured together and stirred for further 48 h without any additional water for hydrolysis. After the surface functional groups of FW200 have reacted with Ti-isopropoxide, the slurry was centrifuged at 4000 rpm for 1 h so that the excess of unreacted Ti-isopropoxide was removed. The sediment was dispersed in 500 mL ethanol and centrifuged and the supernatant was removed again. This procedure was repeated two times to remove the unreacted Ti-isopropoxide. The cleaned sediment was dried at 95 °C for 24 h and used for the electrode preparation.

### Structural and chemical characterization

Scanning electron microscope (SEM) images were recorded with a JEOL JSM 7500F field emission scanning electron microscope operating at 3 kV. Energy dispersive X-ray spectroscopy (EDX) was carried out in the system with an X-Max silicon detector from Oxford Instruments using AZtec software for quantitative analysis. Transmission electron micrographs were taken with a JEOL 2100F transmission electron microscope at 200 kV. Powder samples were prepared by dispersing the powder in ethanol and drop casting them on a copper grid with lacey carbon film (Gatan).

Raman spectra were recorded with Renishaw inVia Raman microscope using a Nd-YAG laser with an excitation wavelength of 523 nm. The spectral resolution was 1.2 cm<sup>-1</sup> and the diameter of laser spot on the sample was 2 μm with a power of 0.2 mW. The spectra were recorded for 20 s and accumulation of 30-times to get high signal-noise and signal-background ratio.

X-ray diffraction (XRD) was conducted per use of a D8 Advance diffractometer (Bruker AXS) with a copper X-ray source (CuK<sub>α</sub>, 40 kV, 49 mA) in point focus (0.5 mm) and a Goebel mirror. A VANTEC-500 (Bruker AXS) 2D detector was employed (25° per step: measurement time 16.7 min per step). The sample was dispersed in ethanol and drop casted on a sapphire wafer and the sample holder was oscillating horizontally to enhance statistics with an amplitude of 5 mm with speed of 0.5 mm s<sup>-1</sup> along the *x*- and 0.2 mm s<sup>-1</sup> along the *y*-axis.

Nitrogen gas sorption measurements at -196 °C were carried out with an Autosorb system (Autosorb 6B, Quantachrome). The powder samples were outgassed at 250 °C for 10 h under vacuum conditions at 10<sup>2</sup> Pa to remove adsorbed water; the outgassing temperature for film electrodes was 120 °C. Nitrogen gas sorption was performed in liquid nitrogen in the relative pressure range from 0.008 to 1.0. The Brunauer-Emmett-Teller specific surface area (BET-SSA)<sup>24</sup> was calculated with the ASiQwin-software in the linear relative pressure range of 0.06–0.1. The density functional theory specific surface area (DFT-SSA) and pore size distribution were calculated *via* quenched-solid density functional theory<sup>25</sup> assuming slit-shaped pores.

Thermogravimetric analysis was carried out on dried hybrid samples at 10 °C min<sup>-1</sup> to 900 °C in flowing synthetic air (20 cm<sup>3</sup> min<sup>-1</sup>) to determine the ash content, which corresponds to the total TiO<sub>2</sub> content in the samples (TG 209F1, Netzsch).

### Electrode preparation

All film electrodes were casted on graphite current collectors using a mixed PVP/PVB polymer binder. We had shown the stability of this binder system in aqueous NaCl solutions in a previous publication<sup>26</sup> and the group of Likun Pan established CDI compatibility when using this binder in a recent study.<sup>27</sup> The carbon hybrid slurry was prepared by dispersing 5 g of as-prepared material and 128 mg of polyvinylpyrrolidone (PVP) in 20 g of ethanol. After tip sonication for 10 min, 319 mg of polyvinyl butyral (PVB; 25 mass% in ethanol) was added and stirred for 30 min. The solid content of pure carbon slurry was set to 10 mass% to ensure castability. Afterwards, the slurry was casted on SGL graphite current collectors (250 μm thickness) and dried at 80 °C for 24 h. The thickness of tape casted electrodes was 100 μm for FW200 and 150 μm and for FW200/TiO<sub>2</sub>.

### Electrochemical measurements

We prepared electrodes by using the same method as introduced for CDI electrodes. The slurry was drop casted on the graphite current collector. The as-prepared electrodes with a diameter of 10 mm were placed into our custom-build cell having spring loaded titanium pistons. A glass fiber mat (GF/A, Whatman) was used as a separator. 1 M NaCl was injected by vacuum backfilling. Electrochemical measurement was conducted with a VSP300 potentiostat/galvanostat (Bio-Logic). For the symmetric full-cell, cyclic voltammetry and galvanostatic cycling techniques were employed. The specific capacitance of the cell was calculated by using eqn (1):

$$C_{\text{specific}} = \frac{1}{Um} \int_{t_1}^{t_2} I dt \quad (1)$$

where, *I* is the measurement current, *t*<sub>2</sub> - *t*<sub>1</sub> is the discharge time, *U* is the applied cell voltage (with respect to iR drop), and *m* is mass of both electrodes.

To monitor the potential development of counter and working electrode in a two electrode setup, we introduced a Ag/AgCl spectator reference electrode to the cell. During constant specific current of 0.1 A g<sup>-1</sup> (charge/discharge), the cathode and



anode potential were monitored by reference electrode and the different of potentials between cathode and anode were determined.

### Oxygen reduction reaction (ORR) evaluation

A rotating disk electrode (RDE) was used to investigate ORR for FW200 and FW200/TiO<sub>2</sub>. The RDE working electrode is a glassy carbon (GC) electrode (Bioanalytical Systems) with a diameter of 5 mm. Prior to use, the RDE-GC was polished on pat with alumina powder slurry several times and dried at 60 °C for 6 h. The carbon hybrid slurry was prepared by the following steps. Active carbon hybrid material (FW200 or FW200/TiO<sub>2</sub>) was mixed with 2.5 mg of PVP in 5 mL absolute ethanol. After that, 23 mg of PVB solution (25 mass% ethanol) was added to the previous mixture and stirred for 15 min. The paste was drop casted on RDE-GC (3 μL of slurry) and dried at 60 °C for 2 h. The as prepared RDE was connected to the RDE apparatus (RRDE-3A, Bioanalytical Systems) having a Pt wire as counter electrode and Ag/AgCl (saturated KCl) as reference electrode. Prior to ORR analysis, 1 M NaCl was bubbled with O<sub>2</sub> gas for 20 min. Linear sweep voltammograms were applied at a sweep rate of 10 mV s<sup>-1</sup> to investigate the ORR on both the FW200 and FW200/TiO<sub>2</sub> electrode. The working electrode potential was scanned from 0.2 to -0.6 V vs. Ag/AgCl. The rotating speed was varied from 0 rpm to 3200 rpm. To subtract the background capacitive current, RDE was tested in an O<sub>2</sub>-free solution at 0 rpm.

The Koutecky–Levich equation (eqn (2) and (3)) was used to estimate the number of electron transfers:<sup>28</sup>

$$\frac{1}{j} = \frac{1}{j_K} + \frac{1}{j_L} = \frac{1}{B} \omega^{-\frac{1}{2}} + \frac{1}{j_K} \quad (2)$$

$$B = 0.62D^{\frac{2}{3}} \nu^{-\frac{1}{6}} n F C_O \quad (3)$$

with  $j$ ,  $j_K$ , and  $j_L$  being the measured, kinetic limited, and mass transfer limited current. Further,  $D$  is the diffusion coefficient of dissolved oxygen in 1 M NaCl ( $2 \times 10^{-5} \text{ cm}^2 \text{ s}^{-1}$ ),<sup>29</sup>  $\nu$  is the kinetic viscosity of 1 M NaCl ( $0.0938 \text{ cm}^2 \text{ s}^{-1}$ ),<sup>30</sup>  $F$  is Faraday's constant ( $96485 \text{ C mol}^{-1}$ ),  $C_O$  is the concentration of oxygen in 1 M NaCl at 25 °C 1 atm ( $2.59 \times 10^{-7} \text{ mol cm}^{-3}$ ),<sup>31</sup> and  $n$  is the number of electron transfers involved in ORR. The parameter  $j_K$  is assumed to be constant after reaching equilibrium potential at one specific mass transfer condition ( $j_L$ ). As shown in eqn (2), the measured current exhibits linear relation with  $\omega^{-1/2}$ ; therefore, the inverse portion of  $B$  indicates the slope of K-L plot which allows the calculation of  $n$  per use of eqn (3).

### CDI measurements

The CDI setup described in ref. 32 with flow-by electrodes (per definition in ref. 1) was used to characterize the desalination performance. The CDI stack was built from the as prepared electrodes and a porous spacer (glass fiber pre-filter, Millipore, 380 μm thickness). The measurements were carried out with three pairs of electrodes. Ion adsorption and desorption steps were carried out using constant potential mode at 1.2 V. The

electrode regeneration was accomplished at 0 V. For all electrochemical operations, we used a VSP300 potentiostat/galvanostat (Bio-Logic) and the duration of each half-cycle was 30 min. All experiments were carried out with a flow rate of 22 mL min<sup>-1</sup> of 5 mM NaCl solution and a 10 L electrolyte tank which was flushed continuously with O<sub>2</sub> gas to ensure oxygen saturation. The salt adsorption capacity (SAC) and the measured charge were defined per mass of active material in both electrodes. For quantification of the electrical charge, the leakage current measured at the end of each half-cycle was subtracted.

## Results and discussion

### Structural and chemical properties

Carbon black type FW200 exhibits micrometer-sized aggregates (Fig. 1A and B), which consist of nanometer-sized primary particles of around 5–15 nm containing highly disordered carbon, as shown by transmission electron microscopy (Fig. 1C). The small size of the carbon black particles was intentionally chosen for providing facile access to the pore volume available for CDI operation and to minimize transport limitations due to impeded ion diffusion. The sol-gel synthesis of titania applied in our experiments yielded a homogenous hybridization of the carbon material (Fig. 1A), as can be seen from the elemental mapping of titanium (Fig. 1B). Quantitative analysis for the EDX spectra (Fig. 1D) yielded for FW200  $91 \pm 1$  mass% carbon and  $9 \pm 1$  mass% oxygen, and for FW200/TiO<sub>2</sub> a composition of  $85 \pm 1$  mass% C,  $13 \pm 1$  mass% O, and  $2 \pm 1$  mass% Ti. High resolution transmission electron microscopy revealed small clusters (*ca.* 1–2 nm) of titania (Fig. 1C, inset). The hybrid powder showed a mass loading of *ca.* 8 mass% titania (=4.8 mass% titanium) as confirmed by thermogravimetric analysis (Fig. 1E). That value is larger than the amount of Ti determined by EDX (2 mass%), because we have to consider the small spot size of the electron beam (effectively probing a small μm<sup>3</sup> volume) and the thermogravimetric analysis is more representative for the total titanium mass in the sample. We see in the thermogram also an onset of the carbon oxidation at much lower temperatures for FW200/TiO<sub>2</sub> compared to just FW200. This is explained by the catalytic effect of the metal oxide on the carbon oxidation reaction.<sup>33</sup>

As seen from the Raman spectra (Fig. 1F), FW200 and FW200/TiO<sub>2</sub> display the typical pattern of carbon which consists of the D-band and the G-band at the wavenumbers of about 1354 cm<sup>-1</sup> and 1603 cm<sup>-1</sup> and a distinct second order spectrum between 2200 and 3200 cm<sup>-1</sup>.<sup>34</sup> The spectra of FW200 and FW200/TiO<sub>2</sub> are virtually indistinguishable (Fig. 1F). We also did not observe any characteristic peaks of titania in FW200/TiO<sub>2</sub> since the domain size of titania (*ca.* 2 nm; Fig. 1B) is too small to yield a detectable Raman signal. X-ray diffraction also shows only the presence of carbon per the peaks at 25.5° 2θ and 42° 2θ, corresponding with the (002) and (110) reflections of graphitic carbon (Fig. 1G). This, too, is in alignment with the presence of few-nanometer-sized titania domains, scattered throughout the network of FW200 particles.



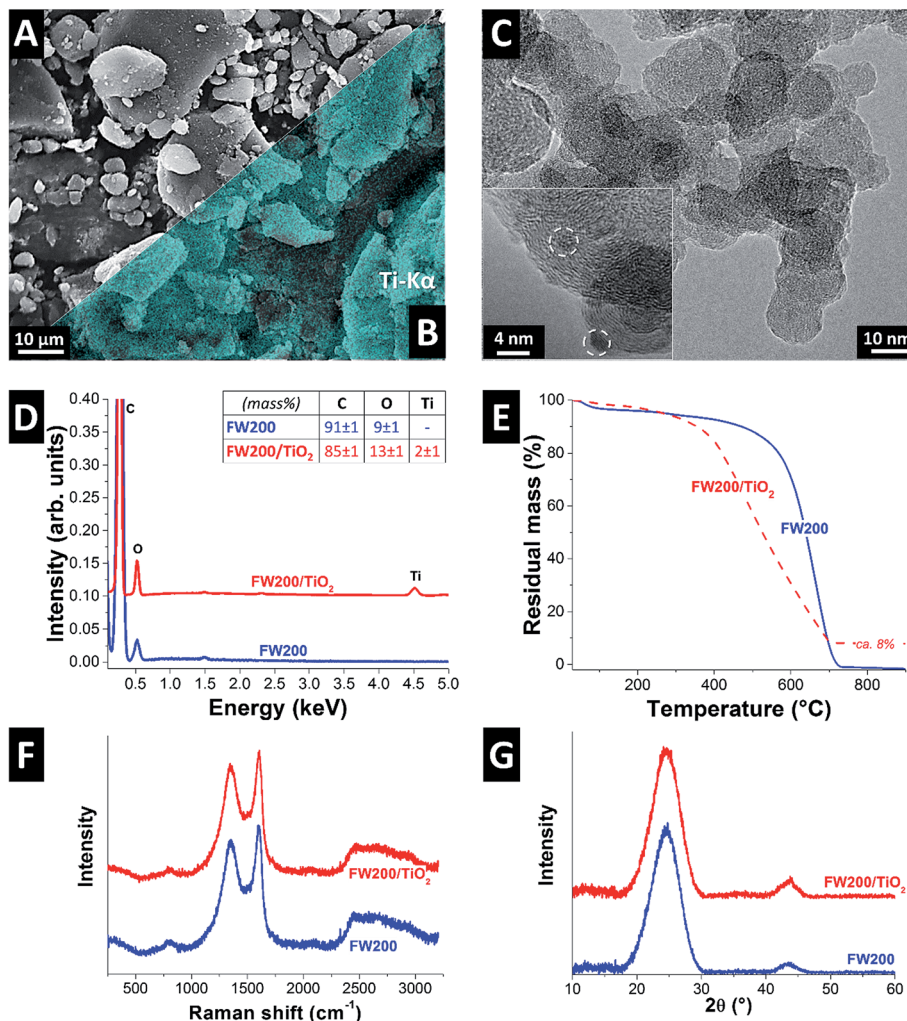


Fig. 1 (A) Scanning electron micrograph and (B) overlaid titanium chemical map (EDX) of hybrid FW200/TiO<sub>2</sub>. (C) Transmission electron micrographs of FW200/TiO<sub>2</sub> showing small titania domains. (D) EDX spectra of FW200 and FW200/TiO<sub>2</sub> along with quantitative data for C, O, and Ti. (E) Thermogravimetric analysis in synthetic air of FW200 and FW200/TiO<sub>2</sub>. (F) Raman spectra and (G) X-ray diffractograms of FW200 and FW200/TiO<sub>2</sub>.

Adding metal oxide to carbons may result in pore blocking of the electrode.<sup>35</sup> By using small amounts of titania and small particles, we were able to limit porosity reduction (Fig. 2). In particular, we see a reduction of the DFT surface area from 549 m<sup>2</sup> g<sup>-1</sup> of FW200 to a value of 404 m<sup>2</sup> g<sup>-1</sup> for FW200/TiO<sub>2</sub> (*i.e.*, -27%). This decrease can already be assessed from the nitrogen sorption isotherms (Fig. 2). Both isotherms are consistent with a material with interparticle nanopores like carbon onions.<sup>36</sup> The measured surface areas align with the presence of pores just in-between the FW200 grains, with an ideal surface area of up to 545 m<sup>2</sup> g<sup>-1</sup> for non-porous carbon spheres of 5–15 nm diameter. Concluding from quenched solid density functional theory, the corresponding decrease in surface area is mostly accomplished by a decrease in micropores (*i.e.*, pores below 2 nm) as a result from certain pore blocking by titania nano-domains (Fig. 2B). The higher density of the metal oxide also contributes towards the reduction of surface area.

### Electrochemical characterization in high ionic strength

The full-cell electrochemical measurements were carried out in oxygen free 1 M NaCl solution to investigate the charge adsorption capability of FW200 and FW200/TiO<sub>2</sub>. As seen in Fig. 3A, the cyclic voltammograms of FW200 and its composite at 5 mV s<sup>-1</sup> exhibit rectangular shape, indicative of charge storage predominately accomplished by double-layer formation (*i.e.*, ion electrosorption).<sup>37</sup> The same is indicated by the pronouncedly triangular shape of galvanostatic charge-discharge plots (Fig. 3B). The specific capacitance of FW200 and FW200/TiO<sub>2</sub> at low specific current of 0.1 A g<sup>-1</sup> is 112 F g<sup>-1</sup> and 101 F g<sup>-1</sup>, respectively, while the specific capacitance at high specific current of 10 A g<sup>-1</sup> is 43 F g<sup>-1</sup> for FW200 and 47 F g<sup>-1</sup> for FW200/TiO<sub>2</sub>, respectively (Fig. 3C). The lower specific surface area of FW200/TiO<sub>2</sub> accounts for the lower specific capacitance, although the difference is much less as might be indicated from the 27% lower accessible surface area compared to FW200.



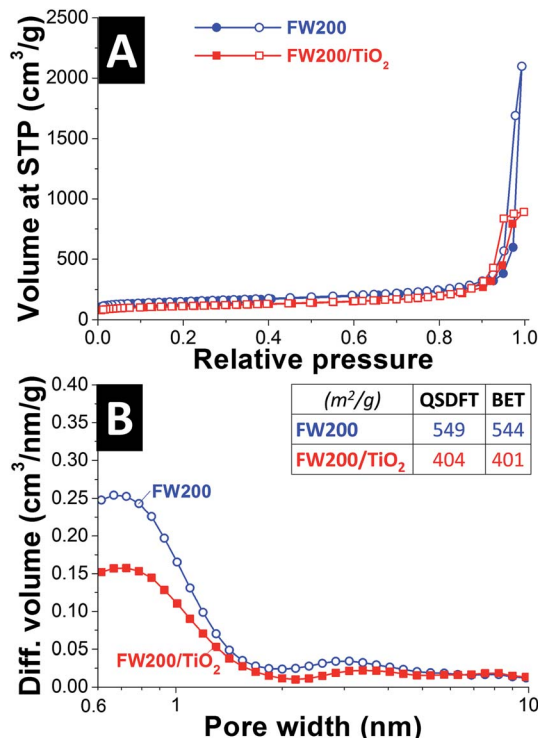


Fig. 2 (A) Nitrogen gas sorption isotherm of FW200 and FW200/TiO<sub>2</sub> showing pore blocking for the latter. (B) Differential pore size distribution calculated via quenched solid density functional theory assuming slit-shaped pores for FW200 and FW200/TiO<sub>2</sub> showing the mixed micro-mesoporous nature of both materials.

The potential development of cathode and anode in the full-cell was benchmarked by introducing an Ag/AgCl spectator electrode (Fig. 3D). The zero charge potentials ( $E_0$ ) of FW200 and FW200/TiO<sub>2</sub> are shifted to positive values vs. Ag/AgCl at all studied cell voltages (*i.e.*, between 0.6 V and 1.4 V). This implies the influence of negatively charged surface groups which get neutralized by cations, leading to an asymmetric potential distribution between cathode ( $\Delta E_{\text{cathode}} = 0.64$  V vs. Ag/AgCl at cell voltage of 1.2 V) and anode ( $\Delta E_{\text{anode}} = -0.56$  V vs. Ag/AgCl at cell voltage of 1.2 V). Nanodecoration with titania further shifts the potentials to positive values of  $\Delta 80$  mV at 0.6 V cell voltages; yet, the differences gradually reduce and virtually vanish at 1.4 V.

### Capacitive deionization performance

The desalination performance of FW200 and FW200/TiO<sub>2</sub> was measured at 1.2 V cell voltage, using a symmetrical two-electrode setup and aqueous 5 mM NaCl saline solution. We bubbled the electrolyte with O<sub>2</sub> to achieve oxygen saturation. This is in stark contrast to the majority of work in the CDI literature, where, with some exceptions (*e.g.*, ref. 38), mostly de-aerated saline media are investigated.<sup>1,2</sup> FW200 carbon electrodes required 35 CDI cycles (*i.e.*, charging and discharging cycles) to achieve equilibrium performance, that is, to obtain the same salt adsorption and salt desorption capacity. Only after such equilibrium is reached, meaningful values for the salt adsorption capacity (SAC) can be obtained and compared to literature.<sup>1</sup> During the 35 conditioning cycles, there were strong fluctuations of the online monitored conductivity of the out-flowing saline solution. We even observed, limited to the early

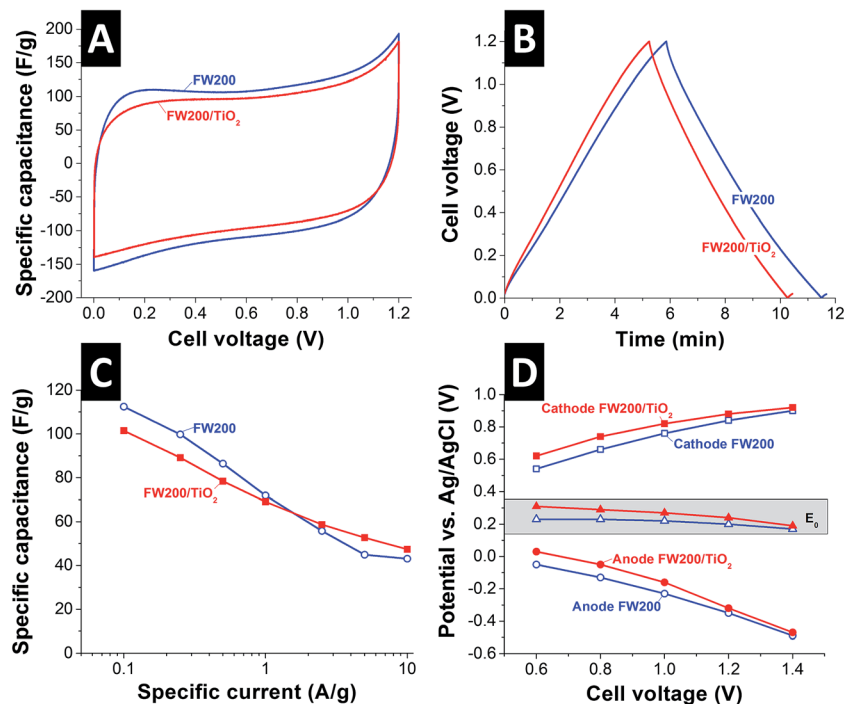


Fig. 3 (A) Cyclic voltammograms at 5 mV s<sup>-1</sup>, (B) galvanostatic charge-discharge curve at 0.1 A g<sup>-1</sup>, (C) rate capability, and (D) cathode, anode and zero charge potential monitoring along with different cell voltages.



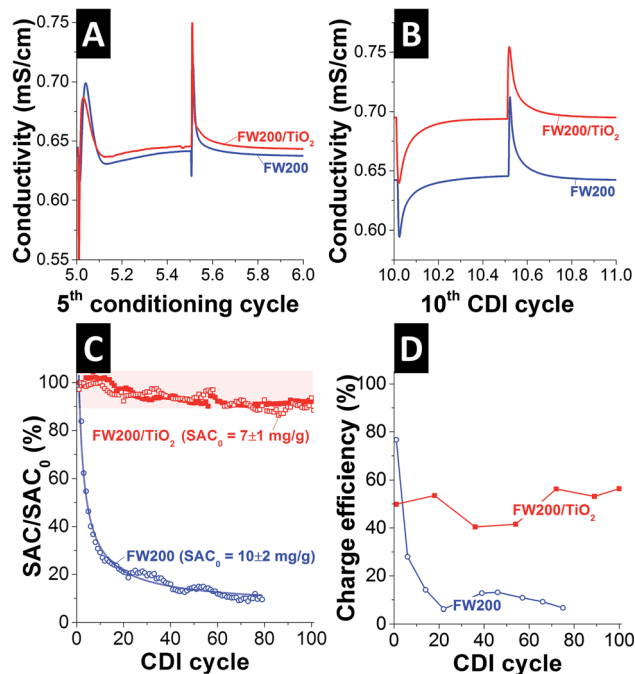


Fig. 4 (A) Typical conductivity curve for a conditioning cycle (shown data for the 5th conditioning cycle) with inverted CDI operation during the desorption cycle (1st half cycle). (B) Typical conductivity curve for conditioned CDI operation (shown data for the 10th CDI cycle) with regular ad- and desorption half-cycles. (C) Salt adsorption capacity (SAC) performance normalized to the first-cycle CDI cycle. The solid lines are fits for an exponential decay (blue; for FW200). For FW200/TiO<sub>2</sub>, two data sets of individual CDI cells are presented. (D) Charge efficiency values corresponding with the data shown in panel (C).

cycles during conditions, evidence of CDI inversion, where ions are desorbed during charging (Fig. 4A).<sup>9,10,38</sup> These high fluctuations are a result of the nanoscopic size of the carbon black primary particles and the obvious reactivity with surface functional groups, which are evidenced by an oxygen content of 9 mass% in FW200, as measured by EDX. After the initial conditioning, conventional CDI adsorption/desorption cycles occurred for FW200, as depicted in Fig. 4B (highlighting the 10th CDI cycle). Prolonged operation of FW200, however, lead to a gradual decrease of the SAC values. Starting from  $10 \pm 2 \text{ mg g}^{-1}$  for the first CDI cycle (averaged over two experiments), the performance decrease follows almost an exponential law and fades by 80% to *ca.*  $2 \text{ mg g}^{-1}$  after 20 CDI cycles and by 90% to  $\sim 1 \text{ mg g}^{-1}$  after 60 CDI cycles.

In case of FW200/TiO<sub>2</sub>, we also observed an initial conditioning phase of 35 cycles (Fig. 4A), following the same pattern as FW200 (Fig. 4B). Obviously, the run-in behavior is dominated by the majority phase (*i.e.*, FW200 = 92 mass%) and its surface chemistry. Yet, the initial SAC of the first CDI cycle (*i.e.*, after conditioning) of  $7 \pm 1 \text{ mg g}^{-1}$  (averaged over three experiments) reduces by only *ca.* 10% after 100 CDI cycles (Fig. 4C). To the best of our knowledge, this is by far the highest performance stability for any CDI system reported so far for oxygen-saturated saline electrolyte without the use of membranes. We also highlight that we used a cell voltage of 1.2 V, instead of a lower voltage, as surveyed for example in ref. 9. The latter reference

illustrates the benefit in performance stability when reducing the cell voltage, for example, from 0.9 V to 0.7 V. The observed performance stability enhancement is clearly linked with the presence of titania. When using standard carbon materials, dissolved oxygen is reduced and consumed to form H<sub>2</sub>O<sub>2</sub> as the major reagent during CDI.<sup>39</sup> Once H<sub>2</sub>O<sub>2</sub> is formed, the oxidation of carbon is boosted and this leads to severe degradation of the carbon electrode material.<sup>16,17</sup> The mechanism for oxygen reduction reaction over carbon material in alkaline media has been reported elsewhere.<sup>40</sup>

Charge efficiency, the ratio between invested charge and removed ions, is a useful tool to further characterize CDI performance and stability.<sup>41</sup> As can be seen from Fig. 4D, the initial charge efficiency for FW200 is high with *ca.* 80%, but drops to *ca.* 10% after 20 cycles. This aligns with the fast decay in SAC, as seen in Fig. 4C, and low values for the charge efficiency are common for carbons with a high heteroatom content in the form of surface functionalities.<sup>42</sup> The titania decorated hybrid electrode displays a lower, but much more stable charge efficiency with an average value of  $50 \pm 6\%$  over 100 cycles (Fig. 4D). The lower value may result from some amounts of transferred charge that is contributing to the modified ORR process and, hence, is not contributing to the actual salt removal.

The CDI evaluation of FW200 and FW200/TiO<sub>2</sub> in de-aerated 5 mM NaCl (*i.e.*, the typical electrolyte used for most CDI work) is shown in Fig. 5. At first, FW200 displays a small inverse peak before starting the adsorption process again (Fig. 5A), but after 15 cycles, the inverse peak vanished (Fig. 5B). The decrease of the inverse peak may be linked to progressing carbon oxidation at the positive electrode. In contrast, FW200/TiO<sub>2</sub> exhibits rather constant inverse peaks (Fig. 5A and B). The salt adsorption performance of FW200 and FW200/TiO<sub>2</sub> is shown in Fig. 5C. The SAC of FW200 and FW200/TiO<sub>2</sub> starts at  $5.5 \text{ mg g}^{-1}$  and slightly decays before stabilizing around  $2 \text{ mg g}^{-1}$  after 20 CDI cycles. Thus, the SAC performance in de-aerated aqueous solution is rather similar for FW200 and FW200/TiO<sub>2</sub>, leading to an unfavorable decay in performance of more than 50% of the initial value over just 10 cycles. Partially inverted CDI also leads to an unfavorably low charge efficiency of 20–30% after 20 CDI cycles (Fig. 5D). Considering these performance values, FW200, with or without titania decoration, is unfavorable for use in de-aerated aqueous solution. Seemingly, the majority phase (FW200) and its associated surface functionalities dominate the electrochemical performance in de-aerated solutions, exhibiting low charge efficiency and fast decay of SAC performance.

For comparison, we synthesized activated carbon/titania hybrids by using the same method as FW200/TiO<sub>2</sub> and tested the CDI performance in oxygen saturated 5 mM NaCl. We chose commercial YP-80F (Kuraray) with a BET surface area of  $2347 \text{ m}^2 \text{ g}^{-1}$ , which is characterized by a large inner porosity.<sup>43</sup> As shown in Fig. S1 (ESI<sup>†</sup>), pristine activated carbon exhibits a SAC of  $9 \text{ mg g}^{-1}$  in the first cycle and a drastic decrease to nearly zero after 15 cycles. This fading in CDI performance of pure activated carbon is related to the oxidization of the anode, comparable to what we have shown for FW200. Once titania is coated on the activated carbon surface, the prolongation of CDI performance



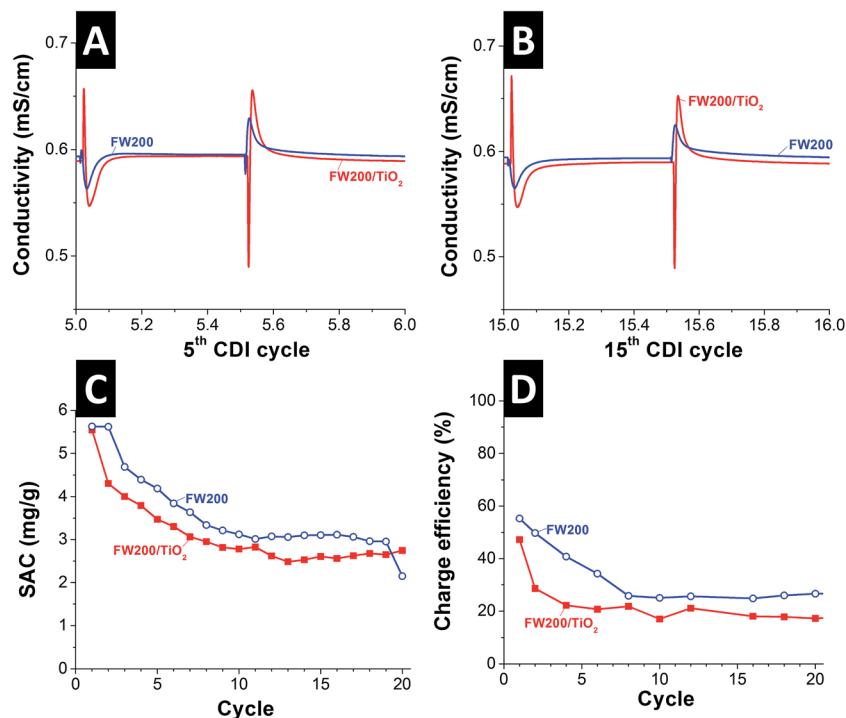
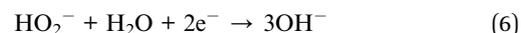
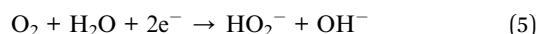


Fig. 5 CDI performance of FW200 and FW200/TiO<sub>2</sub> in de-aerated 5 mM NaCl with 22 mL min<sup>-1</sup> of flow rate. The applied cell voltage is 1.2 V during charging and 0 V during discharging. (A and B) Conductivity at 5th and 15th cycle. (C) Salt adsorption capacity over 30 cycles. (D) Charge efficiency corresponds to the data shown in panel (C).

in oxygen saturated solution can be seen. The activated carbon/titania hybrid shows a very high initial SAC of 18 mg g<sup>-1</sup> in the first cycle, but decreases to a rather constant value of ca. 2 mg g<sup>-1</sup> after 60 cycles. Thus, while titania nanodecoration of activated carbon seemingly improves the performance and CDI stability, the improvement is inferior to what is seen for FW200/TiO<sub>2</sub>, where the majority of surface area is associated with outer surface.

We further studied the catalytic activity (ORR) of titania decoration on FW200 by use of a rotating ring electrode (RDE). As shown in Fig. 6A, linear sweep voltammograms at 10 mV s<sup>-1</sup> and 0 rpm of FW200 and FW200/TiO<sub>2</sub> exhibit an ORR onset potential of -0.086 V and 0.049 V vs. Ag/AgCl, respectively. The higher onset potential of FW200/TiO<sub>2</sub> implies that titania catalyzes ORR. To obtain further information about ORR including the influence of mass diffusion on ORR, RDE measurements with various rotating speeds (200–3200 rpm) were carried out (Fig. 6A and B). For FW200 and FW200/TiO<sub>2</sub>, the diffusion current (*i<sub>L</sub>*) is increased when increasing the rotation speed due to the reduction of diffusion length. The measured current at -0.3 V vs. Ag/AgCl of FW200 and FW200/TiO<sub>2</sub> shows a rather linear correlation with the square root of the rotation speed. The resulting slope of the K-L plot (Fig. 6D) according to eqn (2) and (3) reflects the mechanism by the estimation of *n*. As shown in Fig. 6D, FW200 presents 1.4 electron transfers, while FW200/TiO<sub>2</sub> displays a four electron transfer. As identified in eqn (4)–(6), the four electron transfer (eqn (4)) is favorable for CDI longevity because only hydroxyl ions are formed as reactants. However, in our case, the four

electron pathway is not preferred when carbon has a high amount of oxygen functional groups (9 mass%). Earlier work has shown that oxygen functional groups including carbonyl, carboxyl, and hydroxyl dangling bonds on carbon nanotubes exhibit a two electron pathway at a potential of -0.6 V vs. Ag/AgCl with an onset potential of ca. -0.1 V vs. Ag/AgCl.<sup>44</sup> Therefore, the results shown in the inserted table in Fig. 6D are in good alignment with previous work, since FW200 exhibits 1.4 electron transfers leading to hydrogen peroxide formation (eqn (5)).



We expect initial H<sub>2</sub>O<sub>2</sub> is further reduced on FW200/TiO<sub>2</sub>. The latter has the catalytic ability to modify the oxygen reduction reaction, reducing H<sub>2</sub>O<sub>2</sub> to hydroxide (eqn (6)),<sup>45</sup> as enabled by the four electron transfer in FW200/TiO<sub>2</sub> (inserted table in Fig. 6D). The observed CDI behavior is explained by a transition of the two electron transfer reaction for FW200 that leads to peroxide formation, to a four electron transfer reaction for FW200/TiO<sub>2</sub>, thereby further reducing peroxide evolution and effectively preventing the oxidative carbon degradation. This explanation requires more comprehensive follow-up work to further elucidate the



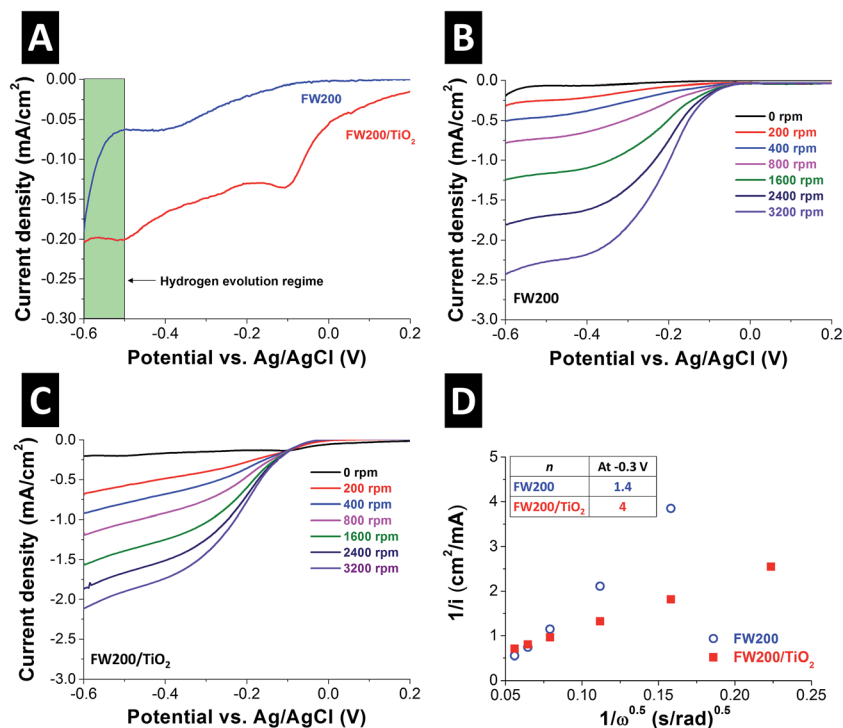


Fig. 6 (A) Linear sweep voltammograms (LSV) at 10 mV s<sup>-1</sup> of FW200 and FW200/TiO<sub>2</sub> in oxygen saturated 1 M NaCl at 0 rpm, (B and C) LSV at 10 mV s<sup>-1</sup> of FW200 (B) and FW200/TiO<sub>2</sub> (C) in O<sub>2</sub> saturated 1 M NaCl with various rotation speeds, and (D) Koutecky–Levich (K–L) plot at -0.3 V vs. Ag/AgCl.

precise mechanisms behind this intriguing performance stability. In absence of excess oxygen, in de-aerated water, ORR does not occur and the carbon degeneration per surface functional groups seemingly dominates the decay of the CDI performance.

## Conclusions

The titania decoration of carbon proved to be an excellent and facile approach to overcome the limited CDI performance stability in oxygen saturated saline solutions. Starting with a promising SAC value of 10 mg g<sup>-1</sup>, carbon black shows a negligible salt removal capacity of 2 mg g<sup>-1</sup> after just 20 CDI cycles. Titania-decorated carbon black showed a stable performance of 7 ± 1 mg g<sup>-1</sup> over a remarkable duration of 100 CDI cycles, being by far the most stable CDI system not using membranes in oxygen saturated media. Future work beyond this proof-of-concept study will have to establish the exact mechanism behind this intriguing performance stability and find the optimized amount of titania loading, while extending the scope to other carbon materials.

## Acknowledgements

This work was carried out within the framework of the Franco-German EEIGM Master's Program in Materials Science at Saarland University. S. P. acknowledges financial support by the German Academic Exchange Service (DAAD award number

91579066). The authors thank Prof. Eduard Arzt (INM) for his continuing support.

## References

- M. E. Suss, S. Porada, X. Sun, P. M. Biesheuvel, J. Yoon and V. Presser, *Energy Environ. Sci.*, 2015, **8**, 2296–2319.
- S. Porada, R. Zhao, A. van der Wal, V. Presser and P. M. Biesheuvel, *Prog. Mater. Sci.*, 2013, **58**, 1388–1442.
- J. W. Blair and G. W. Murphy, in *Saline Water Conversion*, American Chemical Society, 1960, vol. 27, ch. 20, pp. 206–223.
- Y. Liu, C. Y. Nie, X. J. Liu, X. T. Xu, Z. Sun and L. K. Pan, *RSC Adv.*, 2015, **5**, 15205–15225.
- T. Kim, J. E. Dykstra, S. Porada, A. van der Wal, J. Yoon and P. M. Biesheuvel, *J. Colloid Interface Sci.*, 2015, **446**, 317–326.
- X. Xu, L. Pan, Y. Liu, T. Lu, Z. Sun and D. H. C. Chua, *Sci. Rep.*, 2015, **5**, 8458.
- X. Xu, Z. Sun, D. H. C. Chua and L. Pan, *Sci. Rep.*, 2015, **5**, 11225.
- X. Gao, A. Omosebi, J. Landon and K. L. Liu, *Energy Environ. Sci.*, 2015, **8**, 897–909.
- I. Cohen, E. Avraham, Y. Bouhadana, A. Soffer and D. Aurbach, *Electrochim. Acta*, 2013, **106**, 91–100.
- A. Omosebi, X. Gao, J. Landon and K. Liu, *ACS Appl. Mater. Interfaces*, 2014, **6**, 12640–12649.
- X. Gao, A. Omosebi, J. Landon and K. Liu, *J. Electrochem. Soc.*, 2014, **161**, E159–E166.
- A. Omosebi, X. Gao, J. Rentschler, J. Landon and K. Liu, *J. Colloid Interface Sci.*, 2015, **446**, 345–351.



- 13 X. Gao, A. Omosebi, J. Landon and K. Liu, *Environ. Sci. Technol.*, 2015, **49**, 10920–10926.
- 14 X. Gao, S. Porada, A. Omosebi, K.-L. Liu, P. M. Biesheuvel and J. Landon, *Water Res.*, 2016, **92**, 275–282.
- 15 P. B. Peters, R. van Roij, M. Z. Bazant and P. M. Biesheuvel, 2016, ArXiv, 1512.04261.
- 16 D. He, C. E. Wong, W. Tang, P. Kovalsky and T. D. Waite, *Environ. Sci. Technol. Lett.*, 2016, **3**, 222–226.
- 17 T. Kim, J. Yu, C. Kim and J. Yoon, *J. Electroanal. Chem.*, 2016, **776**, 101–104.
- 18 J. Yang, L. Zou, H. Song and Z. Hao, *Desalination*, 2011, **276**, 199–206.
- 19 M. T. Z. Myint and J. Dutta, *Desalination*, 2012, **305**, 24–30.
- 20 M.-W. Ryoo, J. H. Kim and G. Seo, *J. Colloid Interface Sci.*, 2003, **264**, 414–419.
- 21 J.-W. Lee, H.-I. Kim, H.-J. Kim and S.-G. Park, *Appl. Chem. Eng.*, 2010, **21**, 265–271.
- 22 C. Kim, J. Lee, S. Kim and J. Yoon, *Desalination*, 2014, **342**, 70–74.
- 23 J. J. Lado, R. E. Pérez-Roa, J. J. Wouters, M. Isabel Tejedor-Tejedor and M. A. Anderson, *Sep. Purif. Technol.*, 2014, **133**, 236–245.
- 24 S. Brunauer, P. H. Emmett and E. Teller, *J. Am. Chem. Soc.*, 1938, **60**, 309–319.
- 25 G. Y. Gor, M. Thommes, K. A. Cychosz and A. V. Neimark, *Carbon*, 2012, **50**, 1583–1590.
- 26 M. Aslan, D. Weingarh, P. Herbeck-Engel, I. Grobelsek and V. Presser, *J. Power Sources*, 2015, **279**, 323–333.
- 27 X. Xu, M. Wang, Y. Liu, T. Lu and L. Pan, *J. Mater. Chem. A*, 2016, **4**, 5467–5473.
- 28 W. Chen and S. Chen, *Angew. Chem., Int. Ed.*, 2009, **48**, 4386–4389.
- 29 G. W. Hung and R. H. Dinius, *J. Chem. Eng. Data*, 1972, **17**, 449–451.
- 30 J. Kestin, H. E. Khalifa and R. J. Correia, *J. Phys. Chem. Ref. Data*, 1981, **10**, 71–88.
- 31 J. E. Sherwood, F. Stagnitti, M. J. Kokkinn and W. D. Williams, *Limnol. Oceanogr.*, 1991, **36**, 235–250.
- 32 M. Aslan, M. Zeiger, N. Jäckel, I. Grobelsek, D. Weingarh and V. Presser, *J. Phys.: Condens. Matter*, 2016, **28**, 114003.
- 33 B. Gao, G. Z. Chen and G. Li Puma, *Appl. Catal., B*, 2009, **89**, 503–509.
- 34 A. C. Ferrari and J. Robertson, *Phys. Rev. B: Condens. Matter Mater. Phys.*, 2001, **64**, 075414.
- 35 S. Fleischmann, N. Jäckel, M. Zeiger, B. Krüner, I. Grobelsek, P. Formanek, S. Choudhury, D. Weingarh and V. Presser, *Chem. Mater.*, 2016, **28**, 2802–2813.
- 36 M. Zeiger, N. Jäckel, V. N. Mochalin and V. Presser, *J. Mater. Chem. A*, 2016, **4**, 3172–3196.
- 37 F. Beguin, V. Presser, A. Balducci and E. Frackowiak, *Adv. Mater.*, 2014, **26**, 2219–2251.
- 38 Y. Bouhadana, E. Avraham, M. Noked, M. Ben-Tzion, A. Soffer and D. Aurbach, *J. Phys. Chem. C*, 2011, **115**, 16567–16573.
- 39 X. Sun, P. Song, Y. Zhang, C. Liu, W. Xu and W. Xing, *Sci. Rep.*, 2013, **3**, 2505.
- 40 J. Zhang and L. Dai, *ACS Catal.*, 2015, **5**, 7244–7253.
- 41 R. Zhao, P. M. Biesheuvel, H. Miedema, H. Bruning and A. van der Wal, *J. Phys. Chem. Lett.*, 2009, **1**, 205–210.
- 42 S. Porada, F. Schipper, M. Aslan, M. Antonietti, V. Presser and T.-P. Fellingner, *ChemSusChem*, 2015, **8**, 1867–1874.
- 43 N. Jäckel, M. Rodner, A. Schreiber, J. Jeongwook, M. Zeiger, M. Aslan, D. Weingarh and V. Presser, *J. Power Sources*, 2016, **326**, 660–671.
- 44 R.-S. Zhong, Y.-H. Qin, D.-F. Niu, J.-W. Tian, X.-S. Zhang, X.-G. Zhou, S.-G. Sun and W.-K. Yuan, *J. Power Sources*, 2013, **225**, 192–199.
- 45 J. Yu, Z. Liu, L. Zhai, T. Huang and J. Han, *Int. J. Hydrogen Energy*, 2016, **41**, 3436–3445.



## *Supporting Information*

### **High performance stability of titania decorated carbon for desalination with capacitive deionization in oxygenated water**

Srimuk Pattarachai,<sup>1,2</sup> Lucie Ries,<sup>1,2</sup> Marco Zeiger,<sup>1,2</sup> Simon Fleschmann,<sup>2</sup>  
Nicolas Jäckel,<sup>1,2</sup> Aura Tolosa,<sup>1,2</sup> Benjamin Krüner,<sup>1,2</sup> Mesut Aslan,<sup>1</sup> Volker Presser<sup>1,2,\*</sup>

<sup>1</sup>... INM - Leibniz Institute for New Materials, Saarbrücken, Germany

<sup>2</sup>... Department of Materials Science and Engineering, Saarland University, Saarbrücken, Germany

\*... Corresponding author's email address: [volker.presser@leibniz-inm.de](mailto:volker.presser@leibniz-inm.de)

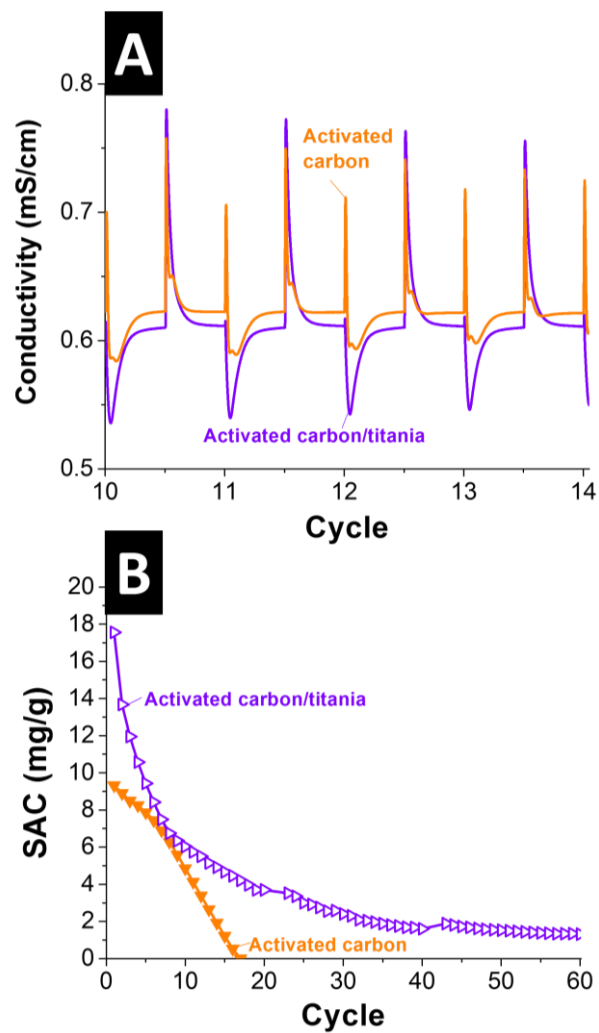


**Figure S1** CDI performance of activated carbon and activated carbon/titania in saturated oxygen 5 mM NaCl. (A) Conductivity profile versus cycle number 10<sup>th</sup> to 14<sup>th</sup>, and (B) salt adsorption capacity (SAC) versus cycle number.

### 4.3 MXene as a novel intercalation-type pseudocapacitive cathode and anode for capacitive deionization

Pattarachai Srimuk,<sup>1,2</sup> Friedrich Kaasik,<sup>1,3</sup> Benjamin Krüner,<sup>1,2</sup> Aura Tolosa,<sup>1,2</sup>  
Simon Fleischmann,<sup>1,2</sup> Nicolas Jäckel,<sup>1,2</sup> Mehmet C. Tekeli,<sup>1,2</sup> Mesut Aslan,<sup>1</sup>  
Matthew E. Suss,<sup>4</sup> Volker Presser<sup>1,2</sup>

<sup>1</sup> INM - Leibniz Institute for New Materials, 66123 Saarbrücken, Germany

<sup>2</sup> Department of Materials Science and Engineering, Saarland University, 66123 Saarbrücken, Germany

<sup>3</sup> IMS Laboratory, Institute of Technology, University of Tartu, Tartu, Estonia

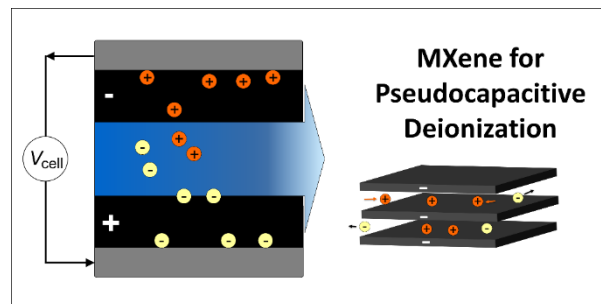
<sup>4</sup> Faculty of Mechanical Engineering, Technion-Israel Institute of Technology, Haifa, 32000, Israel

#### Citation:

P. Srimuk, F. Kaasik, B. Krüner, A. Tolosa, S. Fleischmann, N. Jäckel, M.C. Tekeli, M. Aslan, M.E. Suss, V. Presser, MXENE AS A NOVEL INTERCALATION-TYPE PSEUDOCAPACITIVE CATHODE AND ANODE FOR CAPACITIVE DEIONIZATION, *Journal of Materials Chemistry A* 4(47) (2016) 18265-18271.

#### Own contribution:

Electrode preparation, electrochemistry, analysis, writing



CrossMark  
click for updatesCite this: *J. Mater. Chem. A*, 2016, 4, 18265Received 9th September 2016  
Accepted 2nd November 2016

DOI: 10.1039/c6ta07833h

www.rsc.org/MaterialsA

# MXene as a novel intercalation-type pseudocapacitive cathode and anode for capacitive deionization

Pattarachai Srimuk,<sup>ab</sup> Friedrich Kaasik,<sup>ac</sup> Benjamin Krüner,<sup>ab</sup> Aura Tolosa,<sup>ab</sup> Simon Fleischmann,<sup>b</sup> Nicolas Jäckel,<sup>ab</sup> Mehmet C. Tekeli,<sup>ab</sup> Mesut Aslan,<sup>a</sup> Matthew E. Suss<sup>d</sup> and Volker Presser<sup>\*ab</sup>

In this proof-of-concept study, we introduce and demonstrate MXene as a novel type of intercalation electrode for desalination *via* capacitive deionization (CDI). Traditional CDI cells employ nanoporous carbon electrodes with significant pore volume to achieve a large desalination capacity *via* ion electrosorption. By contrast, MXene stores charge by ion intercalation between the sheets of its two-dimensional nanolamellar structure. By this virtue, it behaves as an ideal pseudocapacitor, that is, showing capacitive electric response while intercalating both anions and cations. We synthesized Ti<sub>3</sub>C<sub>2</sub>-MXene by the conventional process of etching ternary titanium aluminum carbide *i.e.*, the MAX phase (Ti<sub>3</sub>AlC<sub>2</sub>) with hydrofluoric acid. The MXene material was cast directly onto the porous separator of the CDI cell without added binder, and exhibited very stable performance over 30 CDI cycles with an average salt adsorption capacity of 13 ± 2 mg g<sup>-1</sup>.

## 1. Introduction

Capacitive deionization (CDI) is an emerging water treatment technology, ideally suited for the highly energy efficient removal of ions from aqueous<sup>1</sup> or organic electrolytes.<sup>2</sup> CDI has seen tremendous research activities with an exponentially growing number of publications over the last 5 years. Conventional CDI is based on ion removal from a feed stream by electrosorption at the electrically charged fluid/solid interface between the electrolyte and the electrode. Such CDI cells commonly utilize nanoporous carbons as electrodes, with subnanometer pores<sup>3</sup> and/or large overall pore volumes,<sup>4</sup> yielding the best performance values. During charging, ions are continuously removed from the feed stream until the electrode has reached the maximum ion sorption capacity for a given applied voltage. Subsequent discharging or voltage inversion regenerates the

electrodes so that another CDI cycle can begin. One widely used metric to characterize CDI electrode performance is the equilibrium amount of electrosorbed salt per electrode mass (SAC = salt adsorption capacity) and high values up to *ca.* 15–21 mg g<sup>-1</sup> have been reported recently for different carbons.<sup>4,5</sup> For example, commercial activated carbons have been found to yield up to 14 mg g<sup>-1</sup>,<sup>3</sup> exceeded by nanotextured carbons like nitrogen doped graphene foam.<sup>5</sup> Even higher values have been reported by introducing chemical charges to the carbon surfaces by functional groups,<sup>6</sup> which may in the most extreme case even result in inversion of the CDI process (*i.e.*, ion removal during discharging and ion release during charging).<sup>7</sup> Also, in addition to the advent of novel hybrid materials,<sup>8–10</sup> there is further progress with adapting advanced, nanotextured carbon materials for CDI.<sup>11,12</sup>

The discovery and progressing technological adaption of graphene<sup>13</sup> has stimulated the systematic exploration of graphene analogues, that is, 2-dimensional (2-D) nanomaterials beyond carbon.<sup>14</sup> Recently, a novel group of 2-D nanolamellar materials has been introduced, called MXene.<sup>15</sup> First reported in 2011,<sup>16</sup> MXenes are a fast growing group of metal carbides and nitrides that structurally originate from MAX phases. The latter are a large group of ternary transition metal carbides and nitrides with the simplifying formula M<sub>n+1</sub>AX<sub>n</sub>, where *n* = 1, 2, or 3, M is an early transition metal, A belongs mostly to groups 13 or 14, and X is C and/or N.<sup>17</sup> With weaker bonds related to A-site atoms, selective etching, for example with hydrofluoric acid (HF)<sup>18,19</sup> or electrochemical methods,<sup>20</sup> can be achieved to transform MAX phases to MXene. Unlike graphene, MXene layers usually consist of 3, 5, or more atomic layers, depending on the MAX precursor, and the electrical and chemical properties of the exfoliated material strongly reflect the chemical process conditions. For example, MXene can be either metallically conductive, with values as high as 4000 S cm<sup>-1</sup>,<sup>21</sup> or semiconductor-like,<sup>16</sup> depending on the degree of exfoliation and surface functionalization.

MXene has been reported to exhibit a large pseudocapacitance,<sup>22</sup> outperforming the energy storage capacity of most

<sup>a</sup>INM – Leibniz Institute for New Materials, Saarbrücken, Germany. E-mail: volker.presser@leibniz-inm.de

<sup>b</sup>Department of Materials Science and Engineering, Saarland University, Saarbrücken, Germany

<sup>c</sup>IMS Laboratory, Institute of Technology, University of Tartu, Tartu, Estonia

<sup>d</sup>Faculty of Mechanical Engineering, Technion – Israel Institute of Technology, Haifa, 32000, Israel



other capacitive materials, especially when normalizing to the electrode volume. MXene allows for the unique ability to form binder-free electrodes (MXene paper) and to serve as an almost ideal intercalation material with rapid ion insertion between the MXene layers. In particular, MXene has exhibited high measured capacitance ( $>300 \text{ F cm}^{-3}$ ) in lithium or sodium sulfate aqueous media, and is capable of intercalating even much larger ions, like ionic liquids or organic salts.<sup>23,24</sup> Due to its exceptional capacitance and highly reversible intercalation/de-intercalation of ions in aqueous media, we were motivated to explore MXene as a novel electrode material for water desalination by CDI. We here demonstrate and characterize, for the first time, a MXene CDI cell with symmetric geometry (MXene for the positively and negatively polarized electrode), which is, to the best of our knowledge, the first CDI cell with both electrodes based on an intercalation-type material.

## 2. Materials and methods

### 2.1 MAX and MXene synthesis

To obtain MXene, we first synthesized the MAX phase  $\text{Ti}_3\text{AlC}_2$ . Following the literature,<sup>16,25</sup> this was accomplished by mixing elemental titanium (99% purity; abcr), aluminum (99.8% purity; Feinchemikalien und Forschungsbedarf), and carbon (type BP2000; Cabot) in a molar ratio of 3 : 1.1 : 1.88 *via* rigorous planetary ball milling (hard metal container, 10 mm hard metal balls, 20 g total mass in 50 g ethanol, 15 min). The milled material was dried and cold pressed at 50 MPa to form pellets which were heated in a graphite crucible to 1550 °C in argon atmosphere with a heating rate of 10 °C min<sup>-1</sup>, followed by a 2 h heating period, and afterwards cooled to room temperature with a rate of 10 °C min<sup>-1</sup>.

MXene synthesis followed Naguib *et al.* with hydrofluoric acid (HF).<sup>16</sup> For this, 3 g of MAX material was dispersed in 30 mL HF (40–45%) and sealed in a polytetrafluoroethylene cup for 22 h. The resulting material was filtered, obtaining material larger than 2 μm, and then centrifuged 15 times until a pH > 5 was achieved. Afterwards, the material was dried at 80 °C overnight and a yield of 2.3 g (*ca.* 75%) was accomplished.

For comparison, data on commercial activated carbon from Kuraray (type YP-80F) are added and adapted from our previous work.<sup>26</sup> YP-80F electrodes were composed of 95% activated carbon and 5% polytetrafluoroethylene (PTFE) polymer binder. For more information on sample preparation, see ref. 26.

### 2.2 Materials characterization

X-ray diffraction (XRD) experiments were conducted employing a D8 Advance diffractometer (Bruker AXS) with a copper X-ray source (Cu K $\alpha$ , 40 kV, 40 mA) and a nickel filter. Measurements were conducted with a 1D detector (LYNXEYE) and 2D detector (VANTAC).

Scanning electron microscope (SEM) images were recorded with a JEOL JSM 7500F field emission scanning electron microscope (JEOL, Japan) operating at 3 kV. Energy dispersive X-ray spectroscopy (EDX) was carried out at 10 kV in the system with an X-Max Silicon Detector from Oxford Instruments using AZtec software.

Nitrogen gas sorption measurements at -196 °C were carried out with an Autosorb system (Autosorb 6B, Quantachrome). The samples were outgassed at 150 °C for 10 h under vacuum conditions at 10<sup>2</sup> Pa. The BET-specific surface area (BET-SSA) was calculated with the ASiQwin-software using the Brunauer–Emmett–Teller<sup>27</sup> equation in the linear relative pressure range of 0.01–0.05.

### 2.3 Electrode preparation and electrochemical measurements

For full-cell experiments, ethanolic slurries containing MXene powder (250 mg powder in 100 mL ethanol) were prepared by ultrasound assisted stirring in ice bath for 30 min. Porous spacer (glass fiber pre-filter, Millipore, compressed thickness of a single layer is 380 μm) was infiltrated several times by drop casting of the MXene suspension, yielding binder free coatings after drying at 120 °C for 24 h. The exact electrode mass was determined by the mass difference of the spacer prior to and after drop casting and drying. Electrochemical measurements were conducted by symmetric full-cell cyclic voltammetry (CV; scan rate 5 mV s<sup>-1</sup>; up to 1.2 V) and galvanostatic cycling with potential limitation to 1.2 V at 0.1 A g<sup>-1</sup> in 1 M NaCl aqueous solution with a VSP300 potentiostat/galvanostat (Bio-Logic). The cell had a Ag/AgCl spectator reference used to record the electrode potentials, while the cell voltage was not controlled by the reference (but determined as the potential difference between the two symmetric electrodes). The specific capacitance  $C_{sp}$  was calculated according to ref. 28.

For half-cell experiments, 2 mg of MXene was dispersed in 5 mL of ethanol. The suspension was tip-sonicated for 30 min, coated on porous glass fiber separator and dried at 60 °C for 6 h. An electrode disc with a 10 mm diameter was cut, giving a MXene loading of 0.64 mg. As counter electrode, we used 11.4 mg of PTFE-bound (5 mass%) activated carbon (YP-80F) and a glass fiber (GF/A, Whatman) separator.

### 2.4 Capacitive deionization experiments

For CDI experiments, the MXene material was casted directly on the porous separator instead of casting it onto the graphite current collector or using it as a freestanding film. This approach was motivated by the need of filtration to obtain MXene paper and the most facile way of realizing this was to directly use the porous separator used for the CDI cell. To the best of our knowledge, our work is the first time that a CDI electrode was cast on the separator instead of casting onto the current collector. For this, MXene powder was dispersed in ethanol and tip-sonicated for 30 min. Afterwards, the MXene suspension was drop casted over the glass fiber separator and dried at 60 °C for 24 h.

We used a CDI setup described in ref. 26 with flow between electrodes (*i.e.*, feed water flows in parallel to and in-between the electrode pair; see definition from ref. 1). The CDI stack was built from graphite current collectors (SGL Technologies; thickness: 250 μm) with attached MXene electrodes directly deposited onto the porous spacer. The CDI electrode mass was 100 mg with a thickness of 125 μm, as confirmed by SEM. The



measurements were carried out with one symmetric pair of electrodes. The total electrolyte flow rate was  $22 \text{ mL min}^{-1}$ . Ion adsorption and desorption steps were carried out using constant potential mode at 1.2 V and regeneration was accomplished at 0 V. For all electrochemical operations, we used a VSP300 potentiostat/galvanostat (Bio-Logic) and the duration of each half-cycle was 30 min. All experiments were carried out with de-aerated 5 mM NaCl solution in a 10 L electrolyte tank and the electrolyte was de-aerated by flushing nitrogen gas. The salt adsorption capacity and the measured charge were defined per mass of active material (*i.e.*, MXene mass or mass of activated carbon, for comparison) in both electrodes and were calculated as an average value from adsorption and desorption step. For quantification of the electrical charge, the leakage current measured at the end of each half-cycle was subtracted.<sup>29</sup>

The AC experimental data was taken from previous work<sup>26</sup> with  $6 \times 6 \text{ cm}^2$  electrodes with a mass of 500 mg per electrode pair.

### 3. Results and discussion

#### 3.1 Material characterization

The obtained powder of the ternary carbide (Fig. 1A) was typical for the MAX phases with a layered morphology, which transitioned to a much more delaminated structure after HF etching (Fig. 1B).<sup>30</sup> The drastic change in structure is also documented by X-ray powder diffraction (Fig. 1E). In particular, we see a strong shift of the (002)-peak at  $9.52^\circ 2\theta$  (MAX) to  $8.96^\circ 2\theta$  (MXene), which corresponds with an increase in *d*-space of 6.2%. This shift is accompanied by an increase in the full-width at half maximum (FWHM) from  $0.057^\circ 2\theta$  (MAX) to  $0.474^\circ 2\theta$  (MXene).<sup>15,30</sup>

Chemical analysis *via* energy dispersive X-ray spectroscopy (EDX) shows that Al removal was almost fully achieved (Fig. 1D and Table 1). Small amounts of residual aluminum stem from few incompletely transformed MAX grains, which also contribute to the sharp reflections seen in the XRD pattern

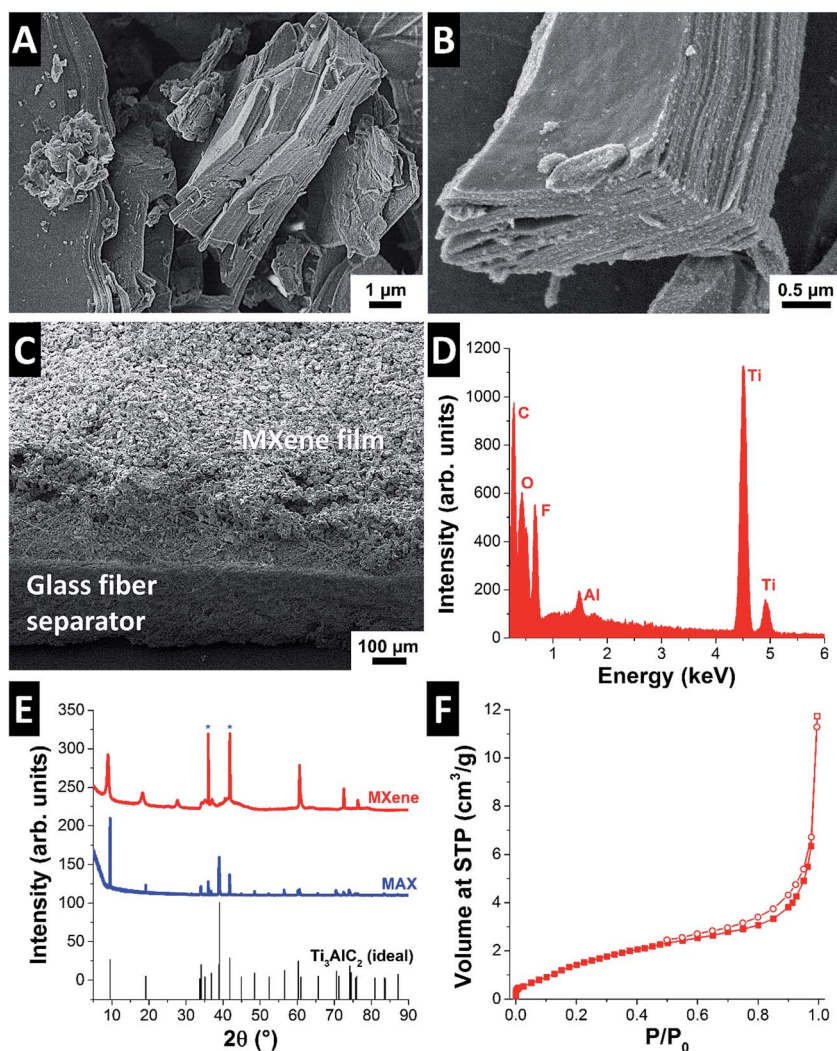


Fig. 1 Scanning electron micrographs of (A) MAX phase  $\text{Ti}_3\text{AlC}_2$ , (B) MXene  $\text{Ti}_3\text{C}_2$ , and (C) MXene  $\text{Ti}_3\text{C}_2$  deposited onto the glass fiber separator (cross section). (D) Energy dispersive X-ray spectrum (EDX) of MXene  $\text{Ti}_3\text{C}_2$ . (E) X-ray diffractograms of MAX and MXene phase compared to the ideal peak positions for  $\text{Ti}_3\text{AlC}_2$  (PDF 52-0875). (F) Nitrogen gas sorption isotherm recorded at  $-196^\circ \text{C}$  of MXene  $\text{Ti}_3\text{C}_2$  with a calculated BET surface area of  $6 \text{ m}^2 \text{ g}^{-1}$ .



**Table 1** Elemental chemical analysis of the initial MXene material and post mortem analysis after CDI cycling

(Mass%)	C	Ti	O	Al	F	Na & Cl
Initial	15 ± 1	59 ± 5	10 ± 2	<1	14 ± 2	—
Post mortem anode	12 ± 3	52 ± 8	29 ± 7	<2	4 ± 1	<2
Post mortem cathode	14 ± 4	62 ± 10	14 ± 5	<1	8 ± 5	<1

(marked by stars in Fig. 1E). In addition to Ti and C, the MXene material also shows significant amounts of F (14 mass%) and O (10 mass%) as shown in Table 1. Etching of MAX in aqueous HF is known to yield an excess of fluorine and oxygen containing surface functional groups, where “surface” refers also the space between the MXene nanosheets.<sup>31</sup>

Although the removal of aluminum induces changes in the morphology and structure, it does not yield a large surface area. Nitrogen gas sorption analysis  $-196\text{ }^{\circ}\text{C}$  showed a BET surface

area of  $6\text{ m}^2\text{ g}^{-1}$  (Fig. 1F). Typical CDI electrodes based on ion electroadsorption into EDLs have BET surface areas exceeding  $1000\text{ m}^2\text{ g}^{-1}$ .<sup>29</sup> However, as we show in this work, ion intercalation in MXene, giving rise to pseudocapacitive charge transfer and ion immobilization, allows for a high SAC without the need for a high BET surface area.

### 3.2 Electrochemical behavior and capacitive deionization

A first assessment of the ion storage capacity and electrochemical behavior of MXene in saline media was carried out by cyclic voltammetry (CV) in aqueous 1 M NaCl (Fig. 2A). As can be seen, the shape of the cyclic voltammogram is highly rectangular for activated carbon and slightly distorted for MXene. The latter features are likely due to the charging (dynamic) response of the rather thick MXene electrode. We here used roughly  $100\text{ }\mu\text{m}$  thick MXene electrodes, while in the literature, usually much thinner MXene electrodes are used, such as  $2\text{ }\mu\text{m}$  in ref. 32. Both MXene and activated carbon are characterized by

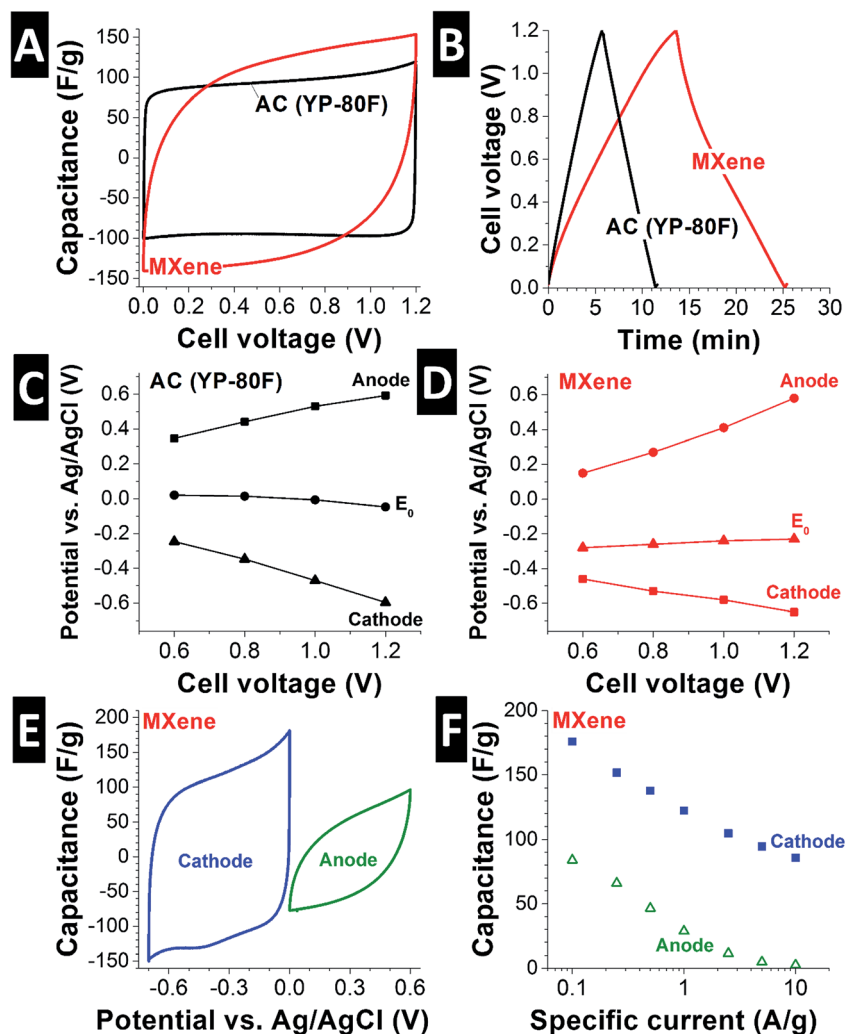


**Fig. 2** (A) Cyclic voltammograms at  $5\text{ mV s}^{-1}$  and (B) galvanostatic charge/discharge at  $0.1\text{ A g}^{-1}$  of MXene and activated carbon (YP-80F; ref. 26) in 1 M NaCl. (C and D) Electrode potential at different cell voltages for anode and cathode of MXene and YP-80F in 1 M NaCl. (E) Cyclic voltammograms at  $5\text{ mV s}^{-1}$  and (F) galvanostatic charge/discharge power handling for MXene half-cell vs. an oversized YP-80F counter electrode in 1 M NaCl.



capacitor-like charge/discharge behavior, which manifests in near-linear voltage curves from galvanostatic charge/discharge cycling (Fig. 2C). At a discharge rate of  $0.1 \text{ A g}^{-1}$ , capacitance values of  $111 \text{ F g}^{-1}$  and  $132 \text{ F g}^{-1}$  were measured for YP-80F activated carbon and MXene, respectively (Fig. 2B). Considering the low surface area of MXene, the high measured capacitance cannot be due to ions electroadsorbed at the fluid/solid interface (like in activated carbon), but instead is attributed to inserted (intercalated) ions between MXene sheets. By this virtue, MXene qualifies not as a double-layer capacitor, but as a pseudocapacitor.<sup>22</sup>

The electrochemical data shown in Fig. 2A and B were derived with a symmetrical two-electrode cell. From galvanostatic charging and discharging at  $0.1 \text{ A g}^{-1}$  to 1.2 V cell voltage, a high coulombic efficiency ( $>97\%$ ; ratio of discharge vs. charge) was calculated. This value indicates a highly reversible charge transfer, for example, accomplished by anion insertion at the positively polarized electrode and cation insertion at the opposite electrode. While most works in the literature have investigated cation intercalation in MXenes,<sup>22</sup> recent works provide experimental evidence also for anion insertion derived from *in situ* X-ray diffraction experiments.<sup>33</sup> By that virtue, MXene is an interesting model material for applying faradaic anion and cation immobilization towards pseudocapacitive desalination.

To further investigate the difference in electrode potential development between activated carbon and MXene electrodes, we added a spectator reference electrode (Ag/AgCl) to the symmetric two-electrode cells (Fig. 2C and D) in 1 M NaCl. The activated carbon electrode pair showed the behavior expected for a symmetric double-layer capacitor: both electrodes see, by increment and opposite by sign, the same increase in electrode potential as the cell voltage is increased. For example, a cell voltage of 1.0 V is accomplished by an anode at +0.5 V and

a cathode at  $-0.5 \text{ V vs. Ag/AgCl}$  (Fig. 2C). MXene electrodes exhibit a different behavior: compared to activated carbon, the potential of the MXene electrode pair is shifted to negative values ( $E_0$ ) by *ca.* 250 mV vs. Ag/AgCl (Fig. 2D). The cell voltage is also differently distributed: a cell voltage of 1.0 V is accomplished by an anode at +0.4 V and a cathode at  $-0.6 \text{ V vs. Ag/AgCl}$ . This behavior is in line with the negative static charge of MXenes because of intrinsic  $-\text{OH}$ ,  $=\text{O}$  and  $-\text{F}$  surface termination.<sup>34</sup>

When performing half-cell experiments vs. an oversized activated carbon counter electrode (YP-80F), we can further investigate the performance of MXene as anode and cathode, that is, during positive or negative polarization. As seen from Fig. 2E, both anodic and cathodic sweeping *via* cyclic voltammetry ( $5 \text{ mV s}^{-1}$ ) yields pseudocapacitive behavior. During positive polarization, a high specific capacitance of  $176 \text{ F g}^{-1}$  is reached, while negative polarization only provides  $84 \text{ F g}^{-1}$  (calculated from galvanostatic discharge at  $0.1 \text{ A g}^{-1}$ ; see Fig. 2F). Evidently, cation insertion is favored, but the ability of MXene to intercalate ions is not limited to cations as seen from the ability of the MXene anode to demonstrate pseudocapacitive charge/discharge characteristics. Surveying different specific currents (Fig. 2F) and from the shape of the CV in Fig. 2E, we also see slower anion intercalation and a more rapid loss of capacitance at higher rates.

To ensure stable performance, the MXene electrodes were cycled between 0 and 1.2 V for 40 times prior CDI experiments in 5 mM NaCl. After this conditioning and wetting process, stable desalination performance was observed with characteristic changes in the effluence salt concentration recorded during potentiostatic cycling (Fig. 3A). The concentration changes compute, based on the averaged data from two separate experiments, to a salt adsorption capacity of  $13 \pm 2 \text{ mg g}^{-1}$  at an average salt adsorption rate (ASAR) of *ca.*  $1 \text{ mg g}^{-1} \text{ min}^{-1}$ .

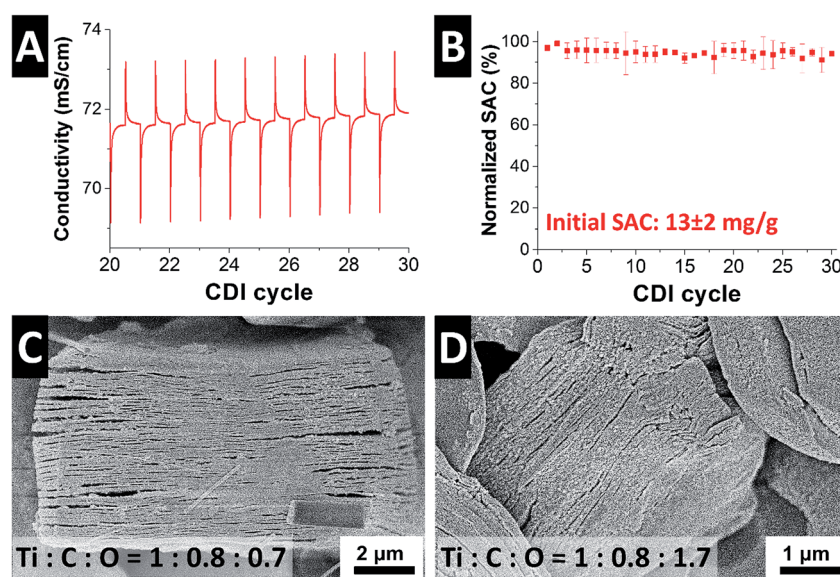


Fig. 3 (A) Conductivity profiles for 10 full cycles in 5 mM NaCl (deaerated) and (B) corresponding salt removal capacity stability of MXene. Error bars in (B) represent the data for two repeat experiments. Post mortem scanning electron micrographs of  $\text{Ti}_3\text{C}_2$  MXene after CDI cycling as (C) negatively and (D) positively polarized electrode. The elemental (molar) ratios noted in (C) and (D) were derived from EDX analysis.



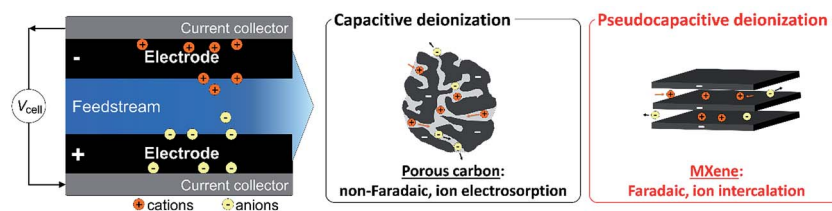


Fig. 4 Concept of electrochemical water desalination. Capacitive deionization accomplishes water desalination by non-faradaic (electrostatic) ion electrosorption at the surface of electrode materials. Pseudocapacitive deionization is accomplished by faradaic ion intercalation between the 2D-sheets of MXene. In both cases, anions and cations are removed.

This value is comparable to YP-80F ( $9 \text{ mg g}^{-1}$ ) and MSP-20 ( $14 \text{ mg g}^{-1}$ ), but higher than other carbons (like carbon xerogel;  $3.3 \text{ mg g}^{-1}$ ).<sup>35</sup> When normalized to the available surface area, we see that MXene accomplishes a desalination capacity of  $1.7 \text{ mg m}^{-2}$ , while YP-80F shows an area-normalized SAC of just  $4.3 \text{ } \mu\text{g m}^{-2}$ . This shows that the ion removal for CDI with MXene cannot be accomplished by the outer surface area, but by ion insertion between the MXene sheets (intercalation). In 5 mM de-aerated NaCl saline solution, the CDI cell exhibited stable performance over 30 cycles (Fig. 3B).

Initial post mortem analysis of the MXene electrodes shows that the overall “open book” morphology is maintained (Fig. 3C and D). Yet, compared to the initial material (Fig. 1B), the MXene electrodes after positive (Fig. 3C) or negative (Fig. 3D) polarization appear more exfoliated. Importantly, we see an increase of the Ti : C : O molar ratio, from initially 1 : 1 : 0.5 (directly after synthesis) to a value of 1 : 0.8 : 0.7 for cathode and 1 : 0.8 : 1.7 for the anode (post mortem; see also Table 1). For ideal  $\text{Ti}_3\text{C}_2$ , we would expect a Ti : C ratio of 1 : 0.7; thus, the higher initial value of the electrode is because of the presence of excess carbon and small amounts of TiC, as common for MXene.<sup>30</sup> Oxidation of MXene is well-known<sup>36</sup> and occurs in the aqueous medium at both electrodes. Triggered by electrochemical oxidation, MXene oxidation occurs to a larger degree at the anode. The reduced relative amount of carbon is a direct result of the carbide oxidation, where carbon is replaced by oxygen in the solid. The combination of repeated ion intercalation/deintercalation and superficial oxidation enhances exfoliation and the morphology of MXene slightly changes. Yet, MXene grains remain overall structural integrity.

## 4. Conclusion

MXene is an interesting novel electrode material for CDI and can be used in a symmetric cell configuration for stable water desalination. The flake structure of the material also enables direct casting onto the porous separator without the need of adding polymer binder. We demonstrated that MXene CDI electrodes accomplished stable performance for 30 cycles with a salt adsorption capacity (SAC) of  $13 \pm 2 \text{ mg g}^{-1}$  (1.2 V cell voltage in 5 mM NaCl saline solution). Thus our results show that the MXene SAC is higher than that of many activated carbons and carbon aerogels commonly used for CDI. However, MXene accomplishes adsorption *via* a completely different ion immobilization mechanism, that is, by ion intercalation instead

of double-layer formation, schematically depicted in Fig. 4. That our initial proof-of-concept cell achieves high performance demonstrates that MXene and CDI *via* intercalation electrodes is a promising direction.

More work is required to better understand the processes of desalination *via* ion insertion in the MXene layered structure and a more rigorous understanding of the concept of charge efficiency in the context of intercalation materials. Also, enhanced performance may be enabled by use of asymmetric MXene CDI cells and hybrid electrodes. We believe that the field of CDI research will see diversification in the near future beyond carbon by employing pseudocapacitive or battery-like processes for enhanced electrochemical desalination, as already predicted by theoretical work.<sup>37</sup>

## Acknowledgements

The authors thank Prof. Eduard Arzt (INM) for his continuing support. We also acknowledge support of the Prof. Lenz Foundation.

## References

- 1 M. E. Suss, S. Porada, X. Sun, P. M. Biesheuvel, J. Yoon and V. Presser, *Energy Environ. Sci.*, 2015, **8**, 2296–2319.
- 2 S. Porada, G. Feng, M. E. Suss and V. Presser, *RSC Adv.*, 2016, **6**, 5865–5870.
- 3 S. Porada, L. Borhardt, M. Oschatz, M. Bryjak, J. S. Atchison, K. J. Keesman, S. Kaskel, P. M. Biesheuvel and V. Presser, *Energy Environ. Sci.*, 2013, **6**, 3700–3712.
- 4 X. Xu, L. Pan, Y. Liu, T. Lu, Z. Sun and D. H. C. Chua, *Sci. Rep.*, 2015, **5**, 8458.
- 5 X. Xu, Z. Sun, D. H. C. Chua and L. Pan, *Sci. Rep.*, 2015, **5**, 11225.
- 6 X. Gao, S. Porada, A. Omosebi, K.-L. Liu, P. M. Biesheuvel and J. Landon, *Water Res.*, 2016, **92**, 275–282.
- 7 X. Gao, A. Omosebi, J. Landon and K. L. Liu, *Energy Environ. Sci.*, 2015, **8**, 897–909.
- 8 B. P. Bastakoti, H. Oveisi, C.-C. Hu, K. C. W. Wu, N. Suzuki, K. Takai, Y. Kamachi, M. Imura and Y. Yamauchi, *Eur. J. Inorg. Chem.*, 2013, 1109–1112.
- 9 B. P. Bastakoti, Y. Kamachi, H.-S. Huang, L.-C. Chen, K. C. W. Wu and Y. Yamauchi, *Eur. J. Inorg. Chem.*, 2013, 39–43.



- 10 J. Lee, S. Kim, C. Kim and J. Yoon, *Energy Environ. Sci.*, 2014, **7**, 3683–3689.
- 11 S. Dutta, S.-Y. Huang, C. Chen, J. E. Chen, Z. A. Allothman, Y. Yamauchi, C.-H. Hou and K. C. W. Wu, *ACS Sustainable Chem. Eng.*, 2016, **4**, 1885–1893.
- 12 N.-L. Liu, S. Dutta, R. R. Salunkhe, T. Ahamad, S. M. Alshehri, Y. Yamauchi, C.-H. Hou and K. C. W. Wu, *Sci. Rep.*, 2016, **6**, 28847.
- 13 A. K. Geim and K. S. Novoselov, *Nat. Mater.*, 2007, **6**, 183–191.
- 14 A. Gupta, T. Sakthivel and S. Seal, *Prog. Mater. Sci.*, 2015, **73**, 44–126.
- 15 M. Naguib, V. N. Mochalin, M. W. Barsoum and Y. Gogotsi, *Adv. Mater.*, 2014, **26**, 992–1005.
- 16 M. Naguib, M. Kortoglu, V. Presser, J. Lu, L. Hultman, J. Niu, M. Heon, Y. Gogotsi and M. W. Barsoum, *Adv. Mater.*, 2011, **23**, 4248–4253.
- 17 M. Naguib and Y. Gogotsi, *Acc. Chem. Res.*, 2014, **48**, 128–135.
- 18 U.S. Department of Energy, *Carbon Sequestration Technology and Program Plan*, 2007.
- 19 M. R. Lukatskaya, O. Mashtalir, C. E. Ren, Y. Dall'Agnese, P. Rozier, P. L. Taberna, M. Naguib, P. Simon, M. W. Barsoum and Y. Gogotsi, *Science*, 2013, **341**, 1502–1505.
- 20 M. R. Lukatskaya, J. Halim, B. Dyatkin, M. Naguib, Y. S. Buranova, M. W. Barsoum and Y. Gogotsi, *Angew. Chem., Int. Ed.*, 2014, **53**, 4877–4880.
- 21 F. Shahzad, M. Alhabeb, C. B. Hatter, B. Anasori, S. Man Hong, C. M. Koo and Y. Gogotsi, *Science*, 2016, **353**, 1137.
- 22 M. D. Levi, M. R. Lukatskaya, S. Sigalov, M. Beidaghi, N. Shpigel, L. Daikhin, D. Aurbach, M. W. Barsoum and Y. Gogotsi, *Adv. Energy Mater.*, 2015, **5**, 1400815.
- 23 J. Come, J. M. Black, M. R. Lukatskaya, M. Naguib, M. Beidaghi, A. J. Rondinone, S. V. Kalinin, D. J. Wesolowski, Y. Gogotsi and N. Balke, *Nano Energy*, 2015, **17**, 27–35.
- 24 Z. Lin, D. Barbara, P.-L. Taberna, K. L. Van Aken, B. Anasori, Y. Gogotsi and P. Simon, *J. Power Sources*, 2016, **326**, 575–579.
- 25 M. Hu, Z. Li, H. Zhang, T. Hu, C. Zhang, Z. Wu and X. Wang, *Chem. Commun.*, 2015, **51**, 13531–13533.
- 26 M. Aslan, M. Zeiger, N. Jäckel, I. Grobelsek, D. Weingarh and V. Presser, *J. Phys.: Condens. Matter*, 2016, **28**, 114003.
- 27 S. Brunauer, P. H. Emmett and E. Teller, *J. Am. Chem. Soc.*, 1938, **60**, 309–319.
- 28 N. Jäckel, M. Rodner, A. Schreiber, J. Jeongwook, M. Zeiger, M. Aslan, D. Weingarh and V. Presser, *J. Power Sources*, 2016, **326**, 660–671.
- 29 S. Porada, R. Zhao, A. van der Wal, V. Presser and P. M. Biesheuvel, *Prog. Mater. Sci.*, 2013, **58**, 1388–1442.
- 30 M. Naguib, O. Mashtalir, J. Carle, V. Presser, J. Lu, L. Hultman, Y. Gogotsi and M. W. Barsoum, *ACS Nano*, 2012, **6**, 1322–1331.
- 31 J. Halim, K. M. Cook, M. Naguib, P. Eklund, Y. Gogotsi, J. Rosen and M. W. Barsoum, *Appl. Surf. Sci.*, 2016, **362**, 406–417.
- 32 J. Halim, S. Kota, M. R. Lukatskaya, M. Naguib, M.-Q. Zhao, E. J. Moon, J. Pitock, J. Nanda, S. J. May, Y. Gogotsi and M. W. Barsoum, *Adv. Funct. Mater.*, 2016, **26**, 3118–3127.
- 33 Z. Lin, P. Rozier, B. Duplicoy, P.-L. Taberna, B. Anasori, Y. Gogotsi and P. Simon, *Electrochem. Commun.*, 2016, **72**, 50–53.
- 34 M. A. Hope, A. C. Forse, K. J. Griffith, M. R. Lukatskaya, M. Ghidui, Y. Gogotsi and C. P. Grey, *Phys. Chem. Chem. Phys.*, 2016, **18**, 5099–5102.
- 35 J. Landon, X. Gao, B. Kulengowski, J. K. Neathery and K. Liu, *J. Electrochem. Soc.*, 2012, **159**, A1861–A1866.
- 36 M. Naguib, O. Mashtalir, M. R. Lukatskaya, B. Dyatkin, C. Zhang, V. Presser, Y. Gogotsi and M. W. Barsoum, *Chem. Commun.*, 2014, **50**, 7420–7423.
- 37 K. C. Smith and R. Dmello, *J. Electrochem. Soc.*, 2016, **163**, A530–A539.



#### 4.4 Two-dimensional molybdenum carbide (MXene) with divacancy ordering for brackish and seawater desalination via cation and anion intercalation

Pattarachai Srimuk,<sup>1,2</sup> Joseph Halim,<sup>3</sup> Juhan Lee,<sup>1,2</sup> Quanzheng Tao,<sup>3</sup>

Johanna Rosen,<sup>3</sup> Volker Presser<sup>1,2</sup>

<sup>1</sup> INM - Leibniz Institute for New Materials, Campus D2 2, 66123 Saarbrücken, Germany

<sup>2</sup> Saarland University, Campus D2 2, 66123 Saarbrücken, Germany

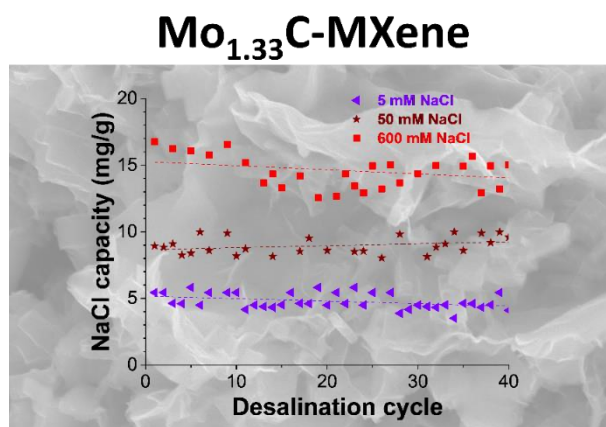
<sup>3</sup> Thin Film Physic, Department of Physic, Chemistry and Biology (IFM), Linköping University, SE-581 83 Linköping, Sweden

##### Citation:

P. Srimuk, J. Halim, J. Lee, Q. Tao, J. Rosen, V. Presser, TWO-DIMENSIONAL MOLYBDENUM CARBIDE (MXENE) WITH DIVACANCY ORDERING FOR BRACKISH AND SEAWATER DESALINATION VIA CATION AND ANION INTERCALATION, ACS Sustainable Chemistry & Engineering 6(3) (2018) 3739-3747.

##### Own contribution:

Electrochemistry, CDI experiment, analysis, writing



**Ion intercalation  
for energy efficient desalination**

# Two-Dimensional Molybdenum Carbide (MXene) with Divacancy Ordering for Brackish and Seawater Desalination via Cation and Anion Intercalation

Pattarachai Srimuk,<sup>†,§</sup> Joseph Halim,<sup>‡</sup> Juhan Lee,<sup>†,§</sup> Quanzheng Tao,<sup>‡</sup> Johanna Rosen,<sup>\*,‡</sup> and Volker Presser<sup>\*,†,§</sup>

<sup>†</sup>INM–Leibniz Institute for New Materials, Campus D2 2, 66123 Saarbrücken, Germany

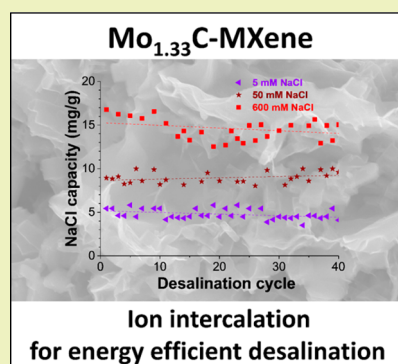
<sup>‡</sup>Thin Film Physics, Department of Physics, Chemistry and Biology (IFM), Linköping University, SE-581 83 Linköping, Sweden

<sup>§</sup>Department of Materials Science and Engineering, Saarland University, Campus D2 2, 66123 Saarbrücken, Germany

## S Supporting Information

**ABSTRACT:** Ion intercalation materials are emerging as a highly attractive class of electrodes for efficient energy water desalination. Most materials and concepts so far have focused on the removal of cations (especially sodium). Anion intercalation, however, remains poorly investigated in water desalination. We present a study on the capability of Mo<sub>1.33</sub>C-MXene for removing cations and anions and demonstrate the desalination performance in brackish water and seawater concentrations. Mo<sub>1.33</sub>C-MXene was prepared via acid treatment of the transition metal carbide MAX phase (Mo<sub>2/3</sub>Sc<sub>1/3</sub>)<sub>2</sub>AlC. Binder-free electrodes were obtained by entangling MXene with carbon nanotubes and tested without the use of any ion exchange membrane at low (5 mM NaCl) and high (600 mM NaCl) salt concentrations. Such electrodes showed a promising desalination performance of 15 mg/g in 600 mM NaCl with high charge efficiency up to 95%. By employing chemical online monitoring of the effluent stream, we separated the cation and anion intercalation capacity of the electrode material.

**KEYWORDS:** Capacitive deionization, Pseudocapacitance, Water desalination, Ion intercalation



## INTRODUCTION

Capacitive deionization (CDI) is a promising water treatment technology for the desalination of saline media with a low salt content (especially below 20 mM), such as brackish water.<sup>1</sup> A conventional CDI cell accomplishes desalination of an inflowing stream through ion electrosorption by the formation of an electrical double layer at fluid/solid interfaces between saline medium and the nanoporous carbon electrode. So far, various carbon materials have been explored as CDI electrodes,<sup>2</sup> such as activated carbon,<sup>3,4</sup> carbon cloth,<sup>5</sup> carbon aerogel,<sup>6</sup> or graphene.<sup>7</sup> However, values for the maximum salt removal capacities of optimized carbon nanomaterials seem to saturate at about 15–25 mg/g at a cell voltage of 1.2 V. While novel cell designs try to overcome this limitation by use of ion exchange membranes<sup>8–10</sup> or suspension electrodes,<sup>11–13</sup> the search for electrode materials beyond carbon is being actively pursued.<sup>14</sup>

Transitioning from conventional capacitive carbon for CDI to Faradaic materials capitalizes on ion intercalation in the crystal structure of the electrode. Some two-dimensional (2D) materials such as transition metal dichalcogenides (TMDs) like MoS<sub>2</sub> (refs 15 or 16) or transition metal carbides (MXenes)<sup>17–19</sup> may show the electric charge vs potential profile of a capacitor and are thereby called pseudocapacitive.<sup>20,21</sup> By this way, the material accomplishes capacitor-like energy storage behavior albeit the energy storage process is

fully Faradaic (ion intercalation); this is in contrast to the non-Faradaic process of ion electrosorption at electrically charged surfaces (conventional CDI and electrical double-layer capacitors).<sup>21–24</sup> Such materials also allow overcoming the intrinsic preference of CDI operation for low molar concentrations: during ion electrosorption, charge is invested to expel ions with the same charge as the electrode (co-ions) and permselective desalination of only counterions (opposite charge than electrode) onsets after depletion of co-ions from carbon nanopores. Accordingly, high molar systems, such as supercapacitors, only show a change of the co-ion/counterion ratio but fail to accomplish actual desalination of the surrounding saline medium.<sup>25,26</sup> Intercalation materials, however, overcome this limitation in the absence of ion exchange membranes by allowing permselective removal of ions at high efficiency even at high molar strength (demonstrated up to 500 mM NaCl; ref 15). In this way, Faradaic deionization is a highly promising technology for energy efficient desalination of seawater or industrial wastewater far above the salinity level of brackish water.<sup>14,27</sup>

Received: November 6, 2017

Revised: January 15, 2018

Published: February 1, 2018

Some novel concepts for electrochemical desalination with Faradaic electrode materials use asymmetric cell designs. The desalination battery, for example, relies on  $\text{Na}_2\text{Mn}_5\text{O}_{10}$ ,  $\text{Na}_2\text{FePO}_4$ , or  $\text{NaTi}_2(\text{PO}_4)_3$  for sodium removal (via ion intercalation; refs 28–30) and Ag or  $\text{BiOCl}$  for chloride removal (via conversion reactions; refs 31–33). TMDs and MXenes show the ability to insert cations or anions, but possibly with different uptake capacities. Yet, the slightly negative charge of many MXenes<sup>34,35</sup> makes the material less attractive to remove chloride and more effective for sodium removal.<sup>18</sup> TMDs like  $\text{MoS}_2$  have a point of zero charge closer to the fully discharged state and are more suitable for anion and cation removal. Compared to the removal of anions by a conversion reaction (like  $\text{Ag}/\text{AgCl}$ ),<sup>31</sup> their removal by intercalation remains much less explored.<sup>15,18</sup> Anion intercalation, however, is well-known for materials like graphite<sup>36,37</sup> and very attractive for desalination technologies.

MXenes are a fast growing group of 2D materials having high potential in many applications,<sup>19</sup> such as energy storage (e.g., batteries and supercapacitors),<sup>38,39</sup> energy conversion (e.g., solar cells and fuel cells),<sup>40,41</sup> membranes,<sup>42–44</sup> and water desalination.<sup>45,46</sup> MXene synthesis and processing can capitalize on existing ceramic manufacturing and is intensively explored for commercial application.<sup>47</sup> Motivated by our recent study on the use of a MXene (namely,  $\text{Ti}_3\text{C}_2$  MXene clay),<sup>18</sup> we now introduce  $\text{Mo}_{1.33}\text{C}$  for water desalination. This MXene originates from a family of 2D atomic laminates with in-plane chemical order, coined *i*-MAX,<sup>48</sup> which after etching allows synthesis of a MXene with ordered divacancies.<sup>49</sup> We provide the first data of MXene at high molar strength from 5 to 600 mM and operate the 2D material as binder-free electrodes in the absence of any ion exchange membrane. By use of online monitoring of the chemical composition of the out-flowing water stream leaving the desalination cell with optical emission spectroscopy, we show the ability of this MXene to intercalate sodium and chloride at the negative and positive electrode, respectively. We chose this MXene as the unique synthesis from the parent  $(\text{Mo}_{2/3}\text{Sc}_{1/3})_2\text{AlC}$  with hydrofluoric acid yields a material with similar specific capacitance (units farads per gram (F/g)) related to anion and cation intercalation. Other MXenes are known to show a significant chemical charge which offset the point of zero charge and modifies, thereby, the ability to uptake cations or anions.<sup>49</sup> The point of zero charge of  $\text{Mo}_{1.33}\text{C}$ -MXene near 0 V should translate for a symmetric cell to a similar desalination capacity for anions and cations, when normalized to the number of intercalated ions.

## ■ EXPERIMENTAL DESCRIPTION

**Materials and Synthesis.** The  $(\text{Mo}_{2/3}\text{Sc}_{1/3})_2\text{AlC}$  MAX phase was synthesized by following previous work (ref 49). Briefly, graphite (99.99%, Sigma-Aldrich), molybdenum (99.99%, Sigma-Aldrich), aluminum (99.8%, Sigma-Aldrich), and scandium (99.99%, Stanford Advanced Material) were mixed in an agate mortar with a Mo:Sc:Al:C stoichiometric ratio of 1.33:0.67:1:1. The mixture was transferred into an alumina crucible and placed inside an argon flow furnace. The sample was heated to 1500 °C and held for 20 h. After cooling the sample to room temperature in the furnace, a loosely packed MAX powder was obtained.

To prepare  $\text{Mo}_{1.33}\text{C}$ -MXene, the as-prepared MAX phase was crushed and sieved through a 450-mesh sieve (particle size <30 μm). A 1 g portion of sieved MAX was etched in 20 mL of concentrated HF (48%, Sigma-Aldrich) and continuously stirred for 24 h. Thereafter, the suspension was filtered and dispersed in water. This process was repeated for five times to remove remaining acid and residual reaction

products. The sample on the filter was then dried at room temperature for 12 h. For the exfoliation of MXene sheets, 100 mg of etched MAX material was put in a centrifuge tube, containing 1 mL of tetrabutylammonium hydroxide (TBAOH). The solution was shaken manually for 5 min and centrifuged at 6000 rpm for 5 min to remove the supernatant. The remaining TBAOH was removed by adding water and carefully rinsed for three times.

**Material Characterization.** X-ray diffraction (XRD) experiments were conducted employing a D8 Advance diffractometer (Bruker AXS) with a copper X-ray source (Cu-Kα, 40 kV, 40 mA) and a nickel filter. Measurements were conducted with a 2-D detector (VANTEC).

Scanning electron microscopy (SEM) was carried out on a JEOL JSM 7500F field emission scanning electron microscope (JEOL, Japan) operating at 3 kV. Energy dispersive X-ray spectroscopy (EDX) was carried out at 10 kV in the system with an X-Max Silicon Detector from Oxford Instruments using AZtec software. Transmission electron microscopy (TEM) was carried out with a JEOL JEM-2100F system operating at 200 kV in a vacuum. Sample material was dispersed and sonicated in ethanol, and drop-casted onto a copper grid with a carbon film.

Nitrogen gas sorption analysis (Supporting Information, Figure S1) was conducted with a Quantachrome Autosorb iQ system. The samples were degassed at 200 °C for 1 h and heated up to 300 °C. To remove volatile surface molecules, this temperature was kept for 20 h at a relative pressure of 0.1 Pa. The nitrogen gas sorption analysis was carried out in liquid nitrogen at −196 °C. The relative pressure of nitrogen was increased from  $5 \times 10^{-7}$  to 1.0 in 35 steps. The calculation of specific surface area (SSA) was performed with the Brunauer–Emmett–Teller equation (BET) in the linear low-pressure regime of the measured isotherms. As can be seen from Figure S1, the  $\text{Mo}_{1.33}\text{C}$ -MXene and  $\text{Mo}_{1.33}\text{C}$ -CNT material is of very small external surface area (BET SSA of ca. 1 m<sup>2</sup>/g, and 30 m<sup>2</sup>/g, respectively).

**Electrode Preparation.** We used a binder-free electrode for all electrochemical measurements (Supporting Information, Figure S2) which was prepared as follows. A 90 mg portion of  $\text{Mo}_{1.33}\text{C}$ -MXene flakes, achieving from TBAOH treatment, were mixed with 300 mL of water and sonicated while stirring in an ice-bath for 10 min. In parallel, 5 mg of multiwall carbon nanotubes (CNTs, Nonacyl NC7000) was added to 100 mL ethanol and sonicated for 20 min. Then, the  $\text{Mo}_{1.33}\text{C}$ -MXene and CNTs mixtures were mixed and further sonicated for 10 min. The  $\text{Mo}_{1.33}\text{C}$ -CNT dispersion was filtered through a porous spacer (glass fiber prefilter, Millipore, compressed thickness of a single layer is 380 μm). Another 5 mg of CNTs was dispersed in 100 mL ethanol and sonicated for 20 min. The CNT dispersion was filtered through the previous  $\text{Mo}_{1.33}\text{C}$ -CNT electrode. The resulting electrode was dried overnight at 60 °C in the oven. The total mass of CNT in the electrode was in the end 10 mass %. The CNTs in the MXene layer prevent the restacking of the layer and avoid loss of MXene to the inflowing water stream during the later desalination application. The only-CNT-layer helps the electrical conductivity of the electrode. The overall small amount of CNTs has also only a minor impact on the electrochemical performance.

**Electrochemical Measurements.** Three-electrode (half-cell) electrochemical measurement was conducted in a custom-built cell outlined in ref 50. A disc of the  $\text{Mo}_{1.33}\text{C}$ -CNT electrode with a diameter of 12 mm (mass loading of 1.2 mg) was used as the working electrode and graphite sheet (SGL carbon) was selected as a current collector for working and counter electrodes (diameter of 12 mm). As a counter electrode, 15 mg of activated carbon (YP80-F, Kuraray) with polytetrafluoroethylene (PTFE) was selected. The detail for carbon electrode preparation can be found in our previous work in ref 51. For cell assembling, the graphite electrode was first placed in the cell following by carbon electrode, 13 mm diameter separator (GF/A, Whatmann),  $\text{Mo}_{1.33}\text{C}$ -CNT, and graphite current collector. The cell was tightly packed by a spring-loaded titanium piston. The  $\text{Ag}/\text{AgCl}$  (3 M KCl, BASi) reference electrode was mounted at the side channel of the cell, where porous frit of reference electrode was close to the working and counter electrode. As an electrolyte, 1 M NaCl was filled into the cell via vacuum backfilling with a syringe.

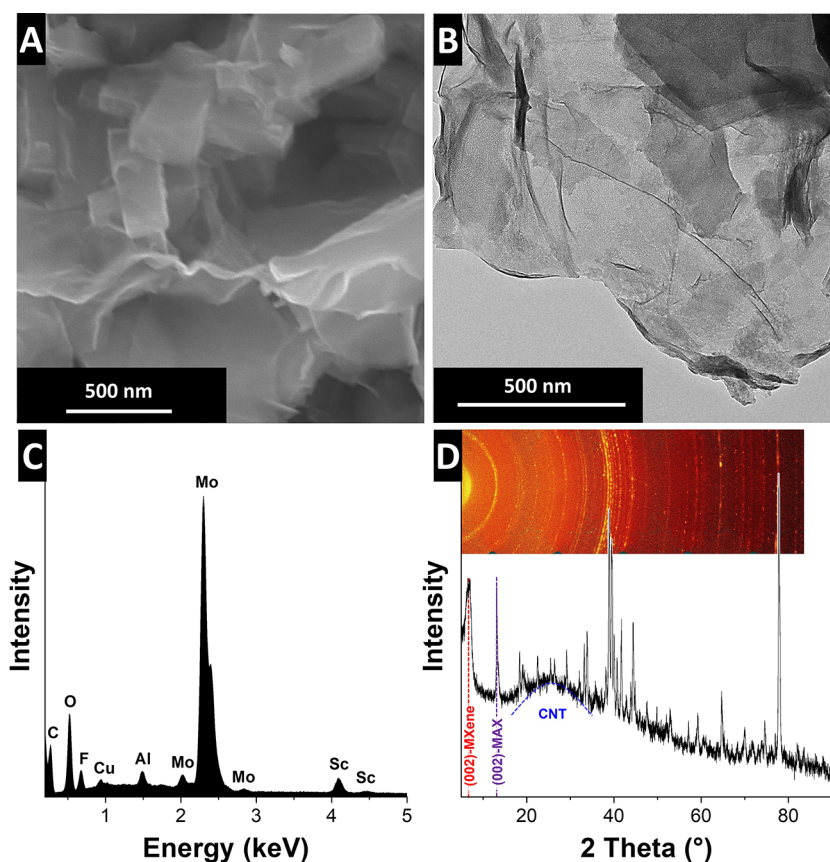


**Figure 1.** Characterization of  $\text{Mo}_{1.33}\text{C-MXene}$  used as electrode material: scanning electron micrograph (A), transmission electron micrograph (B), energy-dispersive X-ray spectrum (C), and X-ray diffractogram and corresponding two-dimensional scattering pattern (D).

The electrochemical measurement was conducted with a VMP300 potentiostat/galvanostat (Bio-Logic). Cyclic voltammetry and galvanostatic cycling were employed with positive and negative polarization starting from 0 V vs Ag/AgCl. For the positive polarization, the potential of the  $\text{Mo}_{1.33}\text{C-CNT}$  electrode was limited at +0.6 V vs Ag/AgCl while  $-0.7$  V vs Ag/AgCl was the limit for negative polarization. For galvanostatic cycling techniques, the  $\text{Mo}_{1.33}\text{C-CNT}$  electrode was applied at different specific current (0.1–10 A/g). The specific capacitance ( $C_{\text{sp}}$ ) was calculated by using eq 1:

$$C_{\text{sp}} = \frac{1}{Um} \int_{t_1}^{t_2} I dt \quad (1)$$

where  $I$  is the applied current,  $t_2 - t_1$  is the time per half-cycle,  $U$  is the potential difference during polarization (excluding the  $iR$  drop), and  $m$  is the total mass of the working electrode.

Two-electrode electrochemical characterization (full-cell configuration) was carried out using the same cell as used in the three-electrode (half-cell) experiment. Two  $\text{Mo}_{1.33}\text{C-CNT}$  electrodes with diameter of 12 mm (total mass 1.4 mg) were separated by a separator with a diameter of 13 mm. Graphite sheets (12 mm diameter) were employed as current collectors. After tightly assembling the cell, 1 M NaCl was injected into the cell by vacuum backfilling. This concentration was chosen to avoid any ion starvation during the experiment; for more information on the correlation between capacitance and ion concentration, see ref 9. To record cyclic voltammograms, we scanned the cell voltage from 0 to 1 V with sweeping rate of 5 mV/s. The cell was charged and discharged with different specific currents, ranging from 0.1 A/g to 10 A/g with cell voltages between 0 and 1 V. To measure potential at zero charge, a Ag/AgCl spectator reference was present in the cell. In this way, the individual potential of each electrode was measured during galvanostatic cycling experiments. The specific capacitance  $C_{\text{sp}}$  was calculated according to ref 52.

**Desalination Measurements.** For desalination experiments, the electrode preparation was the same as for electrochemical analysis. The binder-free  $\text{Mo}_{1.33}\text{C-CNT}$  electrodes were assembled in a flow-by cell described in ref 18. The CDI stack was built from graphite current collectors with attached to  $\text{Mo}_{1.33}\text{C-CNT}$  electrodes. The total mass of electrode including CNT was 300 mg with a thickness of 5  $\mu\text{m}$  (Supporting Information, Figure S1). Afterward, the cell was tightly closed.

The electrochemical desalination measurements were carried out with two symmetric pairs of electrodes where no ion exchange membranes or binder were used. The total electrolyte flow rate was 15 mL/min. Desalination (charging) and salination (discharging) steps were carried out using constant potential mode with a cell voltage of +0.8 V and regeneration was accomplished at 0 V. Note that most CDI works with carbon electrodes use 1.2 V as the cell voltage; such high cell voltages were not suitable for the present electrode material per consideration of the electrochemical stability window. This is in alignment with our previous work on molybdenum disulfide.<sup>15</sup> For all electrochemical operations, we used a VSP300 potentiostat/galvanostat (Bio-Logic), and the duration of each half-cycle was 40 min to ensure near-equilibrium conditions. All experiments were carried out with a concentration of 5, 50, or 600 mM NaCl solution in a 10 L electrolyte tank and the saline medium was deaerated by flushing nitrogen gas. This was done to limit the dissolved oxygen in the solution and allows comparison with the current CDI literature on carbon electrodes without ion exchange membranes.<sup>1</sup> The salt removal capacity and the measured charge were defined per total mass of electrode material (i.e.,  $\text{Mo}_{1.33}\text{C-MXene}$  and -CNTs) and were calculated following our previous works.<sup>15,18</sup>

**Online ICP-OES Monitoring of the Desalination Process.** Two stacked electrode pairs containing  $\text{Mo}_{1.33}\text{C-CNT}$  were assembled in the CDI cell. The adsorption and desorption steps were conducted via chronoamperometry. During charging, a constant voltage of 0.8 V was

**Table 1. Elemental Analysis of Mo<sub>1.33</sub>C-MXene via EDX**

mass %	C	O	F	Al	Sc	Mo
Mo <sub>1.33</sub> C	12.1	8.2	1.3	7.9	5.8	64.6

applied and held for 40 min. Afterward, the cell was discharged at a constant cell voltage of 0 V and held for 40 min. For inductively coupled plasma optical emission spectroscopy (ICP-OES) experiments, the flow rate was 2.5 mL/min to enhance the signal–noise ratio. The saline solution was 5 mM NaCl with a reservoir tank volume of 10 L, which was flushed continuously with N<sub>2</sub> gas to remove dissolved oxygen. To detect the effluent ion concentration, 2 mL/min of solution was constantly extracted from the outlet stream of the cell by the peristaltic pump of the system (ARCOS FHX22, SPECTRO Analytical Instruments). The online intensities from the extracted sample were converted into concentration profiles. The ion removal capacity was calculated for sodium and for chlorine individually using eq 2:

$$\text{ion removal capacity} \left( \frac{m_{\text{ion}}}{m_{\text{electrode}}} \right) = \frac{vM_{\text{ion}}}{m_{\text{electrode}}} \int c \, dt \quad (2)$$

where  $v$  is flow rate (2.5 mL/min),  $M_{\text{ion}}$  is the molecular weight of ion species (Na 23 g/mol, Cl 35.4 g/mol),  $m$  is mass of either positive or negative electrode (mg),  $c$  is the ion concentration of outlet stream (mol/L), and  $t$  is ion removal time (min).

## RESULTS AND DISCUSSION

Mo<sub>1.33</sub>C-MXene was synthesized following the protocol published in a previous work.<sup>49</sup> After HF etching of the ternary metal carbide precursor (Mo<sub>2/3</sub>Sc<sub>1/3</sub>)<sub>2</sub>AlC and tetrabutylammonium hydroxide (TBAOH) intercalation, the resulting MXene shows wrinkle layers morphology (Figure 1A) with a grain size larger than 20 μm. Thin-layer Mo<sub>1.33</sub>C-MXene is shown in Figure 1B, indicating successfully delamination of multilayer Mo<sub>1.33</sub>C-MXene. Chemical analysis via energy dispersive X-ray spectroscopy (EDX) shows small intensities of Al and Sc (Figure 1C), indicating that most of the Al (A-layer) and in-plane Sc (part of the M-layer) were removed during acid treatment. Those atoms were replaced by F- and O-functional groups (Table 1). This is in good alignment with the X-ray diffractogram in Figure 1D, showing reflection of Mo<sub>1.33</sub>C-MXene particles, especially the (002)-reflection at

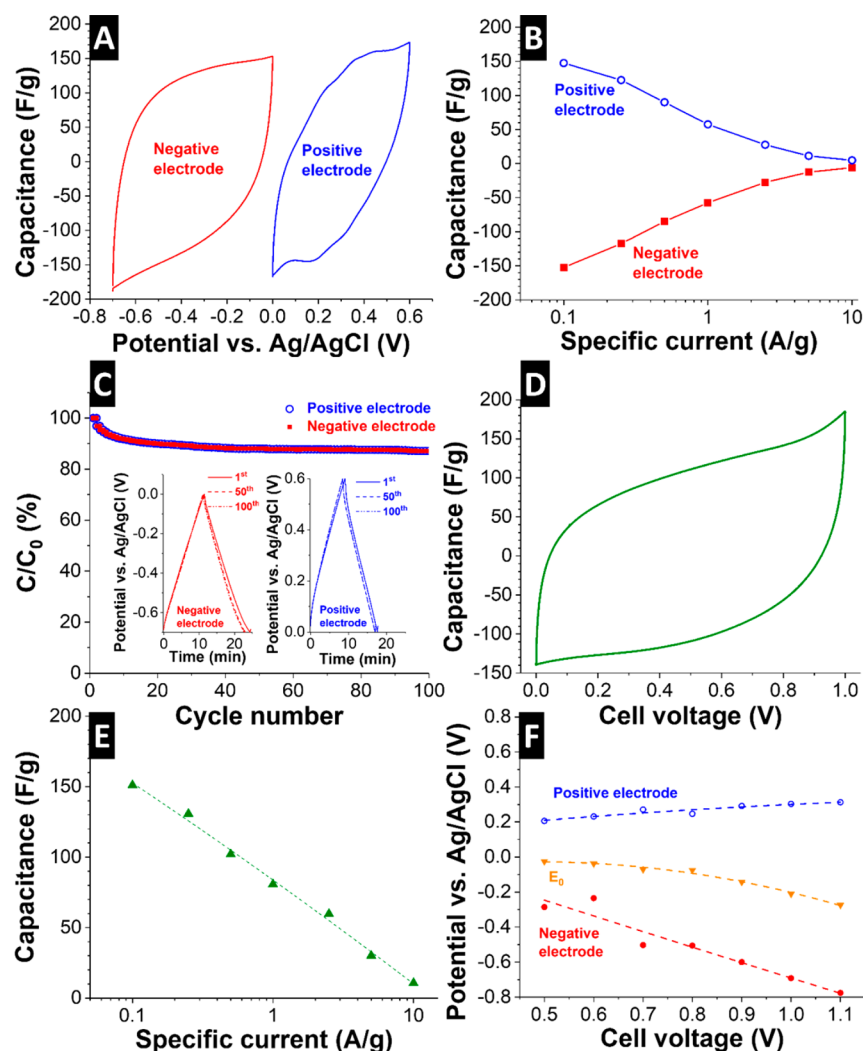


**Figure 2.** Electrochemical characterization of binder-free Mo<sub>1.33</sub>C-CNT electrode in 1 M NaCl: (A) cyclic voltammogram at 5 mV/s, (B) specific capacitance vs specific current, (C) capacitance retention at limiting positive and negative potential, (D) cyclic voltammogram of symmetrical full cell at 5 mV/s, (E) specific capacitance vs specific current of symmetrical full cell, and (F) potential development of the positive electrode, negative electrode, and potential at zero cell voltage.

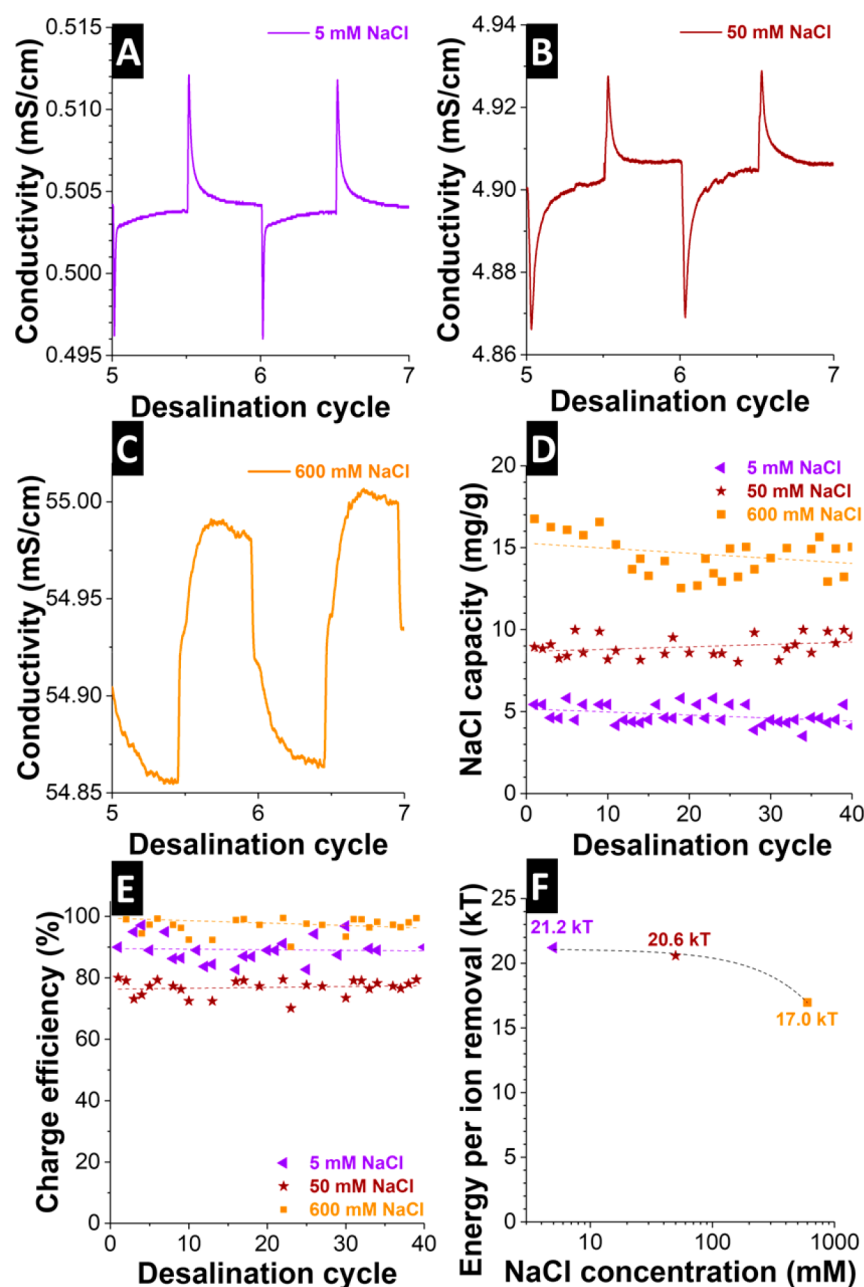


**Figure 3.** Constant voltage desalination with Mo<sub>1.33</sub>C-CNT at 0.8 V at 5, 50, or 600 mM NaCl. (A–C) Conductivity profiles of effluent stream leaving the desalination cell. (D) NaCl removal capacity. (E) Charge efficiency. (F) Energy consumption per removed ion.

6.6°  $2\theta$ . Other reflections correlate to incompletely reacted MAX, for example, the prominent peak at 13.1°  $2\theta$ . A more detailed assignment of the different XRD peaks can be seen in ref 49. The broad reflection at around 24–26°  $2\theta$  originates from the carbon nanotubes (CNT) added during electrode manufacturing. Binder-free Mo<sub>1.33</sub>C-CNT was fabricated by simple filtration of MXene and CNT dispersion through the glass fiber separator (Supporting Information, Figure S1). The total CNT content of 10 mass% effectively avoided MXene restacking and washing-out of the MXene flakes during desalination operation (adopting the approach we used in our previous work on 2D MoS<sub>2</sub><sup>15</sup>).

Prior to desalination testing, we carried out thorough electrochemical analysis with a three-electrode configuration using 1 M NaCl. This half-cell setup allows us to characterize the electrochemical response of the Mo<sub>1.33</sub>C-CNT electrodes

either during positive or negative potential polarization. A cyclic voltammogram (CV) of Mo<sub>1.33</sub>C-CNT is shown in Figure 2A. By sweeping the electrode potential from 0 to +0.6 V vs Ag/AgCl and from 0 to –0.7 V vs Ag/AgCl at a rate of 5 mV/s for each individual cell, we see a pronounced pseudocapacitive response in the form of slightly distorted rectangular shapes. This resistive element in the response (resistive knee) stems from the limited kinetics of ion intercalation in-between MXene sheets. The term pseudocapacitive<sup>21</sup> identifies a capacitorlike electrical behavior which does not originate in ion electro-sorption but is caused by a Faradaic process. In the case of MXene, ions intercalate between the atomic layers not selectively at a certain applied potential but continuously as the charge is accumulated.<sup>20</sup> This gives rise to a linear correlation between charge and potential, as one would expect it for an ideal electrical double-layer capacitor. In a battery-like

system, for comparison, we would see clear redox peaks during charging and discharging, associated with distinct intercalation states, phase transitions, or phase conversions.<sup>24</sup>

For stable cell operation, it is important to determine the electrochemical stability window. As can be seen, the negative limit potential of this MXene is estimated to be  $-0.4$  V vs Ag/AgCl for the negative electrode and the positive limit potential of  $+0.55$  V vs Ag/AgCl for the positive electrode. To estimate specific capacitance of Mo<sub>1.33</sub>C-CNT electrode, galvanostatic charge–discharge was conducted with specific current of 0.1–10 A/g. As shown in Figure 2B, the maximum specific capacitance for the positive electrode is 150 F/g at 0.1 A/g while the maximum specific capacitance for the negative electrode is 155 F/g at 0.1 A/g. The performance is stable and maintains ca. 90% of the initial specific capacitance after 100 galvanostatic charge/discharge cycles at 0.1 A/g (Figure 2C).

Operation of the full cell shows a pseudocapacitive CV shape (Figure 2D). The full cell yields a specific capacitance of 150 F/g at 0.1 A/g as determined by galvanostatic charge/discharge cycling (Figure 2E). An onset of electrochemical decomposition is already indicated by the increase of irreversible current when exceeding a cell voltage of 0.8 V (Figure 2D). This is further confirmed when tracing the potential of the negative and positive electrode by use of a Ag/AgCl spectator reference (Figure 2F): beyond a cell voltage of 0.8 V, the cell potential at zero charge decreases from about 0 V vs Ag/AgCl to about  $-0.2$  V vs Ag/AgCl. The loss of symmetric potential distribution between negative and positive electrode aligns with the emergence of irreversible Faradaic reactions (e.g., decomposition of surface termination group, hydrogen evolution reaction, and oxygen evolution reaction).<sup>53</sup> Therefore, we limited the cell voltage for a symmetric cell (i.e., two Mo<sub>1.33</sub>C-CNT electrodes with same size and mass loading) to 0.8 V. This is the same value as recently found for MoS<sub>2</sub>-CNT electrodes<sup>15</sup> and is significantly lower than most works on CDI by use of carbon electrodes (typically: 1.2 V).<sup>1,27</sup>

Desalination was benchmarked at 5, 50, and 600 mM aqueous NaCl solution to cover the range from brackish water (<17 mM) to seawater ( $\sim 600$  mM = 3.5% salinity). At all three concentrations, we see the characteristic charge/discharge = desalination/salination pattern in the conductivity profiles of the outflowing stream (Figure 3A–C). In alignment with our previous work,<sup>15</sup> we see an increase in desalination capacity (NaCl capacity) from 5 to about 15 mg/g when increasing the salinity from 5 to 600 mM NaCl (all values normalized to the total mass of both electrodes). The increase of desalination capacity with by increasing salinity is a unique feature of desalination of Faradaic materials; in the case of conventional CDI employing nanoporous carbon, the increasing amount of co-ion expulsion consumes an increasing charge and desalination capacity and charge efficiency drop drastically at a concentration above 50 mM. In our case, Mo<sub>1.33</sub>C-CNT electrodes maintain a charge efficiency of ca. 75–97% over 40 desalination cycles at all concentration regimes (Figure 3E). This high charge efficiency is also supported by the stable pH of the outlet stream during desalination process with variations  $\Delta\text{pH} < 0.5$ . It is important to carefully select the upper and lower potential limit to avoid parasitic reactions, low charge efficiency, low salt removal capacity, and rapid performance loss.<sup>54</sup>

In a next step, we calculated the energy consumption per removed ion without considering the energy recovery or pumping energy following the procedure from our previous

work.<sup>49</sup> In this way, we can derive quantitative data to estimate the energy consumption of the electrodes. The energy consumed during desalination was divided by the salt removal capacity. This yields energy in joules per mole of NaCl which is divided by the Boltzmann constant  $k$  (2.48 kJ/mol) to obtain energy consumption in kT. Mo<sub>1.33</sub>C-CNT exhibit energy consumption of 21, 20.5, and 17 kT in 5, 50, and 600 mM NaCl, respectively (Figure 3F). These values are comparable to other materials, for example, nickel hexacyanoferrate (20 kT in 20 mM NaCl),<sup>28</sup> MWCNT h-V<sub>2</sub>O<sub>5</sub> (17.9 kT in 600 mM NaCl),<sup>55</sup> MoS<sub>2</sub>-10CNT (24.6 kT in 500 mM),<sup>15</sup> activated carbon (94.4 kT in 500 mM NaCl using a multichannel membrane CDI unit),<sup>9,56</sup> and activated carbon with ion exchange membrane (20–24 kT in 5–200 mM NaCl).<sup>25</sup> Clearly, desalination using Mo<sub>1.33</sub>C consumes less energy as compared to the use of carbon electrodes (even when the latter are operated in conjunction with ion exchange membranes). For comparison, the energy consumption per ion removal of seawater reverse osmosis is still lower with 7.5 kT for 50% water removal.<sup>57</sup>

The average desalination rates of our system and selected other works are presented in Table 2. The desalination rate of

**Table 2. Comparison of Desalination Capacity and Desalination Rate**

electrode material	cell voltage (V)	salt removal capacity (mg/g)	salt removal rate ( $\mu\text{g}/(\text{g s})$ )	NaCl concentration (mM)	ref
activated carbon (YP-80F)	0.8	15	6.5	5	15
activated carbon (MSP-20)	1.2	23.6	19	10	58
MoS <sub>2</sub> -CNT	0.8	25	7	500	15
MoS <sub>2</sub> -CNT	0.8	9	2.5	5	15
Ti <sub>3</sub> C <sub>2</sub> -MXene	1.2	13	16	5	18
Ti <sub>3</sub> C <sub>2</sub> -MXene	1.2	13	16	5	18
Mo <sub>1.33</sub> C-MXene	0.8	5	2.1	5	this work
Mo <sub>1.33</sub> C-MXene	0.8	15	5.9	600	this work

intercalation materials is typically slower than that of conventional CDI. For instance, a porous carbon electrode exhibits a rate of  $6.5 \mu\text{g}/(\text{g s})$  operating in 5 mM NaCl and 0.8 V, whereas intercalation materials like Mo<sub>1.33</sub>C-MXene show a desalination rate of  $2.1 \mu\text{g}/(\text{g s})$  operating in 5 mM NaCl and 0.8 V. Yet, for a direct comparison and to investigate the intrinsic limitations of different systems, cell parameters (like electrode thickness and mass loading) must be carefully kept constant since thin electrodes, for example, skew the desalination rate toward higher values.<sup>58</sup>

Per the extremely small outer surface area of MXene (ca. 1 m<sup>2</sup>/g; 30 m<sup>2</sup>/g for Mo<sub>1.33</sub>C-CNT, Supporting Information, Figure S1) and assuming an areal capacity of around 0.1 F/m<sup>2</sup>,<sup>52,59</sup> the non-Faradaic contribution to the total measured specific capacitance is negligible (ca. 2%, that is 3 of 150 F/g). Thereby, the only mechanism by which the significant desalination performance can be accomplished is through intercalation between the MXene layers. Our previous studies have shown changes in the lattice distances for Ti<sub>3</sub>C<sub>2</sub>-MXene

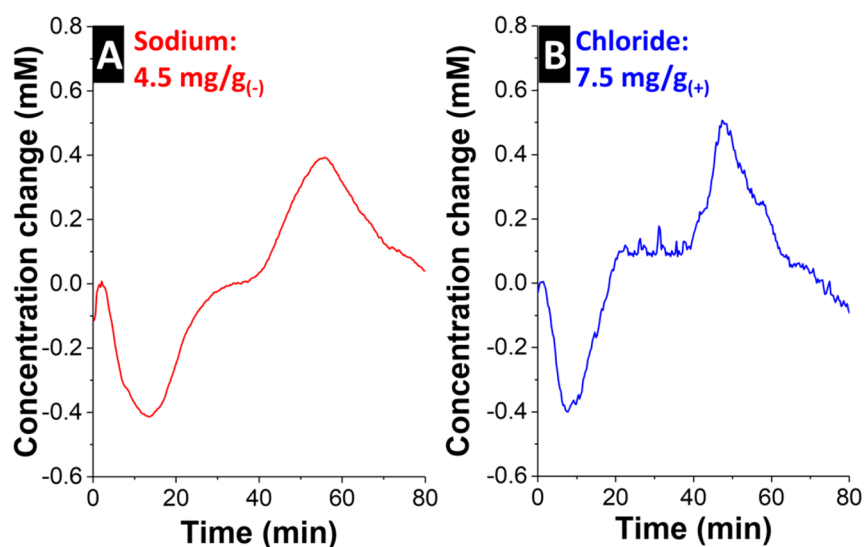


**Figure 4.** Concentration profiles measured with ICP-OES in 5 mM NaCl aqueous solution. The cation uptake capacity (A) is normalized to the mass of the negative electrode (−), and the anion uptake capacity (B) is normalized to the mass of the positive electrode (+).

and MoS<sub>2</sub>-CNT electrodes.<sup>15,18</sup> Also, the electrochemical data clearly show that both positive and negative polarization follow a pseudocapacitive pattern. The only way to explain this behavior is by cation intercalation in the negatively polarized electrode and by anion intercalation in the positively polarized electrode. To further corroborate this ion storage mechanism and to separate the anion and cation removal capacity, we have analyzed the effluent stream's chemical composition with online monitoring with an inductively coupled plasma optical emission spectroscopy (ICP-OES) system. This technique is applied for the first time to an intercalation electrode material and for the study of the anion concentration profiles; so far, ICP-OES studies have only investigated the cation removal and have remained limited to nanoporous carbon electrodes and conventional CDI.<sup>60,61</sup>

As can be seen from the concentration profiles for sodium (Figure 4A) and chlorine (Figure 4B), both follow the concentration profiles expected for electrochemical desalination (Figure 3A–C). Considering the different molar masses, the removal capacity is 4.5 mg/g<sub>(−)</sub> for Na<sup>+</sup> (normalized to the mass of the negative electrode) and 7.5 mg/g<sub>(+)</sub> for Cl<sup>−</sup> (normalized to the mass of the positive electrode), as determined for 5 mM NaCl. On average, this computes to a NaCl removal capacity of 4.8 mg/g normalized to the mass of both electrodes. This value agrees with the desalination capacity determined by conventional conductivity measurements (5 mg/g normalized to the mass of both electrodes; Figure 3D).

## CONCLUSIONS

Our work provides first data for the use of Mo<sub>1.33</sub>C-MXene as sodium ions and chloride ions intercalation via inductive couple plasma optical emission spectroscopy. This MXene accomplishes desalination with ease at low or high salt concentration, (i.e., from brackish water to seawater). By entangling MXene within a CNT network, effective binder-free electrodes are obtained with a promising salt removal capacity of 5, 9, and 15 mg/g in 5, 50, and 600 mM NaCl, respectively; in all cases, we measured a very high charge efficiency up to 97%. The energy consumption during ion removal in seawater concentration (600 mM NaCl) is low (17 kT), which would be impossible to accomplish with conventional carbon electrodes operated with

capacitive deionization. These performance metrics were obtained in absence of any ion exchange membranes, which are major cost-drivers for present-day CDI units. In particular, the compatibility of MXene for desalination of saline media with high molar strength opens new application areas, such as the generation of drinking water from seawater.

## ASSOCIATED CONTENT

### Supporting Information

The Supporting Information is available free of charge on the ACS Publications website at DOI: 10.1021/acssuschemeng.7b04095.

Gas sorption isotherm data and scanning electron microscopy cross-section (PDF)

## AUTHOR INFORMATION

### Corresponding Authors

\*E-mail: johanna.rosen@liu.se (J.R.).

\*E-mail: volker.presser@leibniz-inm.de (V.P.).

### ORCID

Volker Presser: 0000-0003-2181-0590

### Notes

The authors declare no competing financial interest.

## ACKNOWLEDGMENTS

The authors thank Prof. Eduard Arzt (INM) for his continuing support. P.S. acknowledges financial support by the German Academic Exchange Service (DAAD award number 91579066). J.R. acknowledges funding from the Swedish Research Council (642-2013-8020), the Swedish Foundation for Strategic Research (SSF) through the Synergy Grant FUNCASE, and from the Knut and Alice Wallenberg (KAW) Foundation for a Fellowship Grant and Project funding (KAW 2015.0043). We thank Dr. Choudhury, Mr. Zeiger, Mr. Fleischmann, and Ms. Tolosa for technical assistance (all at INM).

## REFERENCES

- (1) Suss, M. E.; Porada, S.; Sun, X.; Biesheuvel, P. M.; Yoon, J.; Presser, V. Water desalination via capacitive deionization: what is it

and what can we expect from it? *Energy Environ. Sci.* **2015**, *8* (8), 2296–2319.

(2) Liu, Y.; Nie, C. Y.; Liu, X. J.; Xu, X. T.; Sun, Z.; Pan, L. K. Review on carbon-based composite materials for capacitive deionization. *RSC Adv.* **2015**, *5* (20), 15205–15225.

(3) Guyes, E. N.; Simanovski, A.; Suss, M. E. Several orders of magnitude increase in the hydraulic permeability of flow-through capacitive deionization electrodes via laser perforations. *RSC Adv.* **2017**, *7* (34), 21308–21313.

(4) Wang, Z.; Yan, T. T.; Chen, G. R.; Shi, L. Y.; Zhang, D. S. High Salt Removal Capacity of Metal–Organic Gel Derived Porous Carbon for Capacitive Deionization. *ACS Sustainable Chem. Eng.* **2017**, *5* (12), 11637–11644.

(5) Kim, C.; Srimuk, P.; Lee, J.; Fleischmann, S.; Aslan, M.; Presser, V. Influence of pore structure and cell voltage of activated carbon cloth as a versatile electrode material for capacitive deionization. *Carbon* **2017**, *122* (1), 329–335.

(6) Suss, M. E.; Baumann, T. F.; Bourcier, W. L.; Spadaccini, C. M.; Rose, K. A.; Santiago, J. G.; Stadermann, M. Capacitive desalination with flow-through electrodes. *Energy Environ. Sci.* **2012**, *5* (11), 9511–9519.

(7) Xu, X.; Sun, Z.; Chua, D. H. C.; Pan, L. Novel nitrogen doped graphene sponge with ultrahigh capacitive deionization performance. *Sci. Rep.* **2015**, *5*, 11225.

(8) Biesheuvel, P. M.; van der Wal, A. Membrane capacitive deionization. *J. Membr. Sci.* **2010**, *346* (2), 256–262.

(9) Kim, C.; Lee, J.; Srimuk, P.; Aslan, M.; Presser, V. Concentration-gradient multi-channel flow stream membrane capacitive deionization cell for ultra-high desalination capacity of carbon electrodes. *ChemSusChem* **2017**, *10* (24), 4914–4920.

(10) Gu, X.; Deng, Y.; Wang, C. Fabrication of Anion-Exchange Polymer Layered Graphene–Melamine Electrodes for Membrane Capacitive Deionization. *ACS Sustainable Chem. Eng.* **2017**, *5* (1), 325–333.

(11) Doornbusch, G. J.; Dykstra, J. E.; Biesheuvel, P. M.; Suss, M. E. Fluidized bed electrodes with high carbon loading for water desalination by capacitive deionization. *J. Mater. Chem. A* **2016**, *4* (10), 3642–3647.

(12) Jeon, S. I.; Park, H. R.; Yeo, J. G.; Yang, S.; Cho, C. H.; Han, M. H.; Kim, D. K. Desalination via a new membrane capacitive deionization process utilizing flow-electrodes. *Energy Environ. Sci.* **2013**, *6* (5), 1471–1475.

(13) Porada, S.; Weingarth, D.; Hamelers, H. V. M.; Bryjak, M.; Presser, V.; Biesheuvel, P. M. Carbon flow electrodes for continuous operation of capacitive deionization and capacitive mixing energy generation. *J. Mater. Chem. A* **2014**, *2* (24), 9313–9321.

(14) Suss, M. E.; Presser, V. Electrochemical water desalination with energy storage electrode materials. *Joule* **2018**, *2*, 10.

(15) Srimuk, P.; Lee, J.; Fleischmann, S.; Choudhury, S.; Jäckel, N.; Zeiger, M.; Kim, C.; Aslan, M.; Presser, V. Faradaic deionization of brackish and sea water via pseudocapacitive cation and anion intercalation into few layered molybdenum disulfide. *J. Mater. Chem. A* **2017**, *5* (30), 15640–15649.

(16) Xing, F.; Li, T.; Li, J.; Zhu, H.; Wang, N.; Cao, X. Chemically Exfoliated MoS<sub>2</sub> for Capacitive Deionization of Saline Water. *Nano Energy* **2017**, *31*, 590–595.

(17) Naguib, M.; Kurtoglu, M.; Presser, V.; Lu, J.; Hultman, L.; Niu, J.; Heon, M.; Gogotsi, Y.; Barsoum, M. W. Two-dimensional nanocrystals produced by exfoliation of Ti<sub>3</sub>AlC<sub>2</sub>. *Adv. Mater.* **2011**, *23* (37), 4248–4253.

(18) Srimuk, P.; Kaasik, F.; Krüner, B.; Tolosa, A.; Fleischmann, S.; Jäckel, N.; Tekeli, M. C.; Aslan, M.; Suss, M. E.; Presser, V. MXene as a novel intercalation-type pseudocapacitive cathode and anode for capacitive deionization. *J. Mater. Chem. A* **2016**, *4* (47), 18265–18271.

(19) Anasori, B.; Lukatskaya, M. R.; Gogotsi, Y. 2D metal carbides and nitrides (MXenes) for energy storage. *Nat. Rev. Mater.* **2017**, *2*, 16098.

(20) Levi, M. D.; Lukatskaya, M. R.; Sigalov, S.; Beidaghi, M.; Shpigel, N.; Daikhin, L.; Aurbach, D.; Barsoum, M. W.; Gogotsi, Y.

Solving the Capacitive Paradox of 2D MXene using Electrochemical Quartz-Crystal Admittance and In Situ Electronic Conductance Measurements. *Adv. Energy Mater.* **2015**, *5* (1), 1400815.

(21) Brousse, T.; Bélanger, D.; Long, J. W. To be or not to be pseudocapacitive? *J. Electrochem. Soc.* **2015**, *162* (5), A5185–A5189.

(22) Conway, B. E. Transition from “Supercapacitor” to “Battery” Behavior in Electrochemical Energy Storage. *J. Electrochem. Soc.* **1991**, *138* (6), 1539–1548.

(23) Bandaru, P. R.; Yamada, H.; Narayanan, R.; Hofer, M. Charge transfer and storage in nanostructures. *Mater. Sci. Eng., R* **2015**, *96*, 1–69.

(24) Salanne, M.; Rotenberg, B.; Naoi, K.; Kaneko, K.; Taberna, P. L.; Grey, C. P.; Dunn, B.; Simon, P. Efficient storage mechanisms for building better supercapacitors. *Nat. Energy* **2016**, *1*, 16070.

(25) Biesheuvel, P. M.; Porada, S.; Levi, M.; Bazant, M. Z. Attractive forces in microporous carbon electrodes for capacitive deionization. *J. Solid State Electrochem.* **2014**, *18* (5), 1365–1376.

(26) Prehal, C.; Koczwara, C.; Jäckel, N.; Schreiber, A.; Burian, M.; Amenitsch, H.; Hartmann, M. A.; Presser, V.; Paris, O. Quantification of ion confinement and desolvation in nanoporous carbon supercapacitors with modelling and in situ X-ray scattering. *Nat. Energy* **2017**, *2* (3), 16215.

(27) He, F.; Biesheuvel, P. M.; Bazant, M. Z.; Hatton, T. A. Theory of water treatment by capacitive deionization with redox active porous electrodes. *Water Res.* **2018**, *132*, 282.

(28) Porada, S.; Shrivastava, A.; Bukowska, P.; Biesheuvel, P. M.; Smith, K. C. Nickel Hexacyanoferrate Electrodes for Continuous Cation Intercalation Desalination of Brackish Water. *Electrochim. Acta* **2017**, *255*, 369–378.

(29) Smith, K. C.; Dmello, R. Na-Ion Desalination (NID) Enabled by Na-Blocking Membranes and Symmetric Na-Intercalation: Porous-Electrode Modeling. *J. Electrochem. Soc.* **2016**, *163* (3), A530–A539.

(30) Lee, J.; Kim, S.; Yoon, J. Rocking Chair Desalination Battery Based on Prussian Blue Electrodes. *ACS Omega* **2017**, *2* (4), 1653–1659.

(31) Pasta, M.; Wessells, C. D.; Cui, Y.; La Mantia, F. A Desalination Battery. *Nano Lett.* **2012**, *12* (2), 839–843.

(32) Kim, S.; Yoon, H.; Shin, D.; Lee, J.; Yoon, J. Electrochemical selective ion separation in capacitive deionization with sodium manganese oxide. *J. Colloid Interface Sci.* **2017**, *506*, 644–648.

(33) Nam, D.-H.; Choi, K.-S. Bismuth as a New Chloride-Storage Electrode Enabling the Construction of a Practical High Capacity Desalination Battery. *J. Am. Chem. Soc.* **2017**, *139* (32), 11055–11063.

(34) Hope, M. A.; Forse, A. C.; Griffith, K. J.; Lukatskaya, M. R.; Ghidui, M.; Gogotsi, Y.; Grey, C. P. NMR reveals the surface functionalisation of Ti<sub>3</sub>C<sub>2</sub> MXene. *Phys. Chem. Chem. Phys.* **2016**, *18* (7), 5099–5102.

(35) Alhabej, M.; Maleski, K.; Anasori, B.; Lelyukh, P.; Clark, L.; Sin, S.; Gogotsi, Y. Guidelines for Synthesis and Processing of 2D Titanium Carbide (Ti<sub>3</sub>C<sub>2</sub>T<sub>x</sub> MXene). *Chem. Mater.* **2017**, *29* (18), 7633–7644.

(36) Placke, T.; Bieker, P.; Lux, F.; Fromm, O.; Meyer, H.-W.; Passerini, S.; Winter, M. Dual-ion Cells Based on Anion Intercalation into Graphite from Ionic Liquid-Based Electrolytes. *Z. Phys. Chem.* **2012**, *226* (5–6), 391.

(37) Fan, H.; Qi, L.; Wang, H. Hexafluorophosphate anion intercalation into graphite electrode from methyl propionate. *Solid State Ionics* **2017**, *300*, 169–174.

(38) Zhang, X.; Zhang, Z.; Zhou, Z. MXene-based materials for electrochemical energy storage. *J. Energy Chem.* **2018**, *27* (1), 73–85.

(39) Liang, X.; Garsuch, A.; Nazar, L. F. Sulfur Cathodes Based on Conductive MXene Nanosheets for High-Performance Lithium–Sulfur Batteries. *Angew. Chem., Int. Ed.* **2015**, *54* (13), 3907–3911.

(40) Bonaccorso, F.; Colombo, L.; Yu, G.; Stoller, M.; Tozzini, V.; Ferrari, A. C.; Ruoff, R. S.; Pellegrini, V. Graphene, related two-dimensional crystals, and hybrid systems for energy conversion and storage. *Science* **2015**, *347* (6217), 1246501.

- (41) Zhong, Y.; Xia, X.; Shi, F.; Zhan, J.; Tu, J.; Fan, H. J. Transition Metal Carbides and Nitrides in Energy Storage and Conversion. *Adv. Sci.* **2016**, *3* (5), 1500286.
- (42) Liu, G.; Shen, J.; Liu, Q.; Liu, G.; Xiong, J.; Yang, J.; Jin, W. Ultrathin two-dimensional MXene membrane for pervaporation desalination. *J. Membr. Sci.* **2018**, *548*, 548–558.
- (43) Ding, L.; Wei, Y.; Wang, Y.; Chen, H.; Caro, J.; Wang, H. A Two-Dimensional Lamellar Membrane: MXene Nanosheet Stacks. *Angew. Chem., Int. Ed.* **2017**, *56* (7), 1825–1829.
- (44) Ren, C. E.; Hatzell, K. B.; Alhabeb, M.; Ling, Z.; Mahmoud, K. A.; Gogotsi, Y. Charge- and Size-Selective Ion Sieving Through  $Ti_3C_2T_x$  MXene Membranes. *J. Phys. Chem. Lett.* **2015**, *6* (20), 4026–31.
- (45) Fard, A. K.; McKay, G.; Chamoun, R.; Rhadfi, T.; Preud'Homme, H.; Atieh, M. A. Barium Removal from Synthetic Natural and Produced Water using MXene as Two Dimensional (2-D) Nanosheet Adsorbent. *Chem. Eng. J.* **2017**, *317*, 331–342.
- (46) Zhang, Q.; Teng, J.; Zou, G.; Peng, Q.; Du, Q.; Jiao, T.; Xiang, J. Efficient phosphate sequestration for water purification by unique sandwich-like MXene/magnetic iron oxide nanocomposites. *Nanoscale* **2016**, *8* (13), 7085–7093.
- (47) Ghidui, M.; Lukatskaya, M. R.; Zhao, M.-Q.; Gogotsi, Y.; Barsoum, M. W. Conductive two-dimensional titanium carbide "clay" with high volumetric capacitance. *Nature* **2014**, *516* (7529), 78–81.
- (48) Dahlqvist, M.; Lu, J.; Meshkian, R.; Tao, Q.; Hultman, L.; Rosen, J. Prediction and synthesis of a family of atomic laminate phases with Kagomé-like and in-plane chemical ordering. *Sci. Adv.* **2017**, *3* (7), e1700642.
- (49) Tao, Q.; Dahlqvist, M.; Lu, J.; Kota, S.; Meshkian, R.; Halim, J.; Palisaitis, J.; Hultman, L.; Barsoum, M. W.; Persson, P. O. Å.; Rosen, J. Two-dimensional  $Mo_{1.33}C$ -MXene with divacancy ordering prepared from parent 3D laminate with in-plane chemical ordering. *Nat. Commun.* **2017**, *8*, 14949.
- (50) Weingarth, D.; Zeiger, M.; Jäckel, N.; Aslan, M.; Feng, G.; Presser, V. Graphitization as a universal tool to tailor the potential-dependent capacitance of carbon supercapacitors. *Adv. Energy Mater.* **2014**, *4* (13), 1400316.
- (51) Aslan, M.; Zeiger, M.; Jäckel, N.; Grobelsek, I.; Weingarth, D.; Presser, V. Improved capacitive deionization performance of mixed hydrophobic/hydrophilic activated carbon electrodes. *J. Phys.: Condens. Matter* **2016**, *28* (11), 114003.
- (52) Jäckel, N.; Rodner, M.; Schreiber, A.; Jeongwook, J.; Zeiger, M.; Aslan, M.; Weingarth, D.; Presser, V. Anomalous or regular capacitance? The influence of pore size dispersity on double-layer formation. *J. Power Sources* **2016**, *326* (1), 660–671.
- (53) He, D.; Wong, C. E.; Tang, W.; Kovalsky, P.; Waite, T. D. Faradaic Reactions in Water Desalination by Batch-Mode Capacitive Deionization. *Environ. Sci. Technol. Lett.* **2016**, *3* (5), 222–226.
- (54) Gao, X.; Porada, S.; Omosebi, A.; Liu, K.-L.; Biesheuvel, P. M.; Landon, J. Complementary surface charge for enhanced capacitive deionization. *Water Res.* **2016**, *92*, 275–82.
- (55) Lee, J.; Srimuk, P.; Aristizabal, K.; Kim, C.; Choudhury, S.; Nah, Y. C.; Mücklich, F.; Presser, V. Pseudocapacitive desalination of brackish water and seawater with vanadium-pentoxide-decorated multiwalled carbon nanotubes. *ChemSusChem* **2017**, *10* (18), 3611–3623.
- (56) Kim, C.; Srimuk, P.; Lee, J.; Aslan, M.; Presser, V. Semi-continuous capacitive deionization using multi-channel flow stream and ion exchange membranes. *Desalination* **2018**, *425* (1), 104–110.
- (57) Elimelech, M.; Phillip, W. A. The Future of Seawater Desalination: Energy, Technology, and the Environment. *Science* **2011**, *333* (6043), 712–717.
- (58) Kim, T.; Yoon, J. CDI ragone plot as a functional tool to evaluate desalination performance in capacitive deionization. *RSC Adv.* **2015**, *5* (2), 1456–1461.
- (59) Centeno, T. A.; Sereda, O.; Stoeckli, F. Capacitance in carbon pores of 0.7 to 15 nm: a regular pattern. *Phys. Chem. Chem. Phys.* **2011**, *13* (27), 12403–6.
- (60) Dykstra, J. E.; Dijkstra, J.; van der Wal, A.; Hamelers, H. V. M.; Porada, S. On-line method to study dynamics of ion adsorption from mixtures of salts in capacitive deionization. *Desalination* **2016**, *390*, 47–52.
- (61) Zhao, R.; van Soestbergen, M.; Rijnaarts, H. H. M.; van der Wal, A.; Bazant, M. Z.; Biesheuvel, P. M. Time-dependent ion selectivity in capacitive charging of porous electrodes. *J. Colloid Interface Sci.* **2012**, *384* (1), 38–44.

## Supporting Information

# **Two-dimensional molybdenum carbide (MXene) with divacancy ordering for brackish and sea water desalination via cation and anion intercalation**

P. Srimuk,<sup>a,b</sup> J. Halim,<sup>b</sup> J. Lee,<sup>a,c</sup> Q. Tao,<sup>b</sup> J. Rosen,<sup>b,\*</sup> and V. Presser<sup>a,c,\*</sup>

<sup>a</sup> *INM - Leibniz Institute for New Materials, Campus D22, 66123 Saarbrücken, Germany*

<sup>b</sup> *Thin Film Physics, Department of Physics, Chemistry and Biology (IFM), Linköping University, SE-581 83 Linköping, Sweden*

<sup>c</sup> *Department of Materials Science and Engineering, Saarland University, 66123 Saarbrücken, Germany*

\* *Corresponding authors' eMail:*

*johanna.rosen@liu.se (JR) & volker.presser@leibniz-inm.de (VP)*

The supporting information includes 2 figures.

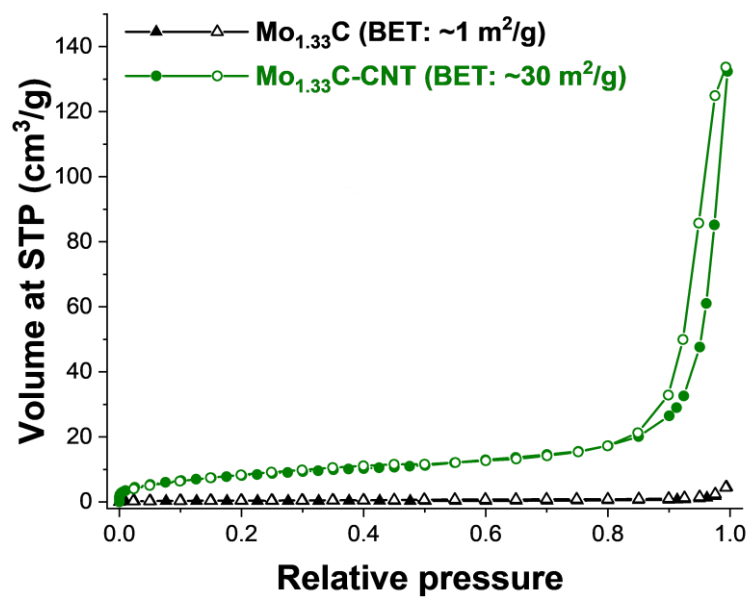


**Fig. S1:** Nitrogen gas sorption isotherm of Mo<sub>1.33</sub>C and Mo<sub>1.33</sub>C-CNT.

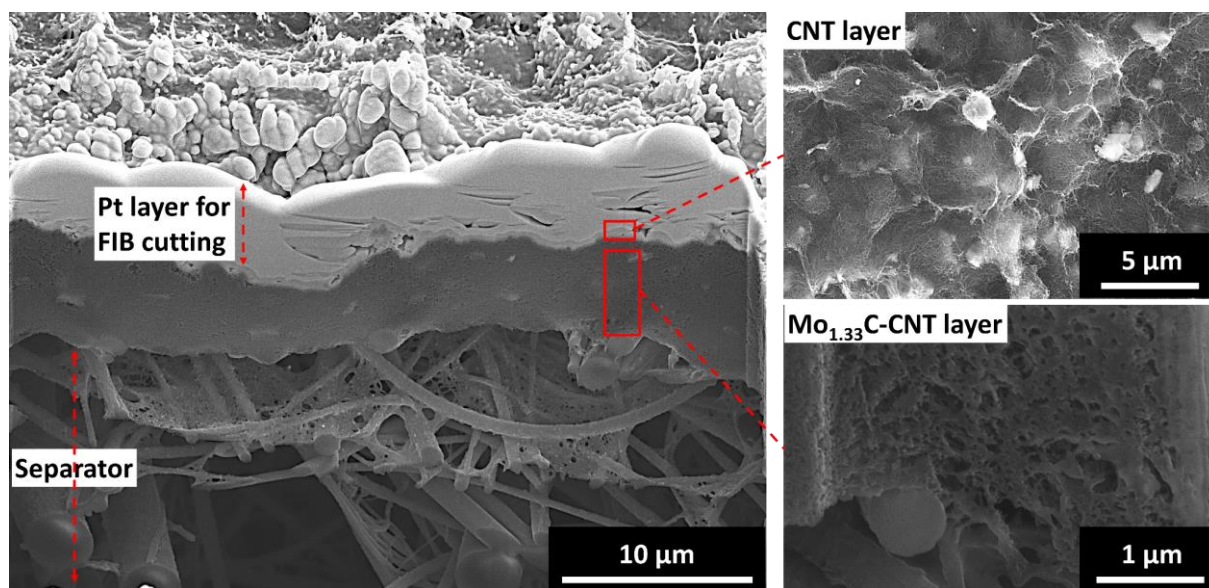


**Fig. S2:** Cross-section scanning electron micrograph of binder-free Mo<sub>1.33</sub>C-CNT electrode prepared via focussed ion beam (FIB).

#### 4.5 Faradaic deionization of brackish and sea water via pseudocapacitive cation and anion intercalation into few-layered molybdenum disulfide

Pattarachai Srimuk,<sup>1,2</sup> Juhan Lee,<sup>1,2</sup> Simon Fleischmann,<sup>1,2</sup> Soumyadip Choudhury,<sup>1,2</sup>  
Nicolas Jäckel,<sup>1,2</sup> Marco Zeiger,<sup>1,2</sup> Choonsoo Kim,<sup>1,2</sup> Mesut Aslan,<sup>1,2</sup> Volker Presser<sup>1,2</sup>

<sup>1</sup> INM - Leibniz Institute for New Materials, Campus D2 2, 66123 Saarbrücken, Germany

<sup>2</sup> Saarland University, Campus D2 2, 66123 Saarbrücken, Germany

##### Citation:

P. Srimuk, J. Lee, S. Fleischmann, S. Choudhury, N. Jäckel, M. Zeiger, C. Kim, M. Aslan, V. Presser, FARADAIC DEIONIZATION OF BRACKISH AND SEA WATER VIA PSEUDOCAPACITIVE CATION AND ANION INTERCALATION INTO FEW-LAYERED MOLYBDENUM DISULFIDE, *Journal of Materials Chemistry A* 5(30) (2017) 15640-15649.

##### Own contribution:

Electrochemistry, CDI experiment, analysis, writing



Cite this: *J. Mater. Chem. A*, 2017, 5, 15640

# Faradaic deionization of brackish and sea water via pseudocapacitive cation and anion intercalation into few-layered molybdenum disulfide†

Pattarachai Srimuk,<sup>ab</sup> Juhan Lee,<sup>ab</sup> Simon Fleischmann,<sup>ab</sup> Soumyadip Choudhury,<sup>a</sup> Nicolas Jäckel,<sup>ab</sup> Marco Zeiger,<sup>ab</sup> Choonsoo Kim,<sup>a</sup> Mesut Aslan<sup>a</sup> and Volker Presser<sup>ab\*</sup>

This work establishes molybdenum disulfide/carbon nanotube electrodes for the desalination of high molar saline water. Capitalizing on the two-dimensional layered structure of MoS<sub>2</sub>, both cations and anions can be effectively removed from a feed water stream by faradaic ion intercalation. The approach is based on the setup of capacitive deionization (CDI), where an effluent water stream is desalinated via the formation of an electrical double-layer at two oppositely polarized carbon electrodes. Yet, CDI can only be effectively applied to low concentrated solutions due to the intrinsic limitation of the electrosorption mechanism. By replacing the conventional porous carbon with MoS<sub>2</sub>/CNT binder-free electrodes, deionization of sodium and chloride ions was achieved by ion intercalation instead of ion electrosorption. This enabled stable desalination performance over 25 cycles in various molar concentrations, with salt adsorption capacities of 10, 13, 18, and 25 mg g<sup>-1</sup> in 5, 25, 100, and 500 mM NaCl aqueous solutions, respectively. This novel approach of faradaic deionization (FDI) paves the way towards a more energy-efficient desalination of brackish water and even sea water.

Received 10th April 2017  
Accepted 4th July 2017

DOI: 10.1039/c7ta03120c

rsc.li/materials-a

## 1. Introduction

The development of energy efficient and cost-effective technologies for the desalination of brackish and saline water is one of the key research activities in environmental engineering.<sup>1–4</sup> Over the last decades, several technologies such as reverse osmosis, multistep distillation, electrodeionization, electro dialysis, and capacitive deionization (CDI) have emerged.<sup>5–7</sup> Among these desalination technologies, CDI is distinguished by a low energy consumption owing to the low operation potential and the simplicity of the system components and configurations.<sup>8</sup> The principle of CDI is based on the electrosorption of ions through electric double-layer (EDL) formation at the interface of carbon electrodes and a feed water stream.<sup>9</sup> When the cell is being charged, the electrodes are polarized positively and negatively, leading to the adsorption of sodium ions and other cations to the negative electrode and chloride ions and other anions to the positive electrode. Thus, the feed water stream is effectively depleted of salt ions.<sup>10</sup> As the cell is discharged, the adsorbed ions are released from the electrode to the effluent water stream

and a fraction of the invested energy is recovered, providing a discharging current.

Porous high surface area carbon electrodes have most commonly been employed in CDI cells, as they provide large interfaces for ion adsorption and offer moderate production costs. Nanoporous carbons exhibit a maximum salt adsorption capacity (SAC) of up to 15–21 mg per gram of the electrode.<sup>8,11</sup> During the CDI operation, the electric double-layer formation in microporous carbon electrodes reestablishes charge neutrality upon charging of the system and is accomplished either by expelling ions of the same charge as the electrode (co-ion expulsion) or by attracting ions of the opposite charge as the electrode (counter-ion adsorption) to the interface.<sup>9,12</sup> Higher salt concentrations of the feed water lead to higher initial ion concentrations in the pores, effectively favoring the mechanism of co-ion expulsion over counter-ion adsorption during EDL formation.<sup>13</sup> Yet, only counter-ion adsorption contributes towards desalination, which is why conventional CDI encounters severely decreased energy efficiency in high saline concentrations as a result of increased amounts of charge being invested in parasitic co-ion desorption.<sup>9</sup> As a consequence, the energy consumption of conventional CDI systems at higher salt concentration strongly exceeds the energy required for reverse osmosis systems.<sup>6</sup>

Therefore, an urgent task of the current research is to overcome this intrinsic limitation of CDI and make the technology accessible beyond brackish water to higher molar

<sup>a</sup>INM – Leibniz Institute for New Materials, Saarbrücken, Germany. E-mail: volker.presser@leibniz-inm.de

<sup>b</sup>Department of Materials Science and Engineering, Saarland University, Saarbrücken, Germany

† Electronic supplementary information (ESI) available. See DOI: 10.1039/c7ta03120c

concentrations (*i.e.*, exceeding 50–100 mM). A highly promising approach is the application of novel electrode materials beyond carbon that offer faradaic reactions,<sup>14–18</sup> effectively replacing ion electrosorption by ion intercalation or surface redox reactions.<sup>19</sup> Pasta *et al.*<sup>14</sup> were the first to introduce a “desalination battery” by removing chloride ions *via* the Ag/AgCl redox reaction and sodium *via* intercalation in sodium manganese oxide (NMO). Later work used nanoporous carbon to accomplish chloride ion removal *via* conventional electrosorption, while using NMO (ref. 16) or Na<sub>2</sub>FeP<sub>2</sub>O<sub>7</sub> (NFP; ref. 17) as sodium intercalation electrodes. This hybrid CDI system achieved a desalination capacity of ~30 mg g<sup>-1</sup> in 100 mM NaCl.<sup>16,17</sup> Yet, this approach requires anion-selective membranes to prevent sodium ion diffusion to the negative electrode. Ion-exchange membranes also play a key role in the so-called sodium ion desalination (NID) proposed by Kyle Smith.<sup>15,20</sup> This approach achieves desalination by insertion or expulsion of sodium ions and the concurrent removal of anions *via* charge balancing. The first studies have presented data for NMO (ref. 15) and nickel hexacyanoferrate (ref. 21), exhibiting a SAC of 30–35 mg g<sup>-1</sup>. Yet, this approach also requires the use of ion-exchange membranes to avoid the need for a chloride insertion electrode like silver or capacitive counter-electrodes as used in hybrid CDI.

In contrast to exclusive cation intercalation, layered two-dimensional materials allow for the intercalation of both cations and anions.<sup>22</sup> This unique ability sets these materials apart from most battery electrodes used exclusively for cation intercalation (*e.g.*, lithium or sodium). These materials have been described as electrodes in the field of pseudocapacitive energy storage,<sup>23</sup> that is, storing charge based on faradaic intercalation reactions showing a capacitor-like electrical response (linear charge–voltage profile).<sup>24</sup> Translation of this behavior to water desalination was recently introduced in 2016 by our group, where the desalination of brackish water with MXene was demonstrated (SAC 13 mg g<sup>-1</sup>).<sup>22</sup> Since the desalination mechanism is based on faradaic intercalation rather than on capacitive electrosorption, it is more accurate to describe the process as faradaic deionization (FDI). A unique advantage of this approach is that no expensive ion-exchange membranes are needed with the cathode and anode having equal size and type of material. Following up on our work, Xing *et al.* used exfoliated molybdenum disulfide (MoS<sub>2</sub>) as a new layered 2D material for desalination and achieved a SAC of 8 mg g<sup>-1</sup> in low molar concentration, and postulated the desalination mechanism to originate from ion electrosorption instead of intercalation.<sup>18</sup> Despite these pioneering works in low concentration media, desalination with layered 2D materials has yet to prove its potential application in high molar solutions, and a clear understanding of the underlying ion removal mechanism has to be established.

In this study, we introduce for the first time molybdenum disulfide/carbon nanotube hybrid electrodes for faradaic deionization of high molar saline water. By rigorous electrochemical and desalination benchmarking, post-mortem analysis, and electrochemical *in situ* measurements, the salt removal mechanism is proven to originate from the pseudocapacitive intercalation of cations and anions into the 2D layered structure

of MoS<sub>2</sub>. We provide comprehensive results for different saline concentrations and establish the first data on the energy consumption of FDI employing MoS<sub>2</sub>/CNT.

## 2. Experimental description

### 2.1 Material synthesis

**MoS<sub>2</sub>-carbon nanotube composite preparation.** Commercially available MoS<sub>2</sub> with a particle size of 20 μm (Sigma-Aldrich) was used as the starting material. Initially, 540 mg of MoS<sub>2</sub> powder was stirred in 240 mL of ethanol for 10 min for pre-dispersion, while 60 mg of carbon nanotubes (Nanocyl NC7000) were separately prepared by mixing with 240 mL of ethanol and ultrasonicated with ice-bath assistance for 15 min. The MoS<sub>2</sub> mixture was tip-sonicated for 15 min before finally being mixed with the carbon nanotube mixture. Subsequently, the mixed solution was further stirred for 10 min and tip-sonicated for 30 min with ice-bath assistance. The mass ratio between the MoS<sub>2</sub> and carbon nanotube was fixed at 90 : 10. Afterwards, 30 mL of the MoS<sub>2</sub>-carbon nanotube mixture was filtered through a glass fiber separator (Millipore, 380 μm thickness, Whatman) and dried at 60 °C for 5 h to obtain free-standing electrodes, labeled as MoS<sub>2</sub>-10CNT.

**Electrochemical activation of MoS<sub>2</sub>.** For the electrochemical activation of MoS<sub>2</sub>, the as-prepared electrode (MoS<sub>2</sub>-10CNT) was employed as a working electrode (positive electrode), whereas a Pt sheet (Mateck) was used as the counter electrode (negative electrode). The MoS<sub>2</sub>-10CNT electrode was clamped with a Pt clip and only the MoS<sub>2</sub>-10CNT part was immersed into 400 mL of 1 M Na<sub>2</sub>SO<sub>4</sub> aqueous solution. The distance between the working and the counter electrode was set to 5 cm. For the activation process, a positive potential was biased on the working electrode with a potential difference of 10 V (Model TOE 8871, Toellner Electronic Instrument GmbH) for 1, 2, or 4 h. Later, the electrodes were cleaned with 500 mL of deionized water (Milli-Q, Merck) for 6 h under continuous stirring to remove residual ions from the electrolyte followed by drying at 60 °C for 5 h. In the next step, the non-activated part which was not dipped into the electrolyte was trimmed off. These binder-free delaminated electrodes are designated as MoS<sub>2</sub>-10CNT-1 h, MoS<sub>2</sub>-10CNT-2 h and MoS<sub>2</sub>-10CNT-4 h reflecting the various holding times applied for electrochemical activation.

### 2.2 Structural and chemical characterization

Scanning electron microscopy (SEM) images were recorded with a field emission scanning electron microscope (FEI, JEOL JSM 7500F) operating at 5 kV. Energy dispersive X-ray spectroscopy (EDX) was carried out in the scanning electron microscope at 10 kV with an X-Max silicon detector from Oxford Instruments using AZtec software for quantitative analysis. Transmission electron micrographs were taken with a JEOL 2100F transmission electron microscope at 200 kV. The powder samples were prepared by dispersing the powders in ethanol and drop casting them on a copper grid with a lacey carbon film (Gatan).

The Raman spectra were recorded with a Renishaw inVia Raman microscope using an Nd:YAG laser with an excitation

wavelength of 532 nm. The spectral resolution was  $1.2 \text{ cm}^{-1}$  and the diameter of the laser spot on the sample was  $2 \text{ }\mu\text{m}$  with a power of 0.2 mW. The spectra were recorded for 20 s with 30 accumulations.

X-ray diffraction (XRD) was conducted in a D8 Advance diffractometer (Bruker AXS) with a copper X-ray source ( $\text{Cu}_{\text{K}\alpha}$ , 40 kV, and 40 mA) and a Goebel mirror in point focus (0.5 mm). We used a VANTEC-500 (Bruker AXS) 2D detector positioned at  $20^\circ$ ,  $40^\circ$ ,  $60^\circ$ , and  $80^\circ$   $2\theta$  with a measurement time of 16.7 min per step. The samples were dispersed in ethanol and drop cast on a sapphire single crystal and the sample holder was oscillated in plane (amplitude of 5 mm with a speed of  $0.5 \text{ mm s}^{-1}$  along the  $x$ - and  $0.2 \text{ mm s}^{-1}$  along the  $y$ -axis) to enhance the signal statistics.

Nitrogen gas sorption measurements at  $-196^\circ \text{C}$  were carried out with an Autosorb iQ system (Quantachrome). The samples were degassed at  $60^\circ \text{C}$  for 10 h under vacuum conditions at  $10^2 \text{ Pa}$ . Nitrogen gas sorption was performed in liquid nitrogen in the relative pressure range from  $10^{-4}$  to 1.0 in 40 steps. The Brunauer–Emmett–Teller specific surface area (BET-SSA)<sup>25</sup> was calculated with Quantachrome's ASiQwin software in the linear relative pressure range of 0.06–0.3.

### 2.3 Electrochemical measurements

**Half-cell experiment.** The electrodes were cut as circular 12 mm discs with a mass of  $\sim 1 \text{ mg}$ . The graphite sheets (SGL Carbon) were cut into a circular shape with a diameter of 12 mm and employed as the current collector. A polytetrafluoroethylene (PTFE)-bound, free-standing activated carbon disc (YP-80F, Kuraray) with an oversized mass of 15 mg was used as the counter electrode. More details on the preparation of free-standing activated carbon electrodes was reported elsewhere.<sup>26</sup> The electrodes were separated by a 13 mm diameter glass fiber mat (GF/A, Whatman) and placed in custom-built cells between spring loaded titanium pistons (see ref. 27). An Ag/AgCl (3 M KCl, BASi) reference electrode was mounted at the side channel of the cell, where a porous frit of the reference electrode is close to the working and counter electrodes. As the electrolyte, 1 M NaCl was injected by vacuum backfilling. The electrochemical measurements were conducted with a VSP300 potentiostat/galvanostat (Bio-Logic). Cyclic voltammetry and galvanostatic cycling techniques were employed. For cyclic voltammetry, the electrode potential was scanned from 0 to  $-0.6 \text{ V vs. Ag/AgCl}$  and from 0 to  $+0.5 \text{ V vs. Ag/AgCl}$  at a scan rate of  $5 \text{ mV s}^{-1}$ . For galvanostatic charge–discharge with potential limitation (GCPL), a specific current between 0.1 and  $10 \text{ A g}^{-1}$  was applied in the electrode potential range between 0 and  $-0.6 \text{ V vs. Ag/AgCl}$  and between 0 and  $+0.5 \text{ V vs. Ag/AgCl}$ . The specific capacitance of the working electrode was calculated by using eqn (1):

$$C_{\text{specific}} = \frac{1}{Um} \int_{t_1}^{t_2} Idt \quad (1)$$

where  $I$  is the applied current,  $t_2 - t_1$  is the time required for polarization,  $U$  is the potential difference during polarization (excluding the iR drop), and  $m$  is the total working electrode mass. In the potential range from 0 to  $-0.6 \text{ V vs. Ag/AgCl}$ , the

oxidation was analyzed with eqn (1) while the reduction was analyzed in the potential range from 0 to  $+0.5 \text{ V vs. Ag/AgCl}$ .

The electrochemical measurements with an EL-CELL *in situ* stage for Raman spectroscopy were conducted to monitor the structural changes during charging and discharging. The cell configuration is shown in the ESI, Fig. S1.† The  $\text{MoS}_2$ -CNT-4 h electrode with a diameter of 8 mm was used as the working electrode and an 8 mm diameter PTFE-bound activated carbon electrode was employed as the oversized counter electrode. The electrodes were separated by a 12 mm diameter glass fiber mat. The graphite sheet was cut into a circular shape with a diameter of 12 mm and used as the current collector. A 5 mm pinhole in the working electrode current collector allowed for the laser beam to reach the electrode surface. Before the cell was sealed, a thin glass slide (LAB0018, EL-CELL GmbH) was introduced to allow spectroscopic investigation of the working electrode. Then, 1 M NaCl was filled into the cell *via* vacuum backfilling. The *in situ* cell was then connected with a GAMRY galvanostat/potentiostat. The cell was chronoamperometrically charged at various potential steps from  $+0.1 \text{ V}$  to  $+0.8 \text{ V}$  or from  $-0.1 \text{ V}$  to  $-0.8 \text{ V}$  for 5 min. Prior to the cell discharge, the Raman spectra were recorded with our Renishaw inVia Raman spectrometer using an Nd:YAG laser with an excitation wavelength of 532 nm. The spectral resolution was  $1.2 \text{ cm}^{-1}$  and the diameter of the laser spot on the sample was  $2 \text{ }\mu\text{m}$  with a power of 2 mW. The spectra were recorded for 20 s with 1 accumulation. To obtain better statistics, we recorded three spectra for each charging step.

### 2.4 Desalination measurements

The desalination performance was evaluated in a conventional CDI setup described in ref. 26 with flow-by electrodes (per definition in ref. 8). The stack used for faradaic deionization was built from the free-standing electrode and a porous separator (glass fiber pre-filter, Millipore,  $380 \text{ }\mu\text{m}$  thickness). The measurements were carried out with three pairs of electrodes. The total mass of the electrodes varied between 80 and 120 mg. Ion adsorption and desorption steps were carried out using constant voltage mode at 0.8 V. The electrode regeneration was accomplished at 0 V. For all electrochemical operations, we used a VSP300 potentiostat/galvanostat (Bio-Logic) and the duration of each half-cycle was 60 min. All experiments were carried out with a flow rate of  $22 \text{ mL min}^{-1}$  at 5, 25, 100, and 500 mM NaCl solutions in a 10 L tank which was flushed continuously with  $\text{N}_2$  gas to obtain an oxygen-free solution.<sup>28</sup> The salt adsorption capacity (SAC) and charge efficiency were calculated using eqn (S1)–(S5) (ESI†). Please note that our use of the term “SAC” is in alignment with the nomenclature in the CDI community; however, it does not indicate that ion removal is accomplished just by electrostatic ion electroadsorption. In fact, in our work, desalination is accomplished by ion intercalation. The SAC and the measured charge were defined by normalization to the entire mass of both electrodes and components (*i.e.*,  $\text{MoS}_2$  and CNT).

Note that normalization by mass complicates the comparison between different materials with different molar masses.

For quantification of the electrical charge, the leakage current at the end of each half-cycle was subtracted. To calculate the energy consumption per removed ion, the energy consumed during adsorption is determined and divided by the salt adsorption capacity.<sup>21</sup> This yields the energy consumption in joules per mol of ions removed ( $\text{J mol}^{-1}$ ).<sup>29</sup> To obtain the energy in  $kT$  as the product of the Boltzmann constant and absolute temperature, the calculated energy in  $\text{J mol}^{-1}$  is divided by the gas constant and the absolute temperature  $RT$  ( $2.48 \text{ kJ mol}^{-1}$  at room temperature).

### 3. Results and discussion

#### 3.1 Structural and chemical compositions

Electrochemical activation (Fig. 1A) of  $\text{MoS}_2$  was facilitated by the electrical conductivity of the carbon nanotubes (CNTs) that were homogeneously dispersed between the  $\text{MoS}_2$  grains (Fig. 1B). In addition to providing electrical conductivity, CNTs also provide mechanical stabilization for a binder-free electrode, effectively holding the activated  $\text{MoS}_2$  sheets together. After tip-sonication with stirring assistance, the  $\text{MoS}_2$ -10CNT

electrode shows particles of 2–5  $\mu\text{m}$  in size, which are uniformly dispersed in the CNT network (Fig. 1B). High-resolution transmission electron microscopy reveals the layered stacking of bulk- $\text{MoS}_2$ -10CNT having a thickness of  $\sim 3.4 \text{ nm}$ , corresponding to five  $\text{MoS}_2$  layers (Fig. 1C). Activation of  $\text{MoS}_2$  (*i.e.*, probably ion intercalation in between the layers) is accomplished by water splitting at high voltages (+10 V), first generating hydroxyl ions around the edges of  $\text{MoS}_2$ , and the hydroxyl ions and sulfate ions will penetrate the  $\text{MoS}_2$  layers and decompose to form oxygen and sulfur dioxide gases. As these gases are accumulated inside the  $\text{MoS}_2$  layered structure, pressure arises between the layers providing enough energy to overcome the van-der-Waals bonds holding the layers together.<sup>30</sup> After electrochemical activation at +10 V for 4 h, the expanded layering of  $\text{MoS}_2$  becomes more pronounced (Fig. 1D) and only a few layers remain *en bloc* (Fig. 1E).

The transition from bulk  $\text{MoS}_2$  grains to few-layered  $\text{MoS}_2$  flakes was confirmed by Raman spectroscopy and X-ray diffraction (Fig. 2). The Raman spectra of bulk and electrochemically activated  $\text{MoS}_2$ -10CNT are shown in Fig. 2A and B. Two Raman peaks of CNTs are observed at  $1350 \text{ cm}^{-1}$  and  $1584$

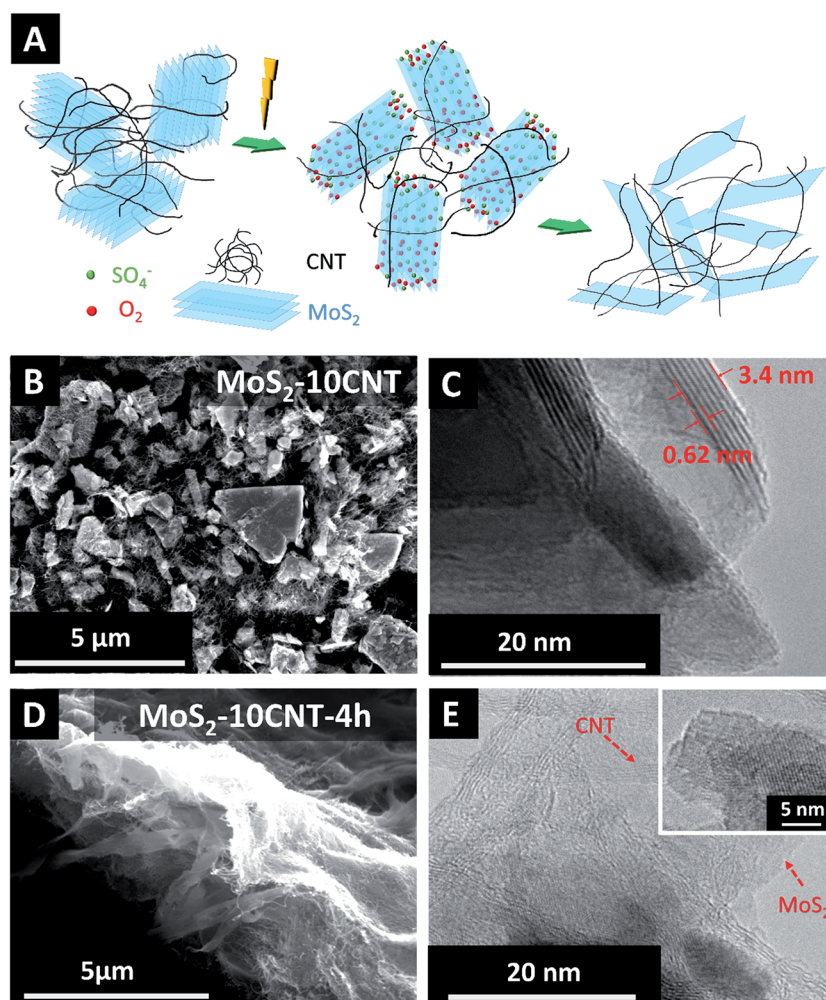


Fig. 1 Schematic illustration of the electrochemical activation process for the  $\text{MoS}_2$ -10CNT electrode (A), scanning electron micrographs of (B)  $\text{MoS}_2$ -10CNT and (D)  $\text{MoS}_2$ -10CNT-4 h. Transmission electron micrographs of (C)  $\text{MoS}_2$ -10CNT and (E)  $\text{MoS}_2$ -10CNT-4 h.

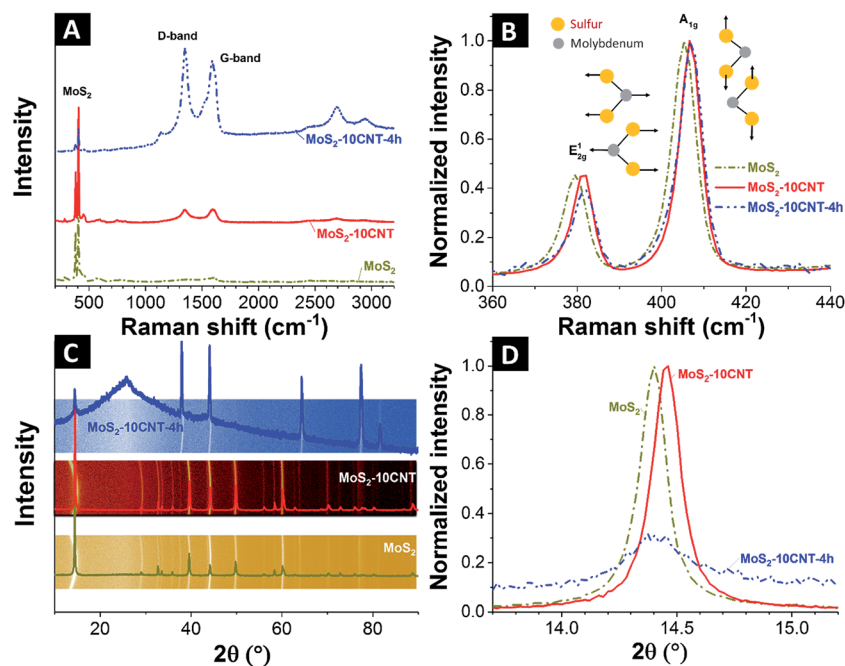


Fig. 2 (A and B) Raman spectra and (C and D) X-ray diffractograms (C and D) with the corresponding two-dimensional scattering pattern (C) of MoS<sub>2</sub>, MoS<sub>2</sub>-10CNT, and MoS<sub>2</sub>-10CNT-4 h.

cm<sup>-1</sup>, indicating the characteristic D-band and G-band of carbon, respectively.<sup>31</sup> The two distinct peaks around 378 cm<sup>-1</sup> and 405 cm<sup>-1</sup> are characteristic peaks of MoS<sub>2</sub> originating from in-plane displacement in Mo and S atoms ( $E_{2g}^1$ ) and out-plane symmetric displacement of sulfur atoms along the *c*-axis ( $A_{1g}$ ).<sup>32</sup> A decreasing intensity of the  $E_{2g}^1$  mode (ESI, Fig. S2A and B†) as well as a blue shift of  $A_{1g}$  vibration with increasing activation time are observed, indicating a reduction of the number of MoS<sub>2</sub> layers per stack.<sup>33</sup>

The X-ray diffractograms of the samples are shown in Fig. 2C and D and in ESI, Fig. S2C and D.† The bulk MoS<sub>2</sub> and MoS<sub>2</sub>-10CNT exhibit a clear diffraction pattern for 2H-MoS<sub>2</sub> with a strong reflection at  $2\theta$  of 14.5°, corresponding to the (002) plane (PDF#37-1492).<sup>34,35</sup> After electrochemical activation, the (002) reflection intensity of MoS<sub>2</sub>-10CNT-4 h decreases (Fig. 2D), indicating a lower number of stacked MoS<sub>2</sub> layers.<sup>30,36</sup>

### 3.2 Electrochemical performance in high concentration saline solution

The charge storage behavior of MoS<sub>2</sub>-10CNT, MoS<sub>2</sub>-10CNT-1 h, and MoS<sub>2</sub>-10CNT-4 h was characterized in a cell with 1 M NaCl by cyclic voltammetry in the potential range from 0 to +0.5 V for the positive electrode and from 0 to -0.6 V for the negative electrode. The cyclic voltammograms (CV) of activated and non-activated MoS<sub>2</sub>-10CNT reveal a capacitor-like (*i.e.*, pseudocapacitive) reduction/oxidation behavior with a rectangular current response (Fig. 3A).<sup>37</sup> The electrochemically activated sample MoS<sub>2</sub>-10CNT-1 h exhibits a higher specific capacitance as compared to pristine CNTs, but does not differ from non-activated MoS<sub>2</sub>-10CNT. In contrast, MoS<sub>2</sub>-10CNT-4 h shows a significantly enhanced capacitance with stable cycling

performance over 200 cycles (ESI, Fig. S3†). Considering the very low specific surface area of the MoS<sub>2</sub>-10CNT-4 h electrode (BET-SSA: 12 m<sup>2</sup> g<sup>-1</sup>; see ESI, Fig. S4†), the enhanced capacitance must originate from faradaic charge storage *via* ion intercalation between the layers of MoS<sub>2</sub>.

The capacitor-like (pseudocapacitive) behavior is confirmed by the triangular galvanostatic charge/discharge profiles (Fig. 3B and C). The MoS<sub>2</sub>-10CNT-4 h electrode demonstrates the highest specific capacitance of 200 F g<sup>-1</sup> and 210 F g<sup>-1</sup> for positive and negative electrode polarizations, respectively (Fig. 3D), being evident for the intercalation of both cations (Na<sup>+</sup>) and anions (Cl<sup>-</sup>) into the activated MoS<sub>2</sub> sheets. A low specific capacitance of 75 F g<sup>-1</sup> was obtained for MoS<sub>2</sub>-10CNT-1 h, which is already higher than that of pristine MoS<sub>2</sub>-10CNT (50 F g<sup>-1</sup>). A small capacitive contribution originates from the electrical double-layer formation on CNTs, owing to their specific surface area of 225 m<sup>2</sup> g<sup>-1</sup> (ESI, Fig. S4†). Yet, this contribution is negligible considering the small amount of CNTs (10 mass%) and the low specific capacitance of CNTs (~20 F g<sup>-1</sup> if the entire electrode would consist only of carbon nanotubes).

For further investigation of the ion insertion mechanism of MoS<sub>2</sub>-10CNT-4 h, half-cells were investigated by electrochemical *in situ* Raman spectroscopy (Fig. 3E and F). As ions intercalate between the MoS<sub>2</sub> layers, the interlayer distance increases, causing a change in the electronic structure and a transition from semiconducting to metal-like conducting MoS<sub>2</sub> (*i.e.*, 2H- to the 1T-phase).<sup>38-42</sup> As long as the cell was operated in the cell voltage range of -0.4 V to +0.4 V, the change in the intensity and the shape of the characteristic MoS<sub>2</sub> peaks are negligible between the reduction and the oxidation at each potential step. In contrast, the characteristic MoS<sub>2</sub> peaks in the Raman spectrum disappeared after applying a cell voltage over +0.4 V or below

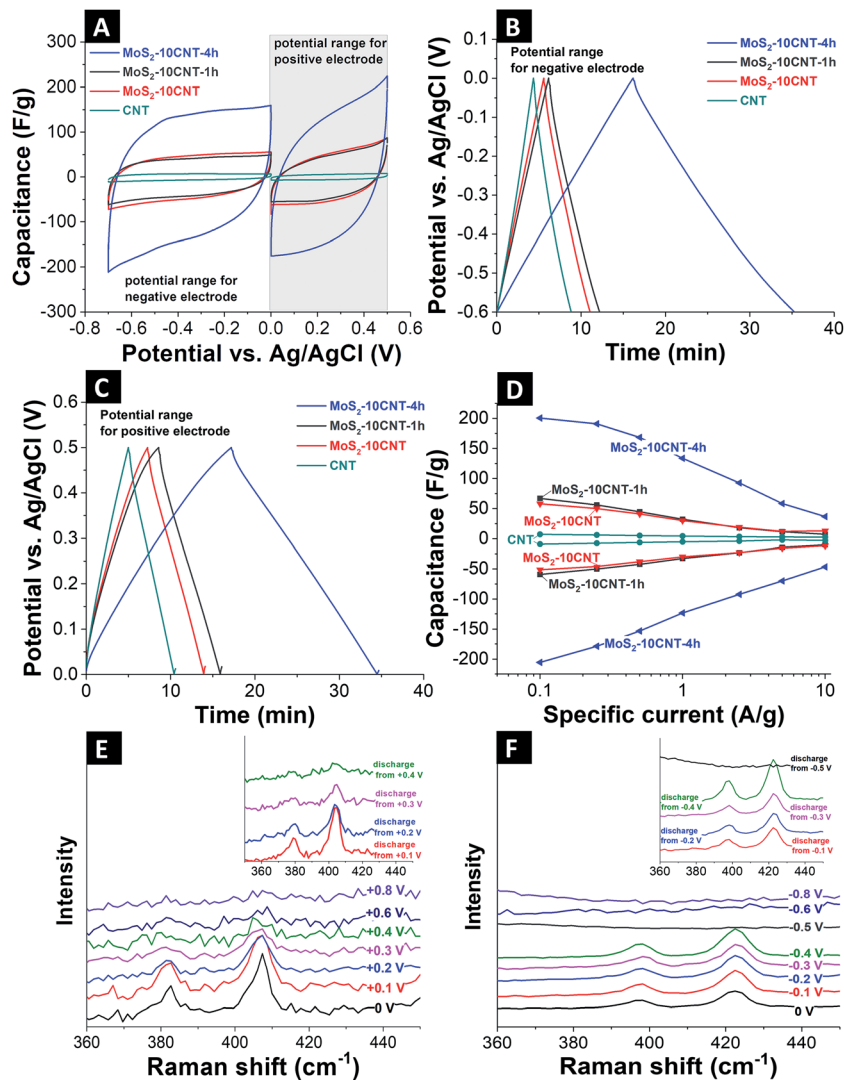


Fig. 3 (A) Cyclic voltammograms at  $5 \text{ mV s}^{-1}$ , (B and C) galvanostatic charge–discharge curves at  $0.1 \text{ A g}^{-1}$ , (D) specific capacitance versus specific current of the as-prepared binder-free electrode, (E) electrochemical *in situ* Raman spectra of  $\text{MoS}_2\text{-10CNT-4 h}$  in aqueous  $1 \text{ M NaCl}$  for positive polarization, and (F) for negative polarization.

$-0.4 \text{ V}$  to the  $\text{MoS}_2\text{-10CNT-4 h}$  electrode, and no restoration of the peaks was observed after reversing the polarity of the electrode to a cell potential of  $0 \text{ V}$ . In the case of the positive electrode, the peak intensity decreases rather gradually while the negative electrode shows a sudden disappearance. This indicates that ion insertion into the  $\text{MoS}_2$  layer structure expands the layer structure, considering that the sizes of the intercalating ions are larger than the interlayer spacing. Considering the ion size, it is possible that chloride intercalation at the positive electrode requires less energy compared to the sodiation of the negative electrode. Such difference and the differences in the ion size may manifest in the sudden phase transformation ( $2\text{H} \rightarrow 1\text{T}$ ) for the negative electrode and a more gradual for the positive.

### 3.3 Capacitive deionization performance at low and high molar concentrations

Considering the attractive pseudocapacitive performance, we selected  $\text{MoS}_2\text{-10CNT-4 h}$  for further investigations as the

desalination electrode at different  $\text{NaCl}$  concentrations (*i.e.*,  $5\text{--}500 \text{ mM}$ ). All experiments were conducted by applying a cell voltage of  $0.8 \text{ V}$  for salt removal and  $0 \text{ V}$  for regeneration. The maximum cell voltage seems low compared to conventional CDI, where voltages up to  $1.2 \text{ V}$  are needed to achieve a high SAC and charge efficiency. Yet, owing to the catalytic properties of  $\text{MoS}_2$  that induce water splitting at voltages above  $0.8 \text{ V}$ ,<sup>39</sup> higher voltages are prohibited.

As shown in Fig. 4A–D, the concentration profiles of the effluent stream exhibit conventional CDI behavior for all cycles. The concentration profile during charging assures that the sodium ions intercalate at the negative electrode and the chloride ions at the positive electrode (otherwise, we would see an inverse profile). Due to the kinetic limitation of the intercalation process, the salt removal step requires  $50 \text{ min}$  to reach equilibrium, while the regeneration step is much faster. This feature is shared with conventional CDI.<sup>8</sup> Compared to CDI with activated carbon, we see a much slower ion removal rate from the

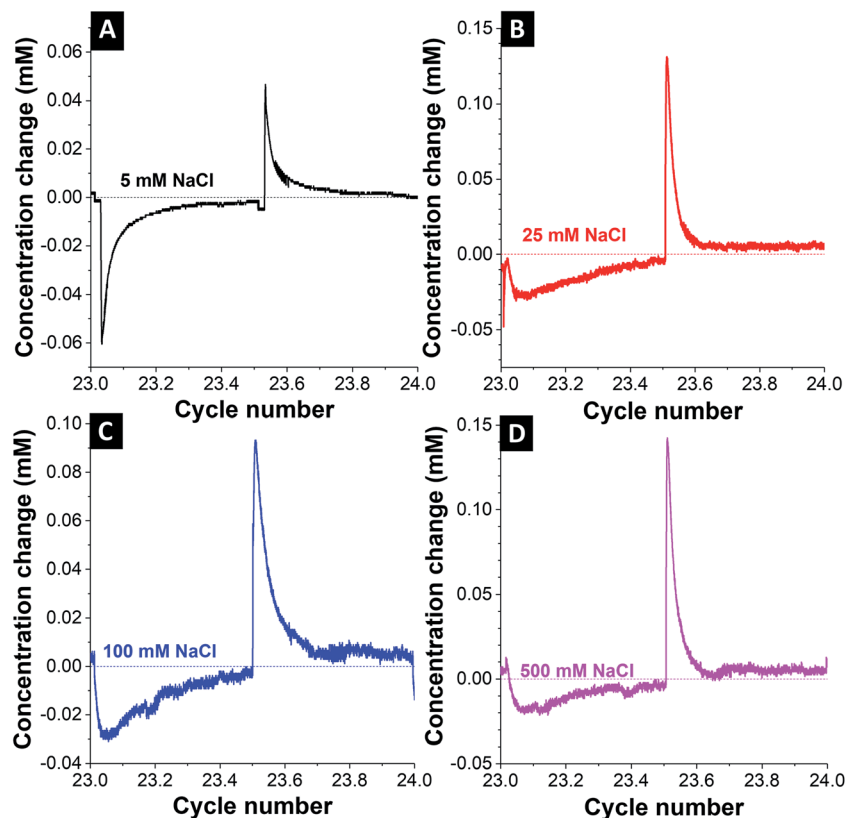


Fig. 4 Desalination performance of MoS<sub>2</sub>-10CNT-4 h at 0.8 V charging and 0 V discharging in aqueous (A) 5 mM NaCl, (B) 25 mM NaCl, (C) 100 mM NaCl, and (D) 500 mM NaCl.

conductivity profiles (ESI, Fig. S5<sup>†</sup>), owing to the different ion removal mechanism of FDI. Yet, the SAC is much higher than carbon at a low bias cell voltage. The SAC of MoS<sub>2</sub>-10CNT-4 h at 0.8 V in the charging step is 8.0, 13, 18, and 25 mg g<sup>-1</sup> at 5, 25, 100 and 500 mM, respectively (Fig. 5A). The sample MoS<sub>2</sub>-10CNT without electrochemical activation shows only a very small SAC of 0.6 mg g<sup>-1</sup> (Table 1 and ESI, Fig. S6<sup>†</sup>). The SAC of MoS<sub>2</sub>-10CNT-4 h is much higher than that of AC, which shows a SAC of 7, 4, 2, and 0.2 mg g<sup>-1</sup> at 5, 25, 100, and 500 mM, respectively (Table 1 and ESI, Fig. S7<sup>†</sup>). For comparison: the salinity in brackish water is between 17 and 513 mM and of sea water between 513 and 856 mM (considering only NaCl); the concentration threshold for fresh water onsets below 17 mM.<sup>1</sup>

The comparison of SAC values normalized to the mass is very useful when comparing different electrodes of the same type of material. However, when comparing MoS<sub>2</sub> and C, we must consider very different molar masses of molybdenum disulfide (160.1 g mol<sup>-1</sup>) and carbon (12.0 g mol<sup>-1</sup>). A practical way is, therefore, to normalize the desalination capacity by the density. Normalizing the SAC by the skeletal density of MoS<sub>2</sub>-CNT (4.8 g cm<sup>-3</sup>) yields 48, 62, 86, and 120 mg cm<sup>-3</sup> at 5, 25, 100, and 500 mM, respectively. These values are considerably higher than those of activated carbon (2.2 g cm<sup>-3</sup>): 14, 8, 4, and 0.4 mg cm<sup>-3</sup> at 5, 25, 100, and 500 mM, respectively. Considering the geometric volume of the electrode, MoS<sub>2</sub>-CNT-4 h with an electrode density of 2.2 g cm<sup>-3</sup> shows a SAC of 18, 29, 39, and 55 mg cm<sup>-3</sup>, while activated carbon with an electrode density of

0.4 g cm<sup>-3</sup> has only a SAC of 3, 2, 1, and 0.1 mg cm<sup>-3</sup> at 5, 25, 100, and 500 mM, respectively.

MoS<sub>2</sub>/CNT electrodes enable high charge efficiencies (*e.g.*, 80% in 5 mM; Fig. 5C) even at low cell voltages. The charge efficiency of MoS<sub>2</sub>-10CNT-4 h even increases for higher saline concentrations (Table 1), reaching 95% at 500 mM. In contrast, the charge efficiency of activated carbon steadily decreases to around 0.1% at 500 mM (ESI, Fig. S7C<sup>†</sup>). The reason for the low charge efficiency and the overall low SAC of activated carbon originates from co-ion expulsion,<sup>43</sup> where ions of the same charge as the electrode must first be removed from the pores. This is effectively avoided in few-layer MoS<sub>2</sub> stacks even at high concentrations, since no co-ions are present between the layers in the uncharged state. This presents a drastic paradigm change: the desalination capacity and charge efficiency for FDI increase with increased salt concentration, while CDI shows the exact opposite behavior.

Water deionization with an intercalation material is not only superior to conventional CDI with nanoporous carbons regarding the desalination capacity and charge efficiency, but also consumes much less energy per removed ion. It is well known that the energy consumption for ion removal *via* conventional CDI increases for higher saline concentrations.<sup>29</sup> When using a cell voltage of 0.8 V (for a fair comparison with MoS<sub>2</sub>-10CNT-4 h operated at the same voltage), we see a tremendous increase of the ion removal energy (Fig. 5D) from 13.3 kJ (5 mM) to 94.4 kJ (100 mM), exceeding 20 000 kJ at

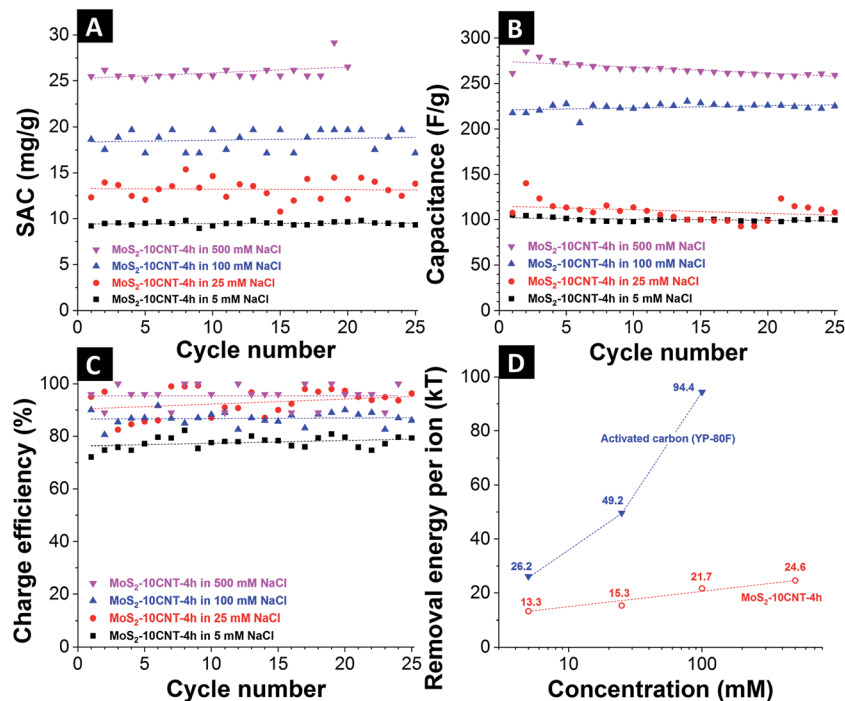


Fig. 5 (A) Salt adsorption capacity (SAC) at 0.8 V, (B) specific capacitance from the FDI cell, (C) charge efficiency, and (D) calculated energy per ion removed of the MoS<sub>2</sub>-10CNT-4 h electrode and activated carbon (YP-80F) in different salt concentrations.

Table 1 Desalination capacities of MoS<sub>2</sub>-CNT and activated carbon in different molar concentrations. The values of the SAC density were obtained by correcting the specific SAC by the material density. Some data are not available from the literature reference (denoted as n.a.)

Material	Cell voltage (V)	NaCl (mM)	Specific SAC (mg g <sup>-1</sup> )	Volumetric SAC (mg cm <sup>-3</sup> )	Charge efficiency (%)	Ref.
Na <sub>4</sub> Mn <sub>9</sub> O <sub>18</sub> /activated carbon	+1.2/-1.2	100	31.2	n.a.	n.a.	16
Na <sub>2</sub> FeP <sub>2</sub> O <sub>7</sub> /activated carbon	+1.2/-1.2	100	30.2	n.a.	n.a.	17
Activated carbon	0.8/0	5	7	14	80	This work
		25	4	8	48	This work
		100	2	4	26	This work
		500	0.2	0.4	0.1	This work
MoS <sub>2</sub> -10CNT	0.8/0	5	0.6	3.5	65	This work
MoS <sub>2</sub> -10CNT-4 h	0.8/0	5	10	40	76	This work
		25	13	65	86	This work
		100	18	90	90	This work
		500	25	125	95	This work

500 mM. For MoS<sub>2</sub>-10CNT-4 h, the energy per removed ion is much smaller and increases only slowly: 12, 15, 23, and 24 kT for 5, 25, 100, and 500 mM, respectively. Additionally, as seen from Table 1, we note that a cell voltage of 0.8 V for MoS<sub>2</sub>-10CNT-4 h is much lower than that in previous studies on hybrid materials (using typically 1.2 V; ref. 17).

Not only the desalination of electrochemically activated MoS<sub>2</sub> increases when increasing the salt concentration, but the specific capacitance also increases as a function of saline concentration of the feed water stream as illustrated in Fig. 5B. The unique ability of intercalation to provide effective desalination also at high concentrations differentiates FDI from CDI and makes it possible to capitalize on the intrinsic benefits of high molar saline solutions. For one, the ion mobility at higher

salt concentration is enhanced, enabling faster desalination kinetics.<sup>44</sup> The latter can also be seen in faster desalination rates at higher concentration in our FDI experiments (Kim-Yoon-plot, also known as CDI Ragone plot; ESI, Fig. S8†). The salt removal rate at the equilibrium state in 5 mM NaCl is 3 μg g<sup>-1</sup> s<sup>-1</sup> and increases to 7 μg g<sup>-1</sup> s<sup>-1</sup> in 500 mM NaCl. Secondly, higher molar concentrations of NaCl lead to a reduced hydration energy and a smaller number of water molecules in the hydration shell.<sup>45,46</sup> Furthermore, the activation energy barrier for ion intercalation is lowered at higher molar concentrations, benefitting more facile ion insertion between the MoS<sub>2</sub> sheets at high concentration.<sup>47-49</sup> At low concentration, a higher energy is needed to overcome the energy barrier than in high concentration, which also aligns with the reduced charge efficiency at

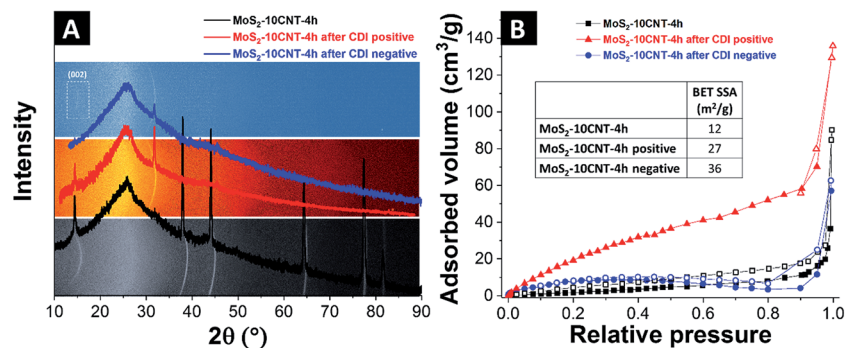


Fig. 6 (A) Post-mortem X-ray diffraction pattern of MoS<sub>2</sub>-10CNT-4 h, and (B) nitrogen gas sorption isotherm of MoS<sub>2</sub>-10CNT-4 before and after FDI cycling.

low concentration as shown in Fig. 5C. To the best of our knowledge, our experimental data represents the first report on the strong concentration dependency of the pseudocapacitive charge storage capacity of MoS<sub>2</sub> in the current literature.

As seen from the *in situ* data and thorough electrochemical analyses (Fig. 3), FDI accomplishes ion removal *via* anion and cation intercalation. The measured (high) values of salt removal capacity cannot be explained by the very small specific surface area (BET-SSA: 12 m<sup>2</sup> g<sup>-1</sup>) or the small mass of carbon nanotubes. Therefore, it is also important to investigate how this ion intercalation process impacts on the initial structure of the electrode material. Post-mortem analysis of MoS<sub>2</sub>-10CNT-4 h is shown in Fig. 6. After desalination and after discharging to 0 V, the positive electrode shows the same diffraction pattern as the initial electrode material (Fig. 6A), yet with a smaller signal intensity. The negative electrode shows a much weaker signal and the MoS<sub>2</sub>-(002) peak is barely visible in the 2D diffraction pattern (Fig. 6A). The results imply a change in the MoS<sub>2</sub> layer structure because of the intercalation of different ions at the negative and positive electrodes.

The different intercalation behavior can originate from the (slight) difference in the sizes of the intercalated ions, including the solvation shells.<sup>50</sup> Sodium ions intercalated at the negative electrode cause a higher expansion of the spacing between the MoS<sub>2</sub> sheets than chloride ions in the positive electrode. Our findings align with the work by Acerce *et al.*<sup>40</sup> reporting that hydrated potassium causes a larger expansion of MoS<sub>2</sub> layers although only slightly different in size compared to hydrated chloride. Post-mortem SEM images indicate that the characteristic layered structure of the MoS<sub>2</sub>/CNT electrodes stayed intact after the desalination operation (ESI, Fig. S9†) without noticeable evidence for the full delamination of the MoS<sub>2</sub> layers. The measured BET-SSA values of 27 m<sup>2</sup> g<sup>-1</sup> for the post-mortem positive electrode and 36 m<sup>2</sup> g<sup>-1</sup> for the post-mortem negative electrode also support the fact that actual delamination (*i.e.*, a complete loss of the *en bloc* layers) does not occur during desalination.

## 4. Conclusions

We introduced, for the first time, faradaic desalination with electrochemically activated, few-layered MoS<sub>2</sub>/CNT electrodes

for both anion and cation removal from saline solutions, ranging from brackish water to sea water. By this novel approach, it was possible to overcome the intrinsic desalination limitation of conventional CDI with porous carbon posed by co-ion desorption in high molarity. In contrast to other desalination technologies involving intercalation materials, our approach does not require the use of ion-exchange membranes. MoS<sub>2</sub>/CNT electrodes demonstrate stable performance over 25 cycles in various concentrations, ranging from brackish water to sea water, exhibiting a high SAC of 10, 13, 18, and 25 mg g<sup>-1</sup> in 5, 25, 100, and 500 mM NaCl, respectively. By capitalizing on ion intercalation instead of on ion electrosorption, an outstanding charge efficiency of 80% is obtained in 500 mM NaCl, a regime not accessible to conventional CDI (0.2 mg g<sup>-1</sup>, charge efficiency *ca.* 2%). The energy consumption per ion removed for FDI using MoS<sub>2</sub>/CNT is calculated to be 21.1 kJ for 100 mM and 24.6 kJ for 500 mM solution; this performance is already promising compared to well-established technologies like reverse osmosis for sea water desalination.

## Acknowledgements

P. S. acknowledges the financial support by the German Academic Exchange Service (DAAD award number 91579066). The authors thank Prof. Eduard Arzt (INM) for his continuing support and Prof. Matthew E. Suss (Technion) for many helpful discussions. The authors thank Benjamin Krüner and Aura Tolosa for conducting XRD and TEM measurements (both at INM).

## References

- 1 M. Elimelech and W. A. Phillip, *Science*, 2011, **333**, 712–717.
- 2 N. Savage and M. S. Diallo, *J. Nanopart. Res.*, 2005, **7**, 331–342.
- 3 M. Noked, A. Soffer and D. Aurbach, *J. Solid State Electrochem.*, 2011, **15**, 1563–1578.
- 4 M. A. Shannon, P. W. Bohn, M. Elimelech, J. G. Georgiadis, B. J. Marinas and A. M. Mayes, *Nature*, 2008, **452**, 301–310.
- 5 Y. Oren, *Desalination*, 2008, **228**, 10–29.

- 6 S. Porada, R. Zhao, A. van der Wal, V. Presser and P. M. Biesheuvel, *Prog. Mater. Sci.*, 2013, **58**, 1388–1442.
- 7 C. Fritzmann, J. Löwenberg, T. Wintgens and T. Melin, *Desalination*, 2007, **216**, 1–76.
- 8 M. E. Suss, S. Porada, X. Sun, P. M. Biesheuvel, J. Yoon and V. Presser, *Energy Environ. Sci.*, 2015, **8**, 2296–2319.
- 9 P. M. Biesheuvel, S. Porada, M. Levi and M. Z. Bazant, *J. Solid State Electrochem.*, 2014, **18**, 1365–1376.
- 10 M. D. Andelman, Flow-through capacitor, *US Pat.* 5415768, 1994.
- 11 Y. Liu, C. Y. Nie, X. J. Liu, X. T. Xu, Z. Sun and L. K. Pan, *RSC Adv.*, 2015, **5**, 15205–15225.
- 12 C. Prehal, C. Koczwara, N. Jäckel, A. Schreiber, M. Burian, H. Amenitsch, M. A. Hartmann, V. Presser and O. Paris, *Nat. Energy*, 2017, **2**, 16215.
- 13 X. Gao, S. Porada, A. Omosebi, K.-L. Liu, P. M. Biesheuvel and J. Landon, *Water Res.*, 2016, **92**, 275–282.
- 14 M. Pasta, C. D. Wessells, Y. Cui and F. La Mantia, *Nano Lett.*, 2012, **12**, 839–843.
- 15 K. C. Smith and R. Dmello, *J. Electrochem. Soc.*, 2016, **163**, A530–A539.
- 16 J. Lee, S. Kim, C. Kim and J. Yoon, *Energy Environ. Sci.*, 2014, **7**, 3683–3689.
- 17 S. Kim, J. Lee, C. Kim and J. Yoon, *Electrochim. Acta*, 2016, **203**, 265–271.
- 18 F. Xing, T. Li, J. Li, H. Zhu, N. Wang and X. Cao, *Nano Energy*, 2017, **31**, 590–595.
- 19 M. Salanne, B. Rotenberg, K. Naoi, K. Kaneko, P. L. Taberna, C. P. Grey, B. Dunn and P. Simon, *Nat. Energy*, 2016, **1**, 16070.
- 20 R. B. Smith, E. Khoo and M. Z. Bazant, 2017, arXiv, 1701.08858.
- 21 S. Porada, P. Bukowska, A. Shrivasa, P. M. Biesheuvel and K. C. Smith, 2016, ArXiv, 1612.08293.
- 22 P. Srimuk, F. Kaasik, B. Krüner, A. Tolosa, S. Fleischmann, N. Jäckel, M. C. Tekeli, M. Aslan, M. E. Suss and V. Presser, *J. Mater. Chem. A*, 2016, **4**, 18265–18271.
- 23 B. Anasori, M. R. Lukatskaya and Y. Gogotsi, *Nat. Rev. Mater.*, 2017, **2**, 16098.
- 24 M. D. Levi, M. R. Lukatskaya, S. Sigalov, M. Beidaghi, N. Shpigel, L. Daikhin, D. Aurbach, M. W. Barsoum and Y. Gogotsi, *Adv. Energy Mater.*, 2015, **5**, 1400815.
- 25 S. Brunauer, P. H. Emmett and E. Teller, *J. Am. Chem. Soc.*, 1938, **60**, 309–319.
- 26 M. Aslan, M. Zeiger, N. Jäckel, I. Grobelsek, D. Weingarh and V. Presser, *J. Phys.: Condens. Matter*, 2016, **28**, 114003.
- 27 D. Weingarh, M. Zeiger, N. Jäckel, M. Aslan, G. Feng and V. Presser, *Adv. Energy Mater.*, 2014, **4**, 1400316.
- 28 P. Srimuk, M. Zeiger, N. Jäckel, A. Tolosa, B. Krüner, S. Fleischmann, I. Grobelsek, M. Aslan, B. Shvartsev, M. E. Suss and V. Presser, *Electrochim. Acta*, 2017, **224**, 314–328.
- 29 R. Zhao, M. Biesheuvel and B. Van der Wal, *Energy Environ. Sci.*, 2012, **5**, 9520–9527.
- 30 N. Liu, P. Kim, J. H. Kim, J. H. Ye, S. Kim and C. J. Lee, *ACS Nano*, 2014, **8**, 6902–6910.
- 31 H. Li, Q. Zhang, C. C. R. Yap, B. K. Tay, T. H. T. Edwin, A. Olivier and D. Baillargeat, *Adv. Funct. Mater.*, 2012, **22**, 1385–1390.
- 32 C. Lee, H. Yan, L. E. Brus, T. F. Heinz, J. Hone and S. Ryu, *ACS Nano*, 2010, **4**, 2695–2700.
- 33 J. Zheng, H. Zhang, S. Dong, Y. Liu, C. Tai Nai, H. Suk Shin, H. Young Jeong, B. Liu and K. Ping Loh, *Nat. Commun.*, 2014, **5**, 2995.
- 34 G. S. Bang, K. W. Nam, J. Y. Kim, J. Shin, J. W. Choi and S.-Y. Choi, *ACS Appl. Mater. Interfaces*, 2014, **6**, 7084–7089.
- 35 M. A. Lukowski, A. S. Daniel, F. Meng, A. Forticaux, L. Li and S. Jin, *J. Am. Chem. Soc.*, 2013, **135**, 10274–10277.
- 36 K. Krishnamoorthy, P. Pazhamalai, G. K. Veerasubramani and S. J. Kim, *J. Power Sources*, 2016, **321**, 112–119.
- 37 T. Brousse, D. Bélanger and J. W. Long, *J. Electrochem. Soc.*, 2015, **162**, A5185–A5189.
- 38 X. Wang, X. Shen, Z. Wang, R. Yu and L. Chen, *ACS Nano*, 2014, **8**, 11394–11400.
- 39 S. J. Rowley-Neale, J. M. Fearn, D. A. C. Brownson, G. C. Smith, X. Ji and C. E. Banks, *Nanoscale*, 2016, **8**, 14767–14777.
- 40 M. Acerce, D. Voiry and M. Chhowalla, *Nat. Nanotechnol.*, 2015, **10**, 313–318.
- 41 M. Azhagurajan, T. Kajita, T. Itoh, Y.-G. Kim and K. Itaya, *J. Am. Chem. Soc.*, 2016, **138**, 3355–3361.
- 42 C. N. R. Rao, U. Maitra and U. V. Waghmare, *Chem. Phys. Lett.*, 2014, **609**, 172–183.
- 43 N. Shpigel, M. D. Levi, S. Sigalov, D. Aurbach, L. Daikhin and V. Presser, *J. Phys.: Condens. Matter*, 2016, **28**, 114001.
- 44 J. Kestin, H. E. Khalifa and R. J. Correia, *J. Phys. Chem. Ref. Data*, 1981, **10**, 71–88.
- 45 V. N. Afanasiev, A. N. Ustinov and I. Y. Vashurina, *J. Phys. Chem. B*, 2009, **113**, 212–223.
- 46 R. Mancinelli, A. Botti, F. Bruni, M. A. Ricci and A. K. Soper, *J. Phys. Chem. B*, 2007, **111**, 13570–13577.
- 47 H. Yildirim, J. Greeley and S. K. R. S. Sankaranarayanan, *J. Phys. Chem. C*, 2011, **115**, 15661–15673.
- 48 A. Van der Ven and G. Ceder, *J. Power Sources*, 2001, **97–98**, 529–531.
- 49 C. Chen, Y. Wen, X. Hu, X. Ji, M. Yan, L. Mai, P. Hu, B. Shan and Y. Huang, *Nat. Commun.*, 2015, **6**, 6929.
- 50 S. Porada, G. Feng, M. E. Suss and V. Presser, *RSC Adv.*, 2016, **6**, 5865–5870.

**Faradaic deionization of brackish and sea water  
via pseudocapacitive cation and anion intercalation  
into few layered molybdenum disulfide**

Pattarachai Srimuk,<sup>1,2</sup> Juhan Lee,<sup>1,2</sup> Simon Fleischmann,<sup>1,2</sup> Soumyadip Choudhury,<sup>1</sup>  
Nicolas Jäckel,<sup>1,2</sup> Marco Zeiger,<sup>1,2</sup> Choonsoo Kim,<sup>1</sup> Mesut Aslan,<sup>1</sup> Volker Presser<sup>1,2,\*</sup>

*Supporting Information*

### Calculation of salt adsorption capacity and charge efficiency

$$SAC = \frac{v \cdot M_{NaCl}}{m_{total}} \int c dt. \quad \text{Equation (S1)}$$

In this equation, v is the flow rate (mL/min),  $M_{NaCl}$  is molecular weight of NaCl (58.44 g/mol),  $m_{total}$  is total mass of electrodes (g), t is the time over the adsorption step (min), and c is the concentration of NaCl (mmol/L).

The concentration of NaCl is calculated by relation of concentration and conductivity:

$$c = \left( \frac{\sigma - 4.5}{121.29} \right)^{1/0.9826} - 0.13 \quad \text{Equation (S2)}$$

where  $\sigma$  is actual conductivity ( $\mu\text{S}/\text{cm}$ ) which subtracts the conductivity by the conductivity of water by measured pH from the measured conductivity:

$$\sigma = \sigma_m - \sigma_w \quad \text{Equation (S3)}$$

where  $\sigma_m$  is measured conductivity (mS/cm) and  $\sigma_w$  is the conductivity of water calculated by:

$$\sigma_w = \frac{e^2}{k_B T} \left( 10^{pH} \cdot N_A \cdot D_{H_3O^+} + \frac{10^{-14}}{10^{-pH}} \cdot N_A \cdot D_{OH^-} \right) \quad \text{Equation (S4)}$$

where  $k_B$  is Boltzmann constant ( $1.38 \cdot 10^{-23} \text{ m}^2 \text{ kg} / \text{s}^2 \text{ K}$ ),  $N_A$  is Avogadro constant ( $6.02 \cdot 10^{23} \text{ mol}^{-1}$ ),  $D_{H_3O^+}$  is diffusion coefficient of hydronium ion ( $9.3 \cdot 10^{-9} \text{ m}^2 / \text{s}$ ), and  $D_{OH^-}$  is the diffusion coefficient of an hydroxyl ion ( $5.3 \cdot 10^{-9} \text{ m}^2 / \text{s}$ ).

$$\text{Charge efficiency (\%)} = \left( \frac{\frac{SAC \left( \frac{mg}{g} \right)}{M_{NaCl} \left( \frac{g}{mol} \right)}}{\frac{\text{Specific capacitance} \left( \frac{C}{g \cdot V} \right) \cdot \text{Cell coltage (V)}}{4 \cdot \text{Faraday constant} \left( \frac{C}{mol} \right)}} \right) \cdot 100 \quad \text{Equation (S5)}$$

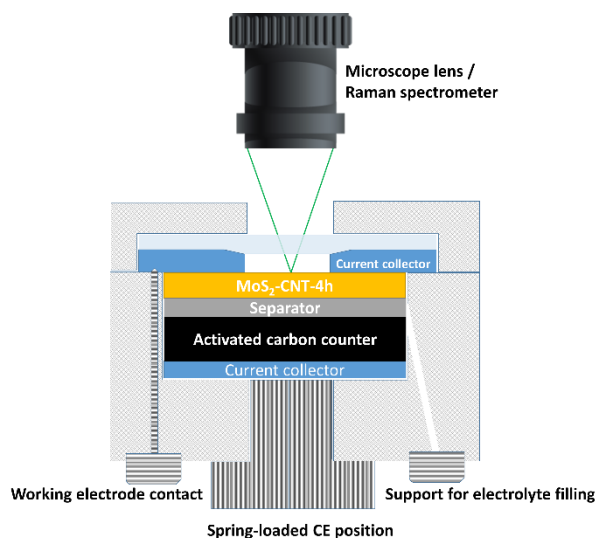


**Figure S1.** Schematic configuration of the electrochemical in situ stage for Raman spectroscopy.

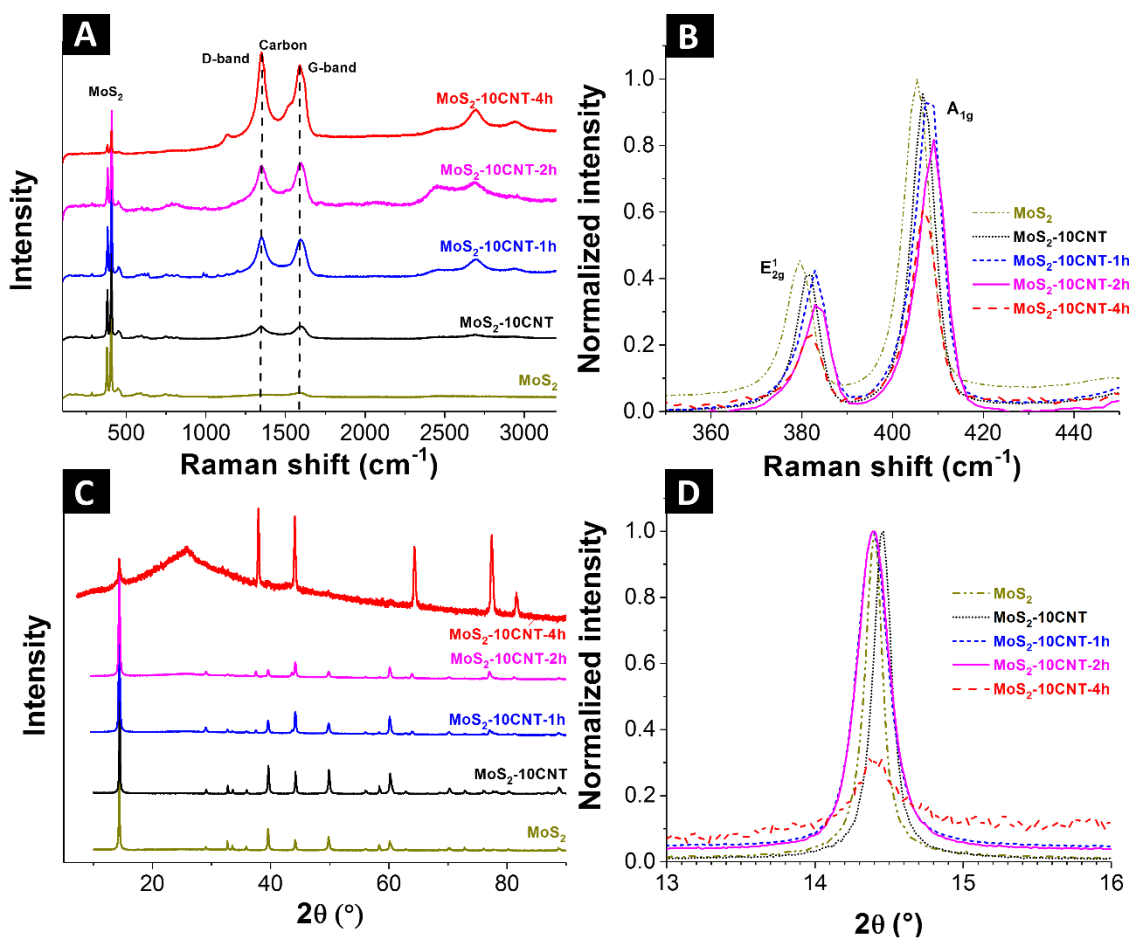


**Figure S2** Raman spectra (A) and (B), X-ray diffractogram of MoS<sub>2</sub>, MoS<sub>2</sub>-10CNT, and electrochemically activated samples (i.e., MoS<sub>2</sub>-10CNT-1h, MoS<sub>2</sub>-10CNT-2h, MoS<sub>2</sub>-10CNT-4h).

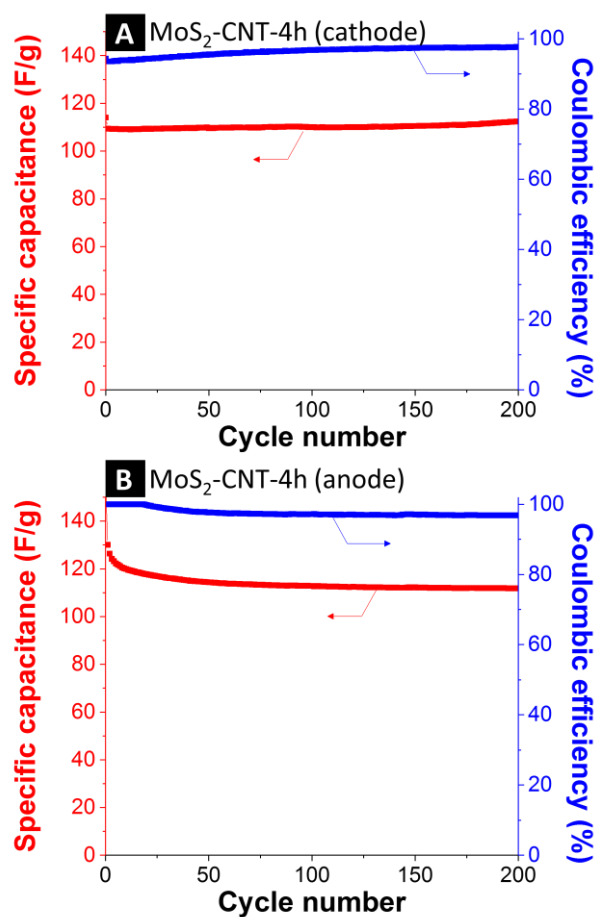


**Figure S3** Cyclic stability of MoS<sub>2</sub>-10CNT-4h at 0.5 A/g in 1 M NaCl. (A) Cathode, (B) anode.

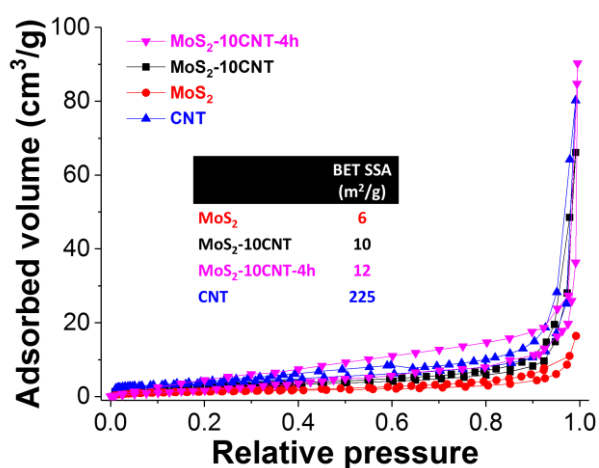


**Figure S4.** Nitrogen gas sorption isotherm recorded at -196 °C of MoS<sub>2</sub>, MoS<sub>2</sub>-10CNT, MoS<sub>2</sub>-10CNT-4h, and pure carbon nanotubes (CNT).

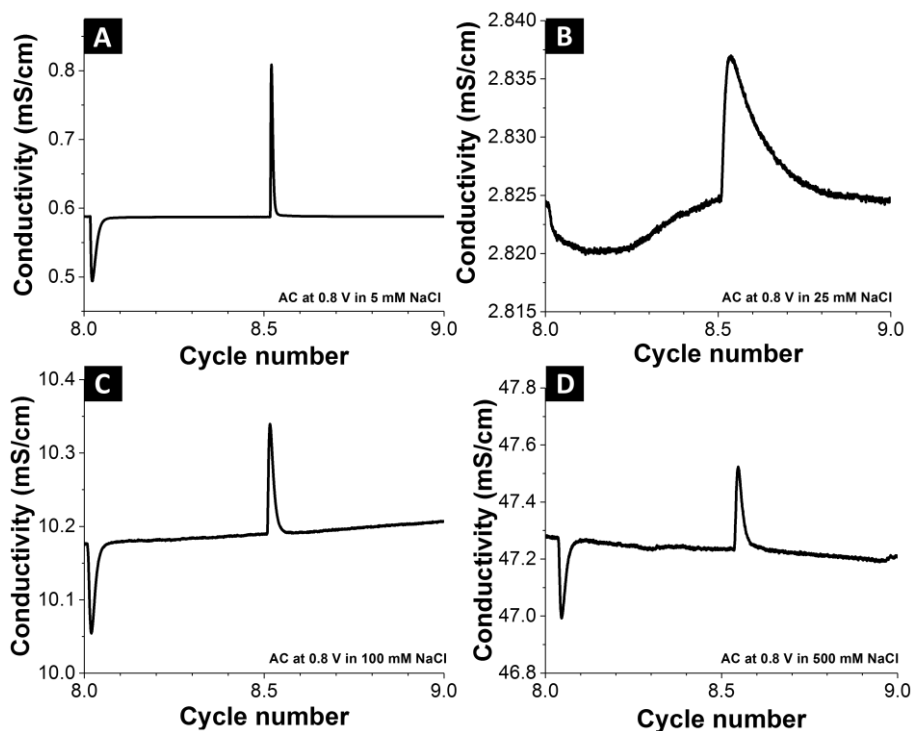


**Figure S5.** CDI performance of AC at 0.8 V charging and 0 V discharging in (A) 5 mM NaCl, (B) 25 mM NaCl, (C) 100 mM NaCl, and (D) 500 mM NaCl.

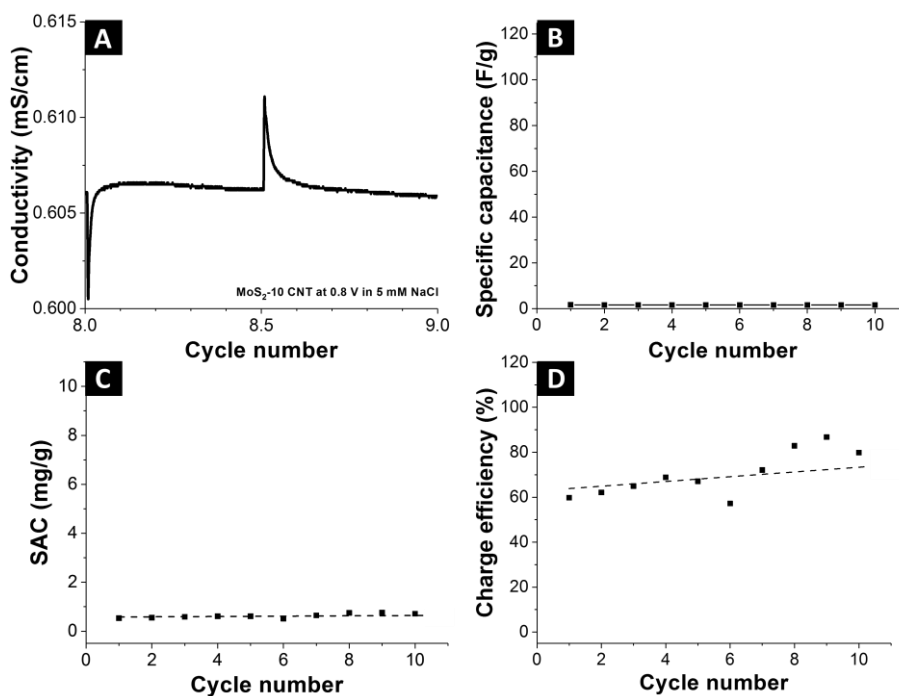


**Figure S6.** (A) CDI performance of MoS<sub>2</sub>-10CNT at 0.8 V charging and 0 V discharging in 5 mM NaCl, (B) specific capacitance from CDI cell, (C) salt adsorption capacity (SAC), and (D) CDI charge efficiency.

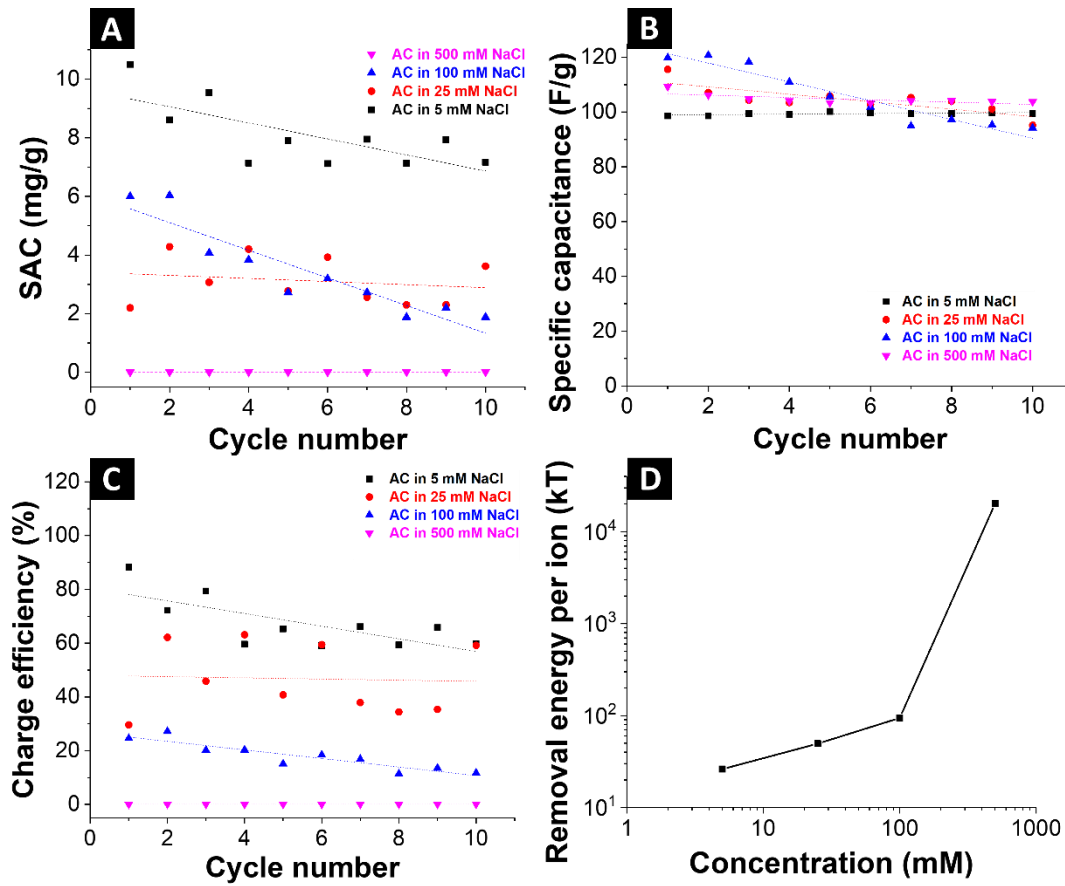


**Figure S7.** Comparative data for CDI with activated carbon (AC). (A) Salt adsorption capacity (SAC), (B) specific capacitance from CDI cell, (C) charge efficiency, and (D) energy per ion removed of AC electrode in different salt concentration.

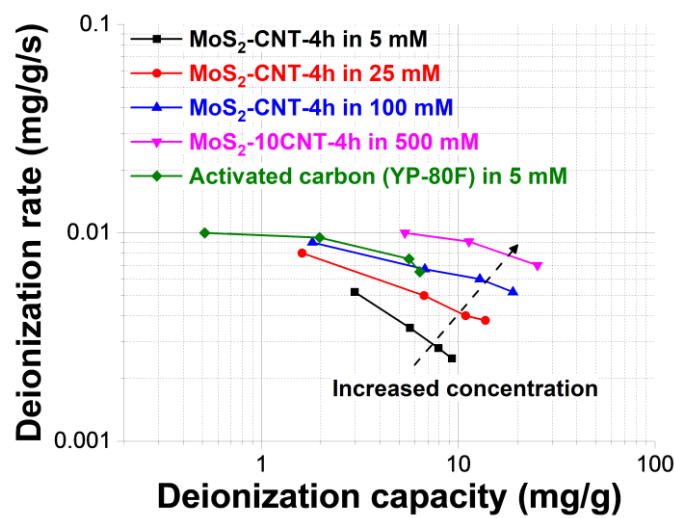


**Figure S8.** Kim-Yoon-Plot (“CDI Ragone plot” for FDI at different molar concentrations.

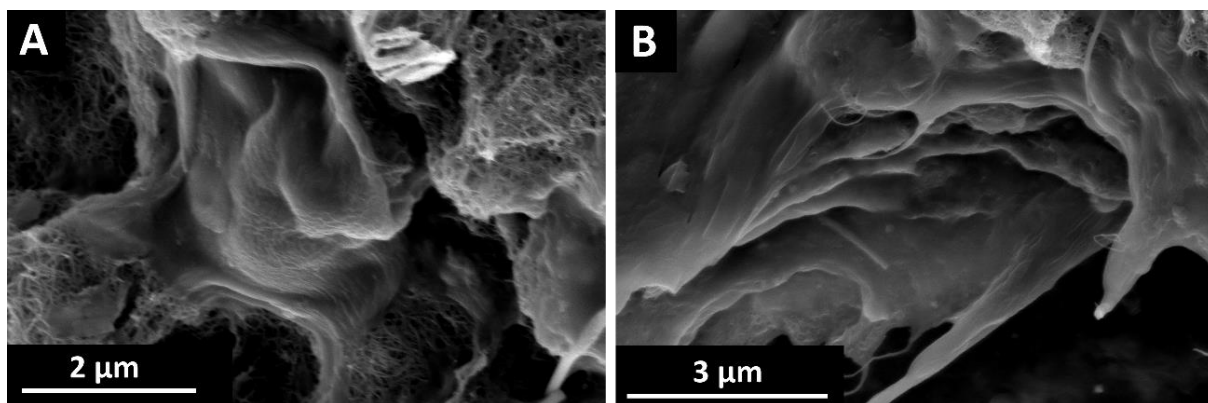


**Figure S9.** Post mortem scanning micrographs (A) negative electrode MoS<sub>2</sub>-10CNT-4h, and (B) positive electrode MoS<sub>2</sub>-10CNT-4h.

#### 4.6 Titanium disulfide: a promising low-dimensional electrode material for sodium ion intercalation for seawater desalination

Pattarachai Srimuk,<sup>1,2</sup> Juhan Lee,<sup>1,2</sup> Aura Tolosa,<sup>1,2</sup> Choonsoo Kim,<sup>1</sup>

Mesut Aslan,<sup>1</sup> Volker Presser<sup>1,2</sup>

<sup>1</sup> INM - Leibniz Institute for New Materials, 66123 Saarbrücken, Germany

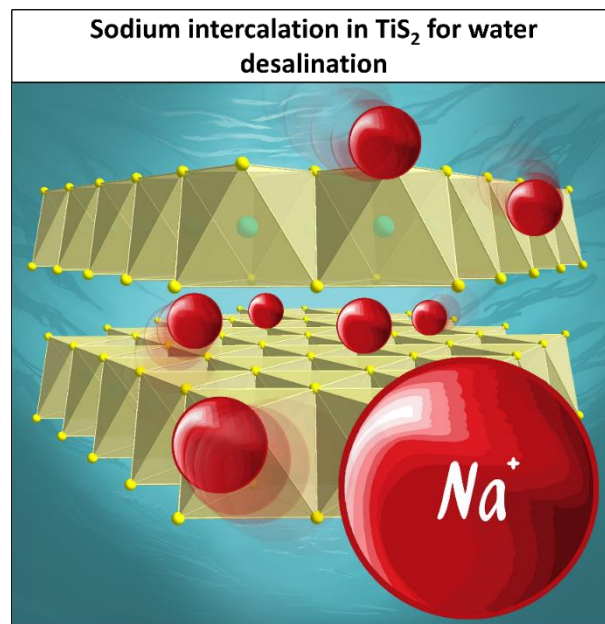
<sup>2</sup> Saarland University, Campus D2 2, 66123 Saarbrücken, Germany

##### Citation:

P. Srimuk, J. Lee, A. Tolosa, C. Kim, M. Aslan, V. Presser, TITANIUM DISULFIDE: A PROMISING LOW-DIMENSIONAL ELECTRODE MATERIAL FOR SODIUM ION INTERCALATION FOR SEAWATER DESALINATION, *Chemistry of Materials* 29(23) (2017) 9964-9973.

##### Own contribution:

Electrochemistry, CDI experiment, ICP-OES, analysis, writing



# Titanium Disulfide: A Promising Low-Dimensional Electrode Material for Sodium Ion Intercalation for Seawater Desalination

Pattarachai Srimuk,<sup>†,‡</sup> Juhan Lee,<sup>†,‡</sup> Aura Tolosa,<sup>†,‡</sup> Choonsoo Kim,<sup>†</sup> Mesut Aslan,<sup>†</sup> and Volker Presser<sup>\*,†,‡</sup>

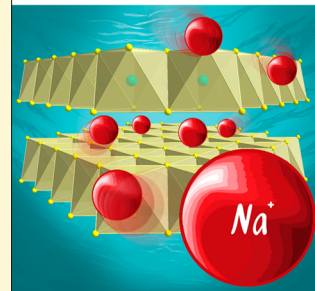
<sup>†</sup>INM, Leibniz Institute for New Materials, Saarbrücken 66123, Germany

<sup>‡</sup>Department of Materials Science and Engineering, Saarland University, Saarbrücken 66123, Germany

## S Supporting Information

**ABSTRACT:** This work introduces for the first time titanium disulfide (TiS<sub>2</sub>)/carbon nanotube (CNT) electrodes for desalination of high molarity saline water. Capitalizing on the two-dimensional layered structure of TiS<sub>2</sub>, cations can be effectively removed from a feedwater stream by intercalation. The TiS<sub>2</sub>-CNT hybrid electrode is paired in an asymmetric cell with microporous activated carbon cloth without an ion exchange membrane. By electrochemical analysis, the correlation between the state of charge and the stability of TiS<sub>2</sub> was investigated. By using post-mortem X-ray diffraction, the sodium-ion intercalation mechanism gives an insight into how the state of charge affects the structure and cyclic stability. Our system showed stable desalination performance over 70 cycles at high molar concentration (600 mM), with a cell salt removal capacity of 14 mg/g (equivalent to a sodium removal capacity of 35.8 mg/g normalized to the mass of TiS<sub>2</sub>-CNT). This novel approach of membrane-free hybrid Faradaic capacitive deionization paves the way toward energy-efficient desalination of seawater.

### Sodium intercalation in TiS<sub>2</sub> for water desalination



## 1. INTRODUCTION

Water provides vital services for human health, food, and sustainability of ecosystems and is a key factor for industry and agriculture. According to the United Nation Water Report of 2016,<sup>1</sup> the fresh water cycle has been interrupted, leading to a rise of water scarcity in many continents.<sup>1</sup> To sustain the basic quality of human life and enable technological advancement, the development of energy efficient and cost-effective technologies for the desalination of brackish and saline water have become key research activities in environmental science and engineering areas.<sup>2–4</sup> There exist several desalination technologies such as reverse osmosis,<sup>5,6</sup> multistep distillation,<sup>7</sup> electrodeionization,<sup>8,9</sup> electro dialysis,<sup>10</sup> and capacitive deionization (CDI).<sup>11,12</sup> In particular, the latter benefits from a very low energy consumption per fresh water production (0.5 Wh/L) for brackish water (lower than 30 mM NaCl), requiring low operating potential (ca. 1 V) and simple system components and configurations.<sup>13</sup>

In principle, CDI employs the mechanism of electric double-layer capacitors (supercapacitors) by means of ion electro-sorption.<sup>14</sup> Commonly, a CDI cell consists of carbon electrodes (such as activated carbon, carbon aerogel, or carbon nanotubes),<sup>15</sup> being separated by a porous separator (Figure 1A). While the saline water is circulating through the separator in the middle of the cell, the cell can be electrically charged. The polarization of the cell leads to the adsorption of cations at the negative electrode and anions at the positive electrode. Thus, the feedwater stream is effectively depleted of salt ions. As the cell is discharged, the adsorbed ions are released from the electrode to the effluent water stream, while a fraction of the

invested energy is recovered by the discharging current. In general, the concentration of the feedwater for conventional CDI systems is limited to around 25 mM due to high energy consumption through low operating efficiency at higher concentrated solutions.<sup>11</sup> Also, the salt adsorption capacity (SAC: the amount of removed salt divided by the total mass of the carbon electrodes in the cell) reaches a saturation, with maximum SAC values being 10–18 mg/g in 10 mM NaCl at present.<sup>15</sup> To enhance SAC values and efficiency of the deionization process, membrane capacitive deionization (MCDI, Figure 1B) was introduced by sealing the electrodes with an anion and a cation exchange membrane.<sup>16–18</sup> The use of membranes can effectively block co-ion expulsion,<sup>19</sup> leading to an increase in salt adsorption capacity and charge efficiency, which is found to be 50% higher than a CDI system in brackish water.<sup>20</sup> However, the use of ion exchange membranes causes high production costs and an increased ionic resistance to the system.<sup>15</sup>

Over the past few years, desalination batteries have emerged as a result of integrated scientific and technological progress on batteries and CDI.<sup>21</sup> Unlike conventional CDI with non-Faradaic (capacitive) ion electro-sorption, desalination batteries rely on Faradaic reactions which can remove ions either by electrochemical conversion reactions or intercalation. The first reported desalination battery consisted of sodium manganese oxide as positive electrode for sodium-ion intercalation and

Received: August 8, 2017

Revised: November 10, 2017

Published: November 11, 2017

## Figures

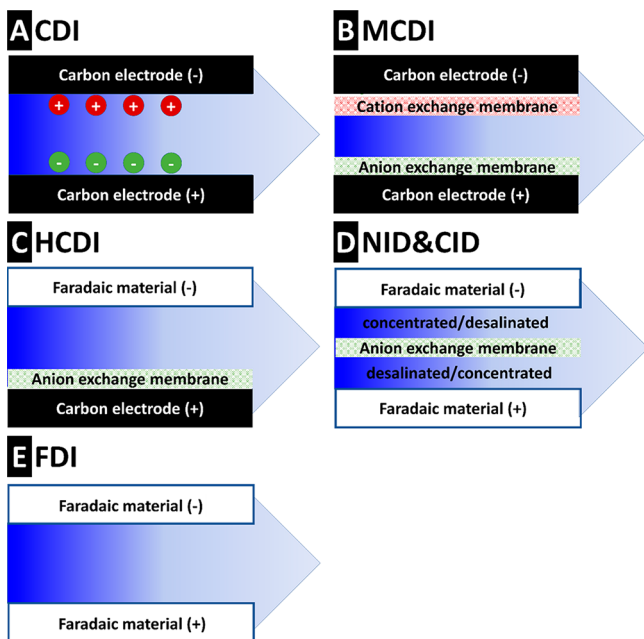


**Figure 1.** Cell configurations of (A) conventional capacitive deionization (without membranes), (B) membrane capacitive deionization, (C) hybrid capacitive deionization with use of an anion exchange membrane, (D) sodium-ion desalination/cation desalination with use of an anion exchange membrane, and (E) Faradaic deionization (without membranes).

silver nanoparticles as negative electrode for the electrochemical incorporation of  $\text{Cl}^-$  via the  $\text{Ag}/\text{AgCl}$  conversion reaction.<sup>21,22</sup> This system did not employ ion exchange membranes and operated in seawater with an energy consumption of 0.29 Wh/L; for comparison, the energy consumption for state-of-the-art reverse osmosis modules is around 0.2 Wh/L.<sup>23</sup> Hybrid capacitive deionization (HCIDI, Figure 1C) introduced by the Yoon group used intercalating materials with redox reactions such as sodium manganese oxide, and sodium iron phosphate as a sodium-ion removal electrode material.<sup>24,25</sup> Those materials exhibit an intercalation potential similar to the carbon electrode, being used as positive electrode. Therefore, anion exchange membranes were necessary for previous HCIDI designs. For chloride immobilization, bismuth can substitute silver and enable chloride removal via the  $\text{Bi}/\text{BiOCl}$  reaction.<sup>26</sup>

More recently, sodium-ion desalination and cation desalination (NID and CID) has been introduced by applying sodium or cation intercalating electrode materials such as manganese oxide, sodium titanium phosphate, sodium nickel hexacyanoferrate, and sodium iron hexacyanoferrate.<sup>27–30</sup> By coupling sodium nickel hexacyanoferrate with sodium iron hexacyanoferrate, SAC can be up to 60 mg/g in 500 mM NaCl.<sup>28</sup> This configuration requires an anion exchange membrane and a double flow-channel, which is necessary for  $\text{Cl}^-$  ion removal because the negative and positive electrodes do not exhibit direct capacity to adsorb, deposit, or intercalate  $\text{Cl}^-$  (Figure 1D). However, the advantage of sodium-ion desalination and cation desalination is that these methods produce both concentrated and desalinated water at the same time, allowing for a continuous process.

Motivated by the advent of two-dimensional (2D) materials for energy storage systems,<sup>31</sup> we introduced desalination with

$\text{Ti}_3\text{C}_2$ -MXene to effectively remove  $\text{Na}^+$  and  $\text{Cl}^-$  via cation and anion intercalation in the layered material using a symmetric cell (with the same material for both electrodes having same size and mass).<sup>32</sup> The layered structure of  $\text{Ti}_3\text{C}_2$ -MXene allowed sodium and chloride ion intercalation without applying any ion exchange membrane (Figure 1E) and yielded a SAC of 13 mg/g in aqueous 5 mM NaCl.<sup>32</sup> Also, molybdenum disulfide ( $\text{MoS}_2$ ), a well-known transition-metal dichalcogenide, was employed for desalination of 400 mM NaCl solution in a symmetric cell, and an SAC value of 9 mg/g was achieved.<sup>33</sup> Even higher performance was obtained for  $\text{MoS}_2$ /carbon nanotube electrodes: 10 mg/g at a charge efficiency of 76% in 5 mM NaCl and 25 mg/g at a charge efficiency of 95% in 500 mM NaCl.<sup>34</sup> Clearly, Faradaic ion intercalation in 2D layered materials such as MXene and transition-metal dichalcogenides is promising to advance electrochemical desalination technologies.

For 2D materials, electrochemical properties greatly depend on the number of layers.<sup>35</sup> Typically, bulk transition-metal dichalcogenides consist of a transition metal coordinated with chalcogens (such as S, Se, or Te). Titanium disulfide ( $\text{TiS}_2$ ) has been successfully employed as electrode material for rechargeable sodium-ion batteries since 1980. However, the material suffers from rapid capacity fading due to the dramatic volume expansion.<sup>36</sup> Recently, Yuping Liu et al. improved the stability of  $\text{TiS}_2$  (~300 cycles) in a sodium-ion battery with an organic electrolyte by engineered nanostructure of  $\text{TiS}_2$  while demonstrating a stable performance.<sup>37</sup> So far,  $\text{TiS}_2$  has not yet been explored for sodium intercalation in aqueous electrolytes for energy storage or for water desalination.  $\text{TiS}_2$  exhibits various features, making it of interest as a material for desalination purposes. First, it shows a battery-like charge/voltage profile; that is, we see clear redox peaks during cation intercalation. By this virtue, it is fundamentally different compared to our previous work on few-layer  $\text{MoS}_2$ , where a nearly ideal pseudocapacitive behavior was observed and where cation and anion intercalation were encountered.  $\text{TiS}_2$  would, therefore, be the first 2D material with battery-like behavior to be explored for electrochemical desalination. Further, the high electrical conductivity of  $\text{TiS}_2$  of  $2 \times 10^2$  S/cm at 25 °C is attractive from an electrode-fabrication point of view, where no conductive additive per se is needed.<sup>38</sup> The lower molar mass of  $\text{TiS}_2$  (112.0 g/mol) compared to that of  $\text{Ti}_3\text{C}_2$ -MXene (167.6 g/mol) or  $\text{MoS}_2$  (160.1 g/mol) could also possibly benefit the mass-normalized performance metrics.

In this work, we introduce membrane-free and binder-free titanium disulfide/carbon nanotube hybrid material for hybrid capacitive desalination by coupling with activated carbon textile. By systematic study through post-mortem X-ray diffraction (XRD) analysis, we confirm that titanium disulfide is capable of sodium removal by a redox intercalation process. We provide comprehensive results at various NaCl concentrations (5, 50, and 600 mM), ranging from brackish water to seawater. Sodium removal is experimentally confirmed by online monitoring of the desalination process with inductively coupled plasma optical emission spectroscopy (ICP-OES).

## 2. EXPERIMENTAL DESCRIPTION

**2.1. Material Synthesis.** Binder-free electrodes were prepared as follows (Figure 2A):  $\text{TiS}_2$  with a particle size of ca. 40  $\mu\text{m}$  (99.99 mass %, Sigma-Aldrich) was used as the starting material. Initially, 100 mg of  $\text{TiS}_2$  powder was stirred and ultrasonicated in 150 mL of ethanol for 30 min for predispersion. In parallel, 11 mg of multiwall carbon

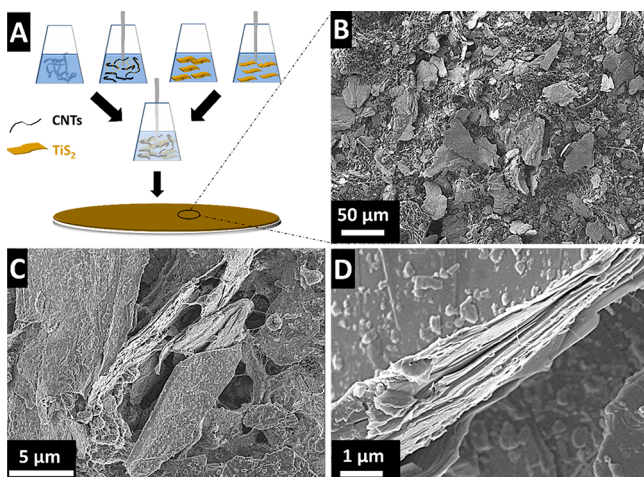


**Figure 2.** (A) Schematic illustration of electrode processing and (B–D) scanning electron micrographs of  $\text{TiS}_2$ -10CNT.

nanotubes (CNT, 99 mass%, Nanocyl NC7000) were separately dispersed by mixing with 150 mL of ethanol and ultrasonicated for 15 min. The  $\text{TiS}_2$  suspension was finally added to the carbon nanotube/ethanol mixture. Subsequently, the  $\text{TiS}_2$ -CNT suspension was further stirred with tip-sonication for 30 min in ethanol. The mass ratio between  $\text{TiS}_2$  and CNT was 9:1. Afterward, the dispersion was filtered through a glass fiber separator (Millipore, 380  $\mu\text{m}$  thickness, Whatman) and dried at 60  $^\circ\text{C}$  for 5 h to obtain binder-free electrodes. The resulting material was labeled  $\text{TiS}_2$ -10CNT.

**2.2. Structural and Chemical Characterization.** Scanning electron microscope (SEM) images were recorded with a field emission scanning electron microscope (JEOL JSM 7500F) operating at 5 kV. Transmission electron micrographs were taken with a JEOL 2100F transmission electron microscope (TEM) at 200 kV. In the TEM, selected area electron diffraction (SAED) was carried on the electrodes. TEM samples were prepared by dispersing the powders in ethanol and drop-casting them on a copper grid with a lacey carbon film.

Raman spectra were recorded with a Renishaw inVia Raman microscope using an Nd:YAG laser with an excitation wavelength of 532 nm. The spectral resolution was 1.2  $\text{cm}^{-1}$  and the diameter of laser spot on the sample was 2  $\mu\text{m}$  with a power of 0.2 mW. The spectra were recorded for 20 s with 30 accumulations.

XRD was conducted in D8 Advance diffractometer (Bruker AXS) with a copper X-ray source (Cu  $K\alpha$ , 40 kV, 40 mA) and a Goebel mirror in point focus (0.5 mm). We used a VANTEC-500 (Bruker AXS) 2D detector positioned at 2 $\theta$ , 40, 60, and 80 $^\circ$  2 $\theta$  with a measurement time of 16.7 min per step. The sample holder was oscillating in plane (amplitude of 5 mm with a speed of 0.5 mm/s along the  $x$ - and 0.2 mm/s along the  $y$ -axis) to enhance the signal statistics.

Nitrogen gas sorption measurements at  $-196$   $^\circ\text{C}$  were carried out by an Autosorb iQ system (Quantachrome). The samples were degassed at 60  $^\circ\text{C}$  for 10 h under vacuum condition at  $10^2$  Pa. Nitrogen gas sorption was performed under liquid nitrogen in the relative pressure range from  $10^{-4}$  to 1.0 in 40 steps. The Brunauer–Emmett–Teller specific surface area (BET-SSA)<sup>39</sup> was calculated by Quantachrome’s ASiQwin software in the linear relative pressure range of 0.06–0.3. The density functional theory specific surface area (DFT-SSA) and pore size distribution (PSD) were calculated via quenched-solid density functional theory (QSDFT)<sup>40</sup> with a model for slit pores, which is an adequate assumption for activated carbons.<sup>41</sup>

**2.3. Electrochemical Measurements.** The binder-free  $\text{TiS}_2$ -10CNT and  $\text{TiS}_2$  electrodes were cut in a circular shape in diameter of 12 mm (mass of  $\sim 1.8$  mg) and employed as a working electrode. Graphite sheets (SGL Carbon) with a diameter of 12 mm were employed as a current collector. A polytetrafluoroethylene-bound, free-standing activated carbon (YP-80F, Kuraray) disc with an

oversized mass of 30 mg was used as a counter electrode. More details on the preparation of free-standing activated carbon electrodes was reported in our previous work.<sup>42</sup> Glass fiber mat (GF/A, Whatman) was cut into a disk with 13 mm diameter and used as a separator. All compartments were placed in custom-built cells between spring-loaded titanium pistons (see ref 43 for the cell design). An Ag/AgCl (3 M KCl, BASi) reference electrode was mounted at the side channel of the cell where a porous frit of the reference electrode is close to the working and counter electrodes. Afterward, 1 M NaCl was injected by vacuum backfilling. Electrochemical measurements were conducted with a VSP300 potentiostat/galvanostat (Bio-Logic).

Commercially available carbon textile (Kynol-S07-20) was applied in this study as denoted “K20”. The properties of K20 are provided and discussed in the Supporting Information, Figure S1 and in ref 44. After cutting K20 discs with a diameter of 12 mm (9 mg), the material was immersed into 1 M NaCl solution for 20 min for initial wetting. Subsequently, a three-electrode cell was assembled with K20 working electrode with the same cell configuration applied for the  $\text{TiS}_2$ -10CNT and  $\text{TiS}_2$  free-standing electrodes.

The specific capacity ( $C_s$ ) of the working electrode was calculated by using eq 1:

$$C_s = \frac{1}{m} \sum_{t_1}^{t_2} I dt \quad (1)$$

where  $I$  is the applied discharge current,  $t_2 - t_1$  is the discharge time, and  $m$  is the total working electrode mass.

After carefully evaluating K20 and  $\text{TiS}_2$ -10CNT electrodes, the mass ratio of the full cell was adjusted by fixing the mass ratio of K20 to  $\text{TiS}_2$ -10CNT of 3-to-1.  $\text{TiS}_2$ -10CNT electrode (12 mm diameter, 5 mg) was selected as a negative electrode while a double stack of K20 disks (12 mm diameter, 17 mg) was selected as a positive electrode. Graphite sheets were also employed as a current collector with a diameter of 12 mm. Positive and negative electrodes were placed in the cell with spring loaded titanium piston with glass fiber (13 mm diameter) as a separator. One molar NaCl was filled into the assembled cell via back vacuum filling. The as-assembled cell was denoted as  $\text{TiS}_2$ -10CNT//K20. To evaluate the cell performance, cyclic voltammetry and galvanostatic charge–discharge measurements were conducted. The cell capacity was calculated by eq 1 with normalization to the combined mass of positive and negative electrodes. To monitor the potential at zero charge and the electrode potentials, we introduced the Ag/AgCl reference electrode at the side of  $\text{TiS}_2$ -10CNT//K20 cell. The reference electrode serves as a spectator in the cell, enabling potential measurement for each individual electrode during cell operation.

**2.4. Desalination Measurements.** The desalination performance was evaluated in a conventional CDI setup described in ref 42 with flow-by electrodes (per definition of ref 11) quasi-single pass flow operation.<sup>45,46</sup> Briefly,  $\text{TiS}_2$ -10CNT (50–60 mg,  $5 \times 5$   $\text{cm}^2$  per electrode) and K20 (250–260 mg,  $5 \times 5$   $\text{cm}^2$  per electrode) were stacked by having a porous separator (glass fiber prefilter, Millipore, 380  $\mu\text{m}$  thickness) between the electrode. Note the density of  $\text{TiS}_2$ -10CNT is 3.14  $\text{g}/\text{cm}^3$  and that for K20 is 1.12  $\text{g}/\text{cm}^3$ . A graphite sheet was used as a current collector on both sides. The cell was filled with NaCl solution and tightly sealed to avoid dead volume with air. The measurements were carried out with one stack electrode pair. The total mass of the electrodes varied between 300 and 330 mg. Ion removal and release steps were carried out using galvanostatic charge–discharging at 0.1 A/g with cycling cell voltage between 0.2 and 0.8 V. In addition, during charging and discharge, the cell was held at 0.8 V (charge) and 0.2 V (discharge) for 15 min during ion removal and release, respectively. The cell was not discharged to 0 V to prevent the potential of the porous carbon crossing zero charge, which leads to the adsorption of chlorides instead of desorption. This feature may become a regular aspect to consider in the future for hybrid systems employing ion intercalation materials. For all electrochemical operations during desalination, we used a VSP300 potentiostat/galvanostat (Bio-Logic). In addition, experiments were carried out with a flow rate of 22 mL/min at 5, 50, and 600 mM NaCl solution in

a 10 L tank which was flushed continuously with nitrogen gas to remove dissolved oxygen from the water.<sup>47</sup> The 10 L tank NaCl solution assures that the change in concentration of inlet stream is negligible. SAC and charge efficiency were calculated by eqs S1–S5 (Supporting Information).<sup>48</sup> Please note that we use the term SAC because it has become a common term in the field of CDI; this does, however, not indicate that ion removal in our system is just accomplished by adsorption but pertains in our work also ion intercalation (which is not an adsorption process per se). The SAC and the measured charge were defined per mass of total material in both electrodes. Note that normalization by total mass complicates the comparison between different materials with different molar mass in asymmetric device architectures. Therefore, we also provide SAC values normalized to individual mass of the positive and negative electrodes by eq S6 (Supporting Information).

To calculate the energy per removed ion, the energy consumed during removal is determined and divided by the salt removal capacity.<sup>49</sup> This yields the energy consumption in joules per mol of ions removed (J/mol). Also, to obtain the energy in (kT) as the product of the Boltzmann constant and absolute temperature, the calculated energy in (J/mol) is divided by the gas constant and the absolute temperature  $RT$  (2.48 kJ/mol at room temperature).

### 2.5. Online ICP-OES Monitoring of the Desalination Process.

Three stacked electrode pairs containing  $\text{TiS}_2$ -10CNT (three individual electrodes, 160 mg) and K20 (three individual electrodes, 700 mg) were assembled in the CDI cell to enhance the ICP-OES signal. The adsorption and desorption steps were conducted via galvanostatic charge–discharge. During charging, constant specific current of 0.1 A/g was applied by limiting the cell voltage to 0.8 V and holding for 30 min. Afterward, the cell was discharged at a constant specific current of 0.1 A/g to a cell voltage of 0.2 V and held for 30 min. For ICP-OES experiments, the flow rate was 3 mL/min to enhance the signal-to-noise ratio. The saline solution was 50 mM NaCl with a reservoir tank volume of 10 L, which was flushed continuously with  $\text{N}_2$  gas to remove dissolved oxygen. To detect the effluent ion concentration, 2 mL/min of solution was constantly extracted from the outlet stream of the cell by the peristaltic pump of ICP-OES instrument (ARCOS FHX22, SPECTRO Analytical Instruments). The calibration curve was made according to the correlation between the intensity of individual wavelength and the concentration of the solution (Supporting Information, Figure S2). The online intensities from extracted sample were converted into concentration profiles. The ion removal capacity was calculated for sodium and chlorine individually using eq 2:

$$\text{ion removal capacity} \left( \frac{m_{\text{ion}}}{m_{\text{electrode}}} \right) = \frac{\nu M_{\text{ion}}}{m_{\text{electrode}}} \int c dt \quad (2)$$

where  $\nu$  is flow rate (3 mL/min),  $M_{\text{ion}}$  is the molecular weight of ion species (Na: 23 g/mol, Cl: 35.5 g/mol),  $m$  is mass of either positive or negative electrode (mg),  $c$  is the ion concentration of outlet stream (mol/L), and  $t$  is ion removal time (min).

## 3. RESULTS AND DISCUSSION

### 3.1. Structural and Chemical Compositions.

Figure 2A shows the schematic synthesis procedure and Figure 2B–C show scanning electron micrographs of the as-prepared  $\text{TiS}_2$ -10CNT electrode. We observed  $\text{TiS}_2$  particle sizes with a planar size in the range of 20–40  $\mu\text{m}$ . The uniformly distributed  $\text{TiS}_2$  was wrapped by entangled CNTs (Figure 2C–D), which can be beneficial to provide an effective electron pathway throughout the electrode.

The diffractogram of the  $\text{TiS}_2$ -10CNT electrode is shown in Figure 3A with the corresponding 2D diffraction pattern. The diffraction pattern identifies as hexagonal  $\text{TiS}_2$  (PDF 88-1967; space group  $P\bar{3}m1$ ,  $a = 2.9508 \text{ \AA}$ ,  $c = 5.6953 \text{ \AA}$ ). The CNTs contribute only a small diffuse signal around  $26^\circ 2\theta$ . We also see from the Debye rings (esp. for the 001-peak) a preferred

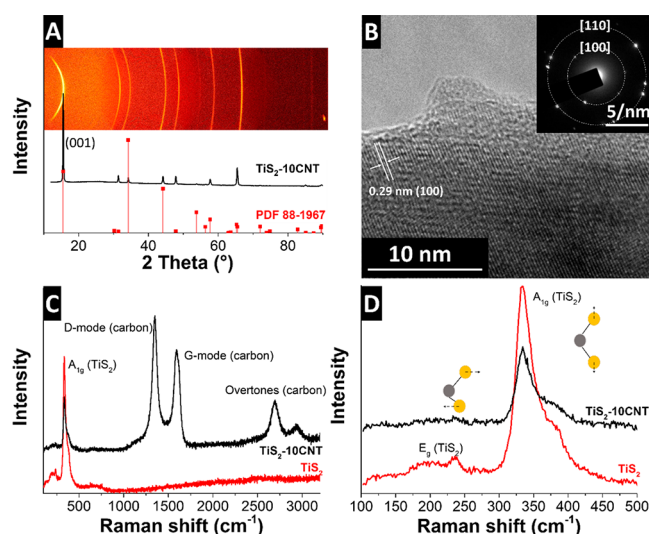


**Figure 3.** (A) X-ray diffractograms with corresponding two-dimensional scattering pattern of  $\text{TiS}_2$ -10CNT, (B) transmission electron micrograph of  $\text{TiS}_2$ -10CNT and selected area electron diffraction pattern, and (C and D) Raman spectra of  $\text{TiS}_2$  and  $\text{TiS}_2$ -10CNT.

(001)-orientation. Transmission electron micrographs reveal the in-plane titanium and sulfur atoms (100-plane) with the distance of 0.29 nm matching well with selected area electron diffraction data (inset Figure 3B). Raman spectra of  $\text{TiS}_2$ -10CNT and  $\text{TiS}_2$  are presented in Figures 3C and D. The characteristic D-band and G-band of CNT are at 1348 and 1592  $\text{cm}^{-1}$ , respectively. The in-plane ( $E_g$ ) and out-plane ( $A_{1g}$ ) vibrations of 1T- $\text{TiS}_2$  are observed at 233 and 332  $\text{cm}^{-1}$ , respectively.<sup>50</sup> Broad peaks around 200 and 380  $\text{cm}^{-1}$  can be assigned to  $\text{TiS}_2$  defects.<sup>51</sup>

### 3.2. Electrochemical Performance in High Concentration Saline Solution.

In the absence of any previous work, we have carried out initial benchmarking of cation intercalation of  $\text{TiS}_2$  in aqueous media. The electrochemical evaluation of  $\text{TiS}_2$ -10CNT and pristine  $\text{TiS}_2$  was carried out in a three-electrode configuration with 1 M NaCl solution. As shown in Figure 4A,  $\text{TiS}_2$ -10CNT was negatively polarized from 0 to  $-0.6 \text{ V}$  vs Ag/AgCl with a scan rate of 1 mV/s. The data show two sharp peaks at  $-0.30$  and  $-0.37 \text{ V}$  vs Ag/AgCl for the negative scan. During the positive scan, two peaks are also detected at  $-0.25$  and  $-0.19 \text{ V}$  vs Ag/AgCl, indicating battery-like ion intercalation behavior with multiple phase transitions. The  $\text{TiS}_2$  electrode was subjected to galvanostatic charge–discharge cycling (Figure 4B). Along the charging and discharging process at 0.1 A/g,  $\text{TiS}_2$ -10CNT exhibits two plateaus at  $-0.30$  and  $-0.37 \text{ V}$  vs Ag/AgCl, which agrees with the data obtained via cyclic voltammetry.

The  $\text{TiS}_2$  electrode gave a maximum specific capacity of 40 mAh/g, which is roughly half that of  $\text{TiS}_2$ -10CNT (68 mAh/g), as determined at a galvanostatic current of 100 mA/g (Figure 4C). CNTs provide an effective conducting network during ion intercalation and deintercalation to enable an optimum electrochemical performance of  $\text{TiS}_2$ .<sup>52</sup> In addition, the entangled CNTs also contribute toward physical structural stability of the electrode during sodiation and desodiation. At a high specific current of 10 A/g,  $\text{TiS}_2$ -10CNT still exhibits a specific capacity of 50 mAh/g (72% retention from the maximum capacity). For comparison, pristine  $\text{TiS}_2$  shows at 10 A/g only 25 mAh/g (62% retention). In the Supporting

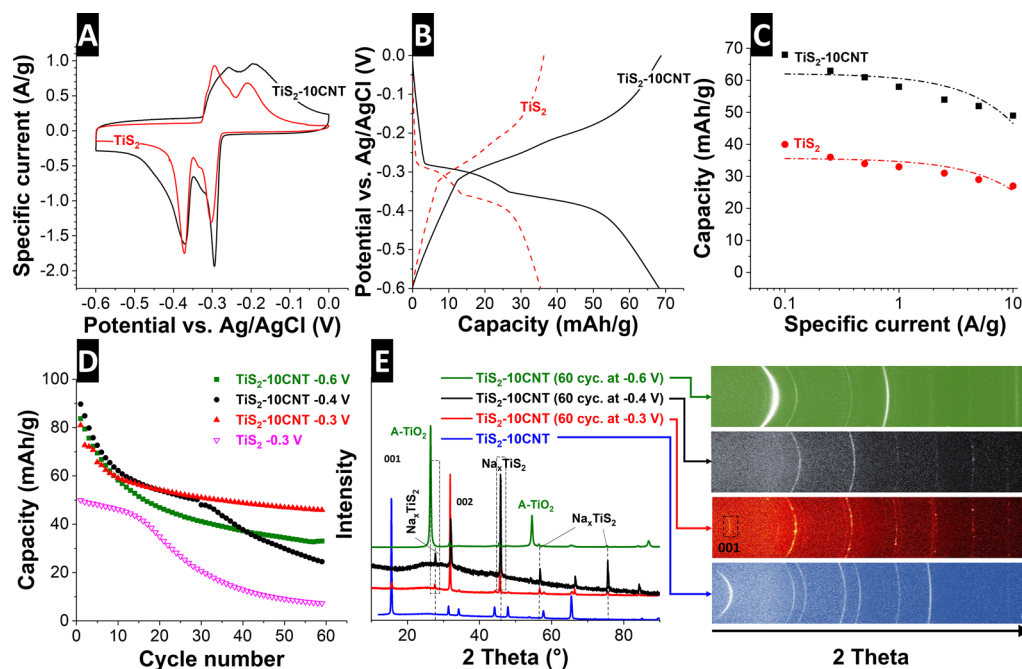


**Figure 4.** (A) Cyclic voltammograms at 1 mV/s, (B) galvanostatic charge–discharge curves at 0.1 A/g, (C) specific capacity versus specific current of the as-prepared  $\text{TiS}_2$ -10CNT and  $\text{TiS}_2$  binder-free electrodes, (D) specific capacity retention of  $\text{TiS}_2$  and  $\text{TiS}_2$ -10CNT electrodes for different potential values, (E) postmortem X-ray diffractogram of desodiated state  $\text{TiS}_2$ -10CNT electrode after 60 cycles and corresponding two-dimensional scattering pattern.

**Information,** further data of the intercalation and deintercalation are shown recorded by postmortem XRD analysis after the electrodes were charged at defined potentials in a three-electrode cell (Figure S3).

Stability testing was assessed via galvanostatic charge–discharge cycling at 0.1 A/g for  $\text{TiS}_2$ -10CNT with various reduction potential limits (Figure 4D).  $\text{TiS}_2$ -10CNT suffers from deep charge at higher negative potential ( $-0.4$  V vs Ag/AgCl), as indicated by poor capacity retentions of 33% for  $-0.6$  V (labeled as  $\text{TiS}_2$ -10CNT  $-0.6$  V) and 27% for  $-0.4$  V; in contrast,  $\text{TiS}_2$ -10CNT at  $-0.3$  V exhibits stable capacity of 50 mAh/g after 15 cycles. The origin of the fast stability degradation at  $-0.6$  V is the phase transition to anatase titania, as evidenced by the postmortem XRD data (Figure 4E).<sup>53</sup> This is further supported by the exfoliated structure observed by SEM images (Supporting Information, Figure S5D). The proposed formation of anatase-type  $\text{TiO}_2$  can be due to the decreasing of local pH.<sup>53</sup> This means that the exfoliated  $\text{TiS}_2$  catalyzed the proton evolution potential, which is expected to occur at  $-0.45$  V vs Ag/AgCl.<sup>54</sup> As a result, the pH near the  $\text{TiS}_2$  surface is slowly decreased by the accumulation of as-produced protons and leads to transformation of  $\text{TiS}_2$  to  $\text{TiO}_2$ .

The capacity decay during continuous cycling operation at  $-0.4$  V (Figure 4D) might originate from a (too) high intercalation/deintercalation depth of  $\text{TiS}_2$ .<sup>55</sup> According to the postmortem XRD analysis for the electrodes collected after the initial cycle (Supporting Information, Figure S3),  $\text{TiS}_2$ -10CNT exhibits a degree of structural expansion at the reduction potential of  $-0.4$  V vs Ag/AgCl higher than that of at  $-0.3$  V vs Ag/AgCl (Supporting Information, Figure S4). The sodiation occurs at potential of  $-0.3$  V vs Ag/AgCl, leading to phase transformation, which is evidenced by the intensified (002) planes (Supporting Information, Figures S3A–C). The fully sodiated state of  $\text{TiS}_2$  appears at  $-0.4$  V vs Ag/AgCl as evidenced by shifting of both (001) and (002) planes toward

larger  $d$ -spacings (Supporting Information, Figure S5, and Supporting Information, Figures S2D–F). After 60 cycles at  $-0.4$  V, the (001) peak disappeared, and we see a weak (002) plane intensity (Figure 4E). This reflects that deep charge state causes volume expansion and disrupts the layered structure of  $\text{TiS}_2$  (Figure 4E and Supporting Information, Figure S5C). In contrast, the presence of (001) is still observed after 60 cycles at  $-0.3$  V vs Ag/AgCl, while reduced intensity compared to that of pristine  $\text{TiS}_2$ -10CNT (Figure 4E) indicates a partial exfoliation of  $\text{TiS}_2$ , as also supported by SEM images (Supporting Information, Figure S5B). Nevertheless, at  $-0.3$  V, the layer structure of  $\text{TiS}_2$  is not further exfoliated, and we see a significant increase in the (002) plane associated with the reordering of  $\text{TiS}_2$  (Supporting Information, Figure S4). In contrast, the intensity of remaining second phase  $\text{Na}_x\text{TiS}_2$  peaks at  $-0.4$  V charging state is much stronger than charging state at  $-0.3$  V. This possibly results from energetically preferable deep intercalation of sodium ions ( $\Delta G^\circ = -48$  kcal/mol at  $x = 1$  for  $\text{TiS}_2 + ne^- + x\text{Na}^+ \rightarrow \text{Na}_x\text{TiS}_2$ ),<sup>56</sup> leading to performance instability during electrochemical cycling.

**3.3. Electrochemical Performance (Aqueous 1 M NaCl).** For electrochemical characterization in realistic conditions, full cells were assembled by coupling  $\text{TiS}_2$ -10CNT (negative electrode) with activated carbon yarn K20 (positive electrode). As the maximum capacity of K20 is 20 mAh/g at 0.1 A/g (Supporting Information, Figure S1F), the mass loading for the positive electrode in the device must be three times higher than that of the  $\text{TiS}_2$ -10CNT electrode. Figure 5A shows the galvanostatic charge–discharge of the device at a current density of 0.1 A/g. It shows plateaus at cell voltages of 0.3 and 0.6 V, which reflects the reversible redox activity of  $\text{TiS}_2$ -10CNT with a Coulombic efficiency of 95%. The cell capacity is measured to be 11 mAh/g (60 mAh/g normalized by  $\text{TiS}_2$ -10CNT mass) at specific current of 10 mA/g<sub>total</sub> and 8 mAh/g at specific current of 1000 mA/g<sub>total</sub>.

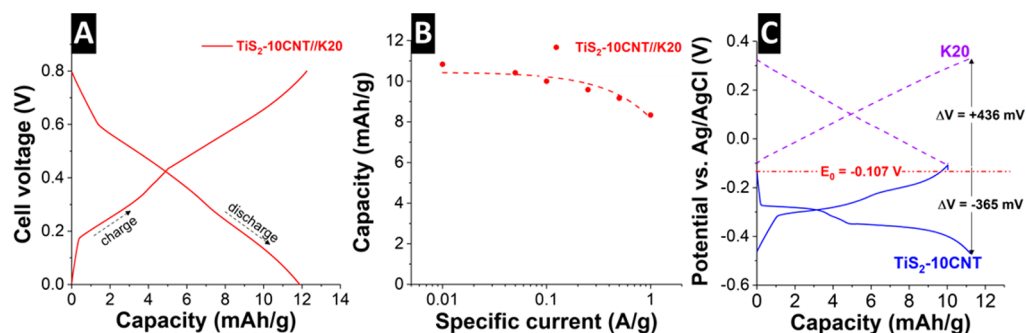


**Figure 5.** Electrochemical cell performance of  $\text{TiS}_2\text{-10CNT//K20}$  (A) galvanostatic charge–discharge cycling at 0.1 A/g, (B) specific capacity versus specific current (dashed line: fitted exponential curve), and (C) potential development of positive and negative electrodes during cell operation from 0 to 0.8 V.

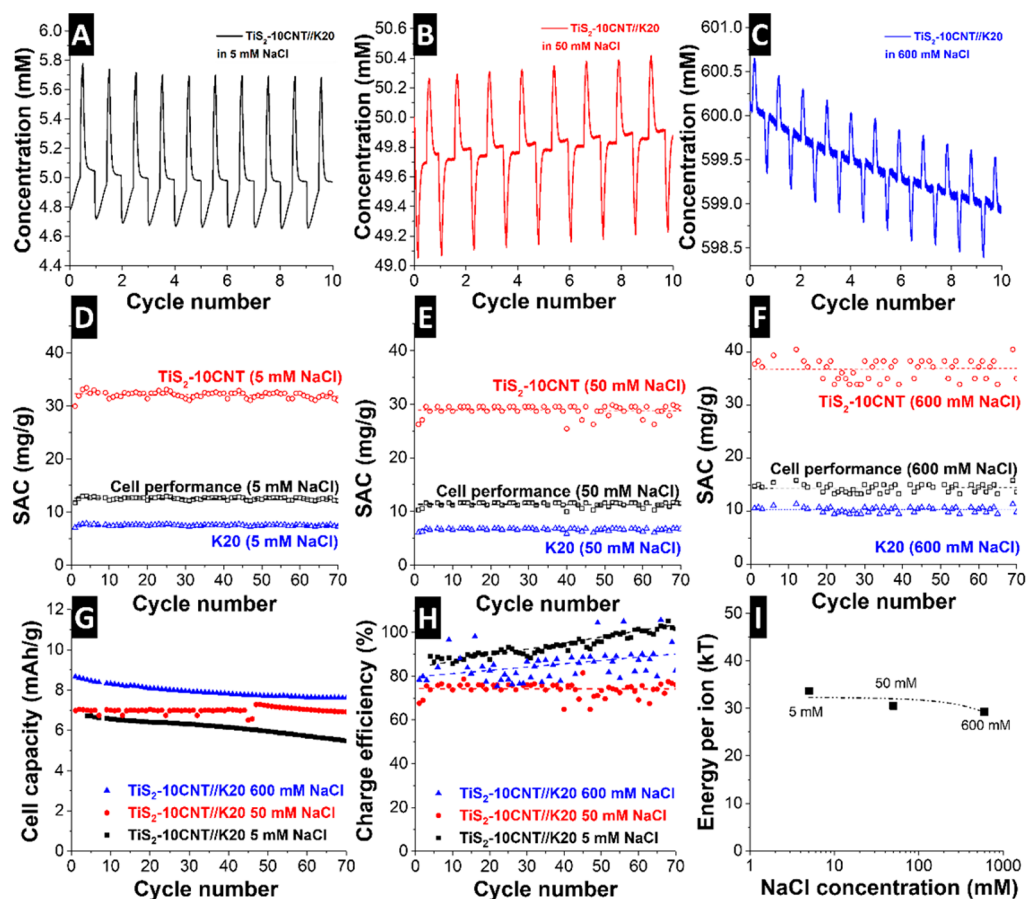


**Figure 6.** Desalination performance of  $\text{TiS}_2\text{-10CNT//K20}$  hybrid faradic deionization (A–C) concentration profile of 5, 50, and 600 mM NaCl; (D–F) SAC over 70 cycles in 5, 50, and 600 mM NaCl; (G) specific capacity; (H) charge efficiency; and (I) energy consumption per ion removal.

This value indicates high capacity retention of 76% at 1000  $\text{mA/g}_{\text{total}}$  (Figure 5B).

The positive and negative electrode potentials were monitored with a Ag/AgCl spectator reference electrode (Figure 5C). It ensures that the potential of  $\text{TiS}_2\text{-10CNT}$  is stable up to cell voltage of 0.8 V; the reduction potential for  $\text{TiS}_2$  is limited to  $-0.4$  V vs Ag/AgCl. The potential at zero charge is  $-107$  mV vs Ag/AgCl and this value suggests preferred cation uptake of the  $\text{TiS}_2\text{-10CNT}$  electrode. This allows us to operate  $\text{TiS}_2\text{-10CNT}$  without applying an ion exchange membrane unlike other HCDCI systems.<sup>24,25</sup>

**3.4. Desalination Performance by Hybrid (Aqueous 5–600 mM NaCl).** Considering the optimized cell perform-

ance of  $\text{TiS}_2\text{-10CNT//K20}$  (11  $\text{mAh/g}$  in 1 M NaCl), we assembled a membrane-free HCDCI cell by using a mass ratio of 5.5:1 (K20: $\text{TiS}_2\text{-10CNT}$ ). The high mass of porous carbon prevents possible side effects of the porous carbon counter electrode through carbon oxidation and oxygen evolution.<sup>57</sup> In addition, the potential of the negative electrode remains within the previously determined stability window. Note that all experiments were conducted without applying an ion exchange membrane; to the best of our knowledge, no hybrid CDI system has been reported without the use of an ion exchange membrane.

The effluent stream concentration is shown in Figures 6A–C. The  $\text{TiS}_2\text{-10CNT//K20}$  cell exhibits salt concentration

**Table 1.** Desalination Capacities for High Concentration Saline Water<sup>a</sup>

material	cell voltage (V)	current	NaCl (mM)	SAC (mg/g)	salt removal (%)	charge efficiency (%)	ref
NMO//Ag	0.7/0 <sup>b</sup>	not available	480		50 <sup>d</sup>	not available	21
NaNiHCF/AEM/NaFeHCF	0.85/0.05	0.1 (A/g)	500	59.9 <sup>e</sup>		90	28
NMO/AEM/AC	1.2/−1.2	54 A/m <sup>2</sup>	100	29.6		not available	25
NTP/AEM/NTP <sup>f</sup>	−0.4/0.4	77 A/m <sup>2</sup>	700		63 <sup>f,e</sup>	not available	27
NiHCF/AEM/NiHCF <sup>f</sup>	−0.4/0.4	54 A/m <sup>2</sup>	700	51		not available	30
MoS <sub>2</sub> (symmetric cell)	1.2/0	not available	400	8.8		not available	33
MoS <sub>2</sub> -10CNT (symmetric cell)	0.8/0	not available	5	10		76	34
		not available	500	25		95	
TiS <sub>2</sub> -10CNT//K20	0.8/0.2	0.1 (A/g)	600	14.5		>85	this work

<sup>a</sup>The values of SAC density were obtained by correcting specific SAC by the material density. NMO = sodium manganese oxide; NaNiHCF = sodium nickel hexacyanoferrate; AEM = anion exchange membrane; NaFeHCF = sodium iron hexacyanoferrate; AC = activated carbon; NTP = sodium titanium phosphate; NiHCF = nickel hexacyanoferrate; CNT = carbon nanotubes; K20 = carbon cloth. <sup>b</sup>The cell voltage was assumed according to the reported potential values for the working and counter electrodes. <sup>c</sup>Double compartment. <sup>d</sup>The percentage of salt removed from the tested solution in the system. <sup>e</sup>Degree of desalination. <sup>f</sup>Calculated value(s).

profiles like a conventional CDI system; that is, sodium and chloride uptake during charging and release of these ions during discharging. While sodium ions are intercalated to the TiS<sub>2</sub>-10CNT, chloride ions are immobilized by electrosorption via the formation of an electrical double-layer in the K20 carbon electrode. Permselective chloride removal is also maintained in absence of any ion exchange membrane even at high concentrations such as 600 mM aqueous NaCl (i.e., synthetic seawater level; Figure 6C). Over 70 cycles, TiS<sub>2</sub>-10CNT//K20 exhibits stable SAC of 11.4, 12.6, and 14.2 mg/g at 5, 50, and 600 mM aqueous NaCl, respectively (Figures 6D–F). If the entire invested charge would perfectly translate to ion uptake (i.e., charge efficiency of 100%), the corresponding SAC values would be 12.6, 14.2, and 15.3 mg/g in 5, 50, and 600 mM aqueous NaCl. Accordingly, our desalination system shows a high charge efficiency of 78–92% over 70 cycles (Coulombic efficiency over 95%). For conventional CDI with two carbon electrodes, achieving such high efficiency and such high desalination values would be impossible at high molar concentration.<sup>19</sup> In addition, high charge efficiency indicates that the potential of positive and negative electrodes remains in the stable regime, as no electro-water splitting occurs during operation. We also avoid the shifting of zero charge potential by discharging the cell always to 0.2 V. As a consequence, we obtain high and stable charge efficiency, and an invert profile (Figures 6A–C) is observed.

The energy consumption of TiS<sub>2</sub>-10CNT//K20 is 0.32 Wh/L in 5 mM NaCl and 1.2 Wh/L in 600 mM NaCl. Considering the salt removal performance, the energy consumption to produce drinkable water (assumed to be <10 mM NaCl solution) is calculated at salt removal of 50% in 600 mM NaCl. Lower values were reported from other FDI systems such as 0.29 Wh/L at salt removal of 30% (equivalent to 0.97 Wh/L at 100% salt removal) for NMO/AgCl system,<sup>21</sup> 1.23 Wh/L at salt removal of 80% (1.5 Wh/L at 100% salt removal) for symmetric NMO system,<sup>27</sup> and 0.34 Wh/L at salt removal of 50% (0.68 Wh/L at 100% salt removal) for the asymmetric NaFeHCF/NaNiHCF system.<sup>28</sup> However, it is important to carefully assess any values provided for the energy consumption in Wh/L because of the strong influence of operation mode, cell engineering, boundary of calculation, and materials. Note that the minimum thermodynamic energy for demixing of seawater (700 mM) is about 1 Wh/L at 50% water salt removal; clearly, energy consumption in the literature is often reported to be lower than theoretical values. The best

comparative values are rather given in energy per removed ion (kT). For example, as reported by Porada et al.,<sup>29</sup> nickel hexacyanoferrate employed in a NID cell shows energy consumption of 12 kT in 20 mM NaCl, while MCDI exhibit a value of 20 kT in 20 mM NaCl. From our measurements for TiS<sub>2</sub>-10CNT//K20, we determined an energy per ion removal of 30–33 kT for brackish water and 29 kT in seawater concentration (Figure 6I). These values are comparable with those of MCDI and CDI (25–35 kT)<sup>49</sup> when operating in brackish water (up to 200 mM). In Table 1, desalination performance values of our cell are compared with literature values of other systems. On the basis of experimental data shown in Table 1, seawater desalination would need to be adapted to scaled versions of our laboratory cell with more electrode mass available to the water treatment process. For example, the TiS<sub>2</sub>-10CNT//K20 system shows a 0.7 mM (0.1%) change in concentration; therefore, the required mass is 400 times (300 mg × 400 = 120 g) higher than our experiment. Yet, the concentration profile in Figure 6C clearly shows that the system can remove the salt in such a highly concentrated solution with an actual flow at 22 mL/min.

For symmetric CDI cells using nanoporous carbon, a normalization for NaCl removal is to be done by using the mass of both electrodes. However, when employing a hybrid cell with different materials for the positive and negative electrode (and in our case, different ion removal mechanisms), the normalization to the mass of both electrodes can mislead the assessment of the actual performance of a single electrode, particularly when the capacity of one electrode is significantly lower than that of the other. It is a common practice to normalize the charge storage capacity to the mass of a single electrode for batteries and supercapacitors.<sup>14</sup> Therefore, we suggest it to be convenient to also normalize the NaCl removal capacity to just one electrode and separately select the sodium or chloride ion depletion capacity (Supporting Information, eq S6). In a system where we must consider only one cation and one anion, such separate calculations are particularly practical and informative. TiS<sub>2</sub> has an intrinsic property to selectively remove sodium ions; thereby, we normalized the amount of removed sodium by the mass of TiS<sub>2</sub>-10CNT electrode. As seen in Figures 6D and E, the sodium ion removal by TiS<sub>2</sub> remains almost constant at 30–40 mg<sub>(Na)g</sub><sup>(negative electrode)</sup> when transitioning from low (5 mM) to high NaCl concentration (600 mM). This value corresponds to a volumetric salt removal capacity of 94.2 mg<sub>(Na)cm</sub><sup>3</sup><sup>(negative electrode)</sup> or 94 g<sub>(Na)/</sub>

$L_{(\text{negative electrode})}$ . In our NaCl system, 1 mol of removed sodium by  $\text{TiS}_2$ -10CNT correlates with 1 mol of removed chloride by the nanoporous carbon electrode. For all concentrations, the chloride removal capacity ranges between 7–10  $\text{mg}_{(\text{Cl})}/\text{g}_{(\text{positive electrode})}$  for the nanoporous carbon electrode or 8.96  $\text{mg}_{(\text{Cl})}/\text{cm}^3_{(\text{positive electrode})}$ .

The data before were based on salt concentration measured by electrical conductivity, which is a well-established method used in the field of CDI. To illustrate the validity of this conventional method, we carried out complementary online monitoring of the Na concentration and Cl concentration separately by ICP-OES. The latter was shown by previous works to be a powerful tool to separate data on the removal of different ions.<sup>58,59</sup> In Figures 7A and B, we exemplify this

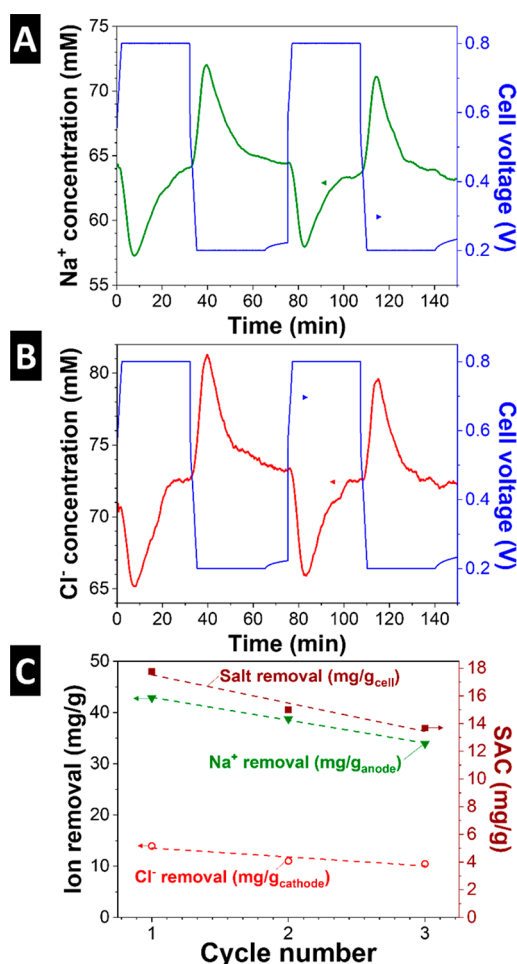


**Figure 7.** Online monitored effluence concentration during desalination via ICP-OES (A) sodium concentration, (B) chloride concentration, and (C) sodium and chloride ion adsorption capacity normalized to mass of the individual negative and positive electrode and salt adsorption capacity corresponding to the mass of both electrodes.

validation for aqueous 50 mM NaCl. While applying a cell voltage of 0.8 V, we clearly see the decreasing concentration of Na<sup>+</sup> and Cl<sup>-</sup>. Correspondingly, we see the release of Na<sup>+</sup> and Cl<sup>-</sup> from the negatively and positively polarized electrodes, respectively, when discharging the cell to 0.2 V. The sodium removal capacity per mass of  $\text{TiS}_2$ -10CNT is 35–39  $\text{mg}_{(\text{Na})}/\text{g}_{(\text{negative electrode})}$ , whereas chloride removal capacity per mass of K20 is 10–14  $\text{mg}_{(\text{Cl})}/\text{g}_{(\text{positive electrode})}$ . This number corresponds

to a total salt removal capacity of 14–17  $\text{mg}_{(\text{NaCl})}/\text{g}_{(\text{both electrodes})}$  of the cell (Figure 7C), which agrees with the value obtained from simple salt concentration measurements depicted in Figures 6D–F. Seemingly, the sodium removal via ion intercalation in  $\text{TiS}_2$  is accompanied by chloride adsorption at the nanoporous carbon. Thereby, we clearly see that the Faradaic charge mechanism at the one electrode forces permselective electrosorption of the porous carbon on the other electrode. Instead of co-ion expulsion or ion swapping, the carbon electrode, in our case, exhibits an effective electrosorption of chloride as being influenced by the sodium intercalation at the other electrode. When not paired with a permselective ion intercalation system but when using just a pair of nanoporous carbon electrodes at such high molar concentration, the system would progressively lose the ability to remove ions from the inflowing water stream.<sup>19,60,61</sup>

Our results show that  $\text{TiS}_2$  allows sodium removal by intercalation mechanisms enabling desalination operation in a typical CDI-cell design for high salt concentration without employing an ion exchange membrane. By this virtue, direct cost will be reduced by no use of membrane. In addition,  $\text{TiS}_2$  can be very interesting for the application in CID systems because these materials have potential for another cation intercalation (i.e., K<sup>+</sup>, and Li<sup>+</sup>). This is in conjunction with the prediction of Smith that cation intercalation materials can also be used for desalination in a broader context, including cation desalination (CID) and electrodialysis (ED).<sup>30</sup>

#### 4. CONCLUSIONS

We introduced hybrid Faradaic desalination with  $\text{TiS}_2$ /CNT hybrid electrodes for cation removal from saline solutions, ranging from brackish to seawater. By this novel approach, it was possible to overcome the intrinsic desalination limitation of conventional CDI with porous carbon posed by co-ion desorption in high molarity. The intrinsic sodium-ion intercalation of  $\text{TiS}_2$  makes it possible to use the activated carbon cloth counter electrode without any ion exchange membrane. The  $\text{TiS}_2$ -10CNT//K20 system showed a salt removal capacity of 14 mg/g in 600 mM NaCl. We also employed a practical and informative way of normalization for battery materials emphasized by in situ desalination ICP-OES. The  $\text{TiS}_2$ -10CNT can effectively remove sodium ions with the capacity of 35.8  $\text{mg}_{(\text{Na})}/\text{g}_{(\text{negative electrode})}$  while K20 shows chloride ion removal of 10  $\text{mg}_{(\text{Cl})}/\text{g}_{(\text{positive electrode})}$ .

#### ■ ASSOCIATED CONTENT

##### Supporting Information

The Supporting Information is available free of charge on the ACS Publications website at DOI: 10.1021/acs.chemmater.7b03363.

Outline of the calculation of salt removal capacity and charge efficiency; supplementary data on the material characterization of activated carbon cloth electrode material; ex situ XRD data; and postmortem scanning electron micrographs investigating the intercalation and deintercalation in  $\text{TiS}_2$  (PDF)

#### ■ AUTHOR INFORMATION

##### Corresponding Author

\*E-mail: volker.presser@leibniz-inm.de.

ORCID 

Volker Presser: 0000-0003-2181-0590

## Notes

The authors declare no competing financial interest.

## ACKNOWLEDGMENTS

The authors gratefully acknowledge financial support by the German Academic Exchange Service (DAAD Award 91579066). The authors thank Prof. Eduard Arzt (INM) for his continuing support. We also thank Ingrid Grobelsek, Simon Fleischmann, Eunho Lim, and Nicolas Jäckel (all at INM) for discussions and technical support. We thank Valeria Lemkova (INM) for her creative graphical assistance.

## REFERENCES

- (1) Stefan Uhlenbrok, R. C. Water and Jobs. *The United Nations Educational, Scientific and Cultural Organization* **2016**, 164.
- (2) Elimelech, M.; Phillip, W. A. The Future of Seawater Desalination: Energy, Technology, and the Environment. *Science* **2011**, *333*, 712–717.
- (3) Charcosset, C. A review of membrane processes and renewable energies for desalination. *Desalination* **2009**, *245*, 214–231.
- (4) Shannon, M. A.; Bohn, P. W.; Elimelech, M.; Georgiadis, J. G.; Marinas, B. J.; Mayes, A. M. Science and technology for water purification in the coming decades. *Nature* **2008**, *452*, 301–310.
- (5) Cath, T. Y.; Childress, A. E.; Elimelech, M. Forward osmosis: Principles, applications, and recent developments. *J. Membr. Sci.* **2006**, *281*, 70–87.
- (6) Lee, K. P.; Arnot, T. C.; Mattia, D. A review of reverse osmosis membrane materials for desalination—Development to date and future potential. *J. Membr. Sci.* **2011**, *370*, 1–22.
- (7) Khawaji, A. D.; Kutubkhanah, I. K.; Wie, J.-M. Advances in seawater desalination technologies. *Desalination* **2008**, *221*, 47–69.
- (8) Arar, Ö.; Yüksel, Ü.; Kabay, N.; Yüksel, M. Various applications of electrodeionization (EDI) method for water treatment—A short review. *Desalination* **2014**, *342*, 16–22.
- (9) Alvarado, L.; Chen, A. Electrodeionization: Principles, Strategies and Applications. *Electrochim. Acta* **2014**, *132*, 583–597.
- (10) Hong, J. G.; Zhang, B.; Glabman, S.; Uzal, N.; Dou, X.; Zhang, H.; Wei, X.; Chen, Y. Potential ion exchange membranes and system performance in reverse electrodialysis for power generation: A review. *J. Membr. Sci.* **2015**, *486*, 71–88.
- (11) Suss, M. E.; Porada, S.; Sun, X.; Biesheuvel, P. M.; Yoon, J.; Presser, V. Water desalination via capacitive deionization: what is it and what can we expect from it? *Energy Environ. Sci.* **2015**, *8*, 2296–2319.
- (12) Porada, S.; Zhao, R.; van der Wal, A.; Presser, V.; Biesheuvel, P. M. Review on the science and technology of water desalination by capacitive deionization. *Prog. Mater. Sci.* **2013**, *58*, 1388–1442.
- (13) Zhao, R.; Porada, S.; Biesheuvel, P. M.; van der Wal, A. Energy consumption in membrane capacitive deionization for different water recoveries and flow rates, and comparison with reverse osmosis. *Desalination* **2013**, *330*, 35–41.
- (14) Béguin, F.; Presser, V.; Balducci, A.; Frackowiak, E. Carbons and Electrolytes for Advanced Supercapacitors. *Adv. Mater.* **2014**, *26*, 2219–2251.
- (15) Liu, Y.; Nie, C.; Liu, X.; Xu, X.; Sun, Z.; Pan, L. Review on carbon-based composite materials for capacitive deionization. *RSC Adv.* **2015**, *5*, 15205–15225.
- (16) Biesheuvel, P. M.; van der Wal, A. Membrane capacitive deionization. *J. Membr. Sci.* **2010**, *346*, 256–262.
- (17) Kim, C.; Lee, J.; Srimuk, P.; Aslan, M.; Presser, V. Concentration-gradient multi-channel flow stream membrane capacitive deionization cell for ultra-high desalination capacity of carbon electrodes. *ChemSusChem* **2017**, DOI: 10.1002/cssc.201700967.
- (18) Kim, C.; Srimuk, P.; Lee, J.; Aslan, M.; Presser, V. Semi-continuous desalination process in capacitive deionization using multi-channel flow stream and ion exchange membranes. *Desalination* **2018**, *425*, 104–110.
- (19) Prehal, C.; Weingarh, D.; Perre, E.; Lechner, R. T.; Amenitsch, H.; Paris, O.; Presser, V. Tracking the structural arrangement of ions in carbon supercapacitor nanopores using in situ small-angle X-ray scattering. *Energy Environ. Sci.* **2015**, *8*, 1725–1735.
- (20) Ding, M.; Shi, W.; Guo, L.; Leong, Z. Y.; Baji, A.; Yang, H. Y. Bimetallic metal-organic framework derived porous carbon nanostructures for high performance membrane capacitive desalination. *J. Mater. Chem. A* **2017**, *5*, 6113–6121.
- (21) Pasta, M.; Wessells, C. D.; Cui, Y.; La Mantia, F. A Desalination Battery. *Nano Lett.* **2012**, *12*, 839–843.
- (22) Chen, F.; Huang, Y.; Guo, L.; Ding, M.; Yang, H. Y. A dual-ion electrochemistry deionization system based on AgCl-Na<sub>0.44</sub>MnO<sub>2</sub> electrodes. *Nanoscale* **2017**, *9*, 10101–10108.
- (23) Kim, S. J.; Ko, S. H.; Kang, K. H.; Han, J. Direct seawater desalination by ion concentration polarization. *Nat. Nanotechnol.* **2010**, *5*, 297.
- (24) Kim, S.; Lee, J.; Kim, C.; Yoon, J. Na<sub>2</sub>FeP<sub>2</sub>O<sub>7</sub> as a Novel Material for Hybrid Capacitive Deionization. *Electrochim. Acta* **2016**, *203*, 265–271.
- (25) Lee, J.; Kim, S.; Kim, C.; Yoon, J. Hybrid capacitive deionization to enhance the desalination performance of capacitive techniques. *Energy Environ. Sci.* **2014**, *7*, 3683–3689.
- (26) Nam, D.-H.; Choi, K.-S. Bismuth as a New Chloride-Storage Electrode Enabling the Construction of a Practical High Capacity Desalination Battery. *J. Am. Chem. Soc.* **2017**, *139*, 11055.
- (27) Smith, K. C.; Dmello, R. Na-Ion Desalination (NID) Enabled by Na-Blocking Membranes and Symmetric Na-Intercalation: Porous-Electrode Modeling. *J. Electrochem. Soc.* **2016**, *163*, A530–A539.
- (28) Lee, J.; Kim, S.; Yoon, J. Rocking Chair Desalination Battery Based on Prussian Blue Electrodes. *ACS Omega* **2017**, *2*, 1653–1659.
- (29) Porada, S.; Shrivastava, A.; Bukowska, P.; Biesheuvel, P. M.; Smith, K. C. Nickel Hexacyanoferrate Electrodes for Continuous Cation Intercalation Desalination of Brackish Water. *Electrochim. Acta* **2017**, *255*, 369–378.
- (30) Smith, K. C. Theoretical evaluation of electrochemical cell architectures using cation intercalation electrodes for desalination. *Electrochim. Acta* **2017**, *230*, 333–341.
- (31) Pomerantseva, E.; Gogotsi, Y. Two-dimensional heterostructures for energy storage. *Nature Energy* **2017**, *2*, 17089.
- (32) Srimuk, P.; Kaasik, F.; Krüner, B.; Tolosa, A.; Fleischmann, S.; Jäckel, N.; Tekeli, M. C.; Aslan, M.; Suss, M. E.; Presser, V. MXene as a novel intercalation-type pseudocapacitive cathode and anode for capacitive deionization. *J. Mater. Chem. A* **2016**, *4*, 18265–18271.
- (33) Xing, F.; Li, T.; Li, J.; Zhu, H.; Wang, N.; Cao, X. Chemically exfoliated MoS<sub>2</sub> for capacitive deionization of saline water. *Nano Energy* **2017**, *31*, 590–595.
- (34) Srimuk, P.; Lee, J.; Fleischmann, S.; Choudhury, S.; Jäckel, N.; Zeiger, M.; Kim, C.; Aslan, M.; Presser, V. Faradaic deionization of brackish and sea water via pseudocapacitive cation and anion intercalation into few layered molybdenum disulfide. *J. Mater. Chem. A* **2017**, *5*, 15640–15649.
- (35) Tan, C.; Zhang, H. Two-dimensional transition metal dichalcogenide nanosheet-based composites. *Chem. Soc. Rev.* **2015**, *44*, 2713–2731.
- (36) Newman, G. H.; Klemann, L. P. Ambient Temperature Cycling of an Na-TiS<sub>2</sub> Cell. *J. Electrochem. Soc.* **1980**, *127*, 2097–2099.
- (37) Liu, Y.; Wang, H.; Cheng, L.; Han, N.; Zhao, F.; Li, P.; Jin, C.; Li, Y. TiS<sub>2</sub> nanoplates: A high-rate and stable electrode material for sodium ion batteries. *Nano Energy* **2016**, *20*, 168–175.
- (38) Ryu, H.-S.; Kim, J.-S.; Park, J.-S.; Park, J.-W.; Kim, K.-W.; Ahn, J.-H.; Nam, T.-H.; Wang, G.; Ahn, H.-J. Electrochemical Properties and Discharge Mechanism of Na/TiS<sub>2</sub> Cells with Liquid Electrolyte at Room Temperature. *J. Electrochem. Soc.* **2013**, *160*, A338–A343.
- (39) Brunauer, S.; Emmett, P. H.; Teller, E. Adsorption of Gases in Multimolecular Layers. *J. Am. Chem. Soc.* **1938**, *60*, 309–319.
- (40) Gor, G. Y.; Thommes, M.; Cychoz, K. A.; Neimark, A. V. Quenched solid density functional theory method for characterization

of mesoporous carbons by nitrogen adsorption. *Carbon* **2012**, *50*, 1583–1590.

(41) Prehal, C.; Koczwara, C.; Jäckel, N.; Amenitsch, H.; Presser, V.; Paris, O. A carbon nanopore model to quantify structure and kinetics of ion electrosorption with in situ small-angle X-ray scattering. *Phys. Chem. Chem. Phys.* **2017**, *19*, 15549–15561.

(42) Aslan, M.; Zeiger, M.; Jäckel, N.; Grobelsek, I.; Weingarh, D.; Presser, V. Improved capacitive deionization performance of mixed hydrophobic/hydrophilic activated carbon electrodes. *J. Phys.: Condens. Matter* **2016**, *28*, 114003.

(43) Lee, J.; Weingarh, D.; Grobelsek, I.; Presser, V. Use of Surfactants for Continuous Operation of Aqueous Electrochemical Flow Capacitors. *Energy Technology* **2016**, *4*, 75–84.

(44) Kim, C.; Srimuk, P.; Lee, J.; Fleischmann, S.; Aslan, M.; Presser, V. Influence of pore structure and cell voltage of activated carbon cloth as a versatile electrode material for capacitive deionization. *Carbon* **2017**, *122*, 329–335.

(45) Lee, J.; Srimuk, P.; Aristizabal, K.; Kim, C.; Choudhury, S.; Nah, Y. C.; Mücklich, F.; Presser, V. Pseudocapacitive desalination of brackish water and seawater via vanadium pentoxide decorated multi-walled carbon nanotubes. *ChemSusChem* **2017**, *10*, 3611.

(46) Porada, S.; Weinstein, L.; Dash, R.; van der Wal, A.; Bryjak, M.; Gogotsi, Y.; Biesheuvel, P. M. Water Desalination Using Capacitive Deionization with Microporous Carbon Electrodes. *ACS Appl. Mater. Interfaces* **2012**, *4*, 1194–1199.

(47) Srimuk, P.; Zeiger, M.; Jäckel, N.; Tolosa, A.; Krüner, B.; Fleischmann, S.; Grobelsek, I.; Aslan, M.; Shvartsev, B.; Suss, M. E.; Presser, V. Enhanced performance stability of carbon/titania hybrid electrodes during capacitive deionization of oxygen saturated saline water. *Electrochim. Acta* **2017**, *224*, 314–328.

(48) Krüner, B.; Srimuk, P.; Fleischmann, S.; Zeiger, M.; Schreiber, A.; Aslan, M.; Quade, A.; Presser, V. Hydrogen-treated, sub-micrometer carbon beads for fast capacitive deionization with high performance stability. *Carbon* **2017**, *117*, 46–54.

(49) Zhao, R.; Biesheuvel, P. M.; van der Wal, A. Energy consumption and constant current operation in membrane capacitive deionization. *Energy Environ. Sci.* **2012**, *5*, 9520–9527.

(50) Xiao, Z.; Yang, Z.; Zhou, L.; Zhang, L.; Wang, R. Highly Conductive Porous Transition Metal Dichalcogenides via Water Steam Etching for High-Performance Lithium-Sulfur Batteries. *ACS Appl. Mater. Interfaces* **2017**, *9*, 18845–18855.

(51) Peters, E. S.; Carmalt, C. J.; Parkin, I. P. Dual-source chemical vapour deposition of titanium sulfide thin films from tetrakisdimethylamidotitanium and sulfur precursors. *J. Mater. Chem.* **2004**, *14*, 3474–3477.

(52) He, Z.; Jiang, Y.; Sun, D.; Dai, L.; Wang, H. Advanced  $\text{LiTi}_2(\text{PO}_4)_3/\text{C}$  anode by incorporation of carbon nanotubes for aqueous lithium-ion batteries. *Ionics* **2017**, *23*, 575–583.

(53) Lim, Y. W. L.; Tang, Y.; Cheng, Y. H.; Chen, Z. Morphology, crystal structure and adsorption performance of hydrothermally synthesized titania and titanate nanostructures. *Nanoscale* **2010**, *2*, 2751–2757.

(54) Zeng, Z.; Tan, C.; Huang, X.; Bao, S.; Zhang, H. Growth of noble metal nanoparticles on single-layer  $\text{TiS}_2$  and  $\text{TaS}_2$  nanosheets for hydrogen evolution reaction. *Energy Environ. Sci.* **2014**, *7*, 797–803.

(55) Seidl, L.; Bucher, N.; Chu, E. M. L.; Hartung, S.; Martens, S.; Schneider, O.; Stimming, U. Intercalation of solvated Na-ions into graphite. *Energy Environ. Sci.* **2017**, *10*, 1631–1642.

(56) Nagelberg, A. S.; Worrell, W. L. A thermodynamic study of sodium-intercalated  $\text{TaS}_2$  and  $\text{TiS}_2$ . *J. Solid State Chem.* **1979**, *29*, 345–354.

(57) He, D.; Wong, C. E.; Tang, W.; Kovalsky, P.; Waite, T. D. Faradaic Reactions in Water Desalination by Batch-Mode Capacitive Deionization. *Environ. Sci. Technol. Lett.* **2016**, *3*, 222–226.

(58) Zhao, R.; van Soestbergen, M.; Rijnaarts, H. H. M.; van der Wal, A.; Bazant, M. Z.; Biesheuvel, P. M. Time-dependent ion selectivity in capacitive charging of porous electrodes. *J. Colloid Interface Sci.* **2012**, *384*, 38–44.

(59) Dykstra, J. E.; Dijkstra, J.; van der Wal, A.; Hamelers, H. V. M.; Porada, S. On-line method to study dynamics of ion adsorption from mixtures of salts in capacitive deionization. *Desalination* **2016**, *390*, 47–52.

(60) Shpigel, N.; Levi, M. D.; Sigalov, S.; Aurbach, D.; Daikhin, L.; Presser, V. Novel in situ multiharmonic EQCM-D approach to characterize complex carbon pore architectures for capacitive deionization of brackish water. *J. Phys.: Condens. Matter* **2016**, *28*, 114001.

(61) Biesheuvel, P. M.; Porada, S.; Levi, M.; Bazant, M. Z. Attractive forces in microporous carbon electrodes for capacitive deionization. *J. Solid State Electrochem.* **2014**, *18*, 1365–1376.

# Titanium disulfide: a promising low-dimensional electrode material for sodium ion intercalation for sea water desalination

Pattarachai Srimuk<sup>1,2</sup>, Juhan Lee<sup>1,2</sup>, Aura Tolosa<sup>1,2</sup>,  
Choonsoo Kim<sup>1</sup>, Mesut Aslan<sup>1</sup>, Volker Presser<sup>1,2,\*</sup>

<sup>1</sup>... INM - Leibniz Institute for New Materials, Saarbrücken, Germany

<sup>2</sup>... Department of Materials Science and Engineering, Saarland University, Saarbrücken, Germany

\*... Corresponding author's email address: [volker.presser@leibniz-inm.de](mailto:volker.presser@leibniz-inm.de)

## *Supporting Information*

### **Calculation of salt adsorption capacity and charge efficiency**

$$SAC = \frac{v \cdot M_{NaCl}}{m_{total}} \int c dt \quad \text{Equation (S1)}$$

in this equation,  $v$  is the flow rate (mL/min),  $M_{NaCl}$  is molecular weight of NaCl (58.44 g/mol),  $m_{total}$  is total mass of electrodes (g),  $t$  is the time over the adsorption step (min), and  $c$  is the concentration of NaCl (mmol/L).

The concentration of NaCl is calculated by relation of concentration and conductivity:

$$c = \left( \frac{\sigma - 4.5}{121.29} \right)^{1/0.9826} - 0.13 \quad \text{Equation (S2)}$$

where  $\sigma$  is the corrected conductivity ( $\mu\text{S}/\text{cm}$ ) which adjusts the measured conductivity  $\sigma_m$  by the measured pH value:

$$\sigma = \sigma_m - \sigma_w \quad \text{Equation (S3)}$$

where  $\sigma_m$  is the measured conductivity (mS/cm) and  $\sigma_w$  is the conductivity of water via:

$$\sigma_w = \frac{e^2}{k_B T} \left( 10^{pH} \cdot N_A \cdot D_{H_3O^+} + \frac{10^{-14}}{10^{-pH}} \cdot N_A \cdot D_{OH^-} \right) \quad \text{Equation (S4)}$$

where  $k_B$  is Boltzmann constant ( $1.38 \cdot 10^{-23} \text{ m}^2 \text{ kg} / \text{s}^2 \text{ K}$ ),  $N_A$  is Avogadro constant ( $6.02 \cdot 10^{23} \text{ mol}^{-1}$ ),  $D_{H_3O^+}$  is diffusion coefficient of hydronium ion ( $9.3 \cdot 10^{-9} \text{ m}^2 / \text{s}$ ), and  $D_{OH^-}$  is the diffusion coefficient of a hydroxyl ion ( $5.3 \cdot 10^{-9} \text{ m}^2 / \text{s}$ ).

$$\text{Charge efficiency (\%)} = \left( \frac{\frac{SAC \left( \frac{mg}{g} \right)}{M_{NaCl} \left( \frac{g}{mol} \right)}}{\frac{\text{Specific capacitance} \left( \frac{C}{g \cdot V} \right) \cdot \text{Cell voltage (V)}}{4 \cdot \text{Faraday constant} \left( \frac{C}{mol} \right)}} \right) \cdot 100 \quad \text{Equation (S5)}$$

### **Calculation of salt adsorption capacity per-half cell**

$$SAC = \frac{v \cdot M_{Na/Cl}}{m_{pos/neg}} \int c dt \quad \text{Equation (S6)}$$

In this equation,  $v$  is the flow rate (mL/min),  $M_{Na/Cl}$  is molecular weight of Na (22.98 g/mol) or Cl (35.44 g/mol),  $m_{pos/neg}$  is total mass of electrodes cathode or anode (g),  $t$  is the time over the adsorption step (min), and  $c$  is the concentration of NaCl (mmol/L).

### Characterization of activated carbon textile (K20)

Commercially available activated carbon textile Kynol-507-20 (K20) is derived from a polymer resin by carbonization and a subsequent activation process. The carbon fibers have a diameter of 10-15  $\mu\text{m}$  (insert **Figure S1A**) and are woven into yarns of ca. 200  $\mu\text{m}$  (**Figure S1A**). The nitrogen sorption isotherm seen in **Figure S1B** is of type I(b) indicative of slit-shaped pore. The specific DFT surface area of K20 is 1870  $\text{m}^2/\text{g}$  (BET surface area: 2200  $\text{m}^2/\text{g}$ ) with a total pore volume of 0.89  $\text{cm}^3/\text{g}$  (**Figure S1C**).

To investigate the electrochemical charge storage performance, a K20 electrode was tested in half-cell configuration. As shown in **Figure S1D**, a K20 electrode was scanned from 0 to +0.6 V vs. Ag/AgCl with a sweep rate of 1 mV/s. The corresponding cyclic voltammogram has a rectangular shape representative of supercapacitor behavior. This is also shown from the linear galvanostatic charge-discharge profile at a specific current of 0.1 A/g seen in **Figure S1E**. The specific capacity at 0.6 V is 20 mAh/g (120 F/g) with a Coulombic efficiency of 98% (**Figure S1E**). As the specific current is increased from 0.1 A/g to 10 A/g (**Figure S1F**), the specific capacity is reduced to ca. 2 mAh/g. This performance aligns with the large diameter of the activated carbon cloth fibers of several micrometers.

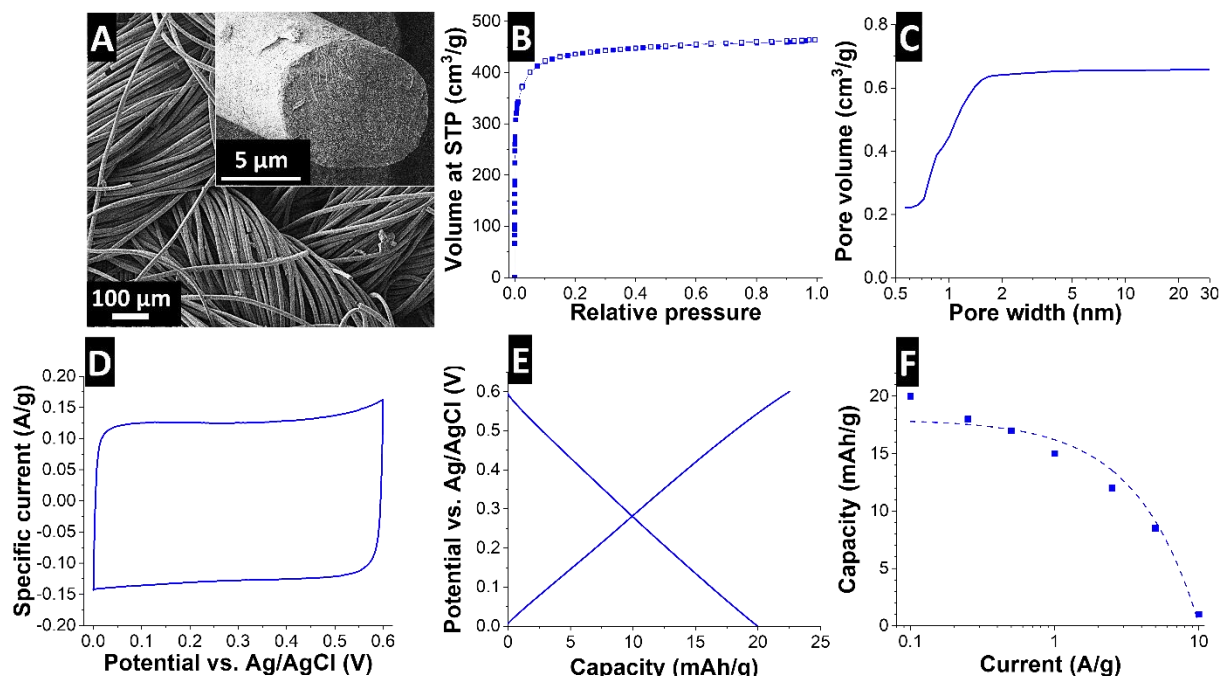


**Figure S1.** (A) Scanning electron micrograph of activated carbon cloth (K20), (B) nitrogen sorption isotherm at -196  $^{\circ}\text{C}$ , (C) cumulative pore size distribution per pore volume, (D) cyclic voltammogram of K20 in half-cell configuration at 1 mV/s, (E) galvanostatic charge-discharge at 0.1 A/g, and (F) specific capacity versus specific current of K20.

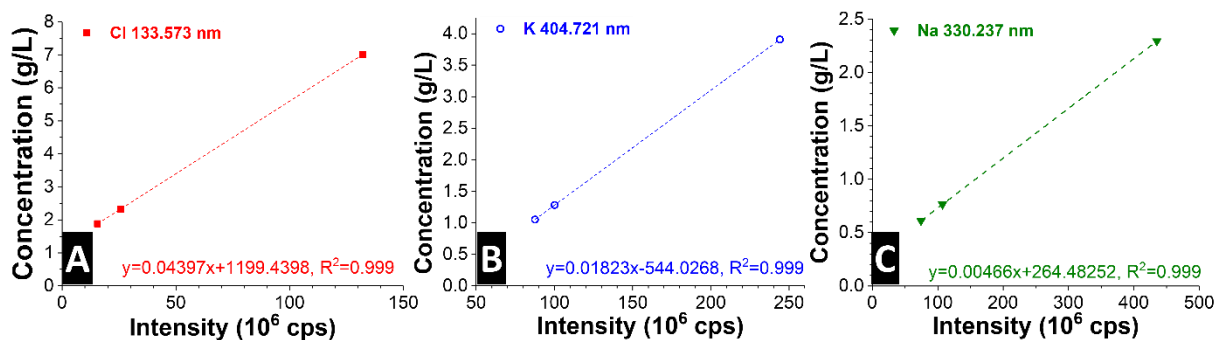


**Figure S2** Calibration curves (i.e., the relation of ion concentration and characteristic peak intensity) of chloride (A), potassium (B), and sodium (C).

### ***Intercalation and deintercalation of $\text{TiS}_2$ via ex-situ XRD***

When  $\text{TiS}_2$ -10CNT is operated at -0.3 V vs. Ag/AgCl, the (001)- $\text{TiS}_2$  peak is shifted to lower angle from 15.57 to 15.49 ° 2 $\theta$  (**Figure S3B**), which is possibly affected by the intensifying of (002) plane (**Figure S3C**). This indicates interlayer expansion of 2.87 Å along the *c*-axis. When the  $\text{TiS}_2$ -10CNT electrode is reduced to -0.4 V, the interspacing expansion is more pronounced compared to that of at -0.3 V. The (001) peak is shifted towards low and high angles after reduction to -0.4 V and oxidation to 0 V (**Figure S3E**), corresponding to the enhanced interlayer expansion and compaction of +0.02 and 0.07 Å at (001) plane, respectively. The reduced interlayer distance also aligns with the change in lattice of (002) plane from 2.82 Å to 2.79 Å (**Figure S3F**). In case of further deep reduction (-0.6 V vs. Ag/AgCl), the (001)- and (002) planes show similar shifting as that of at -0.4 V vs. Ag/AgCl. This reflects that interspacing is not influenced by the stage of charge above -0.4 V. However, the structure transformation during intercalation-deintercalation does not only increase the spacing along the *c*-axis and we also observed deviations of the (100)-plane. This is in conjunction with the appearance of new diffraction peaks from  $\text{Na}_x\text{TiS}_2$ , where  $0 < x < 1$  (**Figure S3A,D,G**).

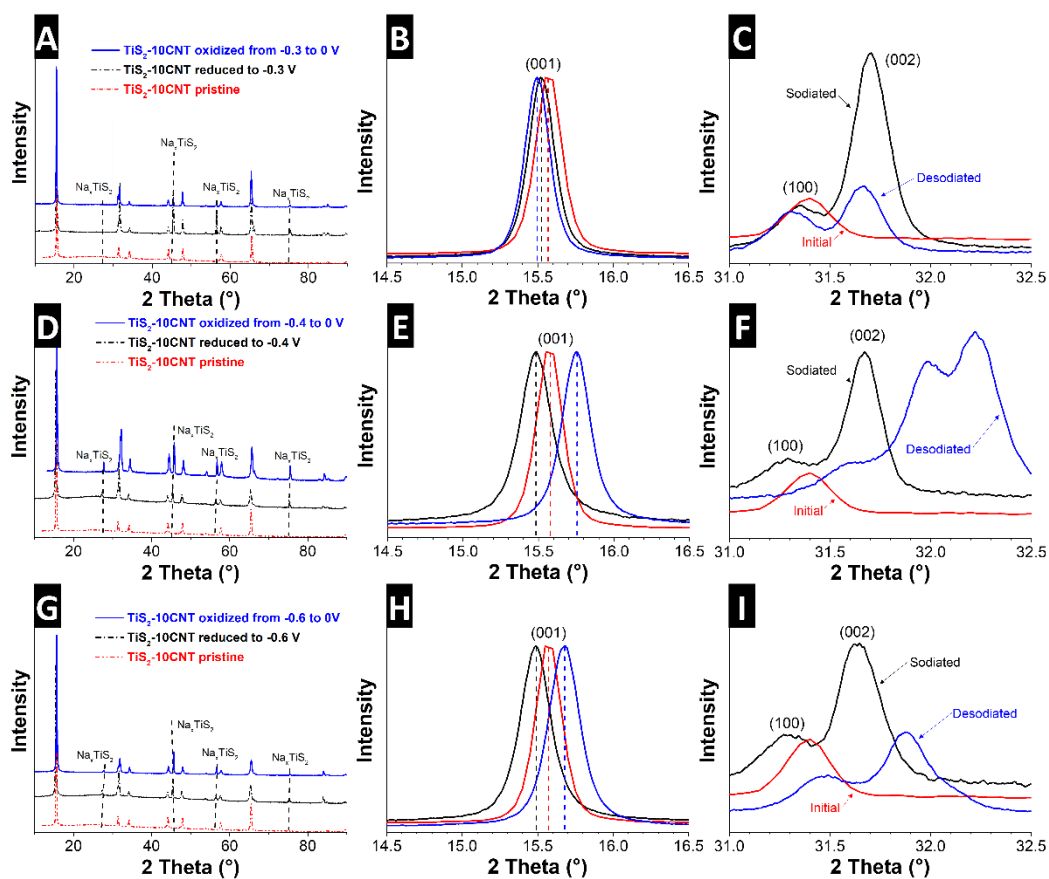


**Figure S3** Ex-situ X-ray diffractogram of  $\text{TiS}_2$ -10CNT electrodes (A-C) 1<sup>st</sup> cycle reduced at -0.3 V and oxidized at 0 V, (D-F) 1<sup>st</sup> cycle reduced at -0.4 V and oxidized at 0 V, and (G-I) 1<sup>st</sup> cycle reduced at -0.6 V and oxidized at 0 V.

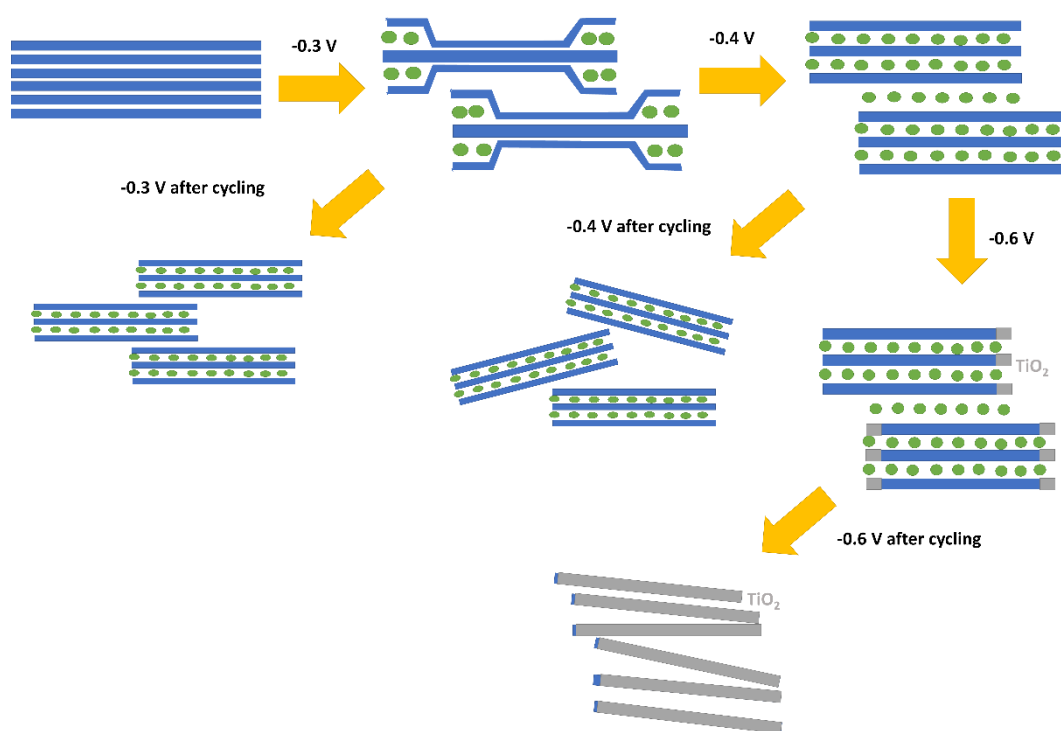


**Figure S4:** Sodium intercalation into  $\text{TiS}_2$  layers at different potentials.

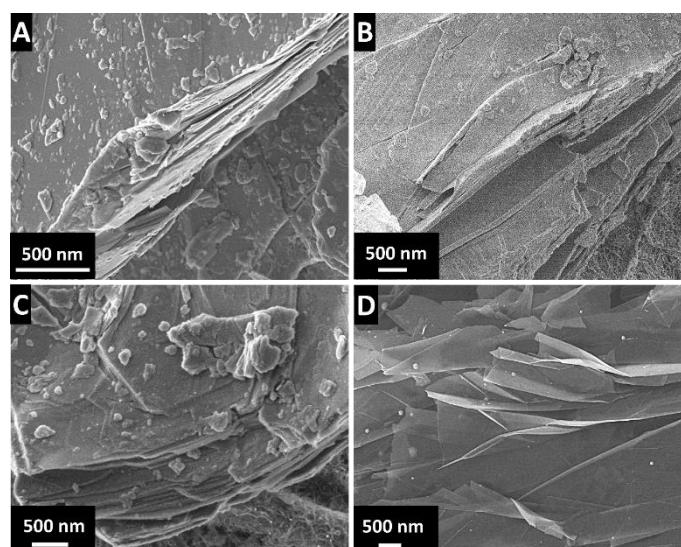


**Figure S5.** Scanning electron micrographs of (A)  $\text{TiS}_2$ -10CNT electrode, (B)  $\text{TiS}_2$ -10CNT after -0.3 V for sixty cycles, (C)  $\text{TiS}_2$ -10CNT after -0.4 V for sixty cycles, and (D)  $\text{TiS}_2$ -10CNT after -0.6 V (also) for sixty cycles.

## 4.7 Potential-dependent, switchable ion selectivity in aqueous media using titanium disulfide

Pattarachai Srimuk,<sup>1,2</sup> Juhan Lee,<sup>1,2</sup> Simon Fleischmann,<sup>1,2</sup>

Mesut Aslan,<sup>1</sup> Choonsoo Kim,<sup>1</sup> Volker Presser<sup>1,2</sup>

<sup>1</sup> INM - Leibniz Institute for New Materials, 66123 Saarbrücken, Germany

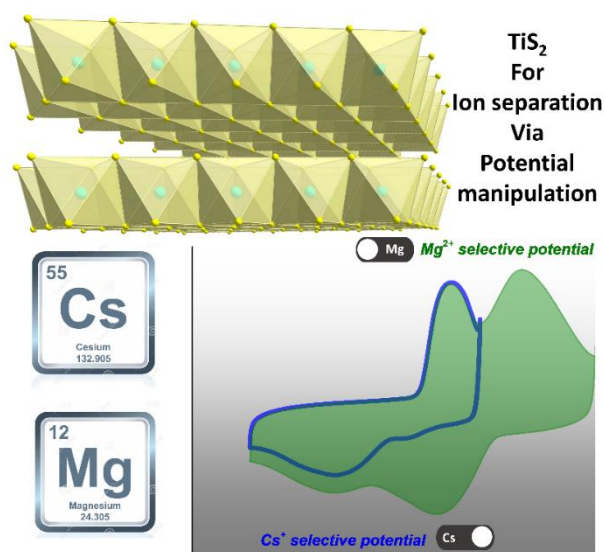
<sup>2</sup> Saarland University, Campus D2 2, 66123 Saarbrücken, Germany

### Citation:

P. Srimuk, J. Lee, S. Fleischmann, M. Aslan, C. Kim, V. Presser, POTENTIAL-DEPENDENT, SWITCHABLE ION SELECTIVITY IN AQUEOUS MEDIA USING TITANIUM DISULFIDE, ChemSusChem 11(13) (2018) 1-11.

### Own contribution:

Electrochemistry, CDI, ICP, analysis, writing



# Potential-Dependent, Switchable Ion Selectivity in Aqueous Media Using Titanium Disulfide

Pattarachai Srimuk<sup>+, [a, b]</sup>, Juhan Lee<sup>+, [a, b]</sup>, Simon Fleischmann,<sup>[a, b]</sup> Mesut Aslan,<sup>[a]</sup> Choonsoo Kim,<sup>[a]</sup> and Volker Presser<sup>\*, [a, b]</sup>

The selective removal of ions by an electrochemical process is a promising approach to enable various water-treatment applications such as water softening or heavy-metal removal. Ion intercalation materials have been investigated for their intrinsic ability to prefer one specific ion over others, showing a preference for (small) monovalent ions over multivalent species. In this work, we present a fundamentally different approach: tunable ion selectivity not by modifying the electrode material, but by changing the operational voltage. We used titanium disulfide, which shows distinctly different potentials for the intercalation of different cations and formed binder-free composite

electrodes with carbon nanotubes. Capitalizing on this potential difference, we demonstrated controllable cation selectivity by online monitoring the effluent stream during electrochemical operation by inductively coupled plasma optical emission spectrometry of aqueous 50 mM CsCl and MgCl<sub>2</sub>. We obtained a molar selectivity of Mg<sup>2+</sup> over Cs<sup>+</sup> of 31 (strong Mg preference) in the potential range between -396 mV and -220 mV versus Ag/AgCl. By adjusting the operational potential window from -219 mV to +26 mV versus Ag/AgCl, Cs<sup>+</sup> was preferred over Mg<sup>2+</sup> by 1.7 times (Cs preference).

## Introduction

The development and utilization of energy-efficient water treatment technologies remain key challenges for a sustainable future. The ability to control the concentration of water-dissolved ions is critical for the generation of drinking water, ensuring process stability in chemical and pharmaceutical production, accomplishing remediation of polluted environmental water, and constitutes the core aspect of ion separation technologies. Accordingly, a wealth of different technologies has appeared in the literature, including reverse osmosis (RO),<sup>[1,2]</sup> thermal adsorption processes,<sup>[3,4]</sup> pH-dependent ion-exchange methods,<sup>[5,6]</sup> and electrochemical processes.<sup>[7,8]</sup> Among them, electrochemical processes are of particular interest owing to potentially high energy efficiency and performance longevity.<sup>[9]</sup>

From a process point of view, electrochemistry may be employed for i) general reduction of the ion concentration (desalination) or ii) selective separation of certain ions from a mixture of different ionic species in water (Figure 1). For desalination, electrochemical concepts such as electrodialysis,<sup>[8]</sup> capacitive deionization (CDI),<sup>[7,10-12]</sup> or battery desalination technologies<sup>[13-16]</sup> are particularly attractive. In the case of electrodialysis

(Figure 1A), desalination is achieved by selective diffusion of ions through ion-selective membranes such as cation- or anion-exchange membranes. As the ions migrate to balance the charge at the interface between the electrode and electrolyte (Figure 1A), a voltage difference exceeding the theoretical limit for water is needed to obtain a sufficient driving force for ion migration. Consequently, the overall energy recovery is small (state-of-the-art is about 30%)<sup>[17]</sup> as significant amounts of charge is consumed by irreversible reactions, including water splitting. Unlike electrodialysis, CDI relies on non-faradaic ion electroadsorption on the surface of nanoporous carbon, which electrochemically behaves like a double-layer capacitor (Figure 1B).<sup>[18]</sup> Effective ion removal with CDI is limited to very low concentrations, typically below 50 mM because of concurrent non-permselective co-ion expulsion and counter-ion adsorption in concentrated solutions.<sup>[19]</sup> Compared to electrodialysis, CDI is more energy efficient; however, electrodialysis can operate effectively at much higher concentrations than CDI. To overcome the low-concentration limitation of CDI, desalination with Faradaic materials (battery electrodes; Figure 1C) has emerged, in which ions are removed by insertion or intercalation into the bulk electrode (e.g., intercalation in MoS<sub>2</sub> or sodium manganese oxide)<sup>[13,14,16,20]</sup> or conversion reactions (e.g., Ag/AgCl reaction).<sup>[21]</sup>

With electrochemistry, it is also possible to achieve ion separation.<sup>[22-24]</sup> First, ion intercalation materials have been shown to exhibit intrinsic cation selectivity (e.g., sodium manganese oxide; Figure 1D).<sup>[13]</sup> The term intrinsic relates to the ability of such intercalation materials to prefer a certain cation over others, typically giving monovalent cations preference over multivalent cations and smaller cations preference over larger

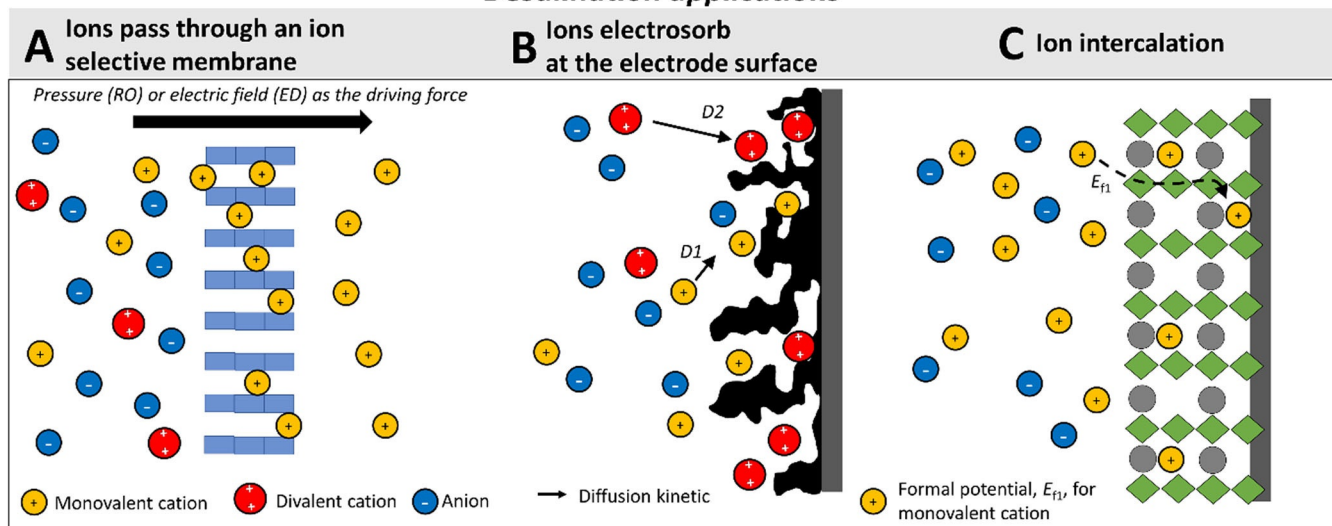
[a] P. Srimuk,<sup>+</sup> J. Lee,<sup>+</sup> S. Fleischmann, Dr. M. Aslan, Dr. C. Kim, Prof. V. Presser  
INM—Leibniz Institute for New Materials  
Saarbrücken (Germany)  
E-mail: volker.presser@leibniz-inm.de

[b] P. Srimuk,<sup>+</sup> J. Lee,<sup>+</sup> S. Fleischmann, Prof. V. Presser  
Department of Materials Science and Engineering, Saarland University  
Saarbrücken (Germany)

[\*] These authors contributed equally.

Supporting Information and the ORCID identification number(s) for the author(s) of this article can be found under:  
<https://doi.org/10.1002/cssc.201800452>.

### Desalination applications



### Separation applications

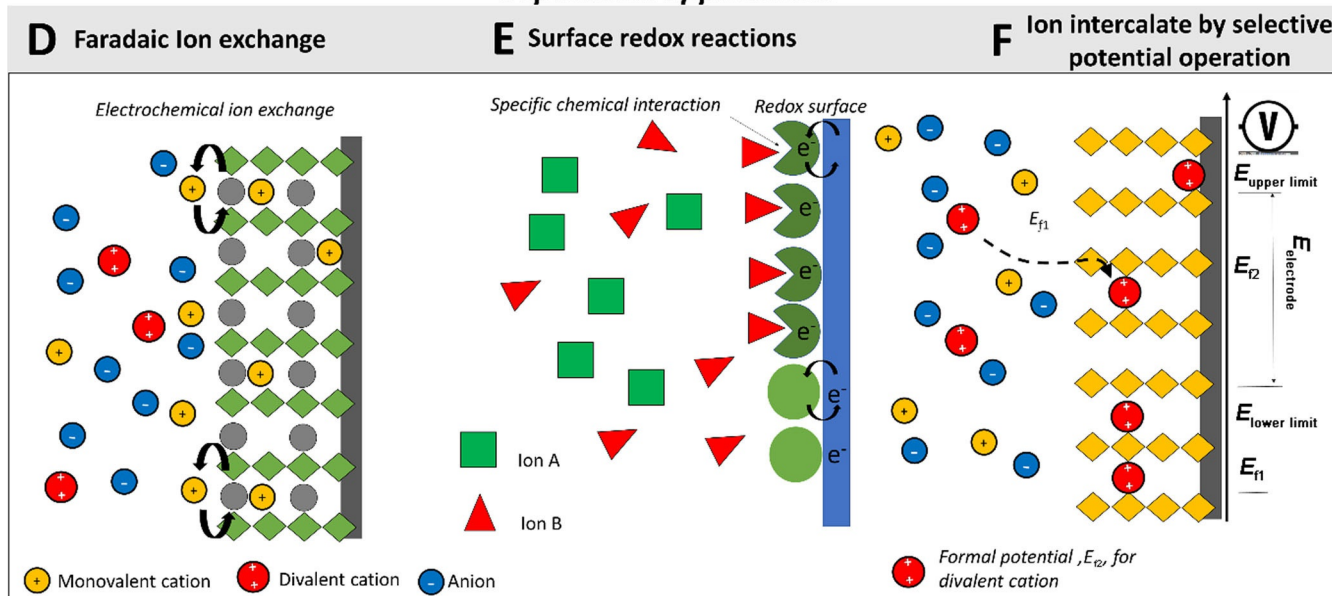


**Figure 1.** Overview of electrochemical separation technologies: (A) electrodialysis, (B) capacitive deionization (kinetic and size selectivity), (C) desalination battery, (D) electrochemical ionic exchange, (E) redox-mediated electroseparation, and (F) potential-controlled electroseparation. ED: electrodialysis; RO: reverse osmosis; D1, D2: diffusion path of monovalent and divalent ions.

cations.<sup>[25–27]</sup> It originates from the nature of ion insertion or intercalation, which is strongly dependent on the material's crystal structure. The crystallographic site at which ion uptake occurs is dependent on the type and size of ion involved.<sup>[25,26,28–34]</sup> Second, separating cations and anions or monovalent and divalent cations can also be accomplished by using an ion-selective membrane during electrodialysis.<sup>[35–37]</sup> However, the latter is insufficient to separate ions in more complex multi-ion systems because it highly relies on the pore size and chemical charges of the membrane. Third, without intercalation and ion exchange membranes, ion separation can also be accomplished by capitalizing on differences in the sorption kinetics of ions during electrosorption in a CDI cell

(Figure 1B).<sup>[38]</sup> For example, monovalent ions are initially preferred, but they become continuously replaced by divalent ions over time in the system  $\text{Na}^+/\text{Ca}^{2+}$ , leading to a  $\text{Ca}^{2+}$  molar selectivity over  $\text{Na}^+$  of approximately 5 (Figure 1B).<sup>[38–40]</sup> Approaches based on ion sorption and replacement kinetics during CDI operation suffer from a low degree of separation.<sup>[38,39]</sup> By modifying the surface functional groups of carbon, it is possible to separate heavy metal ions and alkaline ions. For example, Peiying et al. paired graphene grafted with ethylenediamine triacetic acid and unmodified graphene to obtain a mass-normalized preference for  $\text{Pb}^{2+}$  removal over  $\text{Na}^+$  electroadsorption ions by 0.21 ( $\text{Pb}^{2+}/\text{Na}^+$ ).<sup>[41]</sup> The fourth approach for ion separation employs electrochemical surface

redox reactions (Figure 1E).<sup>[9,32]</sup> This results in a high degree of selectivity ( $> 100$ ) for certain ions because the system is designed to accept a certain ion; however, this technique still suffers from water splitting and is mostly used for organic ion removal.<sup>[9,32,42]</sup>

All these technologies share one central feature: once the electrode materials or membranes are selected, the systems are only suitable for one specific ionic system. However, for a flexible and more adaptive separation process, a technology with tunable selectivity by controlling the process conditions would be preferable. For example, manipulating the cell voltage to select a specific ion to be preferably removed (Figure 1F). In this work, we provide the first proof-of-concept of switchable electrochemical cation selectivity. We used free-standing titanium disulfide/carbon nanotube electrodes, which show a pronounced potential-dependent ion selectivity with clearly identifiable intercalation peaks. Our work specifically exemplifies the controllable preference of  $\text{Cs}^+$  over  $\text{Mg}^{2+}$ , which can be switched to a preference of  $\text{Mg}^{2+}$  over  $\text{Cs}^+$  by adjusting the applied voltage. In addition to electrochemical and material characterization, we used the Nernst equation to identify the formal potential  $E_f$  that is used to predict the selective potential, enabling the precise ion selection (i.e.,  $\text{Cs}^+$  or  $\text{Mg}^{2+}$ ) through variation of the electrode potential.

## Results and Discussion

### Structural characterization of the electrodes

The  $\text{TiS}_2$ -10CNT (composite of  $\text{TiS}_2$  and carbon nanotubes (CNTs) with a constant mass ratio of 9:1) binder-free electrodes were prepared by filtration according to our previous publication.<sup>[43]</sup> SEM and TEM micrographs of the binder-free  $\text{TiS}_2$ -10CNT electrode (Figure S2A and B in the Supporting Information) show CNTs wrapped around  $\text{TiS}_2$  sheets. This is an important feature to ensure electrode integrity of individual  $\text{TiS}_2$  sheets during desalination and sufficient electrical conductivity throughout the electrode.<sup>[16,43]</sup> As confirmed by the four-point probe conductivity measurements, the electronic conductivity of  $\text{TiS}_2$  was very low ( $< 10^{-4}$  S cm, which was the detection limit of the measuring device) compared to that of  $\text{TiS}_2$ -10CNT ( $6.3 \pm 2.3$  S cm). The Raman spectrum of the  $\text{TiS}_2$ -10CNT electrode (Figure S2C) shows the characteristic peaks of CNTs and  $\text{TiS}_2$ . The D-band and G-band peaks of carbon were observed at 1348 and 1592  $\text{cm}^{-1}$ , respectively. The peaks at 233 and 332  $\text{cm}^{-1}$  correspond to in-plane and out-of-plane Ti-S vibrations, respectively.<sup>[44,45]</sup> The diffraction pattern (Figure S2D) was consistent with hexagonal  $\text{TiS}_2$  (PDF #15-0853); no other reflections were observed. As typical for nanocarbons, CNTs contribute a broad signal at approximately  $2\theta = 24^\circ$ , which was lost in the presence of the high-intensity peaks of crystalline  $\text{TiS}_2$ . The preferred orientation of the  $\text{TiS}_2$  plates in the electrode is evident in the 2D diffraction pattern, especially the Bragg ring of the (001) reflection. Clearly, the filtration method used for electrode fabrication leads to a preferred horizontal orientation of the  $\text{TiS}_2$  flakes, as is typical for films prepared from 2D materials such as MXene or clay.<sup>[46,47]</sup>

### Electrochemical performance in aqueous solutions with one type of cation

The  $\text{TiS}_2$ -10CNT electrodes show identifiable intercalation (reduction)/deintercalation (oxidation) peaks, as seen in the cyclic voltammograms depicted in Figure 2A. Also, we observed distinctly different peaks for the corresponding cations  $\text{K}^+$ ,  $\text{Na}^+$ ,  $\text{Cs}^+$ , and  $\text{Mg}^{2+}$  at a high concentration (1 M). The cesium ion showed the highest onset reduction potential at  $-196$  mV versus Ag/AgCl, the potassium and sodium cations at a similar onset reduction potential of  $-268$  mV versus Ag/AgCl, and the magnesium ion at the lowest onset reduction potential of  $-309$  mV versus Ag/AgCl. This indicates that the intercalation/deintercalation of diverse ions is energetically controlled by different energy barriers.<sup>[48,49]</sup>

The intercalation kinetics depend on the type of cations regarding the power performance (Figure 2B). Potassium and sodium cations show much faster intercalation than that of magnesium; therefore, the electrodes maintain more of the initial capacity at high charge/discharge rates during galvanostatic cycling in the potential range from 0 to  $-0.6$  V versus Ag/AgCl (Figure 2B). The electrode shows the highest specific capacity of  $80 \text{ mAh g}^{-1}$  at  $0.1 \text{ Ag}^{-1}$  and  $60 \text{ mAh g}^{-1}$  at  $10 \text{ Ag}^{-1}$  in 1 M KCl. In 1 M CsCl and NaCl, we measured a similar specific capacity of  $70 \text{ mAh g}^{-1}$  at  $0.1 \text{ Ag}^{-1}$ , but the capacity in NaCl at  $10 \text{ Ag}^{-1}$  was much higher than that measured for CsCl. This indicates that cesium ions show slower intercalation kinetic than sodium ions. In 1 M  $\text{MgCl}_2$ , the electrode material exhibited the lowest capacity of  $45 \text{ mAh g}^{-1}$  at  $0.1 \text{ Ag}^{-1}$ . The differences in ion transport and the barrier energy for the intercalation were possibly influenced by the different hydrated ionic radii (Figure 2C).<sup>[48,50]</sup>

Herein, we focus on the first intercalation peak where the intercalation first occurs during electrode reduction. The first peak in the electrochemical signal (Figure 2A) relates to [Eq. (1)]:



in which A is the intercalated cation, and  $n$  is the number of transferred electrons (ideally: 1 for K, Cs, or Na; 2 for Mg).

According to the Nernst equation, the electrode potential can be simplified when not considering the activities of the solid phases [Eq. (2)]<sup>[51-54]</sup>

$$E_e = E_f + \frac{RT}{nF} \ln \left( \frac{[\text{TiS}_{2,\text{Ox}}]}{[\text{TiS}_{2,\text{Re}}]} \right) \quad (2)$$

in which  $E_f$  is the formal redox potential,  $R$  is gas constant ( $8.314 \text{ J mol}^{-1} \text{ K}$ ),  $T$  is temperature (293 K),  $F$  is the Faraday constant ( $96485 \text{ C mol}^{-1}$ ), and  $[\text{TiS}_{2,\text{Re}}]$  and  $[\text{TiS}_{2,\text{Ox}}]$  are the concentrations of the reduced and oxidized  $\text{TiS}_2$ , respectively.

In the case of NaCl and KCl solutions, the formal potential seems to be similar, as indicated by the similar potentials for the first reduction plateau and the last oxidation plateau (Figure 2D). The CsCl solution showed a higher formal potential

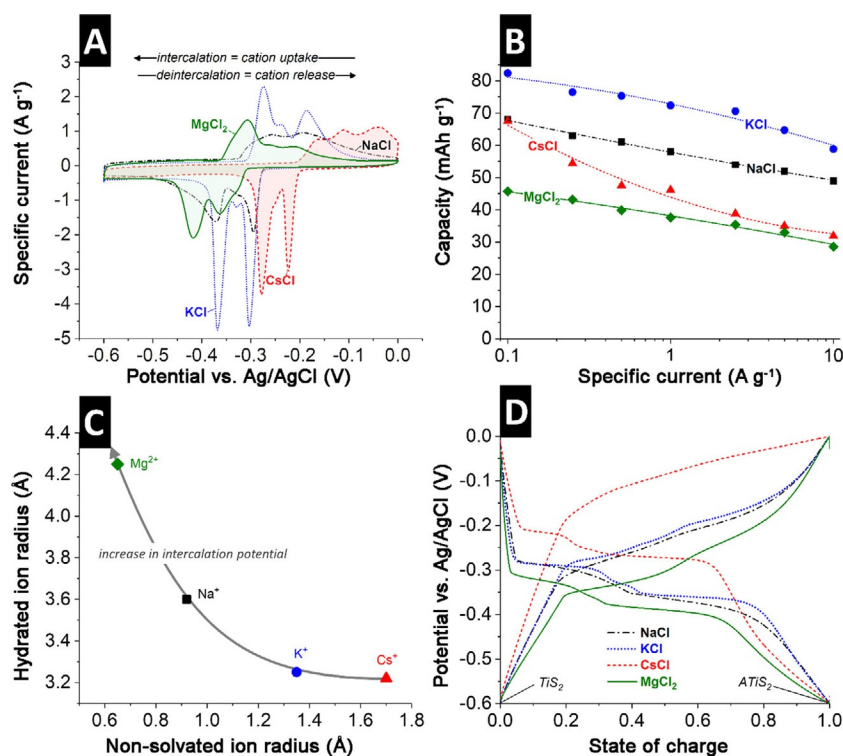


**Figure 2.** Electrochemical response of  $\text{TiS}_2$ -10CNT in 1 M single salt solution: (A) Cyclic voltammograms at  $1 \text{ mV s}^{-1}$ . (B) Specific capacities versus specific current obtained from galvanostatic charge/discharge. (C) Ionic radii with and without a hydration shell. (D) State-of-charge/discharge versus potential.

whereas the  $\text{MgCl}_2$  solution showed the lowest formal potential.

We further evaluated  $\text{TiS}_2$ -10CNT in different salt concentrations of CsCl, KCl, NaCl, and  $\text{MgCl}_2$  using cyclic voltammetry with a sweep rate of  $1 \text{ mV s}^{-1}$  (Figure S3). The formal potential for the intercalation process of  $\text{TiS}_2$  was determined by the half-wave potential of the first redox peak of the cyclic voltammograms. For all tested solutions, the formal potential ( $E_f$ ) became more negative as the cation concentration decreased (Figure 3).  $E_f$  depends on the activity  $a$  of the reduced and oxidized species according to Equation (3):

$$E_f = E_0 + \frac{RT}{nF} \ln \left( \frac{a_{\text{A},\text{Ox}}}{a_{\text{A},\text{re}}} \right) \quad (3)$$

Therefore,  $\text{TiS}_2$  exhibited variable formal potentials in different cations and molar concentrations (Figure 3). Additionally, the standard potentials ( $E_0$ ) of individual cations at standard concentration (1 M) were determined to be  $-159.4 \text{ mV}$  for  $\text{Cs}^+$ ,  $-277.2 \text{ mV}$  for  $\text{Na}^+$ ,  $-282.9 \text{ mV}$  for  $\text{K}^+$ , and  $-323 \text{ mV}$  for  $\text{Mg}^{2+}$  (Table 1). Apparently,  $E_f$  and salt concentration are closely related to the activity of the ion in the system. In the concentration range from 5 mM to 1 M, an almost linear trend was observed. The different standard potentials for different cations can be attributed to the different Gibbs free energy.

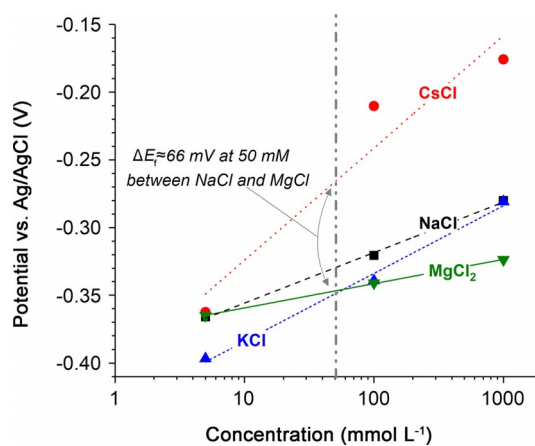


**Figure 3.** Formal potentials of the first intercalation/deintercalation peak versus single-salt concentration.

**Table 1.** Standard potential ( $E_0$ ) of individual salt obtained from a standard concentration (1 M) in water.

Salt	Standard potential $E_0$ [mV]
NaCl	-277.2
CsCl	-159.4
KCl	-282.9
$\text{MgCl}_2$	-323.0

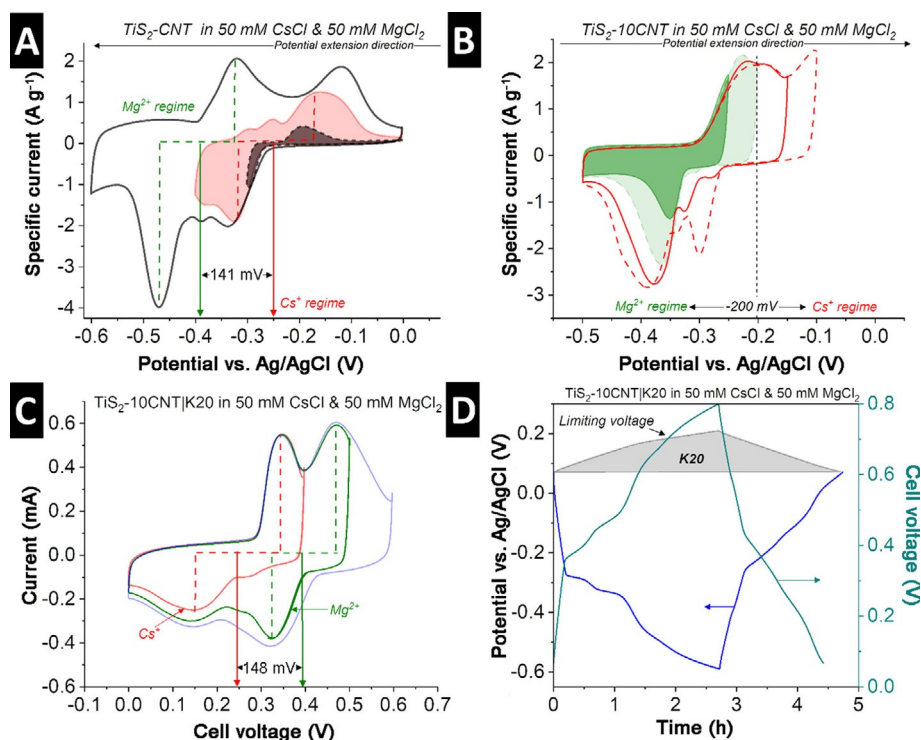
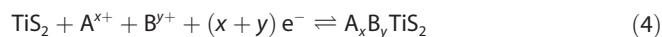


**Figure 4.** (A, B) Cyclic voltammograms of  $\text{TiS}_2\text{-10CNT}$  in 50 mM CsCl and 50 mM  $\text{MgCl}_2$ , (C) cyclic voltammograms of  $\text{TiS}_2\text{-10CNT|K20}$  in 50 mM CsCl and 50 mM  $\text{MgCl}_2$ , and (D) galvanostatic charge/discharge of  $\text{TiS}_2\text{-10CNT|K20}$  with positive and negative potential development.

### Electrochemical performance in aqueous solutions with several types of cations

The formal potentials depend on the type and concentration of the cations in the solution. The distinctly different redox peak positions enable selective separation of ions by applying different potential windows in the mixture solution. In such mixed ionic systems, the standard potential of the mixture solution ( $E_{0,\text{mix}}$ ) must also be considered. The standard potential in a multication system (e.g.,  $\text{Mg}^{2+}$  and  $\text{Cs}^+$ ) shifts when changing the energy of the solution (i.e., entropy of solution and number of solvent molecules in the solvation shell depending on the ion–solvent and ion–ion interaction), whereas the formal potential values will also be different as the activity changes in the Nernst equation. As in Equation (1), the intercalation/deintercalation mechanism changes to [Eq. (4)]:



To understand the effect of multications on the formal potential, we characterized the electrochemical behavior of  $\text{TiS}_2\text{-10CNT}$  in 50 mM  $\text{MgCl}_2$  and CsCl mixture (1:1 molar ratio of  $\text{Mg}^{2+}$  and  $\text{Cs}^+$ ), as those two ion systems exhibit the largest formal potential difference. The cyclic voltammograms in 50 mM CsCl and  $\text{MgCl}_2$  (Figure 4A, note: intercalation potential is extended towards the more negative potential) show an onset reduction potential of  $-260$  mV versus Ag/AgCl whereas the third onset reduction potential occurred at  $-406$  mV versus Ag/AgCl. We assumed that the first and second reduction peaks indicate the insertion of  $\text{Cs}^+$  (Figure 4A), whereas

the third peak was related to the intercalation of  $\text{Mg}^{2+}$ . The emergence of four oxidation peaks while scanning from negative to positive potentials (Figure 4B) also implied that both ions have different deintercalation potential regimes.

The formal potential based on the data presented in Figure 4A is  $-250$  mV for  $\text{Cs}^+$  and  $-391$  mV for  $\text{Mg}^{2+}$ , yielding a potential difference of 141 mV. This value was different from the expected  $E_f$  difference in the single-ion system (66 mV; Figure 3).  $E_f$  of the multication system was shifted by  $+45$  and  $-26$  mV for  $\text{Cs}^+$  and  $\text{Mg}^{2+}$ , respectively. The difference between the single cation and multication system was most probably owed to the activity change, as shown in Equation (3). Despite the slight difference, the formal potentials as a function of the concentration in single-ion systems are still practical for the estimation of multication systems. Considering the formal potentials measured in the multication system ( $-391$  mV for  $\text{Mg}^{2+}$  and  $-250$  mV for  $\text{Cs}^+$ ), it can be used for designing the ion selectivity operation conditions with a boundary potential between  $\text{Mg}^{2+}$  and  $\text{Cs}^+$  of  $-200$  mV (Figure 4B).

In a next step, the  $\text{TiS}_2\text{-10CNT}$  electrode was paired with an oversized activated carbon textile electrode (K20) and tested in a 50 mM mixture of CsCl and  $\text{MgCl}_2$ . As shown in Figure 4C, the cyclic voltammogram with cycling at  $1 \text{ mVs}^{-1}$  had two main peaks at  $+343$  and  $+472$  mV during charging and two peaks at  $+324$  and  $+148$  mV cell voltage during discharging. The cell voltage gap ( $\Delta E_{\text{cell}}$ ) between the two peaks perfectly matched the potential gap between the formal potentials in Figure 4A, indicating that the operation of  $\text{TiS}_2\text{-10CNT}$  with an oversized activated carbon electrode led to precise potential control. As also shown in Figure 4D, the potential develop-

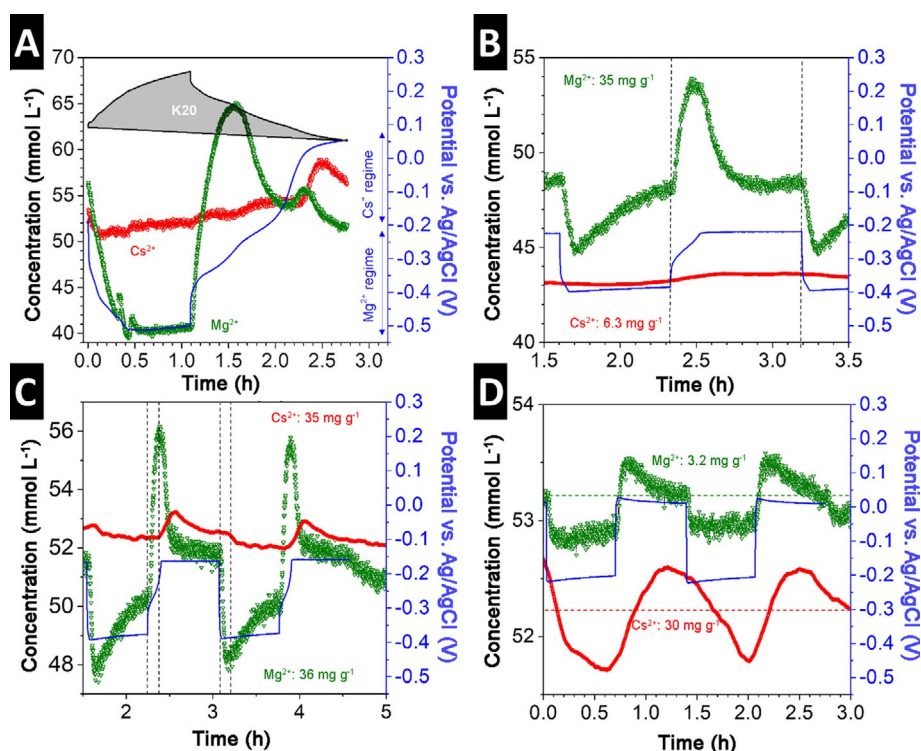


**Figure 5.** Influence of the electrode potential operation range on the effluent concentration of  $\text{Mg}^{2+}$  and  $\text{Cs}^+$  recorded by ICP-OES. The electrode potentials correspond to the following operation ranges: (A) cell voltage between 0 and 0.7 V, (B) cell voltage between 0.34 and 0.49 V, (C) cell voltage between 0.27 and 0.49 V, and (D) cell voltage between 0 and 0.27 V.  $\text{Mg}^{2+}$  and  $\text{Cs}^+$  uptake capacities are normalized to the mass of the  $\text{TiS}_2$ -10CNT electrode.

ment of positive (K20) and negative ( $\text{TiS}_2$ -10CNT) electrode was additionally monitored with the Ag/AgCl reference electrode. The potential contribution of K20 at a cell voltage of 0.8 V was only +125 mV versus Ag/AgCl whereas the majority fraction potential from  $\text{TiS}_2$ -10CNT was +675 mV versus Ag/AgCl. The potentials at the reduction plateaus of  $\text{TiS}_2$ -10CNT in Figure 4D also corresponded to the potentials observed from the three-electrode measurement in Figure 4A. Additionally, the limiting cell voltage was determined to be 0.7 V, which was limited by the negative electrode ( $-0.55$  V vs. Ag/AgCl). Therefore, we limited the negative potential to  $-0.5$  V versus Ag/AgCl in all the following ion selectivity measurements.

### Ion selectivity of $\text{Mg}^{2+}$ and $\text{Cs}^+$ mixture through control of electrode potential

To demonstrate that the intercalation of magnesium and cesium ions can be selectively used for ion separation, we performed desalination measurements using an online monitoring chemical analysis unit (ICP-OES) for the direct measurement of the ion concentration during the electrochemical operation in the desalination cell. During the measurement, the solution (50 mM CsCl and 50 mM  $\text{MgCl}_2$ ) from a 10 L container was continuously fed into the cell with a constant flow rate of  $3 \text{ mL min}^{-1}$ . Simultaneously,  $2 \text{ mL min}^{-1}$  of the effluent was fed into the ICP-OES to detect the concentration change during the ion selectivity process. As shown in Figure 5A, the cell voltage was scanned from 0 to 0.7 V at  $0.05 \text{ A g}_{\text{neg}}^{-1}$  and held for 40 min. The open-circuit voltage (OCV) before applying a cur-

rent was 285 mV, corresponding to +100 mV versus Ag/AgCl for K20 and  $-185$  mV versus Ag/AgCl for  $\text{TiS}_2$ -10CNT. After charging the cell, two plateaus at approximately  $-332$  mV and  $-422$  mV versus Ag/AgCl were observed. Considering the concentration profile of magnesium and cesium ions, both ions intercalated into the  $\text{TiS}_2$  layers, leading to a decreased effluence concentration. After holding the voltage at 0.7 V for 40 min, the positive and negative electrodes were saturated with adsorbed and intercalated ions (fully charged), respectively, resulting in a change of 10 mM for magnesium and 5 mM for cesium ions. Upon discharge to a cell voltage of 0 V, the negative electrode showed two visible plateaus at  $-333$  and  $-190$  mV versus Ag/AgCl. The deintercalation potentials of magnesium and cesium ions remained distinguishable. Magnesium ions were released after the cell was discharged until the negative potential reached  $-160$  mV. Further cell discharge to 0 V led to cesium ion deintercalation with only a small number of magnesium ions being mobilized. This suggests that  $\text{TiS}_2$ -10CNT can be effectively used for magnesium selectivity by modifying the potential.

In the following, we outline three operational regimes: 1) strong Mg preference over Cs, 2) weak Mg preference over Cs, and 3) strong Cs preference over Mg. The corresponding selectivity ratios (per mass and per mol) are also summarized in Table S1. Properties of the system such as the formal potential and selectivity ratio depend on the type and concentration of ions and the structure and phase of the electrode materials. We chose the Cs/Mg system in our proof-of-concept study because of the large potential difference for cation insertion.

Other system parameters and different selectivity ratios will be obtained for other ionic systems and different electrode materials.

### Regime 1: Strong Mg preference over Cs

Magnesium ions can be selectively taken up and released from the  $\text{TiS}_2$ -10CNT electrode in the potential range from  $-220$  mV to  $-396$  mV versus Ag/AgCl, translating to an operational cell voltage of 340–490 mV (Figure 5B), when the threshold for cesium deintercalation of  $-200$  mV versus Ag/AgCl (Figure 4B) is not surpassed. Within this potential regime, we measured a high magnesium uptake capacity of  $35 \text{ mg g}_{\text{neg}}^{-1}$  ( $1458 \text{ } \mu\text{mol g}_{\text{neg}}^{-1}$ ). In addition, a significantly smaller amount of cesium ions was taken up ( $6.3 \text{ mg g}_{\text{neg}}^{-1}$ ,  $47 \text{ } \mu\text{mol g}_{\text{neg}}^{-1}$ ) in this potential range. This confirmed that a magnesium selectivity (molar selectivity ratio of 31 against  $\text{Cs}^+$ / mass selectivity ratio of 5.6 against  $\text{Cs}^+$ ) could be achieved by simply controlling the operational potential of the  $\text{TiS}_2$ -10CNT electrode.

### Regime 2: Weak Mg preference over Cs

We further extended the discharge potential of  $\text{TiS}_2$ -10CNT from  $-220$  to  $-160$  mV versus Ag/AgCl (Figure 5C), which covered the formal potential of cesium and magnesium ions (Figure 4A). Evidently, cesium ions were released exactly when the potential of  $\text{TiS}_2$ -10CNT reached  $-234$  mV versus Ag/AgCl (57 mV difference from the  $\text{Mg}^{2+}$  formal potential and 16 mV difference from the  $\text{Cs}^+$  formal potential). The magnesium uptake capacity at this regime was  $36 \text{ mg g}_{\text{neg}}^{-1}$  ( $1500 \text{ } \mu\text{mol g}_{\text{neg}}^{-1}$ ), which was almost identical to the cesium uptake capacity of  $35 \text{ mg g}_{\text{neg}}^{-1}$  ( $265 \text{ } \mu\text{mol g}_{\text{neg}}^{-1}$ ). In this range, a small preference for magnesium remained, with a molar selectivity ratio between magnesium and cesium of 5.7 (mass selectivity of 1.02). Therefore, the potential range between  $-396$  and  $-160$  mV versus Ag/AgCl was still magnesium selective but at a much lower amplitude compared to the range from  $-220$  to  $-396$  mV versus Ag/AgCl.

### Regime 3: Strong Cs preference over Mg

Without changes to the electrode material or cell design, we can effectively achieve cesium selectivity by shifting the potential of  $\text{TiS}_2$ -10CNT to the cesium regime. As presented in Figure 5D, the potential of  $\text{TiS}_2$ -10CNT was limited between  $-219$  and  $+26$  mV vs. Ag/AgCl. This potential range was much closer to the formal potential of  $\text{Cs}^+$  ( $-250$  mV), but still the influence of  $\text{Mg}^{2+}$  was evident. The cesium uptake with  $30 \text{ mg g}_{\text{neg}}^{-1}$  ( $228 \text{ } \mu\text{mol g}_{\text{neg}}^{-1}$ ) was favored over the magnesium uptake of  $3.2 \text{ mg g}_{\text{neg}}^{-1}$  ( $133 \text{ } \mu\text{mol g}_{\text{neg}}^{-1}$ ). The molar selectivity ratio between cesium and magnesium ( $C_{\text{Cs}}/C_{\text{Mg}}$ ) was 1.7 (mass selectivity: 9.4), indicating that cesium ion removal was preferred over magnesium in this potential regime.

Comparing the data of all three regimes, it is evident that the selectivity between  $\text{Cs}^+$  and  $\text{Mg}^{2+}$  can effectively be controlled by manipulation of the potential. This behavior is reversible, and uptake regimes can be adjusted using the same cell,

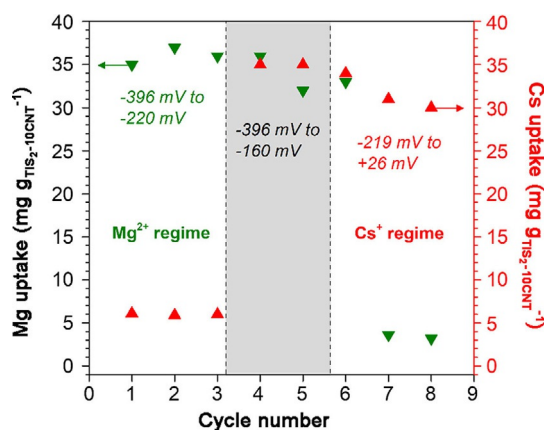


**Figure 6.** Potential dependence of magnesium and cesium ion uptake recorded with online monitoring of the chemical composition of the effluent stream for several operation cycles.

which we confirmed by successively operating one cell in all three described uptake regimes (Figure 6). In Regime 1, the  $\text{Mg}^{2+}$  removal rate was  $0.8$  and  $0.15 \text{ mg g}^{-1} \text{ min}^{-1}$  for  $\text{Cs}^+$ . In Regime 2, the  $\text{Cs}^+$  uptake rate increased to  $0.7 \text{ mg g}^{-1} \text{ min}^{-1}$  whereas the  $\text{Mg}^{2+}$  uptake rate remained unchanged. In Regime 3, the  $\text{Cs}^+$  removal rate was  $0.6 \text{ mg g}^{-1} \text{ min}^{-1}$  but only  $0.06 \text{ mg g}^{-1} \text{ min}^{-1}$  for  $\text{Mg}^{2+}$ . For comparison, the ion removal rate of NaCl using conventional CDI based on nanoporous carbon electrodes ranges between  $0.05$  and  $5.4 \text{ mg g}^{-1} \text{ min}^{-1}$  whereas the NaCl removing rate using faradaic materials is between  $0.4$  and  $0.96 \text{ mg g}^{-1} \text{ min}^{-1}$ . [15,16,55–57]

## Conclusions

Electrochemically switchable ion selectivity was achieved by controlling the potential of the electrode (binder-free  $\text{TiS}_2$ -10CNT). Through thorough electrochemical analysis, we determined that the equilibrium intercalation/deintercalation potential of a  $\text{TiS}_2$ -10CNT electrode depended on the type and concentration of the cations. A formal potential is suggested as guidance for identifying the selective-voltage regime. Throughout the selectivity process, online monitoring by ICP-OES was used to prove that magnesium and cesium ion uptake could be selected by controlling the potential of the negative electrode composed of an intercalation material.  $\text{TiS}_2$  exhibited high magnesium selectivity (molar selectivity of 31 against  $\text{Cs}^+$ ) with a magnesium uptake capacity of  $35 \text{ mg g}_{\text{neg}}^{-1}$  in the potential range between  $-220$  and  $-396$  mV versus Ag/AgCl. Cesium selectivity over magnesium was also observed at a potential between  $+26$  and  $-219$  mV versus Ag/AgCl with a cesium uptake capacity of  $30 \text{ mg g}_{\text{neg}}^{-1}$  and a molar selectivity of 1.71 against the magnesium. Furthermore, the selectivity factor could be enhanced by applying multiple recycle steps.

Our results introduce a novel method to achieve cation selectivity by simple potential adjustment of an intercalation material. This mechanism could be transferred to other intercalation materials and ion systems. Our electrochemical analysis with an online monitoring ICP-OES system with water flow can also be valuable for providing detailed insight into the actual

ion movements in dual-ion battery systems. For separation applications, future work will have to address the longevity of the selectivity rates, the robustness of selective ion removal in multi-ion systems and systems with various electrode materials. Also, it remains important to explore  $\text{TiS}_2$  for other ionic systems for ions with a lower potential difference for insertion/de-insertion and to rigorously benchmark other ion intercalation materials. Issues may arise when structural fatigue or change in the lattice constants alter the electrochemical properties of a battery electrode material, especially the ion insertion potentials during long-term operation.

## Experimental Section

### Material synthesis

Binder-free electrodes were prepared by following the protocol reported in the literature.<sup>[57]</sup> Briefly, 200 mg  $\text{TiS}_2$  (99.99 mass%, Sigma-Aldrich) was mixed in 300 mL ethanol and sonicated for 30 min. Meanwhile, 22 mg carbon nanotubes (multiwall CNT, 99 mass%, Nanocyl NC7000) were separately mixed and sonicated in 300 mL ethanol for 15 min. Afterwards, the CNT dispersion was added to the  $\text{TiS}_2$  dispersion. Subsequently, the  $\text{TiS}_2$ /CNT suspension was further stirred and sonicated for 30 min to obtain a homogeneous mixture. The resulting slurry contained  $\text{TiS}_2$  and CNT with a constant mass ratio of 9:1. The slurry was filtered through a glass fiber separator (Millipore, 380  $\mu\text{m}$  thickness, Whatman) and dried at 60 °C for 5 h to obtain binder-free electrodes. The resulting electrode was labeled  $\text{TiS}_2$ -10CNT.

### Electric conductivity of the electrodes

The electric conductivity of the electrodes was measured by a digital multimeter (DMM 4001, PREMA) with a custom-built spring-loaded four-point probe with blunt gold contacts (tip diameter: 1.5 mm, tip distance: 3 mm). The detection limit of the setup for the conductivity measurement was approximately  $10^{-4}$  S cm.

### Structural and chemical characterization

SEM images were recorded with a field emission scanning electron microscope (JEOL JSM 7500F) operating at 5 kV. TEM images were recorded with a JEOL 2100F transmission electron microscope at 200 kV. The TEM samples were prepared by dispersing the powders in ethanol and drop-casting them on a copper grid with a lacey carbon film.

Raman spectra were recorded with a Renishaw inVia Raman microscope using an Nd:YAG laser with an excitation wavelength of 532 nm. The spectral resolution was 1.2  $\text{cm}^{-1}$ , and the diameter of the laser spot on the sample was 2  $\mu\text{m}$  with a power of 0.2 mW. The spectra were recorded for 20 s with 30 accumulations.

XRD was conducted on a D8 Advance diffractometer (Bruker AXS) with a copper X-ray source ( $\text{Cu K}\alpha$ , 40 kV, 40 mA) and a Goebel mirror in point focus (0.5 mm). We used a VANTEC-500 (Bruker AXS) 2D detector positioned at 20°, 40°, 60°, and 80°  $2\theta$  with a measurement time of 16.7 min per step. The sample holder was oscillating horizontally (amplitude of 5 mm with a speed of 0.5  $\text{mm s}^{-1}$  along the  $x$ -axis and 0.2  $\text{mm s}^{-1}$  along the  $y$ -axis) to enhance the signal statistics.

### Electrochemical measurements

We performed three-electrode measurements to characterize the  $\text{TiS}_2$ -10CNT behavior in four different electrolytes with different concentrations. A binder-free  $\text{TiS}_2$ -10CNT electrode with a diameter of 12 mm was employed as a working electrode, and a pair of graphite discs (12 mm in diameter; SGL Carbon) served as a current collector. As a counter electrode, an oversized polytetrafluoroethylene-bound, free-standing activated carbon electrode (YP-80F, Kuraray) was used. More details on the preparation of free-standing activated carbon electrodes have been reported in our previous work (Ref. [58]). A glass fiber mat (GF/A, Whatman) was cut into circular shape with a diameter of 13 mm and employed as a separator. All components were assembled in custom-built cells between spring-loaded titanium pistons (see Ref. [59] for the cell design). An Ag/AgCl (3 M KCl, BASi) reference electrode was mounted at the side of the cell, where the porous frit of the reference was close to the working and counter electrodes. Afterwards, the electrolyte was injected by vacuum backfilling. We used four different electrolytes (NaCl, KCl, CsCl, and  $\text{MgCl}_2$ ) ranging from low to high concentrations (5 mM to 1 M). The as-assembled cell was tested with a VSP300 potentiostat/galvanostat (Bio-Logic). Throughout this work, cyclic voltammetry was recorded at a scan rate of 1  $\text{mV s}^{-1}$  between 0 and  $-0.6$  V versus Ag/AgCl.

For two-electrode characterization, we used a commercially available activated carbon textile (Kynol-507-20, denoted K20) as a free-standing, binder-free counter electrode. The properties of K20 are provided and discussed in Ref. [60]. After cutting K20 discs with a diameter of 12 mm (9 mg), they were immersed in the salt solution for 20 min for wetting. Full filling of the electrode compartment with electrolyte was ensured by vacuum backfilling. Cyclic voltammetry was performed from 0 to +0.65 V at a sweep rate of 1  $\text{mV s}^{-1}$ .

### Desalination cell assembly

Throughout this study, a flow-by desalination cell was used as described in the Supporting Information (Figure S1). As the negative electrode for cation selectivity, the  $\text{TiS}_2$ -10CNT electrode was cut into squares of 5 × 5 cm with a mass of 90 mg per electrode. To avoid potential shifting, a strongly oversized activated carbon textile electrode (K20) was employed as the counter electrode. The latter was cut to the same size as the  $\text{TiS}_2$ -10CNT electrode but had a mass of 300 mg per electrode. One pair of the  $\text{TiS}_2$ -10CNT electrode (total mass: 180 mg) was coupled with two pairs of K20 (total mass: 1 g), using graphite sheets as current collectors and a porous glass fiber filter as the separator (Millipore, 380  $\mu\text{m}$  thickness) between the electrodes. The skeletal density determined with a helium pycnometer was 3.14  $\text{g cm}^{-3}$  for  $\text{TiS}_2$ -10CNT and 1.12  $\text{g cm}^{-3}$  for K20. To achieve a sufficient clear concentration profile, we employed  $\text{TiS}_2$ -10CNT electrodes that were stacked on top each other (total mass of  $\text{TiS}_2$ -10CNT: 300 mg).

An Ag/AgCl reference was mounted as a spectator at the side of the desalination cell in which the tip of the reference was close to the positive and negative electrode. In this way, the potential of the  $\text{TiS}_2$ -10CNT electrode was monitored. The cell was filled with a salt solution of 50 mM CsCl + 50 mM  $\text{MgCl}_2$  and tightly sealed to avoid any significant dead volume.

### Online ICP-OES monitoring of the ion selectivity process

The as-assembled desalination cell was connected to a VSP300 potentiostat/galvanostat (Bio-Logic). A 10 L salt solution tank was

continuously flushed with N<sub>2</sub> gas to avoid electrode oxidation by dissolved O<sub>2</sub>. The electrolyte was fed into the cell into which the outlet stream was connected to a peristaltic pump, feeding into an inductively coupled plasma optical emission spectrometry (ICP-OES) instrument (ARCOS FHX22, SPECTRO Analytical Instrument).<sup>[57]</sup> Before ion removal, the solution was circulated through the cell at a flow rate of 3 mL min<sup>-1</sup> for 20 min. Afterward, a constant specific current of 0.05 A g<sub>neg</sub><sup>-1</sup> (i.e., normalized to the mass of the negative electrode) was applied by limiting the cell voltage at the desired voltage, at which specific ions were removed. To obtain maximum ion removal, the potential was held at the selected voltage for 40 min. During electrode regeneration, the cell was discharged at a constant specific current of 0.05 A g<sub>neg</sub><sup>-1</sup> to a selected cell voltage and held for 40 min. Also, the individual electrode potential was continuously measured during charge/discharge operation to assure that the negative electrode (TiS<sub>2</sub>-10CNT) was kept at the desired potential. To detect the ion species leaving the cell during operation, an effluent aliquot was extracted at 2 mL min<sup>-1</sup> from the desalination cell outlet by a peristaltic pump and fed into the ICP-OES device.

The ICP-OES calibration was made according to the correlation between the intensity at a specific wavelength and the concentration of the solution. The online intensities from the extracted sample were converted into concentration profiles. The ion removal capacity was calculated for ions individually using Equation (5):

$$\text{Ion removal capacity} \left( \frac{m_{\text{ion}}}{m_{\text{electrode}}} \right) = \frac{\nu \cdot M_{\text{ion}}}{m_{\text{electrode}}} \int c dt \quad (5)$$

in which  $\nu$  is the flow rate (3 mL min<sup>-1</sup>),  $M_{\text{ion}}$  is the molecular weight of the ion species (Cs: 133 g mol<sup>-1</sup>, Mg: 24 g mol<sup>-1</sup>, and Cl: 35 g mol<sup>-1</sup>),  $m$  is the mass of either the positive or negative electrode [mg],  $c$  is the ion concentration of the outlet stream [mol L<sup>-1</sup>], and  $t$  is the ion removal time [min].

## Acknowledgements

S.P. gratefully acknowledges financial support by the German Academic Exchange Service (DAAD award number 91579066). The authors thank Eduard Arzt (INM) for his continuing support. Öznil Budak, Jaehoon Choi, Nicolas Jäckel, and Rafael Linzmeyer Zornitta (all at INM) are thanked for helpful discussions and technical support.

## Conflict of interest

The authors declare no conflict of interest.

**Keywords:** capacitive deionization • ion separation • potential difference • titanium disulfide • water desalination

- [1] K. P. Lee, T. C. Arnot, D. Mattia, *J. Membr. Sci.* **2011**, *370*, 1–22.
- [2] D. M. Stevens, J. Y. Shu, M. Reichert, A. Roy, *Ind. Eng. Chem. Res.* **2017**, *56*, 10526–10551.
- [3] H. M. Qiblawey, F. Banat, *Desalination* **2008**, *220*, 633–644.
- [4] M. Al-Sahali, H. Ettouney, *Desalination* **2007**, *214*, 227–240.
- [5] Q. Zhu, Z. Zhang, M. Sadakane, A. Yoshida, M. Hara, W. Ueda, *New J. Chem.* **2017**, *41*, 4503–4509.
- [6] J. B. Rivest, P. K. Jain, *Chem. Soc. Rev.* **2013**, *42*, 89–96.
- [7] M. E. Suss, S. Porada, X. Sun, P. M. Biesheuvel, J. Yoon, V. Presser, *Energy Environ. Sci.* **2015**, *8*, 2296–2319.

- [8] Ö. Arar, Ü. Yüksel, N. Kabay, M. Yüksel, *Desalination* **2014**, *342*, 16–22.
- [9] X. Su, K.-J. Tan, J. Elbert, C. Ruttiger, M. Gallei, T. F. Jamison, T. A. Hatton, *Energy Environ. Sci.* **2017**, *10*, 1272–1283.
- [10] S. Porada, R. Zhao, A. van der Wal, V. Presser, P. M. Biesheuvel, *Prog. Mater. Sci.* **2013**, *58*, 1388–1442.
- [11] P. Liu, T. Yan, L. Shi, H. S. Park, X. Chen, Z. Zhao, D. Zhang, *J. Mater. Chem. A* **2017**, *5*, 13907–13943.
- [12] C. Zhang, D. He, J. Ma, W. Tang, T. D. Waite, *Water Res.* **2018**, *128*, 314–330.
- [13] J. Lee, S. Kim, C. Kim, J. Yoon, *Energy Environ. Sci.* **2014**, *7*, 3683–3689.
- [14] J. Lee, S. Kim, J. Yoon, *ACS Omega* **2017**, *2*, 1653–1659.
- [15] P. Srimuk, F. Kaasik, B. Krüner, A. Tolosa, S. Fleischmann, N. Jäckel, M. C. Tekeli, M. Aslan, M. E. Suss, V. Presser, *J. Mater. Chem. A* **2016**, *4*, 18265–18271.
- [16] P. Srimuk, J. Lee, S. Fleischmann, S. Choudhury, N. Jäckel, M. Zeiger, C. Kim, M. Aslan, V. Presser, *J. Mater. Chem. A* **2017**, *5*, 15640–15649.
- [17] R. D. Cusick, Y. Kim, B. E. Logan, *Science* **2012**, *335*, 1474–1477.
- [18] F. Béguin, V. Presser, A. Balducci, E. Frackowiak, *Adv. Mater.* **2014**, *26*, 2219–2251.
- [19] P. M. Biesheuvel, S. Porada, M. Levi, M. Z. Bazant, *J. Solid State Electrochem.* **2014**, *18*, 1365–1376.
- [20] S. Porada, A. Shrivastava, P. Bukowska, P. M. Biesheuvel, K. C. Smith, *Electrochim. Acta* **2017**, *255*, 369–378.
- [21] D.-H. Nam, K.-S. Choi, *J. Am. Chem. Soc.* **2017**, *139*, 11055–11063.
- [22] X. Su, H. J. Kulik, T. F. Jamison, T. A. Hatton, *Adv. Funct. Mater.* **2016**, *26*, 3394–3404.
- [23] J. A. Bruce, M. S. Wrighton, *J. Am. Chem. Soc.* **1982**, *104*, 74–82.
- [24] J. Lyskawa, F. Le Derf, E. Levillain, M. Mazari, M. Sallé, L. Dubois, P. Viel, C. Bureau, S. Palacin, *J. Am. Chem. Soc.* **2004**, *126*, 12194–12195.
- [25] M. Pasta, A. Battistel, F. La Mantia, *Energy Environ. Sci.* **2012**, *5*, 9487–9491.
- [26] B. Sun, X.-G. Hao, Z.-D. Wang, G.-Q. Guan, Z.-L. Zhang, Y.-B. Li, S.-B. Liu, *J. Hazard. Mater.* **2012**, *233*, 177–183.
- [27] Z. Wang, Y. Feng, X. Hao, W. Huang, X. Feng, *J. Mater. Chem. A* **2014**, *2*, 10263–10272.
- [28] R. Trócoli, A. Battistel, F. La Mantia, *ChemSusChem* **2015**, *8*, 2514–2519.
- [29] S. Kim, J. Lee, J. S. Kang, K. Jo, S. Kim, Y.-E. Sung, J. Yoon, *Chemosphere* **2015**, *125*, 50–56.
- [30] S. Kim, H. Yoon, D. Shin, J. Lee, J. Yoon, *J. Colloid Interface Sci.* **2017**, *506*, 644–648.
- [31] W. Chen, J. Tang, H.-J. Cheng, X.-H. Xia, *Talanta* **2009**, *80*, 539–543.
- [32] X. Su, T. A. Hatton, *Adv. Colloid Interface Sci.* **2017**, *244*, 6–20.
- [33] P. Ugo, L. M. Moretto, *Electroanalysis* **1995**, *7*, 1105–1113.
- [34] M. Liu, Z. Rong, R. Malik, P. Canepa, A. Jain, G. Ceder, K. A. Persson, *Energy Environ. Sci.* **2015**, *8*, 964–974.
- [35] Y. Zhao, K. Tang, H. Ruan, L. Xue, B. Van der Bruggen, C. Gao, J. Shen, *J. Membr. Sci.* **2017**, *536*, 167–175.
- [36] Y. Oh, D. L. Armstrong, C. Finnerty, S. Zheng, M. Hu, A. Torrents, B. Mi, *J. Membr. Sci.* **2017**, *541*, 235–243.
- [37] J. Abraham, K. S. Vasu, C. D. Williams, K. Gopinadhan, Y. Su, C. T. Cherian, J. Dix, E. Prestat, S. J. Haigh, I. V. Grigorieva, P. Carbone, A. K. Geim, R. R. Nair, *Nat. Nanotechnol.* **2017**, *12*, 546–550.
- [38] R. Zhao, M. van Soestbergen, H. H. M. Rijnaarts, A. van der Wal, M. Z. Bazant, P. M. Biesheuvel, *J. Colloid Interface Sci.* **2012**, *384*, 38–44.
- [39] J. E. Dykstra, J. Dijkstra, A. van der Wal, H. V. M. Hamelers, S. Porada, *Desalination* **2016**, *390*, 47–52.
- [40] M. E. Suss, *J. Electrochem. Soc.* **2017**, *164*, E270–E275.
- [41] P. Liu, T. Yan, J. Zhang, L. Shi, D. Zhang, *J. Mater. Chem. A* **2017**, *5*, 14748–14757.
- [42] X. Su, L. Bromberg, K.-J. Tan, T. F. Jamison, L. P. Padhye, T. A. Hatton, *Environ. Sci. Technol. Lett.* **2017**, *4*, 161–167.
- [43] P. Srimuk, J. Lee, A. Tolosa, C. Kim, M. Aslan, V. Presser, *Chem. Mater.* **2017**, *29*, 9964–9973.
- [44] D. Y. Oh, Y. E. Choi, D. H. Kim, Y.-G. Lee, B.-S. Kim, J. Park, H. Sohn, Y. S. Jung, *J. Mater. Chem. A* **2016**, *4*, 10329–10335.
- [45] C. Lin, X. Zhu, J. Feng, C. Wu, S. Hu, J. Peng, Y. Guo, L. Peng, J. Zhao, J. Huang, J. Yang, Y. Xie, *J. Am. Chem. Soc.* **2013**, *135*, 5144–5151.
- [46] K. Jasmund, G. Lagaly, *Tonminerale und Tone. Struktur, Eigenschaften, Anwendung und Einsatz in Industrie und Umwelt*, Steinkopff Verlag, Darmstadt, **1993**.

- [47] M. Ghidui, M. R. Lukatskaya, M.-Q. Zhao, Y. Gogotsi, M. W. Barsoum, *Nature* **2014**, *516*, 78–81.
- [48] K. Nobuhara, H. Nakayama, M. Nose, S. Nakanishi, H. Iba, *J. Power Sources* **2013**, *243*, 585–587.
- [49] S. P. Ong, V. L. Chevrier, G. Hautier, A. Jain, C. Moore, S. Kim, X. Ma, G. Ceder, *Energy Environ. Sci.* **2011**, *4*, 3680.
- [50] Y. Marcus, *Chem. Rev.* **1988**, *88*, 1475–1498.
- [51] J.-W. Lee, D. Hwang, *Comput. Mater. Sci.* **2015**, *100*, 80–83.
- [52] D. K. Karthikeyan, G. Sikha, R. E. White, *J. Power Sources* **2008**, *185*, 1398–1407.
- [53] M. Jain, A. L. Elmore, M. A. Matthews, J. W. Weidner, *Electrochim. Acta* **1998**, *43*, 2649–2660.
- [54] S. H. Ali, *Ionics* **2005**, *11*, 410–413.
- [55] P. Xu, J. E. Drewes, D. Heil, G. Wang, *Water Res.* **2008**, *42*, 2605–2617.
- [56] B. Krüner, P. Srimuk, S. Fleischmann, M. Zeiger, A. Schreiber, M. Aslan, A. Quade, V. Presser, *Carbon* **2017**, *117*, 46–54.
- [57] P. Srimuk, J. Halim, J. Lee, Q. Tao, J. Rosen, V. Presser, *ACS Sustainable Chem. Eng.* **2018**, *6*, 3739–3747.
- [58] M. Aslan, M. Zeiger, N. Jäckel, I. Grobelsek, D. Weingarh, V. Presser, *J. Phys. Condens. Matter* **2016**, *28*, 114003.
- [59] D. Weingarh, M. Zeiger, N. Jäckel, M. Aslan, G. Feng, V. Presser, *Adv. Energy Mater.* **2014**, *4*, 1400316.
- [60] C. Kim, P. Srimuk, J. Lee, S. Fleischmann, M. Aslan, V. Presser, *Carbon* **2017**, *122*, 329–335.

---

Manuscript received: March 5, 2018

Revised manuscript received: April 10, 2018

Accepted manuscript online: May 1, 2018

Version of record online: June 19, 2018

---

## Supporting Information

### **Potential-Dependent, Switchable Ion Selectivity in Aqueous Media Using Titanium Disulfide**

Pattarachai Srimuk<sup>+, [a, b]</sup> Juhan Lee<sup>+, [a, b]</sup> Simon Fleischmann,<sup>[a, b]</sup> Mesut Aslan,<sup>[a]</sup>  
Choonsoo Kim,<sup>[a]</sup> and Volker Presser<sup>\*, [a, b]</sup>

cssc\_201800452\_sm\_miscellaneous\_information.pdf

# Potential-dependent, switchable ion selectivity in aqueous media using titanium disulfide

Pattarachai Srimuk<sup>1,2,‡</sup>, Juhan Lee<sup>1,2,‡</sup>, Simon Fleischmann,<sup>1,2</sup>

Mesut Aslan<sup>1</sup>, Choonsoo Kim<sup>1</sup>, Volker Presser<sup>1,2,\*</sup>

<sup>1</sup>... INM - Leibniz Institute for New Materials, Saarbrücken, Germany

<sup>2</sup>... Department of Materials Science and Engineering, Saarland University, Saarbrücken, Germany

<sup>‡</sup>... Equal contribution

<sup>\*</sup>... Corresponding author's email address: [volker.presser@leibniz-inm.de](mailto:volker.presser@leibniz-inm.de)

*Supporting Information*

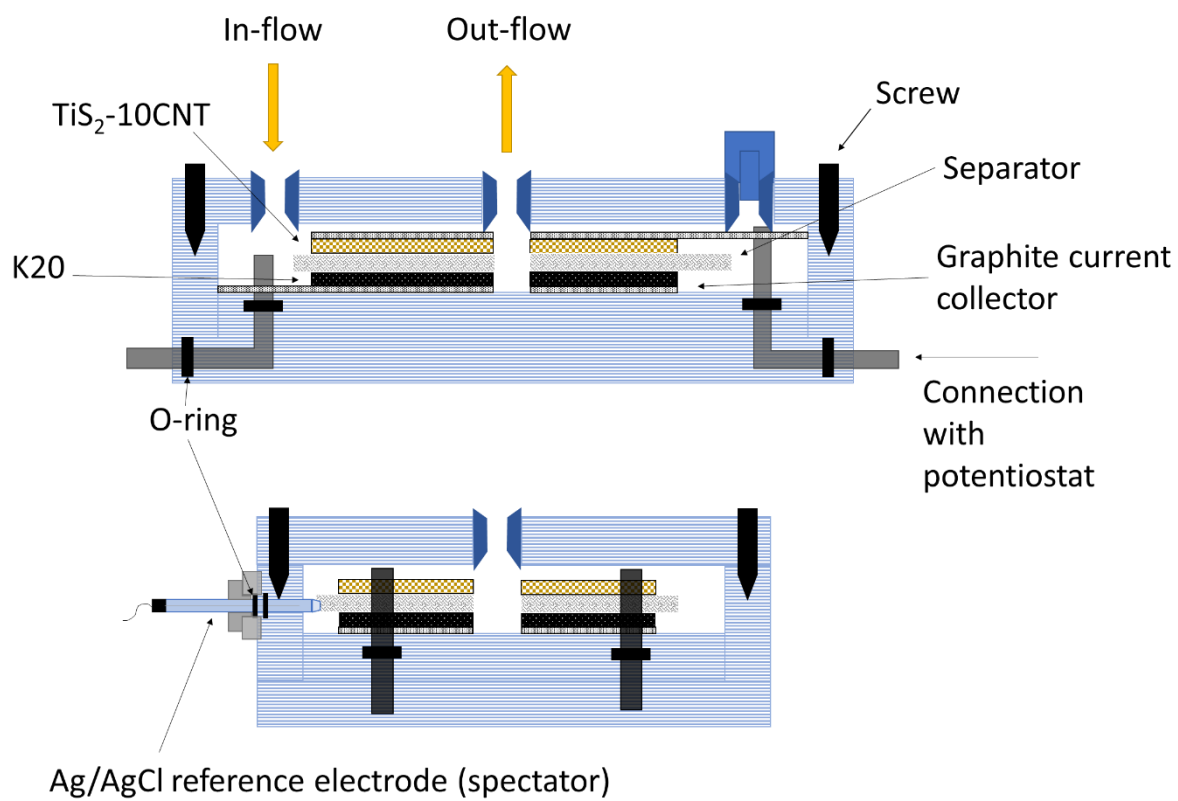


**Figure S1:** Scheme of the CDI cell used in this study.

## 1. Characterization of binder-free $\text{TiS}_2$ -10CNT electrode

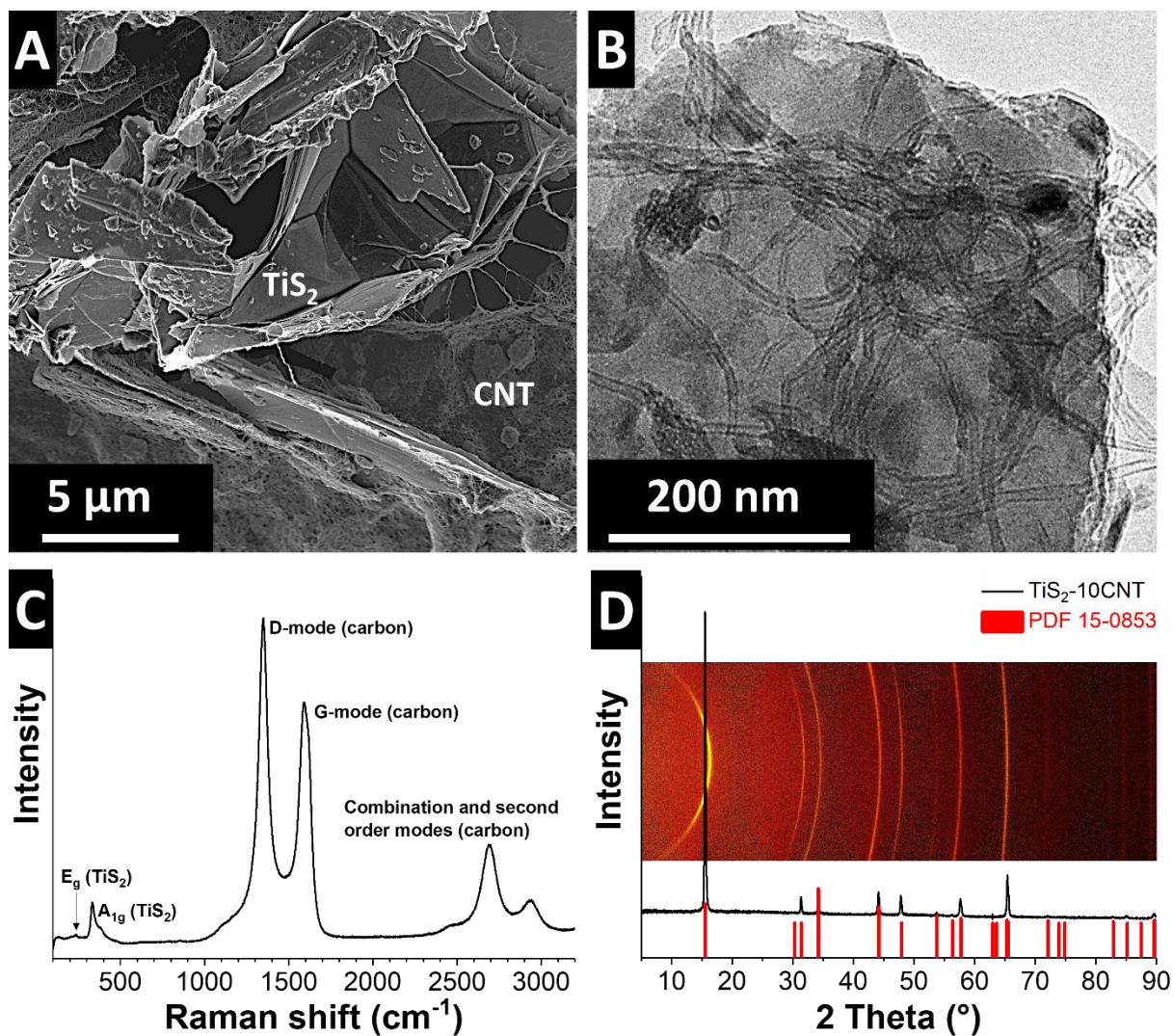


**Figure S2:** (A) scanning electron micrograph, (B) transmission electron micrograph, (C) Raman spectrum, and (D) X-ray diffractogram with corresponding two-dimensional scattering pattern of  $\text{TiS}_2$ -10CNT binder-free electrode.

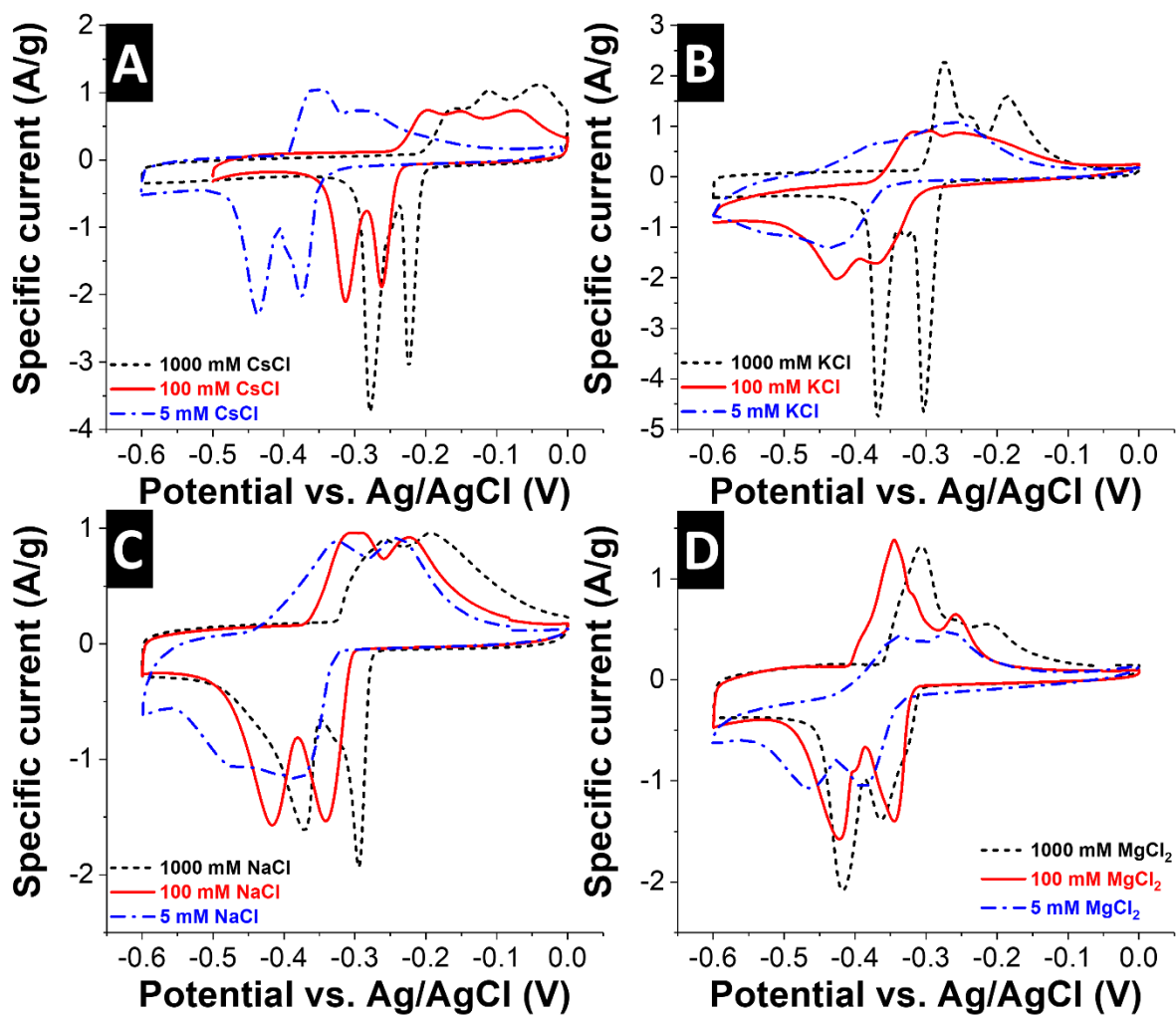


**Figure S3:** Cyclic voltammograms of TiS<sub>2</sub>-10CNT recorded at a scan rate of 1 mV/s using different concentrations of (A) CsCl, (B) KCl, (C) NaCl, and (D) MgCl<sub>2</sub>.

**Table S1:** Summary of ion selectivity values for different operation modes.

Regime	Potential range vs. Ag/AgCl	Molar selectivity: Mg vs. Cs	Mass selectivity: Mg vs. Cs
Regime 1: Strong Mg preference over Cs	-396 mV to -220 mV	31.0	5.6
Regime 2: Weak Mg preference over Cs	-220 mV to -160 mV	5.7	1.0
Regime 3: Strong Cs preference over Mg	-219 mV and +26 mV	0.6	0.1

## 4.8 Sodium ion removal by hydrated vanadyl phosphate for electrochemical water desalination

Juhan Lee,<sup>1,2</sup> Pattarachai Srimuk,<sup>1,2</sup> Rose Zwingelstein,<sup>1,2</sup> Rafael Linzmeyer Zornitta,<sup>1,3</sup>  
Jaehoon Choi,<sup>1,4</sup> Choonsoo Kim,<sup>1</sup> Volker Presser<sup>1,2</sup>

<sup>1</sup> INM - Leibniz Institute for New Materials, 66123 Saarbrücken, Germany

<sup>2</sup> Saarland University, Campus D2 2, 66123 Saarbrücken, Germany

<sup>3</sup> Department of chemical engineering, Federal University of São Carlos, 13565-905 São Carlos, Brazil

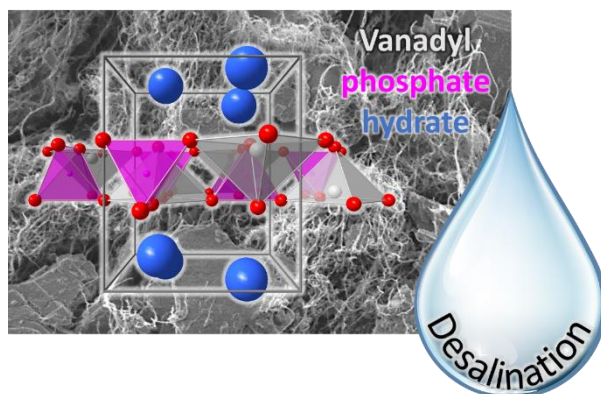
<sup>4</sup> School of Energy, Materials and Chemical Engineering, Korea University of Technology and Education, Chungjeol-ro 1600, 31253 Cheonan, Republic of Korea

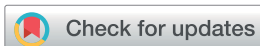
### Citation:

J. Lee, P. Srimuk, R. Zwingelstein, R.L. Zornitta, J. Choi, C. Kim, V. Presser, SODIUM ION REMOVAL BY HYDRATED VANADYL PHOSPHATE FOR ELECTROCHEMICAL WATER DESALINATION, *Journal of Materials Chemistry A* 7(8) (2019) 4175-4184.

### Own contribution:

Electrochemistry, discussion, writing



Cite this: *J. Mater. Chem. A*, 2019, 7, 4175

# Sodium ion removal by hydrated vanadyl phosphate for electrochemical water desalination†

Juhan Lee,<sup>id</sup><sup>ab</sup> Pattarachai Srimuk,<sup>id</sup><sup>ab</sup> Rose Zwingelstein,<sup>ab</sup>  
Rafael Linzmeyer Zornitta,<sup>id</sup><sup>ac</sup> Jaehoon Choi,<sup>ad</sup> Choonsoo Kim<sup>id</sup><sup>a</sup>  
and Volker Presser<sup>id</sup><sup>\*ab</sup>

In recent years, electrochemical water desalination with battery electrode materials has emerged as a promising solution for energy-efficient salt-water desalination. Here, we report the promising desalination performance of a hydrothermally synthesized vanadyl phosphate material (mixed phases of sodium vanadyl phosphate dehydrate and vanadyl hydrogen phosphate hemihydrate) as a new electrode material. We observed robust stability of the synthesized electrode material over 280 cycles during desalination operation for 100 mM NaCl feedwater which was continuously flowing along the electrode material. During the first 100 cycles, the charge storage capacity was enhanced by 47%. This enhancement seems to be caused by a continuous conversion to vanadyl phosphate monohydrate from initial phases according to the post-mortem analysis by X-ray diffraction and infrared spectroscopy. The maximum sodium uptake capacity of the vanadyl phosphate electrode was 24.3 mg g<sup>-1</sup> with charge efficiency of around 85%. We found no detectable level of contamination by phosphorus nor vanadium from the treated water stream indicating that our synthesized electrode is also environmentally safe for water desalination applications.

Received 19th October 2018  
Accepted 27th January 2019

DOI: 10.1039/c8ta10087j

rsc.li/materials-a

## 1 Introduction

For the production of freshwater, desalination removes dissolved salt ions from abundant feed water sources such as seawater and brackish water.<sup>1</sup> Nowadays, water desalination technologies rely mostly on the membrane-based separation or distillation processes; among them, reverse osmosis covers more than half of the worldwide desalination capacity.<sup>2</sup> For more energy-efficient freshwater production, advanced reverse osmosis devices employ efficient membranes, pumps, and motors as well as energy recovery technologies. Today's modern reverse osmosis processes show energy consumption in the range of 2–5 W h per 1 L of generated freshwater.<sup>3,4</sup>

Over recent years, capacitive deionization (CDI) has emerged as a promising new solution for energy-efficient water desalination.<sup>5–7</sup> The low energy consumption of CDI technologies of below 1 W h per L is achieved by highly reversible

electrosorption *via* electrical double-layer (EDL) formation at the interface between an electrode and saline feedwater. Upon electrochemical operations, sodium cations and chloride anions are electroadsorbed (desalination) on the oppositely charged surface of the carbonaceous electrodes or electro-desorbed (regeneration). For a complete cycle, the cell needs to be charged and discharged alternatively while a feed water stream is flowing through the separator during desalination and effluent water is flowing during the regeneration period. A severe limitation of CDI technologies is the notorious co-ion expulsion.<sup>8–10</sup> Instead of electroadsorption of 1 mol of counter-ions (ions with opposite charge as the electrode) per 1 mol of electrons involved for the desalination reaction (charge efficiency of 100%), some of the co-ions (same charge as the electrode) are desorbed or swapped with counter-ions leading to a lower charge efficiency.<sup>11</sup> In low molar media (especially below 100 mM), sufficiently high electrode potentials allow overcoming the non-permselective regime and accomplishing effective desalination of the stream.<sup>12,13</sup> At high molar media ( $\gg 100$  mM), the charge efficiency approaches 0%, and non-permselective ion swapping dominates the entire charge/discharge process.<sup>14–16</sup> Irreversible redox reactions, for example *via* surface functional groups or water decomposition, will further reduce the charge efficiency.<sup>11,17</sup> The issue of co-ion expulsion can, partially, be addressed by placing an ion-exchange membrane in front of the carbon electrodes; thereby, permselective ion access from the flow channel to the

<sup>a</sup>INM – Leibniz Institute for New Materials, Campus D2 2, 66123 Saarbrücken, Germany. E-mail: volker.presser@leibniz-inm.de

<sup>b</sup>Department of Materials Science and Engineering, Saarland University, Campus D2 2, 66123 Saarbrücken, Germany

<sup>c</sup>Department of Chemical Engineering, Federal University of São Carlos, 13565-905 São Carlos, Brazil

<sup>d</sup>School of Energy, Materials and Chemical Engineering, Korea University of Technology and Education, Chungjeol-ro 1600, 31253 Cheonan, Republic of Korea

† Electronic supplementary information (ESI) available. See DOI: 10.1039/c8ta10087j

compartment housing of the electrode is enabled.<sup>18,19</sup> On the side of the ion exchange membrane facing the carbon electrode, co-ions initially present in electrode will be withheld and contribute towards an enhanced salt removal capacity.<sup>7</sup>

In addition to the low charge efficiency of the CDI technologies for highly concentrated saline water desalination, the intrinsically low salt removal capacity (15–25 mg removal of NaCl per 1 g of electrode material) of the carbonaceous electrode materials is also a drawback.<sup>19</sup> The latter is related to the intrinsically low charge storage capacity of carbon electrodes employing ion electrosorption. Therefore, electroactive materials showing faradaic processes<sup>‡</sup> can be used, that is, materials where the charge is being transferred from the liquid phase to the solid electrode.<sup>20</sup> By sole use of faradaic materials or by hybridizing carbon with faradaic materials, the increased charge storage capacity translated to an improved electrochemical desalination performance.<sup>21,22</sup> Faradaic deionization (FDI) relies on the redox reactions such as ion insertion or conversion reactions which provide perm-selective removal of particular ions.<sup>23–26</sup> Due to the latter feature, FDI systems provide high charge efficiency (>85%) even for highly saline feedwater (>500 mM).<sup>14,27–30</sup> The reported salt removal capacity values of FDI systems are commonly in the range of 20–60 mg g<sup>-1</sup>, but even higher values exceeding 100 mg g<sup>-1</sup> were reported for NaTi<sub>2</sub>(PO<sub>4</sub>)<sub>3</sub> paired with reduced graphene oxide,<sup>31</sup> silver,<sup>32</sup> or bismuth.<sup>33</sup> As the energy efficiency (ratio of the energy during discharge to that of during charging) commonly increases for highly concentrated saline water (>100 mM) through higher ionic conductivity, the FDI systems also provide smart energy management in addition to water desalination.<sup>34</sup>

Earlier works have explored vanadyl phosphate as an electrode material for electrochemical energy storage (EES) systems such as lithium ion, sodium ion batteries in organic electrolytes.<sup>35–39</sup> Recently, vanadyl phosphates have also been reported for EES applications in aqueous electrolytes systems exhibiting stable performance over 1000 cycles.<sup>39–41</sup> The facile hydrothermal synthesis of vanadyl phosphates using temperatures of just 200 °C is another attractive feature for this electrode material. As some of the vanadyl phosphates are known to be insoluble to water, for instance, vanadyl phosphate hemihydrate VOHPO<sub>4</sub>·0.5(H<sub>2</sub>O),<sup>35,42</sup> the application of vanadyl phosphates to electrochemical water desalination technologies seems to be promising. To the best of our knowledge, no studies so far have been explored the desalination performance of vanadyl phosphate neither thorough investigations on the stability of the electrode materials regarding water contamination through degradation byproducts.

Here, we report the desalination performance of a hydrothermally synthesized vanadyl phosphate material while feedwater was continuously flowing along the electrode material

(100 mM NaCl input concentration). We chose aqueous NaCl as the most commonly studied saline medium in the research field of electrochemical desalination with nanoporous carbon and battery electrode materials; and peruse of ion exchange membranes, our work quantifies the sodium ion uptake capacity of vanadyl phosphate. The characteristics of the materials are discussed regarding morphology, chemical composition, phase content, and crystal structure by Raman, and infrared spectroscopy, X-ray diffraction (XRD), electron microscopy, and energy dispersive X-ray spectroscopy (EDX). The essential electrochemical properties of the electrode such as reduction, and oxidation limits, maximum charge storage capacity, coulombic efficiency, and cyclic stability are determined by cyclic voltammetry and galvanostatic analysis. In addition, we explain the origin of the charge storage enhancement during the first 100 cycles by post-mortem analyses *via* XRD and infrared spectroscopy.

## 2 Experimental

### 2.1 Materials

For the free-standing and polymer-binder consolidated carbon film electrodes, type YP-80F activated carbon powder (Kuraray) was mixed with polytetrafluoroethylene (PTFE, Sigma-Aldrich) and ethanol, rolled to various thicknesses, and dried in a vacuum oven (120 °C, 203 Pa) for 48 h while controlling the mass ratio of carbon to PTFE to be 95 : 5. The electrodes classify as free-standing without physically or chemically bound to the current collector; for electrochemical testing, the carbon electrodes were mechanically placed onto the current collector. More information on this type of carbon and the electrode fabrication can be found in ref. 43. In short: YP-80F is a mostly microporous carbon with few-micrometer-sized particles with a specific surface area determined by quenched-solid density functional theory of 1786 m<sup>2</sup> g<sup>-1</sup> and an average pore size of 1.3 nm. In the presence of 5 mass% PTFE, the surface area is reduced to 1599 m<sup>2</sup> g<sup>-1</sup> while the average pore size remains to be 1.3 nm.<sup>44</sup>

Vanadyl phosphate was synthesized by hydrothermal processing at 200 °C (5 °C min<sup>-1</sup>) for 24 h in a PTFE-autoclave with a total volume of 200 mL containing 132 mL of aqueous solution of vanadyl sulfate (VOSO<sub>4</sub>, Sigma Aldrich), phosphoric acid (H<sub>3</sub>PO<sub>4</sub>, Sigma Aldrich), and sodium hydroxide (NaOH, Sigma Aldrich). The molar ratio of VOSO<sub>4</sub>, H<sub>3</sub>PO<sub>4</sub>, deionized water, and NaOH was 1 : 1 : 700 : 0.5. The pH value of the precursor solution was adjusted to 1.8 by adding ammonium hydroxide solution (28% NH<sub>3</sub> in H<sub>2</sub>O, Sigma-Aldrich).<sup>45</sup> After the hydrothermal process, the obtained particle-containing solution was centrifuged for 30 min at 4000 rpm. Next, the sediment was collected, mixed with fresh deionized water, and centrifuged again with the same protocol to rinse the remaining dissolved chemicals. After rinsing twice with deionized water, the sediment was further rinsed with ethanol two times. The resulting ethanol-sediment mixture was ball-milled for 30 min and dried under vacuum for 24 h. Then, the dried powder was mixed with 10 mass% of multi-walled carbon nanotubes (NC7000, Nanocyl SA). Afterward, the mixture was sonicated in 150 mL ethanol for

‡ As defined by Brian Evans Conway, a process is faradaic when an “electron transfer does take place across the double layers, with a consequent change of oxidation state, and hence the chemistry of the electroactive materials” for comparison, in non-faradaic materials, “charge accumulation is achieved electrostatically by positive and negative charges residing on two interfaces separated by a vacuum or a molecular dielectric”.

50 min and filtered through a hydrophilic polycarbonate membrane filter (0.22  $\mu\text{m}$  thickness, Isopore, Merck Millipore Ltd.), subsequently. The final free-standing and binder-free electrode was labeled NVP-CNT.

NC7000 consists of multi-wall carbon nanotube, as can be seen from the transmission electron micrographs shown in ESI, Fig. S1.† Argon gas sorption at  $-186^\circ\text{C}$  (ESI, Fig. S2†) yielded a specific surface area of  $207\text{ m}^2\text{ g}^{-1}$  which is mostly dominated by mesopores in-between the carbon nanotubes and tubular bundles. The electrochemical performance of NC7000 in aqueous solutions can be found in our previous work (ref. 27 and 46).

## 2.2 Material characterization

The morphology of the NVP-CNT electrode was examined by a JEOL JSM 7500F field emission scanning microscope (FE-SEM) at an acceleration voltage of 1 kV. The chemical composition of the carbon electrodes was determined by energy dispersive X-ray spectroscopy (EDX) with an X-Max-150 detector (Oxford Instruments) attached to the SEM chamber. The spectra of ten spots were measured using an accelerating voltage range of 12 kV and averaged.

Raman spectroscopy was carried out with a Renishaw inVia Raman Microscope applying an Nd:YAG laser (532 nm). With a grating of 2400 lines per mm, yielding a spectral resolution of approximately  $1.2\text{ cm}^{-1}$ . The spot size on the sample was  $1.2\text{ }\mu\text{m}$  with a numeric aperture of 0.9. Spectra were recorded for various carbon electrodes with an acquisition time of 30 s and ten accumulations. Fourier-transform infrared spectroscopy (FTIR) with attenuated total reflection (ATR) was carried out with a diamond crystal attached to a Bruker Tensor 27 system.

X-ray diffraction (XRD) experiments were conducted using a D8 Advance (Bruker AXS) diffractometer with a copper X-ray source (Cu  $K\alpha$ , 40 kV, 40 mA) and a nickel filter. The system was calibrated with  $\text{LaB}_6$  (purity 99%, Sigma Aldrich). All measurements were measured between  $10\text{--}80^\circ 2\theta$  in step size of  $0.02^\circ$  and a measurement time of 1 s per step. Rietveld refinement was carried out using TOPAS version 5 software (Bruker AXS).

## 2.3 Electrochemical characterization

We used custom-built electrochemical cells in combination with a VMP300 potentiostat/galvanostat (Bio-Logic) in three-electrode (half-cell) configuration; the scheme of the cell design can be found elsewhere.<sup>47,48</sup> An oversized AC electrode (600  $\mu\text{m}$  thickness, 12 mm diameter) and NVP-CNT (185  $\pm$  12  $\mu\text{m}$  thickness, 12 mm diameter) were used as a counter electrode and a working electrode, respectively. A reference electrode (Ag/AgCl, Bioanalytical Systems) was mounted in close contact with the working electrode and the counter electrode. We further used a GF/A glass fiber filter (Whatman) as a separator and a platinum disk as a current collector. After the cell assembly, 1 M NaCl aqueous electrolyte was injected by syringe backfilling.

The specific capacity ( $Q$  in  $\text{mA h g}^{-1}$ ) was obtained from the charge accumulated ( $\text{mA h}$ ) by the reduction/oxidation current

( $I$ ) measured by galvanostatic cycling with potential limitation (GCPL) through eqn (1):

$$Q = \frac{1}{m} \int_{t_1}^{t_2} I dt \quad (1)$$

where  $t_2 - t_1$  is the time required for the reduction/oxidation of the electrode and  $m$  is the total mass of the working electrode. The specific current ( $\text{A g}^{-1}$ ) was obtained by normalizing the applied current by the total mass of the working electrode.

## 2.4 Desalination performance

For the characterization of the desalination performance, we used a custom-built cell shown in ESI, Fig. S3.† The silicone (600  $\mu\text{m}$  thickness) gaskets enable tight sealing of the NVP-CNT working electrode (26 mm diameter, 64 mg) with a cation exchange membrane (FKS-PET-130, FuMA-Tech) and of a double-stack of the AC negative electrode (26 mm diameter,  $550 \pm 50\text{ }\mu\text{m}$  thickness, 362 mg in total) with an anion exchange membrane (FAS-PET-130, FuMA-Tech). These membranes were required purely due to the non-permselective feature of AC counter electrode for chloride removal as well as the influence of CNT conductive additive.<sup>31</sup> The ion exchange membranes are not necessary even at high concentration ( $>100\text{ mM NaCl}$ ) when both working and counter electrodes rely on redox reactions for the electrochemical operation.<sup>32,49</sup> The NaCl solution passed through the middle channel (3 mm thick) provided by a glass fiber separator (Millipore, 7 stacks of 380  $\mu\text{m}$ ). Hence, the total distance between the working and counter electrodes was 3.26 mm. As current collectors, we used a pair of graphite plates (thickness of 10 mm). Through a small opening channel of 4 mm diameter in the current collector at the counter electrode, we inserted an Ag/AgCl reference electrode. The cell was operated by galvanostatic cycling with potential limitation while the potential of the NVP-CNT electrode was controlled by the reference electrode.

An aqueous solution was prepared with NaCl ( $\geq 99.5\%$  purity, Sigma Aldrich) at 100 mM in deionized water (Milli-Q). Desalination cycling was carried out in a flow-by mode with a semi-single pass flow operation.<sup>11,18,50</sup> Using a 10 L reservoir, the stream of water was continuously circulated at a flow rate of  $5\text{ mL min}^{-1}$  with a peristaltic pump. The combination of a large volume of aqueous NaCl reservoir and a comparably small mass of the electrodes assures that the concentration change of the feedwater stream was negligible during desalination operation. The NaCl reservoir was continuously flushed with nitrogen gas to deplete dissolved oxygen. The conductivity of the treated water stream was measured close to the cell. The pH value of the outflow was measured after the solution stream passed through the conductivity meter. The rest of the solution was circulated back to the solution reservoir.

The desalination capacity (equivalent NaCl salt uptake capacity SUC, in  $\text{mg g}^{-1}$ ) of the working electrode was calculated by eqn (2):

$$\text{SUC} = \frac{1}{2m_w} \sum_{n=0}^k (c_0 - c_n) \nu M_{\text{NaCl}} (t_n - t_{n-1}) \quad (2)$$

where  $c_n$  (in M) is the measured molar concentration at time  $t_n$  (in s),  $c_0$  is the initial concentration,  $\nu$  is the volumetric flow rate (in  $\text{L s}^{-1}$ ),  $M_{\text{NaCl}}$  is the molecular mass of NaCl ( $58\,440\text{ mg mol}^{-1}$ ),  $t_n - t_{n-1}$  is the time interval for conductivity measurement, and  $m_w$  (in g) is the mass of the working electrode. The factor of 2 comes from the fact that the SUC value of the cell is the contribution of two electrodes. The SUC value according to eqn (2) is normalized by the mass of the working electrode.<sup>27</sup> The  $\text{Na}^+$  uptake capacity (NUC) was calculated by applying the molecular weight of sodium  $M_{\text{Na}}$  instead of  $M_{\text{NaCl}}$  without introducing the factor 2 in eqn (2).

The concentration of NaCl is calculated by the relation of concentration and conductivity *via* eqn (3):

$$c_n = \frac{1}{1000} \left[ \left( \frac{\sigma_n - 4.5}{121.29} \right)^{1/0.9826} - 0.13 \right] \quad (3)$$

where  $\sigma_n$  is the corrected conductivity ( $\mu\text{S cm}^{-1}$ ) at time  $t_n$  *via* eqn (4):

$$\sigma_n = \sigma_m - \sigma_w \quad (4)$$

where  $\sigma_m$  is the measured conductivity ( $\mu\text{S cm}^{-1}$ ), and  $\sigma_w$  is the conductivity of water.

The conductivity of water  $\sigma_w$  can be calculated with eqn (5):

$$\sigma_w = \frac{10^7 \times e^2}{k_B \times T} \left( 10^{\text{pH}} N_A D_{\text{H}_3\text{O}^+} + \frac{10^{-14}}{10^{-\text{pH}}} N_A D_{\text{OH}^-} \right)$$

where  $k_B$  is the Boltzmann constant ( $1.38 \times 10^{-23}\text{ m}^2\text{ kg s}^{-2}\text{ K}^{-1}$ ),  $N_A$  is the Avogadro constant ( $6.02 \times 10^{23}\text{ mol}^{-1}$ ),  $D_{\text{H}_3\text{O}^+}$  is the diffusion coefficient of hydronium ion ( $9.3 \times 10^{-9}\text{ m}^2\text{ s}^{-1}$ ), and  $D_{\text{OH}^-}$  is the diffusion coefficient of a hydroxyl ion ( $5.3 \times 10^{-9}\text{ m}^2\text{ s}^{-1}$ ).<sup>51,52</sup>

The charge efficiency<sup>41</sup> was calculated by eqn (6):

$$\text{Charge efficiency (\%)} = \frac{F \times \text{NUC}}{36 \times Q \times M_{\text{Na}}} \times 100\% \quad (6)$$

where  $F$  is the Faraday constant, NUC is the  $\text{Na}^+$  uptake capacity, 36 (=100/3600) is multiplied to  $Q$  for the unit conversion from mA h to Coulomb,  $Q$  is the charge, and  $M_{\text{Na}}$  is the molecular weight of sodium.<sup>11,23</sup>

To quantify the vanadium and phosphorus concentration, water samples were collected at the outlet of the desalination cell while feedwater was flowing through the cell at various flow rates. Water samples were also collected from the 10 L reservoir during desalination operation at a different time; the stream of water was continuously circulated at a flow rate of  $5\text{ mL min}^{-1}$ . The water samples were characterized by inductively coupled plasma optical emission spectrometry (ICP-OES; Jobin Yvon Horiba Ultima 2). For calculation of vanadium and phosphorus concentration, the integral intensities at 292.402 nm and 214.914 nm were used, respectively.

## 3 Results and discussion

### 3.1 Material synthesis and characterization

Scanning electron micrographs of the NVP-CNT electrode show micrometer-sized NVP particles effectively entangled by

MWCNTs (Fig. 1A). According to the X-ray diffraction data (Fig. 1B), the NVP particles contain crystalline  $\text{Na}_{0.5}\text{VOPO}_4 \cdot 2(\text{H}_2\text{O})$  (hydrated sodium vanadyl phosphate; PDF 81-1929) and crystalline  $\text{VOHPO}_4 \cdot 0.5(\text{H}_2\text{O})$  (hydrated vanadyl hydrogen phosphate; PDF 84-07612). The presence of vanadyl phosphate in these both crystal structures is further supported by the stoichiometric ratio of the elements in the particles determined by EDX analysis; 1 : 1 : 5 for vanadium, phosphate, and oxygen (Table 1). Also, the sodium to vanadium ratio of 0.4 : 1 implies the sodiated state of the NVP-CNT electrode, in alignment with the presence of  $\text{Na}_{0.5}\text{VOPO}_4 \cdot 2(\text{H}_2\text{O})$  phase in XRD.

According to the infrared spectrum of the NVP-CNT electrode (Fig. 1C), we see in the range of  $2900\text{--}3650\text{ cm}^{-1}$  the O-H stretching mode for coordinated water.<sup>53,54</sup> The presence of the latter is further supported by a band at  $1635\text{ cm}^{-1}$  which can be ascribed to H-O-H bending vibration of water molecules.<sup>54</sup> The presence of P-O bonding is evidenced by multiple bands in the range of  $900\text{--}1200\text{ cm}^{-1}$  responsible for the P-O stretching mode as well as bending mode below  $700\text{ cm}^{-1}$ .<sup>53,55</sup> The bands at  $960\text{ cm}^{-1}$  and  $1081\text{ cm}^{-1}$  can be assigned to the P-O symmetric and antisymmetric stretching mode in hydrated vanadyl phosphate, respectively while the band at  $1030\text{ cm}^{-1}$  can be ascribed to V=O stretching mode.<sup>56</sup> The bands at  $891\text{ cm}^{-1}$  and  $1200\text{ cm}^{-1}$  indicate the existence  $\text{HPO}_4^-$  due to the P-OH stretching and the in-plane bending, respectively.<sup>55,57,58</sup> Furthermore, the band at  $1409\text{ cm}^{-1}$  corresponds to the O-H-O deformation in alignment with strong hydrogen bonding.<sup>57</sup> The other characteristic bands for  $\text{VOHPO}_4 \cdot 0.5(\text{H}_2\text{O})$  have been reported at  $1130\text{ cm}^{-1}$ ,  $1100\text{ cm}^{-1}$ ,  $925\text{ cm}^{-1}$ ,  $531\text{ cm}^{-1}$ , and  $480\text{ cm}^{-1}$  while the characteristic band of  $\text{VOPO}_4 \cdot 2(\text{H}_2\text{O})$  is reported at  $675\text{ cm}^{-1}$  (ESI, Fig. S4A†).<sup>38,53</sup> The positions of these characteristic bands are found almost identical for the electrodes regardless of the degree of sodiation (ESI, Fig. S4B†).

These findings align with the data seen from Raman spectroscopy (Fig. 1D). According to Gulians *et al.*,<sup>59,60</sup> the  $955\text{ cm}^{-1}$  Raman band is characteristic of P-O stretching in  $\text{VOPO}_4 \cdot 2(\text{H}_2\text{O})$  and distinguished from that of  $\text{VOHPO}_4 \cdot 0.5(\text{H}_2\text{O})$ . Therefore, a shoulder at  $955\text{ cm}^{-1}$  implies the presence of the  $\text{VOPO}_4 \cdot 2(\text{H}_2\text{O})$  in the NVP-CNT electrode (Fig. 1D).<sup>38,53</sup> According to Gulians *et al.*, the P-O stretching in  $\text{VOHPO}_4 \cdot 0.5(\text{H}_2\text{O})$  is found at a higher frequency. The band at  $1015\text{ cm}^{-1}$  might be due to P-H stretching in  $\text{VOHPO}_4 \cdot 0.5(\text{H}_2\text{O})$ . The band at  $995\text{ cm}^{-1}$  can correspond to the stretching vibration of V=O in  $\text{VOPO}_4 \cdot 2(\text{H}_2\text{O})$  which is further evidenced by the absence of  $1031\text{ cm}^{-1}$  (V=O stretching in anhydrous vanadyl phosphate) according to Trchova *et al.*; the latter work provided a comparison of anhydrous vanadyl phosphates and its monohydrated and dehydrated forms.<sup>56</sup> The positions of these characteristic bands at  $955\text{ cm}^{-1}$ ,  $995\text{ cm}^{-1}$ , and  $1015\text{ cm}^{-1}$  are found almost identical for the electrodes regardless of the sodiation state (ESI, Fig. S4C†). Additionally, the bands around  $860\text{--}890\text{ cm}^{-1}$  (P-V-O deformation vibration) also indicates the existence of dihydrate as the band positions for anhydrous vanadyl phosphate and monohydrate forms were observed in a lower frequency around  $830\text{ cm}^{-1}$ .<sup>56</sup> The bands at  $1074\text{ cm}^{-1}$  and  $1125\text{ cm}^{-1}$  could be ascribed either to  $\text{VOHPO}_4 \cdot 0.5(\text{H}_2\text{O})$  or

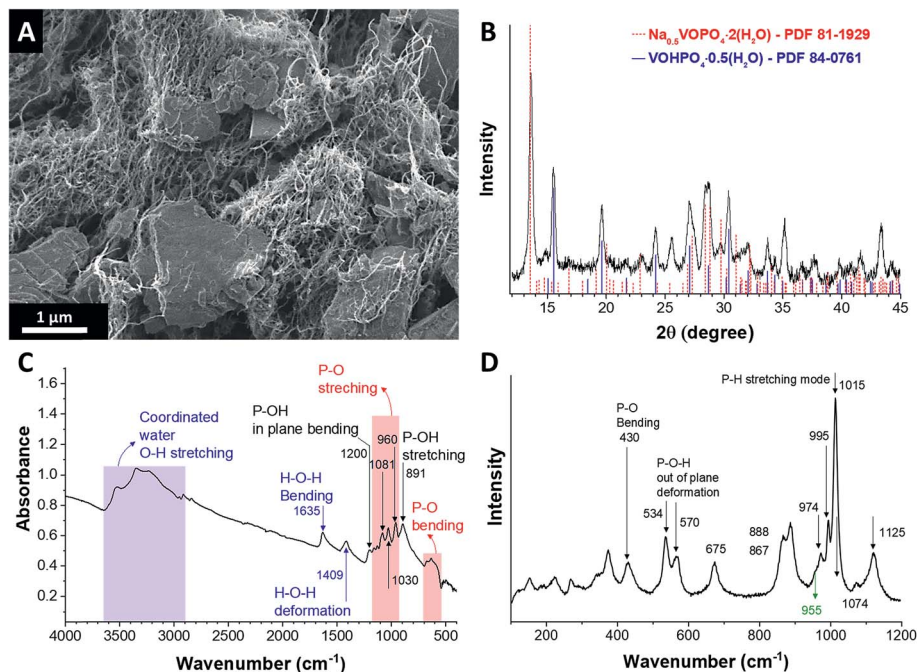


Fig. 1 Material characterizations of the as-synthesized NVP-CNT electrode: (A) scanning electron micrograph, (B) X-ray diffractogram, (C) Fourier-transform infrared spectrum, and (D) Raman spectrum.

Table 1 Sodium, vanadium, phosphorus, and oxygen content of NVP-CNT sample determined by EDX analysis

	Na (atom%)	V (atom%)	P (atom%)	O (atom%)
NVP-CNT	2.39 ± 1.21	7.99 ± 2.03	8.20 ± 2.08	26.8 ± 12.0

$\text{VOPO}_4 \cdot 2(\text{H}_2\text{O})$ . The bands at  $537 \text{ cm}^{-1}$  and  $430 \text{ cm}^{-1}$  seem to be from the coupled V–O and P–O bending modes either in  $\text{VOHPO}_4 \cdot 0.5(\text{H}_2\text{O})$  or  $\text{VOPO}_4 \cdot 2(\text{H}_2\text{O})$ .<sup>53,60</sup> These results from Raman as well as from FT-IR and XRD analyses clearly indicate the presence of both  $\text{VOHPO}_4 \cdot 0.5(\text{H}_2\text{O})$  or sodiated  $\text{VOPO}_4 \cdot 2(\text{H}_2\text{O})$  phases in the as-synthesized NVP-CNT electrode.

### 3.2 Electrochemical performance

To determine the stable electrochemical potential window of the NVP-CNT electrode in 1 M NaCl aqueous solution, we applied cyclic voltammetry at the scan rate of  $1 \text{ mV s}^{-1}$  (Fig. 2A and B). First, the start potential was fixed at  $+0.2 \text{ V vs. Ag/AgCl}$  to focus more on the degradation mechanism during reduction process by avoiding the deintercalation process which at a higher potential ( $+0.32 \text{ V vs. Ag/AgCl}$ ), and the potential limit is extended towards more negative potential values (Fig. 2A). A sharp current increase was observed during reduction at  $-0.16 \text{ V vs. Ag/AgCl}$ . Because no reversible peak current was observed during oxidation, this irreversible reduction reaction at  $-0.16 \text{ V}$  implies a possible electrode degradation. A large reduction current below  $-0.6 \text{ V vs. Ag/AgCl}$  indicates hydrogen gas evolution. To prevent electrode degradation, we chose a reduction potential limit of  $-0.16 \text{ V vs. Ag/AgCl}$ .

In case of the potential extension towards more positive electrode potential values (Fig. 2B), the start potential was fixed to  $+0.17 \text{ V vs. Ag/AgCl}$  to avoid the intercalation process which occurs at a lower potential of  $+0.13 \text{ V vs. Ag/AgCl}$ . The oxidation current starts increasing at  $+0.72 \text{ V vs. Ag/AgCl}$  and soars rapidly as the potential was further scanned towards higher potential values. A large current increase above  $+0.72 \text{ V vs. Ag/AgCl}$  indicates oxygen evolution as well as a possible electrode degradation. Hence, we chose for our continued experiments an oxidation limit potential of  $+0.72 \text{ V vs. Ag/AgCl}$ .

In a potential range from  $-0.1 \text{ V}$  to  $+0.5 \text{ V vs. Ag/AgCl}$ , the NVP-CNT electrode exhibits a clear redox peak pair around  $+0.2 \text{ V vs. Ag/AgCl}$  (Fig. 2C) implying sodiation occurs at  $+0.13 \text{ V vs. Ag/AgCl}$  and desodiation at  $+0.32 \text{ V vs. Ag/AgCl}$ . A small shoulder of the oxidation peak in the initial cyclic voltammogram may relate to the presence of more than one redox peak pairs, thereby implying the presence of two crystal phases in the as-synthesized NVP-CNT. As the cycle number increases, the initially broad redox peaks become narrower. The narrow redox peaks after 150 cycles compared to the initial cyclic voltammogram implies that the intercalation process is mostly governed by one crystal structure in the electrode. For quantitative analysis, the specific capacity of the NVP-CNT electrode is measured at low specific current ( $10 \text{ mA g}^{-1}$ ) in the potential range from  $-0.1 \text{ V}$  to  $+0.5 \text{ V vs. Ag/AgCl}$  after every 30 voltammetric cycles (Fig. 2D, inset). As compared to the initial galvanostatic charging/discharging profile with a broad potential plateau (Fig. 2D, inset), the profile after 30 cycles shows a rather flat potential plateau in alignment with the cyclic voltammograms. The initial specific charge capacity was  $23.0 \text{ mA h g}^{-1}$ ; however, as the cycle number increases, the

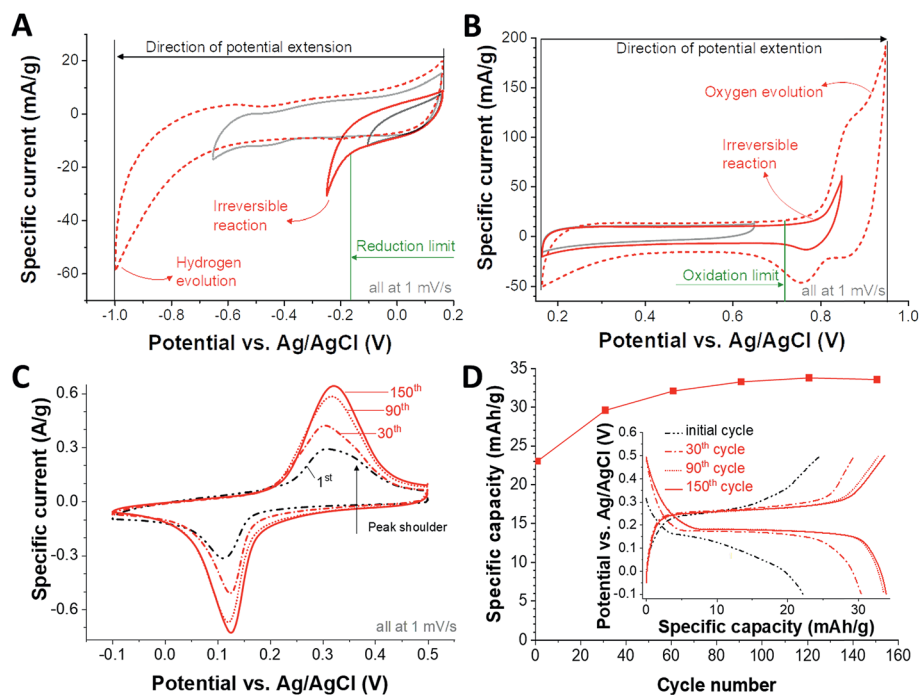


Fig. 2 Electrochemical characterizations of the NVP-CNT electrode: cyclic voltammetry to determine the reduction limit (A) and the oxidation limit (B), (C) cyclic voltammograms obtained at  $1 \text{ mV s}^{-1}$  up to 150 cycles, and (D) specific capacity values obtained by galvanostatic charge and discharge at  $10 \text{ mA g}^{-1}$  (inset) measured after every 30 voltammetric cycles.

specific capacity further increases until the value is stabilized at around  $33.8 \text{ mA h g}^{-1}$  after 120 cycles (Fig. 2D).

Using galvanostatic charge/discharge cycling, we also measured the rate handling performance of the NVP-CNT electrodes at various specific current in the potential range from  $-0.1 \text{ V}$  to  $+0.5 \text{ V vs. Ag/AgCl}$  after 120 cycles (Fig. 3A). The NVP-CNT exhibits a moderate power handling performance in the specific current range of  $0.01\text{--}10 \text{ A g}^{-1}$ ; at high specific current at  $10 \text{ A g}^{-1}$ , the specific capacity of  $4.7 \text{ mA h g}^{-1}$  was maintained (Fig. 3B).

### 3.3 Origin of capacity enhancement

To investigate the origin of the capacity enhancement, we analyzed the NVP-CNT electrodes at different states of

sodiation; as a baseline, we first present the data found for the initial stage of the electrodes. Electrode sodiation was accomplished by applying a specific current of  $10 \text{ mA g}^{-1}$  to  $-0.1 \text{ V vs. Ag/AgCl}$  with subsequent potential holding for 30 min. A desodiated electrode was prepared similarly by oxidizing the NVP-CNT electrode to  $+0.5 \text{ V vs. Ag/AgCl}$  with the subsequent potential holding for 30 min. The half-sodiated electrode was prepared by sodiating the NVP-CNT electrode with the half amount of the initial charge storage capacity of the electrode. Sodiation and desodiation refer to the addition or removal of sodium; therefore, the term desodiation is not intended to indicate the formation of a completely sodium-free NVP phase.

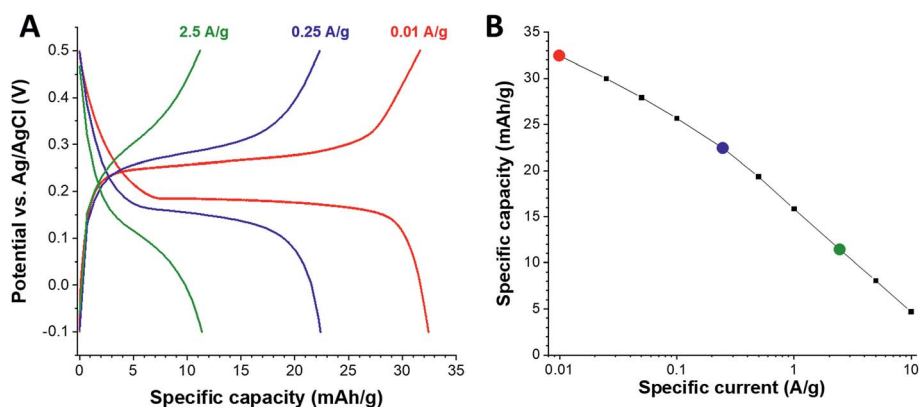


Fig. 3 Rate handling performance of the NVP-CNT electrode: (A) galvanostatic profiles and (B) specific capacity values obtained after 150 cycles at various specific currents ( $0.01\text{--}10 \text{ A g}^{-1}$ ).

The (001) reflection of  $\text{Na}_x\text{VOPO}_4 \cdot 2(\text{H}_2\text{O})$  in the NVP-CNT electrode at  $13.6^\circ$   $2\theta$  shifts to a higher angle indicating a contraction of interlayer separation caused by sodium intercalation (Fig. 4A). As reported by Jacobson *et al.*, the interlayer  $\text{Na}_x\text{VOPO}_4 \cdot 2(\text{H}_2\text{O})$  spacing along the  $c$ -axis contracts upon sodium intercalation while there is an increase along the  $a$ -axis which is in line with the results from our Rietveld analysis (Table 2).<sup>61</sup> Further, the symmetry of  $\text{Na}_x\text{VOPO}_4 \cdot 2(\text{H}_2\text{O})$  structure is changed upon the intercalation/deintercalation as indicated by the distortion of triclinic structure.<sup>62</sup> Unlike the (001) reflection of  $\text{Na}_x\text{VOPO}_4 \cdot 2(\text{H}_2\text{O})$ ,  $\text{Na}_x\text{VOHPO}_4 \cdot 0.5(\text{H}_2\text{O})$  shows an expansion along the  $c$ -axis, as can be seen from the shift of the (001) reflection at  $15.5^\circ$   $2\theta$  towards lower angles. A similar observation was reported by Benziger *et al.* that  $\text{VOHPO}_4 \cdot 0.5(\text{H}_2\text{O})$  expands along the  $c$ -axis upon intercalation with  $n$ -alkylamines.<sup>37</sup> The unit cell volume changes for  $\text{Na}_x\text{VOPO}_4 \cdot 2(\text{H}_2\text{O})$  by +1% in the fully sodiated state as compared to the desodiated state. In contrast to  $\text{Na}_x\text{VOPO}_4 \cdot 2(\text{H}_2\text{O})$ , the  $\text{VOHPO}_4 \cdot 0.5(\text{H}_2\text{O})$  phase in NVP-CNT exhibit almost no volume change during sodiation process (the difference is below 0.1%).

We further analyzed the crystal structure of the NVP-CNT electrodes with different sodiated states after 150 cycles. The sodiated and desodiated electrodes were prepared by following the same protocol described above. In the diffractogram of the desodiated electrode after 150 cycles, we no longer see any of the reflections assigned to  $\text{Na}_x\text{VOHPO}_4 \cdot 0.5(\text{H}_2\text{O})$  (Fig. 4B). The disappearance of  $\text{Na}_x\text{VOHPO}_4 \cdot 0.5(\text{H}_2\text{O})$  is further supported by infrared spectroscopy (Fig. 4C) as evidenced by the absence of the reported characteristic bands of  $\text{VOHPO}_4 \cdot 0.5(\text{H}_2\text{O})$  at  $1635\text{ cm}^{-1}$ ,  $1415\text{ cm}^{-1}$ ,  $1200\text{ cm}^{-1}$ , and  $891\text{ cm}^{-1}$ .<sup>38,53</sup>

The reflections of the desodiated NVP-CNT after 150 cycles (Fig. 4D) indicate the presence of the monohydrate form of

vanadyl phosphate,  $\text{Na}_x\text{VOPO}_4 \cdot (\text{H}_2\text{O})$ ; the positions of the reflexes match well with the results reported by Gautier *et al.* for desodiated  $\text{VOPO}_4 \cdot (\text{H}_2\text{O})$ .<sup>63</sup> Furthermore, the reflection at  $13.7^\circ$   $2\theta$  for the initially desodiated NVP-CNT electrode shifts to  $13.8^\circ$   $2\theta$  after 150 cycles (ESI, Fig. S5A†). These results indicate that the originally observed  $\text{VOHPO}_4 \cdot 0.5(\text{H}_2\text{O})$  and  $\text{Na}_{0.5}\text{VOPO}_4 \cdot 2(\text{H}_2\text{O})$  phases were converted to  $\text{Na}_x\text{VOPO}_4 \cdot (\text{H}_2\text{O})$  phase after 150 cycles and correspond to the data from cyclic voltammetry and galvanostatic analyses (Fig. 2C and D).

Upon sodiation, the reflection at  $13.8^\circ$   $2\theta$  of the desodiated NVP-CNT electrode disappeared after 150 cycles, and we see a large shift of the (001) reflection appears now at  $16.6^\circ$   $2\theta$ . The shifted (001) reflection also exhibits a shoulder towards larger  $d$ -spacings with two maxima at  $14.3^\circ$   $2\theta$  and  $15.6^\circ$   $2\theta$  depending on the measurement spot (Fig. 4D and Fig. S5B in ESI†). Similar shoulders are also observed for the shifted higher order reflections (Fig. 4D, S5C and D†), such as (002) and (003). Such large shifts align with previous work of Zima *et al.* who observed the (001) reflection for  $\text{NaVOPO}_4 \cdot (\text{H}_2\text{O})$  at  $18.3^\circ$   $2\theta$ .<sup>64</sup>

In summary, we see that initial  $\text{VOHPO}_4 \cdot 0.5(\text{H}_2\text{O})$ , and  $\text{Na}_{0.5}\text{VOPO}_4 \cdot 2(\text{H}_2\text{O})$  are slowly converted to  $\text{Na}_x\text{VOPO}_4 \cdot (\text{H}_2\text{O})$  after continued electrochemical cycling; assuming a higher charge storage capacity of the latter phase, we see a continuous increase in the overall electrochemical performance over time until a maximum performance is obtained after 150 cycles (Fig. 2D).

### 3.4 Desalination performance

The desalination performance of CDI systems is usually quantified by use of a full-cell configuration employing the same material and mass for the positive and negative electrodes. Such

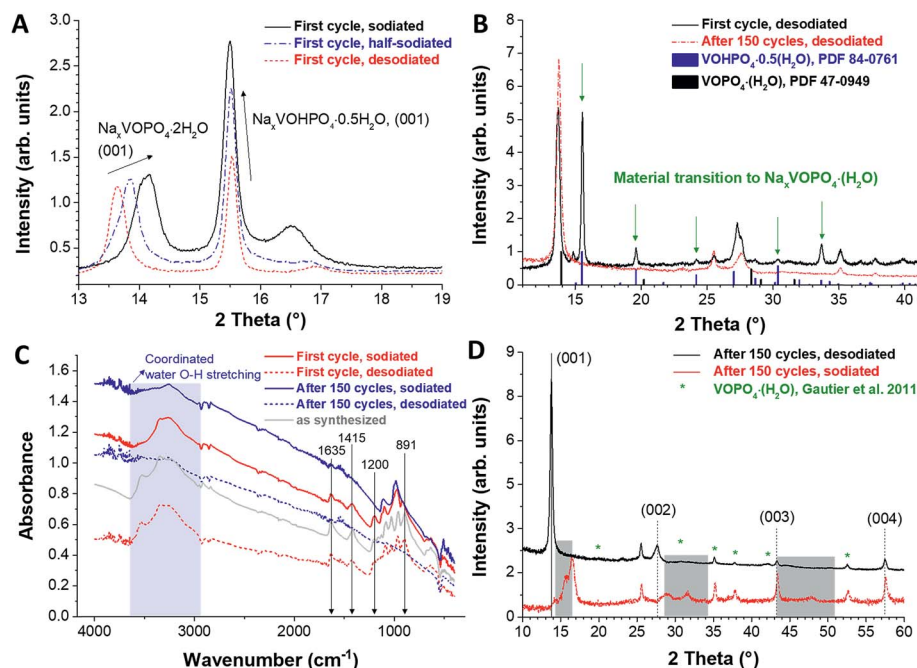


Fig. 4 Post-mortem analyses for the NVP-CNT electrodes prepared with different sodiation states. X-ray diffractograms (A, B and D), and Fourier transform infrared spectra (C).

Table 2 Unit cell parameters obtained by Rietveld refinement analysis based on the reported crystal data

	<i>a</i> (Å)	<i>b</i> (Å)	<i>c</i> (Å)	<i>V</i> (Å <sup>3</sup> )	$\alpha$ (°)	$\beta$ (°)	$\gamma$ (°)	Reference	Structure
<b>Initial cycle</b>									
Desodiated VOPO <sub>4</sub> ·2(H <sub>2</sub> O)	6.27	6.32	13.18	507.48	80.4	87.0	98.7	PDF 81-1929	Triclinic
Half-sodiated VOPO <sub>4</sub> ·2(H <sub>2</sub> O)	6.31	6.33	13.00	504.83	80.7	86.8	98.9	PDF 81-1929	Triclinic
Sodiated VOPO <sub>4</sub> ·2(H <sub>2</sub> O)	6.34	6.38	12.99	513.04	81.5	87.3	98.5	PDF 81-1929	Triclinic
Desodiated VOHPO <sub>4</sub> ·0.5(H <sub>2</sub> O)	7.42	9.62	5.71	407.88	90	90	90	PDF 84-0761	Orthorhombic
Half-sodiated VOHPO <sub>4</sub> ·0.5(H <sub>2</sub> O)	7.43	9.62	5.71	408.71	90	90	90	PDF 84-0761	Orthorhombic
Sodiated VOHPO <sub>4</sub> ·0.5(H <sub>2</sub> O)	7.42	9.62	5.71	408.19	90	90	90	PDF 84-0761	Orthorhombic
<b>After 150 cycles</b>									
Desodiated VOPO <sub>4</sub> ·(H <sub>2</sub> O)	6.15	6.15	6.43	242.98	90	90	90	PDF 47-0949	Tetragonal
Sodiated VOPO <sub>4</sub> ·(H <sub>2</sub> O)	6.19	6.19	11.25	432.05	90	90	90	Ref. 64	Tetragonal

symmetric electrode configuration is also the common configuration for the analysis of electrical double-layer capacitors and pseudocapacitors.<sup>5,17</sup> Yet, to understand the individual processes occurring uniquely at either electrode, half-cell measurements are widely used in the field of electrochemistry. Particularly, the quantification of energy storage materials often employs an oversized counter-electrode with a large enough capacity to assure that one can quantify the maximum charge storage capacity of the working electrode without capacity limitation imposed by the counter electrode. When using a half-cell setup, we can also effectively characterize an individual FDI electrode and its unique ion removal characteristics as demonstrated in earlier work (ref. 27).

In our study, we paired a free-standing NVP-CNT electrode with an oversized counter-electrode of activated carbon (YP-80F) because of the robust performance stability of the latter. Fig. 5A displays the concentration profile during galvanostatic operation at 50 mA g<sup>-1</sup> in the potential range from -0.1 V to +0.4 V vs. Ag/AgCl. This potential range was determined based on the results from Fig. 2A and B to avoid any decomposition process.

After reaching +0.4 V vs. Ag/AgCl, the potential was held for 10 min, and subsequent resting time of 6 min allowed us to determine the baseline concentration. After reaching -0.1 V vs. Ag/AgCl, the potential was held for 15 min with a subsequent

resting time of 6 min. This reduction and oxidation cycle was repeated for 280 times. When the electrode potential is swept from -0.1 V to +0.4 V vs. Ag/AgCl, the concentration of the feed water solution increases which indicates that sodium ions are released from the NVP-CNT electrode material. The amount of total released sodium ions corresponds with 20.7 mg g<sup>-1</sup> (normalized to the mass of the NVP-CNT electrode) during the oxidation process including 10 min of potential holding. The release of sodium ions is balanced by the concurrent release of chloride ions at the activated carbon counter electrode.

During reduction of the electrode from +0.4 V to -0.1 V vs. Ag/AgCl, the concentration of the feed solution decreases because sodium ions are being intercalated into the NVP-CNT electrode (Fig. 5A). The total sodium ion removal of 21.8 mg g<sup>-1</sup> was achieved during the entire reduction process leading to an average NUC of 21.3 mg g<sup>-1</sup> for the initial oxidation/reduction cycle with a charge efficiency of 87%. While sodium ions are removed through the intercalation process at the NVP-CNT electrode, the electrochemical balance was achieved by the concurrent uptake of chloride ions at the activated carbon counter electrode. For that reason, the NVP-CNT electrode can contribute to the NaCl removal of 27.9 mg g<sup>-1</sup> (equivalent NaCl uptake) when a counter electrode with equal charge storage capacity is applied.<sup>27</sup> Up to 126 cycles, the NUC value continuously increases from 21.3 mg

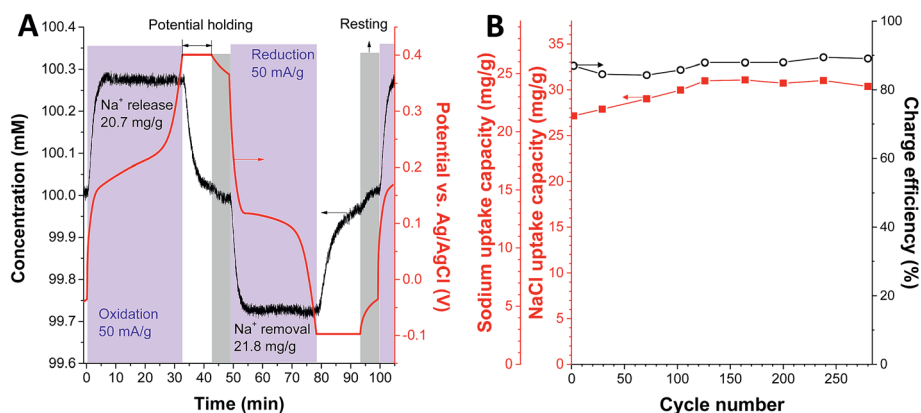


Fig. 5 Characterizations of the electrochemical desalination cell for 100 mM NaCl feed water. (A) Concentration and potential profiles of the cell during galvanostatic operation at 50 mA g<sup>-1</sup>. (B) Salt uptake and sodium uptake capacity, and charge efficiency values obtained for over 280 cycles.

$\text{g}^{-1}$  to  $24.3 \text{ mg g}^{-1}$  (SUC from  $27.2 \text{ mg g}^{-1}$  to  $31.0 \text{ mg g}^{-1}$ ) which aligns with the capacity enhancement observed from the electrochemical analysis in 1 M NaCl solution (Fig. 2D). After that, the SUC value has stabilized with no sign of rapid performance degradation over 280 cycles.

With vanadium and phosphorus being possible leached out of the electrode material during electrochemical cycling, we also analyzed the effluent water exiting the cell at various flow rates ( $1\text{--}40 \text{ mL min}^{-1}$ ) and different times during desalination process. Chemical analysis by ICP-OES is shown in ESI (Fig. S6A and B†), and we see, in the case of different flow rates, no evidence of an increased concentration above the level of the reference water (initially prepared 100 mM NaCl solution) which showed  $7 \pm 2 \mu\text{g L}^{-1}$  and  $11 \pm 18 \mu\text{g L}^{-1}$  for phosphorus and vanadium, respectively (Fig. S6A†). The vanadium concentration as a function of time (Fig. S6B†) shows a low concentration of  $6.2 \pm 0.8 \mu\text{g L}^{-1}$  after 64 h of operation and  $6.3 \pm 0.4 \mu\text{g L}^{-1}$  after 232 h of operation; in the case of phosphorus, the results were in the undetectable range for all samples. The slight initial increase of about  $3 \mu\text{g L}^{-1}$  in vanadium concentration after 62 h (Fig. S6B†) is most probably due to the remaining precursor after the synthesis.

## 4 Conclusions

We used a hydrothermal synthesis to obtain a mixture of  $\text{VOHPO}_4 \cdot 0.5(\text{H}_2\text{O})$  and  $\text{Na}_{0.5}\text{VOPO}_4 \cdot 2(\text{H}_2\text{O})$  and mixed the material with multi-walled carbon nanotubes to obtain well-conductive and free-standing electrodes. As characterized by cyclic voltammetry, the reduction and oxidation limits of the as-synthesized electrode material were determined to be  $-0.16 \text{ V}$  and  $+0.72 \text{ V}$  vs. Ag/AgCl, respectively. We observed that the specific capacity of the electrode was increasing as the electrochemical cyclic process goes by. According to post-mortem analyses by XRD and infrared spectroscopy, the enhancing capacity performance is considered to be due to the conversion of the initial two phases to  $\text{Na}_x\text{VOPO}_4 \cdot (\text{H}_2\text{O})$ . For desalination of a 100 mM NaCl aqueous solution, our electrode material showed a stable performance over 280 cycles and exhibited the maximum sodium uptake capacity of  $24.3 \text{ mg g}^{-1}$  with a charge efficiency of 87%. This sodium uptake capacity is equivalent to NaCl uptake capacity of  $31.0 \text{ mg g}^{-1}$  in case of ideal balance of the cell by applying a counter electrode with the same charge storage capacity. We found no detectable level of contamination by phosphorus nor vanadium from the treated water stream indicating that our synthesized electrode is also environmentally stable for water desalination applications. Our data has provided the first dataset for the desalination performance of vanadyl phosphate, but for defined target applications, like seawater remediation or mining water treatment, further experiments with different ion concentrations and different multi-ion systems are needed.

## Conflicts of interest

There are no conflicts to declare.

## Acknowledgements

Pattarachai Srimuk acknowledges the German Academic Exchange Service DAAD for their financial support (award numbers 91579066) within the frame of the GSSP-Program and DocMASE. Rafael Linzmeyer Zornitta acknowledges his fellowship supported by the São Paulo Research Foundation (FAPESP, processes 2015/26593-3 and 2016/24684-4). The authors thank Eduard Arzt (INM) for his continuing support. The authors thank Öznil Budak, Andrea Jung, Anna Schreiber, and Yuan Zhang (all at INM) for their support. We thank Jeyong Yoon (Seoul National University) for helpful discussions. This work was part of the EEIGM work of Rose Zwingelstein. The work of Jaehoon Choi was part of the joint program between Saarland University, the INM, and KOREATECH and we thank Haiwoong Park for his kind support of the program.

## References

- 1 L. F. Greenlee, D. F. Lawler, B. D. Freeman, B. Marrot and P. Moulin, *Water Res.*, 2009, **43**, 2317–2348.
- 2 M. S. Islam, A. Sultana, A. H. M. Saadat, M. Shammi and M. K. Uddin, *J. Sci. Res.*, 2018, **10**, 77–97.
- 3 Y. Ghalavand, M. S. Hatamipour and A. Rahimi, *Desalin. Water Treat.*, 2015, **54**, 1526–1541.
- 4 A. M. Blanco-Marigorta, A. Lozano-Medina and J. D. Marcos, *Energy*, 2017, **137**, 752–760.
- 5 M. E. Suss and V. Presser, *Joule*, 2018, **2**, 10–15.
- 6 Y. Liu, C. Nie, X. Liu, X. Xu, Z. Sun and L. Pan, *RSC Adv.*, 2015, **5**, 15205–15225.
- 7 M. E. Suss, S. Porada, X. Sun, P. M. Biesheuvel, J. Yoon and V. Presser, *Energy Environ. Sci.*, 2015, **8**, 2296–2319.
- 8 P. Wu, J. Huang, V. Meunier, B. G. Sumpter and R. Qiao, *J. Phys. Chem. Lett.*, 2012, **3**, 1732–1737.
- 9 R. Burt, G. Birkett and X. Zhao, *Phys. Chem. Chem. Phys.*, 2014, **16**, 6519–6538.
- 10 C. Prehal, D. Weingarth, E. Perre, R. T. Lechner, H. Amenitsch, O. Paris and V. Presser, *Energy Environ. Sci.*, 2015, **8**, 1725–1735.
- 11 R. Zhao, P. Biesheuvel, H. Miedema, H. Bruning and A. van der Wal, *J. Phys. Chem. Lett.*, 2009, **1**, 205–210.
- 12 P. M. Biesheuvel, S. Porada, M. Levi and M. Z. Bazant, *J. Solid State Electrochem.*, 2014, **18**, 1365–1376.
- 13 N. Shpigel, M. D. Levi, S. Sigalov, D. Aurbach, L. Daikhin and V. Presser, *J. Phys.: Condens. Matter*, 2016, **28**, 114001.
- 14 P. Srimuk, J. Lee, S. Fleischmann, S. Choudhury, N. Jäckel, M. Zeiger, C. Kim, M. Aslan and V. Presser, *J. Mater. Chem. A*, 2017, **5**, 15640–15649.
- 15 C. Prehal, C. Koczwar, N. Jäckel, A. Schreiber, M. Burian, H. Amenitsch, M. A. Hartmann, V. Presser and O. Paris, *Nat. Energy*, 2017, **2**, 16215.
- 16 C. Prehal, C. Koczwar, H. Amenitsch, V. Presser and O. Paris, *Nat. Commun.*, 2018, **9**, 4145.
- 17 S. Porada, R. Zhao, A. van der Wal, V. Presser and P. M. Biesheuvel, *Prog. Mater. Sci.*, 2013, **58**, 1388–1442.
- 18 P. M. Biesheuvel and A. van der Wal, *J. Membr. Sci.*, 2010, **346**, 256–262.

- 19 C. Kim, J. Lee, P. Srimuk, M. Aslan and V. Presser, *ChemSusChem*, 2017, **10**, 4914–4920.
- 20 B. E. Conway, *Electrochemical Supercapacitors*, Springer, Berlin, 1999.
- 21 J. Lee, S. Kim, C. Kim and J. Yoon, *Energy Environ. Sci.*, 2014, **7**, 3683–3689.
- 22 M. Pasta, C. D. Wessells, Y. Cui and F. La Mantia, *Nano Lett.*, 2012, **12**, 839–843.
- 23 P. Srimuk, J. Lee, S. Fleischmann, M. Aslan, C. Kim and V. Presser, *ChemSusChem*, 2018, **11**, 2091–2100.
- 24 K. C. Smith and R. Dmello, *J. Electrochem. Soc.*, 2016, **163**, A530–A539.
- 25 F. Chen, Y. Huang, L. Guo, M. Ding and H. Y. Yang, *Nanoscale*, 2017, **9**, 10101–10108.
- 26 H. Yoon, J. Lee, S. Kim and J. Yoon, *Desalination*, 2017, **422**, 42–48.
- 27 J. Lee, P. Srimuk, K. Aristizabal, C. Kim, S. Choudhury, Y. C. Nah, F. Mücklich and V. Presser, *ChemSusChem*, 2017, **10**, 3611–3623.
- 28 J. Lee, S. Kim and J. Yoon, *ACS Omega*, 2017, **2**, 1653–1659.
- 29 P. Srimuk, J. Lee, A. Tolosa, C. Kim, M. Aslan and V. Presser, *Chem. Mater.*, 2017, **29**, 9964–9973.
- 30 S. Kim, H. Yoon, D. Shin, J. Lee and J. Yoon, *J. Colloid Interface Sci.*, 2017, **506**, 644–648.
- 31 Y. Huang, F. Chen, L. Guo and H. Y. Yang, *J. Mater. Chem. A*, 2017, **5**, 18157–18165.
- 32 F. Chen, Y. Huang, D. Kong, M. Ding, S. Huang and H. Y. Yang, *FlatChem*, 2018, **8**, 9–16.
- 33 D.-H. Nam and K.-S. Choi, *J. Am. Chem. Soc.*, 2017, **139**, 11055–11063.
- 34 F. Chen, Y. Huang, L. Guo, L. Sun, Y. Wang and H. Y. Yang, *Energy Environ. Sci.*, 2017, **10**, 2081–2089.
- 35 G. J. Hutchings, *J. Mater. Chem.*, 2004, **14**, 3385–3395.
- 36 J. K. Bartley, I. J. Ellison, A. Delimitis, C. J. Kiely, A.-Z. Isfahani, C. Rhodes and G. J. Hutchings, *Phys. Chem. Chem. Phys.*, 2001, **3**, 4606–4613.
- 37 J. B. Benziger, V. Gulians and S. Sundaresan, *Catal. Today*, 1997, **33**, 49–56.
- 38 F. Ben Abdelouahab, R. Olier, N. Guilhaume, F. Lefebvre and J. C. Volta, *J. Catal.*, 1992, **134**, 151–167.
- 39 W. Weng, R. Al Otaibi, M. Alhumaimess, M. Conte, J. K. Bartley, N. F. Dummer, G. J. Hutchings and C. J. Kiely, *J. Mater. Chem.*, 2011, **21**, 16136–16146.
- 40 Y. He, X. Yang, Y. Bai, J. Zhang, L. Kang, Z. Lei and Z.-H. Liu, *Electrochim. Acta*, 2015, **178**, 312–320.
- 41 C. Wu, X. Lu, L. Peng, K. Xu, X. Peng, J. Huang, G. Yu and Y. Xie, *Nat. Commun.*, 2013, **4**, 2431.
- 42 A. A. Rownaghi, Y. H. Taufiq-Yap and F. Rezaei, *Ind. Eng. Chem. Res.*, 2009, **48**, 7517–7528.
- 43 M. Aslan, M. Zeiger, N. Jackel, I. Grobelsek, D. Weingarh and V. Presser, *J. Phys.: Condens. Matter*, 2016, **28**, 114003.
- 44 N. Jäckel, M. Rodner, A. Schreiber, J. Jeongwook, M. Zeiger, M. Aslan, D. Weingarh and V. Presser, *J. Power Sources*, 2016, **326**, 660–671.
- 45 M. Schindler, W. Joswig and W. H. Baur, *J. Solid State Chem.*, 1999, **145**, 15–22.
- 46 J. Lee, P. Srimuk, S. Fleischmann, A. Ridder, M. Zeiger and V. Presser, *J. Mater. Chem. A*, 2017, **5**, 12520–12527.
- 47 D. Weingarh, M. Zeiger, N. Jäckel, M. Aslan, G. Feng and V. Presser, *Adv. Energy Mater.*, 2014, **4**, 1400316.
- 48 J. Lee, D. Weingarh, I. Grobelsek and V. Presser, *Energy Technol.*, 2016, **4**, 75–84.
- 49 P. Srimuk, J. Halim, J. Lee, Q. Tao, J. Rosen and V. Presser, *ACS Sustainable Chem. Eng.*, 2018, **6**, 3739–3747.
- 50 S. Porada, L. Weinstein, R. Dash, A. van der Wal, M. Bryjak, Y. Gogotsi and P. M. Biesheuvel, *ACS Appl. Mater. Interfaces*, 2012, **4**, 1194–1199.
- 51 K. S. Birdi, *Handbook of Surface and Colloid Chemistry*, CRC Press, Boca Raton, 4 edn, 2015.
- 52 R. L. Zornitta, P. Srimuk, J. Lee, B. Krüner, M. Aslan, L. A. M. Ruotolo and V. Presser, *ChemSusChem*, 2018, **13**, 2101–2113.
- 53 W.-S. Dong, J. K. Bartley, N.-X. Song and G. J. Hutchings, *Chem. Mater.*, 2005, **17**, 2757–2764.
- 54 Z. Luo, E. Liu, T. Hu, Z. Li and T. Liu, *Ionics*, 2015, **21**, 289–294.
- 55 J. W. Johnson, D. C. Johnston, A. J. Jacobson and J. F. Brody, *J. Am. Chem. Soc.*, 1984, **106**, 8123–8128.
- 56 M. Trchova, P. Capkova, P. Matejka, K. Melanova, L. Benes and E. Uhlirova, *J. Solid State Chem.*, 1999, **148**, 197–204.
- 57 P. Kolandaivel, R. Parthipan and S. Selvasekarapandian, *Cryst. Res. Technol.*, 1993, **28**, 1139–1145.
- 58 C. Drouet, *BioMed Res. Int.*, 2013, **2013**, 12.
- 59 V. V. Gulians, S. A. Holmes, J. B. Benziger, P. Heaney, D. Yates and I. E. Wachs, *J. Mol. Catal. A: Chem.*, 2001, **172**, 265–276.
- 60 V. V. Gulians, J. B. Benziger and S. Sundaresan, *Chem. Mater.*, 1995, **7**, 1485–1492.
- 61 A. J. Jacobson, J. W. Johnson, J. F. Brody, J. C. Scanlon and J. T. Lewandowski, *Inorg. Chem.*, 1985, **24**, 1782–1787.
- 62 G. A. Gehring and K. A. Gehring, *Rep. Prog. Phys.*, 1975, **38**, 1.
- 63 R. Gautier, N. Audebrand, E. Furet, R. Gautier and E. L. Fur, *Inorg. Chem.*, 2011, **50**, 4378–4383.
- 64 V. Zima, L. Benes, K. Melanova and J. Svoboda, *J. Solid State Chem.*, 2004, **177**, 1173–1178.

## Supplementary Information

# Sodium ion removal by hydrated vanadyl phosphate for electrochemical water desalination

Juhan Lee,<sup>a,b</sup> Pattarachai Srimuk,<sup>a,b</sup> Rose Zwingelstein,<sup>a,b</sup>

Rafael Linzmeyer Zornitta,<sup>a,c</sup> Jaehoon Choi,<sup>a,d</sup> Choonsoo Kim,<sup>a</sup> Volker Presser<sup>a,b,\*</sup>

<sup>a</sup> INM - Leibniz Institute for New Materials, Campus D2 2, 66123 Saarbrücken, Germany

<sup>b</sup> Department of Materials Science and Engineering, Saarland University, Campus D2 2, 66123 Saarbrücken, Germany

<sup>c</sup> Department of Chemical Engineering, Federal University of São Carlos, 13565-905 São Carlos, Brazil

<sup>d</sup> School of Energy, Materials, and Chemical Engineering, Korea University of Technology and Education, Chungjeol-ro 1600, 31253 Cheonan, Republic of Korea

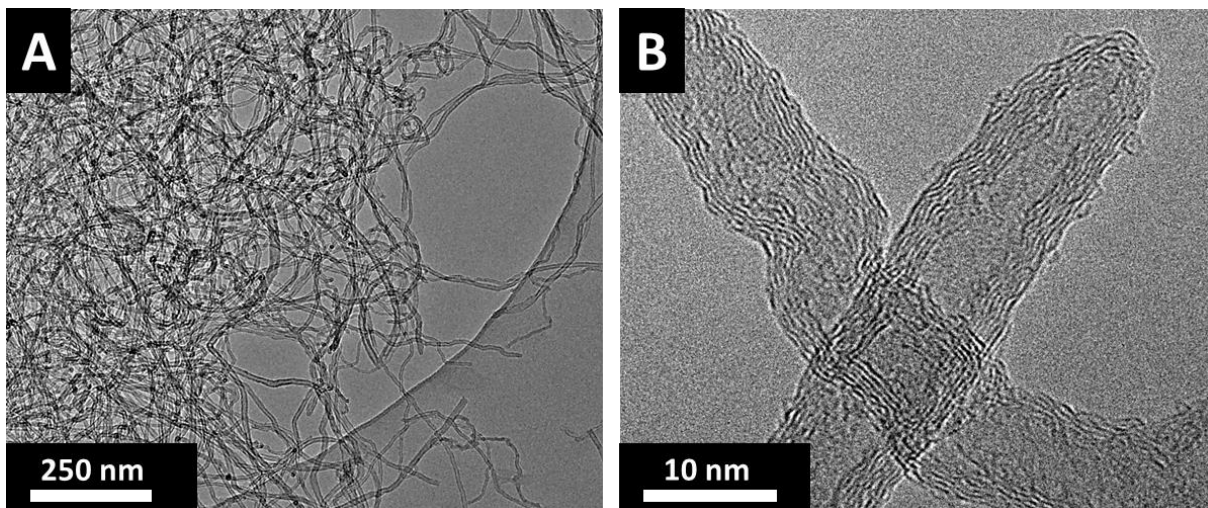


**Figure S1:** Transmission electron micrographs of Nanocyl NC7000 taken with a JEOL 2100F transmission electron microscope at 200 kV. The powder samples were prepared by dispersing the powders in ethanol and drop casting them on a copper grid with a lacey carbon (Gatan).

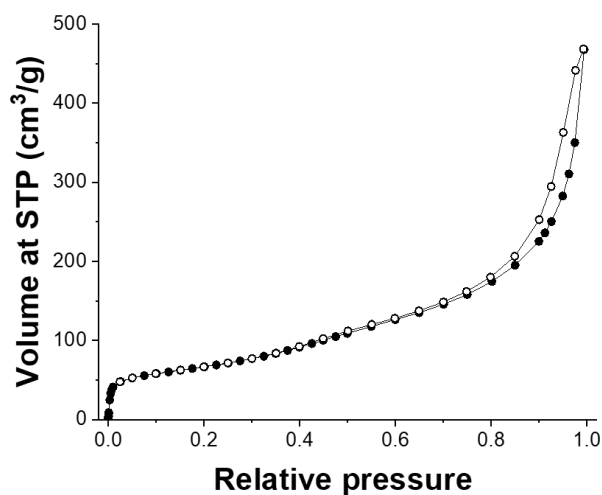


**Figure S2:** Argon gas sorption isotherm recorded at  $-186\text{ }^{\circ}\text{C}$ . The measurement was carried out with an Autosorb iQ system (Quantachrome). The samples were degassed at  $200\text{ }^{\circ}\text{C}$  for 10 h at  $10^2\text{ Pa}$ . The Brunauer-Emmett-Teller specific surface area was calculated in the linear relative pressure range of 0.06-0.3. STP stands for “standard temperature and pressure.”

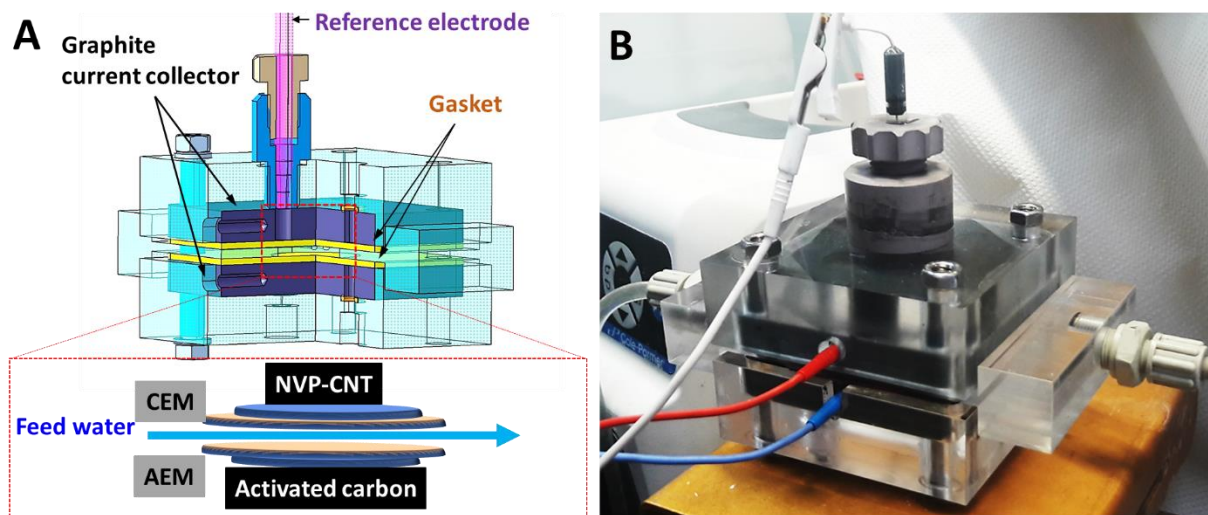


**Figure S3:** (A) Scheme of the cell. (B) A photo of the cell during desalination operation. CEM: cation exchange membrane; AEM: anion exchange membrane.

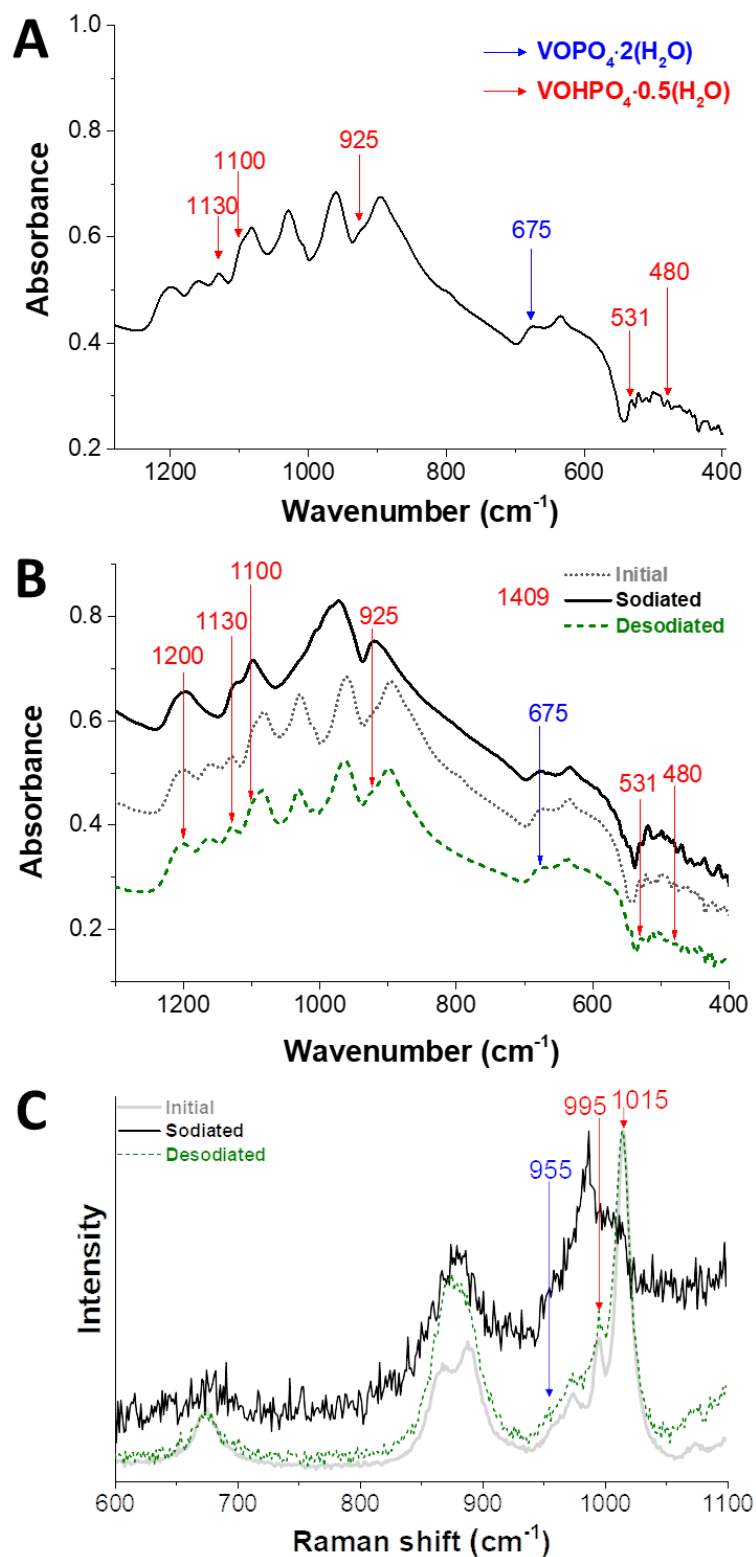


**Figure S4:** (A-B) Infrared spectra of the NVP-CNT electrode initially (A) and after electrochemical operation (B). (C) Raman spectra of the NVP-CNT electrode after electrochemical operation.

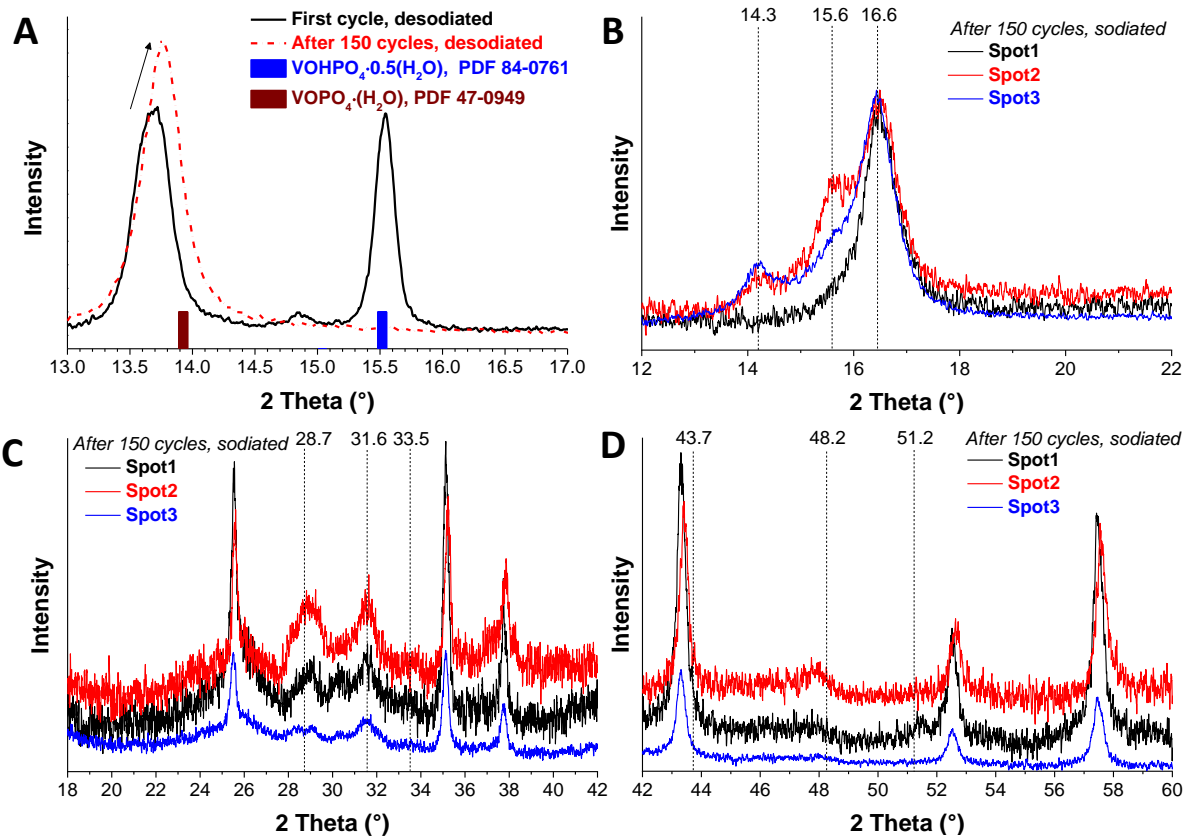


**Figure S5:** X-ray diffractograms of the NVP-CVT electrodes with the desodiated state before and after 150 cycles (A), with the sodiated state after 150 cycles for 3 different spots (B-D).

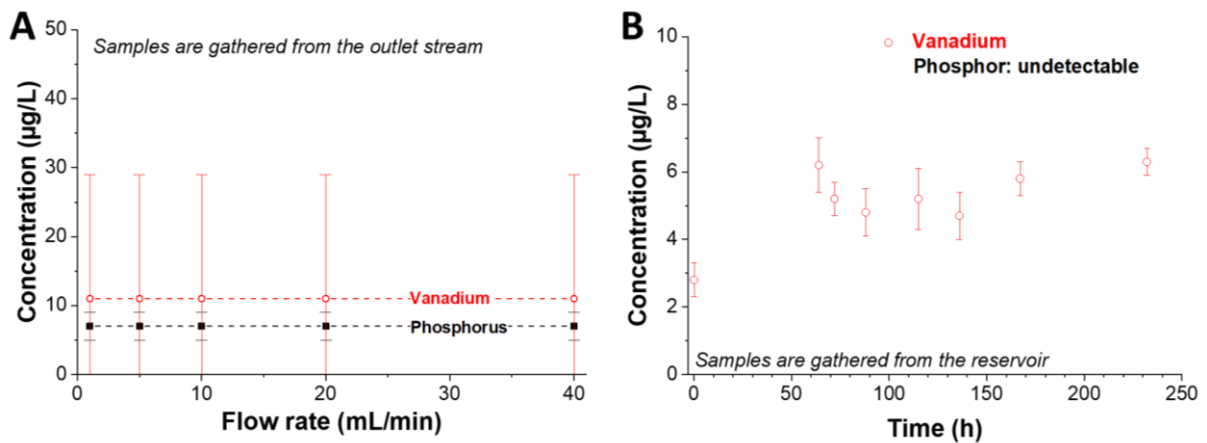


**Figure S6:** Phosphor and vanadium concentration determined by ICP-OES analysis of the water sample collected from the outlet stream of the desalination cell at A) at different flow rates and (B) different times.

## 4.9 Low voltage operation of a silver/silver chloride battery with high desalination capacity in seawater

Pattarachai Srimuk,<sup>1,2</sup>Samantha Husmann,<sup>1</sup> Volker Presser<sup>1,2</sup>

<sup>1</sup> INM - Leibniz Institute for New Materials, 66123 Saarbrücken, Germany

<sup>2</sup> Saarland University, Campus D2 2, 66123 Saarbrücken, Germany

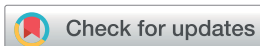
### Citation:

P. Srimuk, S. Husmann, V. Presser, LOW VOLTAGE OPERATION OF A SILVER/SILVER CHLORIDE BATTERY WITH HIGH DESALINATION CAPACITY IN SEAWATER, RSC Advances 9(26) (2019) 14849-14858.

### Own contribution:

Electrochemistry, XRD, CDI, writing





Cite this: *RSC Adv.*, 2019, 9, 14849

# Low voltage operation of a silver/silver chloride battery with high desalination capacity in seawater†

Pattarachai Srimuk,<sup>ab</sup> Samantha Husmann<sup>a</sup> and Volker Presser<sup>\*ab</sup>

Technologies for the effective and energy efficient removal of salt from saline media for advanced water remediation are in high demand. Capacitive deionization using carbon electrodes is limited to highly diluted salt water. Our work demonstrates the high desalination performance of the silver/silver chloride conversion reaction by a chloride ion rocking-chair desalination mechanism. Silver nanoparticles are used as positive electrodes while their chlorination into AgCl particles produces the negative electrode in such a combination that enables a very low cell voltage of only  $\Delta 200$  mV. We used a chloride-ion desalination cell with two flow channels separated by a polymeric cation exchange membrane. The optimized electrode pairing between Ag and AgCl achieves a low energy consumption of 2.5 kJ per ion when performing treatment with highly saline feed (600 mM NaCl). The cell affords a stable desalination capacity of 115 mg g<sup>-1</sup> at a charge efficiency of 98%. This performance aligns with a charge capacity of 110 mA h g<sup>-1</sup>.

Received 5th April 2019  
 Accepted 7th May 2019

DOI: 10.1039/c9ra02570g

rsc.li/rsc-advances

## 1. Introduction

Capacitive deionization (CDI) uses ion electrosorption as a way to immobilize ions at the fluid/solid interface to achieve desalination of a saline medium passing an electrochemical cell.<sup>1–4</sup> By utilizing the formation of an electrical double-layer, this technology may employ additional ion exchange membranes,<sup>5</sup> carbon suspension electrodes,<sup>6–8</sup> or multiple electrolyte flow channels.<sup>9</sup> CDI can achieve a high charge efficiency, that is, most of the invested charge is used for the ion immobilization (desalination) and not lost to redox-reactions that do not contribute towards the actual desalination process.<sup>10,11</sup> Using nanoporous carbon and aqueous saline media, one can typically achieve desalination capacities of 10–25 mg g<sup>-1</sup> (mg NaCl per g of the electrode)<sup>12–16</sup> at cell voltages of about 1 V for low molar concentrations. State-of-the-art nanoporous carbon materials for CDI electrodes include biomass-derived carbon (ref. 17 and 18) and carbons doped by nitrogen, phosphorus, or sulfur (ref. 19–21).

The mechanism of capacitive deionization requires the electrosorption to be accomplished by preferred counter-ion adsorption, with the immobilization of ions with the opposite charge compared to the electrode. Carbon nanopores lack the required permselectivity; therefore, they are already populated

by anions and cations in equal number at the initial uncharged state.<sup>22–24</sup> Thus, charge storage is initially accomplished by concurrent electro-adsorption of counter-ions and ejection of co-ions, which have the same charge sign as the carbon pore wall. Consequently, desalination is only accomplished after the population of co-ions has been depleted; this can be achieved at low and ultralow molar strength, like for brackish water with salinity below 50 mM.<sup>25,26</sup> This limitation still applies to capacitive deionization with nanoporous carbon, but it is increased when using materials capable of other charge storage mechanisms, such as ion insertion (*e.g.*, sodium manganese oxide,<sup>27</sup> hexacyanoferrates,<sup>28</sup> or 2D layered materials<sup>25,29</sup>) or reconstitution/conversion reactions (*e.g.*, Ag/AgCl,<sup>27,30</sup> Bi/BiOCl<sup>31</sup>). Such systems can desalinate highly concentrated saline media (100–900 mM).<sup>32</sup>

The first use of the Ag/AgCl conversion reaction in the context of capacitive deionization, corresponds to the seminal work of Blair and Murphy in 1960, which is considered as the first report of capacitive deionization.<sup>1</sup> In this work, Blair and Murphy investigated half-cells of carbon and modified carbons, most notably, some of them paired with a silver mesh electrode that was anodized at 2 V in concentrated NaCl aqueous solution. The authors created a hybrid capacitive deionization cell by using a pair of one electrosorptive (capacitive) carbon electrode with one redox-active (faradaic) Ag/AgCl electrode.

After the 1960s, Ag/AgCl resurfaced in the context of electrochemical desalination in the seminal work of Pasta *et al.* in 2012.<sup>27</sup> In their work, Pasta *et al.* introduced the so-called desalination battery, which is a cell comprised of one electrode capable of selective sodium uptake and another electrode capable of selective chloride uptake. Specifically, the authors

<sup>a</sup>Department of Materials Science and Engineering, Saarland University, 66123 Saarbrücken, Germany. E-mail: v.presser@mx.uni-saarland.de

<sup>b</sup>INM - Leibniz Institute for New Materials, 66123 Saarbrücken, Germany

† Electronic supplementary information (ESI) available: Supporting electron micrographs, ideal crystal structures, supporting XRD, supporting electrochemical data, and supporting desalination performance. See DOI: 10.1039/c9ra02570g



paired a  $\text{Na}_{2-x}\text{Mn}_5\text{O}_{10}$  (NMO) electrode with an Ag electrode to demonstrate the ability of such a cell to effectively desalinate saline media even at molarity typically found for seawater. The combination of Ag/AgCl and NMO was further explored by Chen *et al.* who reported for 15 mM aqueous NaCl (890 ppm) a desalination performance of 57 mg  $\text{g}^{-1}$  after 100 cycles when sweeping the cell voltage from  $-1.0$  V to  $+1.5$  V.<sup>33</sup>

A novel desalination cell concept, the so-called Na-ion desalination (NID), was introduced by Kyle C. Smith in 2016, with later follow-up work by the same group.<sup>34,35</sup> In its most simplistic form, the NID concept employs two electrodes of the very same material but with different sodiation states. This can be accomplished, for example, by the use of NMO. During charging, one NMO electrode will uptake sodium ions *via* cation insertion while the other NMO electrode will release sodium from the crystal structure. Feedwater passes by these two electrodes in two flow channels which are separated by an anion exchange membrane. As one channel becomes enriched by sodium deinserted from the NMO, chlorine ions cross the ion exchange membrane into that channel; thereby, the other channel becomes depleted by chlorine and, at the same time, depleted from sodium that is being inserted into NMO. This yields concurrently desalination in one channel and salination in the other flow channel. The NID cell concept can be used also for other materials and material pairings, as also shown by Lee *et al.* where sodium nickel hexacyanoferrate was paired with sodium iron hexacyanoferrate.<sup>36</sup> The latter configuration was labeled rocking-chair desalination battery and yielded a desalination capacity of about 60 mg  $\text{g}^{-1}$  in 500 mM NaCl aqueous solution with a cell voltage of 0.8 V. This cell voltage is much lower than what carbon-based CDI devices would employ but still a much higher desalination capacity is obtained.

Whereas the NID cell uses cation-selective electrodes and an anion-exchange membrane, one can invert the concept by employing an anion-selective electrode and a cation-exchange membrane; therefore, we can call the latter in analogy to the NID technology "CID", which stands for Cl-ion desalination. The first CID work predates even the NID work of Smith and Dmello<sup>34</sup> in 2012, Grygolowicz-Pawlak *et al.* used a cation-selective membrane (sulfonated tetrafluoroethylene based fluoropolymer-copolymer; Nafion) coated around silver to achieve desalination of aqueous 600 mM NaCl.<sup>30</sup> This work was adopted and modified for the field of microfluidics by Figuera *et al.* in 2017 when inkjet-printed Ag/AgCl was used as a counter electrode and working electrode for chip-scale water desalination (also using Nafion).<sup>37</sup> While both these works show the desalination effect of the electrochemical operation of silver, their unique designs and reported experimental data do not allow to assess the desalination performance per electrode mass, cycling stability, and basic electrochemical features. The first CID work presented as an inverted NID system was explored in 2019. Arulrajan *et al.* used nanoporous carbon cloth without modification and after chemical surface-functionalization with (3-aminopropyl)triethoxysilane to enable an anion-selective response.<sup>38</sup> This material pair was employed in a modified NID cell with a cation-selective membrane to achieve a desalination capacity of about 50 mg

NaCl per 1 g of electrode material (53 mg  $\text{g}^{-1}$  = 0.91 mmol  $\text{g}^{-1}$ ) when operated in 20 mM NaCl at a cell voltage sweeping between  $-0.9$  V and  $+0.9$  V. Using the same operation parameters of  $\Delta 1.8$  V per one CID cycle, the use of two non-modified carbon electrodes (*i.e.*, in the absence of enabled chloride sensitivity) yielded already a desalination capacity of 25 mg  $\text{g}^{-1}$ . The latter value compares to reports on the same carbon in a conventional CDI cell operating at 0.9 V by division with a factor of 2; the resulting value of 12.5 mg  $\text{g}^{-1}$  is very close to 9 mg  $\text{g}^{-1}$  reported by Kim *et al.* at a lower molar strength of 5 mM NaCl.<sup>39</sup> This work showed the versatility of the NID concept but was limited to low-molar strength and the use of carbon-based electrodes.

In our work, we employed the CID cell based on Ag/AgCl conversion reaction and a polymer-based cation exchange membrane (Fig. 1). This illustrates how promising conversion reactions are for the desalination of seawater or other aqueous/saline media. We do so by using commercially available silver nanoparticles (AgNP) for one electrode, and AgCl obtained from electro-chlorination of AgNP as the other electrode. Therefore, the same Ag/AgCl conversion reaction, on forward- and backward direction, is the mechanism by which chlorine is removed. The overall desalination is then accomplished by charge-balancing of the aqueous media across a polymer-based cation-exchange membrane (Fig. 1C). Also, the use of AgCl in aqueous environments is motivated by the very low solubility of only about 13  $\mu\text{M}$ .<sup>40</sup> Such trace amounts of dissolved AgCl have a useful side effect per the antibacterial property of  $\text{Ag}^+$  ions to disinfect potable water.<sup>41</sup> Here, we demonstrate the electrochemical response of each electrode separately and the use of the Ag/AgCl CID cell for operation in aqueous 600 mM NaCl. This concentration was chosen to illustrate the use of Ag/AgCl CID for seawater desalination but for an ideal saline medium which only contains NaCl. The cell delivers a very high desalination capacity of 115 mg  $\text{g}^{-1}$ , even though a very small cell voltage of just  $\Delta 200$  mV is used. This also translates to a low energy consumption of 2.5 kJ per ion.

## 2. Experimental

### 2.1. Material synthesis and electrode preparation

Silver nanoparticles (AgNPs) (<200 nm, 99%, Sigma Aldrich) were used as a precursor for the silver chloride synthesis *via* electro-chlorination. Prior to AgCl synthesis, the AgNP electrodes were prepared by using two different carbon conductive additive: carbon black and multi-wall carbon nanotubes (CNT).

For AgNP electrode preparation, 80 mass% of the active material (AgNP) was blended with 10 mass% carbon black (C65, IMERYS) in isopropanol. Then, 10 mass% of polyvinylidene fluoride (Sigma Aldrich) was added and mixed with a pestle for 5–10 min in a mortar. *N*-Methyl-2-pyrrolidone (NMP) was dropwise added into the solid mixture while stirring until the slurry achieved a thick viscosity. The as-obtained slurry was doctor-blade casted on a graphite sheet (SGL carbon) with a wet thickness of 150  $\mu\text{m}$  (dry thickness: *ca.* 100  $\mu\text{m}$ ). The coated electrodes were kept in the fume hood for one day and vacuum



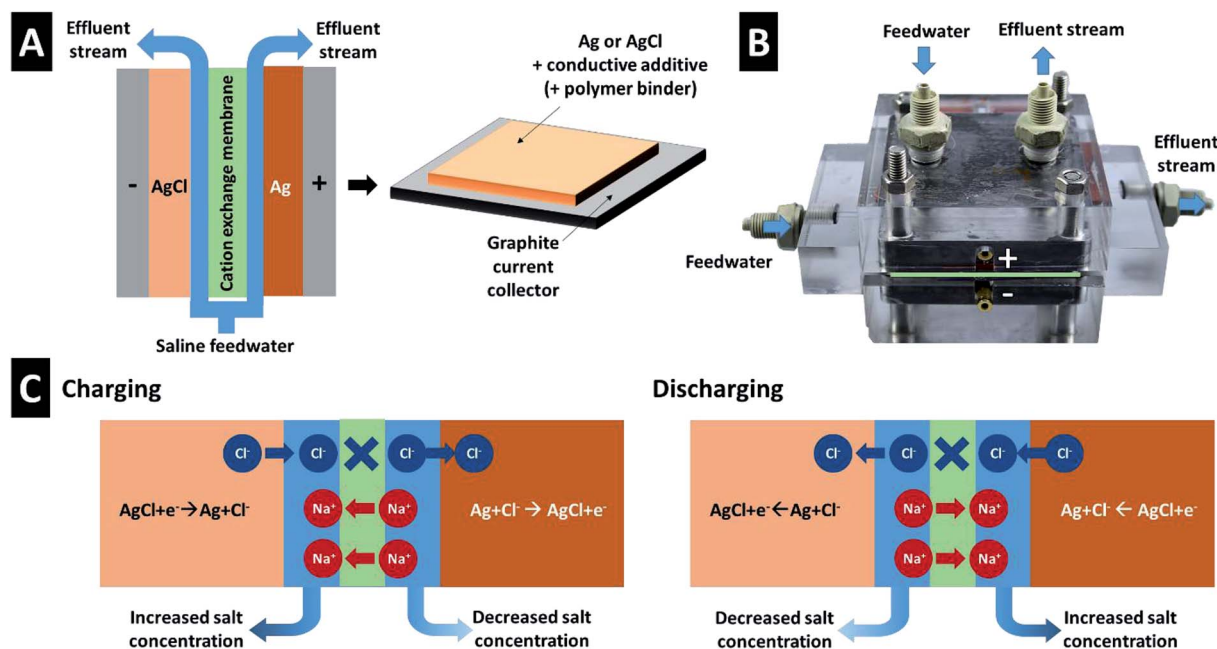


Fig. 1 (A) Scheme of the CID cell and electrode configuration. (B) Photograph of the CID cell. (C) Concept of CID for electrochemical desalination.

dried at 120 °C for 12 h. This electrode was used directly as it is and was labeled AgNP-10CB.

The AgCl electrode was derived *via* electro-chlorination from a binder-free buckypaper electrode composed of AgNP and multi-walled carbon nanotubes. For that, 200 mg of AgNP was mixed with 100 mL of ethanol and sonicated while stirring for 30 min. At the meantime, 50 mg of carbon nanotubes (CNT, Nanocyl NC7000) was mixed with 100 mL of ethanol and sonicated while stirring for 30 min to get a homogeneous suspension. After, the two suspensions were mixed and sonicated for 10 min. Aliquots of 50 mL of the mixed AgNP and CNT suspension were then vacuum filtered through the polymer membrane (Durapore filter, 220 nm pore size). After drying at 60 °C overnight, the free-standing AgNP-CNT electrode was obtained (100 μm thickness) by detaching it from the membrane. The resulting AgNP/CNT electrode had a total content of 20 mass% of CNT.

For the conversion of the AgNP/CNT into AgCl/CNT through an electro-chlorination process, disks with a diameter of 12 mm were cut from the electrode. The electrode was placed in a custom-built electrochemistry cell using spring-loaded titanium piston; for the setup, refer to ref. 42. To assemble the cell, the AgNP/CNT electrode was used as the working electrode. A 13 mm diameter of glass fiber mat (GF/A, Whatman) was employed as the separator. An oversized (50 mg) free-standing film of activated carbon (YP-80F, Kuraray; diameter: 12 mm) blended with polytetrafluoroethylene (PTFE) with 95 : 5 mass% (YP-80F/PTFE 95 : 5) was used as the counter electrode. 1 M NaCl was used as the electrolyte and chloride source at the same time. We connected the assembled cell with a VSP300 potentiostat/galvanostat (Bio-Logic) to apply chronoamperometry at 300 mV *vs.* Ag/AgCl for 3 h. The cell was disassembled, and the electrode was rinsed with deionized

water for several times. The as-obtained chlorinated electrodes were labeled as AgCl-20CNT.

## 2.2. Structural characterization

Scanning electron microscopy (SEM) was carried out using a JEOL JSM-7500F system with an acceleration voltage of 3 kV. The samples were mounted on carbon sticky tape and analyzed without any conductive sputter coating.

X-ray diffraction (XRD) was conducted with D8 Discover diffractometer (Bruker AXS) with a copper source (Cu-K<sub>α</sub>, 40 kV, 40 mA), a Göbel mirror, and a 0.5 mm point focus. A two-dimensional VANTEC-500 detector covered an angular range of 20° 2θ with frames recorded at 20°, 40°, and 80° 2θ using a measurement time of 1000 s per frame. Rietveld analysis was carried out with the Bruker AXS software Topas 5.

## 2.3. Electrochemical characterization

Half-cell characterization was carried out with a custom-built cell using spring-loaded titanium pistons.<sup>42</sup> To assemble the cell, a 12 mm disk of the electrode material (2–4 mg) was employed as the working electrode. A 13 mm diameter of glass fiber mat (GF/A, Whatman) was employed as the separator. A free-standing YP-80F/PTFE 95 : 5 electrode (thickness: 600 μm) was used as the counter electrode. The aqueous NaCl solution was inserted into the cell by vacuum filling with a syringe, and an Ag/AgCl reference electrode (3 M KCl, BASi) was located at the side of the cell body.

The cell was characterized by using VSP300 potentiostat/galvanostat (Bio-Logic). For cyclic voltammetry, the cell was cycled between −0.3 V and +0.3 V *vs.* Ag/AgCl at the scan rate of 1 mV s<sup>−1</sup>. For galvanostatic charge/discharge, the specific current of 0.1–10 A g<sup>−1</sup> was applied to the electrode with the cut-



off potentials of  $-0.3$  V and  $+0.3$  V vs. Ag/AgCl. The specific capacity of the electrode is calculated according to eqn (1).

$$Q = \frac{I \times t}{m_{\text{active}}} \quad (1)$$

where  $Q$  is the specific capacity ( $\text{mA h g}^{-1}$ ),  $I$  is the current (mA),  $t$  is the time (h), and  $m_{\text{active}}$  (g) is the mass of either AgNP or AgCl (*i.e.*, the electrode mass without conductive additive and without polymer binder). To avoid any confusion between specific capacity ( $\text{mA h g}^{-1}$ ) and desalination capacity ( $\text{mg g}^{-1}$ ), we will use the term charge capacity for the specific capacity ( $\text{mA h g}^{-1}$ ) from here on forth.

#### 2.4. Desalination performance

We used an inverted CID cell architecture for electrochemical desalination of aqueous 600 mM NaCl (Fig. 1A and B).<sup>34,38</sup> Two flow channel compartments were separated by 180  $\mu\text{m}$  thick cation exchange membrane (FKS10, FuMa-Tech). Our cell employed AgNP and AgCl as the positive and negative electrode, respectively. The cell was connected to the potentiostat/galvanostat VMP300 (Bio-Logic) using galvanostatic charge/discharge technique with the cut-off voltage of  $\pm 0.1$  V and an applied current of  $0.1 \text{ A g}^{-1}$ . Since the charge capacity of the electrodes does not remain constant, the duration of the desalination operation half-cycles varied from about 300 s (1st cycle) to about 200 s (25th cycle). A reservoir of 10 L of aqueous 600 mM was constantly flushed with  $\text{N}_2$  gas to remove dissolved  $\text{O}_2$ . All measurements were carried out with a feedwater flow rate of  $5 \text{ mL min}^{-1}$ .

The desalination capacity (DC;  $\text{mg g}^{-1}$ ) was calculated by use of eqn (2).

$$\text{DC} = \frac{\nu \times M_{\text{NaCl}}}{m_{\text{active}}} \int c dt \quad (2)$$

where  $c$  (in M) is the measured molar concentration,  $t$  is the time,  $\nu$  is the volumetric flow rate ( $\text{L s}^{-1}$ ),  $M_{\text{NaCl}}$  is the molar mass of NaCl ( $58.440 \text{ g mol}^{-1}$ ), and  $m_{\text{active}}$  (g) is the active electrode mass. The concentration of NaCl was recorded with a Metrohm PT1000 conductometric cell, and the pH values were recorded with a WTW SensoLyt 900P sensor probe.

The charge efficiency (CE; ref. 10) was calculated by eqn (3):

$$\text{CE} = \frac{F \times \text{DC}}{36 \times Q \times M_{\text{NaCl}}} \quad (3)$$

where  $F$  is the Faraday constant ( $96485 \text{ A s mol}^{-1}$ ), DC is the NaCl desalination capacity, 36 ( $=100/3600$ ) is multiplied to  $Q$  for the unit conversion from  $\text{mA h}$  to Coulomb,  $Q$  is the measured charge, and  $M_{\text{Na}}$  is the molecular weight of sodium chloride.

## 3. Results and discussion

### 3.1. Structural characterization

Fig. 2A shows scanning and transmission electron micrographs of AgNP blended with 10 mass% carbon black (AgNP-10CB). The well-dispersed AgNP agglomerates are composed of individual silver particles of around 50–60 nm. As confirmed by X-ray diffraction (Fig. 1B), the structure of AgNP is highly crystalline

and face-centered cubic (space group  $Fm\bar{3}m$ ; ESI, Fig. S1†) with a lattice constant of  $a = 4.0897 \text{ \AA}$  and an average coherence length (domain size) of 75 nm (ESI, Table S1†). The finite domain size also visibly broadens the diffraction cones, as can be seen in the two-dimensional diffraction pattern (Fig. 2B).

As compared to the initial AgNP, the AgCl-20CNT shows a much coarser domain size with AgCl grains entwined within the CNT network (Fig. 2C). A domain size of more than 200 nm and the absence of peak broadening is confirmed by XRD (Fig. 2D). By use of Rietveld refinement, we have determined 85% conversion of Ag to AgCl in the AgCl-20CNT electrodes (ESI, Table S1†). Residual Ag in the AgCl-20CNT electrodes has also lost the nanoscale feature of AgNP and exhibits a lattice spacing of  $a = 4.0905 \text{ \AA}$ . AgCl is also cubic and has a unit cell parameter of  $a = 5.6200 \text{ \AA}$ .

### 3.2. Electrochemical characterization

The characterization of the AgNP and AgCl electrodes in half-cell configuration was performed using aqueous 1 M NaCl to measure the basic electrochemical behavior and to quantify the charge storage capacity (Fig. 3). The overall reaction of Ag to AgCl and of AgCl back to Ag is well-known and given in eqn (4). Following this reaction, metallic silver converts to isolative silver chloride; therefore, our experiments ensured electrical conductivity by the presence of a conductive additive. In addition, the initially 15 mass% of Ag present in the electrochlorinated AgCl-20CNT electrodes may also improve the charge transport process.



Cyclic voltammograms of AgNP-10CB and AgCl-20CNT half-cells are shown in Fig. 3A. As the AgNP-10CB electrode is scanned towards the positive potential and stopped at the cut-off potential of 0.3 V vs. Ag/AgCl, an oxidation peak at +101 mV vs. Ag/AgCl is observed, indicating the formation of AgCl. During the backward scan, the reduction process occurs at  $-121 \text{ mV vs. Ag/AgCl}$  indicative of the reversible reaction of AgCl back to Ag. The AgCl-20CNT electrode shows broad peaks during anodic and cathodic sweeping, with oxidation and reduction peaks at +125 and  $-129 \text{ mV vs. Ag/AgCl}$ , respectively.

The potential of oxidation and reduction potential characterizing the conversion reaction between AgCl and AgNP (eqn (4)) is explained by the Nernst equation (eqn (5) and (6)). Assuming a one electron transfer and high concentration, the formal potential ( $E_f$ ) can be shown as the standard potential ( $E_0$ ) that is between  $-10.5 \text{ mV}$  and  $-10.6 \text{ mV vs. Ag/AgCl}$  (eqn (3)).

$$E_f = E_0 + \frac{RT}{F} \ln\left(\frac{1}{a_{\text{Cl}}}\right) \quad (5)$$

where  $E_f$  is the formal potential,  $E_0$  is the standard potential ( $-10.5 \text{ mV vs. Ag/AgCl}$ ),  $R$  is the gas constant ( $8.314 \text{ J mol}^{-1} \text{ K}^{-1}$ ),  $T$  is the temperature (293 K),  $F$  is the Faraday constant ( $96485 \text{ C mol}^{-1}$ ), and  $a_{\text{Cl}}$  is the activity of chloride ion (equals 1 for high concentrations).



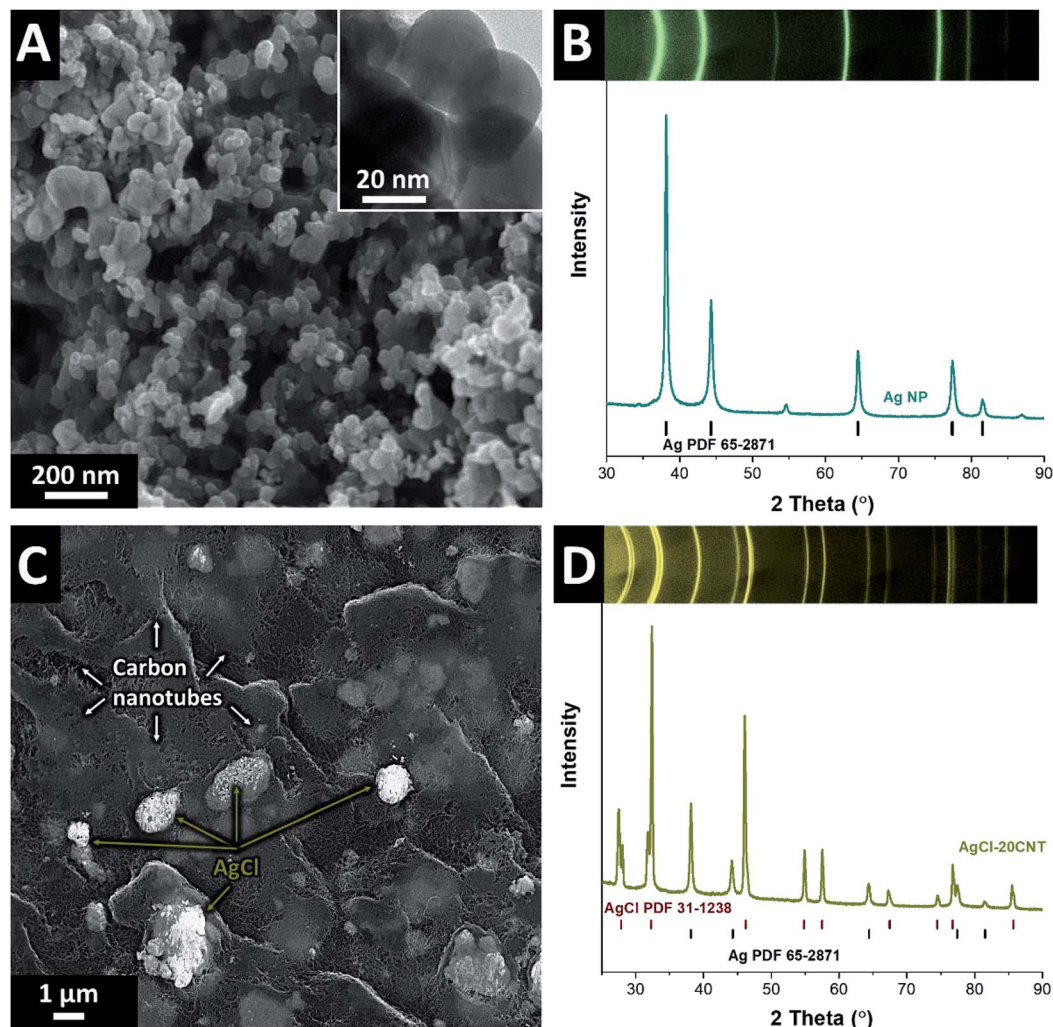


Fig. 2 A) Scanning electron micrograph (inset: transmission electron micrograph) of the AgNP-10CB electrode and (B) X-ray diffraction pattern of the initial AgNP-10CB. (C) Scanning electron micrograph of the AgCl-20CNT electrode and (D) X-ray diffraction pattern of the initial AgCl-20CNT.

$$E_e = E_f + \frac{RT}{F} \ln \left( \frac{c_{\text{AgCl}}}{c_{\text{Ag}} \times c_{\text{Cl}}} \right) \quad (6)$$

where  $E_e$  is the equilibrium potential, and  $c$  gives the concentration of either AgCl, Ag, or chloride ions.

The galvanostatic charge/discharge profiles (Fig. 3B) of AgNP-10CB and AgCl-20CNT in 1 M NaCl exhibit clear plateaus at the potential of  $\pm 50$  mV vs. Ag/AgCl. This very narrow potential range should benefit desalination operation also within a narrow voltage window for the full-cell operation. The charge capacity of AgNP-10CB is  $175 \text{ mA h g}^{-1}$ , which is about 70% of the maximum theoretical capacity of Ag being fully converted to AgCl. When cycling AgCl-20CNT, we obtained  $140 \text{ mA h g}^{-1}$  at  $0.1 \text{ A g}^{-1}$ , which equals 77% of the theoretical maximum.

The overall rate handling of the AgNP-10CB and the AgCl-20CNT electrode is relatively high (Fig. 3C). This may be surprising for a conversion-type redox reaction. Of the initial capacity at  $0.1 \text{ A g}^{-1}$ , AgNP-10CB maintains about 40% at the

very high rate of  $10 \text{ A g}^{-1}$  (corresponding with a C-rate of about 40 C when considering the theoretical capacity of Ag). The AgCl-20CNT electrode also maintains about 30% of the 5th cycle capacity (and 32% of the 1st cycle capacity) at  $10 \text{ A g}^{-1}$  (corresponding with a C-rate of about 53 C when considering the theoretical capacity of AgCl).

As the last step for the basic electrochemical characterization, galvanostatic charge/discharge cycling was performed at a rate of  $0.25 \text{ A g}^{-1}$  (Fig. 3D). These measurements were carried out after cyclic voltammetry and galvanostatic charge/discharge rate handling; therefore, all electrodes had been cycled several times and, thereby, conditioned. Accordingly, AgCl-20CNT, which initially had shown a slight decrease of the charge capacity (Fig. 3C), provides a stable charge capacity of  $100 \text{ mA h g}^{-1}$  with no significant further decrease over the course of 100 cycles (Fig. 3D). The AgNP-10CB electrodes consistently provide a much higher capacity of  $170 \text{ mA h g}^{-1}$  in the first cycle; this capacity is gradually reduced to reach  $137 \text{ mA h g}^{-1}$  after 100 cycles (loss of 19%). Yet, the



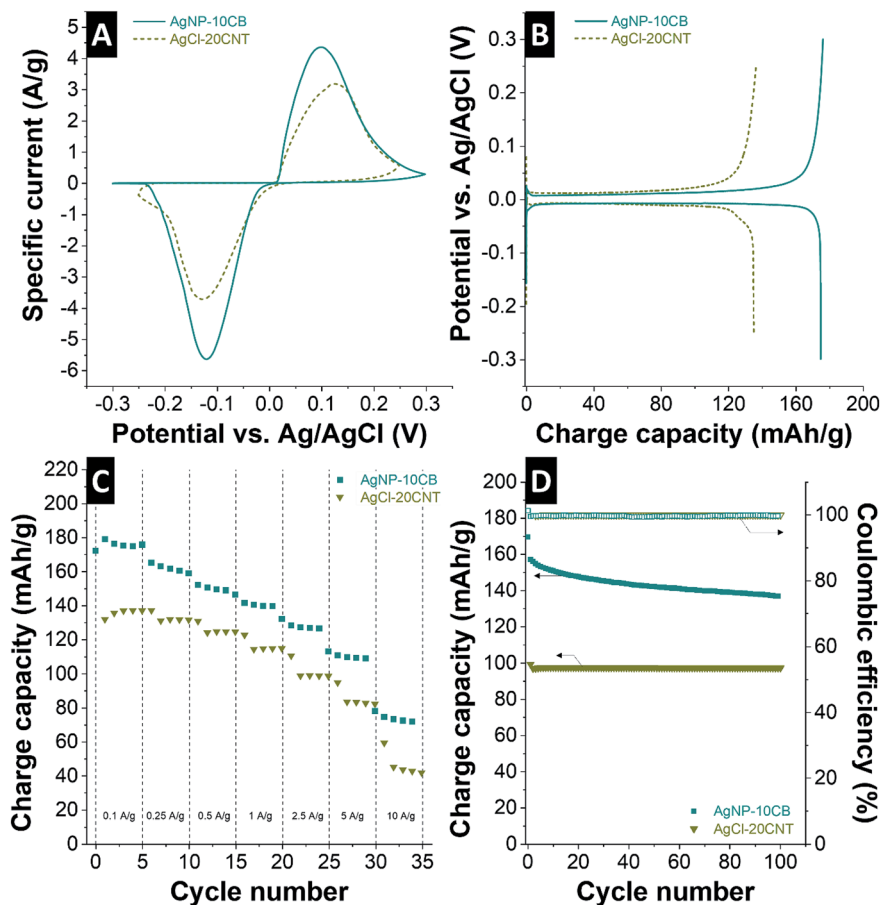


Fig. 3 Electrochemical characterization using a half-cell setup and 1 M NaCl for AgNP-10CB and AgCl-20CNT electrodes. (A) Cyclic voltammetry at  $1 \text{ mV s}^{-1}$ , (B) galvanostatic charge/discharge at  $0.1 \text{ A g}^{-1}$ , (C) galvanostatic rate handling at  $0.1\text{--}10 \text{ A g}^{-1}$ , and (D) galvanostatic charge/discharge cycling stability at  $0.25 \text{ A g}^{-1}$ .

performance loss per cycles decreases over time. Post-mortem analysis of the AgNP-10CB electrodes after electrochemical operation in aqueous 1 M NaCl show that the performance decrease aligns with a potential-induced Ostwald ripening and coarsening of the particle size that leads to incomplete Ag/AgCl conversion; the corresponding X-ray diffraction data and electron micrographs are provided in ESI, Fig. S2.†

### 3.3. Desalination performance

Using the CID cell concept shown in Fig. 1, an AgNP-10CB and an AgCl-20CNT electrode pair was used for the desalination of aqueous 600 mM NaCl. The cell operation was carried out by cycling between  $-0.1 \text{ V}$  and  $+0.1 \text{ V}$ , to yield a net voltage difference of  $\Delta 200 \text{ mV}$ . We chose this range based on the galvanostatic charge/discharge profiles seen in Fig. 3B. As can be seen, the plateaus for the Ag/AgCl conversion reactions are very flat, and material conversion occurs well below  $\pm 0.1 \text{ V}$  vs. Ag/AgCl. The chosen narrow range demonstrates Ag/AgCl-based CID operation at a very small cell voltage. The AgNP-10CB and AgCl-20CNT electrodes were separated by two flow channels and a polymer-based cation exchange membrane. As AgNP is converted to AgCl, chlorine ions are removed from one flow channel, and charge compensation of the electrolyte is

accomplished by transfer of one sodium ion across the ion exchange membrane into the other flow channel (Fig. 1C). The latter is enriched by sodium ions and, at the same time, by chlorine ions which are liberated as AgCl is being converted to Ag. Once both electrodes are fully converted to AgCl or Ag, the operation can be inverted; thereby, the flow channel with increased salt concentration becomes the effluent stream of desalinated water and *vice versa*.

We first measured the electric response of the cell. The characteristic galvanostatic charge/discharge profile for the 1<sup>st</sup>, 10<sup>th</sup>, and 25<sup>th</sup> operation cycle of the CID cell is shown in Fig. 4A. The initial charge capacity of  $205 \text{ mA h g}^{-1}$  during charging is very close to the measured discharge capacity of  $204 \text{ mA h g}^{-1}$ . There are also significant changes in the charge storage capacity of the CID cell over the course of 10 operation cycles (Fig. 4B), but the values stabilize thereafter at a level of  $110 \text{ mA h g}^{-1}$ .

By inverting the cell polarity with a constant current of  $0.1 \text{ A g}^{-1}$ , we see a drastic change in the concentration profile of the effluent stream (Fig. 4C). As desalination is accomplished, the concentration profile of NaCl first decreases before it goes back to the initial value as the electrodes assume their maximum state of charge. Polarity inversion converts AgCl back to Ag and Ag back to AgCl; accordingly, we see an increase in the



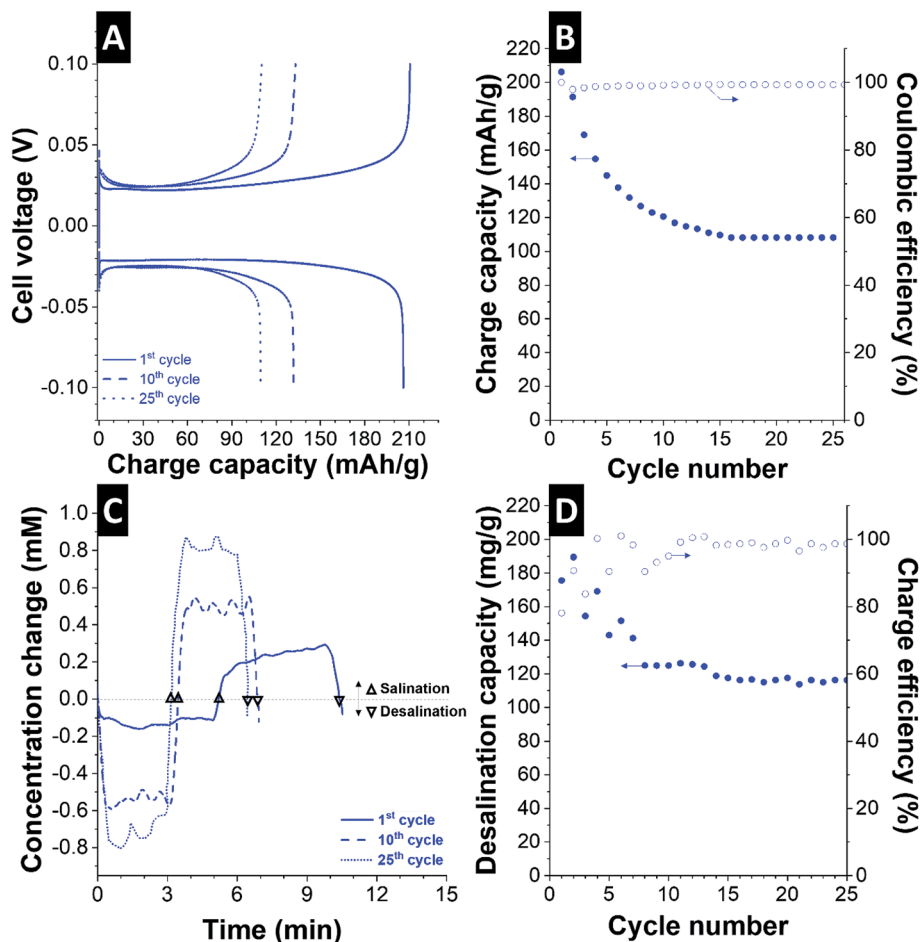


Fig. 4 Electrochemical and desalination performance of AgNP-10CB/AgCl-20CNT CID cell in 600 mM NaCl using a cell voltage of  $\Delta 200$  mV. (A) Charge/discharge profile of the 1st, 10th, and 25th cycle at  $0.1 \text{ A g}^{-1}$  and (B) corresponding cycling stability of the charge capacity. (C) Concentration change during operation and (D) corresponding desalination capacity and charge efficiency values.

concentration profile. The overall concentration change has an amplitude of about  $200 \mu\text{M NaCl}$  for the first cycle and  $600\text{--}700 \mu\text{M NaCl}$  at the 10<sup>th</sup> and 25<sup>th</sup> cycle. This desalination performance is consistent with the small electrode mass of 28 mg that yields the salt removal of  $3.22 \text{ mg NaCl}$  (*i.e.*, desalination capacity of  $115 \text{ mg g}^{-1}$ ). Hence, about 300 g of electrode material would be needed to lower the concentration of 600 mM to 10 mM NaCl for a water volume of 1 L in just one desalination step (and one  $n^{\text{th}}$  of this calculated mass when repeating the process  $n$ -times).

In alignment with the initial changes in the cell's charge storage performance, there are also changes in the desalination capacity (Fig. 4D). We obtained an initial desalination capacity of  $176\text{--}190 \text{ mg g}^{-1}$  in 600 mM NaCl. This very high performance correlates with the very high initial charge capacity in excess of  $200 \text{ mA h g}^{-1}$ . Like the charge capacity, also the desalination capacity fades after a few cycles; thereby, we measured  $125 \text{ mg g}^{-1}$  after 8 cycles, and the performance stabilizes at about  $115 \text{ mg g}^{-1}$  after the 15<sup>th</sup> cycle. This desalination capacity is accomplished at a desalination rate of  $23 \text{ mg g}^{-1} \text{ min}^{-1}$  at the applied current of  $0.1 \text{ A g}^{-1}$ . Concurrently, the initially fluctuating charge efficiency stabilized at a level of about 98% after

the 15<sup>th</sup> cycle. The desalination capacity fading is likely caused by the partially irreversible formation of AgCl at the positive electrode (AgNP-10CB electrode, Fig. S2<sup>†</sup>). This aligns with the decrease charge capacity half-cell performance during cycling of the AgNP-10CB electrode (Fig. 3D).

Based on the desalination performance, we can quantify the effective energy consumption per cycle. Cycling the AgNP-10CB/AgCl-20CNT CID cell in 600 mM between  $-0.1 \text{ V}$  and  $+0.1 \text{ V}$  removes a total of about  $115 \text{ mg g}^{-1} \text{ NaCl}$  and consumes  $97 \mu\text{W h}$  during charging. This value corresponds with an energy consumption of  $2.5 \text{ kT}$  per ion in 600 mM NaCl, which can further be reduced when considering recovered energy during discharging of the cell ( $92 \mu\text{W h}$ ).

#### 3.4. Charge-vs.-desalination correlation and comparison with other works

As seen from eqn (2) and (3), there is a universal correlation between the invested electric charge and the number of removed salt ions. The charge-vs.-desalination (CVD) correlation is not losing validity when we compare different desalination cell concepts but is universally applicable (Fig. 5 and ESI,



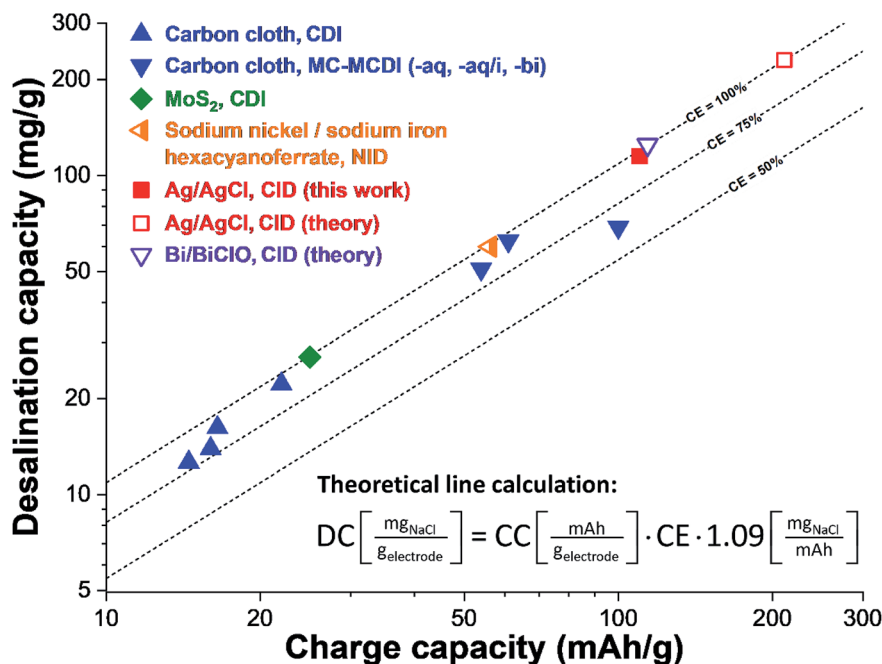


Fig. 5 Charge-vs.-desalination (CVD) plot showing the universal correlation of charge capacity and desalination capacity. The graph shows data for different materials (carbons and non-carbons) and different cell geometries (including CDI, NID, and CID). The theoretical lines assume the stated values for the charge efficiency and are based on eqn (2) and (3). All values are tabulated and with references in ESI, Table S2†. Cell types: CDI (capacitive deionization), MC-MCDI (multi-channel membrane capacitive deionization), NID (sodium-ion desalination), CID (chlorine-ion desalination). Theoretical line calculation: CE (charge efficiency), CC (charge capacity), DC (desalination capacity).

Table S2†). In contrast, the desalination capacity value alone may be misleading as the cell and material performance are strongly intertwined. Assuming a charge efficiency of 100% and ideal ion electrosorption with carbon electrodes, any increase of the cell voltage increases the charge capacity. This can be seen, for example, when we compare the desalination capacity of carbon cloth (Kynol 507-20) operated in a cell cycled between 0 V and 1.2 V ( $DC = 14 \text{ mg g}^{-1}$ ) with the same material cycles between +1.2 V and -1.2 V in a CDI cell modified with ion exchange membranes (MCDI;  $DC = 22 \text{ mg g}^{-1}$ ).<sup>9</sup> The roughly doubled desalination capacity aligns with an increase in the charge capacity (adjusted for a single electrode) from  $16 \text{ mA h g}^{-1}$  to  $22 \text{ mA h g}^{-1}$  and an increase of the charge efficiency from 79% to 95%. Even higher charge capacity values are obtained for carbon when using multi-channel MCDI with concentration gradients or organic/aqueous bi-electrolytes system, with maximum values up to  $54\text{--}61 \text{ mA h g}^{-1}$ .<sup>9,43</sup>

Redox-active electrolytes employing iodide may further enhance the charge storage capacity of carbon electrodes to about  $100 \text{ mA h g}^{-1}$  and the measured desalination capacity of  $69 \text{ mg g}^{-1}$  for a cell operated at 0.7 V aligns with a charge efficiency of 64%.<sup>44</sup> This shows that the CVD plot is not limited to technologies based on ion electrosorption but can also be used to map the performance of non-carbon materials. For example, we see for  $\text{MoS}_2$  a desalination capacity of  $27 \text{ mg g}^{-1}$  in aqueous 600 mM NaCl which aligns with a charge capacity of  $25 \text{ mA h g}^{-1}$ .<sup>25</sup> The NID cell of Lee *et al.* employing nickel hexacyanoferrate and sodium iron hexacyanoferrate yielded a desalination capacity of  $60 \text{ mg g}^{-1}$  for 500 mM NaCl per the charge capacity of  $56 \text{ mA h g}^{-1}$ .<sup>36</sup>

From the CVD plot (Fig. 5), we see that the Ag/AgCl desalination performance using cell voltage of just  $\Delta 0.2 \text{ V}$  is much higher than using carbon electrodes, even when using cell voltages of  $\Delta 2.4 \text{ V}$  or when using multi-channel concentration gradients or redox-active electrolytes. The performance of  $115 \text{ mg g}^{-1}$  at  $110 \text{ mA h g}^{-1}$  of our Ag/AgCl cell is near the theoretical value of the Bi/BiClO conversion reaction operated in a CID cell ( $125 \text{ mg g}^{-1}$  at  $114 \text{ mA h g}^{-1}$ ). Yet, further optimization of the system has great potential for achieving even higher values. When considering the maximum possible charge storage capacity of a well-balanced Ag/AgCl system with 100% charge efficiency and a 100% degree of reversible conversion, we would expect a desalination capacity of  $230 \text{ mg g}^{-1}$  at a charge capacity of  $211 \text{ mA h g}^{-1}$ . Such values, until now, have remained elusive for the fast-growing field of electrochemical desalination.

### 3.5. Remaining challenges for the Ag/AgCl CID concept

Our work has shown the very high desalination performance inherent to the Ag/AgCl conversion reaction process. Yet, grain coarsening and loss of charge capacity caused a corresponding drop of the desalination capacity. The latter stabilized at  $115 \text{ mg g}^{-1}$  which is superior to most materials explored for electrochemical desalination so far, especially when we consider the very small voltage window of  $\Delta 200 \text{ mV}$ . However,  $115 \text{ mg g}^{-1}$  is only half of the theoretical value, and while it is unreasonable to assume 100% utilization of an electrochemical conversion process, there remains significant room for improvement. Clearly, the main electrode design goal must be on maximizing



the amount of Ag and AgCl in the respective electrodes and to use as little conductive additive as possible. Homogeneous phase distribution is of high importance, and we provide in ESI† performance data of non-optimized AgNP and AgCl electrodes. Most specifically, future work will have to address the large loss of the charge capacity of the AgCl electrode and the significant particle coarsening.

## 4. Conclusions

Our work has demonstrated the facile use of silver nanoparticles paired with AgCl as a high-performance desalination battery with two flow-channels separated by a cation-exchange membrane. Such a chloride-ion desalination (CID) cell provides a desalination capacity far beyond the limit of electro-sorptive carbon materials per the large charge capacity of the Ag/AgCl conversion reaction (theoretical maximum: 211 mA h g<sup>-1</sup>). When operated in high molarity aqueous solution of NaCl, electrodes based on AgNP yielded a charge capacity of 175 mA h g<sup>-1</sup>, while AgCl electrodes provided 140 mA h g<sup>-1</sup> when operated at ±0.3 V at a specific current of 0.1 A g<sup>-1</sup>. These values translated in our Ag/AgCl-based desalination cell even at a very small voltage window of ±0.1 V (cell voltage of 200 mV) to a charge capacity of 110 mA h g<sup>-1</sup> and a desalination capacity of 115 mg g<sup>-1</sup> at a charge efficiency of about 98%. The low cell voltage of just Δ200 mV allows for very low energy consumption of about 2.5 kT per ion in 600 mM NaCl. Such high desalination capacity at such small voltages and low energy consumption have not been reported in the literature to the best of our knowledge. Yet, the Ag/AgCl system may even provide higher desalination performance with further optimization, especially regarding a higher degree of reversible AgCl electrode conversion.

## Conflicts of interest

There are no conflicts to declare.

## Acknowledgements

We thank Eduard Arzt (INM) for his continuing support and Aura Tolosa (INM) for helpful discussions. We acknowledge support by the Deutsche Forschungsgemeinschaft (DFG, German Research Foundation) and Saarland University within the funding program Open Access Publishing.

## References

- J. W. Blair and G. W. Murphy, in *Saline Water Conversion*, American Chemical Society, 1960, ch. 20, vol. 27, pp. 206–223.
- S. Porada, R. Zhao, A. van der Wal, V. Presser and P. M. Biesheuvel, *Prog. Mater. Sci.*, 2013, **58**, 1388–1442.
- M. E. Suss, S. Porada, X. Sun, P. M. Biesheuvel, J. Yoon and V. Presser, *Energy Environ. Sci.*, 2015, **8**, 2296–2319.
- M. Noked, A. Soffer and D. Aurbach, *J. Solid State Electrochem.*, 2011, **15**, 1563–1578.
- P. M. Biesheuvel and A. van der Wal, *J. Membr. Sci.*, 2010, **346**, 256–262.
- S. I. Jeon, H. R. Park, J. G. Yeo, S. Yang, C. H. Cho, M. H. Han and D. K. Kim, *Energy Environ. Sci.*, 2013, **6**, 1471–1475.
- Y. Gendel, A. K. E. Rommerskirchen, O. David and M. Wessling, *Electrochem. Commun.*, 2014, **46**, 152–156.
- S. Porada, D. Weingarth, H. V. M. Hamelers, M. Bryjak, V. Presser and P. M. Biesheuvel, *J. Mater. Chem. A*, 2014, **2**, 9313–9321.
- C. Kim, J. Lee, P. Srimuk, M. Aslan and V. Presser, *ChemSusChem*, 2017, **10**, 4914–4920.
- R. Zhao, P. M. Biesheuvel, H. Miedema, H. Bruning and A. van der Wal, *J. Phys. Chem. Lett.*, 2009, **1**, 205–210.
- A. Kalfa, I. Cohen, E. Avraham and D. Aurbach, *J. Electrochem. Soc.*, 2019, **166**, H119–H125.
- X. Xu, L. Pan, Y. Liu, T. Lu, Z. Sun and D. H. C. Chua, *Sci. Rep.*, 2015, **5**, 8458.
- X. Xu, Z. Sun, D. H. C. Chua and L. Pan, *Sci. Rep.*, 2015, **5**, 11225.
- S. Porada, L. Borchardt, M. Oschatz, M. Bryjak, J. S. Atchison, K. J. Keesman, S. Kaskel, P. M. Biesheuvel and V. Presser, *Energy Environ. Sci.*, 2013, **6**, 3700–3712.
- C. Zhang, X. Wang, H. Wang, X. Wu and J. Shen, *Desalination*, 2019, **458**, 45–53.
- S. Hand, X. Shang, J. S. Guest, K. C. Smith and R. D. Cusick, *Environ. Sci. Technol.*, 2019, **53**, 3748–3756.
- C. Zhao, G. Liu, N. Sun, X. Zhang, G. Wang, Y. Zhang, H. Zhang and H. Zhao, *Chem. Eng. J.*, 2018, **334**, 1270–1280.
- S. Porada, F. Schipper, M. Aslan, M. Antonietti, V. Presser and T.-P. Fellinger, *ChemSusChem*, 2015, **8**, 1867–1874.
- J. Zhang, J. Fang, J. Han, T. Yan, L. Shi and D. Zhang, *J. Mater. Chem. A*, 2018, **6**, 15245–15252.
- J. Han, L. Shi, T. Yan, J. Zhang and D. Zhang, *Environ. Sci. Nano*, 2018, **5**, 2337–2345.
- T. Yan, J. Liu, H. Lei, L. Shi, Z. An, H. S. Park and D. Zhang, *Environ. Sci. Nano*, 2018, **5**, 2722–2730.
- C. Prehal, D. Weingarth, E. Perre, R. T. Lechner, H. Amenitsch, O. Paris and V. Presser, *Energy Environ. Sci.*, 2015, **8**, 1725–1735.
- C. Prehal, C. Koczwarra, H. Amenitsch, V. Presser and O. Paris, *Nat. Commun.*, 2018, **9**, 4145.
- C. Prehal, C. Koczwarra, N. Jäckel, A. Schreiber, M. Burian, H. Amenitsch, M. A. Hartmann, V. Presser and O. Paris, *Nat. Energy*, 2017, **2**, 16215.
- P. Srimuk, J. Lee, S. Fleischmann, S. Choudhury, N. Jäckel, M. Zeiger, C. Kim, M. Aslan and V. Presser, *J. Mater. Chem. A*, 2017, **5**, 15640–15649.
- P. M. Biesheuvel, S. Porada, M. Levi and M. Z. Bazant, *J. Solid State Electrochem.*, 2014, **18**, 1365–1376.
- M. Pasta, C. D. Wessells, Y. Cui and F. La Mantia, *Nano Lett.*, 2012, **12**, 839–843.
- S. Porada, A. Shrivastava, P. Bukowska, P. M. Biesheuvel and K. C. Smith, *Electrochim. Acta*, 2017, **255**, 369–378.
- P. Srimuk, F. Kaasik, B. Krüner, A. Tolosa, S. Fleischmann, N. Jäckel, M. C. Tekeli, M. Aslan, M. E. Suss and V. Presser, *J. Mater. Chem. A*, 2016, **4**, 18265–18271.



- 30 E. Grygolicz-Pawlak, M. Sohail, M. Pawlak, B. Neel, A. Shvarev, R. de Marco and E. Bakker, *Anal. Chem.*, 2012, **84**, 6158–6165.
- 31 Y. Liu, Z. Jiang, X. Zhang and P. K. Shen, *J. Mater. Chem. A*, 2018, **6**, 20037–20043.
- 32 M. E. Suss and V. Presser, *Joule*, 2018, **2**, 10–15.
- 33 F. Chen, Y. Huang, L. Guo, M. Ding and H. Y. Yang, *Nanoscale*, 2017, **9**, 10101–10108.
- 34 K. C. Smith and R. Dmello, *J. Electrochem. Soc.*, 2016, **163**, A530–A539.
- 35 K. C. Smith, *Electrochim. Acta*, 2017, **230**, 333–341.
- 36 J. Lee, S. Kim and J. Yoon, *ACS Omega*, 2017, **2**, 1653–1659.
- 37 M. Figuera, P. D. van der Wal and H. Shea, *J. Electrochem. Soc.*, 2017, **164**, H836–H845.
- 38 A. C. Arulrajan, D. L. Ramasamy, M. Sillanpää, A. van der Wal, P. M. Biesheuvel, S. Porada and J. E. Dykstra, *Adv. Mater.*, 2019, **1**, 1806937.
- 39 C. Kim, P. Srimuk, J. Lee, S. Fleischmann, M. Aslan and V. Presser, *Carbon*, 2017, **122**, 329–335.
- 40 T. J. Bruno, W. M. Haynes and D. R. Lide, *CRC handbook of chemistry and physics: a ready-reference book of chemical and physical data*, CRC Press, 2016.
- 41 L. Fewtrell, *Silver: water disinfection and toxicity*, Centre for Research into Environment and Health, 2014.
- 42 D. Weingarh, M. Zeiger, N. Jäckel, M. Aslan, G. Feng and V. Presser, *Adv. Energy Mater.*, 2014, **4**, 1400316.
- 43 C. Kim, P. Srimuk, J. Lee and V. Presser, *Desalination*, 2018, **443**, 56–61.
- 44 J. Lee, P. Srimuk, S. Carpier, J. Choi, R. L. Zornitta, C. Kim, M. Aslan and V. Presser, *ChemSusChem*, 2018, **11**, 3460–3472.



## *Supplementary Information*

### **Low voltage operation of a silver/silver chloride battery with high desalination capacity in seawater**

**Pattarachai Srimuk,<sup>1,2</sup> Samantha Husmann,<sup>1</sup> Volker Presser<sup>1,2,\*</sup>**

<sup>1</sup> INM - Leibniz Institute for New Materials, 66123 Saarbrücken, Germany

<sup>2</sup> Department of Materials Science and Engineering, Saarland University, 66123 Saarbrücken, Germany

\* Corresponding author's eMail: [volker.presser@leibniz-inm.de](mailto:volker.presser@leibniz-inm.de)

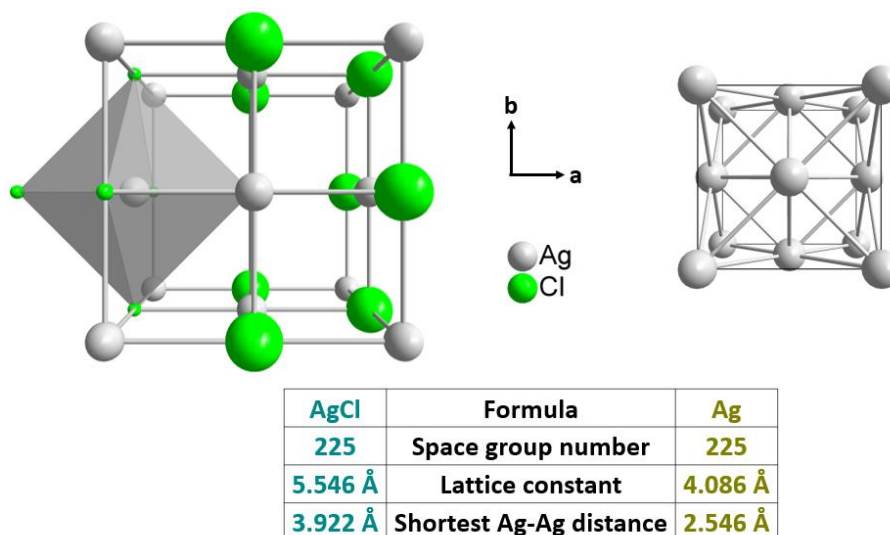


**Figure S1:** Ideal crystal structure of AgCl and Ag along with selected crystallographic information.

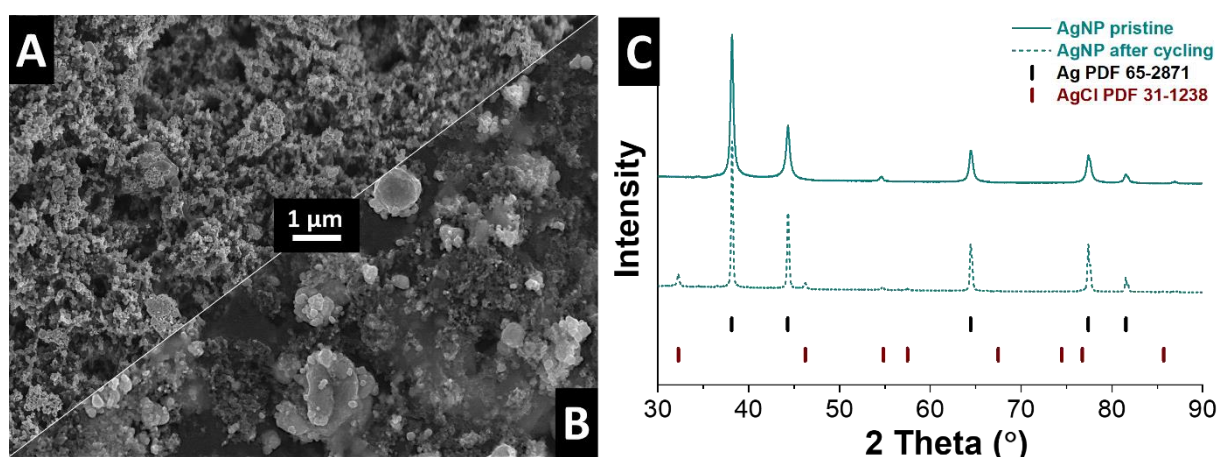


**Figure S2:** A) scanning electron micrograph of AgNP-10CB electrode before (up) and after electrochemistry (bottom) and B) X-ray diffraction pattern of AgNP-10CB electrode before and after electrochemistry.

**Table S1:** Measured crystal structure data obtained via Rietveld analysis of the measured X-ray diffraction pattern.

	Ag			AgCl		
	a (Å)	Size (nm)	Amount (%)	a (Å)	Size (nm)	Amount (%)
AgNP	4.0897	75	>99	-	-	-
AgCl-20CNT	4.0905	>200	15	5.6200	>200	85

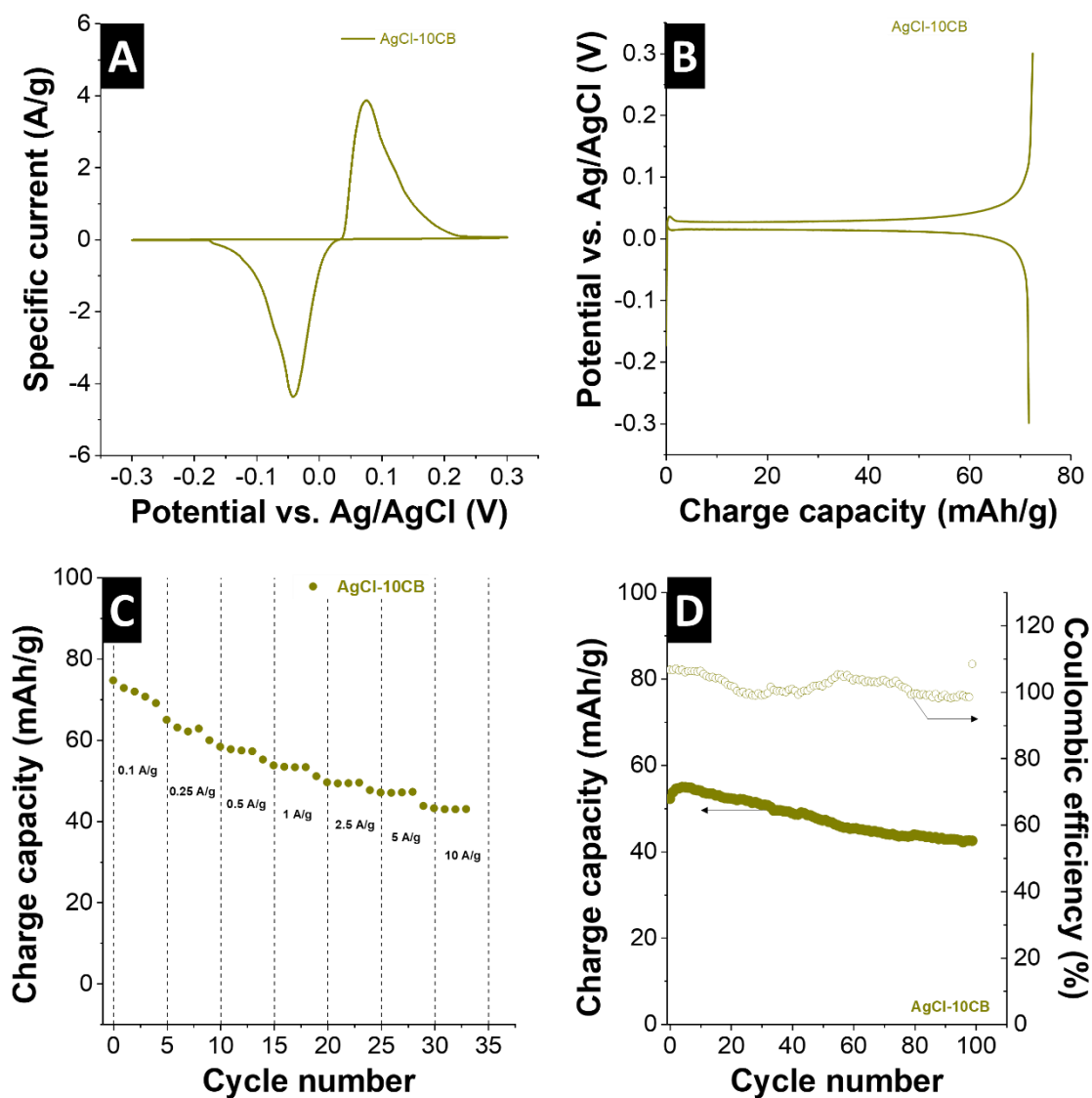


**Figure S3:** Electrochemical characterization using a half-cell setup and 1 M NaCl for AgNP-10CB. For this experiment, AgNP was blended with carbon black the same way as we did for AgCl-20CNT electrodes. A) Cyclic voltammetry at 1 mV/s, B) galvanostatic charge/discharge at 0.1 A/g, C) galvanostatic rate handling at 0.1-10 A/g, and D) galvanostatic charge/discharge cycling stability at 0.25 A/g.

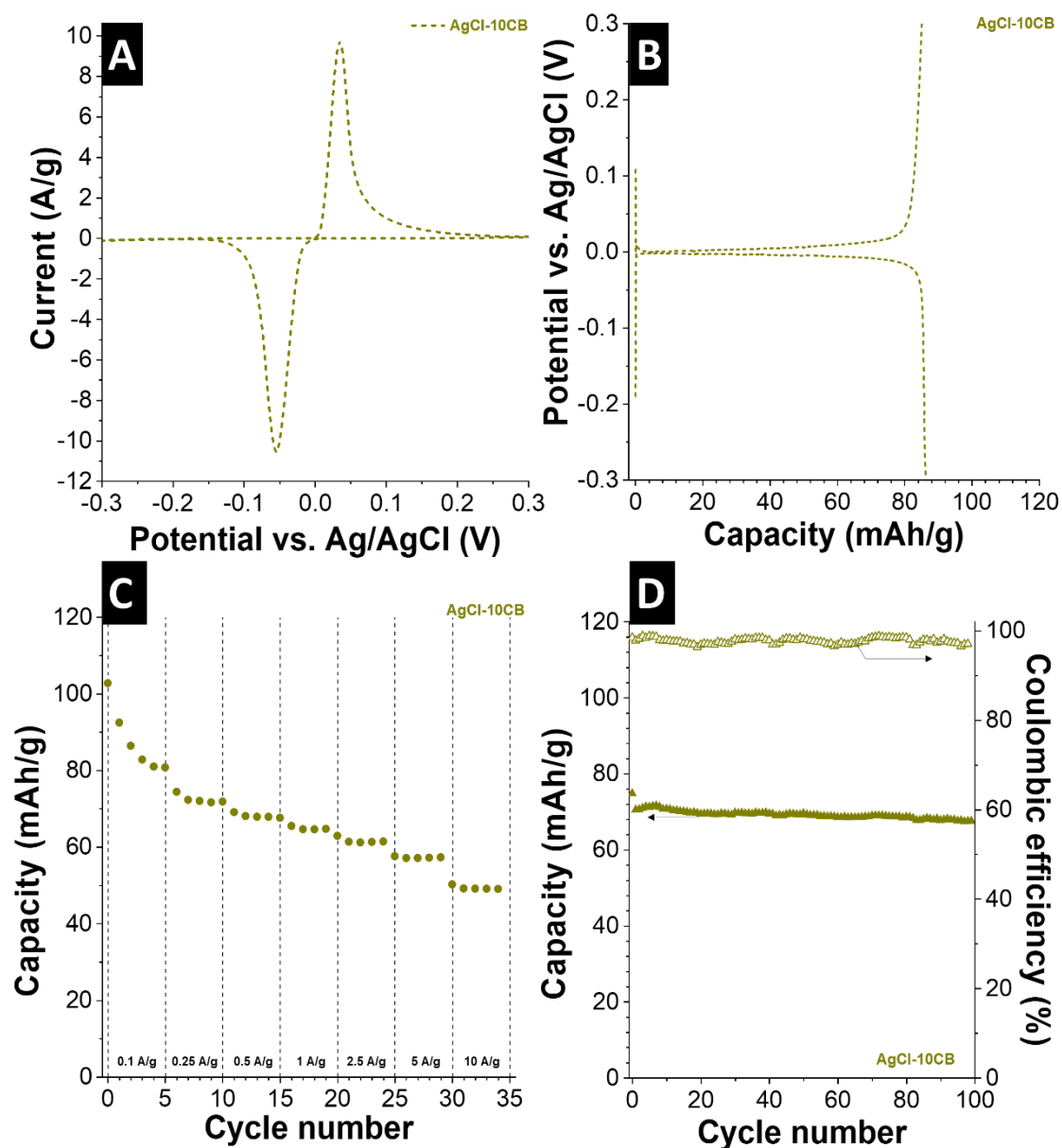


**Figure S4:** Electrochemical characterization using a half-cell setup and 1 M NaCl for AgCl-10CB. For this experiment, Ag was thermally chlorinated at 300 °C for 3 h, achieving full conversion to AgCl. The AgCl powder was then processed like AgNP-10CB electrodes to obtain AgCl-10CB electrodes. A) Cyclic voltammetry at 1 mV/s, B) galvanostatic charge/discharge at 0.1 A/g, C) galvanostatic rate handling at 0.1-10 A/g, and D) galvanostatic charge/discharge cycling stability at 0.25 A/g.

**Table S2:** Desalination performance and corresponding specific capacity for selected literature that provided required data on charge, charge efficiency, and salt removal capacity (considering NaCl as the only salt). NID: sodium-ion desalination. CID: chlorine-ion desalination; CDI: capacitive deionization; MCDI: membrane capacitive deionization. MC-MCDI: multi-channel membrane capacitive deionization (-aq: aqueous media; -bi: organic/aqueous bi-electrolyte).

Material	Cell type	NaCl concentration (mM)	Cell voltage (V)	Charge capacity (mAh/g)	Desalination capacity (mg/g)	Charge efficiency (%)	Comment
Any	Any	Any	Any	100	109	100	Theory, assuming Eq. 3
Any	Any	Any	Any	100	87	80	Theory, assuming Eq. 3
Any	Any	Any	Any	100	55	50	Theory, assuming Eq. 3
Ag/AgCl	CID	600	±0.1	110	115	96	This work
Ag/AgCl	CID	Any	Any	211	230	100	Theory, ideal
Bi/BiClO	CID	Any	Any	114	125	100	Theory, ideal
Kynol 5092-15	CDI	5	1.2	15 <sup>a</sup>	13	76	Ref. <sup>1</sup>
Kynol 507-20	CDI	5	1.2	16 <sup>a</sup>	14	79	Ref. <sup>1</sup>
Kynol 507-20+	CDI	5	1.2	17 <sup>a</sup>	16	89	Ref. <sup>1</sup>
Kynol 507-20	MC-MCDI-aq <sup>b</sup>	5	±1.2	22 <sup>a</sup>	22	93	Ref. <sup>2</sup>
Kynol 507-20	MC-MCDI-aq <sup>c</sup>	5	±1.2	54 <sup>a</sup>	51	87	Ref. <sup>2</sup>
Kynol 507-20	MC-MCDI-bi <sup>d</sup>	5	2.4	61 <sup>a</sup>	63	95	Ref. <sup>3</sup>
Kynol 507-20	MC-MCDI-aq/i <sup>e</sup>	100	0.7	100	69	64	Ref. <sup>4</sup>
MoS <sub>2</sub>	CDI	500	0.8	25	27	96	Ref. <sup>5</sup>
Nickel hexacyanoferrate & sodium iron hexacyanoferrate	NID	500	Δ0.8 <sup>e</sup>	56	60	98	Ref. <sup>6</sup>

<sup>a</sup> Charge storage capacity per one electrode for symmetric cells. <sup>b</sup> side-channel concentration: aqueous 5 mM NaCl. <sup>c</sup> side-channel concentration: aqueous 1000 mM NaCl. <sup>d</sup> side-channel concentration: aqueous 600 mM NaCl and 600 mM NaClO<sub>4</sub> in propylene carbonate. <sup>e</sup> cell was cycled between 0.05 V and 0.85 V.

## Supplementary References

1. C. Kim, P. Srimuk, J. Lee, S. Fleischmann, M. Aslan and V. Presser, *Carbon*, 2017, **122**, 329-335.
2. C. Kim, J. Lee, P. Srimuk, M. Aslan and V. Presser, *ChemSusChem*, 2017, **10**, 4914-4920.
3. C. Kim, P. Srimuk, J. Lee and V. Presser, *Desalination*, 2018, **443**, 56-61.
4. J. Lee, P. Srimuk, S. Carpier, J. Choi, R. L. Zornitta, C. Kim, M. Aslan and V. Presser, *ChemSusChem*, 2018, **11**, 3460-3472.
5. P. Srimuk, J. Lee, S. Fleischmann, S. Choudhury, N. Jäckel, M. Zeiger, C. Kim, M. Aslan and V. Presser, *Journal of Materials Chemistry A*, 2017, **5**, 15640-15649.
6. J. Lee, S. Kim and J. Yoon, *ACS Omega*, 2017, **2**, 1653-1659.

## 4.10 Confined redox reactions of iodide in carbon nanopores for fast and energy-efficient desalination of brackish water and seawater

Juhan Lee,<sup>1,2</sup> Pattarachai Srimuk,<sup>1,2</sup> Sidonie Carpier,<sup>1,2</sup> Jaehoon Choi,<sup>1,3</sup>

Rafael Linzmeyer Zornitta,<sup>1,4</sup> Choonsoo Kim,<sup>1</sup> Mesut Aslan,<sup>1</sup> Volker Presser<sup>1,2</sup>

<sup>1</sup> INM - Leibniz Institute for New Materials, 66123 Saarbrücken, Germany

<sup>2</sup> Saarland University, Campus D2 2, 66123 Saarbrücken, Germany

<sup>3</sup> Department of chemical engineering, Federal University of São Carlos, 13565-905 São Carlos, Brazil

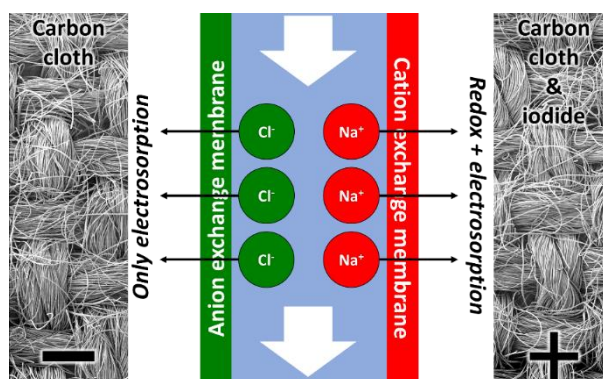
<sup>4</sup> School of Energy, Materials and Chemical Engineering, Korea University of Technology and Education, Chungjeol-ro 1600, 31253 Cheonan, Republic of Korea

### Citation:

J. Lee, P. Srimuk, S. Carpier, J. Choi, R.L. Zornitta, C. Kim, M. Aslan, V. Presser, CONFINED REDOX REACTIONS OF IODIDE IN CARBON NANOPORES FOR FAST AND ENERGY-EFFICIENT DESALINATION OF BRACKISH WATER AND SEAWATER, *ChemSusChem* 11(19) (2018) 3460-3472.

### Own contribution:

Electrochemistry, discussion, writing



# Confined Redox Reactions of Iodide in Carbon Nanopores for Fast and Energy-Efficient Desalination of Brackish Water and Seawater

Juhan Lee,<sup>[a, b]</sup> Pattarachai Srimuk,<sup>[a, b]</sup> Sidonie Carpier,<sup>[a, b]</sup> Jaehoon Choi,<sup>[a, c]</sup>  
Rafael Linzmeyer Zornitta,<sup>[a, d]</sup> Choonsoo Kim,<sup>[a]</sup> Mesut Aslan,<sup>[a]</sup> and Volker Presser\*<sup>[a, b]</sup>

Faradaic deionization is a promising new seawater desalination technology with low energy consumption. One drawback is the low water production rate as a result of the limited kinetics of the ion intercalation and insertion processes. We introduce the redox activities of iodide confined in carbon nanopores for electrochemical desalination. A fast desalination process was enabled by diffusionless redox kinetics governed by thin-layer electrochemistry. A cell was designed with an activated carbon cloth electrode in NaI aqueous solution, which was separated from the feedwater channel by a cation-exchange membrane. Coupled with an activated carbon counter electrode and an anion-exchange membrane, the half-cell in NaI with a cation-exchange membrane maintained performance even at a high

current of  $2.5 \text{ Ag}^{-1}$  ( $21 \text{ mA cm}^{-2}$ ). The redox activities of iodide allowed a high desalination capacity of  $69 \text{ mg g}^{-1}$  (normalized by the mass of the working electrode) with stable performance over 120 cycles. Additionally, we provide a new analytical method for unique performance evaluation under single-pass flow conditions regarding the water production rate and energy consumption. Our cell concept provides flexible performance for low and high salinity and, thus, enables the desalination of brackish water or seawater. Particularly, we found a low energy consumption ( $1.63 \text{ Wh L}^{-1}$ ) for seawater desalination and a high water production rate ( $25 \text{ L m}^{-2} \text{ h}^{-1}$ ) for brackish water.

## Introduction

The ability to purify and desalinate water on a large scale and with low energy consumption is a key asset for sustainable technologies, society, and the economy. At present, industrial freshwater generation is mostly accomplished by filtration technologies, such as reverse osmosis (RO), and distillation processes, such as multistage flash and multiple effect distillation. Among them, RO plants are today the most energy-efficient process and cover more than half of the water desalination capacity.<sup>[1,2]</sup> Continuous technological developments, including high-performance membranes and low-energy pumps and

motors, have drastically decreased the energy consumption of RO plants from  $20 \text{ Wh L}^{-1}$  in the 1970s to  $2 \text{ Wh L}^{-1}$  today.<sup>[3]</sup>

In the pursuit of more energy-efficient water-treatment processes, a wealth of new water-treatment technologies relying on reversible electrochemical reactions have recently emerged. For instance, capacitive deionization (CDI)<sup>[4,5]</sup> and battery desalination<sup>[6–8]</sup> may consume less energy per processed volume ( $< 2 \text{ Wh L}^{-1}$ , 95% recovery of 700 mM feedwater<sup>[9]</sup>) than modern RO plants. Fundamentally, CDI operates in cycles and relies on reversible electrosorption during the formation of an electric double layer at the interface between an electrode and saline feedwater. As exemplified for an aqueous NaCl solution, sodium cations are adsorbed at the negative electrode, and chloride anions are adsorbed at the positive electrode during charging, which consequently allows for desalination of the feedwater stream. An opposite process occurs during discharge, namely, desorption of sodium and chloride ions at the negative and positive electrodes, respectively. The latter process causes an increase in the salt concentration of the effluent stream, and a fraction of the invested energy during cell charge can be recovered. In contrast to this cyclic operation, continuous desalination with CDI can be enabled with flow electrodes (e.g., suspended carbon particles) by operating one cell for charge and the other for discharge with concurrent electrode regeneration.<sup>[10,11]</sup>

Although CDI technologies have been improved in recent years, two fundamental limitations remain.<sup>[4,12,13]</sup> The intrinsically low double-layer charge-storage capacities of porous carbon

[a] J. Lee, P. Srimuk, S. Carpier, J. Choi, R. L. Zornitta, C. Kim, M. Aslan, V. Presser

INM—Leibniz Institute for New Materials  
Campus D2 2, 66123 Saarbrücken (Germany)  
E-mail: volker.presser@leibniz-inm.de

[b] J. Lee, P. Srimuk, S. Carpier, V. Presser  
Department of Materials Science and Engineering  
Saarland University  
Campus D2 2, 66123 Saarbrücken (Germany)

[c] J. Choi  
School of Energy, Materials, and Chemical Engineering  
Korea University of Technology and Education  
1600 Chungjeol-ro, Cheonan 31253 (Republic of Korea)

[d] R. L. Zornitta  
Department of Chemical Engineering  
Federal University of São Carlos  
13565-905 São Carlos (Brazil)

Supporting Information and the ORCID identification number(s) for the author(s) of this article can be found under:  
<https://doi.org/10.1002/cssc.201801538>.

electrodes lead to overall low desalination capacities (desalination capacity for NaCl: 15–25 mg g<sup>-1</sup>).<sup>[14]</sup> Also, the process of co-ion expulsion makes CDI highly inefficient if the feedwater concentration is high (especially above 100 mM).<sup>[15–20]</sup> The latter originates from non-permselective ion electrosorption: instead of removing two ions with opposite charge to the electrodes (counterions), ions with the same charge as the electrode (co-ions) may be released; hence, the ion concentration of the treated water stream is not decreased. As initially present co-ions are depleted during cell charge, more and more counterions are removed from the feedwater, and the resulting charge efficiency (i.e., the charge used for permselective ion removal) will depend on the ion concentration and the applied cell voltage.<sup>[21]</sup>

To enhance the charge-storage capacity and to suppress co-ion expulsion, Faradaic reactions can replace the non-Faradaic process of ion electrosorption for reversible electrochemical desalination processes.<sup>[22]</sup> Faradaic deionization (FDI) accomplishes salt removal by Faradaic processes such as ion intercalation,<sup>[7,23–25]</sup> conversion reactions,<sup>[6,26]</sup> or pseudocapacitive processes.<sup>[27–30]</sup> The best-known FDI system is battery desalination with two battery-type electrodes,<sup>[6]</sup> which was first introduced by Pasta et al. by applying a Na<sub>2-x</sub>Mn<sub>5</sub>O<sub>10</sub> (NMO) positive electrode and a Ag/AgCl negative electrode. In that way, sodium cations were removed by an intercalation process to the NMO structure, whereas chloride anions were removed by a conversion reaction of silver (Ag to AgCl).<sup>[6,26]</sup> Chloride ions can also be removed through anion intercalation into the structure of two-dimensional materials such as transition-metal carbides (MXenes<sup>[28,30,31]</sup>) or transition-metal dichalcogenides (e.g., MoS<sub>2</sub><sup>[29,32]</sup>). The latter materials accomplish anion or cation removal, depending on the polarization of the electrode. Other intercalation-type battery electrodes can be used exclusively for the removal of cations, and a growing number of materials have been explored for sodium-ion intercalation, including sodium manganese oxide,<sup>[25]</sup> sodium iron phosphate,<sup>[24]</sup> nickel hexacyanoferrate,<sup>[7,33]</sup> vanadium oxide,<sup>[27]</sup> and titanium disulfide.<sup>[34]</sup> Most importantly, FDI has demonstrated desalination capacities far superior to those obtained for CDI and approach 100 mg g<sup>-1</sup> with high charge efficiencies over 80% even in saline media at seawater salt concentrations.<sup>[8]</sup> Redox materials may show not only high water desalination performance but also ion selectivity and separability, particularly for the separation of organic ions and heavy-metal ions.<sup>[35,36]</sup> Concerning the latter, using a polyvinyl(ferrocene)-functionalized electrode and a cobaltocenium-containing, polymer-functionalized electrode, Su et al. showed a high preference for organic anions (e.g., carboxylates, sulfonates, and phosphonates) over inorganic anions (e.g., perchlorates) in an aqueous solvent.<sup>[37,38]</sup>

A comprehensive comparison between FDI and RO remains complicated. For instance, most of the energy consumption values for FDI systems are reported with water recovery rates of less than 60%. The water recovery of filtration-based technologies relates to the volume of filtered (or treated) water compared to the feedwater volume.<sup>[2]</sup> Therefore, the water recovery rate must be distinguished from the salt removal ratio, which is the fraction of removed salt compared to the amount

of salt in the feedwater. For instance, modern seawater RO plants can provide water recovery of 40–60% with a salt removal ratio of 99.4–99.7%.<sup>[2,39,40]</sup> As FDI is not a filtration-based technology, we cannot assume the production of 40% of fresh water (< 1 g L<sup>-1</sup> of total dissolved solids) for water recovery of 60%. For that reason, instead of water recovery, the salt removal ratio is a preferable performance parameter for FDI. The highest reported salt removal ratio for FDI was 50%,<sup>[6]</sup> but higher values can be expected for different cell designs or if flow electrodes with small geometric electrode areas are applied. Nevertheless, considering the observed low energy consumption of 0.34 Wh L<sup>-1</sup> at a salt removal of 40% for an aqueous medium with 600 mM NaCl,<sup>[7]</sup> we see the great potential of scaled FDI systems for the future.

One of the primary challenges for the FDI technology compared to CDI systems is intrinsically low desalination rates (mg g<sup>-1</sup> min<sup>-1</sup>: milligram of salt removed per one gram of the electrode material for one minute).<sup>[8]</sup> This mirrors higher charge/discharge rates provided by electrical double-layer capacitors (supercapacitors) relative to that of battery materials.<sup>[41]</sup> The major rate-limiting factors are activation energy barriers for the reactions, low electrical conductivities of many electrode materials, and slow solid-state ion transport. The latter two issues can be addressed through nanoengineering of the electrode materials by using small particles with short intercalation depths (< 100 nm) and a percolating network of a conductive additive for enhanced electron transfer.<sup>[27,29,34]</sup> Alternatively, hybrid deionization (HDI) combines Faradaic and non-Faradaic materials to bridge the performances of CDI and FDI. For example, Kim et al. paired an activated carbon electrode with a sodium iron pyrophosphate electrode with a desalination capacity of 24 mg g<sup>-1</sup> for 100 mM feedwater.<sup>[24]</sup> Thereby, the desalination rate was only marginally reduced to 0.07 mg g<sup>-1</sup> s<sup>-1</sup> for their HDI setup from an initial value of 0.10 mg g<sup>-1</sup> s<sup>-1</sup> upon using two activated carbon electrodes.<sup>[24]</sup>

To enhance the desalination rates further, it is necessary to explore Faradaic processes with rapid redox kinetics. This can be provided only in part by using solid electrodes. The rapid kinetics of redox electrolytes confined in carbon nanopores is a promising new approach for advanced FDI systems.<sup>[42–44]</sup> In the case of redox electrolytes, the redox activities originate from the dissolved ions in the liquid electrolyte.<sup>[45–47]</sup> Electrons are transferred from an electrode to the dissolved ions, and this leads to a change in the oxidation state of the dissolved ions.<sup>[46,48–50]</sup> If redox active ions are further confined in carbon nanopores, diffusion of the redox reactions is governed not by conventional electrochemistry, but by thin-layer electrochemistry.<sup>[51,52]</sup> Owing to the short diffusion length in carbon nanopores, the redox reactions occur rapidly in the thin layer, which leads to redox kinetics as fast as those for electric double-layer formation.<sup>[42,44,53]</sup> Redox electrolyte systems are different from flow batteries, for which nanopores are undesired; instead of confinement, active convection of the ions in carbon macropores is preferred in flow batteries.<sup>[54]</sup> Recently, a new technology applied the principle of flow batteries with nonporous electrodes for water desalination and energy storage.<sup>[55,56]</sup>

Fast redox kinetics, a high charge-storage capacity, and performance stability over thousands of operational cycles make redox electrolytes of high interest for the field of energy storage.<sup>[48,57–60]</sup> To the best of our knowledge, the benefits of the Faradaic reactions of redox electrolytes in the confined space of carbon nanopores have not yet been explored for water desalination. Previous redox electrolyte systems have been applied to electrochemical energy-storage applications different from flow batteries.<sup>[46,60]</sup> Considering the unique characteristics of redox electrolyte systems confined in microporous carbon electrodes, their application to water desalination would be fundamentally different from electrodialysis, for which the highly irreversible water-splitting reaction, which is governed by conventional redox kinetics, is often applied to drive ion migration by applying a high cell voltage.

Here, we demonstrate a proof of concept for the use of the redox activities of iodide in confined carbon nanopores for high-performance water desalination. For that, the sodium iodide containing redox electrolyte was confined in the nanopores of an activated carbon cloth electrode. A cation-exchange membrane (CEM) was used to suppress the diffusion of iodide ions into the treated water stream and to allow for the beneficial electrochemical properties of the redox electrolyte. Our work provides thorough electrochemical analyses for the determination of the oxidation and reduction limits, maximum charge-storage capacities, and redox kinetics. Using a de-

salination cell with a counter electrode made of commercially available activated carbon powder, we quantify desalination capacities and rates. We further introduce a new analytical approach for unique performance evaluation of electrochemical desalination in terms of the water production rate and energy consumption.

## Results and Discussion

### Basic electrochemical performance

Before investigating the desalination performance, we first focused on the basic electrochemical properties of the activated carbon (AC) and activated carbon cloth (ACC) electrodes in different electrolytes. As seen in the cyclic voltammograms (Figure 1b), the AC electrode in 1 M NaCl exhibits a current response with a rectangular shape in the electrode potential range of 0 to  $-0.60$  V (vs. Ag/AgCl). This rectangular shape (Figure 1b, inset) results from a constant current in response to the electrical double-layer formation.<sup>[41]</sup> From the amplitude of this current, the capacitance of the AC electrode is estimated to be approximately  $105 \text{ F g}^{-1}$ . By using  $S$  value analysis,<sup>[61]</sup> we see high reversibility of the oxidation/reduction process for the negative AC electrode until  $-0.60$  V (vs. Ag/AgCl) ( $S$  values below 0.05; Figure 1c). In this potential regime, the predominant charge-storage mechanism is non-Faradaic ion electro-

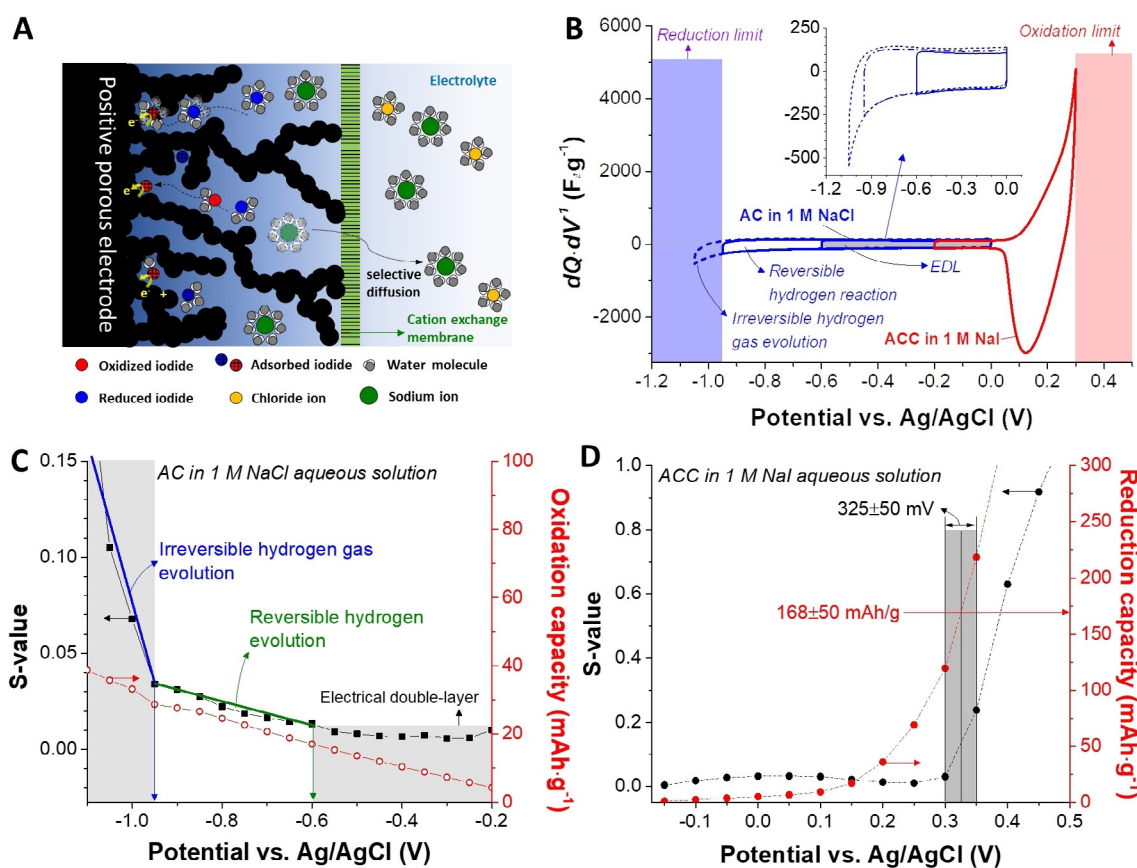


**Figure 1.** a) The desalination process by confined iodide redox activities in nanoporous carbon with the aid of a cation-exchange membrane. b) Cyclic voltammograms of the AC and ACC electrodes in aqueous solutions of NaCl and NaI, respectively.  $S$  value analyses of the c) AC and d) ACC electrodes to determine the reduction and oxidation limits, respectively.

sorption by electrical double-layer formation. Below  $-0.60$  V (vs. Ag/AgCl), the  $S$  value starts to increase and rises exponentially as the electrode potential exceeds  $-0.95$  V (vs. Ag/AgCl). The regime between  $-0.60$  and  $-0.95$  V (vs. Ag/AgCl) corresponds to the reversible adsorption of a dihydrogen intermediate (i.e.,  $C-H_{ad}/H^+$ ) on the carbon surface within the micropores.<sup>[27,49,62–65]</sup> The exponential increase in the  $S$  value below  $-0.95$  V (vs. Ag/AgCl) implies the evolution of hydrogen gas and, therefore, represents the reduction potential limit for reversible energy-storage operations.

The charge-storage capacity of the electrode depends on the chosen potential range (Figure 1c). For instance, scanning the potential of the AC electrode from 0 to  $-0.6$  V provides an oxidation capacity of  $17$  mA h g<sup>-1</sup>. The maximum oxidation capacity of  $29$  mA h g<sup>-1</sup> is achieved at the reduction potential limit of  $-0.95$  V (vs. Ag/AgCl) because of the combined contributions of the Faradaic and non-Faradaic reactions. If 100% of this charge were used for permselective desalination,<sup>[66]</sup> this specific charge would translate into a desalination capacity of  $31$  mg g<sup>-1</sup> [salt uptake capacity (SUC) for NaCl]. This value would be higher than what is typically obtained for CDI with nanoporous carbon ( $15$ – $25$  mg g<sup>-1</sup>)<sup>[12,13]</sup> but lower than the desalination capacity of FDI materials that may accomplish a SUC of  $60$  mg g<sup>-1</sup> or more.<sup>[27]</sup>

In contrast to the AC electrode in  $1$  M NaCl, the ACC electrode in  $1$  M NaI exhibits a distinctive pair of redox peaks at  $+0.2$  V (vs. Ag/AgCl) (Figure 1b). The origin of the redox reactions can be identified by Equation (1):<sup>[67–69]</sup>



On the basis of the  $S$  value analysis (Figure 1d), the oxidation limit is  $(325 \pm 50)$  mV, whereby the ACC electrode in  $1$  M NaI can provide a maximum specific charge of  $(168 \pm 50)$  mA h g<sup>-1</sup>. If used for permselective desalination and assuming a charge efficiency of 100%, this value would correspond to an impressive SUC value of  $(183 \pm 55)$  mg g<sup>-1</sup> (normalized only by the mass of the working electrode).

### Water desalination performance

To capitalize on the high charge-storage capacity, we further investigated the desalination performance of aqueous  $100$  mM NaCl by adopting a membrane CDI (MCDI) cell (Supporting Information, Figure S6).<sup>[27]</sup> The ACC electrode compartment was sealed by a CEM and was filled with aqueous NaI. The CEM suppressed the diffusion of iodide ions to the treated water stream and enabled operation of the redox electrolyte aided hybrid desalination cell (REHDI; Figure 1a). The ACC electrode was chosen because of its attractive characteristics, which include low specific resistivity and binder-free features as well as high performance for both CDI and electric energy-storage applications.<sup>[67,70,71]</sup> The ACC electrode compartment was filled with  $100$  mM NaI for cation removal, and the chloride ions were depleted from the feedwater by an AC electrode compartment in aqueous  $100$  mM NaCl, which was sealed by an anion-exchange membrane. We chose AC because its high

electrochemical stability, and as an oversized counter electrode, it was expected to have a negligible influence on the performance of the ACC working electrode.<sup>[27]</sup> In that manner, the desalination performance of the working electrode half-cell could be discussed by focusing on the confined redox activities of the iodide rather than on the ion electrosorption occurring at the activated carbon counter electrode.<sup>[27,67,70]</sup>

Figure 2a shows the electrode potential profiles of the REHDI cell during constant current charge and discharge ( $\pm 100$  mA g<sup>-1</sup> or  $\pm 0.84$  mA cm<sup>-2</sup>) with a charge limitation of  $20$  mA h g<sup>-1</sup>. This limit ensured the same half-cycle time for all other system configurations at the lowest applied specific current ( $100$  mA g<sup>-1</sup>) for a fair comparison later regarding the desalination kinetics. Resting for  $4$  min between the charge and discharge cycles allowed overpotential measurements and ensured that the concentration of the treated water stream had returned to the initial concentration (Figure 2a, baseline). During cell charge, iodide ions in the nanopores of the ACC working electrode ( $<1$  nm, Figure S1) are oxidized, as evidenced by the potential plateau at  $+0.25$  V (vs. Ag/AgCl). At the same time, the potential of the AC counter electrode decreases linearly from  $0$  to  $-0.28$  V (vs. Ag/AgCl) (Figure 2a). This nearly perfect linear relation aligns with the purely non-Faradaic process at the AC electrode. As soon as the electrodes are polarized, the concentration of the middle channel increases and begins to stabilize at approximately  $100.45$  mM. Therefore, charging at a rate of  $+100$  mA g<sup>-1</sup> causes sodium cations and chloride anions to migrate into the middle channel from the working and counter electrode channels, respectively. The migration of the sodium ions is driven by oxidation of the iodide ions, the state of charge of which becomes more positive, as schematically described in Figure 1a. As a result of the presence of the CEM, the sodium ions selectively leave the working electrode channel to maintain charge neutrality of the NaI electrolyte. The role of the iodide redox activities for the migration of the sodium ions is supported by the evidence of Faradaic reactions in the potential profile (potential plateau) measured for the positive electrodes as well as its relation to the desalination performance (Figure S7c).

In the counter electrode channel, the chloride ions pass through an anion-exchange membrane into the middle channel. The migration of the anions is driven by the adsorption of sodium ions through electrical double-layer formation. Once the cell is discharged at a rate of  $-100$  mA g<sup>-1</sup>, the opposite processes occur, and this leads to the migration of sodium cations and chloride anions from the middle channel into the compartment hosting the ACC and AC electrodes, respectively. As a result, a desalination capacity of  $20.7$  mg g<sup>-1</sup> (normalized by the mass of the working electrode; see Ref. [27]) and a charge efficiency of 96% are achieved for  $100$  mM feedwater (Figure 2a).

For water desalination technologies, the system performance is influenced by the effective residence time of the feedwater. According to the improved modified Donnan model,<sup>[4]</sup> commercially available activated carbon electrodes provide an average salt uptake rate (ASUR) of  $1.5$ – $2.2$  mg g<sup>-1</sup> min<sup>-1</sup> with a desalination capacity of  $4$ – $10$  mg g<sup>-1</sup>

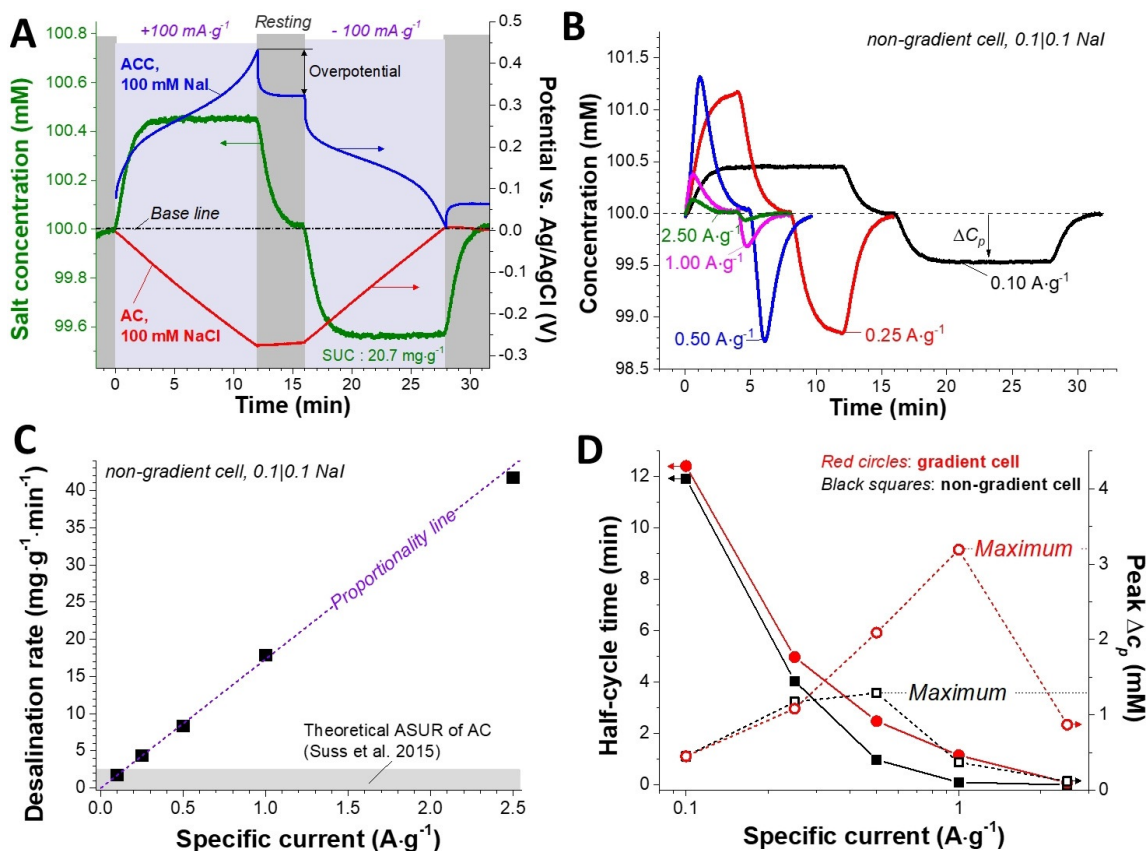


**Figure 2.** a) Concentration profile of the nongradient cell (—) and galvanostatic potential profiles of the individual electrode: the ACC working electrode in 1 M NaI aqueous solution (—) and the AC counter electrode in 1 M NaCl aqueous solution (—). A resting time of 4 min was applied before the sign of the applied current changed. b) Concentration profiles of the nongradient cell at various specific currents. c) Desalination rate (ASUR) obtained at various specific currents. d) Peak concentration difference ( $\Delta C_p$ ) and half-cycle time obtained from the gradient and nongradient cells at various specific currents.

with the half-cycle time (HCT) ranging from 1 to 3 min. In general, the HCT is controlled by electrochemical parameters, whereas the residence time is controlled by flow rates. Hence, a desalination system can be operated with a HCT of 1 min for a desalination rate of 2.2 mg g<sup>-1</sup> min<sup>-1</sup> even with the electrodes exhibiting a low SUC of 4 mg g<sup>-1</sup> for a high water production rate. In this case of a HCT of 1 min, the residence time should be  $\leq 1$  min to achieve effective desalination performance.

For our system, we expected the desalination rate to be proportional to the applied specific current. As the data basis for a feedwater concentration of 100 mM NaCl, we varied the specific current for charge and discharge from 100 mA g<sup>-1</sup> to 2.5 A g<sup>-1</sup> and from 0.84 to 21 mA cm<sup>-2</sup> (Figure 2b) for the 0.1 | 0.1 NaI system (AC in 100 mM NaCl and ACC in 100 mM NaI). As the feedwater ion concentration under the initial conditions is identical to the side compartments, we call this configuration “nongradient cell”, as we will later vary the cell configuration for even more improved performance. The resulting desalination rates (ASUR) increase almost linearly from 1.7 to 41.7 mg g<sup>-1</sup> min<sup>-1</sup> as a function of the applied specific current (Figure 2c). This value is almost ten times greater than that previously reported for the desalination rate of activated carbon electrodes (4.4 mg g<sup>-1</sup> min<sup>-1</sup>; the value originally reported in Ref. [4] is multiplied by a factor of 2 for fair comparison, see the Experimental Section). Most probably, the high ASUR

value is achieved by fast redox kinetics of the iodide ions confined in the carbon nanopores (Figures S4 and S5).<sup>[67]</sup>

With the 0.1 | 0.1 NaI configuration, our system required approximately 4 min to reach the maximum and minimum amplitudes of the concentration for a flow rate of 5 mL min<sup>-1</sup> at a constant current operation with 100 mA g<sup>-1</sup> (Figure 2b). This time period of 4 min relates to ion diffusion in the cell system and is also influenced by the distance between the cell outlet and the conductivity probe. The increase in the specific current decreases the HCT. If the HCT is shorter than the time required for concentration stabilization, no concentration plateau is reached. For example, using a current of 500 mA g<sup>-1</sup> (4.2 mA cm<sup>-2</sup>), we obtained a HCT of approximately 1 min and observed only a sharp peak in the concentration profile with a maximum concentration difference ( $\Delta C_p$ ) of 1.3 mM (Figure 2b). As the specific current increases further, the values of the HCT decrease further (Figure 2d).

The HCT depends on galvanostatic cell operation with the chosen charge limitation and potential limitation; these parameters will also determine the desalination capacity (Figure 3). As shown in Figure 3a, the electric charge capacity of the 0.1 | 0.1 NaI system for 100 mM NaCl feedwater significantly decreases if the applied specific current is increased. This decrease in the capacity at high currents is responsible for the rapid drop in the HCT (Figure 2d). To prevent a rapid increase

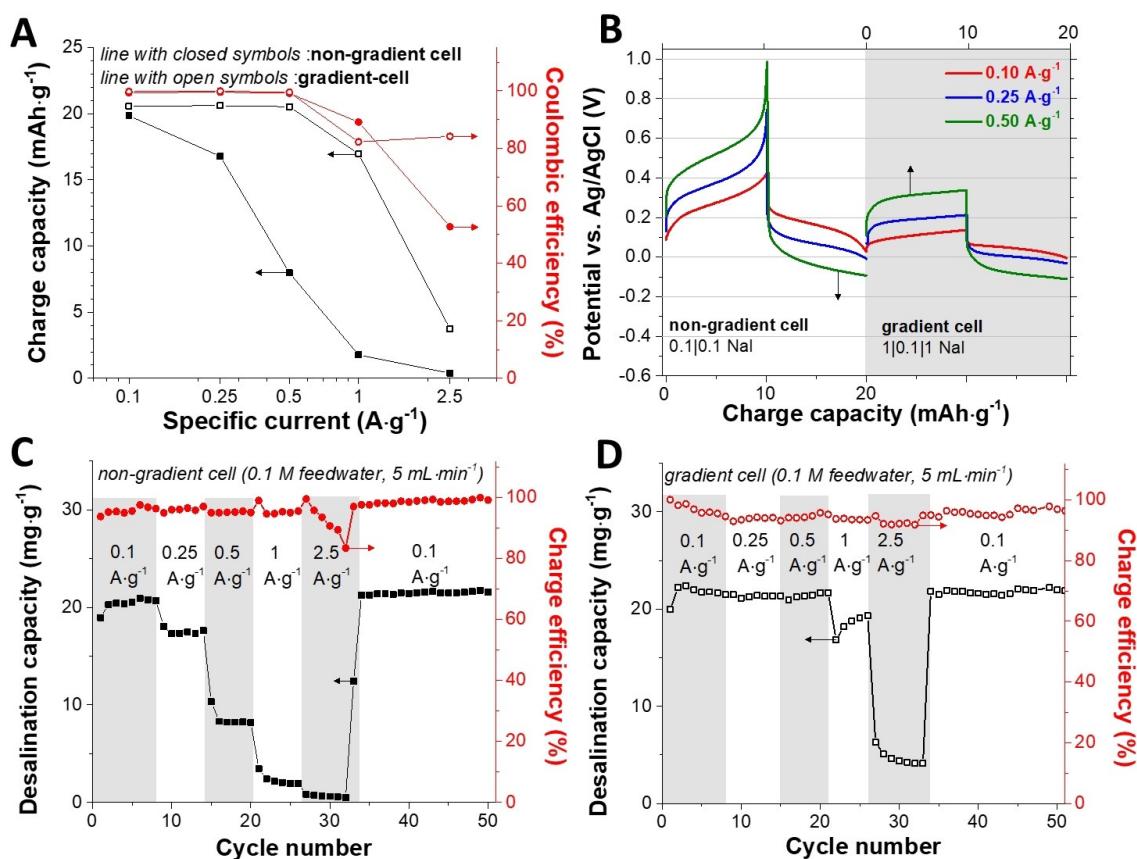


**Figure 3.** a) Charge capacity and Coulombic efficiency values obtained from the gradient and nongradient cells at various specific currents. b) Galvanostatic profiles of the ACC electrode in NaI aqueous solution obtained from the gradient and nongradient cells. The NaCl uptake capacity and charge efficiency values were obtained from the c) nongradient and d) gradient cells at various specific currents.

in the potential in the working electrode, galvanostatic operation was performed by limiting the potential (cell voltage of 1.6 V). Therefore, the decrease in the capacity is mainly caused by the overpotential for the iodide redox reaction with contributions from activation polarization, Ohmic resistance, and concentration polarization (Figure 3 b).<sup>[72]</sup>

The overpotential can be significantly reduced if the concentration of the electrolyte is increased (Figure 3 b). This can be accomplished by adopting our earlier work with the multichannel concentration-gradient membrane CDI concept; in the side channels we used electrolyte concentrations of 1 M NaCl (AC compartment) and 1 M NaI (ACC compartment). We continued using a feedwater concentration of 100 mM NaCl, and the resulting gradient cell system is labeled “1|0.1|1 NaI”. The scheme of our setup can be found in Figure S7 a.<sup>[13,73]</sup> The gradient 1|0.1|1 NaI system was tested by constant current operation with the same limitations on cell voltage and charge capacity as those applied to the nongradient 0.1|0.1 NaI system for fair comparison of the rate handling performance of the desalination process. As compared to the nongradient system, the gradient configuration yields superior rate handling. This can be seen by retention of a higher desalination capacity at high currents. The gradient cell virtually sees no reduction in the desalination capacity of approximately 21 mg g<sup>-1</sup> up to 500 mA g<sup>-1</sup>, whereas the nongradient cell loses more than half

of its initial SUC at the same specific current (Figure 3 c,d). At 1 A g<sup>-1</sup> (8.4 mA cm<sup>-2</sup>), the gradient cell still provides a desalination capacity of 19 mg g<sup>-1</sup> (Figure 3 d), whereas the nongradient cell accomplishes only 2 mg g<sup>-1</sup> (Figure 3 b). The high SUC retention of the gradient cell enables a much higher maximum concentration difference  $\Delta c_p$  of 3.2 mM than the nongradient cell (Figure 2 d).

These results show the importance of considering both the SUC and the HCT. Using the same specific current, a system with a higher desalination capacity may exhibit a longer HCT than a system with a lower desalination capacity because of the dependency of the SUC (in mg g<sup>-1</sup>) on the charge capacity (in mA h g<sup>-1</sup>). For flexible system design and desalination operation, higher SUC values are preferred, as they provide longer HCTs at a given power rate. Simply reporting maximum SUC values without considering the power performance does not provide information for practical desalination performance regarding charge efficiency, water production rate, and energy consumption.

### Energy consumption and water production rate

For water desalination, the actual energy consumption and water production rate are both important to consider. To investigate these parameters adequately for the REHDI concept, we

considered the full-cell performance. In the literature, the energy consumption is often reported by using units of  $kT$ , and the  $E_{kT}$  value represents the energy required per removed ion.<sup>[21]</sup> For the energy calculations, one can either consider only the invested energy ( $kT_{inv}$ ) or include the recovered energy, as schematically shown in Figure 4a.<sup>[74,75]</sup> Values of  $E_{kT}$  for  $kT_{net}$  (considering the net energy) and  $kT_{inv}$  (considering the total invested energy) from the gradient and nongradient cells at a feedwater concentration of 100 mM NaCl are plotted in Figure S7b. With and without considering the recovered energy, the gradient cell consistently consumes less energy during desalination. Therefore, we continued the investigation

only with the gradient cell and studied the variation of the feedwater concentration in the range of 50 to 600 mM.

Typical values of  $E_{kT}$  in the literature for CDI and MCDI are in the range of 20 to 60  $kT$  for desalination of feedwater with a NaCl concentration between 5 and 200 mM.<sup>[4]</sup> In comparison, lower values of 12 to 30  $kT$  are known for FDI and HDI with a NaCl concentration range of 20 to 600 mM.<sup>[28,34]</sup> As the energy consumption strongly depends on the cell and electrode engineering, we also provide  $E_{kT}$  value of an MCDI system measured with a nongradient cell for desalination of 100 mM feedwater by using our setup (cell-voltage limit of 1.2 V without charge-capacity limit; see Figure S7a,c). For the MCDI system with a nongradient cell (100 mM NaCl in the feedwater; Figure 4b), the values were measured to be 34.3  $kT_{inv}$  and 7.8  $kT_{net}$  with a charge efficiency of 97% and an energy efficiency of 77%. Operating the REHDI system at 100  $mA g^{-1}$ , we obtained between 9.6 and 29  $kT_{inv}$  which is below the values of the MCDI system and other values in the literature (Figure 4b). These results indicate that the REHDI system with a gradient cell can provide more energy-efficient water desalination than conventional CDI systems for feedwater concentrations higher than 100 mM.

If the recovered energy is considered, the net energy consumption ( $kT_{net}$ ) is lower at higher concentrations. For a NaCl feedwater concentration of 600 mM, the REHDI system consumes only 2.4  $kT$  per removed ion, although the overall charge efficiency is very low (62%). In comparison, much higher values are found for modern seawater plants (7.2–12.2  $kT$ ).<sup>[2,39,40]</sup> The latter values were converted from the reported values of 3–5  $Wh L^{-1}$  assuming a salt removal ratio of 99.6% and 35  $g L^{-1}$  seawater containing only NaCl. The main contribution to the decrease in the charge efficiency for the concentration regime above 100 mM relates to co-ion expulsion at the AC carbon electrode (Figure S8b). Hence, further improvements in the charge efficiency may be possible by replacing the AC electrode with an intercalation- or conversion-type electrode.

The energy consumption is expected to be related not only to the feedwater concentration but also to the applied specific current.<sup>[75,76]</sup> In Figure 4c, values for  $kT_{inv}$  energy efficiency, and charge efficiency are plotted at various specific currents. We see that the charge efficiency does not depend at all on the applied specific current, because, for all studied conditions, all of the data fall within a margin of  $\pm 1\%$ . The overall energy efficiency decreases at high specific currents because of the increased overpotential at higher currents. For the  $kT_{inv}$  values, we see a pronounced V-shaped profile (Figure 4b: 100  $mA g^{-1}$ ) and an overall increase in the values as the specific current increases (Figure 4c: 100  $mA g^{-1}$  to 1  $A g^{-1}$ ). The results indicate that the V-shape profiles reflect opposing effects of the feedwater concentration on ionic conductivity and co-ion repulsion. At high currents, the  $kT_{inv}$  values become dominated by the reduced overpotential and at higher concentrations through enhanced ionic conductivity.

Energy values in  $kT$  help significantly to compare different electrochemical processes. The energy consumption in  $Wh L^{-1}$  (instead of  $kT$ ) helps us to quantify the entire energy consump-

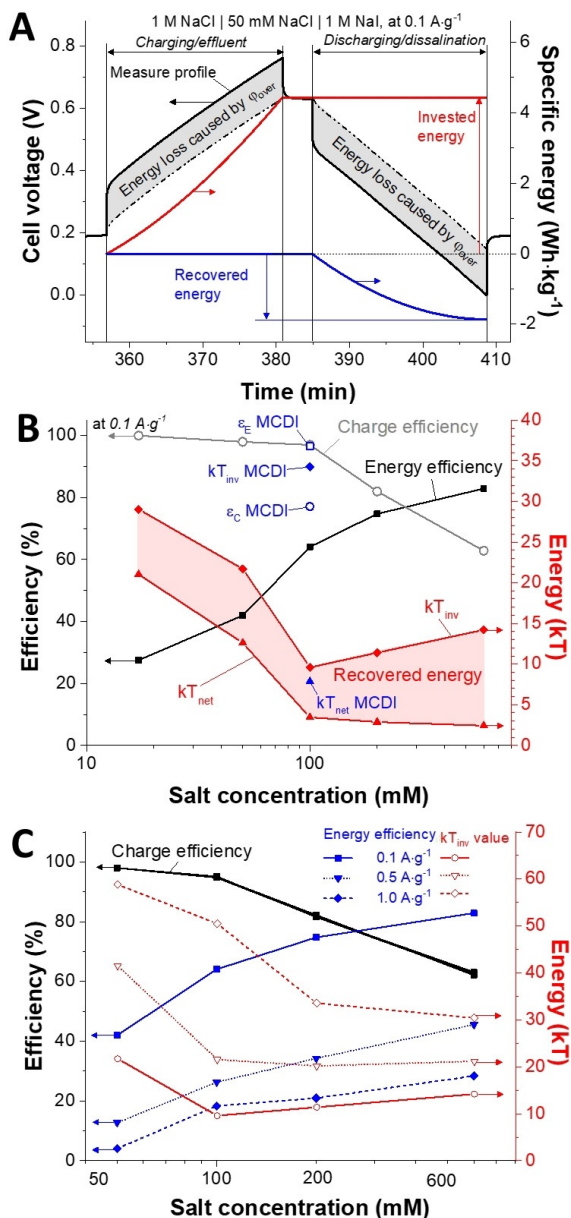


**Figure 4.** a) Galvanostatic cell-voltage profile of the gradient cell obtained during desalination operation for 50 mM NaCl feedwater. Charge and energy efficiency and  $kT$  values obtained from the gradient cell for various feedwater concentrations b) at 0.1  $A g^{-1}$  (0.84  $mA cm^{-2}$ ) and c) at various specific currents. For comparison, values from the membrane capacitive deionization (MCDI) cell are also presented.

tion for the production of water with a desired concentration from feedwater at a given concentration. For instance, the energy consumption of seawater RO plants varies from 3 to 5 WhL<sup>-1</sup> at water recovery values between 40 and 60% with a salt removal ratio of 99.4–99.7%. Brackish water RO plants show energy consumption values between 0.9 and 3 WhL<sup>-1</sup> at water recovery of 75–90% with a salt removal ratio of 95–99%.<sup>[2,39,40]</sup> For the CDI and FDI technologies, the concept of water recovery cannot be easily adapted. By continuous single-pass mode operation, the water recovery would always be 100% (i.e., the ratio of treated water and feedwater, but not the ratio of treated water and the sum of feed water and effluent water). The water recovery for CDI and FDI can also be assumed to be 50% by considering that effluent water is a part of the feedwater if the processed water is not recirculated and the discharge/charging times are equal. Alternatively, one can evaluate the salt removal ratio as a performance parameter. Achieving a high salt removal ratio is a challenging task for small-scale or laboratory-scale systems because of limitations on the electrode mass and cell size. For instance, Dlugolecki and van der Wal used 24 cells with a total electrode area of 1.18 m<sup>2</sup> to achieve a salt removal ratio of 90.6% from 8.6 mM NaCl feedwater with an energy consumption of 0.20 WhL<sup>-1</sup> considering energy recovery even under batch-flow conditions.<sup>[75]</sup>

To overcome the limitations associated with evaluating the energy consumption in units of WhL<sup>-1</sup>, we can estimate the value on the basis of the data from a single-pass mode operation for a specific concentration. For instance, by assuming that the energy required per gram of removed salt ( $E_{\text{salt}}$  in Whg<sup>-1</sup>) at one fixed feedwater concentration remains constant all the way to the desired concentration of fresh water (1 gL<sup>-1</sup>), the energy consumption per 1 L of fresh water ( $E_d$  in WhL<sup>-1</sup>) can be estimated by Equation (2):<sup>[27,34]</sup>

$$E_d = E_{\text{salt}} \cdot (m_s - m_0) \quad (2)$$

in which  $m_s$  is the amount of salt in 1 L of the feedwater, and  $m_0$  [g] is the maximum amount of NaCl in 1 L of drinking water (assumed to be 1 gL<sup>-1</sup>).<sup>[77]</sup> The  $E_{\text{salt}}$  parameter is obtained by dividing the net energy consumption [Wh] by the salt uptake capacity [g] of the cell.

However,  $E_{\text{salt}}$  is a function of the concentration, and therefore, the actual performance can be severely overestimated by using Equation (2). Hence, we suggest an analytical approach involving the use of data obtained in a single-pass mode. In this way, it is possible to estimate more accurately the energy consumption in WhL<sup>-1</sup> for laboratory-scale experiments. As shown in Figure 5a, the energy consumption of the REHDI system is evaluated in Whg<sup>-1</sup> at various feedwater concentrations. If  $E_d$  is integrated in terms of the amount of remaining salt in 1 L of water, then the energy consumption ( $E_d^*$ ) is more accurately estimated by Equation (3) than by Equation (2):

$$E_d^* = \int_{m_0}^{m_s} E_d dm \quad (3)$$

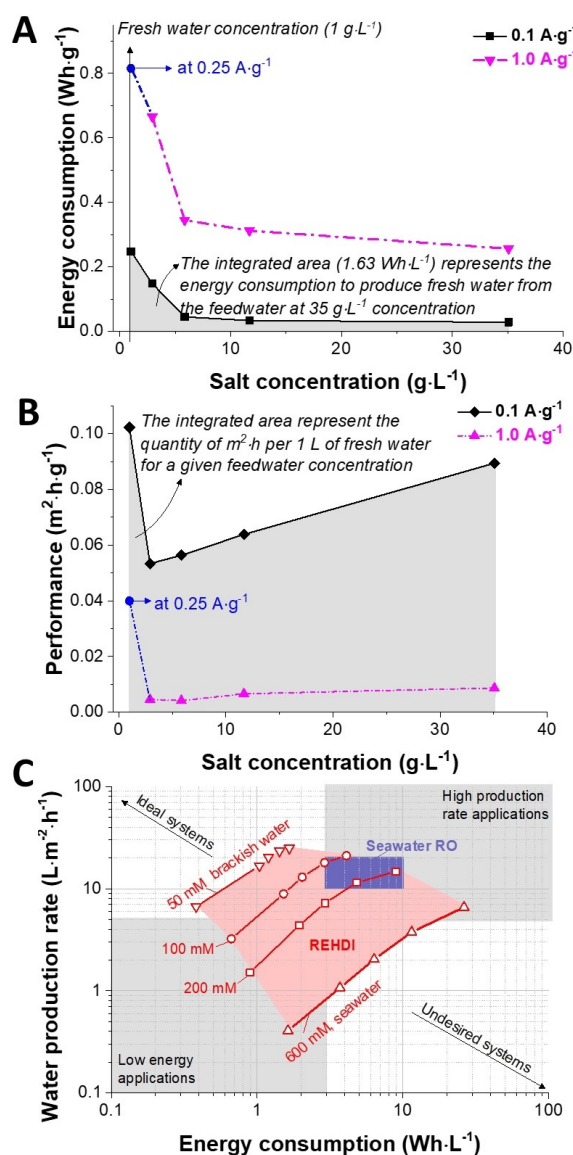


**Figure 5.** a) Energy consumption per gram of removed salt as a function of feedwater concentration. b) Required time and geometrical area of the electrode to remove 1 g of salt as a function of feedwater concentration. c) Water production rate and energy consumption values obtained from the gradient cell. Additional data display the performance range of RO.

For instance, at 0.1 A g<sup>-1</sup>, the total energy consumption for the desalination of 17–600 mM can be estimated by integrating  $E_d$  from  $m_0$  to  $m_s$ . For feedwater with a concentration of 1 gL<sup>-1</sup> (17.1 mM) at a specific current higher than 0.5 A g<sup>-1</sup>, the  $E_d$  values could not be obtained because of the poor rate handling behavior of the system caused by low ionic conductivity. In that case, the next highest  $E_d$  value obtained at a lower current was taken for evaluation. For example, the data at 250 mA g<sup>-1</sup> (2.1 mA cm<sup>-2</sup>) measured for 1 gL<sup>-1</sup> feedwater was applied to the evaluation data set at 1.0 A g<sup>-1</sup> (Figure 5a). In that manner, values for the energy consumption of the REHDI system were obtained at different desalination rates. These data can then be converted into the actual production rate of water and plotted versus the consumed energy, as shown in

Figure 5c. The water production rate,  $\dot{V}_d$  [ $\text{L}\cdot\text{m}^{-2}\cdot\text{h}^{-1}$ ], can be converted from the data set of the desalination rates obtained at various specific currents and feedwater concentrations by Equation (4):

$$\dot{V} = \frac{1}{\int_{m_0}^{m_e} t_E dm} \quad (4)$$

in which  $t_E$  [ $\text{m}^2\cdot\text{h}\cdot\text{g}^{-1}$ ] is the time multiplied by the geometrical area of the electrode required to remove 1 g of NaCl. Normalization by the area provides not only a comparison to other membrane-based desalination technologies but also considers the involvement of cost-expensive ion-exchange membranes to CDI and FDI systems. The datasets used for the calculations with Equation (4) are provided in Figure 5b, as exemplified by the results obtained at 0.1 and 1.0  $\text{A}\cdot\text{g}^{-1}$ .

Using these data, we can evaluate the performance of REHDI at different concentrations and compare the values with seawater RO plants. Figure 5c plots the water production rate in  $\text{L}\cdot\text{m}^{-2}\cdot\text{h}^{-1}$  against the energy consumption in  $\text{Wh}\cdot\text{L}^{-1}$ . In this plot, an ideal system would be located in the upper left corner, whereas the lower right corner represents systems with poor performance. For the REHDI system with a gradient cell, the lowest energy of 0.38  $\text{Wh}\cdot\text{L}^{-1}$  is obtained for the desalination of feedwater with a NaCl concentration of 50 mM. The lowest energy consumption values are 0.66, 0.90, and 1.63  $\text{Wh}\cdot\text{L}^{-1}$  for feedwater concentrations of 100, 200, and 600 mM, respectively. Our REHDI system accomplishes seawater desalination with low energy consumption (1.63  $\text{Wh}\cdot\text{L}^{-1}$ , salt removal ratio 97%) even relative to modern seawater RO plants (3–5  $\text{Wh}\cdot\text{L}^{-1}$ , salt removal ratio of 95–99%).<sup>[2,39,40]</sup>

Higher water production rates become accessible if operating a REHDI system at higher specific currents, but this also results in enhanced higher energy consumption (Figure 5c). Thereby, seawater desalination at a high rate of 6.6  $\text{L}\cdot\text{m}^{-2}\cdot\text{h}^{-1}$  is possible but will show an energy consumption of 26.2  $\text{Wh}\cdot\text{L}^{-1}$ . For 200 mM NaCl feedwater, the maximum water production rate of the gradient cell is 14.7  $\text{L}\cdot\text{m}^{-2}\cdot\text{h}^{-1}$ ; however, a more practical water production rate will be 7.2  $\text{L}\cdot\text{m}^{-2}\cdot\text{h}^{-1}$  with an energy consumption of 2.93  $\text{Wh}\cdot\text{L}^{-1}$ . For 50 mM NaCl feedwater, a low energy consumption (1.66  $\text{Wh}\cdot\text{L}^{-1}$ ) is still maintained at a high water production rate of 25.0  $\text{L}\cdot\text{m}^{-2}\cdot\text{h}^{-1}$ . By comparison, seawater RO systems exhibit values of approximately 10–20  $\text{L}\cdot\text{m}^{-2}\cdot\text{h}^{-1}$  for water recovery in the range of 40 to 50%.<sup>[1,2,78]</sup>

### Performance and cell stability

So far, the water desalination performance of the REHDI system with a gradient cell has been discussed in terms of water production rate and energy consumption. For that, the maximum capacity during the constant-current operation was limited to 20  $\text{mA}\cdot\text{h}\cdot\text{g}^{-1}$ . This capacity limitation allowed the same desalination time for the REHDI system with various configurations at the lowest specific current and, therefore, enabled a comparison regarding the water production rate as well as the reliability for the suggested new analytical approach. To

achieve even higher desalination capacities and to illustrate the promising potential of REHDI, one can also select a higher capacity limit; high SUC values are desired to provide a HCT that is sufficient for flexible engineering of a desalination system. Therefore, the cyclic stability of the REHDI system with a gradient cell for 600 mM feedwater was tested in the cell-voltage window of 0 to 0.73 V at 0.25  $\text{A}\cdot\text{g}^{-1}$  (Figure 6a, inset). The cell-voltage limit was selected not to cross the oxidation limit [(0.325 ± 50) mV] of the ACC electrode in 1 M NaI solution. In the selected cell-voltage window, the potential of the ACC electrode was measured in the range of −0.05 to +0.28 V and exhibited an initial capacity of approximately 100  $\text{mA}\cdot\text{h}\cdot\text{g}^{-1}$ . As seen in Figure 6a, long-time operation over 5 days (120 cycles) yielded stable desalination capacities of (68.9 ± 6.6)  $\text{mg}\cdot\text{g}^{-1}$  with a charge efficiency of approximately 64% and a Coulombic efficiency of almost 100%. The high Coulombic efficiency exceeding 96% obtained by various specific currents (Figure S8a, 0.1–2.5  $\text{A}\cdot\text{g}^{-1}$ ) and feed water concentrations (Figure S8b, 17–600 mM) also assures that the iodide redox activities are highly reversible, which is clearly different from the highly irreversible water-splitting reaction of electrodesialysis.

Not all desalination technologies are applied to the generation of potable water. Yet, all desalination technologies will re-

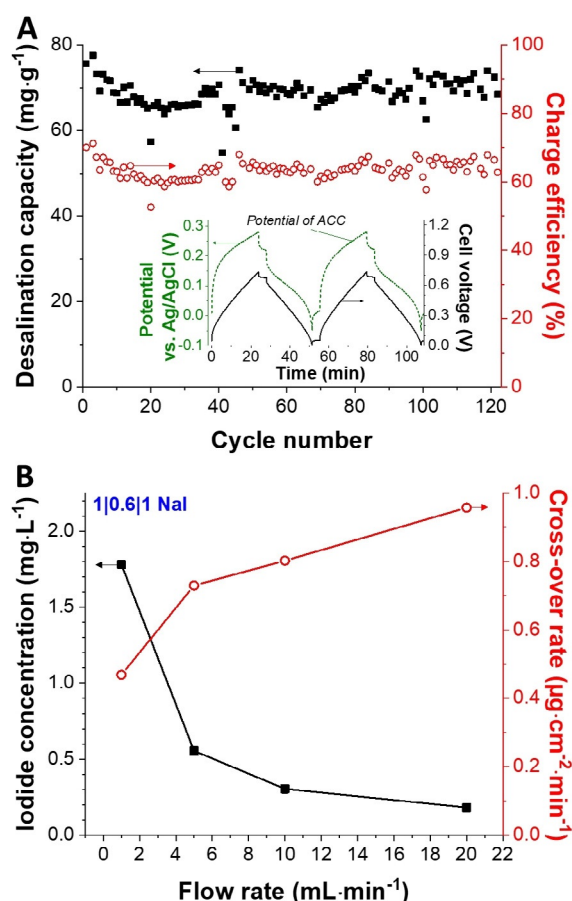


**Figure 6.** a) Performance stability of the ACC electrode in NaI aqueous as coupled with an AC counter electrode in terms of salt uptake capacity and charge efficiency. b) Iodide cross-over to the middle channel as a function of the flow rate.

quire a thorough investigation of possible leakage from the iodide through the ion-exchange membrane and into the treated water stream. After passing through the REHDI cell unit, the iodide concentration of the water stream was measured to be  $(0.56 \pm 0.03) \text{ mg L}^{-1}$  at a flow rate of  $5 \text{ mL min}^{-1}$ . We found that the iodide concentration in the treated water stream depended on the flow rate (Figure 6b). At a lower rate ( $1 \text{ mL min}^{-1}$ ), the iodide concentration was  $(1.78 \pm 0.01) \text{ mg L}^{-1}$ , and a lower concentration of  $(0.18 \pm 0.02) \text{ mg L}^{-1}$  was found at  $20 \text{ mL min}^{-1}$ . The obtained lowest value is in the range of iodide concentrations from natural groundwater.<sup>[79]</sup> If the values are converted into cross-over rates normalized by the size of the geographical area of the electrode, the highest rate was measured to be  $0.958 \mu\text{g cm}^{-2} \text{ min}^{-1}$  at  $20 \text{ mL min}^{-1}$ , and the lowest rate was measured to be  $0.469 \mu\text{g cm}^{-2} \text{ min}^{-1}$  at  $1 \text{ mL min}^{-1}$ . Most probably, the higher cross-over rate was caused by the higher dynamics of water at higher flow rates. Our results imply that using our current setup without using different or thicker membranes may eventually require replenishing the iodide electrolyte in the ACC compartment per the depletion of the iodide.

The leakage of elemental iodine into the effluent stream will have to be considered depending on the target application and the associated water composition requirements. For the generation of potable water, our data show that REHDI is still a viable technology. Iodide is essential for life and the human body and is considered to have low toxicity. According to a document published by the World Health Organization (WHO) in 1996, no serious health issue had been found in a five-year study of people consuming water with an iodide concentration of  $1 \text{ mg L}^{-1}$ .<sup>[80]</sup> The iodide concentration in groundwater depends on the geographical location and the soil.<sup>[80]</sup> Instead, many people suffer from iodine-deficiency disorders in areas with low iodine concentrations.<sup>[81]</sup> According to studies by Ünak et al. in 1999 and by Delange in 1994, at least 1 billion people are currently at risk of iodine-deficiency disorders.<sup>[81,82]</sup>

## Conclusions

As proof of concept, we demonstrated that confined iodide activities in nanoporous carbon could be applied for energy-efficient water desalination even at seawater concentrations with broad and flexible applications to brackish water. Through a diffusionless iodide reaction at an activated carbon cloth electrode, the desalination capacity was well maintained, even at high specific currents of  $2.5 \text{ A g}^{-1}$  if a gradient cell configuration was used. The origin of this high retention was the improved ionic conductivity at the side channel in the gradient cell, as evidenced by a reduced overpotential for the reaction. The gradient cell exhibited low energy consumption in the range of  $14.2$  to  $29.0 \text{ kT}_{\text{inv}}$  depending on the feedwater concentration ( $17$ – $600 \text{ mM NaCl}$ ). Owing to opposite effects of concentration on co-ion expulsion and overpotential, the lowest  $\text{kT}_{\text{inv}}$  value was observed for feedwater at a  $100 \text{ mM}$  concentration at low specific currents ( $<0.5 \text{ A g}^{-1}$ ). At higher specific currents, the energy consumption in  $\text{kT}_{\text{inv}}$  was dominated by the overpotential, which was reduced significantly at

higher concentrations through improved ionic conductivity. By considering the restored energy, the overall net energy consumption was low and varied from  $21$  to  $2.4 \text{ kT}$  at different feedwater concentrations. The optimized cell exhibited a highly stable desalination process with a desalination capacity of  $69 \text{ mg g}^{-1}$  throughout  $120$  cycles. Mainly, considering a high water production rate ( $25 \text{ L m}^{-2} \text{ h}^{-1}$ ) for brackish water and low energy consumption for seawater ( $1.63 \text{ Wh L}^{-1}$ ), the confined iodide reaction in nanoporous carbon is believed to play an essential role for future desalination technology.

## Experimental Section

### Materials

As electrodes, we used activated carbon cloth (ACC; type ACC-507-20 from Kynol; more details found in Ref. [70]) and free-standing film electrodes of activated carbon (AC; type YP-80F from Kuraray; more details found in Ref. [83]). For the preparation of the free-standing AC electrode, the powder form of the activated carbon was mixed with polytetrafluoroethylene (PTFE, Sigma-Aldrich) and ethanol, rolled to form a film, and dried in a vacuum oven ( $120^\circ\text{C}$ ,  $203 \text{ Pa}$ ) for  $48 \text{ h}$  while controlling the mass ratio of carbon to PTFE at  $95:5$ . Aqueous sodium iodide (NaI) solutions were prepared with NaI ( $\geq 99.999\%$  purity, Sigma Aldrich) either at  $100 \text{ mM}$  or  $1 \text{ M}$  in deionized water (Milli-Q). NaI was stored and weighted in a glove box.

### Material characterization

For electrochemical characterization, custom-built cells were measured with a VMP300 potentiostat/galvanostat (Bio-Logic) in a three-electrode configuration. The configuration of our cell design can be found elsewhere.<sup>[84,61]</sup> For the half-cell characterization of the AC ( $200 \mu\text{m}$  thickness,  $12 \text{ mm}$  diameter,  $\approx 10 \text{ mg}$  mass loading) in aqueous NaCl, a double stack of oversized AC electrodes ( $600 \mu\text{m}$  thickness,  $12 \text{ mm}$  diameter,  $\approx 30 \text{ mg}$ ) was used as the counter electrode. For half-cell characterization of the ACC ( $5 \text{ mm}$  diameter,  $\approx 1.7 \text{ mg}$ ) in aqueous NaI, a triple stack of oversized AC electrodes was used. At the side of the cell, a reference electrode (Ag/AgCl, Bioanalytical Systems) was mounted in close contact with the working and counter electrodes. We used GF/A glass fiber filters (Whatman) as the separators and platinum disks as the current collectors. After cell assembly, the aqueous electrolyte was injected by syringe for backfilling.

The specific capacity,  $Q [\text{mAh g}^{-1}]$ , was obtained from the charge accumulated [mAh] by the reduction or oxidation current ( $I$ ) measured by cyclic voltammetry by using Equation (5):

$$Q = \frac{1}{m} \int_{t_1}^{t_2} I dt \quad (5)$$

in which  $t_2 - t_1$  is the time required for the reduction or oxidation of the electrode and  $m$  is the active mass of the working electrode.

To determine the electrochemical stability (anodic and cathodic potential limits),  $S$  value analysis was performed following the general procedure reported elsewhere.<sup>[43,85]</sup> Briefly, the potential of the electrode was scanned from the fixed starting potential, whereas the end potential was extended in potential intervals of  $50 \text{ mV}$ .

The  $S$  values were calculated by using Equations (6) and (7):

$$S_a = \frac{Q_a}{Q_c} - 1 \quad (6)$$

$$S_c = \frac{Q_c}{Q_a} \quad (7)$$

in which  $S_a$  is the  $S$  value for the anodic limit,  $S_c$  is the  $S$  value for the cathodic limit,  $Q_a$  is the charge accumulated by the anodic current, and  $Q_c$  is the charge accumulated by the cathodic current. The applied currents were all normalized either by the full mass or the geometrical area of the working electrode, as indicated in the Discussion section. The specific current values in this study were obtained by normalizing the applied current by the active mass of the working electrode or the geometrical area of the working electrode.

### Desalination performance

For characterization of the desalination performance, we used the custom-built cell shown in Figure S6. The gaskets enabled tight sealing of the ACC working electrode [24 mm diameter, (37.8 ± 0.9) mg] with a cation-exchange membrane (FKS-PET-130, FuMA-Tech) and of the AC negative electrode [30 mm diameter, (550 ± 20) μm thickness, (157.6 ± 2.1) mg] with an anion-exchange membrane (FAS-PET-130, FuMA-Tech). In both electrode compartments, there was no excess electrolyte volume except for the geometrical volume of the electrode to prevent overestimation of the performance.<sup>[43]</sup> As our previous study indicated, as long as the type and size of the electrode and the volume of the electrode compartment were the same, comparison of the performances of the tested systems was fair regardless of the normalization by the volume of the cell or mass of the electrode.<sup>[43]</sup> As we provide the diameters and masses of the working electrodes, all reported performance values in our paper can be easily converted into the values normalized by the geometrical electrode area. For the water production rate [L m<sup>-2</sup> h<sup>-1</sup>], we applied the area of the geometrical area of the electrode, as a slightly larger size of the membrane was used for firm sealing with the gasket. For large-scale applications, we expect that the size of this sealed part of the membrane will be negligibly small relative to the effective area of the membrane, which will be the same size of the electrode.

The NaCl solution passed through the middle channel (thickness of 3 mm) provided by a glass fiber separator (Millipore, 7 stacks of 380 μm). Hence, the total distance between the working and counter electrodes was 3.26 mm. As current collectors, we used a pair of graphite plates (thickness of 10 mm). Through a small opening channel with 4 mm diameter in the current collector at the counter electrode, we inserted a Ag/AgCl reference electrode. By using Ag/AgCl as a spectator reference, we recorded the potential of the AC electrode (vs. Ag/AgCl) electrode while the cell was operated in a full-cell fashion.

Aqueous solutions were prepared with NaCl (≥99.5% purity, Sigma-Aldrich) at various concentrations (17–600 mM) in deionized water (Milli-Q). All desalination experiments were performed in a flow-by mode with semisingle pass flow operation.<sup>[86–88]</sup> Using a 10 L reservoir, the stream of water was continuously circulated at a flow rate of 5 mL min<sup>-1</sup> with a peristaltic pump. The large volume of aqueous NaCl assured that the concentration change in the feedwater stream was negligible despite the desalination operation owing to the small masses of the electrodes in the cell. The NaCl

reservoir was continuously flushed with nitrogen to deplete dissolved oxygen. The conductivity of the treated water stream was measured close to the cell. The pH value of the outflow was measured after the solution stream passed through the conductivity meter. The rest of the solution was circulated back into the solution reservoir.

The desalination capacity (salt uptake capacity, SUC [mg g<sup>-1</sup>]) of the working electrode was calculated by using Equation (8):

$$\text{SUC} = \frac{1}{2 \cdot m_w} \sum_{n=0}^k ([c_0 - c_n] \cdot \nu \cdot M_{\text{NaCl}} \cdot [t_n - t_{n-1}]) \quad (8)$$

in which  $c_n$  [M] is the measured molar concentration at time  $t_n$  [s],  $c_0$  is the initial concentration,  $\nu$  is the volumetric flow rate [L s<sup>-1</sup>],  $M_{\text{NaCl}}$  is the molecular mass of NaCl (58440 mg mol<sup>-1</sup>),  $t_n - t_{n-1}$  is the time interval for the conductivity measurement, and  $m_w$  [g] is the mass of the working electrode. The factor of 2 comes from the fact that the SUC value of the cell is the contribution of two electrodes. Note that the SUC value according to Equation (8) is normalized by the mass of the working electrode. For the SUC value of the entire cell performance (SUC<sub>cell</sub>), the values were normalized by the mass of both the working and counter electrodes ( $m_c$ ) instead of  $2 m_w$ .<sup>[27]</sup> Even though no electrochemical cell works without having a counter electrode in the cell, normalization only by the mass of the working electrode is a common practice in many applications such as reporting electrochemical properties of batteries, supercapacitors, and catalysts.<sup>[89–91]</sup> For instance, the performance of lithium battery half-cells using (redox-active) lithium metal as a counter electrode is commonly normalized only by the mass of the working electrode if there is controlled or negligible influence of the counter electrode. The charge capacity is normalized mostly by the mass of the working electrode in the case of electrochemical energy-storage systems, as the capacity of the half-cell is limited by the working electrode.<sup>[27,92]</sup> Likewise, the SUC is also limited by the capacity of the working electrode in a half-cell, as validated by our previous work.<sup>[27]</sup> The term “uptake” is used to prevent the incorrect description that the salt removal mechanism of our system is based on an “adsorption” process.

The concentration of NaCl is calculated, after correcting for the pH value, by converting the measured conductivity by Equation (9):

$$c_n = \frac{1}{1000} \cdot \left( \left[ \frac{\sigma_n - 4.5}{121.29} \right]^{0.9826} - 0.13 \right) \quad (9)$$

in which  $\sigma_n$  is the corrected conductivity [μS cm<sup>-1</sup>] at time  $t_n$  by Equation (10):

$$\sigma_n = \sigma_m - \sigma_w \quad (10)$$

in which  $\sigma_m$  is the measured conductivity [μS cm<sup>-1</sup>]. The conductivity of water,  $\sigma_w$  [μS cm<sup>-1</sup>], can be obtained from Equation (11):

$$\sigma_w = \frac{10^6 \cdot e^2}{k_B \cdot T} \cdot \left( 10^{\text{pH}} \cdot N_A \cdot D_{\text{H}_3\text{O}^+} + N \frac{10^{-14}}{10^{-\text{pH}}} \cdot N_A \cdot D_{\text{OH}^-} \right) \quad (11)$$

in which  $k_B$  is the Boltzmann constant (1.38 × 10<sup>-23</sup> m<sup>2</sup> kg s<sup>-2</sup> K<sup>-1</sup>),  $N_A$  is the Avogadro constant (6.02 × 10<sup>23</sup> mol<sup>-1</sup>),  $D_{\text{H}_3\text{O}^+}$  is the diffusion coefficient of the hydronium ion (9.3 × 10<sup>-9</sup> m<sup>2</sup> s<sup>-1</sup>), and  $D_{\text{OH}^-}$  is the diffusion coefficient of a hydroxy ion (5.3 × 10<sup>-9</sup> m<sup>2</sup> s<sup>-1</sup>).

The charge efficiency, following Ref. [88], was calculated by Equation (12):

$$\text{Charge efficiency} = \left( \frac{F \cdot \text{SUC}_{\text{cell}}}{3600 \cdot Q_{\text{cell}} \cdot M_{\text{NaCl}}} \right) \cdot 100\% \quad (12)$$

in which  $F$  is the Faraday constant ( $96485.3 \text{ C mol}^{-1}$ ),  $Q_{\text{cell}}$  is the specific capacity of the cell (normalized to  $m_t$ ), and 3600 converts  $Q_{\text{cell}}$  from Ah to Coulomb. In the manuscript, the specific capacity values are mostly reported as being normalized by the mass of the working electrode to express more the performance of the ACC electrode in NaI solution than that of the full cell.

The energy consumption per gram of electrode materials [ $\text{Wh g}^{-1}$ ] was quantified with Equation (13):

$$E_{\text{cell}} = \frac{1}{3.6 \cdot m_t} \int_{t_1}^{t_2} U dt \quad (13)$$

in which  $I$  [mA] is the applied current,  $t_2 - t_1$  is the operating time either for charge or discharge, and  $U$  is the measured cell voltage during galvanostatic operation. A factor of 3.6 is introduced to convert the unit from  $\text{mJ g}^{-1}$  to  $\text{Wh g}^{-1}$ .

The energy required per removed NaCl ion ( $E_{\text{KT}}$  in kT) is calculated by using Equation (14):

$$E_{\text{KT}} = \frac{3600}{R \cdot T} \cdot \frac{E_{\text{cell}} \cdot M_{\text{NaCl}}}{\text{SUC}_{\text{cell}}} \quad (14)$$

in which the factor of 3600 converts the unit from Watt-hour of  $E_{\text{cell}}$  [ $\text{Wh g}^{-1}$ ] into Joule, and  $R$  is the gas constant ( $8.314 \text{ J mol}^{-1} \text{ K}^{-1}$ ).

Average salt uptake rate (ASUR [ $\text{mg g}^{-1} \text{ min}^{-1}$ ]) was calculated by using Equation (15):

$$\text{ASUR} = \frac{\text{SUC}}{\Delta t_d} \quad (15)$$

in which  $\Delta t_d$  [min] is the time required for the desalination period during cell discharge. For the ASUR calculations, one could consider the total cycle time; however, the resulting value will be the average of the rates for salt uptake and salt release. We prefer to report ASUR to represent the salt removal performance for desalination rather than the salt release. As we provide ASUR, the Coulombic efficiency, and the charge efficiency values, values for the average salt uptake and release rate can be easily obtained. We also did not consider the resting time for the calculation of ASUR, as it is highly related to analytical techniques and cell engineering, which we discuss in more detail in the manuscript by introducing new parameters such as concentration stabilization time and peak concentration difference.

To determine the iodine concentration, water samples were collected at the outlet of the desalination cell while feedwater was flowing through the cell at various flow rates. The water samples were characterized by inductively coupled plasma optical emission spectrometry (ICP-OES; Jobin Yvon Horiba Ultima 2). To calculate the iodine concentration, the integral intensities at  $\lambda = 182.976 \text{ nm}$  were used; calibration aqueous solutions with 0, 10, and 50 ppm iodine were prepared by adding potassium iodide (Roth).

## Acknowledgements

P.S. acknowledges the German Academic Exchange Service DAAD for financial support (award number 91579066) within the frame of the GSSP-Program and DocMASE. R.L.Z. acknowledges his fellowship supported by the São Paulo Research Foundation (FAPESP, processes 2015/26593-3 and 2016/24684-4). The authors thank Eduard Arzt (INM) for his kind and continuing support. The authors thank Andrea Jung and Anna Schreiber (both at INM) for technical support. This work was part of the EEIGM work of Sidonie Carpier. The work of J.C. was part of the joint program between Saarland University, the INM, and KOREATECH, and we thank Haiwoong Park for his kind support of the program.

## Conflict of interest

The authors declare no conflict of interest.

**Keywords:** deionization · desalination · electrochemistry · energy recovery · redox chemistry

- [1] B. L. Pangarkar, M. G. Sane, M. Guddad, *ISRN Mater. Sci.* **2011**, *2011*, 1–9.
- [2] L. F. Greenlee, D. F. Lawler, B. D. Freeman, B. Marrot, P. Moulin, *Water Res.* **2009**, *43*, 2317–2348.
- [3] A. M. Blanco-Marigorta, A. Lozano-Medina, J. D. Marcos, *Energy* **2017**, *137*, 752–760.
- [4] M. E. Suss, S. Porada, X. Sun, P. M. Biesheuvel, J. Yoon, V. Presser, *Energy Environ. Sci.* **2015**, *8*, 2296–2319.
- [5] S. Porada, R. Zhao, A. van Der Wal, V. Presser, P. Biesheuvel, *Prog. Mater. Sci.* **2013**, *58*, 1388–1442.
- [6] M. Pasta, C. D. Wessells, Y. Cui, F. La Mantia, *Nano Lett.* **2012**, *12*, 839–843.
- [7] J. Lee, S. Kim, J. Yoon, *ACS Omega* **2017**, *2*, 1653–1659.
- [8] M. E. Suss, V. Presser, *Joule* **2018**, *2*, 10–15.
- [9] K. C. Smith, R. Dmello, *J. Electrochem. Soc.* **2016**, *163*, A530–A539.
- [10] S. Porada, D. Weingarth, H. V. M. Hamelers, M. Bryjak, V. Presser, P. M. Biesheuvel, *J. Mater. Chem. A* **2014**, *2*, 9313–9321.
- [11] S.-i. Jeon, H.-r. Park, J.-g. Yeo, S. Yang, C. H. Cho, M. H. Han, D. K. Kim, *Energy Environ. Sci.* **2013**, *6*, 1471–1475.
- [12] Y. Liu, C. Y. Nie, X. J. Liu, X. T. Xu, Z. Sun, L. K. Pan, *RSC Adv.* **2015**, *5*, 15205–15225.
- [13] C. Kim, J. Lee, P. Srimuk, M. Aslan, V. Presser, *ChemSusChem* **2017**, *10*, 4914–4920.
- [14] F. Béguin, V. Presser, A. Balducci, E. Frackowiak, *Adv. Mater.* **2014**, *26*, 2219–2251.
- [15] P. Wu, J. Huang, V. Meunier, B. G. Sumpter, R. Qiao, *J. Phys. Chem. Lett.* **2012**, *3*, 1732–1737.
- [16] R. Burt, G. Birkett, X. S. Zhao, *Phys. Chem. Chem. Phys.* **2014**, *16*, 6519–6538.
- [17] W. Y. Tsai, P. L. Taberna, P. Simon, *J. Am. Chem. Soc.* **2014**, *136*, 8722–8728.
- [18] C. Prehal, C. Koczwara, N. Jäckel, A. Schreiber, M. Burian, H. Amenitsch, M. A. Hartmann, V. Presser, O. Paris, *Nat. Energy* **2017**, *2*, 16215.
- [19] C. Prehal, D. Weingarth, E. Perre, R. T. Lechner, H. Amenitsch, O. Paris, V. Presser, *Energy Environ. Sci.* **2015**, *8*, 1725–1735.
- [20] P. M. Biesheuvel, S. Porada, M. Levi, M. Z. Bazant, *J. Solid State Electrochem.* **2014**, *18*, 1365–1376.
- [21] R. Zhao, P. M. Biesheuvel, A. van der Wal, *Energy Environ. Sci.* **2012**, *5*, 9520–9527.
- [22] C. Zhang, D. He, J. Ma, W. Tang, T. D. Waite, *Water Res.* **2018**, *128*, 314–330.
- [23] S. Kim, H. Yoon, D. Shin, J. Lee, J. Yoon, *J. Colloid Interface Sci.* **2017**, *506*, 644–648.
- [24] S. Kim, J. Lee, C. Kim, J. Yoon, *Electrochim. Acta* **2016**, *203*, 265–271.

- [25] J. Lee, S. Kim, C. Kim, J. Yoon, *Energy Environ. Sci.* **2014**, *7*, 3683–3689.
- [26] H. Yoon, J. Lee, S. Kim, J. Yoon, *Desalination* **2017**, *422*, 42–48.
- [27] J. Lee, P. Srimuk, K. Aristizabal, C. Kim, S. Choudhury, Y. C. Nah, F. Mücklich, V. Presser, *ChemSusChem* **2017**, *10*, 3611–3623.
- [28] P. Srimuk, J. Halim, J. Lee, Q. Z. Tao, J. Rosen, V. Presser, *ACS Sustainable Chem. Eng.* **2018**, *6*, 3739–3747.
- [29] P. Srimuk, J. Lee, S. Fleischmann, S. Choudhury, N. Jäckel, M. Zeiger, C. Kim, M. Aslan, V. Presser, *J. Mater. Chem. A* **2017**, *5*, 15640–15649.
- [30] P. Srimuk, F. Kaasik, B. Krüner, A. Tolosa, S. Fleischmann, N. Jäckel, M. C. Tekeli, M. Aslan, M. E. Suss, V. Presser, *J. Mater. Chem. A* **2016**, *4*, 18265–18271.
- [31] W. Z. Bao, X. Tang, X. Guo, S. Choi, C. Y. Wang, Y. Gogotsi, G. X. Wang, *Joule* **2018**, *2*, 778–787.
- [32] F. Xing, T. Li, J. Y. Li, H. R. Zhu, N. Wang, X. Cao, *Nano Energy* **2017**, *31*, 590–595.
- [33] S. Porada, A. Shrivastava, P. Bukowska, P. M. Biesheuvel, K. C. Smith, *Electrochim. Acta* **2017**, *255*, 369–378.
- [34] P. Srimuk, J. Lee, A. Tolosa, C. Kim, M. Aslan, V. Presser, *Chem. Mater.* **2017**, *29*, 9964–9973.
- [35] X. Su, T. A. Hatton, *Phys. Chem. Chem. Phys.* **2017**, *19*, 23570–23584.
- [36] X. Su, T. A. Hatton, *Adv. Colloid Interface Sci.* **2017**, *244*, 6–20.
- [37] X. Su, H. J. Kulik, T. F. Jamison, T. A. Hatton, *Adv. Funct. Mater.* **2016**, *26*, 3394–3404.
- [38] X. Su, K. J. Tan, J. Elbert, C. Ruttiger, M. Gallei, T. F. Jamison, T. A. Hatton, *Energy Environ. Sci.* **2017**, *10*, 1272–1283.
- [39] M. Elimelech, W. A. Phillip, *Science* **2011**, *333*, 712–717.
- [40] M. Kurihara, H. Yamamura, T. Nakanishi, S. Jinno, *Desalination* **2001**, *138*, 191–199.
- [41] M. Salanne, B. Rotenberg, K. Naoi, K. Kaneko, P. L. Taberna, C. P. Grey, B. Dunn, P. Simon, *Nat. Energy* **2016**, *1*, 16070.
- [42] R. Narayanan, P. R. Bandaru, *J. Electrochem. Soc.* **2014**, *162*, A86–A91.
- [43] J. Lee, S. Choudhury, D. Weingarh, D. Kim, V. Presser, *ACS Appl. Mater. Interfaces* **2016**, *8*, 23676–23687.
- [44] P. R. Bandaru, H. Yamada, R. Narayanan, M. Hofer, *Mater. Sci. Eng. R* **2015**, *96*, 1–69.
- [45] J. Lee, B. Krüner, A. Tolosa, S. Sathyamoorthi, D. Kim, S. Choudhury, K. H. Seo, V. Presser, *Energy Environ. Sci.* **2016**, *9*, 3392–3398.
- [46] B. Akinwolemiwa, C. Peng, G. Z. Chen, *J. Electrochem. Soc.* **2015**, *162*, A5054–A5059.
- [47] S. T. Senthilkumar, R. K. Selvan, J. S. Melo, *J. Mater. Chem. A* **2013**, *1*, 12386–12394.
- [48] S. E. Chun, B. Evanko, X. Wang, D. Vonlanthen, X. Ji, G. D. Stucky, S. W. Boettcher, *Nat. Commun.* **2015**, *6*, 7818.
- [49] E. Frackowiak, M. Meller, J. Menzel, D. Gastol, K. Fic, *Faraday Discuss.* **2014**, *172*, 179–198.
- [50] B. Akinwolemiwa, G. Chen, *Curr. Top. Electrochem.* **2017**, *19*, 47–65.
- [51] A. T. Hubbard, *J. Electroanal. Chem. Interfacial Electrochem.* **1969**, *22*, 165–174.
- [52] A. T. Hubbard, F. C. Anson, *Anal. Chem.* **1966**, *38*, 58–61.
- [53] I. Streeter, G. G. Wildgoose, L. D. Shao, R. G. Compton, *Sens. Actuators B* **2008**, *133*, 462–466.
- [54] A. Z. Weber, M. M. Mench, J. P. Meyers, P. N. Ross, J. T. Gostick, Q. H. Liu, *J. Appl. Electrochem.* **2011**, *41*, 1137–1164.
- [55] D. Desai, E. S. Beh, S. Sahu, V. Vedharathinam, Q. van Overmeere, C. F. de Lannoy, A. P. Jose, A. R. Völkel, J. B. Rivest, *ACS Energy Lett.* **2018**, *3*, 375–379.
- [56] X. Hou, Q. Liang, X. Hu, Y. Zhou, Q. Ru, F. Chen, S. Hu, *Nanoscale* **2018**, *10*, 12308–12314.
- [57] J. Lee, A. Tolosa, B. Krüner, N. Jäckel, S. Fleischmann, M. Zeiger, D. Kim, V. Presser, *Sustainable Energy Fuels* **2017**, *1*, 299–307.
- [58] B. Krüner, J. Lee, N. Jäckel, A. Tolosa, V. Presser, *ACS Appl. Mater. Interfaces* **2016**, *8*, 9104–9115.
- [59] E. Mourad, L. Coustan, P. Lannelongue, D. Zigah, A. Mehdi, A. Vioux, S. A. Freunberger, F. Favier, O. Fontaine, *Nat. Mater.* **2017**, *16*, 446–453.
- [60] B. Evanko, S. W. Boettcher, S. J. Yoo, G. D. Stucky, *ACS Energy Lett.* **2017**, *2*, 2581–2590.
- [61] J. Lee, D. Weingarh, I. Grobelsek, V. Presser, *Energy Technol.* **2016**, *4*, 75–84.
- [62] M. He, K. Fic, E. Frackowiak, P. Novák, E. J. Berg, *Energy Storage Mater.* **2016**, *5*, 111–115.
- [63] M. L. He, K. Fic, E. Frackowiak, P. Novak, E. J. Berg, *Energy Environ. Sci.* **2016**, *9*, 623–633.
- [64] K. Fic, M. Metier, E. Frackowiak, *J. Electrochem. Soc.* **2015**, *162*, A5140–A5147.
- [65] P. Ratajczak, M. E. Suss, F. Kaasik, F. Béguin, *Energy Storage Mater.* **2019**, *16*, 126–145.
- [66] S. Porada, L. Borchardt, M. Oschatz, M. Bryjak, J. S. Atchison, K. J. Keesman, S. Kaskel, P. M. Biesheuvel, V. Presser, *Energy Environ. Sci.* **2013**, *6*, 3700–3712.
- [67] J. Lee, P. Srimuk, S. Fleischmann, A. Ridder, M. Zeiger, V. Presser, *J. Mater. Chem. A* **2017**, *5*, 12520–12527.
- [68] G. Lota, E. Frackowiak, *Electrochem. Commun.* **2009**, *11*, 87–90.
- [69] E. Frackowiak, K. Fic, M. Meller, G. Lota, *ChemSusChem* **2012**, *5*, 1181–1185.
- [70] C. Kim, P. Srimuk, J. Lee, S. Fleischmann, M. Aslan, V. Presser, *Carbon* **2017**, *122*, 329–335.
- [71] J. Lee, S. Badie, P. Srimuk, A. Ridder, H. Shim, S. Choudhury, Y. C. Nah, V. Presser, *Sustainable Energy Fuels* **2018**, *2*, 577–588.
- [72] K. Y. Lian, C. M. Yang, *J. Power Sources* **2013**, *231*, 239–245.
- [73] C. Kim, P. Srimuk, J. Lee, M. Aslan, V. Presser, *Desalination* **2018**, *425*, 104–110.
- [74] R. Zhao, S. Porada, P. M. Biesheuvel, A. van der Wal, *Desalination* **2013**, *330*, 35–41.
- [75] P. Dlugolecki, A. van der Wal, *Environ. Sci. Technol.* **2013**, *47*, 4904–4910.
- [76] E. Frackowiak, Q. Abbas, F. Béguin, *J. Energy Chem.* **2013**, *22*, 226–240.
- [77] H. A. Gorrell, *AAPG Bull.* **1958**, *42*, 2513.
- [78] M. S. Mohsen, S. Gammoh, *Desalin. Water Treat.* **2010**, *14*, 265–272.
- [79] D. D. Voutchkova, S. M. Kristiansen, B. Hansen, V. Ernstsens, B. L. Sorensen, K. H. Esbensen, *Environ. Geochem. Health* **2014**, *36*, 1151–1164.
- [80] *Guidelines for Drinking-Water Quality, Vol. 2, Health Criteria and Other Supporting Information*, World Health Organization, New York, USA, **1996**.
- [81] F. Delange, *Thyroid* **1994**, *4*, 107–128.
- [82] P. Unak, Ş. Darcan, F. Yurt, Z. Biber, M. Çoker, *Biol. Trace Elem. Res.* **1999**, *71*, 463–470.
- [83] M. Aslan, M. Zeiger, N. Jackel, I. Grobelsek, D. Weingarh, V. Presser, *J. Phys. Condens. Matter* **2016**, *28*, 114003.
- [84] D. Weingarh, M. Zeiger, N. Jackel, M. Aslan, G. Feng, V. Presser, *Adv. Energy Mater.* **2014**, *4*, 1400316.
- [85] D. Weingarh, H. Noh, A. Foelske-Schmitz, A. Wokaun, R. Kötz, *Electrochim. Acta* **2013**, *103*, 119–124.
- [86] P. M. Biesheuvel, A. van der Wal, *J. Membr. Sci.* **2010**, *346*, 256–262.
- [87] S. Porada, L. Weinstein, R. Dash, A. van der Wal, M. Bryjak, Y. Gogotsi, P. M. Biesheuvel, *ACS Appl. Mater. Interfaces* **2012**, *4*, 1194–1199.
- [88] R. Zhao, P. M. Biesheuvel, H. Miedema, H. Bruning, A. van der Wal, *J. Phys. Chem. Lett.* **2010**, *1*, 205–210.
- [89] S. Li, C. Cheng, A. Thomas, *Adv. Mater.* **2017**, *29*, 1602547.
- [90] S. Li, D. Wu, H. Liang, J. Wang, X. Zhuang, Y. Mai, Y. Su, X. Feng, *ChemSusChem* **2014**, *7*, 3002–3006.
- [91] S. Li, C. Cheng, H.-W. Liang, X. Feng, A. Thomas, *Adv. Mater.* **2017**, *29*, 1700707.
- [92] D. Linden, T. Reddy, *Linden's Handbook of Batteries, 3rd ed.* McGraw-Hill, New York, **2002**.

Manuscript received: July 8, 2018

Accepted manuscript online: July 31, 2018

Version of record online: August 22, 2018

## Supporting Information

### **Confined Redox Reactions of Iodide in Carbon Nanopores for Fast and Energy-Efficient Desalination of Brackish Water and Seawater**

Juhan Lee,<sup>[a, b]</sup> Pattarachai Srimuk,<sup>[a, b]</sup> Sidonie Carpier,<sup>[a, b]</sup> Jaehoon Choi,<sup>[a, c]</sup>  
Rafael Linzmeyer Zornitta,<sup>[a, d]</sup> Choonsoo Kim,<sup>[a]</sup> Mesut Aslan,<sup>[a]</sup> and Volker Presser<sup>\*[a, b]</sup>

cssc\_201801538\_sm\_miscellaneous\_information.pdf

## Section 1: Material characterization

The shape of the measured nitrogen sorption isotherms (**Fig. S1A**) recorded at  $-196\text{ }^{\circ}\text{C}$  of AC can be classified as Type I(b). The isotherms for ACC is Type I(a) implying that the material contains narrower pores ( $<1\text{ nm}$ ) than AC. The pore size distribution (PSD) patterns of AC and ACC were calculated with quenched-solid density functional theory (QSDFT) assuming slit pores. As can be seen from **Fig. S1B**, all samples are predominately microporous; the pore structure parameters (surface area, pore volume, and average pore size) are summarized in **Table S1**.

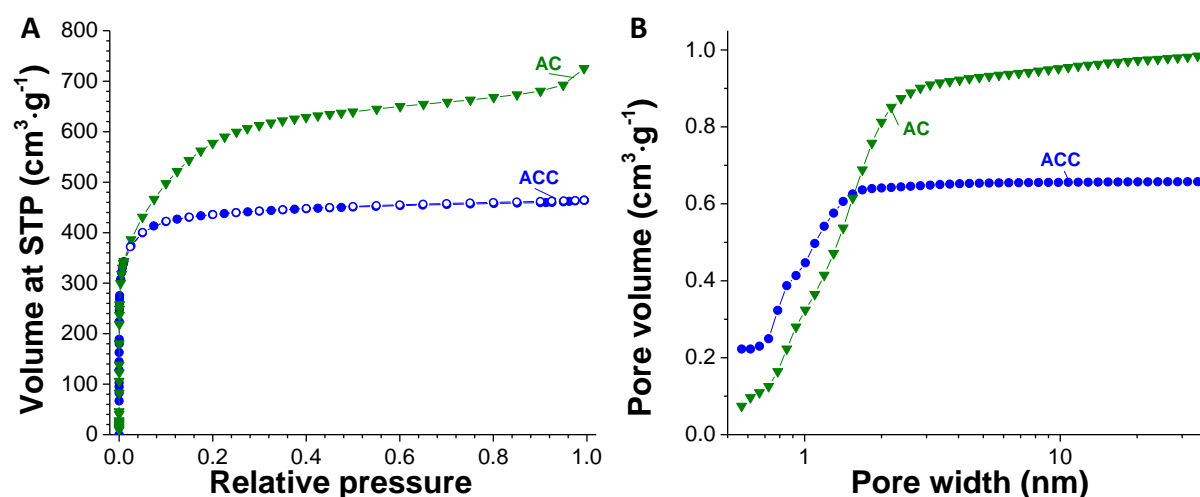


**Fig. S1:** Nitrogen gas sorption analysis of the carbon electrodes applied for this work. a) Nitrogen gas sorption isotherms at  $-196\text{ }^{\circ}\text{C}$ . b) Cumulative pore size distribution per volume.

**Table S1:** Specific surface area and total pore volume of various carbon electrodes as calculated either by density functional theory or BET equation as well average pore size from nitrogen sorption analysis.

Sample	SSA DFT ( $\text{m}^2 \cdot \text{g}^{-1}$ )	SSA BET ( $\text{m}^2 \cdot \text{g}^{-1}$ )	Total pore volume ( $\text{cm}^3 \cdot \text{g}^{-1}$ )	Average pore size (nm)
ACC	1638	1694	0.66	0.8
AC	1648	2094	1.05	1.4

The morphology of the carbon electrodes was examined by a JEOL JSM 7500F field emission scanning microscope operated at 3 kV (**Fig. S2**). The chemical composition of the carbon electrodes was determined by energy dispersive X-ray spectroscopy (EDX) with an X-Max-150 detector (Oxford Instruments) attached to the SEM chamber (**Table S2**). The spectra were measured using an accelerating voltage of 10 kV and the data of ten spots were averaged; for the calibration, silicon crystal was applied. ACC electrode shows a highly-intertwined network of porous carbon fibers with an average diameter of about 5  $\mu\text{m}$  and a length of up to several centimeters (**Fig. S2A**). The fibers themselves have a high internal porosity, as seen on the fiber surfaces and fracture cross-sections (**Fig. S2A**). AC electrode consists of particles in the size of several microns, which are connected by fibers of the polytetrafluoroethylene binder (**Fig. S2B**). These particles show large pores of up to 1  $\mu\text{m}$  on the surface, which lead to a hierarchical, interparticle pore network.

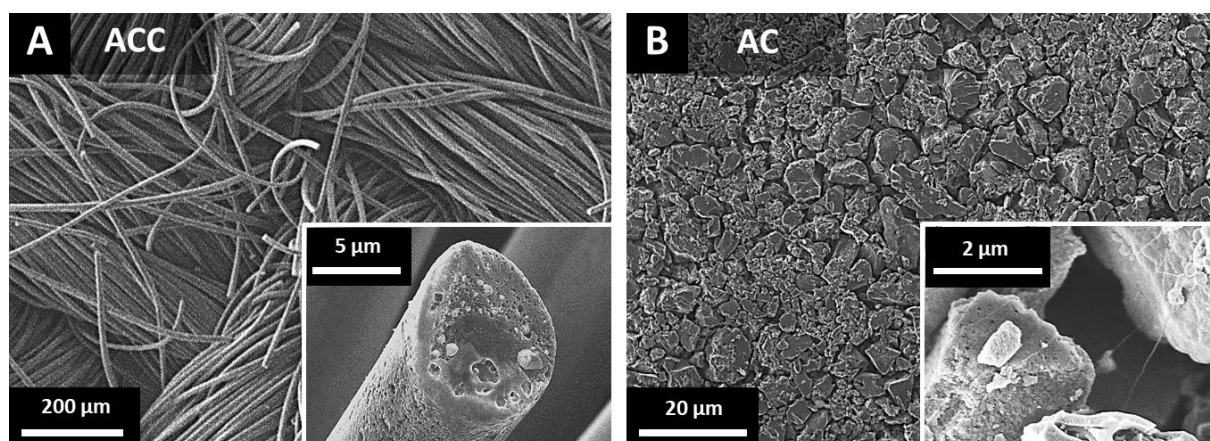


**Fig. S2:** Scanning electron micrographs of activated carbon cloth (ACC) and activated carbon (AC).

**Table S2:** Chemical composition of the carbon electrodes determined by EDX.

Sample	C (mass%)	O (mass%)	Al + F + Na + K + Si (mass%)
ACC	>95	2-4	<1
AC	>95	4-5	<1

Raman spectroscopy was carried out with a Renishaw inVia Raman microscope applying an Nd:YAG laser (532 nm) with a power of ca. 0.25 mW. With a grating of 2400 lines·mm<sup>-1</sup>, yielding a spectral resolution of approximately 1.2 cm<sup>-1</sup>. The spot size on the sample was about 2 μm with a numeric aperture of 0.75. Spectra were recorded for various carbon electrodes with an acquisition time of 30 s and 10 accumulations. D- and G-band deconvolution was carried out with baseline-subtracted, D-band normalized Raman spectra, employing four Voigt peaks. The quantitative results are found in **Table S3**, Raman spectra are given in **Fig. S3**.

I<sub>D</sub>/I<sub>G</sub> ratios of 2.79 and 2.61 were obtained and FWHM for D-band of 129 and 96 for ACC and AC, respectively. Both a higher I<sub>D</sub>/I<sub>G</sub> ratio, as well as a higher FWHM of the D-signal are generally associated with an increase in structural carbon disorder that is linked to defects in the hexagonal graphite structure. These defects originate mainly from micropores that disrupt the graphitic carbon lattice.

**Table S3:** Results of the peak deconvolution from the Raman spectra regarding the D- and G-mode of carbon. The peak positions and values for the full width at half maximum (FWHM) are given, as well as the areal intensity ratio I<sub>D</sub>/I<sub>G</sub>.

Sample	D-mode		G-mode		I <sub>D</sub> /I <sub>G</sub> ratio
	Position (cm <sup>-1</sup> )	FWHM (cm <sup>-1</sup> )	Position (cm <sup>-1</sup> )	FWHM (cm <sup>-1</sup> )	
ACC	1338	126	1604	53	2.79
AC	1337	96	1602	55	2.61

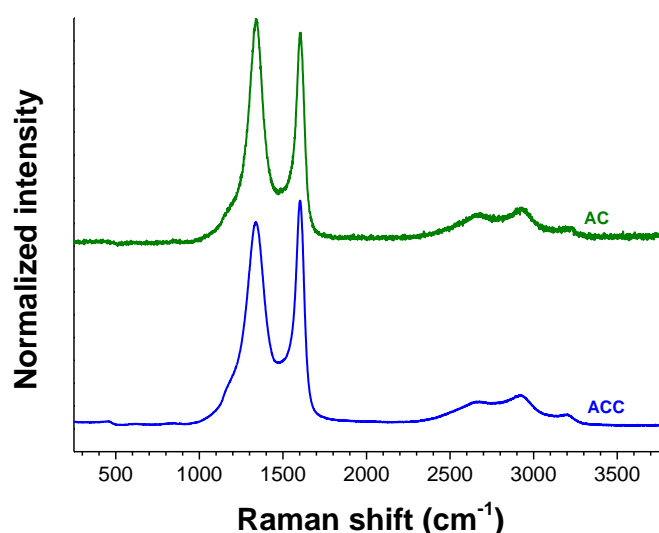


**Fig. S3:** Raman spectra of activated carbon cloth (ACC; type ACC-507-20 from Kynol) and activated carbon (AC; type YP-80F from Kuraray).

## Section 2: Redox kinetics of potassium ferricyanide and iodide in nanoporous carbon

To investigate the kinetic of redox electrolyte in nanoporous carbon electrodes, we first benchmarked a well-established standard redox couple with one electron transfer, namely 1 M of potassium ferricyanide, PFC. The inset in **Fig. S4A** shows cyclic voltammograms of a flat surface electrode (5 mm diameter glassy carbon, GC, ALS GmbH) and nanoporous activated carbon (AC-1.4) coated on GC at a scan rate of  $100 \text{ mV}\cdot\text{s}^{-1}$ . The detailed preparation of the carbon coated GC can be found in Ref. <sup>1</sup>. The CVs of GC and AC-1.4 electrodes exhibit half-wave potential of +0.26 V and +0.21 V vs. Ag/AgCl, respectively, with different oxidation and reduction current response. The reduction currents of GC and AC-1.4 electrodes versus scan rate follow a power law ( $y=ax^e+b$ ) with an exponent of 0.3 for GC and 1.0 for AC-1.4 (**Fig. S4A**). Therefore, the redox kinetics in AC-1.4 electrode seems to follow the recently suggested thin layer diffusion electrochemistry (exponent close to 1) than the planar diffusion electrochemistry (exponent close to 0.5).<sup>2-4</sup>

So far, the thin layer diffusion electrochemistry has been studied mostly with the carbon nanotubes with various arrangement for different type of pore space between the tubes. After the pioneering modeling and simulation work for the thin layer electrochemistry,<sup>3,5</sup> enhanced redox kinetics in porous carbon electrode were reported in case of macroporous and mesoporous carbons via diffusion-less redox reactions and fast ion diffusion in the confined carbon pores, respectively.<sup>2,6</sup> Our results of microporous activated carbon electrode (AC-1.4) strongly support the electrochemical thin layer process from previous reported meso- and macroporous carbon studies. Since the contribution of electric double-layer (EDL) formation is reported to be significant for high surface carbon electrode in case ferricyanide/ferrocyanide redox couple,<sup>7</sup> the conventional electrochemical analyses could be misleading when the influence of ELD is not considered. Therefore, the influence of the electric double-layer must be excluded for the analysis. The implementation of rotating disk electrode (RDE, RRDE-3A, ALS GmbH) allows us to investigate the redox kinetic in nanoporous carbon since the contribution of electric double-layer can be kept at a constant scan rate while kinetic condition is varied via rotational speed of the electrode.

The bulk hydrodynamic diffusion generated via the spinning of the electrode leads to a thin and constant diffusion layer. Hence, the rate is limited mostly to the diffusion of redox species near the charges transfer zone. **Fig. S4B-C** shows cyclic voltammograms at  $100 \text{ mV}\cdot\text{s}^{-1}$  with different rotational speed. By increasing the rotational speed of electrode from 200 rpm to 3200 rpm, the  $\text{Fe}(\text{CN}_6)^{4-}$  ions in bulk regime are transported faster into the diffusion layer. Therefore, the reduction current is increasing as a function of increasing rotational speed. This phenomenon is explained by Koutecky-Levich equation,<sup>1, 8</sup>

$$\frac{1}{j} = \frac{1}{j_k} + \frac{1}{j_L} = \frac{1}{B} \omega^{-0.5} + \frac{1}{nFkC} \quad \text{Eq. (S1)}$$

where,  $j$  is the measured current,  $j_k$  the intrinsic kinetic limit current,  $j_L$  is the mass transfer limit current,  $F$  is Faraday constant,  $C$  is bulk concentration, and  $n$  is number of electron involved in the reaction which is the proportional to the square root of angular velocity ( $\omega$ ) of RDE electrode. The proportionality is defined as  $B$ ,

$$B = 0.62D^{2/3}\nu^{-1/3}nFC \quad \text{Eq. (S2)}$$

where,  $\nu$  is the kinematic viscosity of the electrolyte and  $D$  is diffusion coefficient of reactant.

We assume  $j_k$  to be constant at certain potential with rate constant ( $k$ ).

As shown in **Fig. S4D**, the linear relation between response current and angular speed is obtained. The slope of the graph ( $B^{-1}$ ) corresponds to the diffusion coefficient. The diffusion coefficient was calculated by using  $\nu = 0.00921 \text{ cm}^2\cdot\text{s}^{-1}$ ,  $n=1$ ,  $F=96485 \text{ mol}^{-1}$ , and  $C=0.001 \text{ mol}\cdot\text{cm}^{-3}$ . In case of nanoconfined redox ions (AC-1.4), the diffusion coefficient of  $2.1\cdot 10^{-7} \text{ cm}^2\cdot\text{s}^{-1}$  was obtained while the diffusion coefficient for GC flat electrode was calculated to be  $1.6\cdot 10^{-7} \text{ cm}^2\cdot\text{s}^{-1}$ . The higher diffusion coefficient of the nanoporous carbon than that of GC flat electrode confirms the redox kinetic is enhanced in nanoporous carbon as enabled by the fast diffusion of redox ions in the confinement of carbon nanopores.

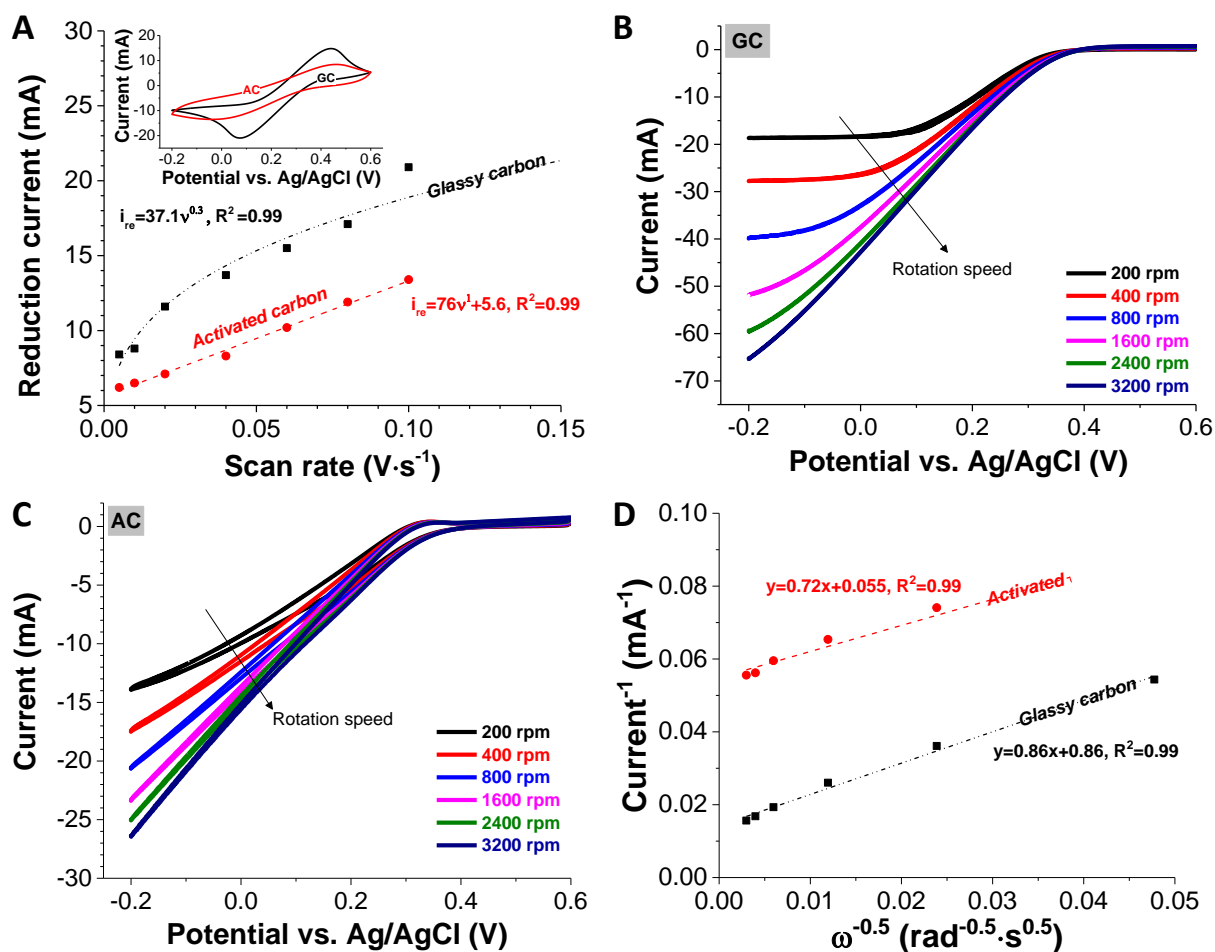


**Fig. S4:** Kinetic study of redox couple (1 M potassium ferricyanide) with cyclic voltammetry under static and dynamic condition. Dynamic condition was given by rotation disk electrode. A) the reduction current versus scan rate corresponding result from cyclic voltammogram (inset) in 1 M potassium ferricyanide, B-C) cyclic voltammogram of GC and AC electrode with different rotational speed and D) Koutecky-Levich relation plot.

The same strategy can be applied to study kinetic of potassium iodide (KI). Iodide is the complex redox reaction which undergo oxidation by donating two electrons to form iodine/and triiodide at standard potential of 0.54 V vs SHE, afterward the resulting iodine can be reacted with water to form iodate at a potential of 1.2 V vs SHE. The latter is an irreversible reaction consuming the iodide ions leading to poor charge efficiency particularly. Therefore, we avoid the second reaction by limiting potential lower than 0.6 V vs. SHE (0.4 V vs. Ag/AgCl):



**Fig. S5A** shows the cyclic voltammograms of AC-1.4 and GC electrode in 0.1 M KI and 0.5 M  $K_2SO_4$ . In the case of GC, the onset oxidation potential of iodide ( $I^-$ ) ion was observed to be at +0.12 V vs. Ag/AgCl. The oxidation current is sharply increase up to 0.15 mA at +0.3 V vs. Ag/AgCl; afterwards, the electrode was backward scanned, leading to reduction of triiodide/iodine( $I_2/I_3^-$ ). The ratio of oxidation and reduction current ( $I_{re}/I_{ox}$ ) is 0.57 suggesting irreversible process possibly due to redox shuttling and precipitation of  $I_2$ .<sup>9, 10</sup> The latter is strongly depended on the identity of electrode such as microstructure and surface chemistry. The cyclic voltammogram of 0.1 M KI and 0.5 M  $K_2SO_4$  performs differently in AC-1.4 compared to the flat electrode (GC). The onset oxidation potential was observed to be 0.12 V vs. Ag/AgCl, which is 0.18 V lower than in GC electrode possibly via the higher local concentration which trapped inside pores and thin layer diffusion.<sup>2</sup> The  $I_{re}/I_{ox}$  of AC-1.4 is 0.98, confirming that nanoporous carbon mitigate the redox shuttling and favor to form triiodide instead of iodine resulting high degree of reversible reaction.

**Fig. S5B** illustrates the reduction current of triiodine on AC-1.4 and GC electrode plotted against the scan rate. By fitting the curve with a power law, the kinetic limit can be identified (**Fig. S5B**): AC-1.4 exhibits an exponent of 0.4 and the GC flat electrode of 0.2. Because the oxidation potential was not scanned till the peak current appears, the low exponent numbers (<0.5) do not necessarily indicate slow redox kinetics in both cases. The reduction current is rather reduced due to the larger peak separation at higher scan rate than the kinetic limitations since the non-equilibrium state of the reaction to the oxidation peak current is growing as the peak separation is getting broader in a fixed potential window for the scanning. Because the thin layer electrochemistry in carbon pores is also featured by the narrow peak separation with less distortion in shape,<sup>2-4, 11</sup> the lower exponent number for AC-1.4 than that of GC flat electrode still implies that the redox kinetics of iodide system in nanopores is faster than on the flat electrode.

Further studies with RDE in 0.1 M KI and 0.5 M  $K_2SO_4$  (**Fig. S5C**) show that the reduction current for AC-1.4 is slightly increased by increasing of rotating speed being good align with Koutecky-Levich equation (**Fig. S5D**). The curve's slope of 1.26 translates to a diffusion coefficient of  $5.3 \cdot 10^{-3} \text{ cm}^2 \cdot \text{s}^{-1}$ . As compared to a previous study, the diffusion coefficient of  $I^-$  on GC electrode estimated from static condition is between  $1.6 \cdot 10^{-5}$  and  $2.6 \cdot 10^{-7} \text{ cm}^2 \cdot \text{s}^{-1}$  depending on the concentration.<sup>10, 12</sup> These values are much lower than that of AC-1.4 electrode. In addition, the RDE result in GC electrode does not fit to the Koutecky-Levich since

we observed no change of reduction and oxidation current when the electrode rotation speed is increased. This is possible when the formation of triiodide ions is dominated by deposition/adsorption of iodine/iodide leading to continuous shuttling process of oxidized triiodide/iodine ion. Since the redox reactions are confined in the case of porous carbons in narrow pores,<sup>2</sup> this active site blocking does not play an influential role in case of AC-1.4. Considering the specific adsorption behavior of iodide,<sup>13</sup> confining iodide into the carbon micropores seems to be crucial for enhanced redox kinetics as well as high reversibility enabled by low-degree of redox shuttling.

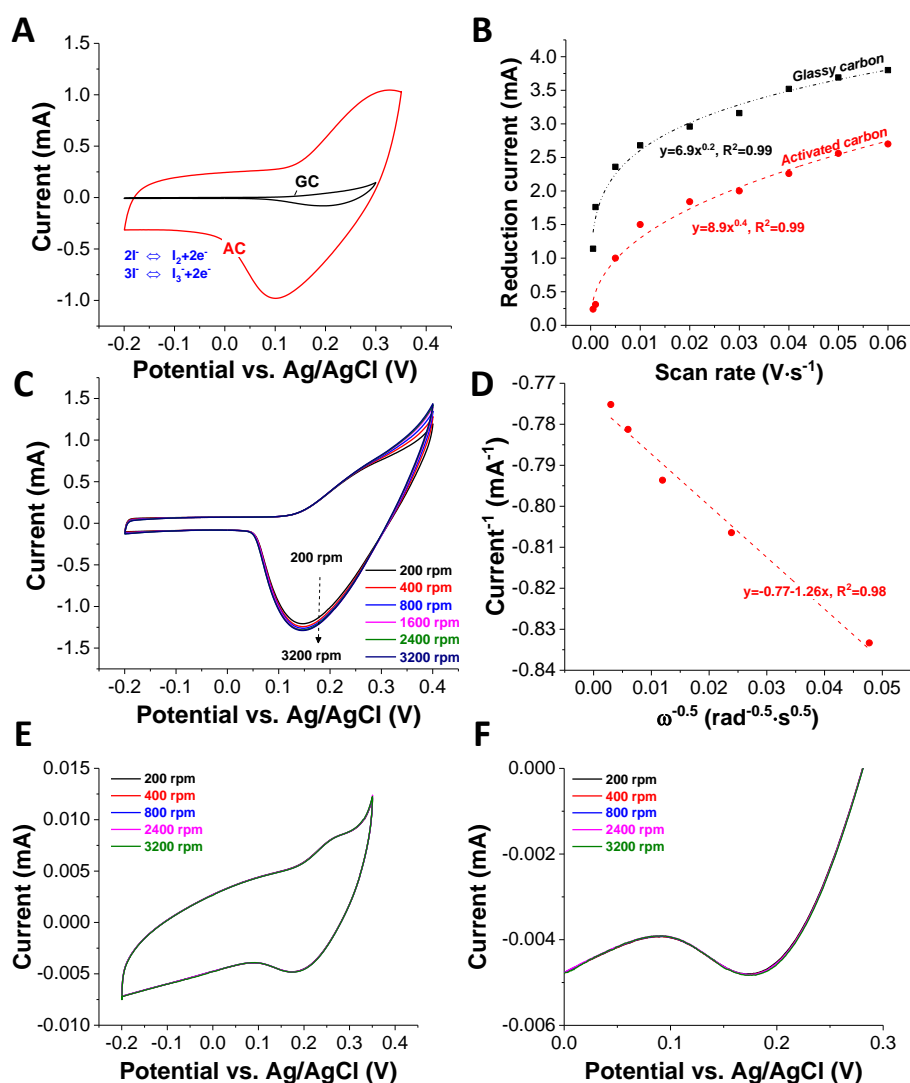


**Fig. S5:** The kinetic study of iodide on GC and AC electrode with cyclic voltammetry under static and dynamic condition. a) Cyclic voltammogram of GC and AC electrode in 0.1 M KI and 0.5 M  $K_2SO_4$ , b) plot of reduction current versus scan rate respecting result from cyclic voltammogram, c) cyclic voltammogram of AC electrode in 0.1 M KI and 0.5 M  $K_2SO_4$  with different rotational speed, d) Koutecky-Levich relation plot, e) and f) cyclic voltammogram of GC electrode in 0.1 M KI and 0.5 M  $K_2SO_4$  with different rotational speed.

### Section 3: Desalination measurements

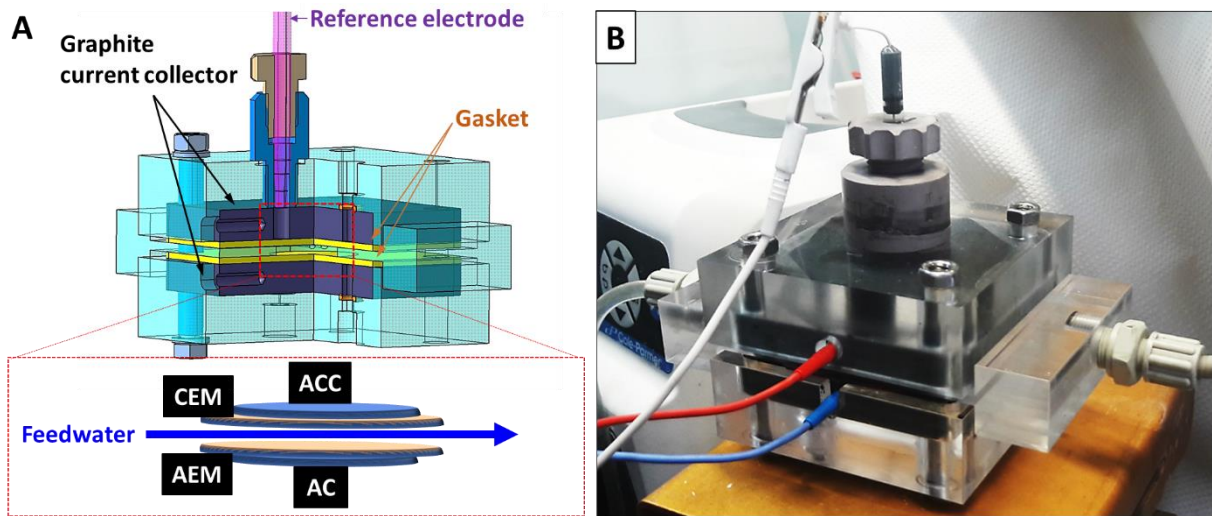
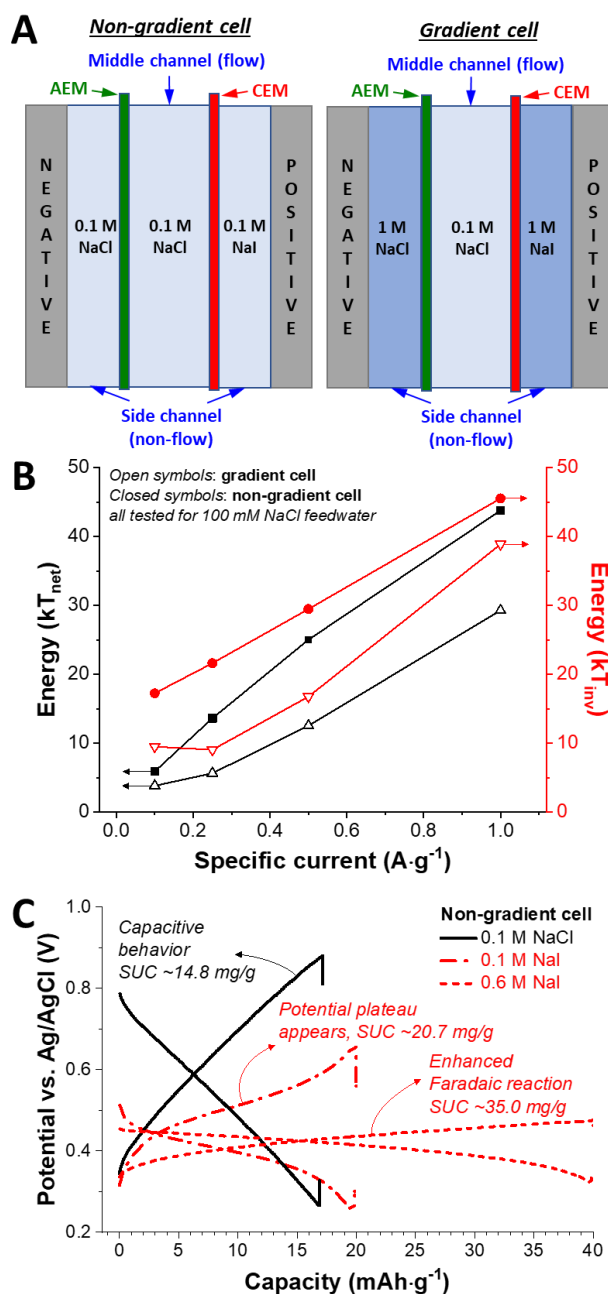
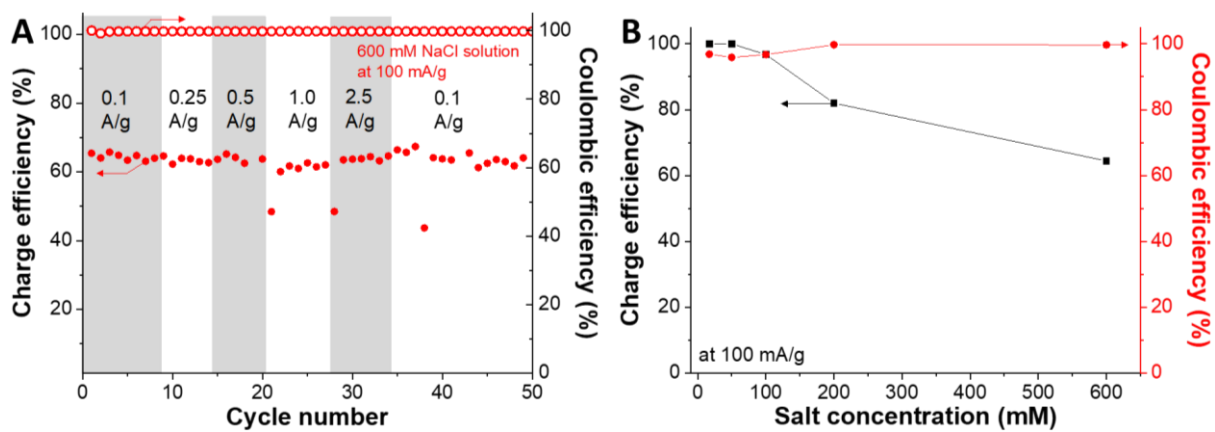


Figure S6: (A) Scheme of the cell. (B) A photo of the cell during desalination operation.



**Figure S7:** (A) Schemes of the gradient and non-gradient cells. For the gradient cell, 1 M NaI was applied to the side channel between the positive electrode and the cation exchange membrane (CEM) and 1 M NaCl to the channel between the negative electrode and the anion exchange membrane (AEM). For the non-gradient cell, the same concentration was applied to all channels. (B) Energy consumption (in kT) of the gradient and non-gradient cells.  $kT_{inv}$  represents only the invested energy during cell charging whereas  $kT_{net}$  represents the net energy consumption which is the difference between the invested and restored energy. (C) Potential profiles of the positive electrodes measured from non-gradient cells for 0.1 M NaCl, 0.1 M NaI, and 0.6 M NaI. For 0.1 M NaCl, the AEM was arranged next to the AC positive electrode, and the CEM to the AC negative electrode to represent the performance of a conventional MCDI performance.



**Figure S8:** Coulombic efficiency and charge efficiency obtained from the REHDI system at specific currents of 0.1-2.5 A/g for 600 mM feedwater (A) and for various salt concentrations in the range from 17 mM to 600 mM (B).

## References

- [1] P. Srimuk, L. Ries, M. Zeiger, S. Fleischmann, N. Jäckel, A. Tolosa, B. Krüner, M. Aslan, V. Presser *RSC Advances*. **2016**, *6*, 106081-106089.
- [2] R. Narayanan, P. R. Bandaru *Journal of the Electrochemical Society*. **2014**, *162*, A86-A91.
- [3] I. Streeter, G. G. Wildgoose, L. D. Shao, R. G. Compton *Sensors and Actuators B*. **2008**, *133*, 462-466.
- [4] K. R. Ward, L. H. J. Xiong, N. S. Lawrence, R. S. Hartshorne, R. G. Compton *Journal of Electroanalytical Chemistry*. **2013**, *702*, 15-24.
- [5] A. Z. Weber, M. M. Mench, J. P. Meyers, P. N. Ross, J. T. Gostick, Q. H. Liu *Journal of Applied Electrochemistry*. **2011**, *41*, 1137-1164.
- [6] S. M. Chathoth, E. Mamontov, A. I. Kolesnikov, Y. Gogotsi, D. J. Wesolowski *EPL (Europhysics Letters)*. **2011**, *95*, 56001.
- [7] J. Lee, S. Choudhury, D. Weingarh, D. Kim, V. Presser *ACS Applied Materials & Interfaces*. **2016**, *8*, 23676-23687.
- [8] P. Srimuk, M. Zeiger, N. Jäckel, A. Tolosa, B. Krüner, S. Fleischmann, I. Grobelsek, M. Aslan, B. Shvartsev, M. E. Suss, V. Presser *Electrochimica Acta*. **2017**, *224*, 314-328.
- [9] E. I. Rogers, D. S. Silvester, L. Aldous, C. Hardacre, R. G. Compton *The Journal of Physical Chemistry C*. **2008**, *112*, 6551-6557.
- [10] C. L. Bentley, A. M. Bond, A. F. Hollenkamp, P. J. Mahon, J. Zhang *Electrochimica Acta*. **2013**, *109*, 554-561.
- [11] M. C. Henstridge, E. J. F. Dickinson, M. Aslanoglu, C. Batchelor-McAuley, R. G. Compton *Sensors and Actuators B*. **2010**, *145*, 417-427.
- [12] C. L. Bentley, A. M. Bond, A. F. Hollenkamp, P. J. Mahon, J. Zhang *The Journal of Physical Chemistry C*. **2015**, *119*, 22392-22403.
- [13] S. E. Chun, B. Evanko, X. Wang, D. Vonlanthen, X. Ji, G. D. Stucky, S. W. Boettcher *Nature Communications*. **2015**, *6*, 7818.

## 5. Summary, conclusions, and outlook

My doctoral work has investigated and developed a new generation of electrochemical water desalination materials beyond nanoporous carbon. Selected aspects and performance ranges are graphically depicted in **Figure 26**. There are three main categories of materials that have been studied: 1) titania-enhanced carbon, 2) Faradaic materials, including ion insertion materials and conversion reaction materials, and 3) redox-electrolyte enabled carbon.

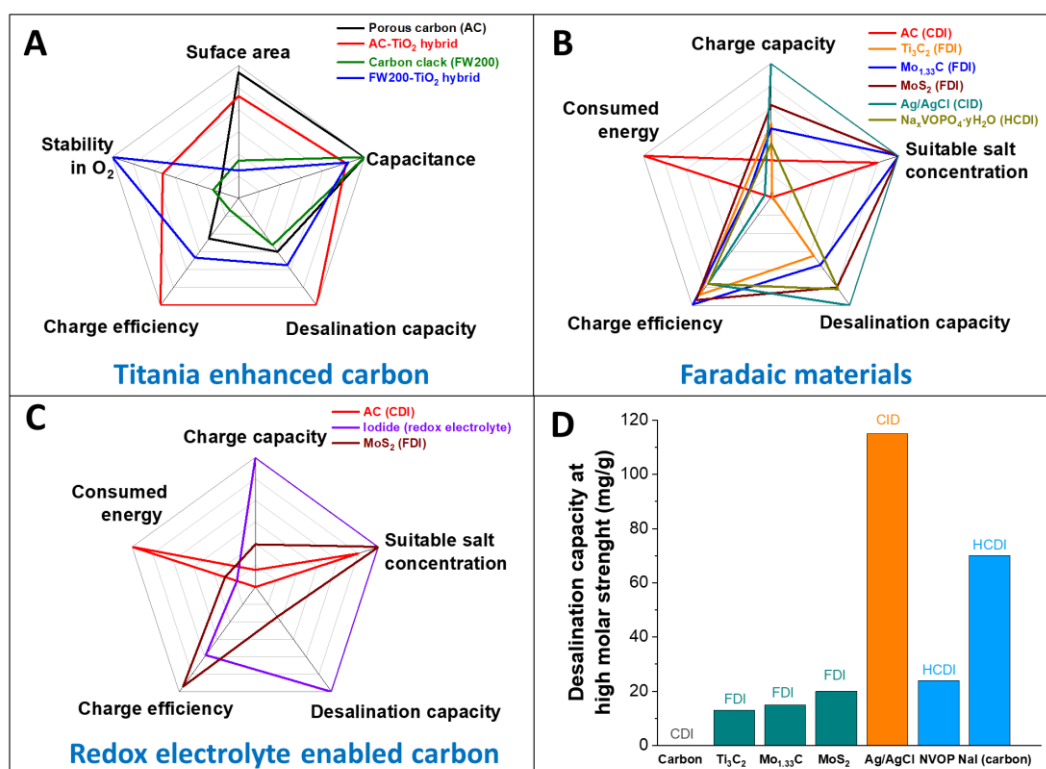


**Figure 26.** Summary water desalination performance from three main material categories A) Hybrid material compared with carbon, B) Insertion materials compared with carbon, C) Redox electrolyte compared with MoS<sub>2</sub> and carbon, and D) desalination capacity through this Ph.D. work. Note: the desalination capacity of NaI system and Na<sub>x</sub>VOPO<sub>4</sub>·yH<sub>2</sub>O (NVOP) was normalized by the mass of a single (working) electrode.

Titania/carbon hybrid materials were developed with the main objective to enable robust and stable desalination of oxygen-saturated water. The remediation of the latter causes well-known issues for conventional capacitive deionization in the absence of (expensive) ion exchange membranes. Due to the incomplete oxygen reduction reaction on the surface of carbon, we see a constant peroxide formation, resulting in carbon oxidation and poor cycling stability. By hybridizing carbon with titania nanoparticle, the cyclic stability is significantly enhanced (**Figure 26A,D**). Yet, sol-gel implementation of nano-titania domains on the surface of carbon is not compatible with the large inner surface of microporous carbons; therefore, only carbon materials dominated by an external surface area are suitable candidates for this stabilization approach. This limitation may be addressed by using other metal oxide deposition methods, such as atomic layer deposition, and the use of highly mesoporous carbons. The combination and benefit of mesoporous carbon and thin-layer deposition of metal oxides were already shown to be promising in the field of electrochemical energy storage.[218]

Even the best carbon with the most stable performance during cyclic desalination operation cannot overcome two intrinsic limitations: the limited charge storage capacity of carbon of about 100-200 F/g and the limitations imposed by the process of ion electrosorption itself. The first aspect limits the desalination capacity, depending on the cell voltage range, to a maximum of about 20-25 mg/g. The second aspect limits the applicability of capacitive deionization to brackish water. A more promising aspect, therefore, is to leave carbon altogether behind and to explore other materials. This comes along with a second change: the implementation of charge-transfer processes, such as ion insertion, redox-reactions of ions, or conversion reactions of electrode materials. As shown by our work, Faradaic materials allow much higher desalination performance compared to carbon, as shown in **Figure 26B,D**, that is higher desalination capacity, lower energy consumption, and possible operation at higher molar strength. This particularly pertains to conversion reaction systems.

My journey along these lines started with our proof-of-concept work on the use of  $\text{Ti}_3\text{C}_2$ -MXene for symmetric desalination cells. Among other materials, MXene is capable of cation and/or anion insertion between the layers of its two-dimensional structure. The overall performance for desalination of aqueous 5 mM NaCl electrolyte was on a par with activated carbon, which also had a very comparable charge storage capacity. Yet, the full potential of Faradaic materials not limited by the mechanisms of ion electrosorption unfolds when increasing the salt concentration. We demonstrated for  $\text{Mo}_{1.33}\text{C}$ -MXene the ability to operate not only well in aqueous media with seawater-like concentrations of NaCl but also to show an enhanced performance compared to low molar strength water. The desalination capacity of  $\text{MoS}_2$  and  $\text{Mo}_{1.33}\text{C}$  MXene were 25 mg/g and 15 mg/g in 600 NaCl, which was in stark contrast to what we observed for carbon (0.1 mg/g). This performance increase pertains to both charge efficiency and overall desalination capacity and is probably linked to the lower energetic barrier of ion insertion at high molar concentration.

There is a rich wealth of materials capable of reversible ion insertion. Among interesting materials with a layered, two-dimensional structure, we also explored  $\text{TiS}_2$  and  $\text{Na}_x\text{VOPO}_4 \cdot y\text{H}_2\text{O}$ . The latter show, unlike most MXenes, distinct redox-peaks in their electrochemical signature during charging and discharging operation corresponding with sodiation and de-sodiation. Cell design using such materials require careful consideration of the insertion potential(s). In the case of  $\text{TiS}_2$ , the ability to insert sodium and the sodiation/desodiation potential below -0.2 V vs. Ag/AgCl allows us to pair the Faradaic material with positively polarized carbon; thereby, Na and Cl removal is accomplished on the respective sides of the electrode pair in the absence of an ion exchange membrane. A different case is encountered when using materials that show a sodium insertion potential at more positive values. For example, the sodium insertion of  $\text{Na}_x\text{VOPO}_4 \cdot y\text{H}_2\text{O}$  above +0.1 V vs. Ag/AgCl makes the use of an ion exchange membrane at a carbon counter electrode necessary to allow desalination performance. For other materials, like the Ag/AgCl conversion reaction system, we do need an ion exchange membrane peruse of the CID system with two flow channels; by this way, we can exceed 100 mg/g at a cell voltage of just 0.2 V. This shows the importance of careful cell design by considering the positive and negative electrode processes separately. Only this way will allow the implementation of Faradaic material in desalination cells, either paired with carbon or with another Faradaic electrode.

Redox-processes are not just found when ions are inserted into a host crystal, when materials undergo conversion reactions, or when ions react with surface groups; instead, we can also capitalize on charge transfer processes that occur when dissolved ions in the electrolyte undergo redox-processes. For example, this can be achieved using NaI, where we capitalize on the redox-activity of iodide. This system requires the use of an ion exchange membrane to prevent leakage of iodide into the effluent stream but allows, per the fast kinetics of redox ion charging/discharging, the fast desalination/salination operation in addition to a large desalination capacity (**Figure 26C,D**). Another advantage of this approach is the possibility to continue the use of activated carbon as the electrode materials, and we benefit from the enhanced charge transfer of redox ions confined in carbon nanopores.

It is exciting to see the Cambrian explosion like the unfolding of a new generation of electrochemical desalination materials, cells, and concepts. Many of these approaches directly adapt electrode materials so-far explored in the context of sodium-ion battery technology. Many other of these approaches make links to energy storage by investing charge in a reversible fashion during desalination (in times with excess energy supply) and the charge recovery during cell regeneration (to resupply energy to the power grid when power consumption exceeds power generation). The unique ability to not only provide energy efficient tools for water remediation but also enable energy storage is a valuable tool for the continued transition of our technology towards more sustainability. Yet, the excitement of our current gold-digging times should not hide the need for exerting rigor for the technological maturity and actual implementation perspective. For example, the degradation mechanisms and ways to overcome electrode and/or membrane fouling in the context of electrochemical desalination remains poorly explored. Also, it remains unknown if the energy efficiency and low energy consumption will be enough to enable commercial use of this technology in view of the costs for the electrode materials, (expensive) membranes, and (also expensive) system design. All of that requires more work with focus on establishing universally accepted benchmarking parameters to enable fair and direct comparison between materials, cell designs, and technologies.

## 6. References

- [1] Natural-based solutions for water, The United Nations Educational, Scientific and Cultural Organization (UNESCO), 2018.
- [2] T. Oki, S. Kanae, Global Hydrological Cycles and World Water Resources, *Science* 313(5790) (2006) 1068-1072.
- [3] Water in a changing world, The United Nations Educational, Scientific and Cultural Organization (UNESCO), 2008.
- [4] M.M. Mekonnen, A.Y. Hoekstra, Four billion people facing severe water scarcity, *Science Advances* 2(2) (2016) e1500323.
- [5] L.F. Greenlee, D.F. Lawler, B.D. Freeman, B. Marrot, P. Moulin, Reverse osmosis desalination: Water sources, technology, and today's challenges, *Water Research* 43(9) (2009) 2317-2348.
- [6] A. Deshmukh, C. Boo, V. Karanikola, S. Lin, A.P. Straub, T. Tong, D.M. Warsinger, M. Elimelech, Membrane distillation at the water-energy nexus: limits, opportunities, and challenges, *Energy & Environmental Science* 11(5) (2018) 1177-1196.
- [7] N.M. Wade, Distillation plant development and cost update, *Desalination* 136(1) (2001) 3-12.
- [8] M. Al-Sahali, H. Ettouney, Developments in thermal desalination processes: Design, energy, and costing aspects, *Desalination* 214(1) (2007) 227-240.
- [9] H.T. El-Dessouky, H.M. Ettouney, F. Mandani, Performance of parallel feed multiple effect evaporation system for seawater desalination, *Applied Thermal Engineering* 20(17) (2000) 1679-1706.
- [10] C.E. Reid, E.J. Breton, Water and ion flow across cellulosic membranes, *Journal of Applied Polymer Science* 1(2) (1959) 133-143.
- [11] A.E. Allegrezza, B.S. Parekh, P.L. Parise, E.J. Swiniarski, J.L. White, Chlorine resistant polysulfone reverse osmosis modules, *Desalination* 64 (1987) 285-304.
- [12] I. Cabasso, C.N. Tran, Polymer alloy membrane. I. Cellulose acetate–poly(bromophenylene oxide phosphonate) dense and asymmetric membranes, *Journal of Applied Polymer Science* 23(10) (1979) 2967-2988.
- [13] B. Kunst, S. Sourirajan, Effect of casting conditions on the performance of porous cellulose acetate membranes in reverse osmosis, *Journal of Applied Polymer Science* 14(3) (1970) 723-733.
- [14] J.E. Cadotte, R.J. Petersen, R.E. Larson, E.E. Erickson, A new thin-film composite seawater reverse osmosis membrane, *Desalination* 32 (1980) 25-31.
- [15] S.S. Shenvi, A.M. Isloor, A.F. Ismail, A review on RO membrane technology: Developments and challenges, *Desalination* 368 (2015) 10-26.
- [16] D.M. Stevens, J.Y. Shu, M. Reichert, A. Roy, Next-Generation Nanoporous Materials: Progress and Prospects for Reverse Osmosis and Nanofiltration, *Industrial & Engineering Chemistry Research* 56(38) (2017) 10526-10551.
- [17] X.-H. Ma, Z.-K. Yao, Z. Yang, H. Guo, Z.-L. Xu, C.Y. Tang, M. Elimelech, Nanofoaming of Polyamide Desalination Membranes To Tune Permeability and Selectivity, *Environmental Science & Technology Letters* 5(2) (2018) 123-130.
- [18] J.R. Werber, C.O. Osuji, M. Elimelech, Materials for next-generation desalination and water purification membranes, *Nature Reviews Materials* 1 (2016) 16018.
- [19] G. Hummer, J.C. Rasaiah, J.P. Noworyta, Water conduction through the hydrophobic channel of a carbon nanotube, *Nature* 414 (2001) 188.
- [20] S. Dervin, D.D. Dionysiou, S.C. Pillai, 2D nanostructures for water purification: graphene and beyond, *Nanoscale* 8(33) (2016) 15115-15131.
- [21] D. Cohen-Tanugi, J.C. Grossman, Water Desalination across Nanoporous Graphene, *Nano Letters* 12(7) (2012) 3602-3608.

- [22] J.W. Blair, G.W. Murphy, Electrochemical Demineralization of Water with Porous Electrodes of Large Surface Area, Saline Water Conversion, American Chemical Society 1960, pp. 206-223.
- [23] B.B. Arnold, G.W. Murphy, Studies on the electrochemistry of carbon and chemically-modified carbon surfaces, *The Journal of Physical Chemistry* 65(1) (1961) 135-138.
- [24] S. Evans, W.S. Hamilton, The Mechanism of Demineralization at Carbon Electrodes, *Journal of The Electrochemical Society* 113(12) (1966) 1314-1319.
- [25] G.W. Murphy, D.D. Caudle, Mathematical theory of electrochemical demineralization in flowing systems, *Electrochimica Acta* 12(12) (1967) 1655-1664.
- [26] A.M. Johnson, J. Newman, Desalting by Means of Porous Carbon Electrodes, *Journal of The Electrochemical Society* 118(3) (1971) 510-517.
- [27] P.M. Biesheuvel, B. van Limpt, A. van der Wal, Dynamic Adsorption/Desorption Process Model for Capacitive Deionization, *The Journal of Physical Chemistry C* 113(14) (2009) 5636-5640.
- [28] P.M. Biesheuvel, Y. Fu, M.Z. Bazant, Diffuse charge and Faradaic reactions in porous electrodes, *Physical Review E* 83(6) (2011) 061507.
- [29] P.M. Biesheuvel, R. Zhao, S. Porada, A. van der Wal, Theory of membrane capacitive deionization including the effect of the electrode pore space, *Journal of Colloid and Interface Science* 360(1) (2011) 239-248.
- [30] M. Müller, B. Kastening, The double layer of activated carbon electrodes: Part 1. The contribution of ions in the pores, *Journal of Electroanalytical Chemistry* 374(1) (1994) 149-158.
- [31] J.M. Griffin, A.C. Forse, W.-Y. Tsai, P.-L. Taberna, P. Simon, C.P. Grey, In situ NMR and electrochemical quartz crystal microbalance techniques reveal the structure of the electrical double layer in supercapacitors, *Nature Materials* 14(8) (2015) 812-819.
- [32] C. Prehal, D. Weingarth, E. Perre, R.T. Lechner, H. Amenitsch, O. Paris, V. Presser, Tracking the structural arrangement of ions in carbon supercapacitor nanopores using in situ small-angle X-ray scattering, *Energy & Environmental Science* 8(6) (2015) 1725-1735.
- [33] P. Srimuk, J. Lee, Ö. Budak, J. Choi, M. Chen, G. Feng, C. Prehal, V. Presser, In Situ Tracking of Partial Sodium Desolvation of Materials with Capacitive, Pseudocapacitive, and Battery-like Charge/Discharge Behavior in Aqueous Electrolytes, *Langmuir* 34(44) (2018) 13132-13143.
- [34] S. Porada, R. Zhao, A. van der Wal, V. Presser, P.M. Biesheuvel, Review on the science and technology of water desalination by capacitive deionization, *Progress in Materials Science* 58(8) (2013) 1388-1442.
- [35] C. Prehal, C. Koczvara, H. Amenitsch, V. Presser, O. Paris, Salt concentration and charging velocity determine ion charge storage mechanism in nanoporous supercapacitors, *Nature Communications* 9(1) (2018) 4145.
- [36] C. Prehal, C. Koczvara, N. Jäckel, A. Schreiber, M. Burian, H. Amenitsch, M.A. Hartmann, V. Presser, O. Paris, Quantification of ion confinement and desolvation in nanoporous carbon supercapacitors with modelling and in situ X-ray scattering, *Nature Energy* 2 (2017) 16215.
- [37] P. Srimuk, J. Lee, S. Fleischmann, S. Choudhury, N. Jäckel, M. Zeiger, C. Kim, M. Aslan, V. Presser, Faradaic deionization of brackish and sea water via pseudocapacitive cation and anion intercalation into few-layered molybdenum disulfide, *Journal of Materials Chemistry A* 5(30) (2017) 15640-15649.
- [38] C. Kim, P. Srimuk, J. Lee, S. Fleischmann, M. Aslan, V. Presser, Influence of pore structure and cell voltage of activated carbon cloth as a versatile electrode material for capacitive deionization, *Carbon* (122) (2017) 329-335.
- [39] E. Avraham, M. Noked, I. Cohen, A. Soffer, D. Aurbach, The Dependence of the Desalination Performance in Capacitive Deionization Processes on the Electrodes PZC, *Journal of The Electrochemical Society* 158(12) (2011) P168-P173.
- [40] Y. Bouhadana, E. Avraham, M. Noked, M. Ben-Tzion, A. Soffer, D. Aurbach, Capacitive Deionization of NaCl Solutions at Non-Steady-State Conditions: Inversion Functionality of the Carbon Electrodes, *The Journal of Physical Chemistry C* 115(33) (2011) 16567-16573.

- [41] X. Gao, A. Omosebi, J. Landon, K. Liu, Surface charge enhanced carbon electrodes for stable and efficient capacitive deionization using inverted adsorption–desorption behavior, *Energy & Environmental Science* 8(3) (2015) 897-909.
- [42] X. Gao, A. Omosebi, J. Landon, K. Liu, Enhanced Salt Removal in an Inverted Capacitive Deionization Cell Using Amine Modified Microporous Carbon Cathodes, *Environmental Science & Technology* 49(18) (2015) 10920-10926.
- [43] P. Srimuk, L. Ries, M. Zeiger, S. Fleischmann, N. Jäckel, A. Tolosa, B. Krüner, M. Aslan, V. Presser, High performance stability of titania decorated carbon for desalination with capacitive deionization in oxygenated water, *RSC Advances* 6(108) (2016) 106081-106089.
- [44] P. Srimuk, M. Zeiger, N. Jäckel, A. Tolosa, B. Krüner, S. Fleischmann, I. Grobelsek, M. Aslan, B. Shvartsev, M.E. Suss, V. Presser, Enhanced performance stability of carbon/titania hybrid electrodes during capacitive deionization of oxygen saturated saline water, *Electrochimica Acta* 224 (2017) 314-328.
- [45] D. He, C.E. Wong, W. Tang, P. Kovalsky, T.D. Waite, Faradaic Reactions in Water Desalination by Batch-Mode Capacitive Deionization, *Environmental Science & Technology Letters* 3(5) (2016) 222-226.
- [46] I. Cohen, E. Avraham, Y. Bouhadana, A. Soffer, D. Aurbach, The effect of the flow-regime, reversal of polarization, and oxygen on the long term stability in capacitive de-ionization processes, *Electrochimica Acta* 153 (2015) 106-114.
- [47] B. Shapira, E. Avraham, D. Aurbach, Side Reactions in Capacitive Deionization (CDI) Processes: The Role of Oxygen Reduction, *Electrochimica Acta* 220 (2016) 285-295.
- [48] I. Cohen, E. Avraham, Y. Bouhadana, A. Soffer, D. Aurbach, Long term stability of capacitive de-ionization processes for water desalination: The challenge of positive electrodes corrosion, *Electrochimica Acta* 106 (2013) 91-100.
- [49] M. He, K. Fic, E. Fr̄ckowiak, P. Novák, E.J. Berg, Ageing phenomena in high-voltage aqueous supercapacitors investigated by in situ gas analysis, *Energy & Environmental Science* 9(2) (2016) 623-633.
- [50] R.L. Zornitta, P. Srimuk, J. Lee, B. Krüner, M. Aslan, L.A.M. Ruotolo, V. Presser, Charge and potential balancing for optimized capacitive deionization using lignin - derived, low - cost activated carbon electrodes, *ChemSusChem* 11(13) (2018) 2101-2113.
- [51] N. Jäckel, M. Rodner, A. Schreiber, J. Jeongwook, M. Zeiger, M. Aslan, D. Weingarth, V. Presser, Anomalous or regular capacitance? The influence of pore size dispersity on double-layer formation, *Journal of Power Sources* 326 (2016) 660-671.
- [52] J. Chmiola, G. Yushin, Y. Gogotsi, C. Portet, P. Simon, P.L. Taberna, Anomalous Increase in Carbon Capacitance at Pore Sizes Less Than 1 Nanometer, *Science* 313(5794) (2006) 1760-1763.
- [53] S. Porada, L. Borhardt, M. Oschatz, M. Bryjak, J.S. Atchison, K.J. Keesman, S. Kaskel, P.M. Biesheuvel, V. Presser, Direct prediction of the desalination performance of porous carbon electrodes for capacitive deionization, *Energy & Environmental Science* 6(12) (2013) 3700-3712.
- [54] S. Porada, F. Schipper, M. Aslan, M. Antonietti, V. Presser, T.-P. Fellingner, Capacitive Deionization using Biomass-based Microporous Salt-Templated Heteroatom-Doped Carbons, *ChemSusChem* 8(11) (2015) 1867-1874.
- [55] M. Winter, R.J. Brodd, What Are Batteries, Fuel Cells, and Supercapacitors?, *Chemical Reviews* 104(10) (2004) 4245-4270.
- [56] F. Béguin, V. Presser, A. Balducci, E. Frackowiak, Carbons and Electrolytes for Advanced Supercapacitors, *Advanced Materials* 26(14) (2014) 2219-2251.
- [57] N. Jäckel, P. Simon, Y. Gogotsi, V. Presser, Increase in Capacitance by Subnanometer Pores in Carbon, *ACS Energy Letters* 1(6) (2016) 1262-1265.
- [58] M.K.B. Gratiuto, T. Panyathanmaporn, R.A. Chumnanklang, N. Sirinuntawittaya, A. Dutta, Production of activated carbon from coconut shell: Optimization using response surface methodology, *Bioresource Technology* 99(11) (2008) 4887-4895.
- [59] L. Khezami, A. Chetouani, B. Taouk, R. Capart, Production and characterisation of activated carbon from wood components in powder: Cellulose, lignin, xylan, *Powder Technology* 157(1) (2005) 48-56.

- [60] G. Wang, B. Qian, Q. Dong, J. Yang, Z. Zhao, J. Qiu, Highly mesoporous activated carbon electrode for capacitive deionization, *Separation and Purification Technology* 103 (2013) 216-221.
- [61] G. Wang, Q. Dong, Z. Ling, C. Pan, C. Yu, J. Qiu, Hierarchical activated carbon nanofiber webs with tuned structure fabricated by electrospinning for capacitive deionization, *Journal of Materials Chemistry* 22(41) (2012) 21819-21823.
- [62] B. Krüner, P. Srimuk, S. Fleischmann, M. Zeiger, A. Schreiber, M. Aslan, A. Quade, V. Presser, Hydrogen-treated, sub-micrometer carbon beads for fast capacitive deionization with high performance stability, *Carbon* 117 (2017) 46-54.
- [63] M. Suzuki, Activated carbon fiber: Fundamentals and applications, *Carbon* 32(4) (1994) 577-586.
- [64] J. Lee, J. Kim, T. Hyeon, Recent Progress in the Synthesis of Porous Carbon Materials, *Advanced Materials* 18(16) (2006) 2073-2094.
- [65] C. Liang, Z. Li, S. Dai, Mesoporous Carbon Materials: Synthesis and Modification, *Angewandte Chemie International Edition* 47(20) (2008) 3696-3717.
- [66] Z. Ma, T. Kyotani, Z. Liu, O. Terasaki, A. Tomita, Very High Surface Area Microporous Carbon with a Three-Dimensional Nano-Array Structure: Synthesis and Its Molecular Structure, *Chemistry of Materials* 13(12) (2001) 4413-4415.
- [67] Z. Ma, T. Kyotani, A. Tomita, Preparation of a high surface area microporous carbon having the structural regularity of Y zeolite, *Chemical Communications* (23) (2000) 2365-2366.
- [68] S.A. Johnson, E.S. Brigham, P.J. Ollivier, T.E. Mallouk, Effect of Micropore Topology on the Structure and Properties of Zeolite Polymer Replicas, *Chemistry of Materials* 9(11) (1997) 2448-2458.
- [69] P. Zhang, F. Sun, Z. Xiang, Z. Shen, J. Yun, D. Cao, ZIF-derived in situ nitrogen-doped porous carbons as efficient metal-free electrocatalysts for oxygen reduction reaction, *Energy & Environmental Science* 7(1) (2014) 442-450.
- [70] P. Zhang, F. Sun, Z. Shen, D. Cao, ZIF-derived porous carbon: a promising supercapacitor electrode material, *Journal of Materials Chemistry A* 2(32) (2014) 12873-12880.
- [71] H.-x. Zhong, J. Wang, Y.-w. Zhang, W.-l. Xu, W. Xing, D. Xu, Y.-f. Zhang, X.-b. Zhang, ZIF-8 Derived Graphene-Based Nitrogen-Doped Porous Carbon Sheets as Highly Efficient and Durable Oxygen Reduction Electrocatalysts, *Angewandte Chemie International Edition* 53(51) (2014) 14235-14239.
- [72] L. Zhang, Z. Su, F. Jiang, L. Yang, J. Qian, Y. Zhou, W. Li, M. Hong, Highly graphitized nitrogen-doped porous carbon nanopolyhedra derived from ZIF-8 nanocrystals as efficient electrocatalysts for oxygen reduction reactions, *Nanoscale* 6(12) (2014) 6590-6602.
- [73] C.T. Kresge, M.E. Leonowicz, W.J. Roth, J.C. Vartuli, J.S. Beck, Ordered mesoporous molecular sieves synthesized by a liquid-crystal template mechanism, *Nature* 359(6397) (1992) 710-712.
- [74] J.S. Beck, J.C. Vartuli, W.J. Roth, M.E. Leonowicz, C.T. Kresge, K.D. Schmitt, C.T.W. Chu, D.H. Olson, E.W. Sheppard, S.B. McCullen, J.B. Higgins, J.L. Schlenker, A new family of mesoporous molecular sieves prepared with liquid crystal templates, *Journal of the American Chemical Society* 114(27) (1992) 10834-10843.
- [75] R. Ryoo, S.H. Joo, S. Jun, Synthesis of Highly Ordered Carbon Molecular Sieves via Template-Mediated Structural Transformation, *The Journal of Physical Chemistry B* 103(37) (1999) 7743-7746.
- [76] J.H. Knox, B. Kaur, G.R. Millward, Structure and performance of porous graphitic carbon in liquid chromatography, *Journal of Chromatography A* 352 (1986) 3-25.
- [77] K.K. Unger, H. Mueller, Prospects for Carbon as Packing Material in High-Performance Liquid Chromatography, *Journal of Liquid Chromatography* 6(sup001) (1983) 1-36.
- [78] K.P. Gierszal, M. Jaroniec, Carbons with Extremely Large Volume of Uniform Mesopores Synthesized by Carbonization of Phenolic Resin Film Formed on Colloidal Silica Template, *Journal of the American Chemical Society* 128(31) (2006) 10026-10027.

- [79] A.A. Zakhidov, R.H. Baughman, Z. Iqbal, C. Cui, I. Khayrullin, S.O. Dantas, J. Marti, V.G. Ralchenko, Carbon Structures with Three-Dimensional Periodicity at Optical Wavelengths, *Science* 282(5390) (1998) 897-901.
- [80] Z. Lei, Y. Zhang, H. Wang, Y. Ke, J. Li, F. Li, J. Xing, Fabrication of well-ordered macroporous active carbon with a microporous framework, *Journal of Materials Chemistry* 11(8) (2001) 1975-1977.
- [81] S. Kang, J.-S. Yu, M. Kruk, M. Jaroniec, Synthesis of an ordered macroporous carbon with 62 nm spherical pores that exhibit unique gas adsorption properties, *Chemical Communications* (16) (2002) 1670-1671.
- [82] L. Li, L. Zou, H. Song, G. Morris, Ordered mesoporous carbons synthesized by a modified sol-gel process for electrosorptive removal of sodium chloride, *Carbon* 47(3) (2009) 775-781.
- [83] L. Zou, L. Li, H. Song, G. Morris, Using mesoporous carbon electrodes for brackish water desalination, *Water Research* 42(8) (2008) 2340-2348.
- [84] Y. Gogotsi, V. Presser, *Carbon Nanomaterials*, CRC Press, Boca Raton, 2013.
- [85] Y. Gogotsi, A. Nikitin, H. Ye, W. Zhou, J.E. Fischer, B. Yi, H.C. Foley, M.W. Barsoum, Nanoporous carbide-derived carbon with tunable pore size, *Nature Materials* 2 (2003) 591.
- [86] A. Jänes, T. Thomberg, H. Kurig, E. Lust, Nanoscale fine-tuning of porosity of carbide-derived carbon prepared from molybdenum carbide, *Carbon* 47(1) (2009) 23-29.
- [87] A. Tolosa, B. Krüner, S. Fleischmann, N. Jäckel, M. Zeiger, M. Aslan, I. Grobelsek, V. Presser, Niobium carbide nanofibers as a versatile precursor for high power supercapacitor and high energy battery electrodes, *Journal of Materials Chemistry A* 4(41) (2016) 16003-16016.
- [88] J.K. Ewert, D. Weingarh, C. Denner, M. Friedrich, M. Zeiger, A. Schreiber, N. Jäckel, V. Presser, R. Kempe, Enhanced capacitance of nitrogen-doped hierarchically porous carbide-derived carbon in matched ionic liquids, *Journal of Materials Chemistry A* 3(37) (2015) 18906-18912.
- [89] M. Oschatz, M. Zeiger, N. Jäckel, P. Strubel, L. Borchardt, R. Reinhold, W. Nickel, J. Eckert, V. Presser, S. Kaskel, Emulsion soft templating of carbide-derived carbon nanospheres with controllable porosity for capacitive electrochemical energy storage, *Journal of Materials Chemistry A* 3(35) (2015) 17983-17990.
- [90] W. Gu, G. Yushin, Review of nanostructured carbon materials for electrochemical capacitor applications: advantages and limitations of activated carbon, carbide - derived carbon, zeolite - templated carbon, carbon aerogels, carbon nanotubes, onion - like carbon, and graphene, *Wiley Interdisciplinary Reviews: Energy and Environment* 3(5) (2014) 424-473.
- [91] A. Tolosa, B. Krüner, N. Jäckel, M. Aslan, C. Vakifahmetoglu, V. Presser, Electrospinning and electrospaying of silicon oxycarbide-derived nanoporous carbon for supercapacitor electrodes, *Journal of Power Sources* 313 (2016) 178-188.
- [92] M. Oschatz, E. Kockrick, M. Rose, L. Borchardt, N. Klein, I. Senkovska, T. Freudenberg, Y. Korenblit, G. Yushin, S. Kaskel, A cubic ordered, mesoporous carbide-derived carbon for gas and energy storage applications, *Carbon* 48(14) (2010) 3987-3992.
- [93] Y. Korenblit, M. Rose, E. Kockrick, L. Borchardt, A. Kvit, S. Kaskel, G. Yushin, High-Rate Electrochemical Capacitors Based on Ordered Mesoporous Silicon Carbide-Derived Carbon, *ACS Nano* 4(3) (2010) 1337-1344.
- [94] M. Rose, Y. Korenblit, E. Kockrick, L. Borchardt, M. Oschatz, S. Kaskel, G. Yushin, Hierarchical Micro- and Mesoporous Carbide-Derived Carbon as a High-Performance Electrode Material in Supercapacitors, *Small* 7(8) (2011) 1108-1117.
- [95] S. Porada, L. Weinstein, R. Dash, A. van der Wal, M. Bryjak, Y. Gogotsi, P.M. Biesheuvel, Water Desalination Using Capacitive Deionization with Microporous Carbon Electrodes, *ACS Applied Materials & Interfaces* 4(3) (2012) 1194-1199.
- [96] R.W. Pekala, J.C. Farmer, C.T. Alviso, T.D. Tran, S.T. Mayer, J.M. Miller, B. Dunn, Carbon aerogels for electrochemical applications, *Journal of Non-Crystalline Solids* 225 (1998) 74-80.
- [97] B. Jia, W. Zhang, Preparation and Application of Electrodes in Capacitive Deionization (CDI): a State-of-Art Review, *Nanoscale Research Letters* 11(1) (2016) 1-25.

- [98] T. Horikawa, J.i. Hayashi, K. Muroyama, Controllability of pore characteristics of resorcinol–formaldehyde carbon aerogel, *Carbon* 42(8) (2004) 1625-1633.
- [99] P. Xu, J.E. Drewes, D. Heil, G. Wang, Treatment of brackish produced water using carbon aerogel-based capacitive deionization technology, *Water Research* 42(10) (2008) 2605-2617.
- [100] J.C. Farmer, D.V. Fix, G.V. Mack, R.W. Pekala, J.F. Poco, Capacitive, deionization with carbon aerogel electrodes: Carbonate, sulfate, and phosphate, United States, 1995.
- [101] J.C. Farmer, D.V. Fix, G.V. Mack, R.W. Pekala, J.F. Poco, Capacitive Deionization of NaCl and NaNO<sub>3</sub> Solutions with Carbon Aerogel Electrodes, *Journal of The Electrochemical Society* 143(1) (1996) 159-169.
- [102] J.C. Farmer, D.V. Fix, G.V. Mack, R.W. Pekala, J.F. Poco, Capacitive deionization of NH<sub>4</sub>ClO<sub>4</sub> solutions with carbon aerogel electrodes, *Journal of Applied Electrochemistry* 26(10) (1996) 1007-1018.
- [103] K.S. Novoselov, A.K. Geim, S.V. Morozov, D. Jiang, Y. Zhang, S.V. Dubonos, I.V. Grigorieva, A.A. Firsov, Electric Field Effect in Atomically Thin Carbon Films, *Science* 306(5696) (2004) 666-669.
- [104] P. Avouris, C. Dimitrakopoulos, Graphene: synthesis and applications, *Materials Today* 15(3) (2012) 86-97.
- [105] G. Eda, G. Fanchini, M. Chhowalla, Large-area ultrathin films of reduced graphene oxide as a transparent and flexible electronic material, *Nature Nanotechnology* 3 (2008) 270.
- [106] S. Stankovich, D.A. Dikin, R.D. Piner, K.A. Kohlhaas, A. Kleinhammes, Y. Jia, Y. Wu, S.T. Nguyen, R.S. Ruoff, Synthesis of graphene-based nanosheets via chemical reduction of exfoliated graphite oxide, *Carbon* 45(7) (2007) 1558-1565.
- [107] V. Augustyn, Y. Gogotsi, 2D Materials with Nanoconfined Fluids for Electrochemical Energy Storage, *Joule* 1(3) (2017) 443-452.
- [108] H. Li, T. Lu, L. Pan, Y. Zhang, Z. Sun, Electrosorption behavior of graphene in NaCl solutions, *Journal of Materials Chemistry* 19(37) (2009) 6773-6779.
- [109] W. Kong, X. Duan, Y. Ge, H. Liu, J. Hu, X. Duan, Holey graphene hydrogel with in-plane pores for high-performance capacitive desalination, *Nano Research* 9(8) (2016) 2458-2466.
- [110] K. Dai, L. Shi, J. Fang, D. Zhang, B. Yu, NaCl adsorption in multi-walled carbon nanotubes, *Materials Letters* 59(16) (2005) 1989-1992.
- [111] Y. Liu, C. Nie, X. Liu, X. Xu, Z. Sun, L. Pan, Review on carbon-based composite materials for capacitive deionization, *RSC Advances* 5(20) (2015) 15205-15225.
- [112] B. Lee, N. Park, K.S. Kang, H.J. Ryu, S.H. Hong, Enhanced Capacitive Deionization by Dispersion of CNTs in Activated Carbon Electrode, *ACS Sustainable Chemistry & Engineering* 6(2) (2018) 1572-1579.
- [113] D. Zhang, L. Shi, J. Fang, K. Dai, Removal of NaCl from saltwater solution using carbon nanotubes/activated carbon composite electrode, *Materials Letters* 60(3) (2006) 360-363.
- [114] Z. Peng, D. Zhang, L. Shi, T. Yan, High performance ordered mesoporous carbon/carbon nanotube composite electrodes for capacitive deionization, *Journal of Materials Chemistry* 22(14) (2012) 6603-6612.
- [115] D. Zhang, X. Wen, L. Shi, T. Yan, J. Zhang, Enhanced capacitive deionization of graphene/mesoporous carbon composites, *Nanoscale* 4(17) (2012) 5440-5446.
- [116] M. Pasta, C.D. Wessells, Y. Cui, F. La Mantia, A Desalination Battery, *Nano Letters* 12(2) (2012) 839-843.
- [117] J. Lee, S. Kim, C. Kim, J. Yoon, Hybrid capacitive deionization to enhance the desalination performance of capacitive techniques, *Energy & Environmental Science* 7(11) (2014) 3683-3689.
- [118] S. Kim, J. Lee, C. Kim, J. Yoon, Na<sub>2</sub>FeP<sub>2</sub>O<sub>7</sub> as a Novel Material for Hybrid Capacitive Deionization, *Electrochimica Acta* 203 (2016) 265-271.
- [119] P. Srimuk, J. Lee, A. Tolosa, C. Kim, M. Aslan, V. Presser, Titanium Disulfide: A Promising Low-Dimensional Electrode Material for Sodium Ion Intercalation for Seawater Desalination, *Chemistry of Materials* 29(23) (2017) 9964–9973.

- [120] P. Srimuk, F. Kaasik, B. Krüner, A. Tolosa, S. Fleischmann, N. Jäckel, M.C. Tekeli, M. Aslan, M.E. Suss, V. Presser, MXene as a novel intercalation-type pseudocapacitive cathode and anode for capacitive deionization, *Journal of Materials Chemistry A* 4(47) (2016) 18265-18271.
- [121] F. Xing, T. Li, J. Li, H. Zhu, N. Wang, X. Cao, Chemically exfoliated MoS<sub>2</sub> for capacitive deionization of saline water, *Nano Energy* 31 (2017) 590-595.
- [122] M. Acerce, D. Voiry, M. Chhowalla, Metallic 1T phase MoS<sub>2</sub> nanosheets as supercapacitor electrode materials, *Nature Nanotechnology* 10(4) (2015) 313-8.
- [123] F. Chen, Y. Huang, L. Guo, L. Sun, Y. Wang, H.Y. Yang, Dual-ions electrochemical deionization: a desalination generator, *Energy & Environmental Science* 10(10) (2017) 2081-2089.
- [124] K.C. Smith, R. Dmello, Na-Ion Desalination (NID) Enabled by Na-Blocking Membranes and Symmetric Na-Intercalation: Porous-Electrode Modeling, *Journal of The Electrochemical Society* 163(3) (2016) A530-A539.
- [125] J. Lee, S. Kim, J. Yoon, Rocking Chair Desalination Battery Based on Prussian Blue Electrodes, *ACS Omega* 2(4) (2017) 1653-1659.
- [126] T. Kim, C.A. Gorski, B.E. Logan, Low Energy Desalination Using Battery Electrode Deionization, *Environmental Science & Technology Letters* 4(10) (2017) 444-449.
- [127] E. Grygolowicz-Pawlak, M. Sohail, M. Pawlak, B. Neel, A. Shvarev, R. de Marco, E. Bakker, Coulometric Sodium Chloride Removal System with Nafion Membrane for Seawater Sample Treatment, *Analytical Chemistry* 84(14) (2012) 6158-6165.
- [128] M. Fighera, P.D. van der Wal, H. Shea, Microfluidic Platform for Seawater Desalination by Coulometric Removal of Chloride Ions through Printed Ag Electrodes, *Journal of The Electrochemical Society* 164(12) (2017) H836-H845.
- [129] A.C. Arulrajan, D.L. Ramasamy, M. Sillanpää, A.d. Wal, P.M. Biesheuvel, S. Porada, J.E. Dykstra, Exceptional Water Desalination Performance with Anion - Selective Electrodes, *Advanced Materials* 31(10) (2019) e1806937.
- [130] P. Srimuk, S. Husmann, V. Presser, Low voltage operation of a silver/silver chloride battery with high desalination capacity in seawater, *RSC Advances* 9(26) (2019) 14849-14858.
- [131] B.E. Conway, *Electrochemical Supercapacitors scientific fundamental and technological applications*, springer, Heidelberg, 1999.
- [132] J.B. Clarke, J.W. Hastie, L.H.E. Kihlborg, R. Metselaar, M.M. Thackeray, Definitions of terms relating to phase transitions of the solid state (IUPAC Recommendations 1994), *Pure and Applied Chemistry* 66(3) (1994) 577.
- [133] C. Delmas, H. Cognac-Auradou, J.M. Cocciantelli, M. Ménétrier, J.P. Doumerc, The Li<sub>x</sub>V<sub>2</sub>O<sub>5</sub> system: An overview of the structure modifications induced by the lithium intercalation, *Solid State Ionics* 69(3) (1994) 257-264.
- [134] H. Shi, J. Barker, M.Y. Saïdi, R. Koksang, Structure and Lithium Intercalation Properties of Synthetic and Natural Graphite, *Journal of The Electrochemical Society* 143(11) (1996) 3466-3472.
- [135] J.P. Zheng, P.J. Cygan, T.R. Jow, Hydrrous Ruthenium Oxide as an Electrode Material for Electrochemical Capacitors, *Journal of The Electrochemical Society* 142(8) (1995) 2699-2703.
- [136] T. Brousse, D. Bélanger, J.W. Long, To Be or Not To Be Pseudocapacitive?, *Journal of The Electrochemical Society* 162(5) (2015) A5185-A5189.
- [137] P. Srimuk, J. Lee, S. Fleischmann, M. Aslan, C. Kim, V. Presser, Potential - dependent, switchable ion selectivity in aqueous media using titanium disulfide, *ChemSusChem* (11) (2018) 1-11.
- [138] A. Van der Ven, J. Bhattacharya, A.A. Belak, Understanding Li Diffusion in Li-Intercalation Compounds, *Accounts of Chemical Research* 46(5) (2013) 1216-1225.
- [139] D. Bin, F. Wang, A.G. Tamirat, L. Suo, Y. Wang, C. Wang, Y. Xia, Progress in Aqueous Rechargeable Sodium - Ion Batteries, *Advanced Energy Materials* 8(17) (2018) 1703008.
- [140] J. Lee, P. Srimuk, K. Aristizabal, C. Kim, S. Choudhury, Y.-C. Nah, F. Mücklich, V. Presser, Pseudocapacitive desalination of brackish water and seawater via vanadium pentoxide decorated multi-walled carbon nanotubes, *ChemSusChem* (10) (2017) 3611-3623.

- [141] P. Srimuk, J. Halim, J. Lee, Q. Tao, J. Rosen, V. Presser, Two-Dimensional Molybdenum Carbide (MXene) with Divacancy Ordering for Brackish and Seawater Desalination via Cation and Anion Intercalation, *ACS Sustainable Chemistry & Engineering* 6(3) (2018) 3739-3747.
- [142] W. Bao, X. Tang, X. Guo, S. Choi, C. Wang, Y. Gogotsi, G. Wang, Porous Cryo-Dried MXene for Efficient Capacitive Deionization, *Joule* 2(4) (2018) 778-787.
- [143] V. Augustyn, P. Simon, B. Dunn, Pseudocapacitive oxide materials for high-rate electrochemical energy storage, *Energy & Environmental Science* 7(5) (2014) 1597-1614.
- [144] A. Eftekhari, On the Theoretical Capacity/Energy of Lithium Batteries and Their Counterparts, *ACS Sustainable Chemistry & Engineering* 7(4) (2019) 3684-3687.
- [145] J.-Y. Hwang, S.-T. Myung, Y.-K. Sun, Sodium-ion batteries: present and future, *Chemical Society Reviews* 46(12) (2017) 3529-3614.
- [146] H. Kim, D.J. Kim, D.-H. Seo, M.S. Yeom, K. Kang, D.K. Kim, Y. Jung, Ab Initio Study of the Sodium Intercalation and Intermediate Phases in  $\text{Na}_{0.44}\text{MnO}_2$  for Sodium-Ion Battery, *Chemistry of Materials* 24(6) (2012) 1205-1211.
- [147] A.D. Tevar, J.F. Whitacre, Relating Synthesis Conditions and Electrochemical Performance for the Sodium Intercalation Compound  $\text{Na}_4\text{Mn}_9\text{O}_{18}$  in Aqueous Electrolyte, *Journal of The Electrochemical Society* 157(7) (2010) A870-A875.
- [148] S. Boyd, V. Augustyn, Transition metal oxides for aqueous sodium-ion electrochemical energy storage, *Inorganic Chemistry Frontiers* 5(5) (2018) 999-1015.
- [149] F. Chen, Y. Huang, L. Guo, M. Ding, H.Y. Yang, A dual-ion electrochemistry deionization system based on AgCl-NMO Electrodes, *Nanoscale* 9(28) (2017) 10101-10108.
- [150] Z.Y. Leong, H.Y. Yang, A Study of  $\text{MnO}_2$  with Different Crystalline Forms for Pseudocapacitive Desalination, *ACS Applied Materials & Interfaces* 11(14) (2019) 13176-13184.
- [151] S. Devaraj, N. Munichandraiah, Effect of Crystallographic Structure of  $\text{MnO}_2$  on Its Electrochemical Capacitance Properties, *The Journal of Physical Chemistry C* 112(11) (2008) 4406-4417.
- [152] B.W. Byles, D.A. Cullen, K.L. More, E. Pomerantseva, Tunnel structured manganese oxide nanowires as redox active electrodes for hybrid capacitive deionization, *Nano Energy* 44 (2018) 476-488.
- [153] M. Naguib, M. Kurtoglu, V. Presser, J. Lu, J. Niu, M. Heon, L. Hultman, Y. Gogotsi, M.W. Barsoum, Two-Dimensional Nanocrystals Produced by Exfoliation of  $\text{Ti}_3\text{AlC}_2$ , *Advanced Materials* 23(37) (2011) 4248-4253.
- [154] M. Naguib, V.N. Mochalin, M.W. Barsoum, Y. Gogotsi, 25th Anniversary Article: MXenes: A New Family of Two-Dimensional Materials, *Advanced Materials* 26(7) (2014) 992-1005.
- [155] B. Anasori, M.R. Lukatskaya, Y. Gogotsi, 2D metal carbides and nitrides (MXenes) for energy storage, *Nature Reviews Materials* 2(2) (2017) 16098.
- [156] V.M. Hong Ng, H. Huang, K. Zhou, P.S. Lee, W. Que, J.Z. Xu, L.B. Kong, Recent progress in layered transition metal carbides and/or nitrides (MXenes) and their composites: synthesis and applications, *Journal of Materials Chemistry A* 5(7) (2017) 3039-3068.
- [157] J. Pang, R.G. Mendes, A. Bachmatiuk, L. Zhao, H.Q. Ta, T. Gemming, H. Liu, Z. Liu, M.H. Rummeli, Applications of 2D MXenes in energy conversion and storage systems, *Chemical Society Reviews* 48(1) (2018) 72-133.
- [158] T. Schultz, N.C. Frey, K. Hantanasirisakul, S. Park, S.J. May, V.B. Shenoy, Y. Gogotsi, N. Koch, Surface termination dependent work function and electronic properties of  $\text{Ti}_3\text{C}_2\text{T}_x$  MXene, *Chemistry of Materials* (2019) DOI:10.1021/acs.chemmater.9b00414.
- [159] M.R. Lukatskaya, O. Mashtalir, C.E. Ren, Y. Dall'Agnese, P. Rozier, P.L. Taberna, M. Naguib, P. Simon, M.W. Barsoum, Y. Gogotsi, Cation Intercalation and High Volumetric Capacitance of Two-Dimensional Titanium Carbide, *Science* 341(6153) (2013) 1502-1505.
- [160] E. Quain, T.S. Mathis, N. Kurra, K. Maleski, K.L. Aken, M. Alhabeab, H.N. Alshareef, Y. Gogotsi, Direct Writing of Additive - Free MXene - in - Water Ink for Electronics and Energy Storage, *Advanced Materials Technologies* 4(1) (2018) 1800256.

- [161] N. Shpigel, M.D. Levi, S. Sigalov, T.S. Mathis, Y. Gogotsi, D. Aurbach, Direct assessment of nano-confined water in 2D  $\text{Ti}_3\text{C}_2$  (MXene) electrode interspaces by a surface acoustic technique, *Journal of the American Chemical Society* 140(28) (2018) 8910-8917.
- [162] M. Hu, T. Hu, Z. Li, Y. Yang, R. Cheng, J. Yang, C. Cui, X. Wang, Surface Functional Groups and Interlayer Water Determine the Electrochemical Capacitance of  $\text{Ti}_3\text{C}_2\text{T}_x$  MXene, *ACS Nano* 12(4) (2018) 3578-3586.
- [163] Q.H. Wang, K. Kalantar-Zadeh, A. Kis, J.N. Coleman, M.S. Strano, Electronics and optoelectronics of two-dimensional transition metal dichalcogenides, *Nat Nano* 7(11) (2012) 699-712.
- [164] D. Voiry, A. Mohite, M. Chhowalla, Phase engineering of transition metal dichalcogenides, *Chemical Society Reviews* 44(9) (2015) 2702-2712.
- [165] K.F. Mak, C. Lee, J. Hone, J. Shan, T.F. Heinz, Atomically Thin  $\text{MoS}_2$ : A New Direct-Gap Semiconductor, *Physical Review Letters* 105(13) (2010) 136805.
- [166] T. Korn, S. Heydrich, M. Hirmer, J. Schmutzler, C. Schüller, Low-temperature photocarrier dynamics in monolayer  $\text{MoS}_2$ , *Applied Physics Letters* 99(10) (2011) 102109.
- [167] H. He, P. Lu, L. Wu, C. Zhang, Y. Song, P. Guan, S. Wang, Structural Properties and Phase Transition of Na Adsorption on Monolayer  $\text{MoS}_2$ , *Nanoscale Research Letters* 11(1) (2016) 330.
- [168] J. Xiao, D. Choi, L. Cosimbescu, P. Koech, J. Liu, J.P. Lemmon, Exfoliated  $\text{MoS}_2$  Nanocomposite as an Anode Material for Lithium Ion Batteries, *Chemistry of Materials* 22(16) (2010) 4522-4524.
- [169] K. Chang, W. Chen, l-Cysteine-Assisted Synthesis of Layered  $\text{MoS}_2$ /Graphene Composites with Excellent Electrochemical Performances for Lithium Ion Batteries, *ACS Nano* 5(6) (2011) 4720-4728.
- [170] G.S. Bang, K.W. Nam, J.Y. Kim, J. Shin, J.W. Choi, S.Y. Choi, Effective liquid-phase exfoliation and sodium ion battery application of  $\text{MoS}_2$  nanosheets, *ACS Applied Materials & Interfaces* 6(10) (2014) 7084-9.
- [171] M.A. Bissett, I.A. Kinloch, R.A. Dryfe, Characterization of  $\text{MoS}_2$ -Graphene Composites for High-Performance Coin Cell Supercapacitors, *ACS Applied Materials & Interfaces* 7(31) (2015) 17388-98.
- [172] C.N. Rao, K. Gopalakrishnan, U. Maitra, Comparative Study of Potential Applications of Graphene,  $\text{MoS}_2$ , and Other Two-Dimensional Materials in Energy Devices, Sensors, and Related Areas, *ACS Applied Materials & Interfaces* 7(15) (2015) 7809-32.
- [173] N. Savjani, E.A. Lewis, M.A. Bissett, J.R. Brent, R.A.W. Dryfe, S.J. Haigh, P. O'Brien, Synthesis of Lateral Size-Controlled Monolayer  $1\text{H-MoS}_2$ @Oleylamine as Supercapacitor Electrodes, *Chemistry of Materials* 28(2) (2016) 657-664.
- [174] S. Zhang, R. Hu, P. Dai, X. Yu, Z. Ding, M. Wu, G. Li, Y. Ma, C. Tu, Synthesis of rambutan-like  $\text{MoS}_2$ /mesoporous carbon spheres nanocomposites with excellent performance for supercapacitors, *Applied Surface Science* 396 (2017) 994-999.
- [175] X. Geng, Y. Zhang, Y. Han, J. Li, L. Yang, M. Benamara, L. Chen, H. Zhu, Two-Dimensional Water-Coupled Metallic  $\text{MoS}_2$  with Nanochannels for Ultrafast Supercapacitors, *Nano Letters* 17(3) (2017) 1825-1832.
- [176] D. Wu, C. Zhang, S. Xu, Y. Zhu, D. Xiong, L. Wang, P.K. Chu, Fabrication and enhanced supercapacitance of hollow nanostructured  $\text{MoS}_2$  prepared by a CATB-assisted hydrothermal process, *Materials Letters* 184 (2016) 96-99.
- [177] K. Krishnamoorthy, P. Pazhamalai, G.K. Veerasubramani, S.J. Kim, Mechanically delaminated few layered  $\text{MoS}_2$  nanosheets based high performance wire type solid-state symmetric supercapacitors, *Journal of Power Sources* 321 (2016) 112-119.
- [178] B.D. Falola, T. Wiltowski, I.I. Suni, Electrodeposition of  $\text{MoS}_2$  for Charge Storage in Electrochemical Supercapacitors, *Journal of The Electrochemical Society* 163(9) (2016) D568-D574.
- [179] S. Balendhran, S. Walia, H. Nili, J.Z. Ou, S. Zhuiykov, R.B. Kaner, S. Sriram, M. Bhaskaran, K. Kalantar-zadeh, Two-Dimensional Molybdenum Trioxide and Dichalcogenides, *Advanced Functional Materials* 23(32) (2013) 3952-3970.

- [180] K. Kalantar-zadeh, J.Z. Ou, T. Daeneke, A. Mitchell, T. Sasaki, M.S. Fuhrer, Two dimensional and layered transition metal oxides, *Applied Materials Today* 5 (2016) 73-89.
- [181] Y. Zheng, G. Chen, Y. Yu, Y. Hu, Y. Feng, J. Sun, Urea-assisted synthesis of ultra-thin hexagonal tungsten trioxide photocatalyst sheets, *Journal of Materials Science* 50(24) (2015) 8111-8119.
- [182] X.K. Hu, Y.T. Qian, Z.T. Song, J.R. Huang, R. Cao, J.Q. Xiao, Comparative Study on MoO<sub>3</sub> and H<sub>x</sub>MoO<sub>3</sub> Nanobelts: Structure and Electric Transport, *Chemistry of Materials* 20(4) (2008) 1527-1533.
- [183] B. Hu, L. Mai, W. Chen, F. Yang, From MoO<sub>3</sub> Nanobelts to MoO<sub>2</sub> Nanorods: Structure Transformation and Electrical Transport, *ACS Nano* 3(2) (2009) 478-482.
- [184] K.R. Kendall, C. Navas, J.K. Thomas, H.-C.z. Loye, Recent developments in perovskite-based oxide ion conductors, *Solid State Ionics* 82(3) (1995) 215-223.
- [185] L. Athouël, F. Moser, R. Dugas, O. Crosnier, D. Bélanger, T. Brousse, Variation of the MnO<sub>2</sub> Birnessite Structure upon Charge/Discharge in an Electrochemical Supercapacitor Electrode in Aqueous Na<sub>2</sub>SO<sub>4</sub> Electrolyte, *The Journal of Physical Chemistry C* 112(18) (2008) 7270-7277.
- [186] A.G. El-Deen, N.A.M. Barakat, H.Y. Kim, Graphene wrapped MnO<sub>2</sub>-nanostructures as effective and stable electrode materials for capacitive deionization desalination technology, *Desalination* 344 (2014) 289-298.
- [187] B. Chen, Y. Wang, Z. Chang, X. Wang, M. Li, X. Liu, L. Zhang, Y. Wu, Enhanced capacitive desalination of MnO<sub>2</sub> by forming composite with multi-walled carbon nanotubes, *RSC Advances* 6(8) (2016) 6730-6736.
- [188] B.W. Byles, B. Hayes-Oberst, E. Pomerantseva, Ion Removal Performance, Structural/Compositional Dynamics, and Electrochemical Stability of Layered Manganese Oxide Electrodes in Hybrid Capacitive Deionization, *ACS Applied Materials & Interfaces* 10(38) (2018) 32313-32322.
- [189] S. Ferlay, T. Mallah, R. Ouahès, P. Veillet, M. Verdaguer, A room-temperature organometallic magnet based on Prussian blue, *Nature* 378(6558) (1995) 701-703.
- [190] D. Su, A. McDonagh, S.Z. Qiao, G. Wang, High - Capacity Aqueous Potassium - Ion Batteries for Large - Scale Energy Storage, *Advanced Materials* 29(1) (2017) 1604007.
- [191] P. Jian, W. Jinsong, Y. Haocong, H. WenJing, Y. Yonghui, Y. Jinwen, S. Yi, L. Yi, L. Jiahuan, X. Yue, W. Peng, L. Yuyu, J. Yu, D. Yu, M. Ling, J. Jianjun, H. Jiantao, H. Yunhui, A Dual - Insertion Type Sodium - Ion Full Cell Based on High - Quality Ternary - Metal Prussian Blue Analogs, *Advanced Energy Materials* 8(11) (2018) 1702856.
- [192] R. Bors, J. Yun, P. Marzak, J. Fichtner, D. Scieszka, A.S. Bandarenka, Chromium(II) Hexacyanoferrate-Based Thin Films as a Material for Aqueous Alkali Metal Cation Batteries, *ACS Omega* 3(5) (2018) 5111-5115.
- [193] B. Paulitsch, J. Yun, A.S. Bandarenka, Electrodeposited Na<sub>2</sub>VO<sub>x</sub>[Fe(CN)<sub>6</sub>] films As a Cathode Material for Aqueous Na-Ion Batteries, *ACS Applied Materials & Interfaces* 9(9) (2017) 8107-8112.
- [194] C. Erinwingbovo, M.S. Palagonia, D. Brogioli, F. La Mantia, Intercalation into a Prussian Blue Derivative from Solutions Containing Two Species of Cations, *ChemPhysChem* 18(8) (2017) 917-925.
- [195] W. Chen, J. Tang, H.-J. Cheng, X.-H. Xia, A simple method for fabrication of sole composition nickel hexacyanoferrate modified electrode and its application, *Talanta* 80(2) (2009) 539-543.
- [196] L. Hu, J.-y. Mei, Q.-w. Chen, P. Zhang, N. Yan, Magnetically separable Prussian blue analogue Mn<sub>3</sub>[Co(CN)<sub>6</sub>]<sub>2</sub>·nH<sub>2</sub>O porous nanocubes as excellent absorbents for heavy metal ions, *Nanoscale* 3(10) (2011) 4270-4274.
- [197] S. Choi, B. Chang, S. Kim, J. Lee, J. Yoon, J.W. Choi, Battery Electrode Materials with Omnivalent Cation Storage for Fast and Charge - Efficient Ion Removal of Asymmetric Capacitive Deionization, *Advanced Functional Materials* 28(35) (2018) 1802665.

- [198] S. Vafakhah, L. Guo, D. Sriramulu, S. Huang, M. Saeedikhani, H.Y. Yang, Efficient Sodium Ion Intercalation into the Free-Standing Prussian blue/Graphene Aerogel Anode in Hybrid Capacitive Deionization System, *ACS Applied Materials & Interfaces* 11(6) (2019) 5989-5998.
- [199] D. Kundu, E. Talaie, V. Duffort, L.F. Nazar, The Emerging Chemistry of Sodium Ion Batteries for Electrochemical Energy Storage, *Angewandte Chemie International Edition* 54(11) (2015) 3431-3448.
- [200] J. Fang, S. Wang, Z. Li, H. Chen, L. Xia, L. Ding, H. Wang, Porous  $\text{Na}_3\text{V}_2(\text{PO}_4)_3/\text{C}$  nanoparticles enwrapped in three-dimensional graphene for high performance sodium-ion batteries, *Journal of Materials Chemistry A* 4(4) (2016) 1180-1185.
- [201] Z. Li, D.B. Ravnsbæk, K. Xiang, Y.-M. Chiang,  $\text{Na}_3\text{Ti}_2(\text{PO}_4)_3$  as a sodium-bearing anode for rechargeable aqueous sodium-ion batteries, *Electrochemistry Communications* 44 (2014) 12-15.
- [202] P. Senguttuvan, G. Rouse, M.E. Arroyo y de Dompablo, H. Vezin, J.M. Tarascon, M.R. Palacín, Low-Potential Sodium Insertion in a NASICON-Type Structure through the Ti(III)/Ti(II) Redox Couple, *Journal of the American Chemical Society* 135(10) (2013) 3897-3903.
- [203] Y. Huang, F. Chen, L. Guo, H.Y. Yang, Ultrahigh performance of a novel electrochemical deionization system based on a  $\text{NaTi}_2(\text{PO}_4)_3/\text{rGO}$  nanocomposite, *Journal of Materials Chemistry A* 5(34) (2017) 18157-18165.
- [204] D.-H. Nam, K.-S. Choi, Bismuth as a New Chloride-Storage Electrode Enabling the Construction of a Practical High Capacity Desalination Battery, *Journal of the American Chemical Society* 139(32) (2017) 11055-11063.
- [205] Y. Huang, F. Chen, L. Guo, J. Zhang, T. Chen, H.Y. Yang, Low energy consumption dual-ion electrochemical deionization system using  $\text{NaTi}_2(\text{PO}_4)_3$ -AgNPs electrodes, *Desalination* 451 (2018) 241-247.
- [206] J. Cao, Y. Wang, L. Wang, F. Yu, J. Ma,  $\text{Na}_3\text{V}_2(\text{PO}_4)_3/\text{C}$  as Faradaic Electrodes in Capacitive Deionization for High Performance Desalination, *Nano Letters* 19(2) (2019) 823-828.
- [207] W. Zhao, M. Ding, L. Guo, H.Y. Yang, Dual-Ion Electrochemical Deionization System with Binder-Free Aerogel Electrodes, *Small* 15(9) (2019) e1805505.
- [208] R.A. Huggins, *Advanced Batteries Materials Science Aspects*, Springer, Heidelberg, 2009.
- [209] F. Wang, R. Robert, N.A. Chernova, N. Pereira, F. Omenya, F. Badway, X. Hua, M. Ruotolo, R. Zhang, L. Wu, V. Volkov, D. Su, B. Key, M.S. Whittingham, C.P. Grey, G.G. Amatucci, Y. Zhu, J. Graetz, Conversion Reaction Mechanisms in Lithium Ion Batteries: Study of the Binary Metal Fluoride Electrodes, *Journal of the American Chemical Society* 133(46) (2011) 18828-18836.
- [210] H. Yoon, J. Lee, S. Kim, J. Yoon, Hybrid capacitive deionization with Ag coated carbon composite electrode, *Desalination* 422 (2017) 42-48.
- [211] Y.-C. Tsai, R.-a. Doong, Hierarchically ordered mesoporous carbons and silver nanoparticles as asymmetric electrodes for highly efficient capacitive deionization, *Desalination* 398 (2016) 171-179.
- [212] P.R. Bandaru, H. Yamada, R. Narayanan, M. Hofer, Charge transfer and storage in nanostructures, *Materials Science and Engineering R* 96 (2015) 1-69.
- [213] J. Lee, P. Srimuk, S. Fleischmann, X. Su, T.A. Hatton, V. Presser, Redox-electrolytes for non-flow electrochemical energy storage: A critical review and best practice, *Progress in Materials Science* 101 (2019) 46-89.
- [214] J. Lee, B. Krüner, A. Tolosa, S. Sathyamoorthi, D. Kim, S. Choudhury, K.-H. Seo, V. Presser, Tin/vanadium redox electrolyte for battery-like energy storage capacity combined with supercapacitor-like power handling, *Energy & Environmental Science* 9(11) (2016) 3392-3398.
- [215] J. Lee, P. Srimuk, S. Fleischmann, A. Ridder, M. Zeiger, V. Presser, Nanoconfinement of redox reactions enables rapid zinc iodide energy storage with high efficiency, *Journal of Materials Chemistry A* 5(24) (2017) 12520-12527.
- [216] J. Lee, P. Srimuk, S. Carpiër, J. Choi, R.L. Zornitta, C. Kim, M. Aslan, V. Presser, Confined redox reactions of iodide in carbon nanopores for fast and energy-efficient desalination of brackish water and seawater, *ChemSusChem* 11(19) (2018) 3460-3472.

- [217] J. Lee, P. Srimuk, R.L. Zornitta, M. Aslan, B.L. Mehdi, V. Presser, High electrochemical seawater desalination performance enabled by an iodide redox electrolyte paired with a sodium superionic conductor, *ACS Sustainable Chemistry & Engineering* 7(11) (2019) 10132-10142.
- [218] S. Fleischmann, D. Leistenschneider, V. Lemkova, B. Krüner, M. Zeiger, L. Borchardt, V. Presser, Tailored mesoporous carbon/vanadium pentoxide hybrid electrodes for high power pseudocapacitive lithium and sodium intercalation, *Chemistry of Materials* 29(20) (2017) 8653-8662.
- [219] L. Zou, G. Morris, D. Qi, Using activated carbon electrode in electrosorptive deionisation of brackish water, *Desalination* 225(1) (2008) 329-340.
- [220] M. Aslan, M. Zeiger, N. Jäckel, I. Grobelsek, D. Weingarth, V. Presser, Improved capacitive deionization performance of mixed hydrophobic/hydrophilic activated carbon electrodes, *Journal of Physics: Condensed Matter* 28(11) (2016) 114003.
- [221] P. Liu, T. Yan, L. Shi, H.S. Park, X. Chen, Z. Zhao, D. Zhang, Graphene-based materials for capacitive deionization, *Journal of Materials Chemistry A* 5(27) (2017) 13907-13943.
- [222] G. Wang, C. Pan, L. Wang, Q. Dong, C. Yu, Z. Zhao, J. Qiu, Activated carbon nanofiber webs made by electrospinning for capacitive deionization, *Electrochimica Acta* 69 (2012) 65-70.
- [223] Z. Chen, C. Song, X. Sun, H. Guo, G. Zhu, Kinetic and isotherm studies on the electrosorption of NaCl from aqueous solutions by activated carbon electrodes, *Desalination* 267(2) (2011) 239-243.
- [224] X. Quan, Z. Fu, L. Yuan, M. Zhong, R. Mi, X. Yang, Y. Yi, C. Wang, Capacitive deionization of NaCl solutions with ambient pressure dried carbon aerogel microsphere electrodes, *RSC Advances* 7(57) (2017) 35875-35882.
- [225] C. Tsouris, R. Mayes, J. Kiggans, K. Sharma, S. Yiacoumi, D. DePaoli, S. Dai, Mesoporous Carbon for Capacitive Deionization of Saline Water, *Environmental Science & Technology* 45(23) (2011) 10243-10249.
- [226] H. Li, L. Zou, L. Pan, Z. Sun, Novel Graphene-Like Electrodes for Capacitive Deionization, *Environmental Science & Technology* 44(22) (2010) 8692-8697.
- [227] H. Wang, D. Zhang, T. Yan, X. Wen, J. Zhang, L. Shi, Q. Zhong, Three-dimensional macroporous graphene architectures as high performance electrodes for capacitive deionization, *Journal of Materials Chemistry A* 1(38) (2013) 11778-11789.
- [228] Z.Y. Yang, L.J. Jin, G.Q. Lu, Q.Q. Xiao, Y.X. Zhang, L. Jing, X.X. Zhang, Y.M. Yan, K.N. Sun, Sponge - Templated Preparation of High Surface Area Graphene with Ultrahigh Capacitive Deionization Performance, *Advanced Functional Materials* 24(25) (2014) 3917-3925.
- [229] X. Xu, Z. Sun, D.H.C. Chua, L. Pan, Novel nitrogen doped graphene sponge with ultrahigh capacitive deionization performance, *Scientific Reports* 5 (2015) 11225.
- [230] H. Li, L. Pan, T. Lu, Y. Zhan, C. Nie, Z. Sun, A comparative study on electrosorptive behavior of carbon nanotubes and graphene for capacitive deionization, *Journal of Electroanalytical Chemistry* 653(1) (2011) 40-44.
- [231] N.-L. Liu, S. Dutta, R.R. Salunkhe, T. Ahamad, S.M. Alshehri, Y. Yamauchi, C.-H. Hou, K.C.W. Wu, ZIF-8 Derived, Nitrogen-Doped Porous Electrodes of Carbon Polyhedron Particles for High-Performance Electrosorption of Salt Ions, *Scientific Reports* 6 (2016) 28847.
- [232] X. Xu, M. Wang, Y. Liu, T. Lu, L. Pan, Metal-organic framework-engaged formation of a hierarchical hybrid with carbon nanotube inserted porous carbon polyhedra for highly efficient capacitive deionization, *Journal of Materials Chemistry A* 4(15) (2016) 5467-5473.
- [233] J. Zhang, J. Fang, J. Han, T. Yan, L. Shi, D. Zhang, N, P, S co-doped hollow carbon polyhedra derived from MOF-based core-shell nanocomposites for capacitive deionization, *Journal of Materials Chemistry A* 6(31) (2018) 15245-15252.

## Appendix: Tables

Sample name	Precursor	Activation method	SSA (m <sup>2</sup> /g)	Pore volume (cm <sup>3</sup> /g)	d <sub>50</sub> (nm)	Salt concentration (mM)	Cell voltage (V)	DC (mg/g)	Ref.
Activated carbon	Unknown	3 MKOH at 80 °C	BET: 889	0.64	4.2	8.5	2	n.a.	[219]
ACF/CB900	Polyacrylonitrile and carbon black	CO <sub>2</sub> , 700-900 °C	BET: 428	0.34	n.a.	1.5	1.6	9.1	[61]
ACs1	Coconut shell	Unknown	BET: 917	0.52	n.a.	0.85	1.6	2.5	[60]
ACs2	Coconut shell	Unknown	BET: 1,040	0.51	n.a.	0.85	1.6	3.2	[60]
ACph	Phenolic resin	Unknown	BET: 1,445	0.74	n.a.	0.85	1.6	3.3	[60]
ACk1	Petroleum coke	Unknown	BET: 1,828	1.0	n.a.	0.85	1.6	4	[60]
ACk2	Petroleum coke	Unknown	BET: 1,968	1.1	n.a.	0.85	1.6	4.2	[60]
ACk3	Petroleum coke	Unknown	BET: 2,030	1.1	n.a.	0.85	1.6	4.5	[60]
AC (YP80)	Unknown	Unknown	DFT: 1,786	1.1	1.3	5	1.2	10-11	[220]
PNC-CO <sub>2</sub>	Novolac	CO <sub>2</sub> , 1000 °C	DFT: 1,905	1.26	1.5	5	1.2	6-8	[221]
ACF900	Polyacrylonitrile	CO <sub>2</sub> , 900 °C	BET: 712	0.36	2.0	n.a.	1.6	4.6	[222]
AC	Unknown	Unknown	BET: 1,153	n.a.	2.0	1.7-34	1.2	10	[223]
ACC-507-15	Polymer resin	Unknown	DFT: 1,499	0.5	0.66	5	1.2	10	[38]
ACC-5092-15	Polymer resin	Unknown	DFT: 1,550	0.56	0.68	5	1.2	12	[38]
ACC-507-20	Polymer resin	Unknown	DFT: 1,940	0.89	0.96	5	1.2	14	[38]
ACC-5092-20	Polymer resin	Unknown	DFT: 1,876	0.81	0.89	5	1.2	14.5	[38]
ACC-507-20+	ACC-507-20	CO <sub>2</sub> , 950 °C	DFT: 2,191	1.22	1.26	5	1.2	17	[38]

Sample name	Precursor	Activation method	SSA (m <sup>2</sup> /g)	Pore volume (cm <sup>3</sup> /g)	d <sub>50</sub> (nm)	Salt concentration (mM)	Cell voltage (V)	DC (mg/g)	Ref.
CDC-1	TiC	Unknown	BET: 1,100	0.5	n.a.	5	1.2	11.7	[95]
CDC-2	TiC	Unknown	BET: 1,200	0.6	n.a.	5	1.2	8.8	[95]
TiC-CDC	TiC	Cl <sub>2</sub> , 800 °C	DFT: 1,376	0.52	0.67	5	1.2	10	[53]
Emulsion SiC-CDC	SiC	Cl <sub>2</sub> , 700 °C	DFT: 2,120	1.14	1.24	5	1.2	11.1	[53]
SiC-CDC	SiC	Cl <sub>2</sub> , 800 °C	DFT: 2,260	1.98	4	5	1.2	12.8	[53]
Carbon aerogel	Resorcinol/formaldehyde	CO <sub>2</sub> , 1050 °C	BET: 600-800	n.a.	n.a.	8.5	1.2	2.9	[101]
Carbon aerogel micro sphere	Resorcinol/formaldehyde	CO <sub>2</sub> , 850 °C	BET: 910	0.77	3.4	11	1.4	5.5	[224]
Ordered mesoporous carbon	P123/TEOS/Ni salt	unknown	BET: 1491	1.59	3.7	0.8	0.8	0.9	[82]
Self-assembled mesoporous carbon	Phloroglucinol/Pluronic F127	KOH at 850	BJH: 1700	0.54	n.a.	76	1.2	14.5	[225]
Reduced graphene oxide	Graphene oxide	unknown	BET: 14	n.a.	7.2	8.5	2.0	1.85	[108]
Graphene nano flakes	Graphene oxide	unknown	BET: 222	n.a.	n.a.	8.5	2.0	1.35	[226]

Sample name	Precursor	Activation method	SSA (m <sup>2</sup> /g)	Pore volume (cm <sup>3</sup> /g)	d <sub>50</sub> (nm)	Salt concentration (mM)	Cell voltage (V)	DC (mg/g)	Ref.
3-D macropore graphene	Graphene oxide/Polystyrene	unknown	BJH: 339	n.a.	295.9	n.a.	1.6	3.9	[227]
Sponge-templated graphene	Graphene oxide	unknown	BJH: 305	n.a.	3.5	n.a.	1.5	4.95	[228]
Nitrogen doped graphene	Graphene oxide	unknown	BJH: 526	3.13	n.a.	8.5	1.5	21	[229]
Holey graphene	Graphene oxide	H <sub>2</sub> O <sub>2</sub>	MB: 1261	n.a.	n.a.	85	1.2	26.8	[109]
Multi-walled carbon nanotubes	CH <sub>4</sub> /La <sub>2</sub> NiO <sub>4</sub>	unknown	BET: 129	0.38	n.a.	50	1.2	1.7	[110]
Single-walled carbon nanotube	unknown	unknown	BET: 453	n.a.	n.a.	1.6	2.0	0.12	[230]
Double-walled carbon nanotube	unknown	unknown	BET: 415	n.a.	n.a.	1.6	2.0	0.14	[230]
3-D ZIF-8 derived carbon	ZIF-8	unknown	BET: 798	0.5	n.a.	1	1.2	8.52	[231]
Porous carbon polyhedral/CNT	ZIF-8 growth on CNT	unknown	BET: 898	1.31	5.8	17	1.2	20	[232]
Halogen doped hollow carbon polyhedral	ZIF-8 growth on PZS	unknown	BET: 929	1.6	n.a.	8.5	1.2	22	[233]